Conference Proceedings of the Society for Experimental Mechanics Series

W. Carter Ralph · Raman Singh · Gyaneshwar Tandon
Piyush R. Thakre · Pablo Zavattieri · Yong Zhu *Editors*

Mechanics of Composite and Multi-functional Materials, Volume 7

Proceedings of the 2016 Annual Conference on Experimental and Applied Mechanics

Springer

Conference Proceedings of the Society for Experimental Mechanics Series

Series Editor

Kristin B. Zimmerman, Ph.D.
Society for Experimental Mechanics, Inc.
Bethel, CT, USA

More information about this series at http://www.springer.com/series/8922

W. Carter Ralph • Raman Singh • Gyaneshwar Tandon
Piyush R. Thakre • Pablo Zavattieri • Yong Zhu
Editors

Mechanics of Composite and Multi-functional Materials, Volume 7

Proceedings of the 2016 Annual Conference on Experimental and Applied Mechanics

Springer

Editors
W. Carter Ralph
Southern Research
Birmingham, AL, USA

Raman Singh
Oklahoma State University
Tulsa, OK, USA

Gyaneshwar Tandon
University of Dayton Research Institute
Dayton, OH, USA

Piyush R. Thakre
The Dow Chemical Company
Midland, MI, USA

Pablo Zavattieri
Purdue University
West Lafayette, IN, USA

Yong Zhu
North Carolina State University
Raleigh, NC, USA

ISSN 2191-5644 ISSN 2191-5652 (electronic)
Conference Proceedings of the Society for Experimental Mechanics Series
ISBN 978-3-319-41765-3 ISBN 978-3-319-41766-0 (eBook)
DOI 10.1007/978-3-319-41766-0

Library of Congress Control Number: 2016951852

Printed on acid-free paper

This Springer imprint is published by Springer Nature
The registered company is Springer International Publishing AG Switzerland

Preface

Mechanics of Composite and Multifunctional Materials represents one of ten volumes of technical papers presented at the 2016 SEM Annual Conference & Exposition on Experimental and Applied Mechanics organized by the Society for Experimental Mechanics and held in Orlando, FL, June 6–9, 2016. The complete Proceedings also includes volumes on *Dynamic Behavior of Materials; Challenges In Mechanics of Time-Dependent Materials; Advancement of Optical Methods in Experimental Mechanics; Experimental and Applied Mechanics; Micro and Nanomechanics; Mechanics of Biological Systems and Materials; Fracture, Fatigue, Failure and Damage Evolution; Residual Stress, Thermomechanics & Infrared Imaging, Hybrid Techniques and Inverse Problems; and Joining Technologies for Composites and Dissimilar Materials*.

This volume presents early findings from experimental and computational investigations in an important area within Composite, Hybrid, and Multifunctional Materials.

Composites are increasingly the material of choice for a wide range of applications from sporting equipment to aerospace vehicles. This increase has been fueled by increases in material options, greater understanding of material behaviors, novel design solutions, and improved manufacturing techniques. The broad range of uses and challenges requires a multidisciplinary approach between mechanical, chemical, and physical researchers to continue the rapid rate of advancement.

New materials are being developed from recycled source materials, leading to composites with unique properties and more sustainable sources. Existing materials are being used in new and critical applications, requiring deeper understanding of their behaviors and failure mechanisms on multiple scales. In addition, the unique properties of composites present many challenges in manufacturing and in joining them with other materials. Testing needs to be performed on these materials to characterize their properties and new test methods, and technologies must be developed in order to perform these studies and to evaluate parts during manufacture and use.

Birmingham, AL — W. Carter Ralph
Tulsa, OK — Raman Singh
Dayton, OH — Gyaneshwar Tandon
Midland, MI — Piyush R. Thakre
West Lafayette, IN — Pablo Zavattieri
Raleigh, NC — Yong Zhu

Contents

Chapter 1
Mechanical and Tribological Properties of Scrap Rubber Based Composites Reinforced with Glass Fiber, Al and TiO_2

L.M.P. Ferreira, I. Miskioglu, E. Bayraktar, and D. Katundi

Abstract Scrap rubber/Epoxy composites reinforced with Aluminium, Glass Fibre (GF) and TiO_2 particles were prepared and mechanical and tribological properties of these composites were investigated. Basically, these composites are aimed to use in automotive and aeronautics applications. A detail microstructure and matrix/reinforcement interface analyze was made by means of Scanning Electron Microscope (SEM) The wear performance of hard particles reinforced composites were evaluated. Quasi static and dynamic compression tests were carried out and damaged specimens were studied by SEM. The hardness (short test) values of the composites were reviewed related to the reinforcement elements, Glass Fibre-fiber and TiO_2 added in the matrix.

Keywords Recycling materials • Rubber/epoxy composites • Low-cost engineering • Wear resistance

1.1 Introduction

In engineering applications, there are many possibilities for usage of recycling of scrap rubber and most of them are used in automotive industry and domestic area, etc. Other main areas such as the aerospace and microelectronics industries have enourmous demand for high performance (ductile and high toughness) structural adhesive systems like epoxy and/or elastomers reinforced composites [1–9]. Today, additionally, the main component of these waste rubbers is styrene–butadiene rubber (SBR) and, in spite of the different uses for recycling it, the research for new applications is still a need because of the extremely high amount of waste rubber produced every year [5–8, 10–16].

Additionally, these materials are commonly used for long term applications at ambient or at moderately elevated temperature conditions. Conforming to these needs, elastomers (rubbers) should be used by simple processing with various materials in different conditions by addition of new alloying elements [7–11].

The present work reviews manufacturing facilities of scrap elastomers (SBR-rubbers) + epoxy resin composites with different proportions of particulate reinforcements. Main objective of this research was to determine the ductility and toughness of scrap elastomer (SBR rubber) matrix composites containing GF, TiO_2, B, etc. as basic reinforcements. Basically, these composites are aimed to use in automotive and aeronautics applications as bumpers and as internal furniture as ductile and tough and sound materials. Scanning electron microscopy (SEM) was used to study the microstructure and fracture surfaces of these composites.

L.M.P. Ferreira
Materials Science Department, UNICAMP—University of Campinas, Campinas, São Paulo, Brazil

School of Mechanical and Manufacturing Engineering, Supmeca-Paris, Paris, France

I. Miskioglu
Department of ME-EM, Michigan Technological University, Houghton, MI, USA

E. Bayraktar (✉)
School of Mechanical and Manufacturing Engineering, Supmeca-Paris, Paris, France
e-mail: bayraktar@supmeca.fr

D. Katundi
Materials Science Department, UNICAMP—University of Campinas, Campinas, São Paulo, Brazil

W.C. Ralph et al. (eds.), *Mechanics of Composite and Multi-functional Materials, Volume 7*,
Conference Proceedings of the Society for Experimental Mechanics Series, DOI 10.1007/978-3-319-41766-0_1

1.2 Experimental Conditions

At the beginning of the composite design, scrap rubber powders were chemically treated by toluene, acrylic acid and vinyltriethoxysilane (2 %) then dried in an oven to eliminate trace of the chemicals. After chemical treatment, 60 % of scrap rubber and 40 % of epoxy were mixed used as matrix. TiO_2 was chosen as main reinforcing element together; with aluminum, glass-fiber, as minor reinforcement elements, boron and Cu were also added in the matrix (Table 1.1).

Four basic compositions were prepared after here will be called RETIG-1, 2, 3 and 4.

After preliminary blending of the basic elements (scrap rubber + epoxy) of the composites, reinforcement elements were added in the structure and entire of the mixture have been milled for 2 h to obtain a homogenous compound. At the final stage, the specimens were manufactured by hot compacting (double uniaxial action) under a pressure of 70 MPa at the temperature of 180 °C. The dwell time for the compacting process was 15 min. All of the specimens (30 mm diameter, 6 mm thick) were cooled down slowly. The post curing was concluded under isothermal conditions at 80 °C for 48 h. Shore D hardness test was performed on the polished flat surfaces of the specimens according to ASTM D 2240 using durometer Shore test device, (type HBD-100-0). Shore D was also performed for the samples exposed to Ultra Violet (UV) conditions during exposing time: 2 months (every week during months) to evaluate resistance of these composites against degradation by UV.

Macroindentation test was carried out at room temperature using a stainless steel ball with 3 mm diameter. For this test, ten specimens for each composition were prepared with diameter of 40 mm. Thickness of the specimens was variable from 6 up to 10 mm. Maximum force (F_{max}) at failure and fracture surface were evaluated by SEM analysis.

Again, dynamic compression (drop weight tests) was carried out using a universal drop weight test device, Dynatup Model 8200 machine, with a total weight of 1.9 kg, punch height of 600 mm and with an impact velocity of around 3 m/s.

Wear resistance were evaluated by nanoindentation tests under two different normal loads (20 and 50 mN) applied over a linear track of 500 μm for 50 cycles. Wear is performed with a conical tip that has 90 degree apex angle. One cycle is defined as a pass and return of the tip over the track; the total distance for one test was 0.050 m. The speed of the tip during wear tests was 50 μm/s. A total of 10 wear test was performed for each sample.

1.3 Results and Discussion

General microstructure of the specimens was presented in the Fig. 1.1 for four compositions. All of the microstructures of the composites presented here are more and less homogenous. Chemical fusion bonding of rubber with epoxy powders were made perfectly thanks to the initial chemical treatment of the scrap rubber.

Certain area in the structure shows weakly agglomeration of the reinforcements. This type of agglomeration can be improved by milling in longer time.

Comparison of hardness (Shore D) results were compared in the Fig. 1.2 for four different compositions after exposing to ultraviolet (UV) during 7, 14, 21, 28 and 45 days. As seen from this graphics, there is no change significantly on the measured values for each period. In reality, all of the specimens have kept their original structure any decohesion between chemical bindings (not chemical deterioration). Addition of boron is always a positive effect on the hardness behaviour of these composites even if its percentage is very low. However, some small cracks appeared on the thin specimens at the end of long exposing time (around 2 months). This behaviour is worthy for the pieces aimed on the production of external parts used for example in the car industry (i.e. bumpers) [7–13]. All of the four composites gave the same level of hardness.

Table 1.1 General compositions of the rubber based composites (RETIG)

Compositions	Matrix Rubber 60 % Epoxy 40 %	Al	Glass-fiber	**TiO_2**	B	Cu
RETIG-1	B	7	7	**0**	1	1
RETIG-2	B	7	7	**7**	1	1
RETIG-3	B	7	7	**10**	1	1
RETIG-4	B	7	7	**15**	1	1

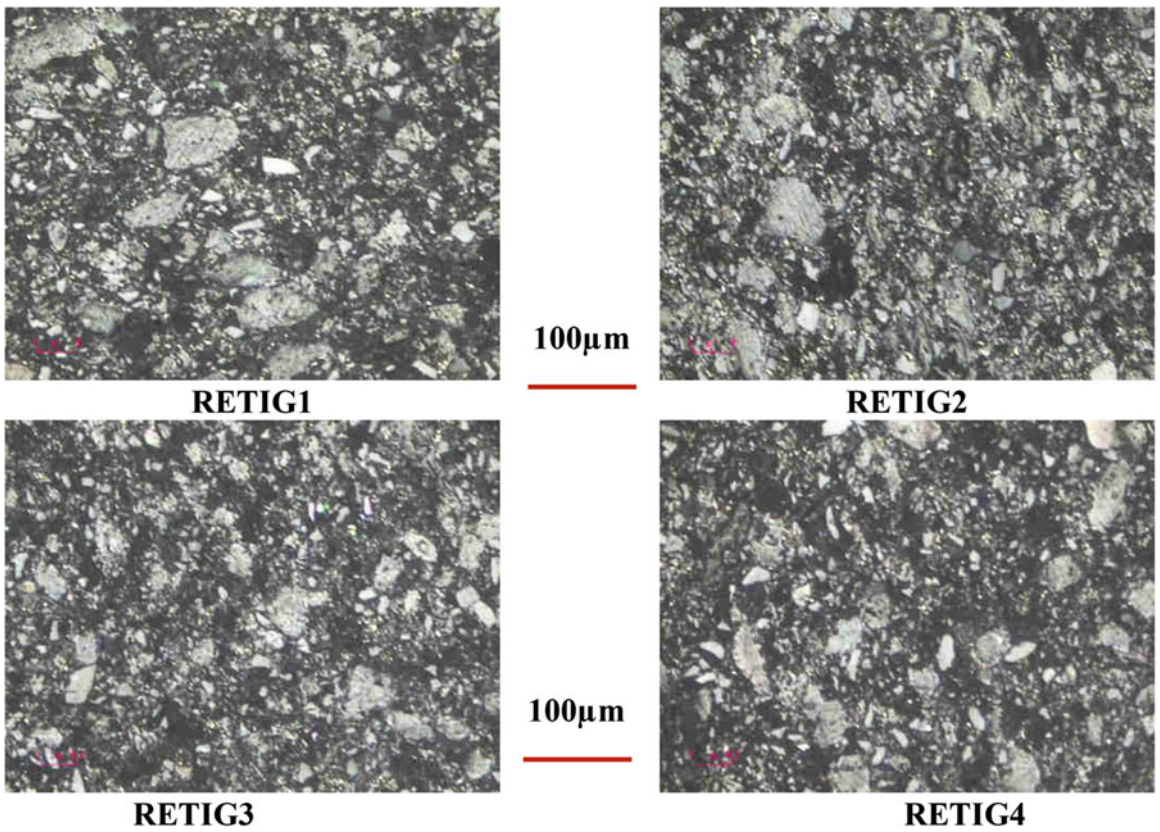

Fig. 1.1 General microstructures of the compositions in transversal section

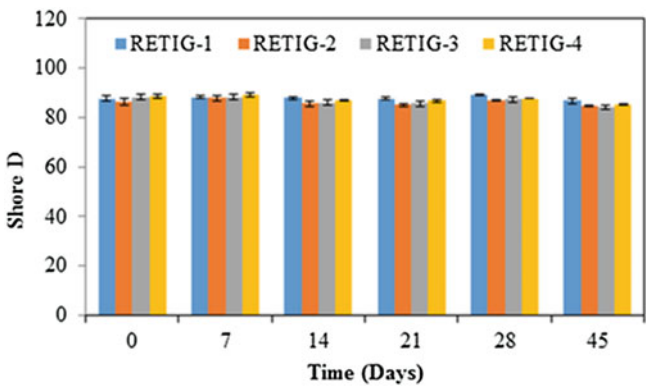

Fig. 1.2 Comparison of Shore D results for four different compositions after exposing to ultraviolet (UV) during 7, 14, 21, 28 and 45 days

Macroindentation test results were presented in the Fig. 1.3 presented with maximum forces at the failure. A considerable scattering on the values was found for each composite. This type of the damage analysis is very well-meaning related the structure of this type of composites. Damaged surfaces obtained from this test were evaluated by SEM (Fig. 1.4).

Fracture surfaces for all of the composites have shown very tough structure without internal defects (porosity, decohesion of the particulate reinforcements, etc.). Ductility is observed in many parts of the surfaces and increasing from the first composite (RETIG-1, TiO_2 value is 0 %) up to the fourth composite (RETIG-4, TiO_2 value is 15 %) these observations are justified with the results observed from Fig. 1.3.

Another damage analysis has been performed by dynamic compression and/or drop weight test as given the entire test conditions in the former section (experimental conditions) and absorbed energy were calculated for each composite via "Mat lab" from the data base (Fig. 1.5).

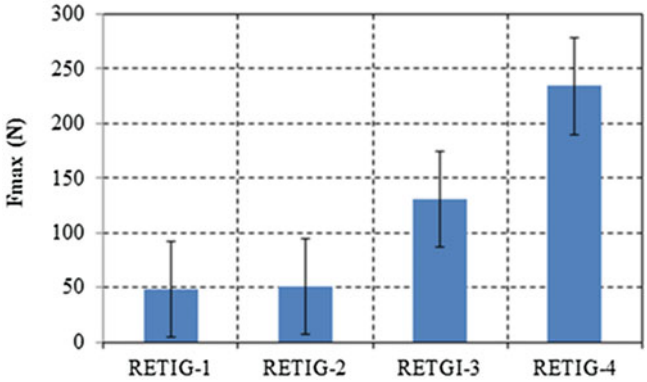

Fig. 1.3 Maximum values (F_{max}) obtained for each composition obtained by macroindentation test

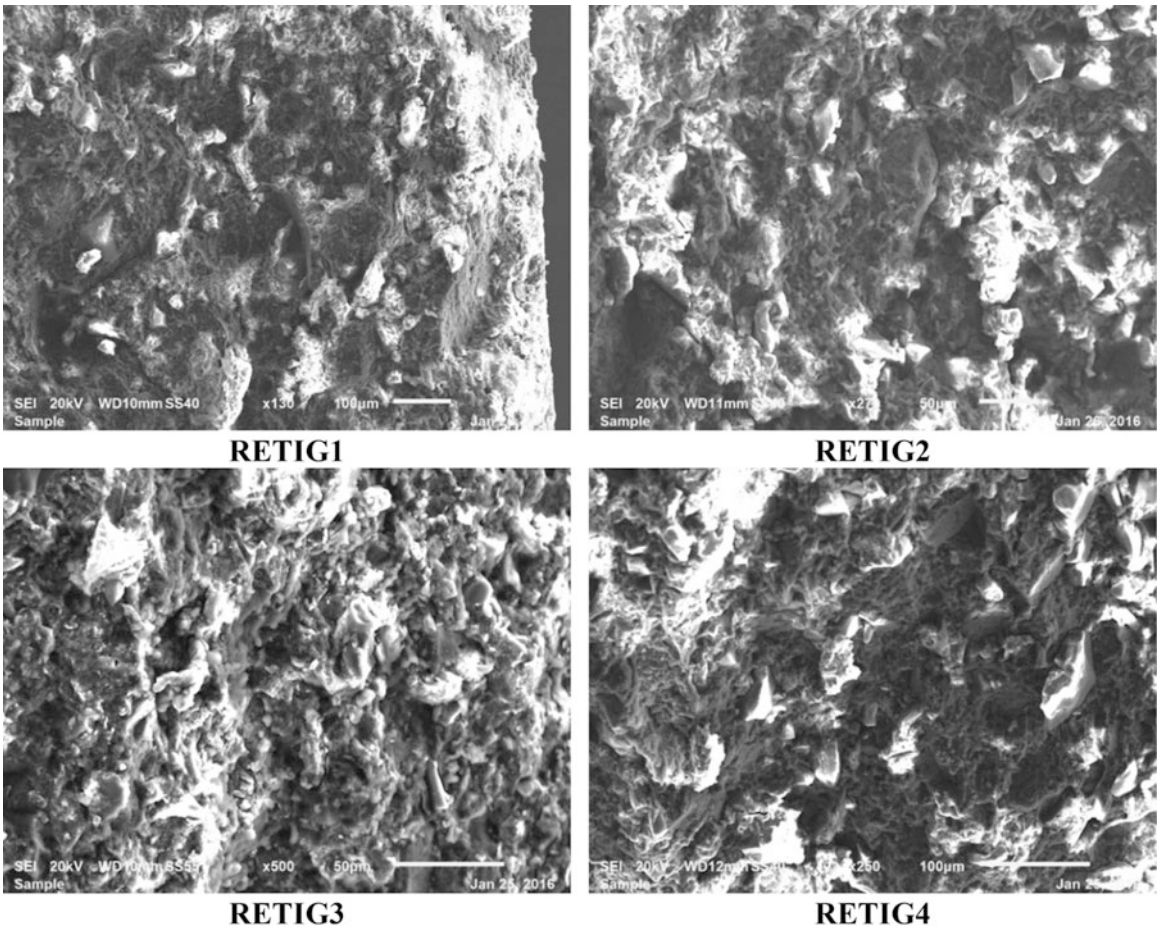

Fig. 1.4 Fracture surfaces of the samples for the compositions after macroindentation test presented in this work

Fracture surfaces of this test were evaluated in the Fig. 1.6. Again, the glass fibers added in the structure play a role like a bridge between the matrix and reinforcements. In fact, ductile behaviour of these composites is a combined effect of the main reinforcement of TiO_2 and glass fibers. Even if the slope is weakly incremental, addition of glass fibre together with TiO_2 improves ductility agreement with former papers published in [4, 14, 16]. All of these results obtained by dynamic compression tests confirmed well former results discussed in the Figs. 1.3 and 1.4.

Wear track deformation by using nanoindentation tests gave much more information on the micromechanical properties of the composites proposed in this work. Wear resistance were evaluated by nanoindentation tests under two different

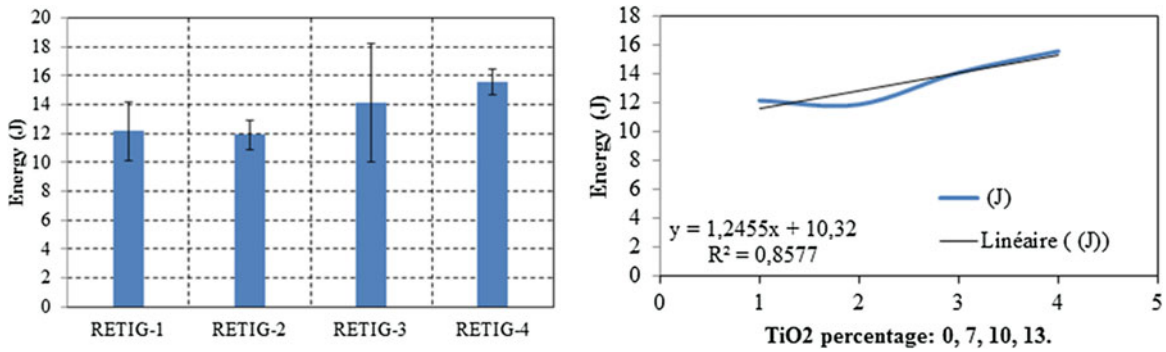

Fig. 1.5 Energy and liner tendency as a function of the particulate reinforcements found for four compositions obtained by dynamic compression test

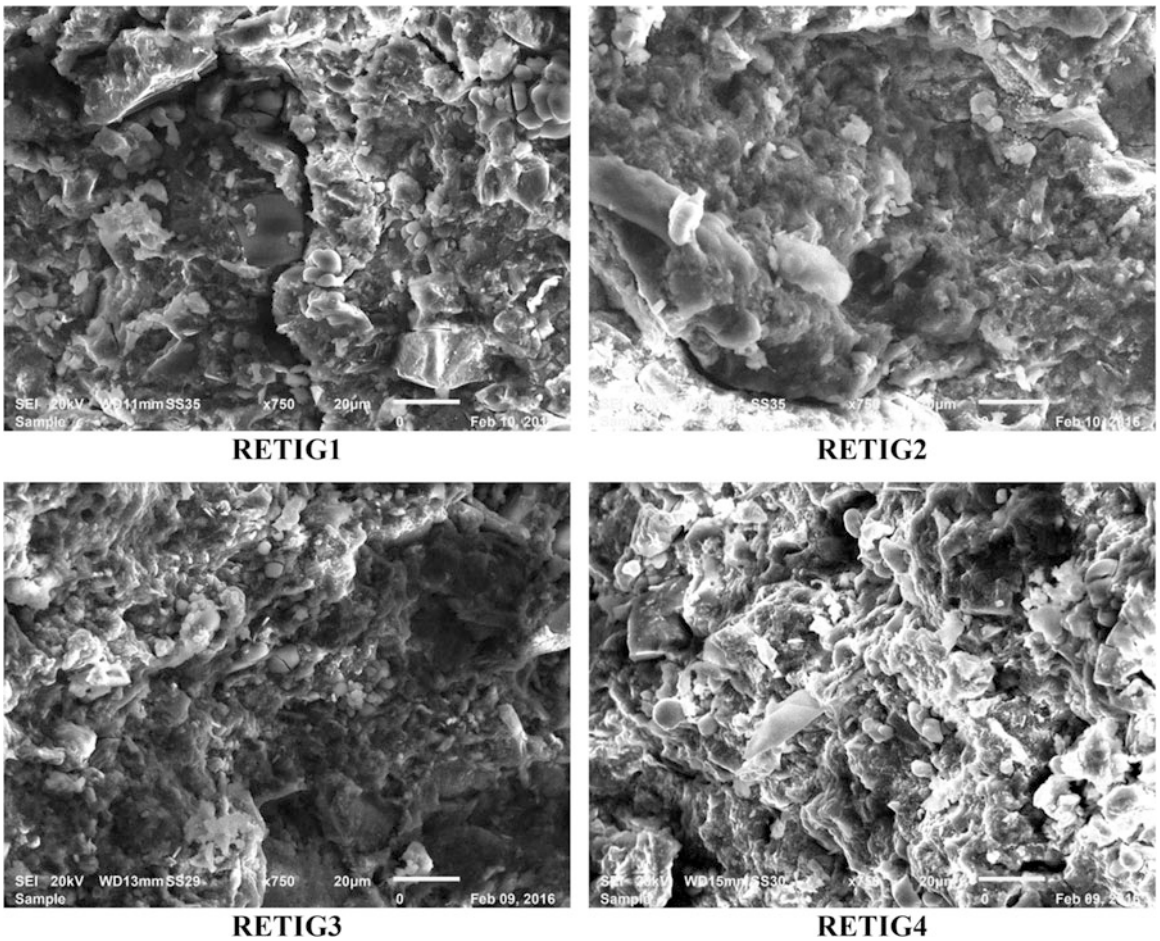

Fig. 1.6 Fracture surface of the samples taken from four compositions obtained by dynamic compression tests

normal loads (20 and 50 mN) applied over a linear track of 500 μm for 50 cycles. Wear damage was performed with a conical tip that has 90 degree apex angle. Figure 1.7 presents total results of this evaluation. Each column in the figure gives mean value of 10 wear tests. One may observed that the wear tracks are not perfectly straight, apparently the conical tip is not fracturing the hard particles (i.e. boron), and just going around them. Another reason can be attributed to the well adhesion of the particles that they are not pulled out of the matrix (without debonding, they keep their positions in the matrix). It means that very good adhesion related to very good interface passage between the particles and the matrix was observed on all of the compositions.

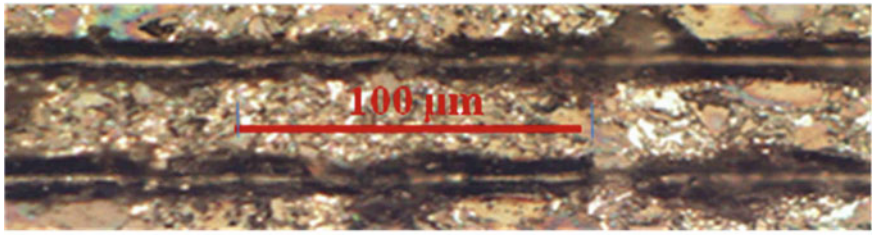

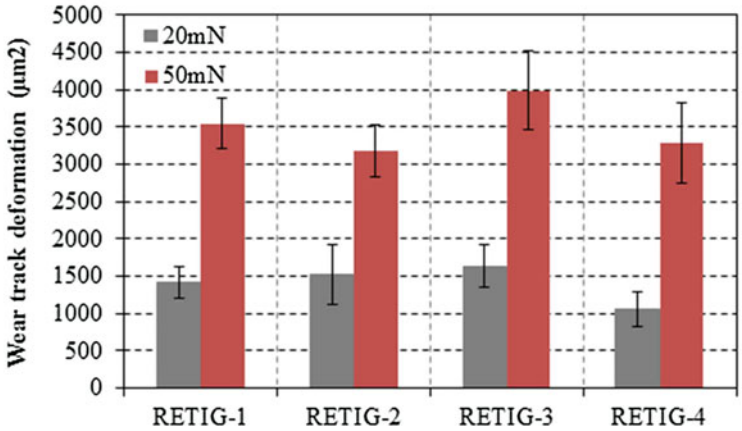

Fig. 1.7 Comparison of wear track deformation results tested on the four compositions under the loads of 20 and 50 mN

1.4 Conclusions

In the frame of the common research project going on, four new composites were designed from scrap elastomers (SBR) matrix powders essentially reinforced with GF, Al, TiO_2, B, B, and pretreated with fine epoxy resin. Chemical treatment of rubber powders with vinyltriethoxysilane gave very successful mixture with epoxy resin resulted by well adhesion bonding with particulate reinforcements. Experimental results obtained from the four different compositions were discussed in the present work. Mechanical and tribological properties of these composites were evaluated under different test conditions. Degradation of the specimens was too low after a long exposure 2 months against UV. Combined effect of TiO_2 and glass fibres gives a ductile behaviour in case of impact (drop weight) damage tests. Homogeneous distribution of the reinforcements in the matrix can be improved by longer milling time at the beginning of the process.

References

1. Zaimova, D., Bayraktar, E., Katundi, D., Dishovsky, N.: Elastomeric matrix composites: effect of processing conditions on the physical, mechanical and viscoelastic properties. J. Achiev. Mater. Manuf. Eng. **50**(2), 81–91 (2012)
2. Papadopoulos, A.M.: State of the art in thermal insulation materials and aims for future developments. Energy Build. **37**, 77–86 (2005)
3. Zaimova, D., Bayraktar, E., Miskioglu, I.: Manufacturing and damage analysis of epoxy resin-reinforced scrap rubber composites for aeronautical applications. In: Tandon, G.P., Tekalur, S.A., Ralph, C., Sottos, N.R., Blaiszik, B. (eds.) Experimental Mechanics of Composite, Hybrid, and Multifunctional Materials, vol. 6, pp. 65–76. Springer, New York (2014)
4. Zaimova, D., Bayraktar, E., Miskioglu, I., Katundi, D.: Manufacturing of new elastomeric composites: mechanical properties, chemical and physical analysis. In: Tandon, G. (ed.) Composite, Hybrid, and Multifunctional Materials, vol. 4, pp. 139–150. Springer, New York (2015)
5. Kaynak, C., Sipahi-Saglam, E., Akovali, G.: A fractographic study on toughening of epoxy resin using ground tyre rubber. Polymer **42**, 4393–4399 (2001)
6. Yesilata, B., Turgut, P.: A simple dynamic measurement technique for comparing thermal insulation performances of anisotropic building materials. Energy Build. **39**, 1027–1034 (2007)
7. Bessri, K., Montembault, F., Bayraktar, E., Bathias, C.: Understanding of mechanical behaviour and damage mechanism in elastomers using X-ray computed tomography at several scales. Int. J. Tomogr. Stat. **14**, 29–40 (2010)
8. Bayraktar, E., Antholovich, S., Bathias, C.: Multiscale observation of fatigue behaviour of elastomeric matrix and metal matrix composites by X-ray tomography. Int. J. Fatigue **28**, 1322–1333 (2006)
9. Bayraktar, E., Miskioglu, I., Zaimova, D.: Low-cost production of epoxy matrix composites reinforced with scarp rubber, boron, glass bubbles and alumina. In: Ralph, C., Silberstein, M., Thakre, P.R., Singh, R. (eds.) Mechanics of Composite and Multifunctional Materials, vol. 7, pp. 163–172. Springer, New York (2015)

10. Bayraktar, E., Isac, N., Bessri, K., Bathias, C.: Damage mechanisms in natural (NR) and synthetic rubber (SBR): nucleation, growth and instability of the cavitations. Int. J. Fatigue Fract. Struct. Mater. **31**(1), 1–13 (2008)
11. Pacheco-Torgal, F., Ding, Y., Jalali, S.: Properties and durability of concrete containing polymeric wastes (tyre rubber and polyethylene terephthalate bottles): an overview. Construct. Build Mater. **30**, 714–724 (2012)
12. Luong, R., Isac, N., Bayraktar, E.: Damage initiation mechanisms of rubber. J. Arch. Mater. Sci. Eng. **28**(1), 19–26 (2007)
13. Zaimova, D., Bayraktar, E., Miskioglu, I., Dishovsky, N.: Optimization and service life prediction of elastomeric based composites used in manufacturing engineering. In: Tandon, G.P., Tekalur, S.A., Ralph, C., Sottos, N.R., Blaiszik, B. (eds.) Experimental Mechanics of Composite, Hybrid, and Multifunctional Materials, vol. 6, pp. 157–166. Springer, New York (2014)
14. Zaimova, D., Bayraktar, E., Miskioglu, I.: Characteristics of elastomeric composites reinforced with carbon black and epoxy. In: Ralph, C., Silberstein, M., Thakre, P.R., Singh, R. (eds.) Mechanics of Composite and Multifunctional Materials, vol. 7, pp. 191–202. Springer, New York (2015)
15. Nacif, G.L., Panzera, T.H., Strecker, K., Christoforo, A.L., Paine, K.A.: Investigations on cementitious composites based on rubber particle waste additions. Mater. Res. **16**(2), 259–268 (2013)
16. Zaimova, D., Bayraktar, E., Miskioglu, I., Katundi, D.: Study of influence of SiC and Al2O3 as reinforcement elements in elastomeric matrix composites. In: Tandon, G. (ed.) Composite, Hybrid, and Multifunctional Materials, vol. 4, pp. 129–138. Springer, New York (2015)

Chapter 2
Investigating Hemp Concrete Mechanical Properties Variability Due to Hemp Particles

César Niyigena, Sofiane Amziane, and Alaa Chateauneuf

Abstract Nowadays, the use of bio-source and recyclable materials are experiencing considerable success. They include among others, the wood, the bamboos and the innovative concrete in which vegetable origin aggregates are used. In this latter case, several types of aggregates are used like sunflower, hemp particles, etc. Hemp particles are increasingly used thanks to its environmental asset, such as the positive CO_2 balance and its easiness lifecycle management. In construction applications, they have also other advantages like good thermal and acoustic insulation properties. However, its major drawback is related to low mechanical performance. The present work investigates the impact of hemp aggregates on the mechanical properties of hemp concrete. Nine different hemp particles from different origins (country, region, etc.) with varied properties (size, water absorption, etc.) are used in the same conditions (binder, specimen fabrication, etc.). Fabricated specimens were submitted to mechanical compression test, then compressive strength and moduli are analysed. The obtained results show high variability. Hemp particles impact results in a mechanical response with low, medium and high levels of deformation. A factor close to 10 is observed between the minimum and maximum compressive strengths. The performed analyses show that the interaction between the hemp particles and the binder is likely to contribute to the mechanical response. Hence, further investigations taking into account their chemical composition may allow to better understand this interaction impact.

Keywords Hemp particles • Mechanical properties • Variability • Hemp concrete

2.1 Introduction

The impact of hemp particles on hemp concrete have been treated in some differents studies [1–3]. In those studies, the used hemp are of limited varibility. Morever, the considered properties in those studies are mainly based on particle size and hemp origin [1, 2]. Within those studies, since many parametres are taken into account at the same time, such as the humidity, the binder type, the curing conditions [1], the specimen size [3], etc. then it comes difficult to assess the real impact of hemp particles due to parameter interferences.

This study focuses on the variability of hemp concrete due to hemp particles. The selection procedure for nine hemp particles has been developped in a previous study [4] in which many different characteristics are taken into account such as: the water absorption capacity, the hemp particles size including the specific area, the width and length of particles, its mass and also the density. Beyond the selection, the main aim is to predict the imapct of selected hemp particles on hemp concrete mechanical performance. The outcome of this research revealed three categories of hemp particles: category 1 is supposed to result in high mechanical performance, the category 2 in medium performance and the category 3 in low mechanical performance. In this study, it is recommended to conduct laboratory testing in order to validate the predicted results. The main aim of the herein study is to analyse the obtained results. As it will be presented so far, the obtained results are characterized by three main mechanical response behaviors with compressive strengths ranging from 0.11 to 1.10 MPa.

C. Niyigena (✉) • S. Amziane • A. Chateauneuf
Clermont Université, Institut Pascal, Polytech' Clermont-Ferrand, 63174 Aubière Cédex, France
e-mail: cesar.niyigena@polytech.univ-bpclermont.fr; cesar.niyigena@univ-bpclermont.fr; sofiane.amziane@univ-bpclermont.fr; alaa.chateauneuf@gmail.com

W.C. Ralph et al. (eds.), *Mechanics of Composite and Multi-functional Materials, Volume 7*,
Conference Proceedings of the Society for Experimental Mechanics Series, DOI 10.1007/978-3-319-41766-0_2

2.2 Materials and Method

Cylindrical specimens of 11 cm in diameter and 22 cm of height were used with nine hemp particles and the same commercial hydraulic binder. The characterization results for bulk density, water absorption and particle size distribution, are detailed in the previous study [4]. The protocols and methods related to manufacturing, mixing process are given in Sect. 2.2. The compressive strength tests have been made using Zwick machine under the same protocol detailed in [3], and the experimental results were collected for variability analysis. The considered mechanical properties are compressive strength and moduli (apparent and elastic); in this later case, the protocol for calculation is detailed in [3].

2.2.1 Hemp Shiv Characterization

The used hemp particles have been characterized in [4], where the main properties considered for their characterization are mainly: the bulk density, the particle size and the water absorption capacity. The main results are given in Table 2.1. Among these 13 characterized hemp particles, based on the recommandations in [4], only 9 have been selected to fabricate specimens of the herein study. They are underlined in the Table 2.1.

2.2.2 Preparation of Compression Specimen

2.2.2.1 Mix Proportioning

In construction, hemp concrete has several applications, such as: filling wooden frame walls, roofing insulation, etc. To each application, corresponds a given number of specifications such as minimum compressive strength and Young's modulus [5], which can be met by specific formulations. For the purpose of the herein study, it has been decided to use a unique formulation corresponding to wall application [5], as the objective is to analyze the effect of hemp particles rather than formulation itself, any other one may have been used. The quantities in kilograms per batch of 100 L are detailed in Table 2.2; these quantities are calculated by taking into account a mean bulk density for hemp particles equal to 120 kg/m^3.

Table 2.1 Characterization results of differents used hemp particles [4]

Nomenclature	Bulk density (kg/m^3)	Initial water absorption (%)	Final water absorption (%)	Particle mean area (mm^2)	Particle mass (mg)	Particle mean length (mm)	Particle mean width (mm)	Particle elongation	Particle equivalent diameter (mm)
C1	70.83	159.83	293.05	0.91	0.18	0.64	0.19	2.62	0.32
C2	89.74	194.15	379.22	4.89	0.84	3.4	1.04	3.47	1.79
C3	118.03	242.59	432.49	1.57	0.28	1.11	0.32	2.63	0.58
C4	118.27	233.79	358.33	1.94	0.35	1.45	0.44	2.6	0.76
C5	125.66	153.99	351.28	8.1	1.77	5.88	1.4	4.97	2.78
C6	128.2	181.39	358.53	5.31	1.14	4.2	1.27	3.95	2.23
C7	129.91	163.59	321.94	3.25	0.79	1.93	0.42	3.19	0.84
C8	143.55	152.73	328.04	6.96	1.51	5.59	1.23	5.52	2.53
C9	147.5	211.77	381.47	6.95	1.5	5.11	1.38	4.47	2.58
C10	130.65	112.23	307.31	0.82	0.15	0.77	0.25	2.28	0.41
C11	95.4	165.85	344.58	1.72	0.23	1.46	0.34	3.32	0.66
C12	103.93	162.89	338.7	1.18	0.18	1.02	0.28	2.77	0.5
C13	158.85	226.16	375.06	1.36	0.22	1.11	0.52	2.27	0.8
Minimum	70.83	112.23	293.05	0.82	0.15	0.64	0.19	2.27	0.32
Maximum	158.85	242.59	432.49	8.1	1.77	5.88	1.4	5.52	2.78
Mean	120.04	181.61	351.54	3.46	0.7	2.59	0.7	3.39	1.29
Standard deviation	24.72	37.97	36.38	2.64	0.6	1.96	0.48	1.05	0.94

Table 2.2 Tested formula for wall application per batch

Shiv (kg)	Binder (kg)	Water (kg)	Ratio water/binder	Ratio shiv/binder
11.4	23.75	28.5	1.2	0.48

Fig. 2.1 Different mixer type, (**a**) for classic concrete and (**b**) specific for hemp concrete

2.2.2.2 Mixing of Hemp Concrete

The hemp aggregates are put in the mixer with prewetting water equal to a quarter of total amount of necessary water. After few minutes of mixing, the second quarter of water is added with the binder. The mixing is maintained, then depending on the homogeneity of the mixture the third and last quarter of water are added and keep mixing until the perfect mixture homogeneity is obtained. For a good homogeneity, it is better to use a suitable mixer; a specific one for hemp concrete is shown in Fig. 2.1b below.

In fact, on one hand, the conventional mixer has primary and secondary blades both fixed on vertical rotating axes (Fig. 2.1a). Only the axis for primary blades is motorised and allow the mixing. During the mixing process the secondary blades are then entrained by the concrete mixture in opposite direction to primary blades. This rotation in both direction allows a good homogeneity for the mixture. In the case of hemp concrete, as it is lightweight, it becomes difficult to induce secondary blades rotation. In opposite, the hemp concrete is stuck inside the blades thus forming a kind of bloc which rotates in the mixer without mixing the constituants properly, which makes this conventinal mixer unsuitable for hemp concrete.

On the other hand, a mixer with horizonal rotating axis with blades ramified to it, is well adapted for hemp concrete (Fig. 2.1b). As all blades are connected to the horizontal motorized axis and their possibile rotation in both directions, it becomes more easier and practical to properly mix the hemp concrete.

2.2.2.3 Numbering of Fabricated Specimens

According to the recommmendations in [4] for a given hemp particles type, 3 or 9 specimens are fabricated for each type of the 9 selected hemp particles. To identify hemp particles: 9 specimens are considered for “primary test” (C2, C4, C5 and C12), and 3 specimens are considered for “secondary test” (C3, C6, C10, C11 and C13). Therefore the numbering of specimens is as following: P and S for primary and secondary tests, respectively, 11 stands for the size of specimen 11 $\times$ 22 cm, Ci repersents a given hemp particles type and n is the number of the specimen. For example, “P-C2-11-3” stands for primary test from hemp particles C2, size 11 $\times$ 22 cm specimen number 3.

2.3 Results and Discussion

2.3.1 Mechanical Response

Three main hemp concrete mechanical behaviors have been observed, they differ in their level of strain. On one hand, a law strain around 3 % has been observed (Fig. 2.2); in this case, the maximum compressive stress is observed during the third loading phase before the end of test. On the other hand, a high level deformation is observed and may reach in some cases values beyond 20 % (Fig. 2.5), this last value correponds to the maximum level choosen for the compressive test protocol [3]. Another intermediate behavior is also observed and is characterized by moderate levels with maximum strength values around 5 % of strain (Fig. 2.3).

The low level of strain is observed in the case of hemp concrete with small particle size with 1.36 mm^2 for particle mean area and a high mean specific area equal to 18,822 mm^2/3 g, C13. In fact, for this hemp type, the particules prevent the good

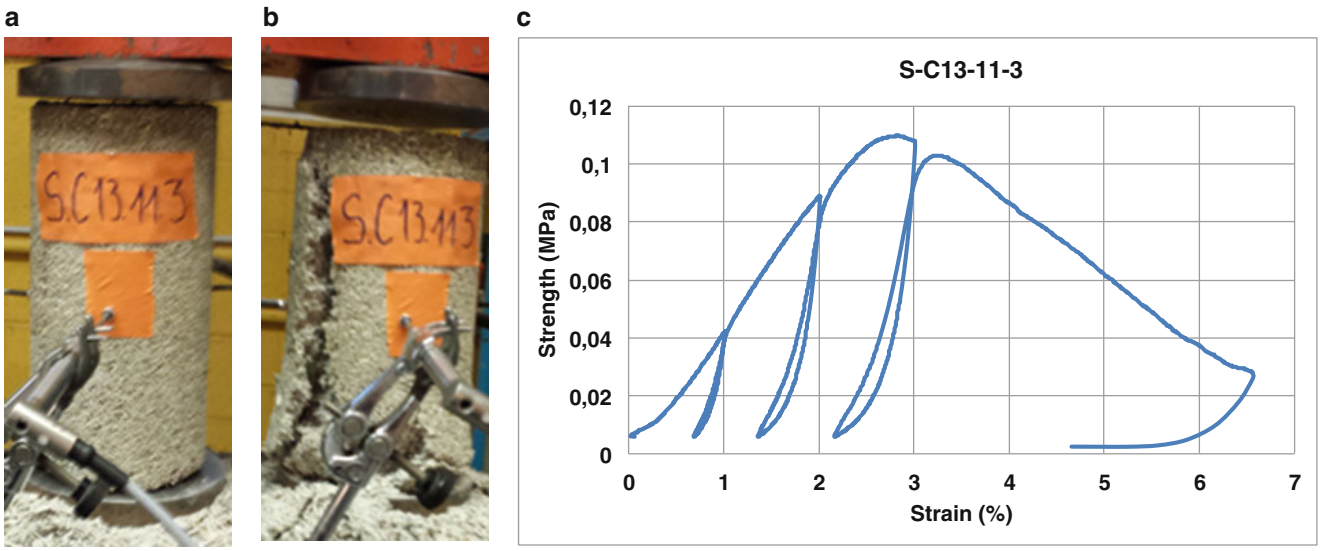

Fig. 2.2 Mechanical response: low deformation, specimen before (**a**) and after (**b**) test with strength-strain curve (**c**)

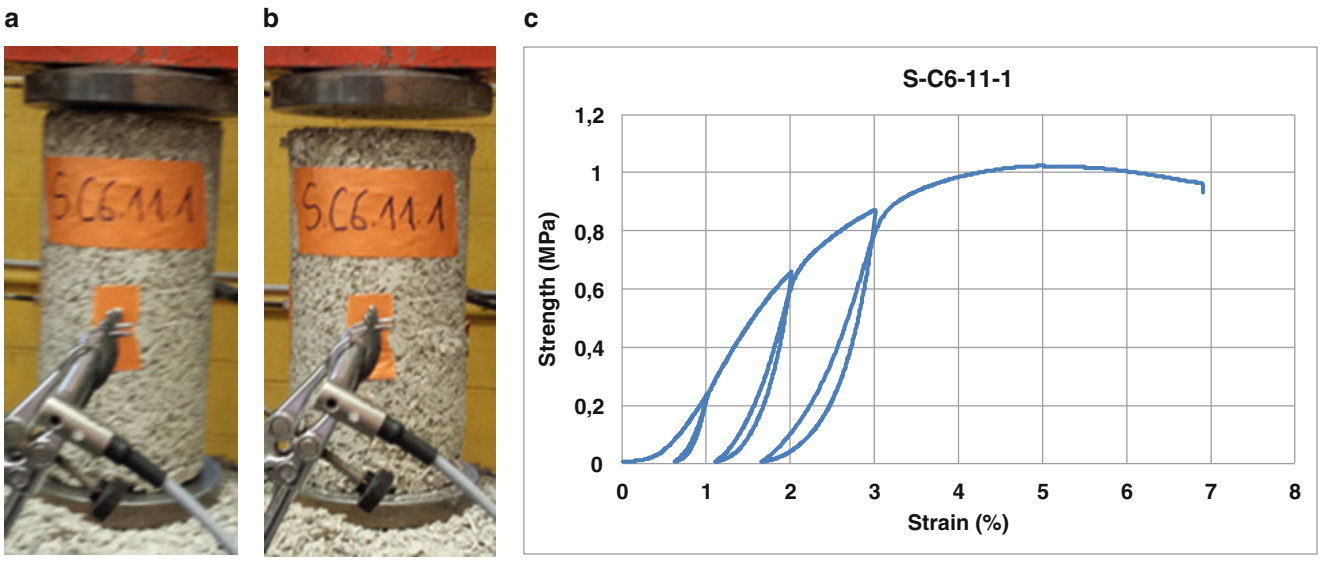

Fig. 2.3 Mechanical response with medium deformation, specimen before (**a**) and after (**b**) test with strength-strain curve (**c**)

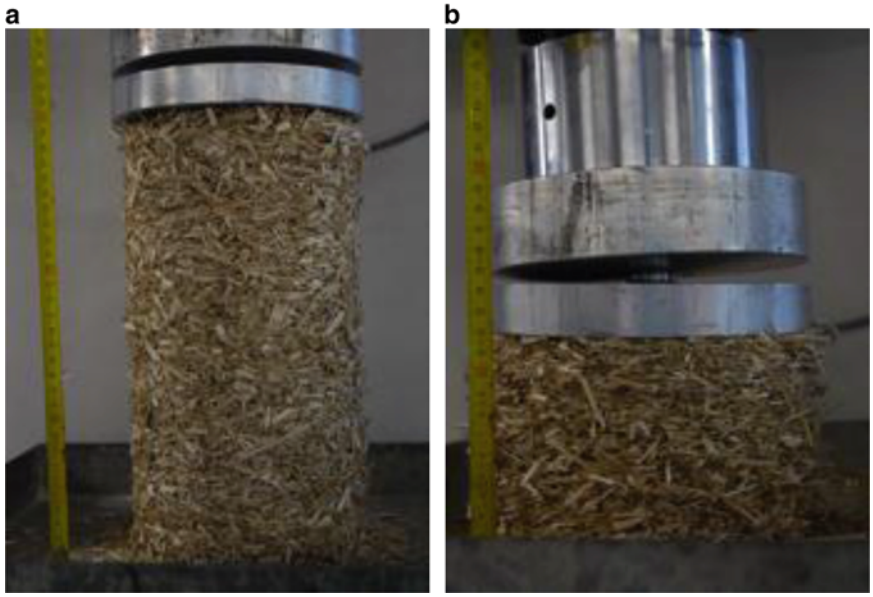

Fig. 2.4 Hemp particles mechanical response, before (**a**) and after (**b**) compression test [8]

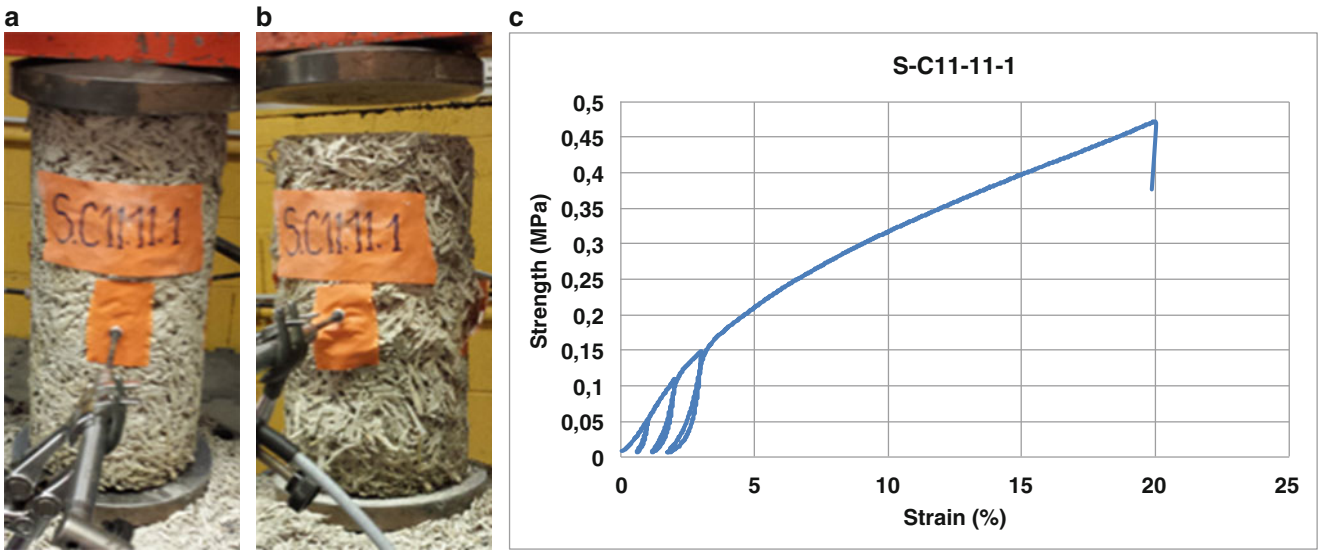

Fig. 2.5 Mechanical response with low deformation, specimen before (**a**) and after (**b**) test with strength-strain curve (**c**)

connection in bonding matrix, thus weakening the whole material (specimen) and finally resulting in low strength. The failure mode is characterized by the total squashing of the specimen in vertical direction as shown in Fig. 2.2b.

In the case of high strain, due to compressive loading, hemp particles rearranged themselves as a stack of layers. In fact, this rearrangement is facilitated by the particle shape, thanks to its high elongation (3.32), resulting is a good overlapping of the particles against each others. Furthermore, it is possible that the high water absorption capacity for this type of hemp (340 % after 48 h) amplifies the level of deformation. As it has been proved [6], there is a competition of water absorption between the binder and the hemp particles. Since this hemp shiv has a high water absorption capacity, the water required for the setting and the hardening process of the binder is absorbed by hemp particles; probably the false setting phenomenon occurs. Then the binder does no longer fulfill its mechanical role, and load is transmitted to hemp particles. As a result, the observed mechanical behavior is similar to that of hemp particles under compression as illustrated in Figs. 2.4b and 2.5b for hemp particles and concrete, respectively. It should be noted that these findings are not necessarily generalizable for all the analysed nine hemp particles types. This let us assume that the chemical interaction between the binder and the hemp

particles used can also contribute to the observed mechanical response. The study of the chemical composition and molecules in plant cell surface may help to better understand the impact of the chemical interaction hemp particles/binder on the setting and hardening process of hemp concrete material. In previous studies [6, 7], it was shown that these chemical compounds "extracts" may affect significantly the setting process for hydraulic binders.

2.3.2 *Hemp Particles Impact on the Mechanical Performance*

The previous section illustrates how the mechanical response differs depending on hemp particles. At this stage, only the main behaviors have been discussed. This section, focus on the obtained results for all the nine hemp particles. The main considered properties are the compressive strength and the modulus.

2.3.2.1 Compression Strength

The compressive strength results show considerable dispersion at two levels. On one hand, we observe the variability related to used hemp particles with a factor equal to 10 between the minimum and maximum strengths, particularly between hemp particles C13 and C6, respectively (Fig. 2.6). On the other hand, we also observed the significant dispersion within a given type of hemp particle. For example, we have a minimum of 0.47 MPa and 0.65 MPa with a maximum of 0.65 MPa and 0.99 MPa for hemp C2 and C5, respectively (Fig. 2.6). This intrinsic variability of the material shows to what extend the number of samples considered may impact the result, hence it is necessary to take enough samples for statistical significance of results. To our knowledge, there is no specific study for this issue in the case of hemp concrete. In the herein study 9 and 3 samples were used for primary and secondary tests, respectively. The obtained results are presented in the current section, the analysis is proposed later in Sect. 3.3.

2.3.2.2 Elastic Modulus

The observed dispersions for compressive strength are also confirmed in the case of the elastic modulus, although we observe low dispersion for C2 hemp concrete. These results highlight also the sensitivity of the variability with respect to the relevant property and of course its measurement method. In [3], the low variability were observed for density, while compressive strength and elastic modulus had high variabilities.

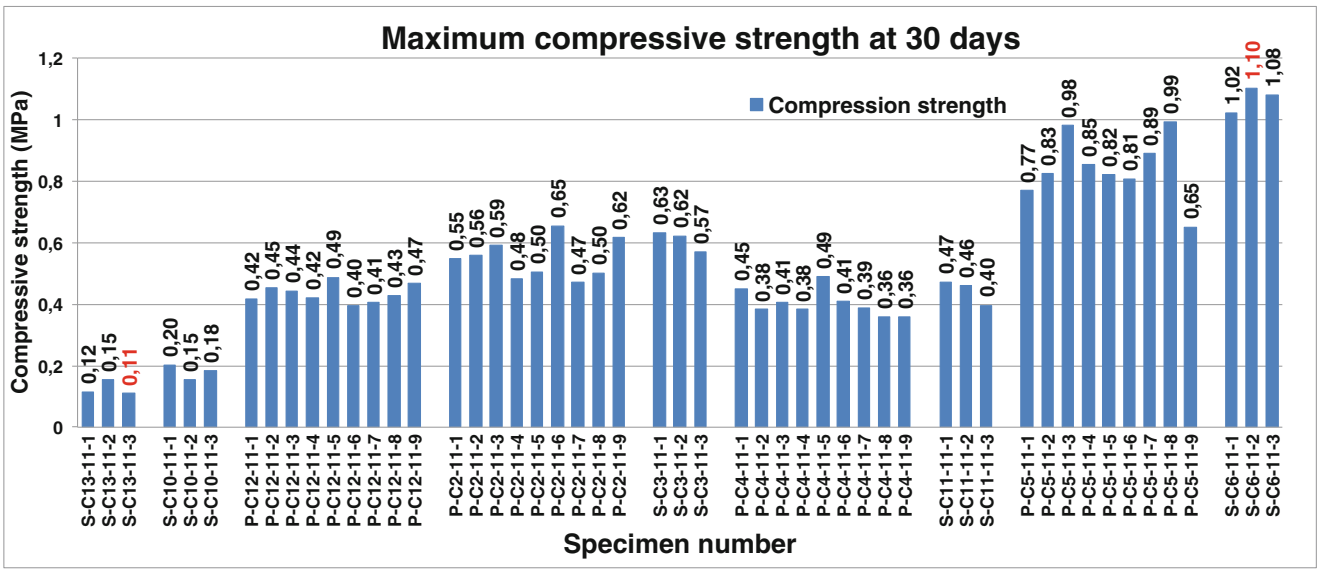

Fig. 2.6 Compressive strength results for differents hemp concrete

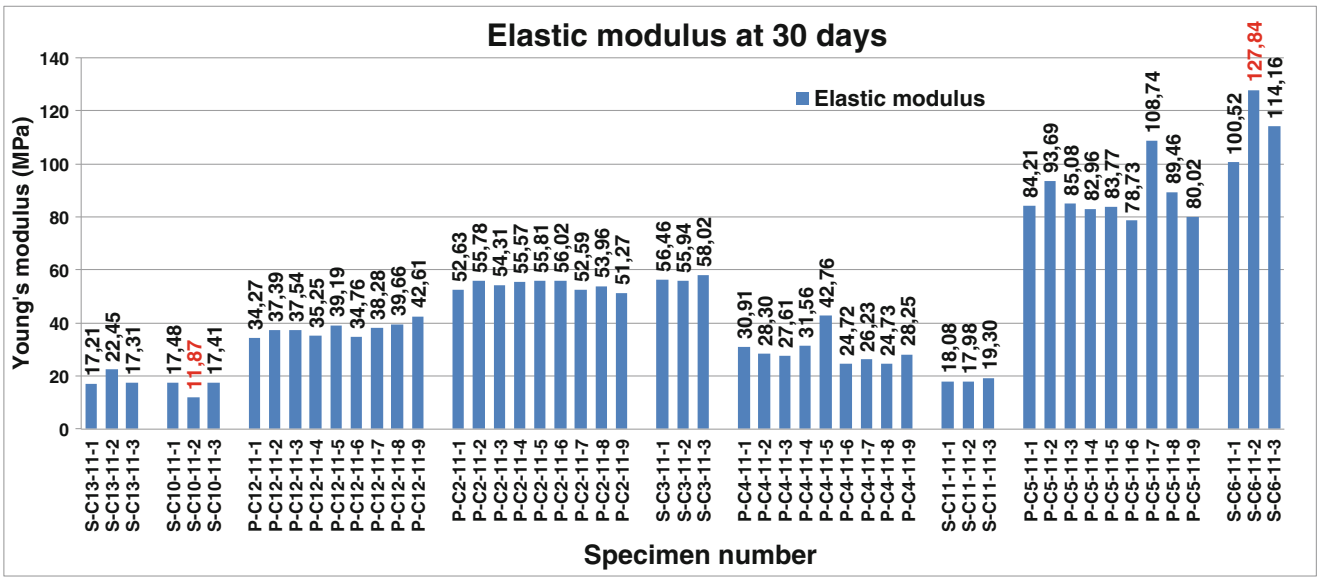

Fig. 2.7 Elastic modulus results for different hemp particles

Table 2.3 Summary of results at 30 days

	Specimen number	Maximum strength	Strength at 5 % of strain	Apparent modulus	Elastic modulus
Mean value	P-C2-11	0.55	0.51	29.49	54.22
	P-C4-11	0.40	0.34	15.00	29.45
	P-C5-11	0.84	0.79	46.77	87.41
	P-C12-11	0.44	0.40	16.39	37.66
	S-C3-11	0.61	0.60	33.49	56.81
	S-C6-11	1.07	1.05	61.00	114.17
	S-C10-11	0.18	0.16	4.89	15.59
	S-C11-11	0.44	0.22	6.17	18.45
	S-C13-11	0.13	0.05	5.68	18.99
Standard deviation	P-C2-11	0.06	0.03	6.06	1.73
	P-C4-11	0.04	0.04	4.74	5.53
	P-C5-11	0.11	0.08	13.17	9.20
	P-C12-11	0.03	0.02	1.43	2.67
	S-C3-11	0.03	0.03	3.38	1.08
	S-C6-11	0.04	0.03	15.53	13.66
	S-C10-11	0.03	0.02	1.72	3.22
	S-C11-11	0.04	0.01	0.15	0.74
	S-C13-11	0.02	0.04	1.42	3.00
Coefficient of variation	P-C2-11	11.59	6.15	20.56	3.19
	P-C4-11	10.53	12.19	31.63	18.78
	P-C5-11	12.48	10.47	28.17	10.53
	P-C12-11	6.90	4.92	8.75	7.09
	S-C3-11	5.62	4.66	10.10	1.91
	S-C6-11	3.82	2.59	25.46	11.96
	S-C10-11	14.18	11.77	35.26	20.64
	S-C11-11	9.21	2.80	2.42	3.99
	S-C13-11	19.05	86.62	24.92	15.79

The detailed results for all samples (3 for secondary test and 9 for primary test) allowed us to show the variability within a given hemp particles type as illustrated in Figs. 2.6 and 2.7 for both compressive strength and moduli, respectively. For a detailed analysis, the Tables 2.3 and 2.4 give the mean values of all specimens for each hemp particles, the standard deviation and the coefficient of variation. These results are given at 30 days and 180 days, respectively.

Table 2.4 Summary of results at 180 days

	Specimen number	Maximum strength	Strength at 5 % of strain	Apparent modulus	Elastic modulus
Mean value	P-C2-11	0.57	0.55	29.09	58.84
	P-C4-11	0.42	0.31	15.09	33.12
	P-C5-11	0.87	0.82	40.42	88.97
	P-C12-11	0.42	0.36	14.12	35.22
	S-C3-11	0.66	0.61	30.99	55.98
	S-C6-11	1.07	1.02	42.79	103.44
	S-C10-11	0.25	0.18	7.68	20.94
	S-C11-11	0.40	0.21	10.91	20.08
	S-C13-11	0.13	0.10	12.27	20.72
Standard deviation	P-C2-11	0.04	0.03	4.36	6.72
	P-C4-11	0.07	0.08	2.95	5.95
	P-C5-11	0.06	0.06	12.09	11.90
	P-C12-11	0.07	0.05	1.21	4.84
	S-C3-11	0.05	0.04	3.42	4.54
	S-C6-11	0.14	0.15	14.94	22.93
	S-C10-11	0.00	0.00	1.15	0.78
	S-C11-11	0.05	0.01	2.15	1.78
	S-C13-11	0.02	0.05	4.76	4.70
Coefficient of variation	P-C2-11	7.68	5.08	14.99	11.42
	P-C4-11	17.16	24.32	19.52	17.97
	P-C5-11	6.72	7.90	29.90	13.38
	P-C12-11	15.68	13.82	8.58	13.75
	S-C3-11	7.15	6.69	11.05	8.11
	S-C6-11	13.45	14.18	34.92	22.17
	S-C10-11	1.96	0.91	15.00	3.72
	S-C11-11	13.40	3.92	19.67	8.85
	S-C13-11	15.41	50.71	38.77	22.67

2.3.3 Variability of Result with Respect to Used Hemp Particles

2.3.3.1 Compression Strength

Due to the different levels of deformability, especially in the case of high deformation, it is not relevant to assess the compression strength by considering only its maximum value. Because, as discussed early, some types of hemp may be compressed up to high level of deformation, almost infinitely, without breaking (Fig. 2.5c). Therefore, the deformation level reached does not necessarily correspond to the allowable deformation in practice. For this matter, it is important to analyse the compressive strength by considering the associated strain. As result, in the herein study we discuss not only the maximum compressive strength but also the compressive strength at 5 % of strain.

According to the obtained results, significant differences are observed with respect to hemp particles type used with a factor equal to 8.2 between the lowest mean value of maximum strength and the highest one, this is the case for hemp C13 and C6, respectively. The obtained coefficient of variation in the case of maximum compressive strength and at 5 % of deformation varies from 1 to 25 % for all criteria (type of hemp, date of test, etc.). This shows to what extend hemp particles induce variability in results.

However, in some cases, we observe a relatively high coefficient of variation as for C13 with 86.62 % at 30 days, or 50.71 % at 180 days for the same hemp particles. Note that these dispersions are observed for the compressive strength at 5 % of strain. Indeed, since C13 has low levels of deformation as shown in Fig. 2.2, it follows that the compressive strength values obtained at 5 % are too dispersed.

2.3.3.2 Modulus

Since it is known that there is a relationship between compressive strength and modulus, one can expected to have the same variability for modulus results as for compressive strength ones. However, the analysis in the case of modulus indicates that these dispersions are not necessarily the same.

The mean values obtained vary from 4.89 MPa to 61.00 MPa and 15.59 MPa to 114.17 MPa for the apparent and elastic modulus, respectively. Such dispersions are obtained by considering different types of hemp particles and both testing dates. Furthermore, in the same configurations, the observed coefficient of variation varies from 2.4 % to 38.8 % and 1.9 % to 22.7 % for the apparent and elastic modulus, respectively.

2.4 Conclusion

In this study, the problem for suitable hemp concrete mixer has been discussed and it has been highlighted that the use of classic mixer result in non-homogeneous mixture. The results of the study show that hemp particles may impact considerably the hemp concrete mechanical properties. By changing only hemp particles, a factor of 10 has been observed between minimum and maximum values for compressive strength. It has also been highlighted the three main mechanical response behaviors for hemp concrete material characterized by the low, medium and high level of strain. These observed behaviors are related to hemp particles shape and their water absorption capacity. It has also been highlighted that probably the hemp particles/binder chemical interaction may also impact the observed behavior, thus, it is necessary to undertake more investigations, which may focus on the chemical composition and molecules in plant cell surface as they may affect significantly the setting and hardening process for the binder.

Acknowledgments The authors would like to thank the Auvergne Region Council for their financial support of this work.

References

1. Arnaud, L., Gourlay, E.: Experimental study of parameters influencing mechanical properties of hemp concretes. Constr. Build. Mater. **28**(1), 50–56 (2012)
2. Stevulova, N., Kidalova, L., Cigasova, J., Junak, J., Sicakova, A., Terpakova, E.: Lightweight composites containing hemp hurds. Procedia Eng. **65**, 69–74 (2013)
3. Niyigena, C., Amziane, S., Chateauneuf, A., Arnaud, L., Laetitia, B., Collet, F., Escadeillas, G., Lanos, C., Lawrence, M., Magniont, C.: RRT3: statistical analysis of hemp concrete mechanical properties variability. In: First International Conference on Bio-Based Building Materials, Clermont-Ferrand, France (2015)
4. Niyigena, C., Amziane, S., Chateauneuf, A.: Etude de la variabilité des caractéristiques de granulats de chanvre. Rencontres Universitaires de Génie Civil, Bayonne, France (2015)
5. FFB: Construire en chanvre: Règles professionnelles d'exécution. Fédération Française du Bâtiment. Collection recherche développement métier (2009)
6. Diquélou, Y., Gourlay, E., Arnaud, L., Kurek, B.: The impact of hemp shiv on cement setting and hardening: the influence of extracts and study of the interface. In: Proceeding of the International Inorganic-Bonded Fiber Composites Conference, Acton, Australia. pp. 41–50 (2012)
7. Diquelou, Y.: Interactions entre les granulats de chanvre et les liants à base de ciment et de chaux: Mécanismes de la prise et propriétés des interfaces formées dans les agrobétons. Reims (2013)
8. Gourlay, E.: Caractérisation expérimentale des propriétés mécaniques et hygrothermiques du béton de chanvre. Détermination de l'impact des matières premières et de la méthode de mise en oeuvre. ENTPE (2014)

Chapter 3
Recycling of Scrap Aluminium (AA7075) Chips for Low Cost Composites

L.F.P. Ferreira, E. Bayraktar, M.H. Robert, and I. Miskioglu

Abstract Aluminium chips are generally recycled via foundry methods. In this research, the use of a combined method through powder metallurgy techniques (Sintering + thixoforging) has been proposed as a more effective low cost and alternative processing for recycling of scrap aluminium chips (AA7075). Aluminium chips, TiO_2 and spherical ceramic powder are mixed and pre-milled as matrix and reinforcement, respectively, and other additives (Pure Boron, BN and TiC and Graphite) in different amounts, are used as well to improve the properties of the final composition. The effects of the different additives in the microstructure, mechanical properties essentially impact shock values are compared. Fracture surfaces were analyzed by scanning electron microscopy (SEM) for detailed damage evaluation.

Keywords Recycle of AA7075 • Powder metallurgy • Thixoforging • Impact resistance • Damage analysis

3.1 Introduction

Many types of the well-known composites in engineering applications (aeronautics, automotive, etc.) are based on aluminium based composites (AMMCs) that are used as matrix and particulate reinforcements such as alumina, SiC, boron and/or intermetallics and other ceramic oxide, etc. [1–7]. Different processing methods have been developed for these composites, among which liquid state and solid state sintering as powders (the mixture of matrix and the reinforcements) and also the semi-solid condition (thixoforming mainly for graded materials), etc. are well known. Usually, supplementary application of pressure is necessary to decrease internal (structural) defects and improve homogeneity of the final product. Advantages of using SSM technology to produce MMCs must be yet fully exploited; one possible approach is the direct thixoforming of an assembly of matrix and reinforcing particles, to produce near net shape products. A particular kind of MMC, the, can be successfully produced by thixoforming [2, 5–7].

On the other hand, powder metallurgy is a complex and expensive way for processing of these composites (longer mixing + milling step and longer sintering time, higher temperatures, etc.) [3–8]. For this reason, it is necessary to use another method, in an economic and safe way for processing MMCs in engineering applications. For example, recycling of metallic wastes is an important subject today mainly in large scale manufacturing that yield very large amount of scarp (i.e. scrap aluminium chips coming from machining processes). This case is much more important in the aeronautical industry, where very large quantities of scrap aluminium chips are produced in machining of aeronautical parts [7–13].

The present work proposes a new and a simple idea for the development of low cost engineering manufacturing of AMMCs using scrap aluminium chips, via a combined method of powder metallurgy (pre-sintering) and thixoforming of reinforced with particulates such as metallic and ceramic oxides. Mechanical behaviour—impact damage—analyses have been carried out. Microstructural evaluation and fracture surfaces as well as interface analyses by Scanning Electron Microscopy (SEM) were studied in detail.

L.F.P. Ferreira
Materials Science Department, UNICAMP—University of Campinas, Campinas, São Paulo, Brazil

School of Mechanical and Manufacturing Engineering, Supmeca-Paris, Paris, France

E. Bayraktar (✉)
School of Mechanical and Manufacturing Engineering, Supmeca-Paris, Paris, France
e-mail: bayraktar@supmeca.fr

M.H. Robert
Materials Science Department, UNICAMP—University of Campinas, Campinas, São Paulo, Brazil

I. Miskioglu
ME-EM Department, Michigan Technological University, Houghton, MI, USA

W.C. Ralph et al. (eds.), *Mechanics of Composite and Multi-functional Materials, Volume 7*,
Conference Proceedings of the Society for Experimental Mechanics Series, DOI 10.1007/978-3-319-41766-0_3

3.2 Experimental Procedures

Scrap aluminium (AA7075) alloy (5.1wt%Zn, 2.2wt%Mg, 1.5wt%Cu), as recycled chips (d < 1.7 mm) coming from cutting process of aeronautical parts was used as matrix of the composites proposed in the present work. Scrap aluminium chips were initially processed by milling in a conventional ball mill to reduce their dimensions to desired conditions as presented highly deformed structure in the Fig. 3.1. A little amount recrystallization can be observed after milling (Fig. 3.1b). Addition of pure aluminium fine powder (A1050-5 wt%) during milling as stabilizer together with the ceramic particles seems to improve distribution of particles homogenously. TiO_2 was chosen as main reinforcing elements and also boron nitride, boron, graphite, and spherical ceramic particles were added in different amounts to the matrix (Table 3.1). Total milling time of the mixture was chosen as 2 h after that hot compaction of the mixture was performed under a double action pressure of 250 MPa at the temperature of 200 °C for 30 min. At the second step, these preformed specimens (diameter: 40 mm and thickness: 15–20 mm) were placed in the tool die and heated in the oven under argon atmosphere up to 600 °C with a waiting time of 10 min, and then followed by thixoforging at two stages: first pressure was 15 MPa and 20 s later, final pressure applied was 70 MPa. After thixoforming final diameter of the specimens was 40 mm and their thickness varied from 8 to 10 mm.

Thixoforming conditions of AA7075 alloy and the value of liquid fraction, df_l/dT (f_l = liquid fraction) in the solidification range have been studied using differential scanning calorimetry (DSC) and the actual thixoforming temperature was determined. For this case, software called "Thermocalc®" (version 4.1) was used for the calculation of phase transformation temperatures of AA7075 and liquid percentage in the solid matrix was chosen for the test temperature. Fine microstructural evaluation and fracture surfaces after impact test as well as interface analyses by Scanning Electron Microscopy (SEM) were carried out in detail. Microhardness measurements ($HV_{0.25}$) were made on the polished and etched metallographic specimens. Seven measurements were taken for each composition in three different zones, matrix, interface and reinforcement particles, respectively. The same specimens were also used in microindentation tests. Instrumented micro-indentation testing was conducted to estimate certain micro mechanical properties using CSM indentation test device with a Vickers diamond indenter. Nine indentations were performed 1 mm apart from each other and then the results were averaged. The maximum indentation load (F_{max}) was 600 mN. The indentation hardness and indentation modulus were measured by using the Oliver and Pharr method [14].

Impact tests (EN-10045) were performed to determine the energy absorption capacity of the composites manufactured in this study. Four or five specimens were tested for each composition. The fracture surfaces of the failed specimens were analyzed by SEM.

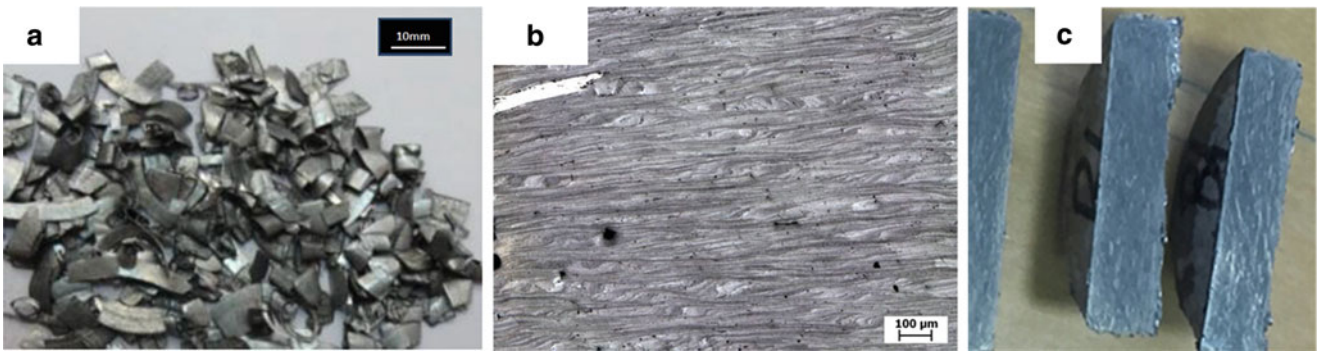

Fig. 3.1 (**a**) Al-chips as raw materials and (**b**) microstructure of Al-chips after milling and (**c**) preformed specimens compacted at 200 °C before thixoforming

Table 3.1 Weight percentage of reinforcement particles for the compositions of the Al-chips based composites (EC)

Composites	AA7075	TiO_2	Boron	BN	**TiC**	Graphite	Spherical ceramic
EC-1	B	2.5	3	2	**3**	3	3
EC-2	B	5	3	2	**3**	3	3
EC-3	B	10	3	2	**3**	3	3

3.3 Results and Discussion

From DSC results, the variation of liquid fraction (f_l) with temperature ($f_l \times T$) of the AA7075 chips was determined and results are shown in Fig. 3.2. In the present work, processing temperature was defined as 600 °C at which the liquid fraction was about 15 % (Table 3.2). As the total liquid fraction in the processing is not so high, this sensibility can be afforded without much risk for the processing stability. Because thixoforming processing of these composites were designed at two steps: thixoforging operation was performed on the compacted and presintered specimens in the matrix at this temperature (600 °C) at 15 MPa pressure at the beginning and at 70 MPa as final pressure.

In fact, a special case for thixoforming process is to create globular structure that interactions among globules in the semi-solid structure are important parameters as far as viscosity is concerned. These structural characteristics depend on the mechanisms involved in the spheroidization of the structure during the heating to the semi-solid condition. In this work, globular structure was carried out quasi perfectly thanks to a novel combined process that was explained in the former section (experimental conditions).

As known, ideal mechanism for globular structure is recrystallization phenomenon contained by the heavily deformed material. In this case, ideal thixotropic structure was obtained by the combined method; presintering at low temperature and large deformation after thixoforming [5, 7]. In the production of AMMCs, it would then be projected the separation of globules and penetration of particulate reinforcements in the liquid area among them, providing a good dispersion in the matrix to give a strong a tough structure [2, 5, 7].

General microstructure and some details of the interfaces between matrix and reinforcements are presented in Fig. 3.3 obtained by SEM. The general appearance for structural information (first column) and more details of the structure related to the interfaces inside of the matrix (second and third columns) have been presented for three compositions EC-1, EC-2 and EC-3,

Again, Fig. 3.4 gives more detail about the thixotropic structure and evolution of globular forms as well as general microstructural analysis made by EDS was presented in this figure. However, from these pictures, another critical observation should be explained here. It means that there is not perfect globular structural formation in everywhere of the specimen, mainly certain chips keep theirs structure even if they contain eutectic zones solidified after the pushing of the reinforcement inside of the matrix with liquid parts. Although their internal structure is globular, as shown in

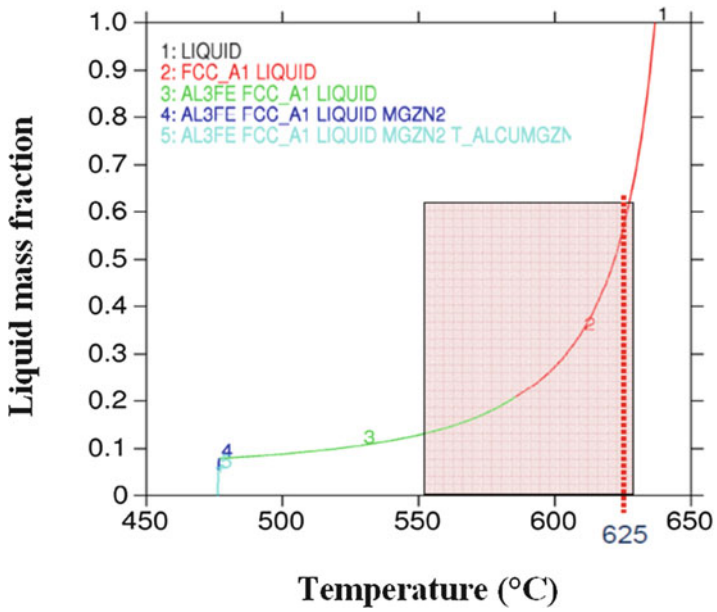

Fig. 3.2 Liquid mass fraction as function of temperature obtained by Thermocalc® software [5, 7]

Table 3.2 DSC analysis for AA7075 chips: liquid fraction (f_l) as a function of temperature

Temperature (°C)	550	560	570	580	**600**	620	625	660
f_l (%)	–	0.02	1.05	3.38	**14.50**	40.40	51.30	100

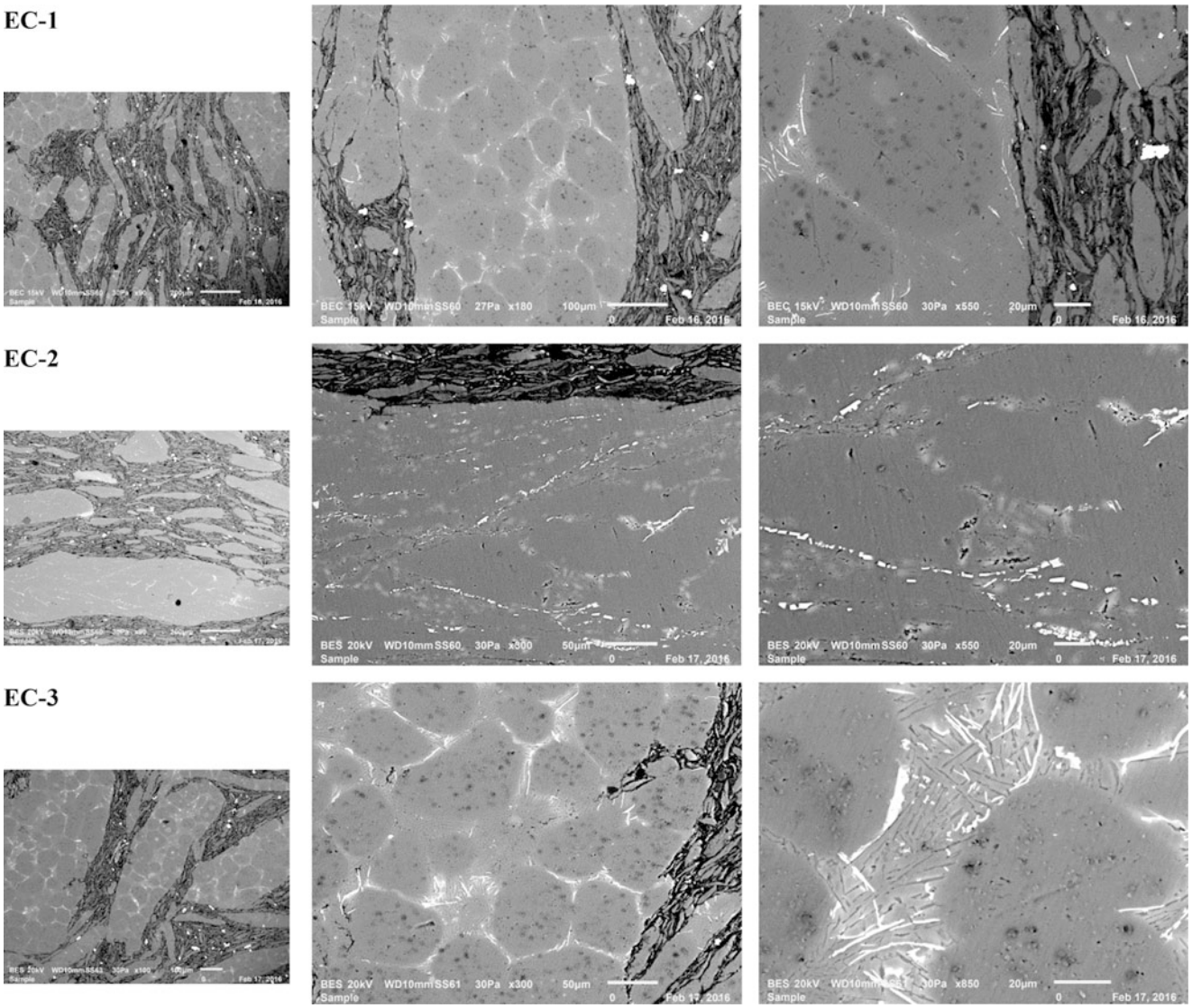

Fig. 3.3 General microstructure (*first column*) and some details of the structure and inside of the matrix for three compositions EC-1, EC-2 and EC-3, obtained by SEM (*second and third columns*)

Figs. 3.3 and 3.4, globules were not entirely detached. Therefore, even though the heating temperature and time were enough to cause partial melting and to stimulate a globular microstructure in the chips, those with large dimensions were not desegregated during thixoforming. Most probably, the main reason is the heating time that should be optimized and thixoforging pressure should be increased for improving the formation of the globular structure [5, 7].

As for the porosity in the final structure, all of the produced samples presented here, does not contain porosity or very low porosity (quasi zero) is observed in the structure that is much lower than products obtained by conventional manufacturing process (simple sintering in powder metallurgy and or other classical foundry etc.).

Microhardness ($HV_{0.25}$) measurements were taken from three different zones: matrix, interface and reinforcement and presented in the Fig. 3.5. All of the measurements for each composition do not change significantly. Most probably these results are due to the homogenous structures of the composites proposed in this study; it means that the distribution of reinforcement are more homogeneous thanks to the combined process applied for each composition carried out in two steps with application of high pressure in final stage of the process.

For the comparison of micromechanical properties, microindentation tests results are presented in the Table 3.3. The penetration depth and contact area between the indenter and the sample describe the mechanical properties of the material. Consequently, if the structure has hard particle reinforcements, they can behave as barriers to the penetration movement, and

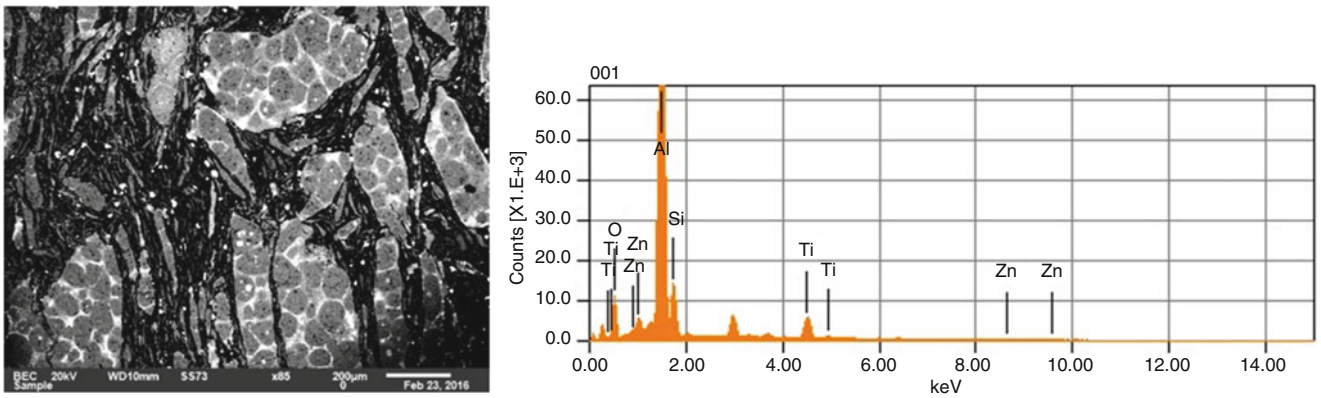

Fig. 3.4 General morphologies of AA7075 composites observed by SEM and also "EDS" spectrum analysis

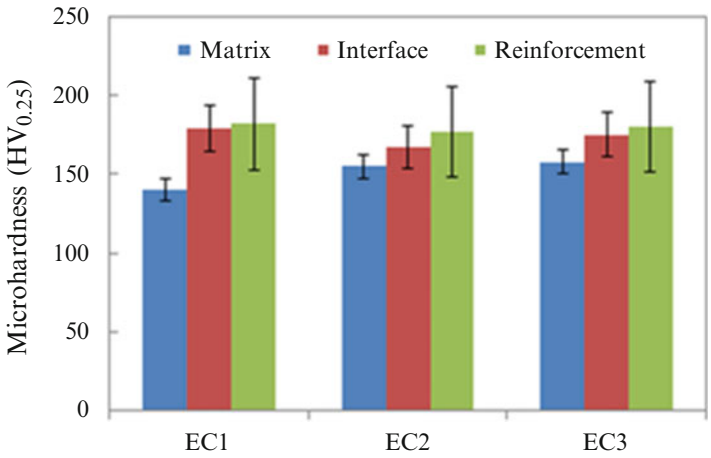

Fig. 3.5 Microhardness ($HV_{0.25}$) measurements taken from three different zones: matrix, interface and reinforcement

Table 3.3 Micromechanical properties of AA7075 composites obtained from instrumented microindentation testing only for the comparison

Composition N°	F_{max} (mN)	Indentation hardness (MPa)	Indentation modulus (GPa)
EC-1	600	1564	92
EC-2	600	1710	98
EC-3	600	1738	113

The value taken from literature [9] for AA7075, T6 (HV175, and E = 72 GPa

evidently there will be less area of contact between the bodies and better mechanical properties are observed The maximum indentation load (F_{max}) was taken as 600 mN for all of three composites. The indentation hardness and indentation modulus were measured. It is observed that both indentation hardness and modulus increase slightly depending on the amount of TiO_2 in the structure. It means that the structures of three composites are tough and solid. They have homogeneous structures with well distributed reinforcements in the matrix. For this reason, addition of TiO_2 has not so significant effect on the mechanical properties. Similarities of these results are related essentially to the homogeneous structure obtained with the combined process of the composites.

As another mechanical property, energy absorption of the three composites, EC1, EC2 and EC3 were determined by means of impact tests. Figure 3.6 shows the impact response of the three composites. The energy (absorbed energy) values presented are the average of 4 or 5 tests for each composite. It can be observed that there is no significant difference between the absorbed energy values of the composites. These results confirm what is discussed in Fig. 3.5 and Table 3.3; homogenous structure and well distributed particle reinforcements with very low porosity (quasi zero) in the structure. And also the effect of main particulate reinforcement should influence these results. Here, the addition of TiO_2 in the structure did not have a considerable effect on the different properties as seen in the Figs. 3.5 and 3.6 an also in Table 3.3. Fracture surfaces taken from failed specimen during impact tests are presented in Fig. 3.7. Fracture surfaces have shown that rigidity increased with

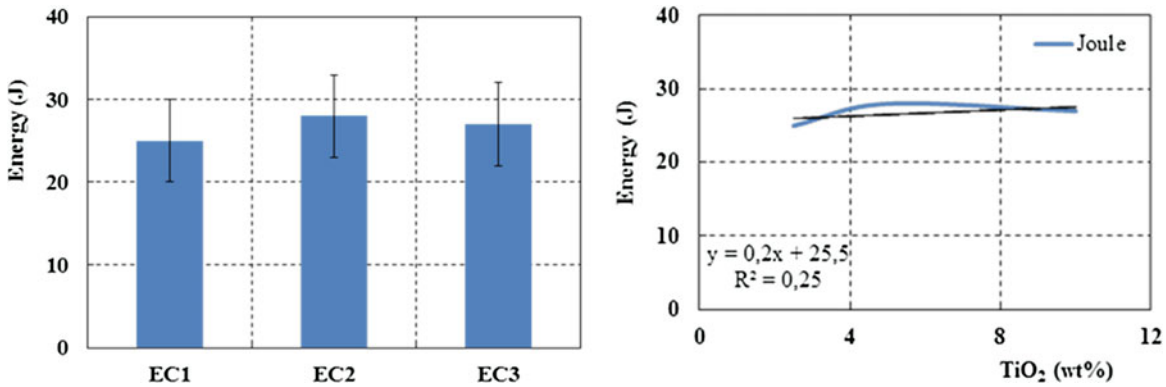

Fig. 3.6 Absorbed energy (*left side*) and linear tendency (*right side*) during impact test for three compositions

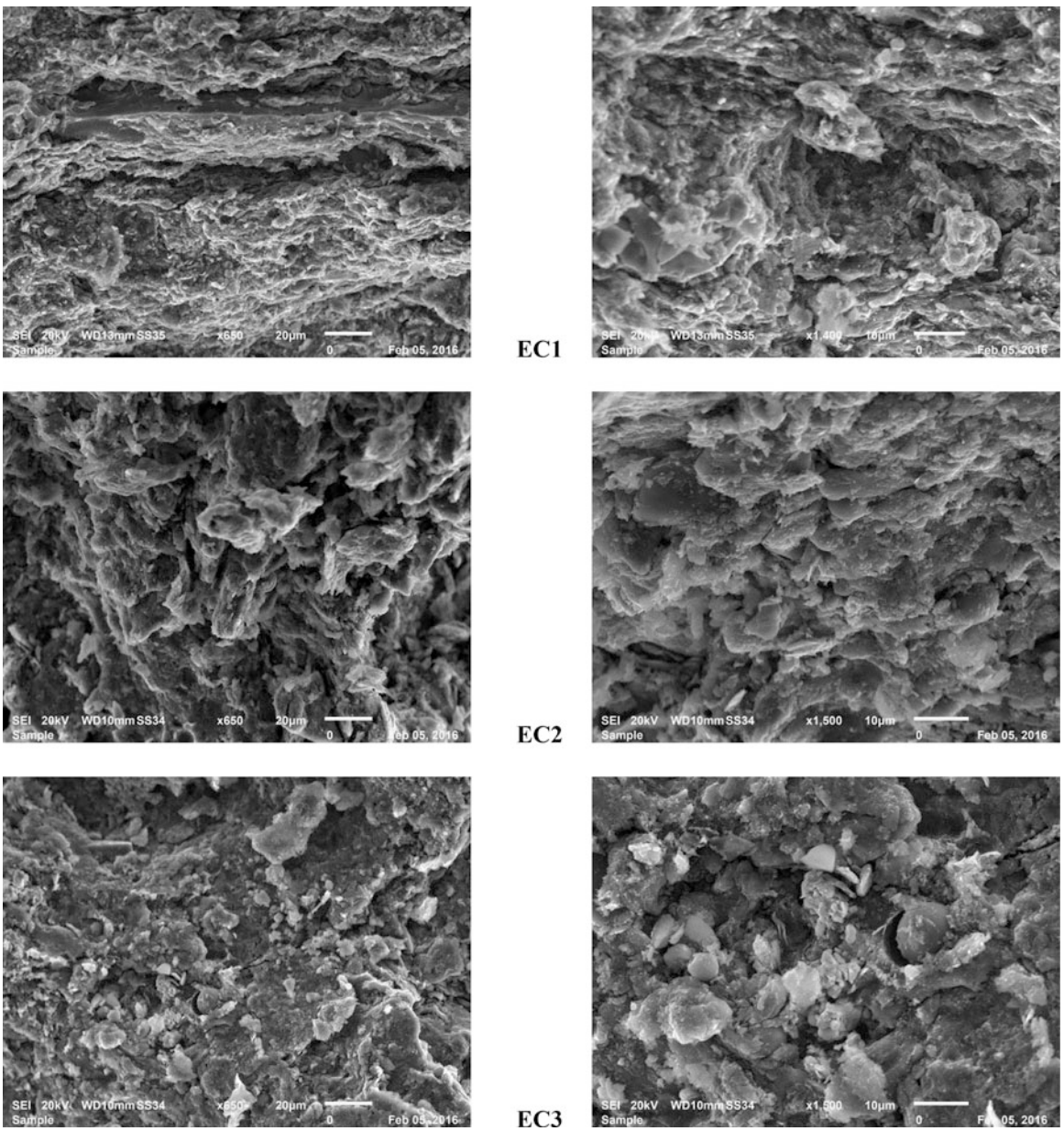

Fig. 3.7 Fracture surfaces taken from broken specimen by impact test

higher pressure during the thixoforming. There is any internal defect and/or porosity observed from these pictures. Reinforcements are well integrated in the matrix without debonding during impact due to strong interface of the particles with matrix.

3.4 Conclusions

Novel composites created by combined method of sintering + thixoforming have been carried out successfully in an economic way with quasi zero porosity. Homogenous microstructure with graded distribution of the reinforcing particles could be obtained successfully by novel process proposed in this work. In the final product, particulate reinforcements and ceramic particles are located well in the matrix dragged by the liquid in the semi-solid material. Addition of pure Al fine powder as stabilizer together with the ceramic particles seems to improve homogenous distribution of the particles. Fracture surfaces have shown that rigidity increased with higher pressure during the thixoforming. For this reason, interfaces between matrix and reinforcing particles can be improved by increment of dwell time at the maximum temperature during this processing and also is worthy to increase applied pressure at the second stage of thixoforming process. In summary, processing conditions still needs to be optimized, in order to achieve high homogeneity of reinforcement dispersion in the matrix. By this way, semi solid aluminium chips in the structure can be disaggregated very easily and then globules can be detached from original structure by penetration of hard particles of the reinforcement in the liquid phase.

References

1. Lang, Y.J., et al.: Effect of strain-induced precipitation on the low angle grain boundary in AA7050 aluminum alloy. Mater. Des. **32**, 4241–4246 (2011)
2. Ferreira, L.M.P., Robert, M.H., Bayraktar, E., Zaimova, D.: New design of aluminium based composites through combined method of powder metallurgy and thixoforming. Adv. Mater. Res. **939**, 68–75 (2014)
3. Mortensen, A., Jinn, I.: Solidification processing of metal matrix composites. Int. Mater. Rev. **37**, 101–128 (1992)
4. Huang, Y., et al.: Characterization of a powder metallurgy SiC/Cu–Al composite. J. Mater. Process. Technol. **197**, 43–48 (2008)
5. Ferreira, L.M.P., Robert, M.H., Bayraktar, E.: Effect of operational parameters in the semi-solid processing of al/sic composites from machining chips. In: ECCM16—16th European Conference on Composite Materials, Seville, Spain, 22–26 June 2014
6. Min, S.: Effects of volume fraction of SiC particles on mechanical properties of SiC/Al composites. Trans. Nonferrous Met. Soc. China **19**, 1400–1404 (2009)
7. Ferreira, L., Robert, M.H., Bayraktar, E.: Production of aluminum/SiC/$NiAl_2O_4$ AMMCs by thixoforming of recycled chips. Solid State Phenom. **217–218**, 286–293 (2015)
8. Zoqui, E.J., Paes, M., Robert, M.H.: Effect of macro and microstructure on the viscosity of the A356 alloy in the semi-solid state. J. Mater. Process. Technol. **153–154**, 300–306 (2004)
9. MATWEB: Material Property data. www.matweb.com
10. Yu, Z., Wu, G., Jiang, L.: Effect of coating Al_2O_3 reinforcing particles on the interface and mechanical properties of 6061 alloy aluminium matrix composites. Mater. Lett. **59**, 2281–2284 (2005)
11. Shin, J.H., Choi, H.J., Cho, M.K., Bae, D.H.: Effect of the interface layer on the mechanical behavior of TiO_2 nanoparticle reinforced aluminum matrix composites. J. Compos. Mater. **48**(1), 99–106 (2014)
12. Ferreira, L.-M.-P., Bayraktar, E., Miskioglu, I., Robert, M.-H.: Effect of the reinforcement particles on the microstructure and electrical properties of aluminium matrix composites (AMCs). In: AMPT-2015, International Conference of Advanced Materials Processing Technologies, Madrid, Spain, 14–17 Dec 2015
13. Shi, Z., Yang, J.M., Lee, J.C.: The interfacial characterization of oxidized SiC/2014 Al composites. Mater. Sci. Eng. **303**, 46–53 (2001)
14. Oliver, W.C., Pharr, G.M.: An improved technique for determining hardness and elastic modulus using load and displacement sensing indentation experiments. J. Mater. Res. **7**, 1564–1583 (1992)

Chapter 4
Scrap Rubber Based Composites Reinforced with Ceramic Oxides and Silica

D. Zaimova, L.-M.P. Ferreira, E. Bayraktar, and I. Miskioglu

Abstract The paper presents results of investigation on composition of some ceramic oxides used for scrap rubber-based composites. The paper reports results of investigation on the influence of boron, boron oxide (B_2O_3) and silica presence of Zr_2O_3 in the composition. Silica is added as the agent controlling the composite transformation. The process of scrap rubber matrix reinforced with certain ceramic reinforcements during heating was examined by DSC/TG technique. Microstructure was evaluated by Scanning Electron Microscope (SEM). Mechanical and wear properties are also studied depending on the composition. The mechanical properties of the composite structure were found to significantly increase with increasing B_2O_3 and Zr_2O_3 contents.

Keywords Recycled rubber • Composites • Low cost production • Ceramic reinforcements • Damage analyse

4.1 Introduction

Around 22 million tons of rubber that is processed every year worldwide goes into making vehicle tires or other manufacturing of the pieces from rubber. Due to the complexity of processing, rubber can be somewhat difficult to recycle, even when the rubber residues are reclaimed and re-used to make new products, the lack of techniques for producing high-quality materials means that the recyclables are transferred to secondary products [1–3], etc.

For this reason, a new idea should be found to optimize the recycling of rubber waste in powder and researchers have been working on the processing of scrap rubber to create novel composite materials reinforced with hard particles. It has been shown that dramatic improvements in mechanical properties can be achieved by addition of a few weight percentages of ceramic materials consisting of oxides/silicates in matrices [4–13]. The large aspect ratios of silicates for example are thought to be mainly responsible for the enhanced mechanical properties of particulate–polymer nanocomposites.

In this work, the influence of the addition of ceramic particles in matrix from treated (silane) a scrap rubber to create a new composite was studied. The results of density, hardness and macroindentation and impact test results were discussed. The dielectric properties, dielectric loss angle tangent (tan delta) were analyzed using a Dielectric Thermal Analyzer (DETA) and a Dynamic Mechanical Thermal Analysis (DMTA). Microstructure and fracture surfaces were analyzed by Scannin Electron Microscopy (SEM).

D. Zaimova
UTCM—University of Chemical Technology and Metallurgy, Sofia, Bulgaria

L.-M.P. Ferreira
Mechanical and Materials Engineering Faculty, University of Campinas, Campinas, São Paulo, Brazil

School of Mechanical and Manufacturing Engineering, Supmeca-Paris, Paris, France

E. Bayraktar (✉)
School of Mechanical and Manufacturing Engineering, Supmeca-Paris, Paris, France
e-mail: bayraktar@supmeca.fr

I. Miskioglu
ME-EM Department, Michigan Technological University, Houghton, MI, USA

W.C. Ralph et al. (eds.), *Mechanics of Composite and Multi-functional Materials, Volume 7*,
Conference Proceedings of the Society for Experimental Mechanics Series, DOI 10.1007/978-3-319-41766-0_4

4.2 Experimental Conditions

Scrap rubber powder was chemically treated by toluene, acrylic acid and vinyltriethoxysilane (2 %) then dried in an oven to entirely eliminate any trace of the chemicals. The main reinforcing element used is Zr_2O and the additional elements such as B, $B2O_3$, SiO_2, Si and Epoxy were also added in different amounts according to design of the five compositions as indicated in the Table 4.1. After here, they are called as DI-0, DI-1, DI-2, DI-3, DI-4.

The scrap rubber and the reinforcement elements were mixed and milled for 2 h to obtain a homogenous compound. At the final stage, the specimens were manufactured by hot compacting (double uniaxial action) under a pressure of 70 MPa at the temperature of 180 °C. The dwell time for the compacting process was 15 min. All of the specimens (30 mm diameter, from 6 up to 10 mm thickness) were cooled down in the tool die. The post curing was concluded under isothermal conditions at a temperature of 80 °C for 48 h.

After post curing, hardness and density measurements on the specimens were performed. "Shore D" hardness test measurements on the polished flat surfaces of the specimens were carried out according to ASTM D 2240 using durometer Shore test device (type HBD-100-0).

Macroindentation test was carried out at room temperature using a stainless steel ball with 3 mm diameter. For this test, samples with diameter of 40 mm and thickness from 6 up to 10 mm thickness were prepared. Maximum stress levels at failure were then compared. The fracture surfaces of the failed specimens were analyzed by SEM and EDS analysis for the checking of the composition.

Impact tests (EN-10045) were performed to determine the energy absorption capacity of the composites manufactured in this study. Four or five specimens were tested for each composition.

Dielectric properties, permittivity and tan delta, were carried out by DETA-Rheometric Scientific at three different frequencies, 100 Hz, 1 and 10 kHz. For this analysis, samples with diameter of 30 mm and thickness of 2 mm were produced. Again for Dynamic Mechanical Thermal Analysis (DMTA), all of the composites designed here were tested for the DMTA was used to characterize them as a function of temperature, using a constant time, stress, and atmosphere. For this test, three frequencies were tested, 100 Hz, 1 kHz and 10 kHz. The measurements of stiffness and damping are reported as modulus and tan delta. For DMTA tests, rectangular specimens of 10 mm wide, 2 mm thickness and length of 30 mm were prepared; three or four samples for each composition were tested. Tested specimens for dielectricity and DMTA, are called DiSi for only registration in the software. It means they are in fact DI-1, 2, 3, 4 and 5 as indicated in the Table 4.1.

4.3 Results and Discussion

General microstructures of the specimens were presented in the Fig. 4.1a, b for four compositions respectively. All of the microstructures of the composites presented here are more and less homogenous. Chemical fusion bonding of rubber with particulate reinforcements were made perfectly thanks to the initial chemical treatment of the scrap rubber powders. Certain area in the structure shows weakly agglomeration of the reinforcements. This type of agglomeration can be improved by milling and heating under pressure in longer time.

Absolute density and Shore D hardness measurements for these composites were presented in the Fig. 4.3.

Absolute densities (Archimed) for each composition were compared (Fig. 4.2a) after that Shore D hardness test measurements on the polished surfaces of the specimens were carried out according to ASTM D 2240. Five measurements for each specimen were made and mean values were presented again in the Fig. 4.2b. All of the values discussed here have shown the same levels with low dispersions. Again, only DI-3 and DI-4 have given more dispersion in the measurements.

Macroindentation test results were presented in the Fig. 4.3 presented with maximum forces at the failure. A considerable scattering on the values was found for each composite. This type of the damage analysis is very well-meaning related the

Table 4.1 General design of five compositions based on the scrap rubber

Composites	Matrix (SBR)	**Zr_2O_3**	B	B_2O_3	SiO_2	Si	Epoxy
DI-0	Balance	–	10	25	10	3	–
DI-1	Balance	**10**	10	25	10	3	–
DI-2	Balance	**20**	10	25	10	3	–
DI-3	Balance	**30**	10	25	10	3	–
DI-4	Balance	**40**	10	25	10	3	10

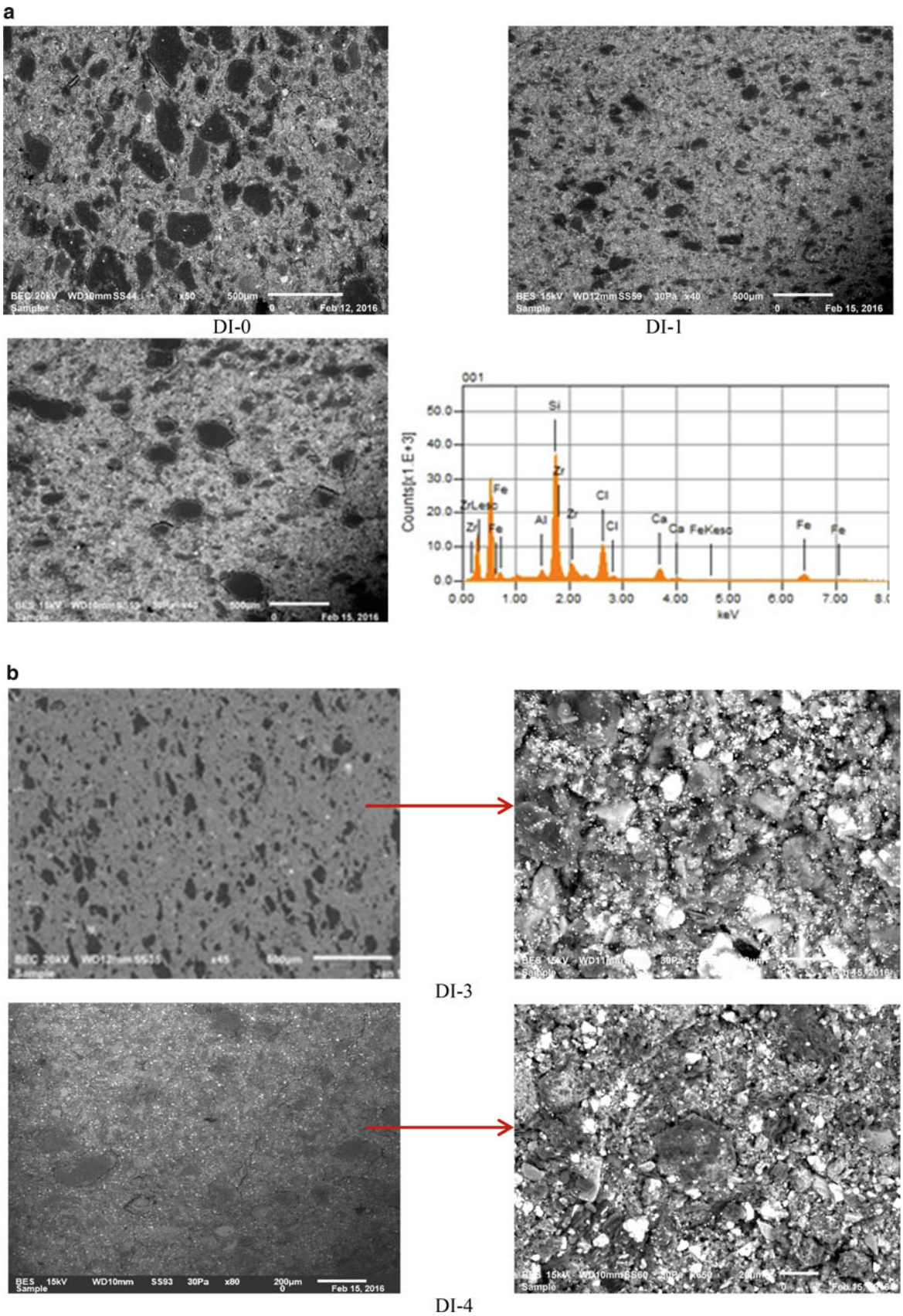

Fig. 4.1 (**a**) General microstructures of the compositions in transversal section for DI-1 and DI-2 and EDS analyses. (**b**) General microstructures of the compositions in transversal section for DI-3 and DI-4 (pictures in high magnification were put in the *right column*)

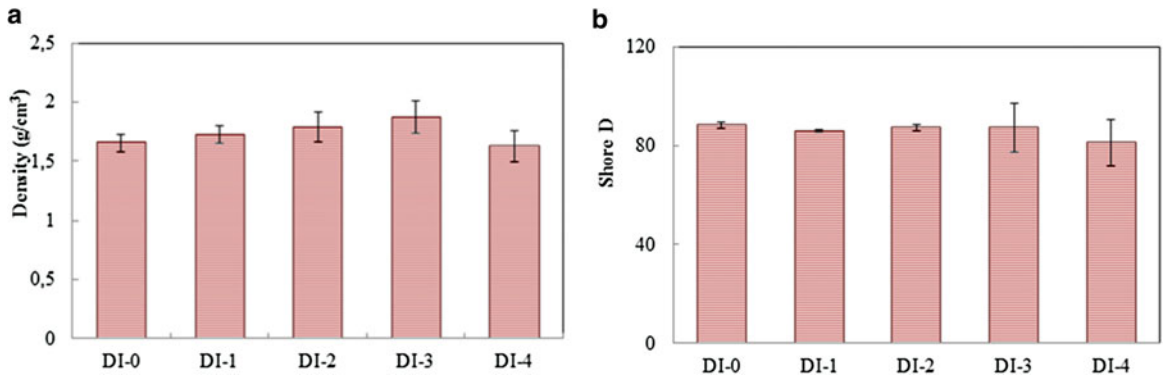

Fig. 4.2 Density and Shore D measurements for five compositions created in this work

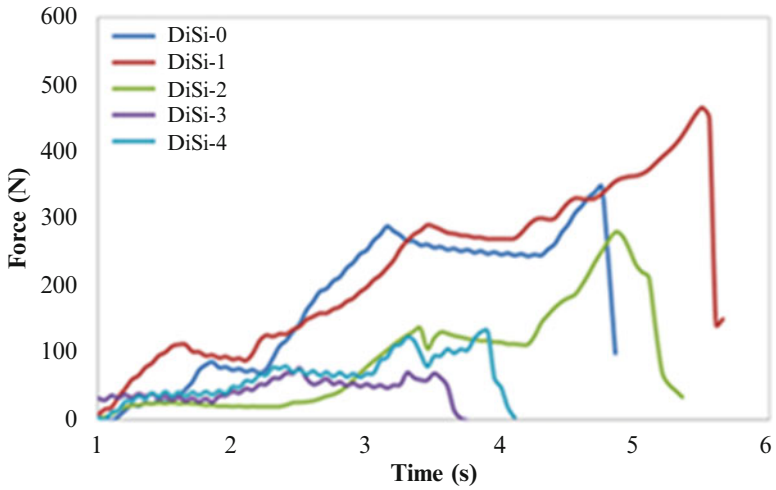

Fig. 4.3 Macroindentation test results in compression test for five compositions. These values only one series of the tests repeated at least four and five times for each composite

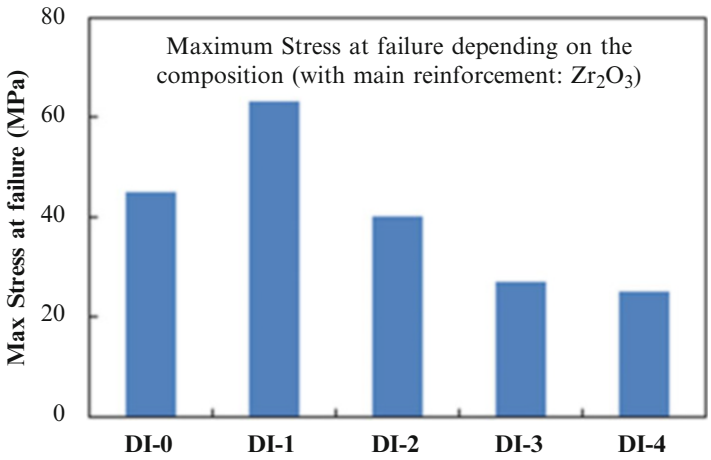

Fig. 4.4 Maximum stress values at failure from macroindentation test. These values are means values taken from five measurements for each composite

structure of this type of composites. Figure 4.4 summarizes maximum stress (mean) values at failure. However, very big dispersion was obtained in these tests. In reality, evolution of the values for each composition is strongly related with hard particles added in the structure. Combined effect of Zr_2O_3 with boron increases brittleness and gives a practical solution to optimize the composition. Impact tests (EN-10045) were performed to determine the energy absorption capacity of the composites manufactured in this study (Fig. 4.5). Four or five specimens were tested for each composition. These values are means values taken from five measurements for each composite. These results confirm well the former tests discussed in the

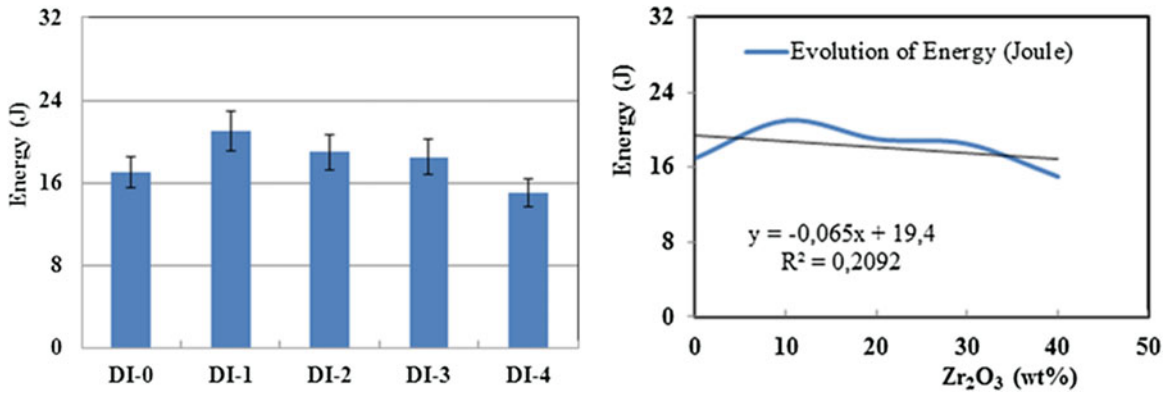

Fig. 4.5 Absorbed energy and liner tendency as a function of the particulate reinforcements found for five compositions obtained by impact test

Figs. 4.3, 4.4, and 4.6 that shows fracture surfaces taken from the specimens failed at the maximum stress levels. It means that ductility decreases with increment of hard particles essentially this effect is considerable in case of the last composition called DI-4 with combined effect of Zr_2O_3 with boron and epoxy resin together [4, 6, 9, 11].

Dynamic mechanical thermal analysis (DMTA) was used to determine the storage modulus (E') and dynamic mechanical loss angle tangent (tan δ). The storage modulus (E') is the measure of the sample elastic behavior, the loss modulus (E") is the measure of the viscous response of the materials. The ratio of the loss modulus to the storage modulus (E"/E') is the dynamic mechanical loss angle tangent (tan δ) and it is a measure of the energy dissipation in the material. Tan δ is also an indicator of the viscoelasticity of the sample [14].

Figures 4.7 and 4.8 present evolution of storage modulus and tan delta of the composites depending on the temperature interval from −60 to 120 °C, respectively. These Figs. 4.7 and 4.8 indicate very clearly that the storage modulus decreases with increasing the temperature for all of the composites. There is no dependence observed concerning the different quantity of Zr_2O_3 or the addition of epoxy in the composition DI-4. Although it is seen from these figures that composite DiSi-1 has the highest value for the storage modulus. These values are worthy to compare with former tests discussed in the Figs. 4.3, 4.4, and 4.5. This means that the polymer chain mobility in composite DI-1 is more restricted comparing to the other studied composites. It is also seen from these curves that these composites does not behave like elastomers although that the matrix is originally waste rubber. Probably this is due to the effect of the additional elements used to obtain these composites. Similar conclusions can be made for tan delta. Hard particles and mainly the combined effect of Zr_2O_3—boron and for final composition (DI-4) epoxy resin changed the physical chemistry behaviour of the composites.

As for the dielectric permittivity (E') of these composites, this property shows the ability of a material to store electric potential energy under the influence of an external electric field, which is proportional to the capacitance and measures the alignment of dipoles [15]. Figure 4.9a–d shows the variation of E' as a function the temperature for several different frequencies. It is observed from the figures that the E' continuously decreased with increasing the frequency. The decrease in E' on increasing the frequency is well expected in most of the dielectric materials. This may be attributed to the tendency of dipoles in macromolecules to orient themselves in the direction of the external alternating electric field and the uniform dispersion of the filler aggregates in the polymer matrix. It is also observed that E' is increasing with increasing of the temperature for all composites [7, 9, 11, 14, 15].

It is also known that as the temperature increases the intermolecular forces between polymer chains is broken which enhances thermal agitation. At lower temperature, the segmental motion of the chain is practically frozen and this is the reason why the dielectric constant is reduced. This tendency is strongly observed for all composites investigated in this paper. Concerning the different quantities of Zr_2O_3, there is relation observed. It is seen that the results for DI-0 (without Zr_2O_3) and DI-4 (maximum content of Zr_2O_3 plus epoxy) are very similar. The ratio between the dielectric losses with the dielectric constant is quantified as tan δ [15]. Concerning the dielectric loss angle tangent, there is no clear relation between the temperature and the quantity additives for the studied composites.

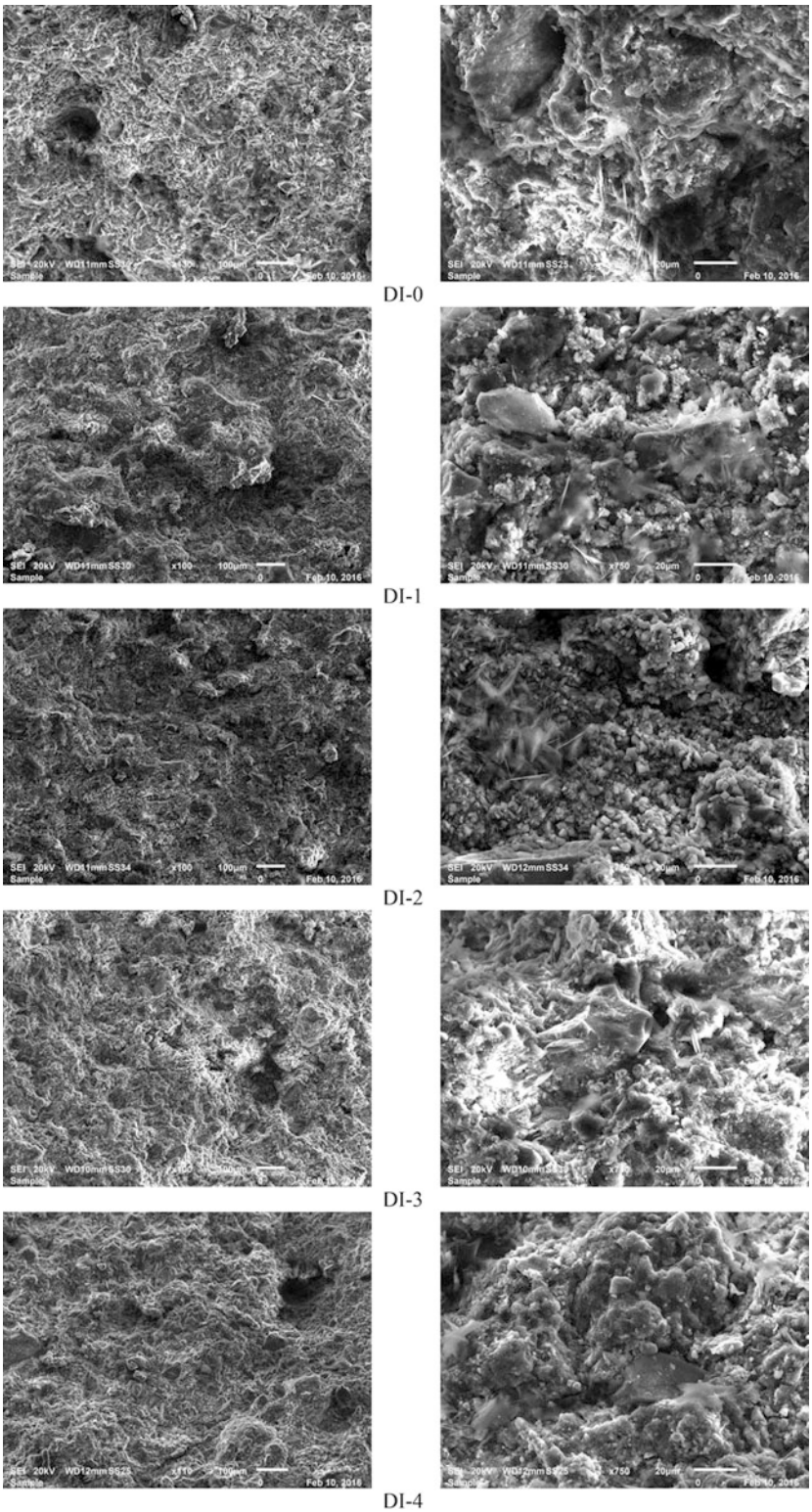

Fig. 4.6 Fracture surface of the samples after macroindentation test

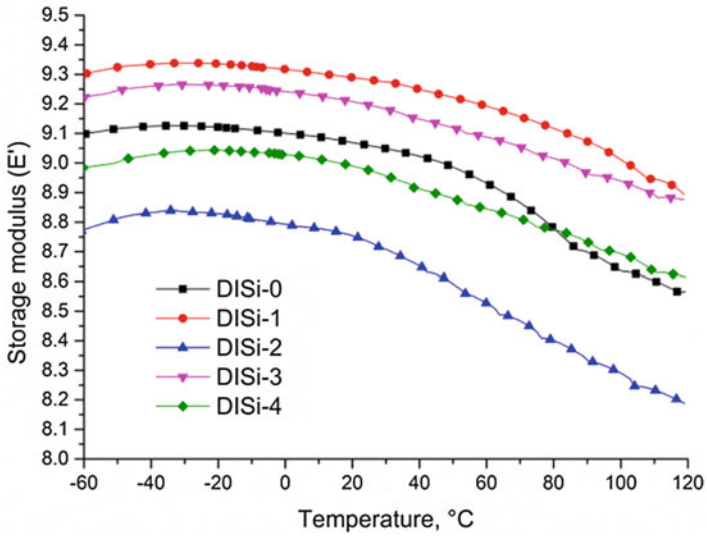

Fig. 4.7 Evolution of storage modulus (E') as a function of temperature for the five composites studied in this work

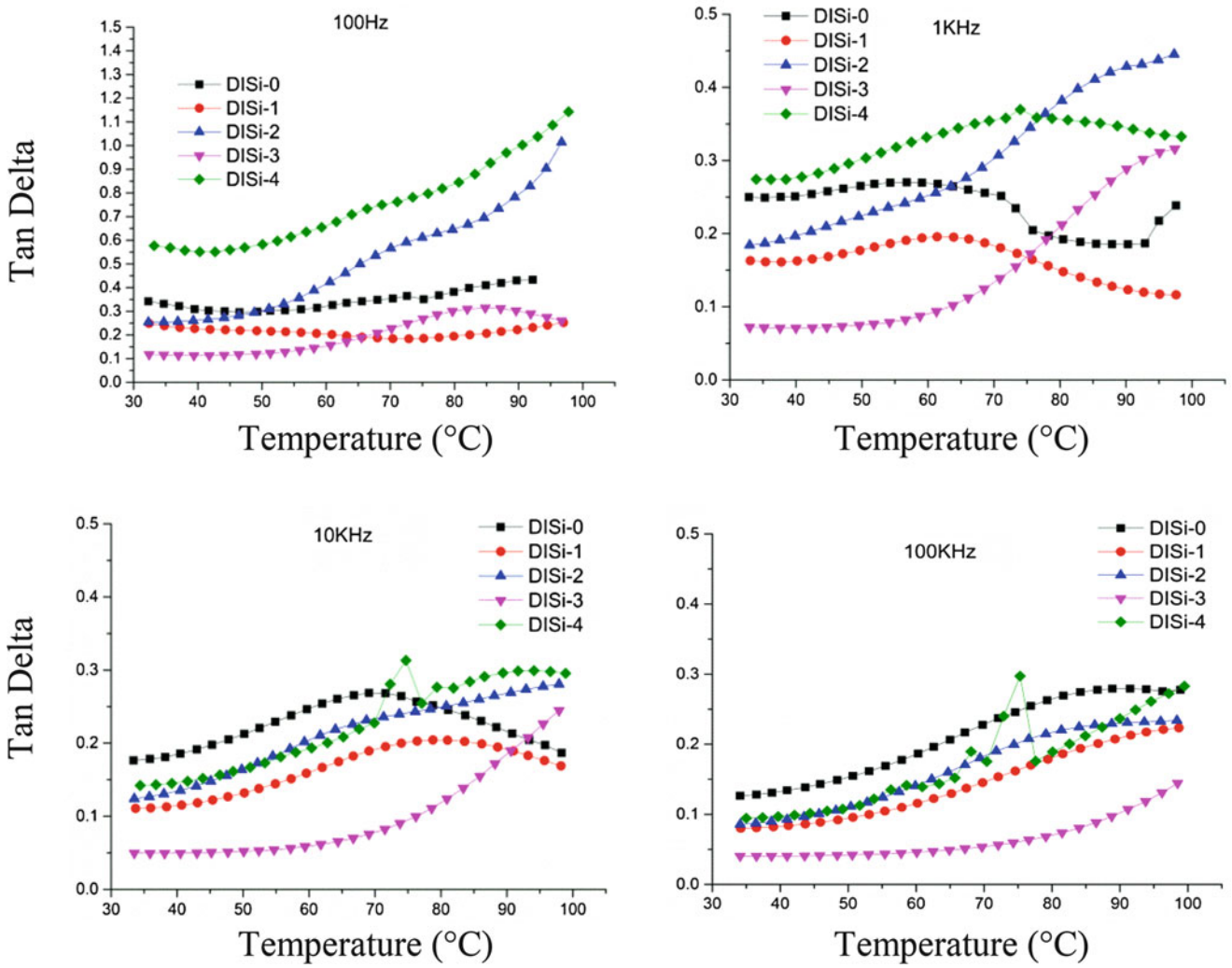

Fig. 4.8 Evolution of "Tan delta" as a function of temperature for the five composites studied in this work

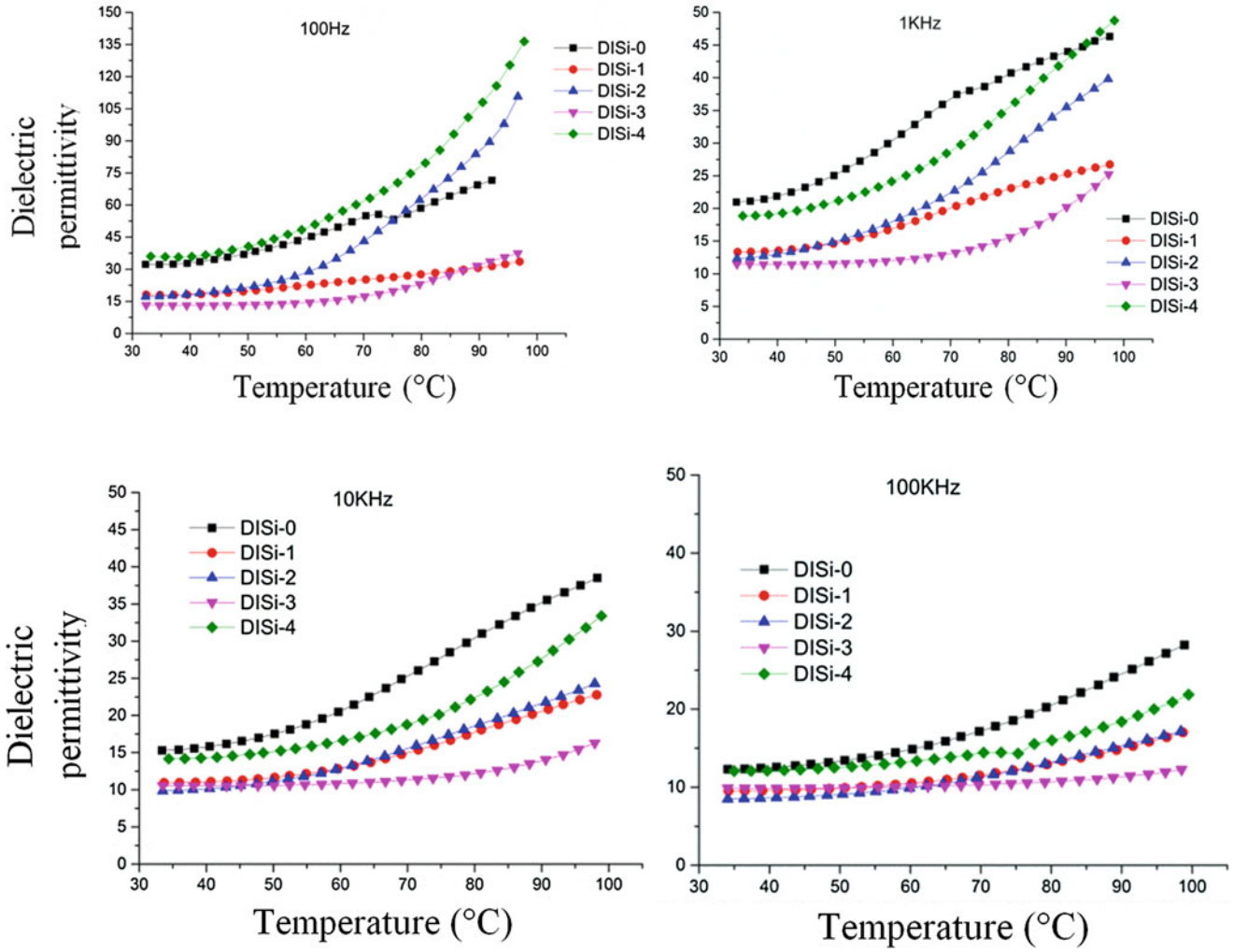

Fig. 4.9 Dielectric permittivity as a function of temperature for the composites in different frequencies

4.4 Conclusions

In the frame of common research project, five novel composites were proposed from scarp rubber in powders reinforced with ceramic oxides mainly as hard particles, Zr_2O_3, boron, B_2O_3, SiO_2, and Si. Mechanical properties and physical chemistry behaviour of these composites were compared with at least 100 specimens tested for these comparisons.

Many results presenting different properties show very close interpretations quasi the same evolution for each composite. As a practical solution, these results are worthy to use for optimization of the compositions. These composites have shown a mixed behaviour far away from classical rubber properties. Mainly ductility should be improved by using new formulation for optimal composition. Combined effect of Zr_2O_3 with boron should be considered as brittleness in the structure. For this reason these points will be redesigned for the next combination of these composites that they will be used in internal furniture in automotive industry, may be will find another industrial applications in future depending on the development of the present work that is already going on.

References

1. Zaimova, D., Bayraktar, E., Miskioglu, I., Katundi, D.: Manufacturing of new elastomeric composites: mechanical properties, chemical and physical analysis. In: Tandon, G. (ed.) Composite, Hybrid, and Multifunctional Materials, vol. 4, pp. 139–150. Springer, New York (2015)

2. Decker, E.H., et al.: Energy and material flow through the urban ecosystem. Annu. Rev. Energy Env. **25**, 685–740 (2012)
3. Bandyopadhyay, S., et al.: An overview of rubber recycling. Prog. Rubber Plast. Recycl. Technol. **24**, 73–112 (2008)
4. Zaimova, D., Bayraktar, E., Miskioglu, I., Dishovsky, N.: Optimization and service life prediction of elastomeric based composites used in manufacturing engineering. In: Tandon, G.P., Tekalur, S.A., Ralph, C., Sottos, N.R., Blaiszik, B. (eds.) Experimental Mechanics of Composite, Hybrid, and Multifunctional Materials, vol. 6, pp. 157–166. Springer, New York (2014)
5. Kim, M.H., Park, C.I., Choi, W.M., Lee, J.W., Lim, J.G.: Synthesis and material properties of syndiotactic polystyrene/organophilic clay nanocomposites. J. Appl. Polym. Sci. **92**, 2144–2150 (2004)
6. Zaimova, D., Bayraktar, E., Miskioglu, I.: Characteristics of elastomeric composites reinforced with carbon black and epoxy. In: Ralph, C., Silberstein, M., Thakre, P.R., Singh, R. (eds.) Mechanics of Composite and Multifunctional, Materials, pp. 191–202. Springer, New York (2015)
7. Zaimova, D., Bayraktar, E., Miskioglu, I.: Manufacturing and damage analysis of epoxy resin-reinforced scrap rubber composites for aeronautical applications. In: Tandon, G.P., Tekalur, S.A., Ralph, C., Sottos, N.R., Blaiszik, B. (eds.) Experimental Mechanics of Composite, Hybrid, and Multifunctional Materials, vol. 6, pp. 65–76. Springer, New York (2014)
8. Wang, Z., Lan, T., Pinnavaia, T.J.: Hybrid organic–inorganic nano-composites formed from an epoxy polymer and a layered silicic acid (magadiite). Chem. Mater. **8**, 2200–2204 (1996)
9. Zaimova, D., Bayraktar, E., Miskioglu, I., Katundi, D.: Study of influence of SiC and Al2O3 as reinforcement elements in elastomeric matrix composites. In: Tandon, G. (ed.) Composite, Hybrid, and Multifunctional Materials, vol. 4, pp. 129–138. Springer, New York (2015)
10. Wong, C.P., Bollampally, R.S.: Thermal conductivity, elastic modulus, and coefficient of thermal expansion of polymer composites filled with ceramic particles for electronic packaging. J. Appl. Polym. Sci. **74**, 3396–3403 (1999)
11. Zaimova, D., Bayraktar, E., Katundi, E., Dishovsky, D.: Design of new elastomeric composites used in manufacturing engineering. In: 14th International Materials Symposium—IMSP 2012, Pamukkale, Turkey, vol. 1, pp. 1–13 (2012)
12. Wang, M., Berry, C., Braden, M., Benfield, W.: Young's and shear moduli of ceramic particle filled polyethylene. J. Mater. Sci. Mater. Med. **9**, 621–624 (1998)
13. Verbeek, C.J.R.: The influence of interfacial adhesion, particle size and size distribution on the predicted mechanical properties of particulate thermoplastic composites. Mater. Lett. **57**, 1919–1924 (2003)
14. Shaw, M.T., MacKnight, W.J.: Introduction to Polymer Viscoelasticity. Wiley, New York (2005)
15. Ahmad, Z.: Chapter 1. Polymer Dielectric Materials "Dielectric Material". In: Silaghi, M.A. (ed.), 3 Oct 2012. ISBN: 978-953-51-0764-4

Chapter 5
Mechanical and Tribological Properties of Scrap Rubber Reinforced with Al_2O_3 Fiber, Aluminium and TiO_2

L.M.P. Ferreira, I. Miskioglu, E. Bayraktar, and D. Katundi

Abstract Scrap rubber/Epoxy composites reinforced with Aluminium, Alumina Fibre and TiO_2 particles were prepared and mechanical and tribological properties of these composites were investigated. Basically, these composites are aimed to use in many engineering applications. A detail microstructure and matrix/reinforcement interface analyze was made by means of Scanning Electron Microscope (SEM) The wear performance of hard particles reinforced composites were evaluated in view of micromechanical properties. Quasi static and dynamic compression tests were carried out and damaged specimens were studied by SEM. Degradation behaviour of the structure for each composite was compared after exposing against UV. The hardness (short test) values of the composites were reviewed related to the reinforcement elements.

Keywords Recycling materials • Rubber/epoxy composites • Low-cost engineering • Wear resistance

5.1 Introduction

Recycling of scrap rubber reinforced with different particles is used very often in industrial applications, in civil engineering, shoe industry and pieces for other internal and external furniture. Recently, new composites from recycled rubbers became very attractive in automotive and domestic applications; requirements for high performance structural systems like elastomeric based composites [1–8, 9]. Today, many industrial research on the novel composites from recycled materials concentrate on the processing of these recycled materials and production methods for low cost engineering applications. One of the crucial subjects is the optimal processing of the scrap rubber coming from production in high amount of waste rubber produced every year [5–8, 10–16]. These rubber based composites are usually used for long term applications at ambient or at moderately elevated temperature conditions. For this reason, recycled rubbers should be used by simple processing with various materials in different conditions by addition of new and simple reinforcements [7, 8, 9–11].

The present work presents processing of scrap rubbers treated with epoxy resin to create novel composites in economic way. Main objective of this research was to determine the mechanical and tribological properties of these composites by using scrap rubber powders as a matrix reinforced with aluminium, alumina fibre and TiO_2 particles were prepared and mechanical and tribological properties were investigated. Basically, these composites are aimed to use in automotive applications as internal furniture as ductile and tough and sound materials. Scanning electron microscopy (SEM) was used to study the microstructure and fracture surfaces of these composites

L.M.P. Ferreira
Materials Science Department, UNICAMP—University of Campinas, Campinas, São Paulo, Brazil

School of Mechanical and Manufacturing Engineering, Supmeca-Paris, Paris, France

I. Miskioglu
ME-EM Department, Michigan Technological University, Houghton, MI, USA

E. Bayraktar (✉)
School of Mechanical and Manufacturing Engineering, Supmeca-Paris, Paris, France
e-mail: bayraktar@supmeca.fr

D. Katundi
Materials Science Department, UNICAMP—University of Campinas, Campinas, São Paulo, Brazil

W.C. Ralph et al. (eds.), *Mechanics of Composite and Multi-functional Materials, Volume 7*,
Conference Proceedings of the Society for Experimental Mechanics Series, DOI 10.1007/978-3-319-41766-0_5

5.2 Experimental Conditions

At the beginning of the composite design, scrap rubber powders were chemically treated by toluene, acrylic acid and vinyltriethoxysilane (2 %) then dried in an oven to eliminate trace of the chemicals. After chemical treatment, 60 % of scrap rubber and 40 % of epoxy were mixed used as matrix. TiO_2 was chosen as main reinforcing element together; with aluminum, alumina-fiber. And also, boron and Cu were added as minor reinforcement elements in the matrix (Table 5.1).

Four basic compositions were prepared after here will be called RETI-1, 2, 3 and 4.

After preliminary blending of the basic elements (scrap rubber + epoxy) of the composites, reinforcement elements were added in the structure and entire of the mixture have been milled for 2 h to obtain a homogenous compound. At the final stage, the specimens were manufactured by hot compacting (double uniaxial action) under a pressure of 70 MPa at the temperature of 180 °C. The dwell time for the compacting process was 15 min. All of the specimens (30 mm diameter, 6 mm thick) were cooled down slowly. The post curing was concluded under isothermal conditions at 80 °C for 48 h. Shore D hardness test was performed on the polished flat surfaces of the specimens according to ASTM D 2240 using durometer Shore test device (type HBD-100-0). Shore D was also performed for the samples exposed to Ultra Violet (UV) conditions during exposing time: 2 months (every week during months) to evaluate resistance of these composites against degradation by UV.

Macroindentation test was carried out at room temperature using a stainless steel ball with 3 mm diameter. For this test, 10 specimens for each composition were prepared with diameter of 40 mm. Thickness of the specimens was variable from 6 up to 10 mm. Maximum force (F_{max}) at failure and fracture surface were evaluated by SEM analysis.

Again, dynamic compression (drop weight tests) was carried out using a universal drop weight test device, Dynatup Model 8200 machine, with a total weight of 1.9 kg, punch height of 600 mm and with an impact velocity of around 3 m/s.

Wear resistance were evaluated by nanoindentation tests under two different normal loads (20 and 50 mN) applied over a linear track of 500 μm for 50 cycles. Wear is performed with a conical tip that has 90 degree apex angle. One cycle is defined as a pass and return of the tip over the track; the total distance for one test was 0.050 m. The speed of the tip during wear tests was 50 μm/s. A total of 10 wear test was performed for each sample.

5.3 Results and Discussion

General microstructure of the specimens was presented in the Fig. 5.1 for four compositions. All of the microstructures of the composites presented here are more and less homogenous. Adhesion of rubber with epoxy powders were made perfectly thanks to the initial chemical treatment (silane) of the scrap rubber. Distribution of the reinforcements is more and less homogeny and small agglomeration of the reinforcements were observed in the specimens from first composite (RETI-1). This type of agglomeration can be improved by milling in longer time and longer heating time.

Comparison of hardness (Shore D) results were compared in the Fig. 5.2 for four different compositions after exposing to ultraviolet (UV) during 7, 14, 21, 28 and 45 days. As seen from this graphics, there is no change significantly on the measured values for each period. In reality, all of the specimens have kept their original structure any decohesion between chemical bindings without chemical deterioration. Addition of boron is always a positive effect on the hardness behaviour of these composites even if its percentage is very low. This behaviour is worthy for the pieces aimed on the production of external parts used for example in the industry [7, 8, 9–13]. All of the four composites gave the same level of hardness.

There is not significant variation in the hardness values during the long period of exposing to UV.

Generally, the properties of interest in composites are mechanical properties. The aim is to achieve optimum mechanical properties required for specific applications. For this reason, macroindentation test results were conducted and presented in

Table 5.1 General compositions of the rubber based composites (RETI)

Composites	Matrix R 60 % E 40 %	Al	Al_2O_3 Fiber	Al_2O_3 Powder	**TiO_2**	B	Cu
RETI-1	Balance	13	6	1	**0**	1	1
RETI-2	Balance	13	6	1	**7**	1	1
RETI-3	Balance	13	6	1	**10**	1	1
RETI-4	Balance	13	6	1	**15**	1	1

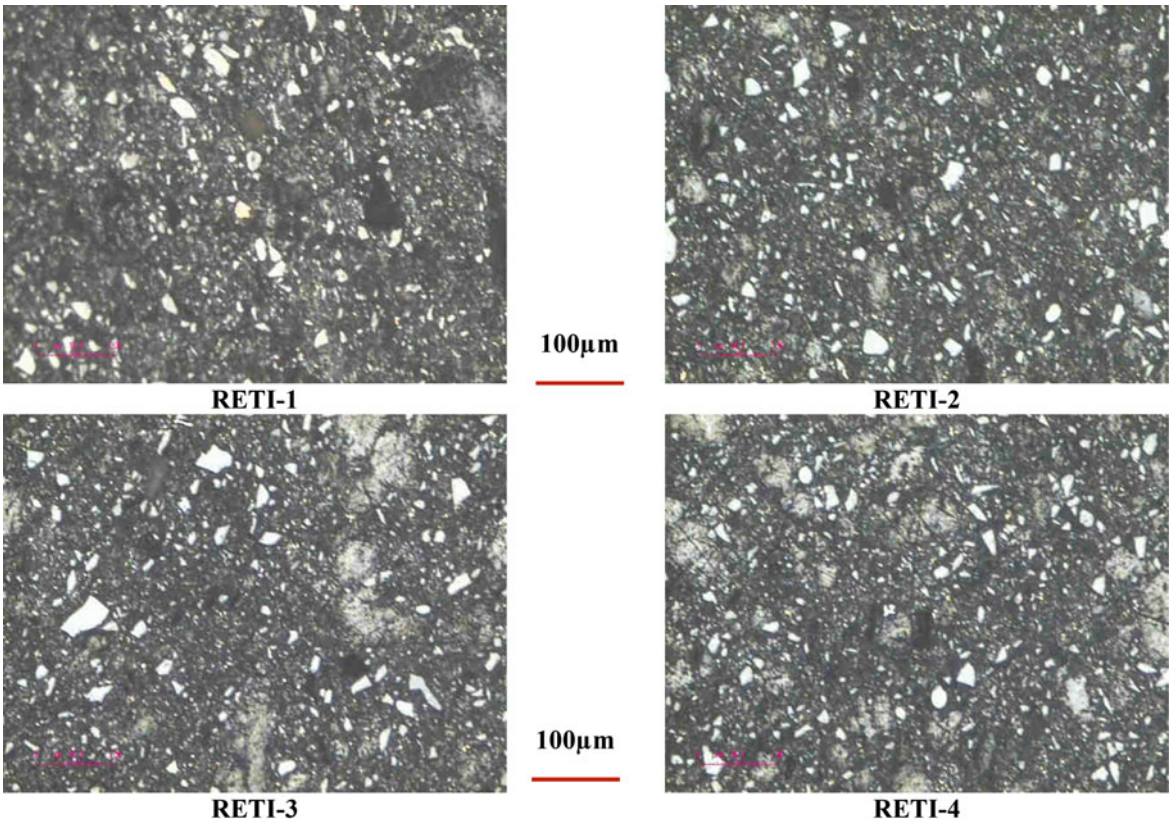

Fig. 5.1 General microstructures of the compositions in transversal section

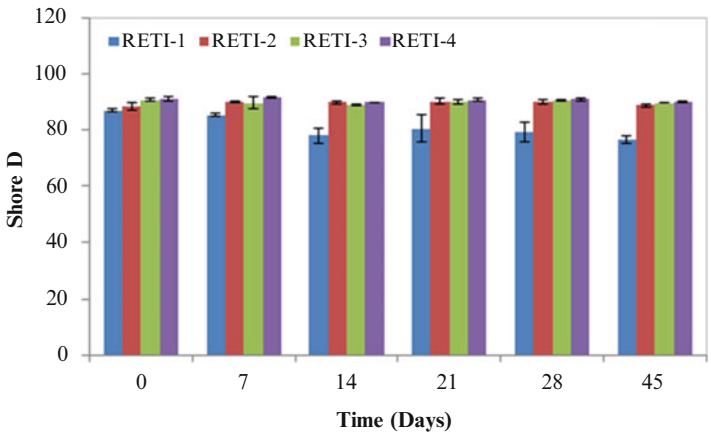

Fig. 5.2 Comparison of Shore D results for four different compositions after *exposing to ultraviolet* (UV) during 7, 14, 21, 28 and 45 days

the Fig. 5.3. These values were compared with maximum forces at the failure. A considerable scattering on the values was found for each composite. This type of the damage analysis is very well-meaning related the structure of this type of composites. Probably, Addition of alumina fibre and alumina and boron together increase the brittleness. Damaged surfaces obtained from this test were evaluated by SEM as shown in the Fig. 5.4.

Fracture surfaces for all of the composites have shown brittle structure but little porosity was observed in some local area. But there is any decohesion of the particulate reinforcements.

Another damage analysis has been performed by dynamic compression and/or drop weight test as given the entire test conditions in the former section (experimental conditions) and absorbed energy were calculated for each composite via "Mat lab" from the data base (Fig. 5.5).

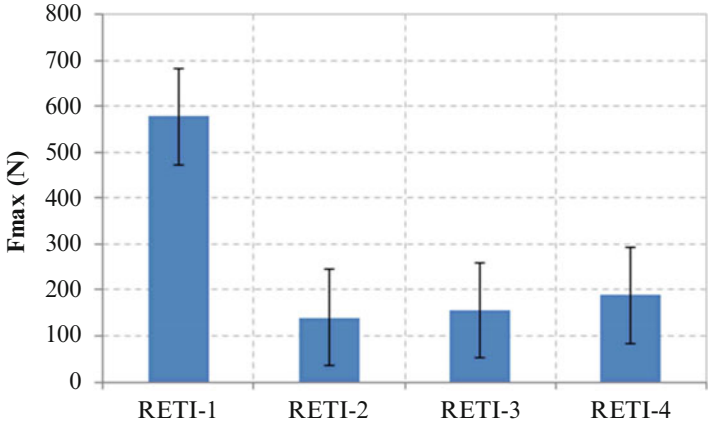

Fig. 5.3 Maximum values (F_{max}) obtained for each composition obtained by macroindentation test

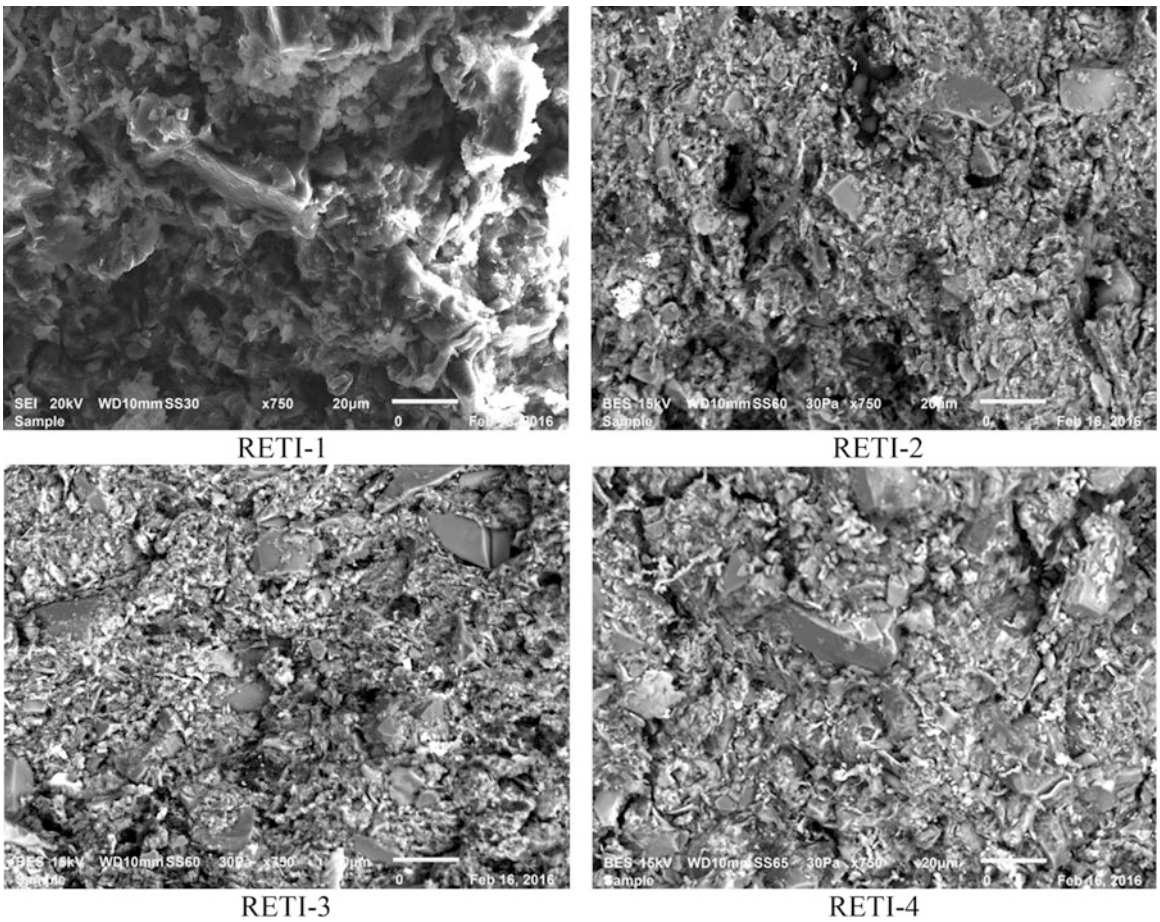

Fig. 5.4 Fracture surfaces of the samples for the compositions after macroindentation test presented in this work

Fracture surfaces of this dynamic test were evaluated in the Fig. 5.6. Again, the alumina fibers and alumina and also boron added together in the structure play on the brittle damage behaviour, however, very good interface was observed between the matrix and reinforcements in all of the composites studied here.

Even if the slope shows a slight decreasing effect, final results gave satisfaction. Some works performed in the literature studied similar results [4, 14, 16]. All of these results obtained by dynamic compression tests confirmed well former results discussed in the Figs. 5.3 and 5.4.

Wear track deformation by using nanoindentation tests gave much more information on the micromechanical properties of the composites proposed in this work. Wear resistance were evaluated by nanoindentation tests under two different

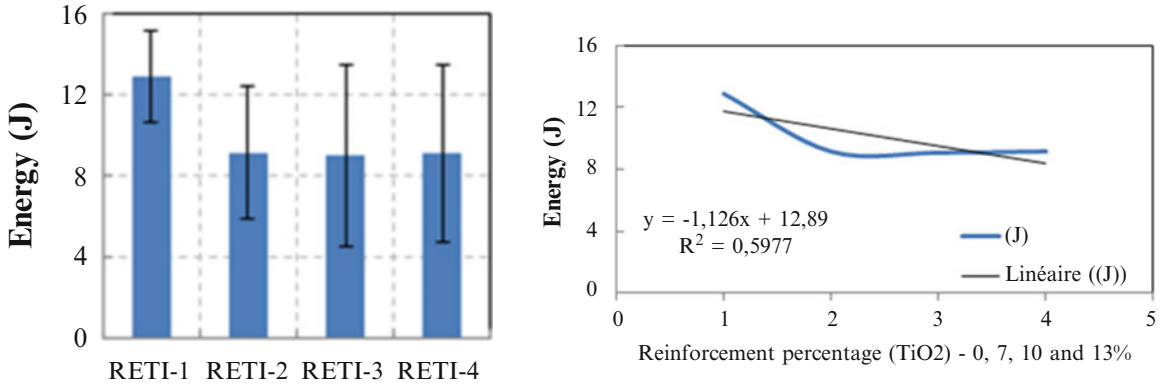

Fig. 5.5 Energy and liner tendency as a function of the particulate reinforcements found for four compositions obtained by dynamic compression test

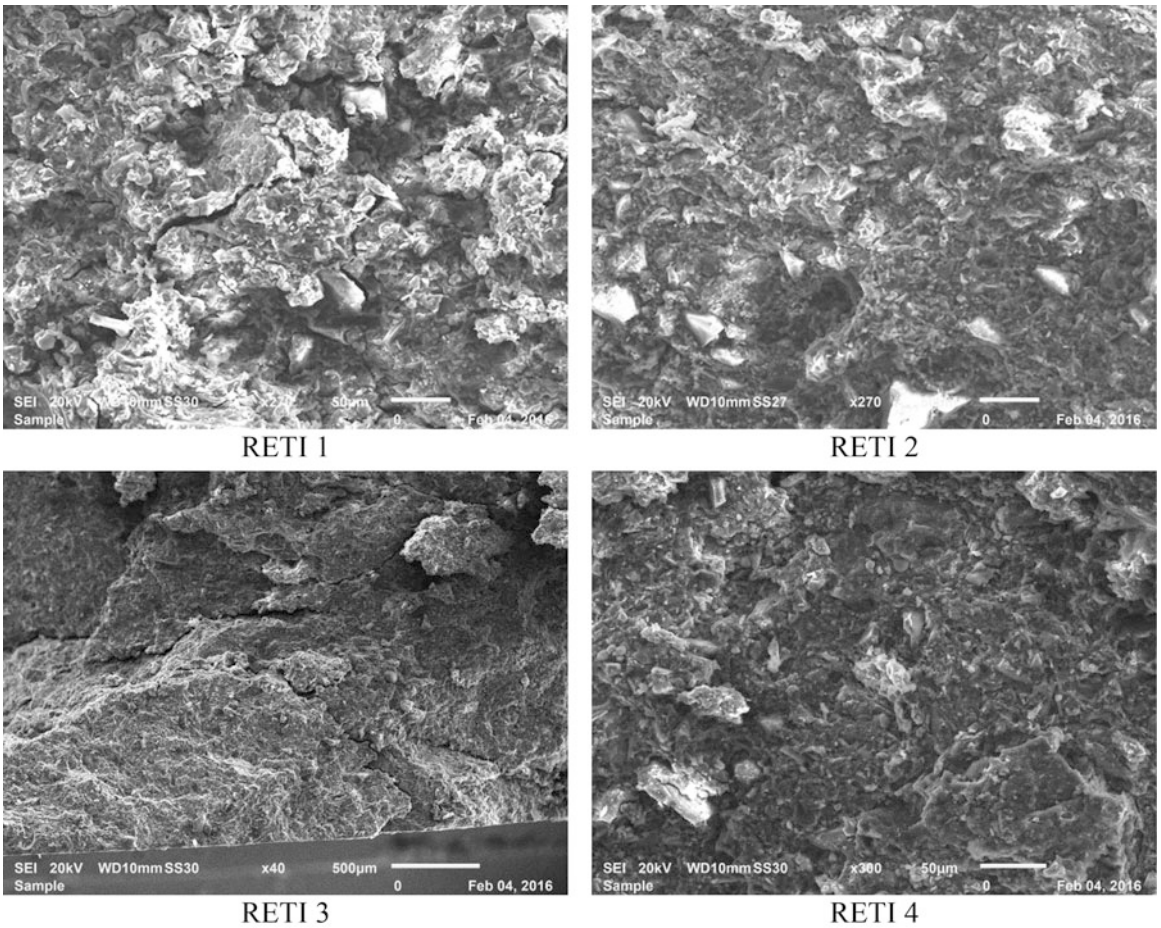

Fig. 5.6 Fracture surface of the samples taken from four compositions obtained by dynamic compression tests

normal loads (20 and 50 mN) applied over a linear track of 500 µm for 50 cycles. Wear damage was performed with a conical tip that has 90 degree apex angle.

Figure 5.7 shows comparison of two wear tracks (initial and final/residual traces) performed on the specimen of RETI-2 under 50 mN wear load, 50 cycles over 500 micrometer track. This graph was given only as an example.

Figure 5.8 presents total results of this evaluation. Each column in the figure gives mean value of 10 wear tests. One may observed that the wear tracks are not perfectly straight, apparently the conical tip is not fracturing the hard particles (i.e. alumina fibre, boron), and just going around them.

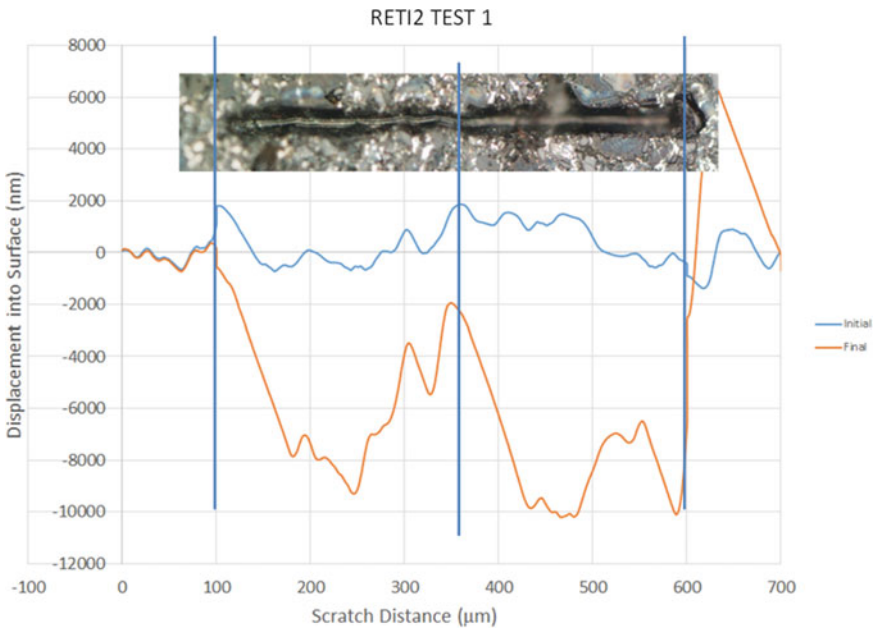

Fig. 5.7 Comparison of two wear tracks (initial and final traces) performed on the specimen of RETI-2 under 50 mN wear load, 50 cycles over 500 micrometer track

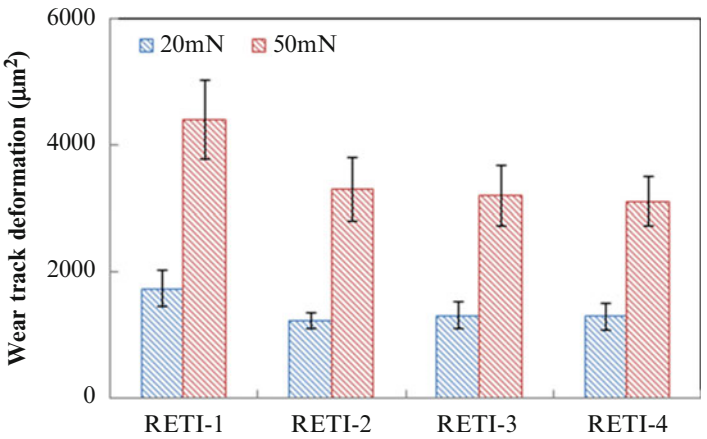

Fig. 5.8 Comparison of wear track deformation results tested on the four compositions under the loads of 20 and 50 mN

Another reason can be attributed to the well adhesion of the particles that they are not pulled out of the matrix (without debonding, they keep their positions in the matrix). It means that very good adhesion related to very good interface passage between the particulate reinforcements and the matrix was observed on all of the compositions.

5.4 Conclusions

In the frame of the common research project going on, four new composites were designed from scrap elastomers (SBR) matrix powders essentially reinforced with alumina fibre, Al, TiO_2, B, after treatment with fine epoxy resin. Chemical treatment of rubber powders with vinyltriethoxysilane gave very successful mixture with epoxy resin resulted by well adhesion bonding with particulate reinforcements. Experimental results obtained from the four different compositions were discussed in the present work. Mechanical and tribological properties of these composites were evaluated under different test conditions. Degradation of the specimens was too low after a long exposure 2 months against UV. Addition of alumina fibre and alumina together with TiO_2 in the matrix gave brittle behaviour in case of impact (drop weight) damage tests. Homogeneous distribution of the particulate reinforcements in the matrix can be improved by longer milling time and longer heating time during the mixture at the beginning of the process.

References

1. Markovic, G., et al.: Composites based on waste rubber powder and rubber blends: BR/CSM. Composites Part B **45**(1), 178–184 (2013)
2. Zaimova, D., Bayraktar, E., Miskioglu, I., Dishovsky, N.: Optimization and service life prediction of elastomeric based composites used in manufacturing engineering. In: Tandon, G.P., Tekalur, S.A., Ralph, C., Sottos, N.R., Blaiszik, B. (eds.) Experimental Mechanics of Composite, Hybrid, and Multifunctional Materials, vol. 6, pp. 157–166. Springer, New York (2014)
3. Zaimova, D., Bayraktar, E., Miskioglu, I.: Characteristics of elastomeric composites reinforced with carbon black and epoxy. In: Ralph, C., Silberstein, M., Thakre, P.R., Singh, R. (eds.) Mechanics of Composite and Multifunctional Materials, vol. 7, pp. 191–202. Springer, New York (2015)
4. Nacif, G.L., Panzera, T.H., Strecker, K., Christoforo, A.L., Paine, K.A.: Investigations on cementitious composites based on rubber particle waste additions. Mater. Res. **16**(2), 259–268 (2013)
5. Zaimova, D., Bayraktar, E., Miskioglu, I., Katundi, D.: Study of influence of SiC and Al2O3 as reinforcement elements in elastomeric matrix composites. In: Tandon, G. (ed.) Composite, Hybrid, and Multifunctional Materials, vol. 4, pp. 129–138. Springer, New York (2015)
6. Anifantis, N.K., et al.: Advances in elastomers II. Adv. Struct. Mater. **12**, 11–68 (2013)
7. Papadopoulos, A.M.: State of the art in thermal insulation materials and aims for future developments. Energy Build. **37**, 77–86 (2005)
8. Zaimova, D., Bayraktar, E., Miskioglu, I.: Manufacturing and damage analysis of epoxy resin-reinforced scrap rubber composites for aeronautical applications. In: Tandon, G.P., Tekalur, S.A., Ralph, C., Sottos, N.R., Blaiszik, B. (eds.) Experimental Mechanics of Composite, Hybrid, and Multifunctional Materials, vol. 6, pp. 65–76. Springer, New York (2014)
9. Bayraktar, E., Miskioglu, I., Zaimova, D.: Low-Cost Production of Epoxy Matrix Composites Reinforced with Scarp Rubber, Boron, Glass Bubbles and Alumina. Mechanics of Composite and Multifunctional, Materials, SEM, **7**, 163–172 (2015)
10. Bayraktar, E., Isac, N., Bessri, K., Bathias, C.: Damage mechanisms in natural (NR) and synthetic rubber (SBR): nucleation, growth and instability of the cavitations, IJFSM, International Journal of Fatigue and Fracture of the Structural Materials, 31, 1, 1–13 (2008)
11. Pacheco- Torgal, F., Ding, Y., Jalali, S.: Properties and durability of concrete containing polymeric wastes (tyre rubber and polyethylene terephthalate bottles): An overview, Construction and Building Materials, **30**, 714–724 (2012)
12. Luong R., Isac N., Bayraktar E.: Damage initiation mechanisms of rubber, JAMME, journal of archives of materials science and engineering, **28**(1), 19–26 (2007)
13. Zaimova, D., Bayraktar, E., Miskioglu, I., Dishovsky, N.: Optimization and Service Life Prediction of Elastomeric Based Composites Used in Manufacturing Engineering, Experimental Mechanics of Composite, Hybrid, and Multifunctional Materials, SEM, **6**, 157–166 (2014)
14. Zaimova, D., Bayraktar, E., Miskioglu, I.: Characteristics of Elastomeric Composites Reinforced with Carbon Black and Epoxy, Mechanics of Composite and Multifunctional, Materials, SEM, pp. 191–202 (2015)
15. Nacif, G.L., Panzera, T.H., Strecker, K., Christoforo, A.L., Paine, K.A.: Investigations on cementitious composites based on rubber particle waste additions, Materials Research, **16** (2), 259–268 (2013)
16. Zaimova, D., Bayraktar, E., Miskioglu, I., Katundi, D.: Study of Influence of SiC and Al2O3 as Reinforcement Elements in Elastomeric Matrix Composites, Composite, Hybrid, and Multifunctional Materials, SEM, **4**, 129–138 (2015)

Chapter 6
Thermo-mechanical Investigation of Fused Deposition Modeling by Computational and Experimental Methods

Koohyar Pooladvand and Cosme Furlong

Abstract Real-time thermo-mechanical process monitoring backed with numerical predictions in additive manufacturing (AM) can help understand relevant fundamental mechanics and the interaction between thermal, mechanical, and material relationships in order to design and produce components with consistent quality and performance. Process monitoring imposes technical challenges while the development of accurate models is hindered by complex phenomena comprising multiple domains and boundary conditions. In this paper, we present the results of our efforts in modeling rapid prototyping processes by Fused Deposition Modeling (FDM). A transient enthalpy formulation with moving boundary conditions is developed to predict temperature profiles and heat flow during layer-by-layer (LBL) deposition and the calculated results compared with in-situ experimental measurements obtained with an IR camera to validate the solution and calibrate the modeling parameters. The outcome is a reliable computational model, which will be expanded to predict the interaction of heat flow and temperature with mechanical properties, phase transformation, and part performance.

Keywords Additive manufacturing • Fused deposition modeling • Transient thermo-mechanical modeling • IR imaging • Numerical modeling validation

6.1 Introduction

Additive manufacturing (AM) is revolutionizing manufacturing processes due to its flexibility over conventional manufacturing. Where conventional manufacturing becomes restrictive, additive manufacturing can offer a solution [1]. Design flexibility, customization, optimization, and sustainability are just some of the benefits of AM; however, uncertainties in mechanical properties, geometry, performance, and microstructure of the manufactured products limit its applications [1, 2].

In order to produce reliable and consistent final products, developing a control strategy over manufacturing parameters, optimized product consolidation plan, and monitoring in addition to closed-loop feedback control systems with real-time measurements are required [1–3]. Multiphysics modeling of AM processes through sensitivity analysis provide insight on product realization and, therefore, allowing the identification of the manufacturing parameters that required monitoring.

King et al. [4] simulated an AM process numerically, including melting, vaporization, phase change, and melt pool characteristics. The developed multi-scale and multiphysics model was computationally expensive because of its mathematical and physical complexity, as schematically shown in Fig. 6.1. Tolochko et al. [5] considered a two-dimensional model of laser sintering that accounted for the metallurgical and morphological properties of the deposited powder. The proposed model considered the powder as a scattering medium and different laser intensities interacting with powder were investigated to study phase change and melting. Experiments and models were aimed at investigation laser to solid interactions without taking to consideration fabrication parameters and considering the laser at a fixed location [5]. Developed numerical models in these two studies produced results that had relatively good correlation with experimental observations. However, incorporating such models as part of the manufacturing control loop for AM may be impractical due to their complexity and computational run-time.

Fused deposition modeling (FDM), as shown in Fig. 6.2, is available from industrial to home applications where the material is laid layer-by-layer to define a part. Modeling this type of AM process is based on the energy added to the last layer by the fused filament. Layer-by-layer deposition produces thermo-mechanical cycles that are introduced by melting

K. Pooladvand (✉) • C. Furlong
Center for Holographic Studies and Laser micro-mechaTronics—CHSLT, Department of Mechanical Engineering, Worcester Polytechnic Institute (WPI), Worcester, MA 01609, USA
e-mail: kpooladvand@wpi.edu

W.C. Ralph et al. (eds.), *Mechanics of Composite and Multi-functional Materials, Volume 7*,
Conference Proceedings of the Society for Experimental Mechanics Series, DOI 10.1007/978-3-319-41766-0_6

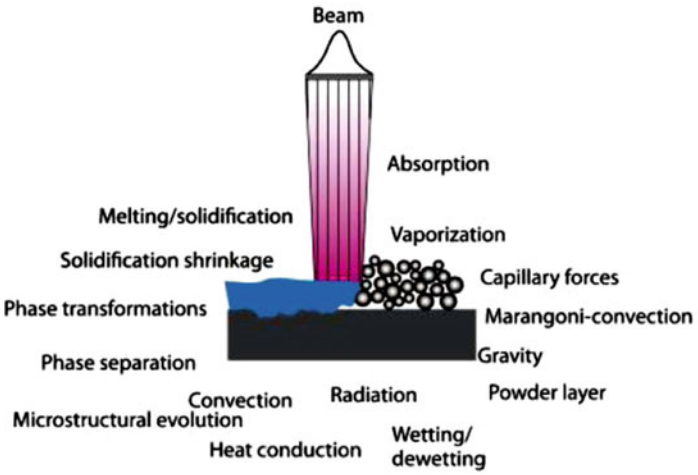

Fig. 6.1 Representative image of additive manufacturing by layer deposition that includes multiscale and multiphysics investigations [4, 6]

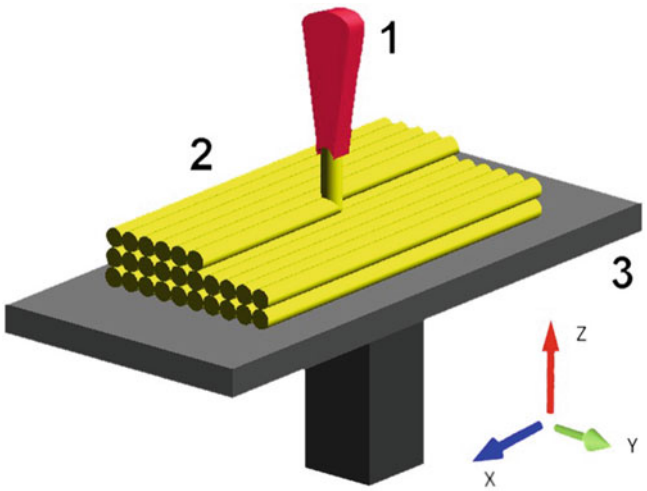

Fig. 6.2 Schematic of layer-by-layer deposition by FDM (1-Extruder, 2-deposited layers, 3-Platform) [7]. Deposition takes place in three orthogonal directions

and solidification, including rapid changes in heat flux and temperature [1, 4] that affect the final mechanical properties of the part as well as its quality and shape.

The processes of formation and production in FDM involve all mechanics of heat transfer: radiation, convention, and conduction. Radiation plays a significant role at the high temperature regions, specifically during the first phases of material deposition and forming. In addition, a highly concentrated heat source that initiates melt pool formation where energy transport by convection in the fluid region may be dominant [8–10].

From the heat transfer perspective, properly modeling conduction, radiation, and convection for temperature dependent material property and boundary conditions is rather complex. To realize the modeling of FDM, radiation, transient conditions, as well as natural/force convection need to be incorporated together with moving boundaries and conditions.

6.2 Methodology

Because of the complex multiphysics involved in FDM and the need for reliable simulations, we are developing 3D thermal models to study FDM by combining modeling and experimentation. Our efforts to model FDM in 3D begins by first considering a 1D thermal problem. In this case, a cylindrical domain of finite radius is selected where material is incrementally deposited layer-by-layer in one dimension along the vertical direction. The radius of the domain is selected such as the ratio of convection and conduction effects, i.e., Biot number, satisfies lumped model conditions.

Cylinders of specific dimensions are fabricated while thermograms are recorded during the consolidation and cooling phases. These recorded thermographic data are utilized to estimate the combined convection-radiation heat transfer coefficient, i.e., the total heat transfer coefficient (THTC), which we assume it can be described by a mathematical function [11–13]. An iterative procedure based on a least squares error minimization algorithm is employed to determine the parameters of this function and it proceeds as follows:

1. Assume a mathematical model to describe the THTC (incorporating radiation and convection heat transfer coefficients),
2. Set up an initial 1D transient numerical model with assumed boundary conditions and thermal parameters,
3. Record thermograms in-situ while a part is fabricated with specific manufacturing parameters,
4. Run the numerical simulation,
5. Quantitatively compare numerical and experimental results,
6. Adjust the total heat transfer coefficient following the assumed mathematical function,
7. Repeat steps 4 to 6 until meet the convergence criterion.

With the estimated THTC in 1D, the model is expanded to 3D in a similar cylindrical coordinate system by modeling the layer-by-layer deposition in radial, i.e., r, and axial, i.e., z, directions simultaneously. At each axial position, radial deposition of material is modeled by progressing from the perimeter to the center of the cylinder with radial steps or rings of specific increments. When reaching the center, a new axial layer is added and radial deposition is started again. This approach adds the capability of controlling the deposition rate in radial and axial directions as well as in each deposition and time increments. During all steps of deposition, the estimated THTC from the 1D analysis is used on the boundaries to model local heat dissipation. The transient simulations are based on the hypothesis that the estimated THTC from 1D is able to predict realistic heat transfer effects in 3D. Such hypothesis is tested by fabricating, modeling, and experimenting with cylindrical specimen of different diameters, i.e., 10, 20 and 30 mm, and same height, i.e., 50 mm ± 0.3 mm. Software to carry out the entire 1D and 3D simulations was developed in MATLAB™.

6.2.1 Mathematical Formulation

The mathematical and physical basis are based on conservation of mass, momentum, and energy, while also considering melt pool hydrodynamics and changes in material properties [4, 5, 8, 10, 14–17]. For each incremental deposition, conservation of energy indicates that

$$\dot{E}_{advection,in} - \dot{E}_{advection,out} + \dot{E}_{conduction,in} - \dot{E}_{conduction,out} + \dot{W}_{net,on\ \ CV} + \dot{E}_{Energy\ \ Generation} = \dot{E}_{internal}, \tag{6.1}$$

where, E is energy, W is work, and CV is control volume. Equation (6.1) is used to develop the governing equation for transient heat transfer with phase transition and with enthalpy formulation described as [4, 5, 8, 16, 18].

$$\frac{\partial \rho u}{\partial t} + V \cdot \nabla \rho h = \nabla \cdot (k \nabla T) + \dot{q}\,, \tag{6.2}$$

where, t is time, u is internal energy, ρ is mass density, V is velocity vector, h is enthalpy, k is conductivity, T is temperature, and $\dot{q}$ is volumetric heat generation [16]. Figure 6.3 illustrates the control volume for 1D modeling, where z is the axial deposition direction that occurs at constant velocity U_z. For this case, Eq. (6.2) is simplified to

$$\frac{\partial \rho u}{\partial t} + U_z \frac{\partial \rho h}{\partial z} = \frac{\partial}{\partial z}\left(k \frac{\partial T}{\partial z}\right) + \dot{q}\,. \tag{6.3}$$

Furthermore, by realizing that $du = dh = c_p dT$, the governing equation in cylindrical coordinates (r, θ, z) for 3D modeling considering symmetry about the θ axis is [4, 5, 14]

$$\rho c_p \frac{\partial T}{\partial t} + \rho c_p U_z \frac{\partial T}{\partial z} + \rho c_p U_r \frac{\partial T}{\partial r} = \frac{\partial}{\partial z}\left(k \frac{\partial T}{\partial z}\right) + \frac{1}{r}\frac{\partial}{\partial r}\left(kr \frac{\partial T}{\partial r}\right) + \dot{q}\,. \tag{6.4}$$

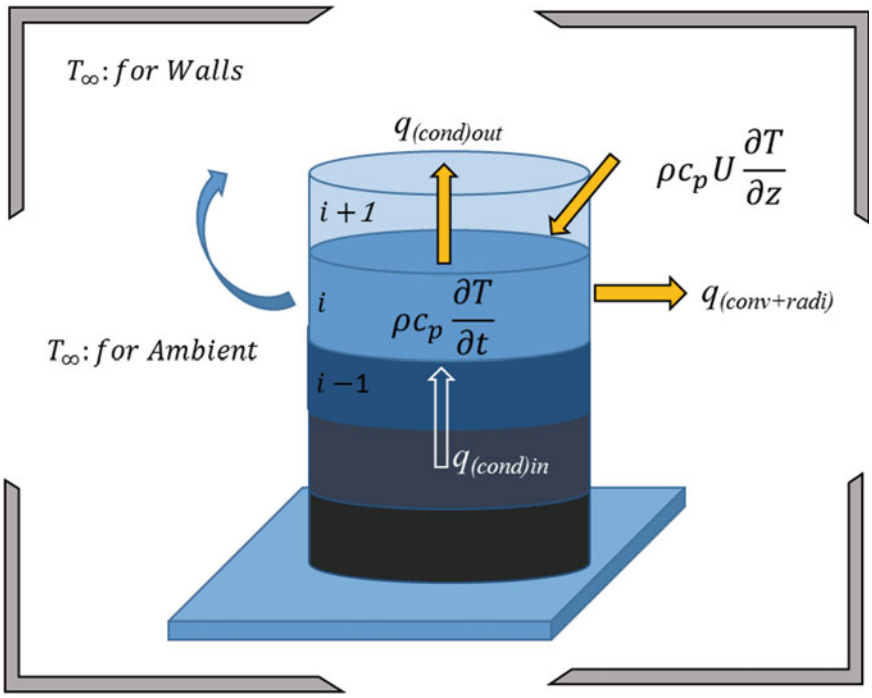

Fig. 6.3 Representative schematic of energy balance for a 1D model in a cylindrical coordinates system for deposition of the *i*th layer

By considering a 1D model and lumped conditions, the temperature across each axial layer, dz, is constant and by applying boundary conditions depicted in Fig. 6.3, energy balance indicated that

$$A \cdot dz \cdot \rho c_p \frac{\partial T}{\partial t} + A \cdot dz \cdot \rho c_p U_z \frac{\partial T}{\partial z} = q_{(cond)in} - q_{(cond)out} - q_{(conv+rad)}, \tag{6.5a}$$

$$q_{(cond)in} - q_{(con)out} = \frac{\partial}{\partial z}\left(k\frac{\partial T}{\partial z}\right) \cdot A, \tag{6.5b}$$

$$q_{(conv+rad)} = 2\pi r \cdot dz\left[h_{conv}(T - T_\infty) + \varepsilon\sigma\left(T^4 - T_\infty^4\right)\right], \tag{6.5c}$$

where A is cross sectional area, ε is emissivity, and σ is Stefan-Boltzmann constant. By substituting Eqs. (6.5b) and (6.5c) into Eq. (6.5a), it is obtained that

$$\rho c_p \frac{\partial T}{\partial t} + \rho c_p U_z \frac{\partial T}{\partial z} = k\left(\frac{\partial^2 T}{\partial z^2}\right) - \frac{4h_{conv}}{d}(T - T_\infty) - \frac{4h_{rad}}{d}(\mathrm{T} - T_\infty), \tag{6.6}$$

where, T and T_∞ are the surface and environment-wall temperatures, respectively, d is diameter, and h_{rad} is the radiation heat transfer coefficient described with [11–13]

$$h_{rad} = \varepsilon\sigma\left(T^2 + T_\infty^2\right)(T + T_\infty). \tag{6.7}$$

This radiation heat transfer coefficient is added to the convection heat transfer, h_{conv}, to define the total heat transfer coefficient, h_t, as follows

$$h_t = h_{rad} + h_{conv} = \varepsilon\sigma\left(T^2 + T_\infty^2\right)(T + T_\infty) + h_{conv}. \tag{6.8}$$

Determination of accurate values for h_t is crucial for accurate simulations. However, h_t is difficult to determine because it combines radiation and convection parameters, which are usually obtained experimentally. Empirical approximations of

h_t have been proposed with the most accepted being exponential functions, such as those proposed in [13, 19] and expressed as

$$h_t = \alpha \varepsilon T^{\beta}, \tag{6.9}$$

where α and β are determined by experimental investigations and procedures. In this paper, α and β are determined using 1D model and expanded to 3D.

6.2.2 Numerical Formulation

To solve the governing equations numerically, an implicit Euler finite differences scheme is utilized. Details of such formulation is described in [14–16, 18].

6.2.2.1 1D Discretization

To numerically solve the transient heat transfer governing equation in 1D, Eq. (6.6), forward finite differences are used for both, time and first order derivative in the direction of deposition whereas central differences are used for the second order differential in the direction of deposition as follows

$$\rho c_p \frac{T_i^{l+1} - T_i^l}{\Delta t} + \rho c_p U \frac{T_{i+1}^{l+1} - T_i^{l+1}}{\Delta z} = +k\left(\frac{T_{i+1}^{l+1} - 2T_i^{l+1} + T_{i-1}^{l+1}}{(\Delta z)^2}\right) - \frac{4h_t}{d}\left(T_i^{l+1} - T_\infty\right), \tag{6.10}$$

where Δt is time increment, i indicates ith deposited layer in z direction, and l indicates lth time step. In addition, to assemble the complete set of equations for the entire domain at each Δt increment, boundary conditions at the top and bottom of the domain are applied with combined convection-radiation condition at the top layer and constant temperature at the bottom, respectively.

6.2.2.2 3-D Discretization

In 3D, deposition is modeled by defining discrete elements in the same cylindrical coordinate system as in 1D, but without lumped model simplifications. Modeling is performed layer-by-layer with each layer deposited in the z direction. At each layer, the domain is discretized in (r, θ, z) with elements having finite dimensions of $(dr, rd\theta, dz)$, as shown in Fig. 6.4a, with symmetry in the θ direction to volumetrically integrate Eq. (6.4) at nodal position, i, j, located at the centroid of each element in the (r, z) plane for each time increment Δt as

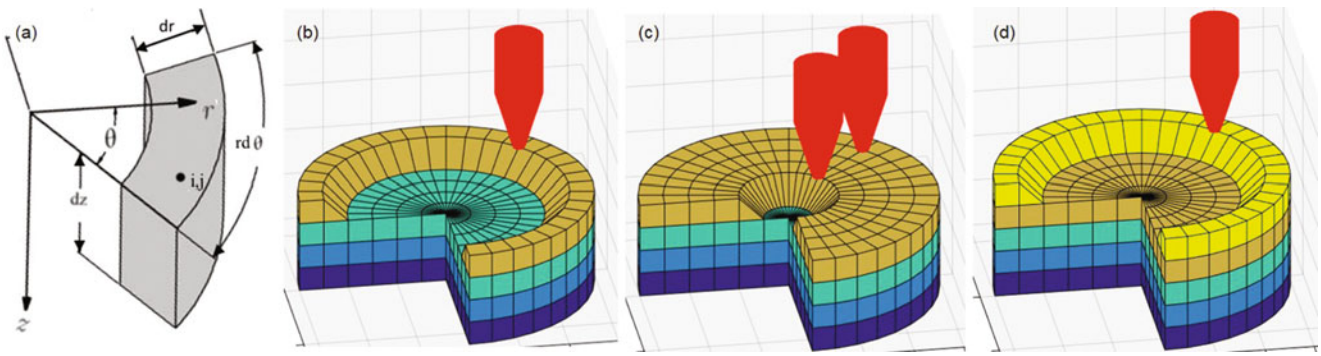

Fig. 6.4 3D element and schematic representation of the fabrication model: (**a**) cylindrical element at node i, j; (**b**) first radial ring is being deposited; (**c**) last radial ring is being deposited on the same layer; and (**d**) first radial ring is being deposited on the next layer

$$\int_{i-\frac{1}{2}}^{i+\frac{1}{2}}\int_{j-\frac{1}{2}}^{j+\frac{1}{2}}\int_{t}^{t+\Delta t}\rho c_p\frac{\partial T}{\partial t}drdzdt=\int_{t}^{t+\Delta t}\int_{i-\frac{1}{2}}^{i+\frac{1}{2}}\int_{j-\frac{1}{2}}^{j+\frac{1}{2}}\frac{\partial}{\partial z}\left(k\frac{\partial T}{\partial z}\right)drdzdt+\int_{t}^{t+\Delta t}\int_{i-\frac{1}{2}}^{i+\frac{1}{2}}\int_{j-\frac{1}{2}}^{j+\frac{1}{2}}\left[\frac{1}{r}\frac{\partial}{\partial r}\left(kr\frac{\partial T}{\partial r}\right)\right]drdzdt, \tag{6.11}$$

where i is in z direction and j is r direction. In Eq. (6.11), $\dot{q}$, U_z, and U_r are zero except at the last deposited ring where advection effects need to be considered. After integration, it is obtained the following

$$\Delta r\Delta z\rho\, c_{p,i}^{l+1}\int_{t}^{t+\Delta t}\frac{\partial T}{\partial t}dt=k\frac{\partial T}{\partial z}\Big)_{i+\frac{1}{2}}\Delta r\Delta t-k\frac{\partial T}{\partial z}\Big)_{i-\frac{1}{2}}\Delta r\Delta t+kr\frac{\partial T}{\partial r}\Big)_{j+\frac{1}{2}}\frac{\Delta z\Delta t}{r_{j+\frac{1}{2}}}-kr\frac{\partial T}{\partial r}\Big)_{j-\frac{1}{2}}\frac{\Delta z\Delta t}{r_{j-\frac{1}{2}}}. \tag{6.12}$$

Figure 6.4 shows intermediate steps of deposition, which starts by depositing rings of material from the perimeter to the center of the cylinder. When the center has been reached, a layer has been defined and radial deposition is started again at a new axial location. This process is repeated until the final layer is deposited after which the model continues in order to simulate the cooling process.

Boundary conditions are considered for the layer at the bottom of the cylinder as having constant temperature whereas on the perimeter and top layers convection-radiation heat transfer conditions are applied. The assembled system of equations at each deposition step is solved by alternating direction implicit (ADI) methods rather than fully implicit in order to define tridiagonal matrices that can efficiently be solved to reduce the total computational time.

6.3 Results and Discussions

An XYZ Da Vinci 2.0 Duo FDM 3D printer was utilized. The thermo-mechanical specifications of the ABS filament utilized includes, mass density $\rho = 940 \pm 5$ kg/cm^3 (the density is measured experimentally based on the cubic printed sample), conductivity $k = 0.17$ W/m K, and specific heat $c_p = 1400$ J/kg K [20, 21]. The part geometries and manufacturing parameters considered are included in Table 6.1. A calibrated IR FLIR A320 camera was utilized to perform in-situ measurements during part fabrication.

6.3.1 Determination of Total Heat Transfer Coefficient

The initially approximation for convection-radiation total heat coefficient was chosen from the values reported by Vinokurov [19] and were selected to be $\alpha = 2.4 \times 10^{-3}$ and $\beta = 1.61$. The procedures and methodology described in Sect. 6.2 were applied to estimate values for α and β to describe the geometry and manufactured parameters considered, i.e., $D = 10$ mm and deposition velocity of 100 mm/min. After application of the least square error minimization approach to the 1D computational-experimental problem, it was obtained that $\beta = 1.61$ and $\alpha = 0.65 \times 10^{-3}$ define an optimal set of parameters. Figure 6.5 shows computational and experimental profiles while illustrating the effects of different values for parameter α.

After determining the optimal values for α and β, computational and experimental investigation were performed in order to compare corresponding temperature profiles for 1D models. Figure 6.6 shows representative computational and experimental temperature profiles obtained throughout the fabrication and cooling of a 1D model. Comparisons show good correlation between simulations and experiments.

Table 6.1 Part geometries and manufacturing parameters considered

Part geometry		Manufacturing parameters	
Sample length, L	50 ± 0.3 mm	Deposition velocity in z for $D = 10$ mm, in 1D)	100 mm/min
Part diameters, D	1. 10 ± 0.35 mm	Linear deposition velocity for 3D	750 mm/min
	2. 20 ± 0.35 mm		
	3. 30 ± 0.35 mm		
Part initial length, Z_0	0.3 mm	Ambient temperature T_∞	293.15 K
Emissivity	0.85	Extruder temperature T_{Exd}	393.15 K
		Platform temperature T_b	343.15 K

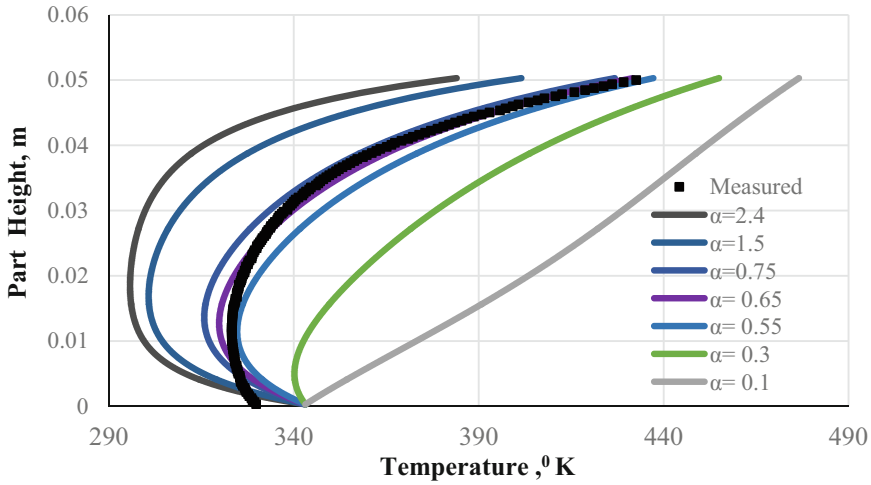

Fig. 6.5 Computationally and experimentally obtained temperature profiles for a 1D fabrication model showing the effects of parameter α. Profiles correspond to temperatures right after fabrication is completed

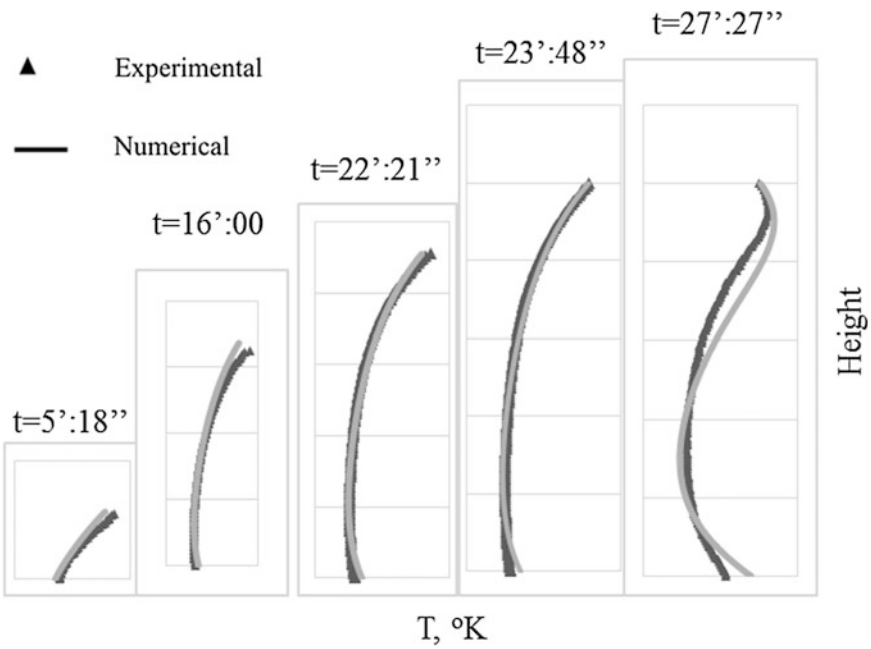

Fig. 6.6 Comparisons between computational and experimental temperature profiles along the height of the part during fabrication and cooling. Maximum part height is 50 mm, and temperature varies from 293.15 to 453.15 K

6.3.2 3D Modeling

After completing series of 1D simulations and experiments to define the THTC, 3D investigation were performed. Computational simulations utilized the defined THTC and the results verified experimentally. Figure 6.7 shows comparisons between computationally and experimentally obtained result for geometries defined by $D = 20$ and 30 mm fabricated using a linear deposition rate of 750 mm/min. Results shown in Fig. 6.7 correspond to instances when the part is at 25 % and 75 % from being completed and computational-experimental temperature profiles indicate reasonable agreement, which demonstrates that the approach to define the THTC is valid although further investigation may be needed.

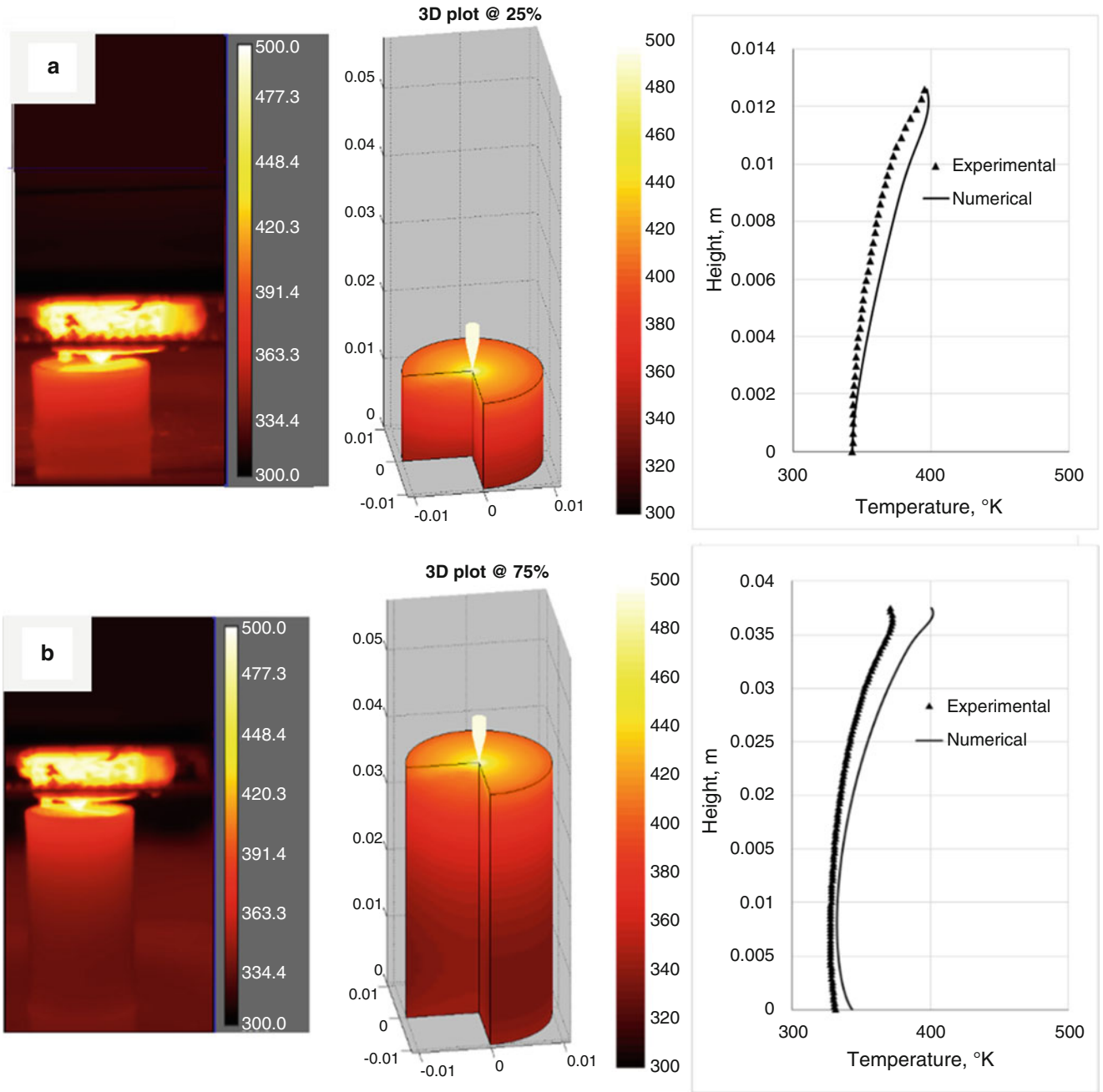

Fig. 6.7 Comparisons between computational and experimental temperature results: (**a**) at 25 % completion, $D = 20$ mm; (**b**) at 75 % completion, $D = 20$ mm; (**c**) at 25 % completion, $D = 30$ mm; and (**d**) at 75 % completion, $D = 30$ mm. Reported temperature are in Kelvin

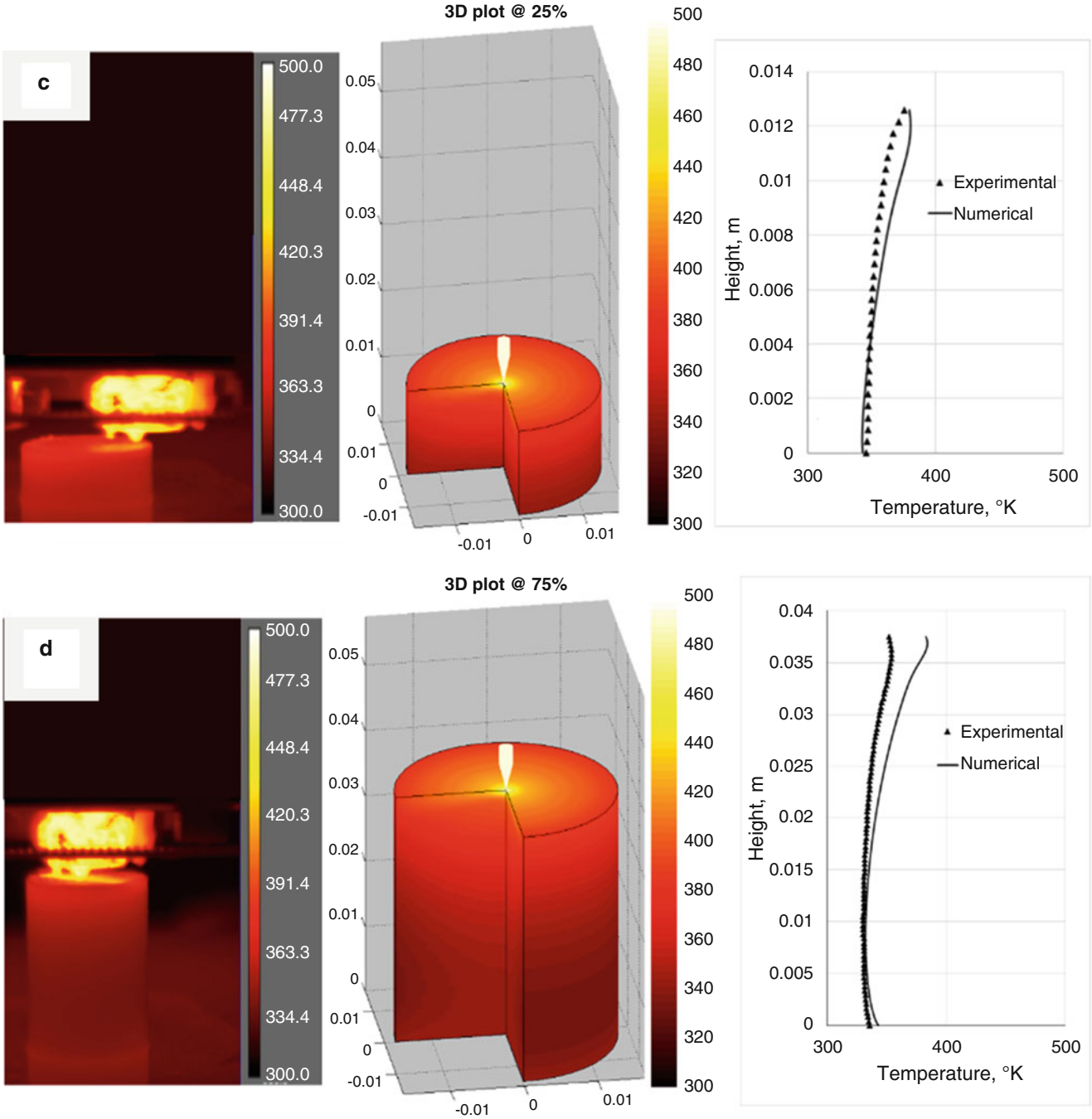

Fig. 6.7 (continued)

6.4 Conclusions and Future Work

In this paper, we presented our preliminary investigations toward understanding of AM by FDM. Computational and experimental investigations were focused on the some of the thermal aspects of FDM. Because the phenomena are sensitive to accurate convection and radiation parameters, an approach to define these parameters was proposed in which computational and experimental methods are combined with the hypothesis that the parameters vary following an exponential function. The function is determined through the investigation of 1D models that satisfy lumped conditions. Correlations between 1D and 3D computational and experimental results indicate the validity of the approach although further

investigations are required. In addition, the approaches suggests the feasibility of using a simplified 1D model in the environment of an AM machine to account for specific materials and to understand the effects of actual heat transfer conditions. As demonstrated in our preliminary results, the approach has the potential to be expanded for the investigation of elaborated 3D components while utilizing numerical models that are computationally cost effective.

For future work, material properties, emissivity, and absorptivity dependency to temperature will be needed to be considered individually in the numerical model. In addition, thermo-mechanical effects that produce part distortions and deformations due to phase change, phase transformation, and temperature gradient between layers will be included. These data will be incorporated together with sensitivity analysis and optimization to control manufacturing parameters, i.e., temperature, layer thickness, direction of deposition, and speed to improve par quality and performance.

Acknowledgments This work has been partially supported by the NSF, award CMMI-1428921. The authors would like to gratefully acknowledge the support of the Mechanical Engineering Department of Worcester Polytechnic Institute (WPI) and the contributions by members of the CHSLT.

References

1. Frazier, W.E.: Metal additive manufacturing: a review. J. Mater. Eng. Perform. **23**(6), 1917–1928 (2014)
2. Qian, M.: Metal powder for additive manufacturing. JOM **67**(3), 536–537 (2015)
3. Yang, S., Zhao, Y.F.: Additive manufacturing-enabled design theory and methodology: a critical review. Int. J. Adv. Manuf. Technol. **80**(1–4), 327–342 (2015)
4. King, W., Anderson, A.T., Ferencz, R.M., Hodge, N.E., Kamath, C., Khairallah, S.A.: Overview of modelling and simulation of metal powder bed fusion process at Lawrence Livermore National Laboratory. Mater. Sci. Technol. **31**(8), 957–968 (2015)
5. Tolochko, N.K., Arshinov, M.K., Gusarov, A.V., Titov, V.I., Laoui, T., Froyen, L.: Mechanisms of selective laser sintering and heat transfer in Ti powder. Rapid Prototyping J. **9**(5), 314–326 (2003)
6. Körner, C., Attar, E., Heinl, P.: Mesoscopic simulation of selective beam melting processes. J. Mater. Process. Technol. **211**(6), 978–987 (2011)
7. Wikipedia: Fused deposition modeling. en.wikipedia.org/wiki/Fused_deposition_modeling (2016)
8. Zhang, W., Roy, G.G., Elmer, J.W., DebRoy, T.: Modeling of heat transfer and fluid flow during gas tungsten arc spot welding of low carbon steel. J. Appl. Phys. **93**(5), 3022–3033 (2003)
9. Zhang, W., Kim, C.H., DebRoy, T.: Heat and fluid flow in complex joints during gas metal arc welding—Part II: Application to fillet welding of mild steel. J. Appl. Phys. **95**(9), 5220–5229 (2004)
10. Manvatkar, V., De, A., Debroy, T.: Heat transfer and material flow during laser assisted multi-layer additive manufacturing. J. Appl. Phys. **116**(12), 124905 (2014)
11. Howell, J.R., Siegel, R., Mengüç, M.P.: Thermal radiation heat transfer, 5th edn. CRC Press, Boca Raton (2011)
12. Jones, H.R.N.: Radiation heat transfer. Oxford University Press, New York (2000)
13. Frewin, M.R., Scott, D.A.: Finite element model of pulsed laser welding. Weld J. **78**(1), 15s–22s (1999)
14. Ho, J.R., Grigoropoulos, C.P., Humphrey, J.A.C.: Computational study of heat-transfer and gas-dynamics in the pulsed-laser evaporation of metals. J. Appl. Phys. **78**(7), 4696–4709 (1995)
15. Majumdar, P.: Computational methods for heat and mass transfer. Taylor & Francis, New York (2005)
16. van Elsen, M., Baelmans, M., Mercelis, P., Kruth, J.P.: Solutions for modelling moving heat sources in a semi-infinite medium and applications to laser material processing. Int. J. Heat Mass Transfer **50**(23–24), 4872–4882 (2007)
17. Holman, J.P.: Heat transfer, 10th edn. McGraw-Hill, Boston (2010)
18. Dowden, J.M.: The mathematics of thermal modeling: an introduction to the theory of laser material processing. Chapman & Hall/CRC, Boca Raton (2001)
19. Vinokurov, V.A.: Welding stresses and distortion: determination and elimination. British Library Lending Division, London (1977)
20. Stratasys: 3D print in 9 colors with standard thermoplastic. www.stratasys.com/materials/fdm/absplus (2016)
21. XYZPrinter: 3D printer. www.xyzprinters.com (2016)

Chapter 7
Non-linear Contact Analysis of Self-Supporting Lattice

A. Aremu, I. Ashcroft, R. Wildman, and R. Hague

Abstract Using additive manufacturing (AM) techniques for end user parts is quite attractive for performance enhancement and product customization since designs are less constrained via this technique. The extent to which this could influence design is still to be determined. An interesting way to exploit AM capabilities for mechanical components is to embed lattice structures in such components. However, constraints inherent on some AM machines might limit the range of suitable lattices. For selective laser melting (SLM), supports are needed for features inclined at an angle lower than 45°. This does imply that lattices without such features are better suited for SLM. Despite this constraint, a number of lattices can be made via the SLM technique. In this paper, we determine the structural properties of four of these self-supporting lattices via non-linear contact analysis. A minimal surface lattice show superior properties to those of the other three strut based lattices.

Keywords Additive manufacturing • Lattice • Contact • Non-linear • Finite element

7.1 Introduction

Traditional lattice and foam manufacturing techniques have previously been used to realize topologies with closed architecture as seen in [1]. Some of these include vapour deposition, casting, gas entrapment, slurry foaming, electrochemical deposition, reaction sintering, spray forming and gasars. It is difficult to achieve other topologies using these techniques especially those with complicated three dimensional domains. Fortunately, additive manufacturing (AM) provides a less constrained approach to manufacture lattices. AM employs sliced CAD data to selectively cure input material, and then consolidates processed layers to form three dimensional parts [2]. This eliminates the need for tools thereby offering a way to realize highly complicated parts. However, it should be noted that AM techniques are more suitable for lattices with open architecture which allows the separation of a part from processed and unprocessed material. This is because it is difficult to reach redundant material residing in closed voids during post processing. Also, some AM techniques have other constraints which include a maximum feature angle and length beyond which support structures are needed to prevent distortion and shrinkage [3]. While supports are helpful for different topologies, it is not practical to remove supports from lattice structures. Therefore, lattices that could self-support are better suited to AM techniques with such constraints. Some AM techniques include selective laser sintering, selective laser melting, fused deposition modelling, ink-jet printing, ultrasonic AM, stereolithography, fused filament fabrication and multiple layered laser cladding [4]; all of which can be used to manufacture parts with functional lattice structures.

In recent times, a lot of work has been done to understand the behaviour of AM lattices. Yan et al. [5] investigated the stainless steel gyroid lattices with selective laser melting (SLM). The yield strength of the lattice reduced as the cell size was decreased. Smith et al. [6] investigated the effects of reinforcements on body centred cubic lattices. Mullen et al. [7] used SLM to study how titanium lattices could be used to support bone growth and McKown [8] investigated the behaviour of body centred cubic lattice under impact loading; showing that the failure modes could be significantly affected by the configuration of this lattice. Merkt et al. [9] found that 316L lattices would perform better that TiAl6V4 for energy absorption applications. Hussein et al. [10] showed that, Ti64Al gyroid and diamond lattices with low volume fraction could act as supports for cantilever parts manufactured with direct metal laser sintering machine. It is impractical to understand all the failure mechanisms of these lattices via manufacture and testing alone; owing to the vast amount of lattice configurations. Virtual testing techniques have therefore been used to understand lattice behaviour under numerous loading conditions.

A. Aremu (✉) • I. Ashcroft • R. Wildman • R. Hague
Faculty of Engineering, EPSRC Centre for Innovative Manufacturing in Additive Manufacturing,
University of Nottingham, Nottingham NG7 2RD, UK
e-mail: adedeji.aremu@nottingham.ac.uk

W.C. Ralph et al. (eds.), *Mechanics of Composite and Multi-functional Materials, Volume 7*,
Conference Proceedings of the Society for Experimental Mechanics Series, DOI 10.1007/978-3-319-41766-0_7

According to Noor [11] lattices can be virtually analysed by direct, discrete field, periodic structure or substitute methods. Direct method involves discrete finite element analysis where the structure is divided into simpler elements. The contributions of each element are evident in global matrix assembled from the properties of the element. This method is computationally expensive for lattices in large domains, which is the case for lattices embedded in mechanical parts. In the discrete field methods, the repetitive nature of the lattice is used to construct compatibility and equilibrium equations which are then solved. This works best for lattices with simple topology and is unsuitable for relatively complex lattices. When analysing lattices with periodic approaches, finite element and matrix methods are used to reduce the size of the lattice. Again, this method requires the exact representation of the behaviour of a member which might not be easily available for complex lattices. The most versatile methods are substitute methods since they allow the replacement of the lattice by a suitable continuum model with similar characteristics to the original lattice. There is significant discrepancies in literature on how best to substitute these lattices; it is therefore paramount that the methods are validated. Advancement in computational resources has allowed the use of direct approaches on relatively smaller lattices. This therefore offers a way to validate efficient substitution methods on large lattices.

Luxner et al. [12] used beam elements to investigate elastic and plastic deformation in simple cubic lattices. Highly ordered simple cubic lattices were found to perform better than their disordered counterpart, though they are susceptible to localized damage. Meguid et al. [13] showed that shell elements within a representative unit cell model can represent the crushing behaviour of metallic lattice. Giorgi et al. [14] modelled closed cell aluminium lattice with shell elements and Smith et al. [15] modelled the body centred cubic lattice and its hybrid with continuum three dimensional and beam elements; demonstrating the effects of cellular architecture on SLM built lattices. Some of this work include aspect of material non-linearity, little has been done to include non-linear deformation caused by changes in the boundary and geometry. Material non-linearity is associated with the existence of stresses greater that the yield as such the stress-strain relationship is not linear [16]. Geometric non-linearity is caused by the changing shape of the loaded lattice which affects the stiffness of the structure. The stiffness matrix of the lattice is therefore iteratively updated for each load increment. Also, the deformation of the lattice could cause the boundary conditions to change in a non-linear manner. Non-linear contact analysis is therefore a powerful technique that allow better insight into the deformation mechanism of AM lattices. In this paper, four self-supporting lattice are subjected to compressive loads via non-linear contact analysis. The lattice are explicitly modelled as the computational expense is tolerable for the size of the domain considered.

7.2 Contact Finite Element Study

7.2.1 Lattice models

The non-linear behaviour of the four lattice types shown in Fig. 7.1 was investigated. The BCC, BCCZ and FCC unit cells shown in Fig. 7.1a, b, d belong to a family of lattices with cylindrical member connected at joints. The truncated members form the cylindrical members of the lattices when the cells are tessellated in a Cartesian coordinate system. The radius of the member controls the density of the densities of cell and their corresponding lattices. The inclinations of the members to a horizontal plane (which is usually parallel to a build platform) is greater than or equal to 45°, thereby minimizing the need for supports. Previous work on AM lattice has been largely focused on this sort of structures. The double gyroid cell shown in Fig. 7.1c belongs to a family of relatively unexplored lattices called minimal surfaces. These are surfaces with a mean curvature of zero and topologies that locally minimize their total surface area. The double gyroid lattice is structured in a manner that do not require support when manufactured via an AM technique. It is governed by a trigonometric equation which can be seen in [17].

The four cells were embedded in a 18 mm cubic domain within a Cartesian coordinate system shown in Fig. 7.2. The unit cell size was set at 4.5 mm, thereby giving lattices with four cells in the x, y, and z directions. Also, a common density, 0.23, was enforced across the lattices to ensure a fair comparison can be made. Such a constraint imply that lattice with more cylindrical member would have smaller radii.

7.2.2 Problem Formulation and Mesh Generation

Hexahedral meshes were constructed for the four lattices which experience compressive displacement from two rigid bodies as illustrated in Fig. 7.2. The meshes were constituted with approximately 200,000 elements as preliminary

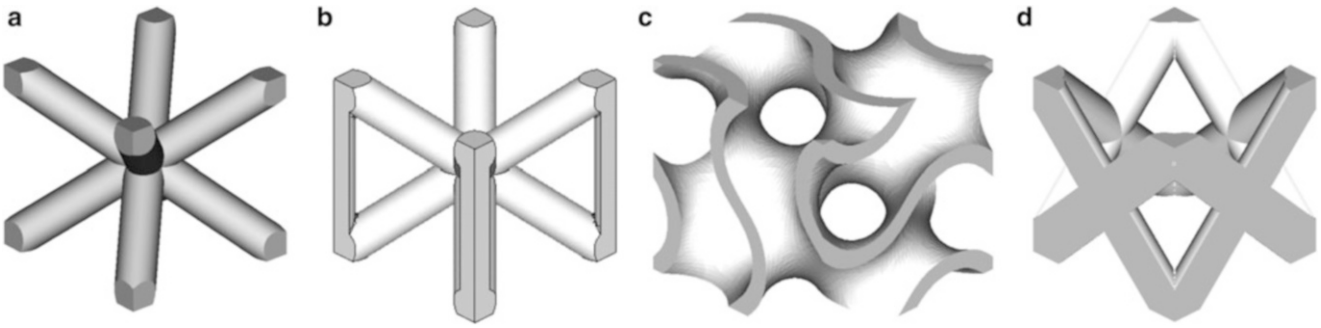

Fig. 7.1 Self-supporting lattice unit cells: (**a**) BCC; (**b**) BCCZ; (**c**) double gyroid; (**d**) FCC

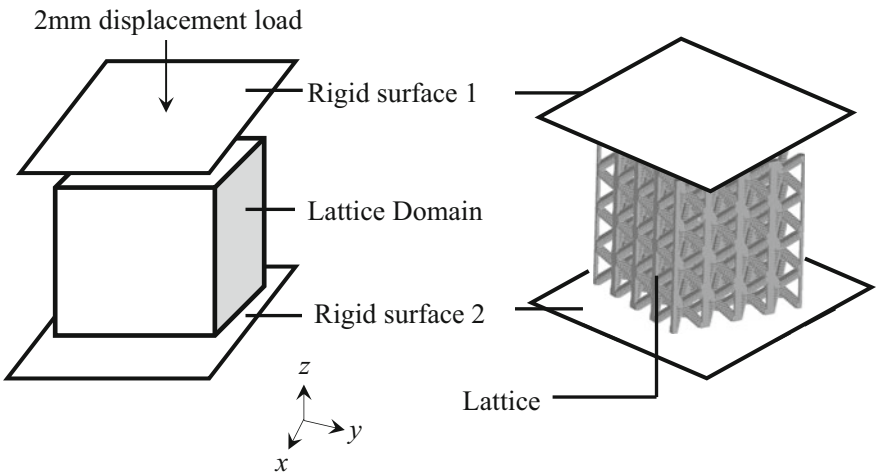

Fig. 7.2 Non-linear contact model consisting of two rigid surfaces and lattice mesh

convergence study suggested this was sufficient to minimize discretization errors. The aspect ratio of the elements in the mesh was set at one to avoid elemental distortion. The Youngs modulus assumed a value of 115 GPa with Poisson ratio of 0.31 and a yield stress of 0.9 GPa.

The lattices were loaded along the z and then y axes. The analysis was perform with Marc Mentat® and python scripts were used to extract and process stress and strain data. During the analysis, the displacement of rigid Surface 1 was iteratively increased from 0 to 2 mm to simulate a linearly increasing compressive load on the top face of the mesh. Rigid Surface 2 was fixed for all degrees of freedom. The time step was set at 0.0004 s to obtain a detailed stress-strain relationship. The interaction between the contact bodies and mesh were assumed to be touching. By definition, rigid surfaces are undeformable bodies, having considerably greater stiffness than the mesh body. Therefore, the displacement on the rigids due to the mesh are negligible when in contact. Also, for this problem displacement loads suggests the rigids would not be in contact with each other. Therefore, the model did not account for such an occurrence. The solver was set to full Newton-Raphson and convergence was achieved via relative force and displacement tolerance which both assumed a value of 0.1. The contact detection method was set to segment to segment which has been shown to be more efficient than other methods.

7.3 Results and Discussion

The displacement imposed on the lattices corresponds to strain values between 0 and 0.12. As such, Fig. 7.3 shows the plot of the average Von Mises stresses against strains in this strain range. The load plane is the top most plane of the lattice which is in contact with rigid Surface 1 during the simulation. Figure 7.3a shows results when the lattices are loaded in the z while Fig. 7.3b represents those for the y direction. As the load is increased, a linear relationship exist initially between the stress and strain. The slope of the curves is the effective modulus, E_{eff}, for the lattices. It can be seen that the modulus of the double

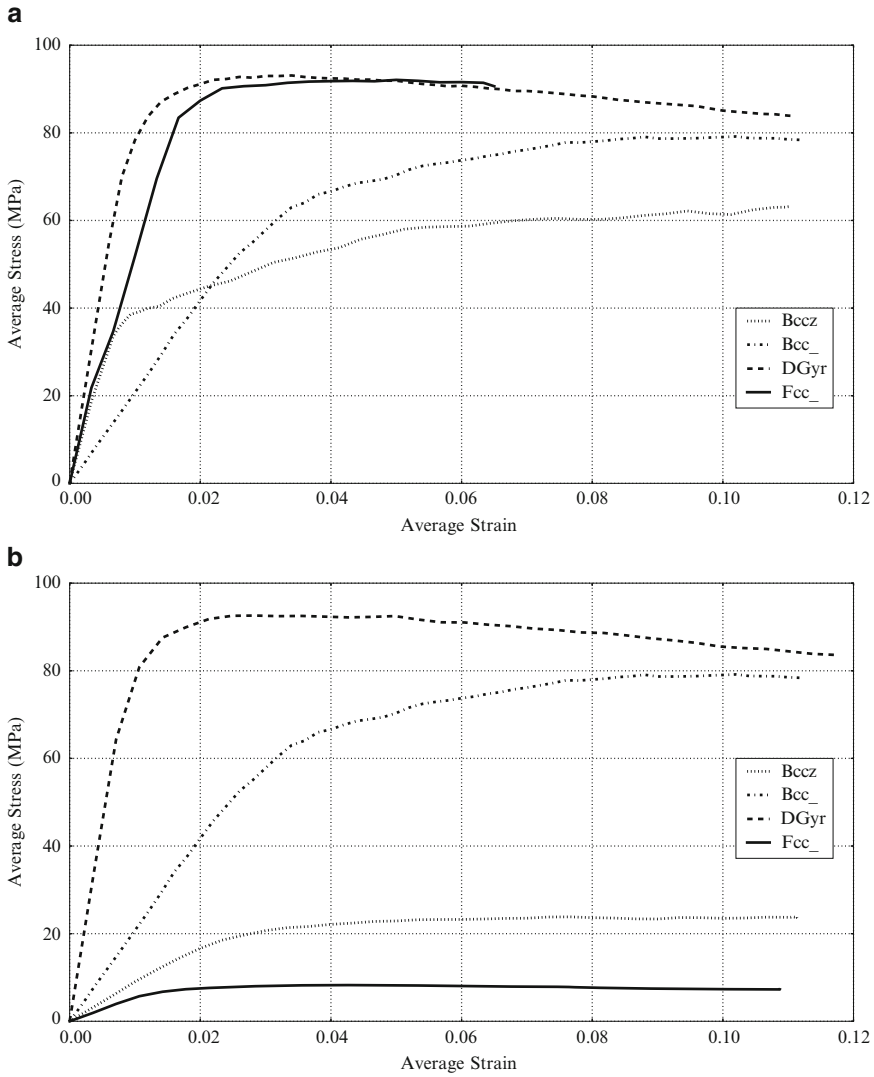

Fig. 7.3 Average stress-strain on load plane (**a**) *z* (**b**) *y*

gyroid lattice is the greatest for both the *z* and *y* directions. This is more evident in the *y* direction where the slope of the curve suggests the modulus of the double gyroid is greater than that of the others by some other of magnitudes. The numerical value for the E_{eff} is determine using data in the elastic region and shown in Table 7.1. Along the *z* direction, the double gyroid lattice has a E_{eff} which is approximately twice that of BCCZ, four times greater than the BCC lattice and also superior to the FCC lattice.

Though the E_{eff} for the double gyroid is lower in the *y* direction, suggesting some degree of anisotropic behaviour, it superior performance can still be seen along this axis. From the figures and table, the FCC lattice has the second largest modulus in the *z* but is inferior to all the other three lattices in the *y*. A similar trend can be seen for the BCCZ lattice which is relatively weaker in the *y* axis. The stress-strain profiles for the BCC and double gyroid lattice are largely similar in both *z* and *y* axis; in contrast to the BCCZ and the FCC lattices which show a high degree of anisotropy. This is expected since the vertical members in the BCCZ and the members in FCC are aligned with the *z* axis as seen in Fig. 7.1 and such features are absent in the *y* axis. The onset of inelastic behaviour differs for the lattices which could be a consequence of geometric and boundary non-linear, since the same material properties were assumed for the four lattices. Within the non-linear region, the lattices become insensitive to increased strain. The FCC lattice appear to be the less sensitive to the strain increase in both axes, though this occurs at a more lower stress in the *y* axis. Both BCC and BCCZ loose their sensitivity to increased strain at a greater strain value that of FCC or double gyroid when loaded in the *z*. In the *y* axis, BCCZ becomes insensitive at approximately similar strain as FCC. Unlike the other three, the gradient of the curve for the double gyroid lattice continuously reduce at strains above 0.03. This suggests that the double gyroid lattice is unable to completely sustain it

Table 7.1 Effective modulus E_{eff} for the BCC, BCCZ, double gyroid and FCC lattices as determined from average stress-strain curves

Lattice	E_{eff} (MPa) (z axis)	E_{eff} (MPa) (y axis)
BCC	2081	2081
BCCZ	3798	886
DGYR	8636	5102
FCC	4813	456

high load bearing capacity at strain values beyond this value. At 0.06 strain, the FCC lattice performs slightly better that the double gyroid in the z axis. However, the FCC is approximately ten times weaker in the y. Comparing the performance of the BCC and BCCZ lattice along the z direction, the BCCZ lattice performs better than the BCC at lower strain values between 0 and 0.21. Beyond this range the BCC sustains more stress than the BCCZ for a similar strain value. At 0.1 strain, the BCC lattice can sustain 25 % more stress than the BCCZ lattice. It should also be noted that the non-linear analysis for the FCC lattice converged prematurely when loaded along the z *axis*, so data shown in Fig. 7.3a for this lattice reached a maximum strain of 0.065.

The Von Mises stress distribution for the deformed lattices are shown in Fig. 7.4. These represent those at the last iteration most of which is beyond a strain value of 0.1. From the scales it can be seen that the BCC and the double gyroid lattices have lower stress values than the FCC, BCCZ. Members along the edges of the FCC and BCCZ lattice buckled which contributed to the relatively lower performance. For the BCCZ lattice, the buckling can be in Fig. 7.4c where the lattice was loaded along the z axis. Due to immature convergence, an inference cannot be made about the FCC lattice experiencing a load along the z beyond 0.065. However, it can be seen from Fig. 7.4h that some members residing on the sides of the FCC lattice buckled. Generally regions at the center of the lattices experienced lower stresses than those at the edges, though this is less evident for the double gyroid lattice. Loading the FCC in the y axis does not follow this trend since it's central region seem to experience more load than the edges.

7.4 Summary and Conclusions

Non-linear contact analysis was performed to ascertain the structural response of a four lattice types. The lattices were selected to avoid support requirements on an AM technique. The BCC, BCCZ, double gyroid and FCC lattices were deformed with two rigid bodies with strain below 0.12. This was performed in both z and y directions. The double gyroid lattice performed better than the other three with significantly higher effective modulus on the loaded axes and sustaining a higher level of stress at a given strain in the non-elastic region. While the FCC lattice performed better that the BCC and BCCZ along the z axis, it was relative weaker in the y. At lower strains, the BCCZ lattice performs better than the BCC lattice. This is rapidly reversed at higher strain values where the BCC lattice sustains higher load for a given strain. An inference could not be made for the FCC lattice when loaded in the z direction beyond a strain of 0.065 due to premature convergence. Also, the stress in the double gyroid lattice was more evenly distributed that the other three lattice.

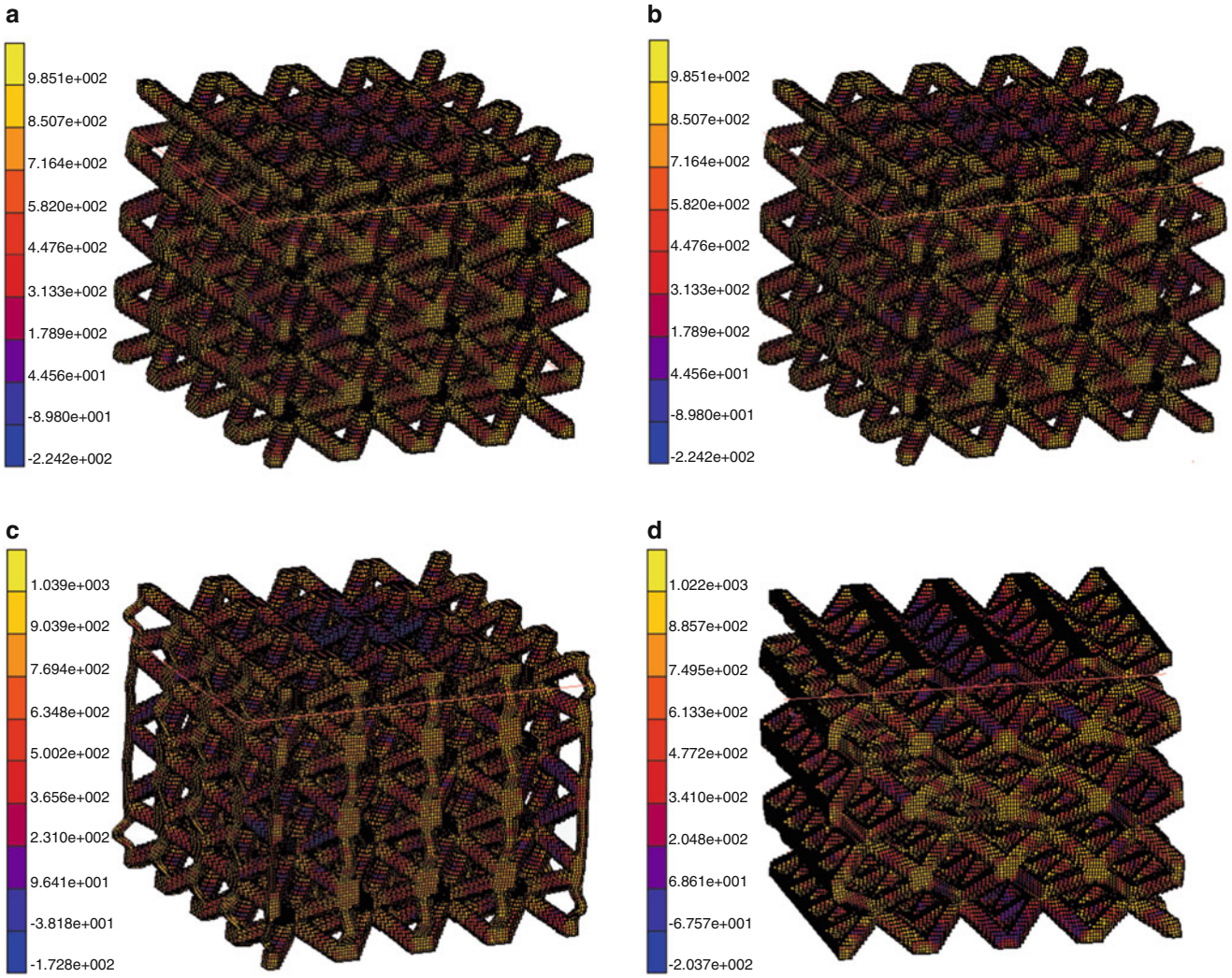

Fig. 7.4 Von misses stress distribution in lattices at the last iteration. (**a**) BCC, *z*-axis; (**b**) BCC, *y*-axis; (**c**) BCCZ, *z*-axis; (**d**) BCC, *y*-axis; (**e**) DG, *z*-axis; (**f**) DG, *y*-axis; (**g**) FCC, *z*-axis; (**h**) FCC, *y*-axis

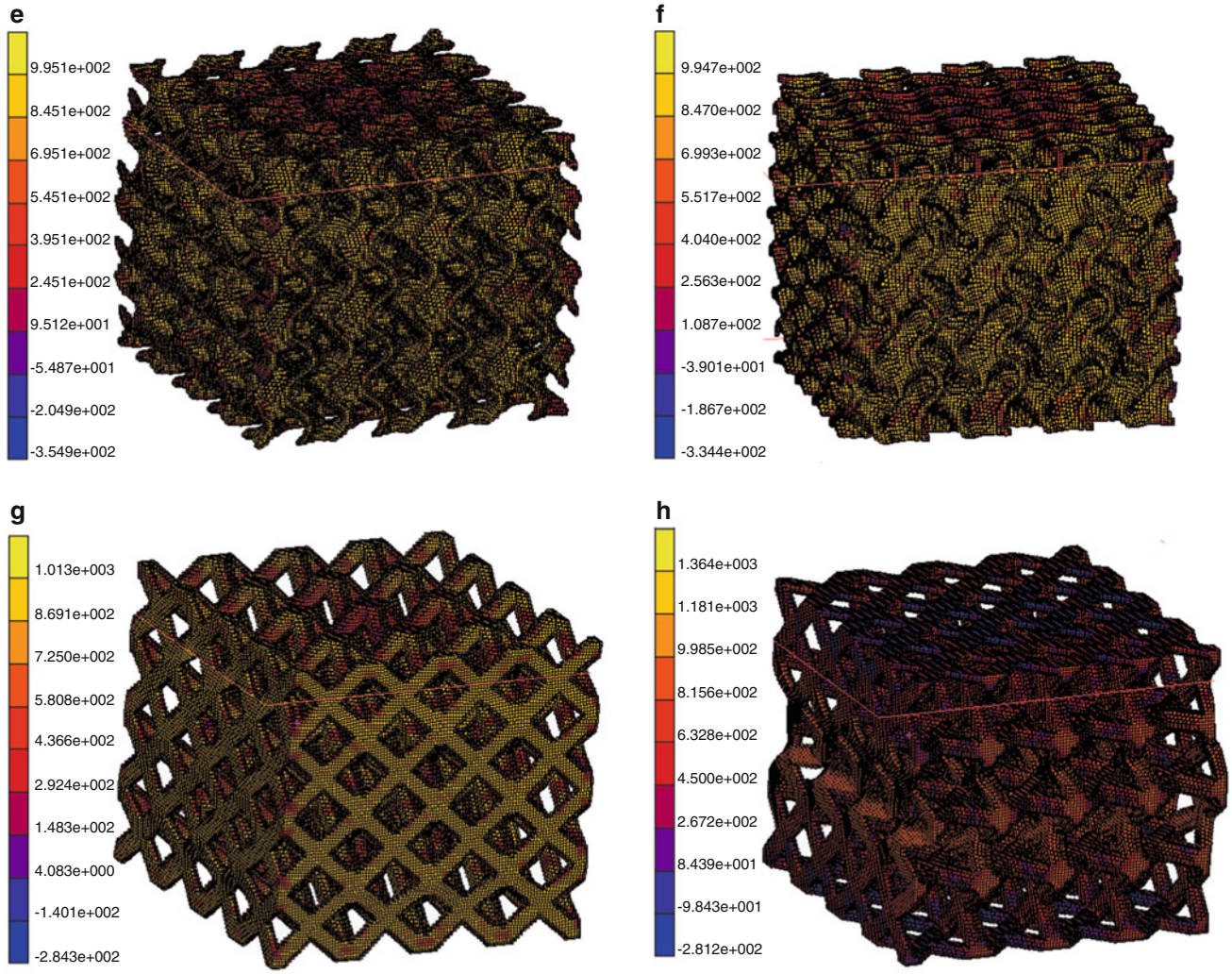

Fig. 7.4 (continued)

Acknowledgements This work is funded by the engineering and physical science research council (EPSRC).

References

1. Banhart, J.: Manufacture, characterisation and application of cellular metals and metal foams. Progress Mater. Sci. **46**, 559–632 (2001)
2. Gibson, I., Rosen, D., Stucker, B.: Additive Manufacturing Technologies, 2nd edn, p. 498. Springer, New York (2014)
3. Serphos, R.: Incorporating AM-specific manufacturing constraints into topology optimization. Master of Science Thesis, Faculty of Mechanical, Maritime and Materials Engineering (3mE) (2014)
4. Pinkerton, A.J.: Lasers in additive manufacturing. Opt. Laser Technol. **78**, 25–32 (2016)
5. Yan, C., Hao, L., Hussein, A., Raymont, D.: Evaluations of cellular lattice structures, manufactured using selective laser melting. Int. J. Mach. Tools Manuf. 32–38 (2012)
6. Smith, M., Guan, Z., Cantwell, W.J.: Finite element modelling of the compressive response of lattice structures manufactured using the selective laser melting technique. Int. J. Mech. Sci. **67**, 28–41 (2013)
7. Mullen, L., Stamp, R.C., Brooks, W.K., Jones, E., Sutcliffe, C.J.: Selective laser melting: a regular unit cell approach for the manufacture of porous, titanium, bone in-growth constructs, suitable for orthopaedic applications. J. Biomed. Mater. Res. B Appl. Biomater. **89B**, 325–334 (2009). doi:10.1002/jbm.b.31219
8. Mckwon, S., Shen, Y., Brookes, W.K., Sutcliffe, C.J., Cantwell, W.J., Langdon, G.S., Nurick, G.N., Theobald, M.D.: Quasi-static and blast loading response of lattice structures. Int. J. Impact Eng. **35**, 795–810 (2008)

9. Merkt, S., Hinke, J., Bultmann, J., Brandt, M., Xie, Y.M.: Mechanical response of TiAl6V4 lattice structures manufactured by selective laser melting in quasistatic and dynamic compression tests. J. Laser Appl. **27**, 7 (2015)
10. Hussein, A., Hao, L., Yan, C., Everson, R., Young, P.: Advanced lattice support structures for metal additive manufacturing. J. Mater. Process. Technol. **213**, 1019–1026 (2013)
11. Noor, A.K.: Continuum modelling for repetitive lattice structures. Appl. Mech. Rev. **41**(7), 285–296 (1988)
12. Luxner, L.M., Woesz, A., Stampfl, J., Fratzl, P., Pettermann, H.E.: A finite element study on the effects of disorder in cellular structures. Acta Biomater. **5**, 381–390 (2009)
13. Meguid, S., A., Cheon, S.S., El-Abbasi, N.: FE modelling of deformation localization in metallic foams. Finite Elem. Anal. Des. **38**(7), 631–643 (2002)
14. De Giorgi, M., Carofalo, A., Dattoma, V., Nobile, R., Palano, F.: Aluminium foams structural modelling. Comput. Struct. **88**(1), 25–35 (2010)
15. Smith, M., Guan, Z., Cantwell, W.J.: Finite element modelling of the compressive response of lattice structures manufactured using the selective laser melting technique. Int. J. Mech. Sci. **67**, 28–41 (2013)
16. Reddy, J.N.: An Introduction to Nonlinear Finite Element Analysis, p. 482. Oxford University Press, New York (2005)
17. Aremu, A.O., Maskery, I.A., Tuck, C.J., Ashcroft, I.A., Wildman, R.D., Hague, R.J.M.: Effects of net and solid skins on self-support lattice structures. Chall. Mech. Time Depend. Mater. **2**, 83–89 (2015)

Chapter 8
Process Parameter Effects on Interlaminar Fracture Toughness of FDM Printed Coupons

G.P. Tandon, T.J. Whitney, R. Gerzeski, H. Koerner, and J. Baur

Abstract In Fused Deposition Modeling (FDM), filaments of heated thermoplastic are extruded from a tip that moves in a raster-like motion. Depending on filament material properties and the processing parameters, the extruded beads and the fusion-bond between them could result in anisotropic properties (particularly with regard to strength). In this work, the focus is on characterizing the interlaminar fracture toughness of coupons produced by FDM with varying road-to-road offsets producing positive, zero and negative air gaps between neighboring roads resulting in coupons of varying density (void content). The resulting bond line formation is assessed through measuring and analyzing changes in the mesostructure and the contact attained at the interfaces between the adjoining roads. The bond quality is assessed by evaluating plane-strain fracture toughness using compact tension specimens. Results demonstrate an approximate five-fold increase in fracture toughness with varying air gaps.

Keywords Additive manufacturing • Fused deposition modeling • Ultem*9085 • Fracture toughness • Air gap

8.1 Introduction

Additive manufacturing (AM) technologies such as FDM provide a means of producing parts of complex, 3-D geometry [1] by depositing material layer-by-layer. As successive layers are built up, new molten material will heat previously deposited roads causing their outer surfaces to melt. The formation of bonds among polymer filaments in FDM parts is driven by the thermal energy of the extruded material. The bonding quality depends on the growth of the neck formed between the adjacent filaments and on the molecular diffusion and randomization of the polymer chains across the interface. The bonding phenomenon is thermally driven and determines the integrity and mechanical properties of the resulting structure [2]. Suspected reasons include the presence of voids inherent to the FDM process (creating stress concentration and crack initiation sites) and the thermal history to which the material is exposed during the process (leading to large residual stresses). Test results also show that the mechanical strength properties depend on the given inner part structure as a result from the build direction and the toolpath generation [3]. The fact that the mechanical properties of the part depend on the orientation and path becomes particularly critical when FDM technology is used to produce components directly for end use [4]. The quality of FDM processed parts mainly depends on careful selection of process variables. Thus, identification of the FDM process parameters that significantly affect the quality of FDM processed parts is important [5].

FDM structures built with rasters (beads of material) oriented at bias angles to the primary axis of the structure morphologically resemble laminated composite materials. The "laminate analogy" and respectively application of classical lamination plate theory methods for mechanics of FDM parts appears to hold for these materials [6]. That is, each layer of the FDM structure can be treated as composite lamina with anisotropic stiffness and strength properties (the magnitude of which decrease as the density of the FDM build increases).

G.P. Tandon (✉)
University of Dayton Research Institute, 300 College Park, Dayton, OH 45469-0060, USA

Air Force Research Laboratory, WPAFB, OH 45433, USA
e-mail: Gyaneshwar.Tandon.ctr@us.af.mil

T.J. Whitney
University of Dayton, Dayton, OH 45469, USA

R. Gerzeski • H. Koerner • J. Baur
Air Force Research Laboratory, WPAFB, OH 45433, USA

W.C. Ralph et al. (eds.), *Mechanics of Composite and Multi-functional Materials, Volume 7*,
Conference Proceedings of the Society for Experimental Mechanics Series, DOI 10.1007/978-3-319-41766-0_8

While AM methods have been around for decades, only within the last 5–10 years has the application to primary load-bearing structure been considered. The American Society for Testing and Materials (ASTM), committee F42 on Additive Manufacturing Technologies, has existed for almost 6 years, but focuses almost exclusively on metallic additive methods. ASTM committee D30 on Composite Materials has many standards at various scales that provide "starting points" for additive methods, since additive structures resemble layered composites. However, no industry-wide momentum has yet developed for a test methods program, developed specifically for OMC additive structures. For example, no methods exist for assessing bond-line strength or residual stress for two "roads" laid side-by-side or on top of each other (layer-to-layer), much less assessing the distribution of such parameters within a component (the distribution being required to use the data at the next higher scale). These methods will be critical in experimentally validating models which seek to predict component-scale physical or mechanical response based on simulation at the lower scales.

8.2 Experimental Methods

The current study focuses on ULTEM© 9085, a commercially available polyetherimide (PEI)/polycarbonate (PC) blend of interest to the aerospace industry for its flame retardant and smoke-and-toxicity rating. It processes at a relatively high temperature compared to other thermoplastics currently available for FDM.

Three different plates measuring $6'' \times 6''$ were printed on the FORTUS 400MC with ULTEM 9085 material with "low", "medium" and "high" density of the roads. The density terminology (low, nominal, high) represent a set of "typical" machine settings for the nominal case, and then there are other settings that represent a lower and higher density. The setting that results in these density differences is the "raster-to-raster gap," which controls how far the tip moves laterally at the end of a row in order to start the next row. The setting value itself doesn't mean much, because each machine will produce a different density for the same machine setting, due to the achievable tolerances in the machine (actual tip opening diameter, play in the drive belts, variations in the stepper motor, etc.). That's why each machine really needs to go through frequent density calibrations (if density is important to the builds), to know what parameters to use for a desired density.

For this study, the raster-to-raster air gaps (in inches) for the low, nominal, and high density panels were 0.001, 0.000, and −0.001, respectively. All three plates had the roads oriented unidirectionally. In addition, the values of other parameters that are adjustable were as follows:

- Height of raster: 0.010 in (This is the "slice height" for each printed layer).
- Tip: T16 (0.016 in. diameter)
- Temperatures: standard print temperature (tips and liquefier were at 325 °C, chamber was at 195 °C)
- Print speed—we used the standard extrusion rate, fixed by the machine.
- Raster width was adjusted based on air gap. For the panels studied, the center-line-to-center-line distance was fixed at 0.020 in. So for an air gap of 0.001 in. the raster width was 0.019 in. For a 0.000 air gap, the raster width was 0.020 in., and for the −0.001 air gap, the raster width was 0.021 in.
- Contours width was fixed at 0.020 in.
- Contour-to-raster gap was 0.000 in.

The microstructure of the printed plates was first examined using optical microscopy techniques to quantify the effect of variations in raster-to-raster air gaps on the inter-road porosity and contact between the adjacent roads. Next, compact tension specimens were prepared for fracture toughness evaluation from the printed plates with "low", "medium" and "high" density of the roads. A schematic of the compact tension specimen is shown in Fig. 8.1. Specimen dimension 'W' is fixed by the fabrication process and is $.514'' \pm .0005''$. The specimen thickness was measured using a Mitutoyo digital micrometer; this measurement was made at the center of the specimen. The initial crack length 'a' was measured using a Mitutoyo toolmakers microscope with a micrometer driven stage.

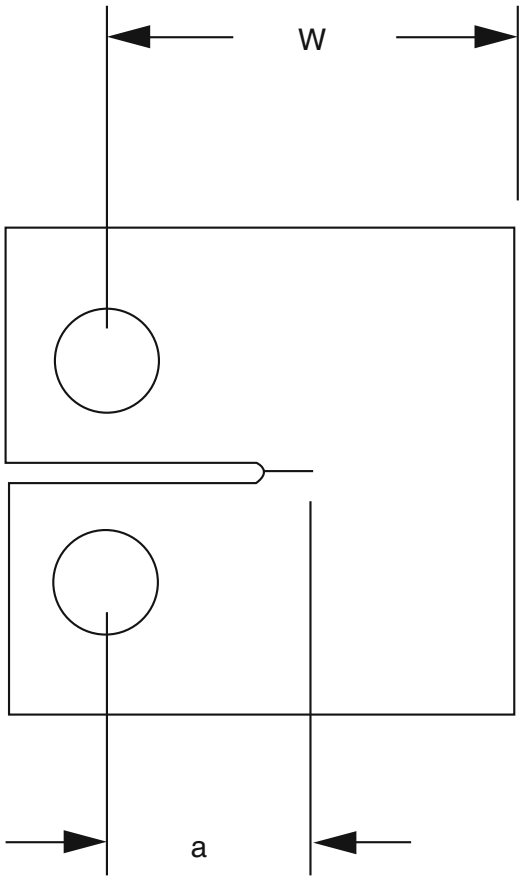

Fig. 8.1 Schematic of a compact tension specimen for fracture toughness evaluation

8.3 Results and Discussion

8.3.1 Microstructure Characterization

Figures 8.2, 8.3, and 8.4 show the cross-sections of three unidirectional specimens with "low", "medium" and "high" density of the roads oriented (a) parallel and (b) perpendicular to the road direction, respectively.

In the longitudinal direction, one sees waviness in the roads. This does sometimes happen at specific points on the build platform due to anomalies in the hardware or software, such as in the stepper motors, belts, or even the diameter of the feedstock. Maybe a better word would be "uncertainty" or "tolerance" of the raster's with respect to parallelism. There is also a recognized phenomenon in the Stratasys machines known as "twinning," in which sets of adjacent roads (two roads) will be well connected, but the connections between these sets will have gaps due to waviness. It's possible that we may be cutting through one of these gaps, or possibly, the section was not taken quite parallel to the raster, so that one sees rasters appear and disappear.

In the transverse directions, the cross-sections were further analyzed for porosity and for contact length measurements both parallel and perpendicular to the adjacent roads. These measurements were performed over several random locations and the averages computed. Figures 8.5, 8.6, and 8.7 show examples of the magnified regions over which porosity calculations were done using image analysis. A representative volume element which enclosed 16 "pores" was randomly selected. The boundary of the voids was outlined using short linear segments and then the area fraction enclosed by the voids was computed. Table 8.1 summarizes the pore volume fraction calculations for low, normal and high density specimens.

Figure 8.8 shows an example of the magnified region of the cross-section of a "nominal" road density specimen over which road and contact length measurements were made using optical microscopy in the plane of the roads and in the thickness direction. Several roads were randomly selected and the contact distance was measured along the top and bottom interfaces, and along the left and right edges of adjacent roads. Table 8.2 summarizes the average measured road dimensions and the calculated road area using average width and height measurements while approximating the road cross-section as an

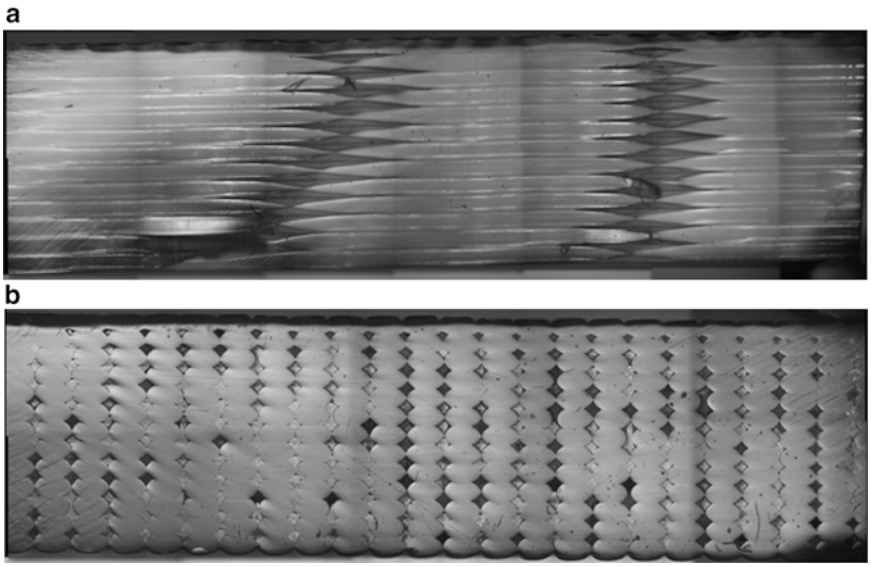

Fig. 8.2 (**a**) Longitudinal, and (**b**) transverse cross-sections of "low" road density specimen

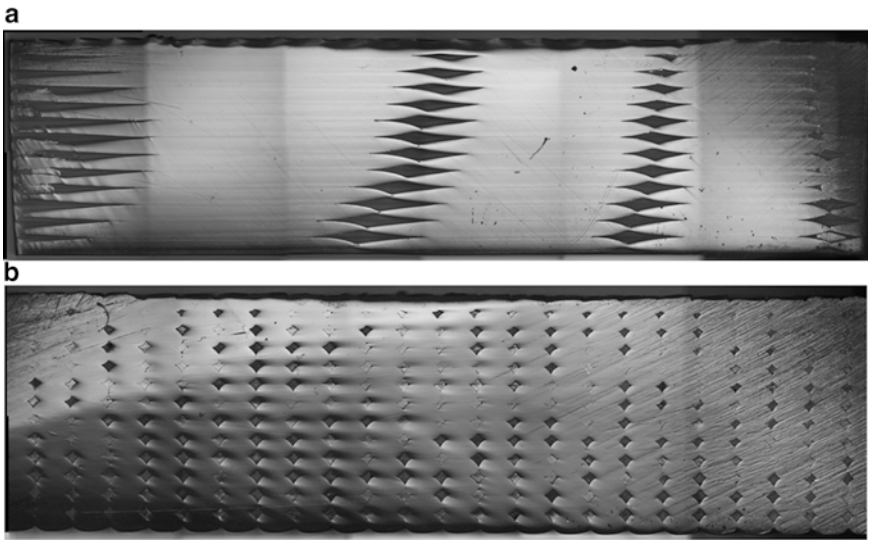

Fig. 8.3 (**a**) Longitudinal, and (**b**) transverse cross-sections of "nominal" road density specimen

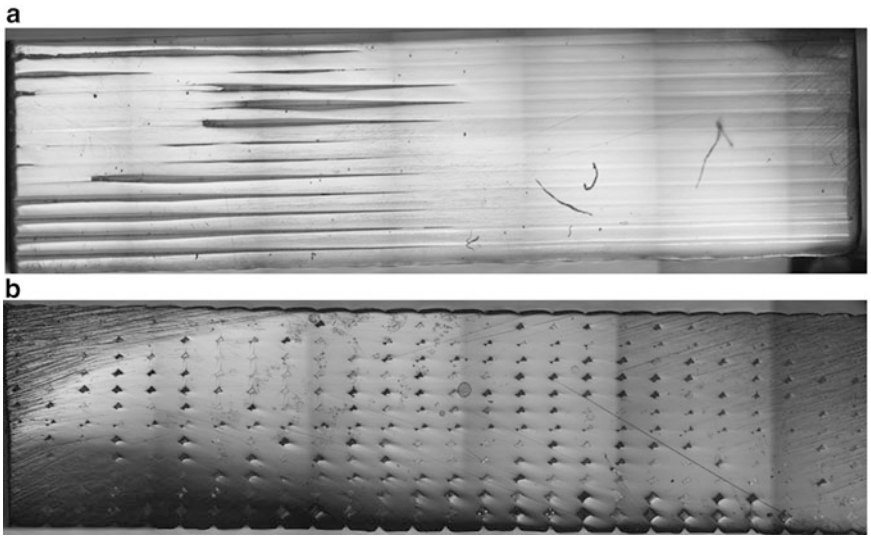

Fig. 8.4 (**a**) Longitudinal, and (**b**) transverse cross-sections of "high" road density specimen

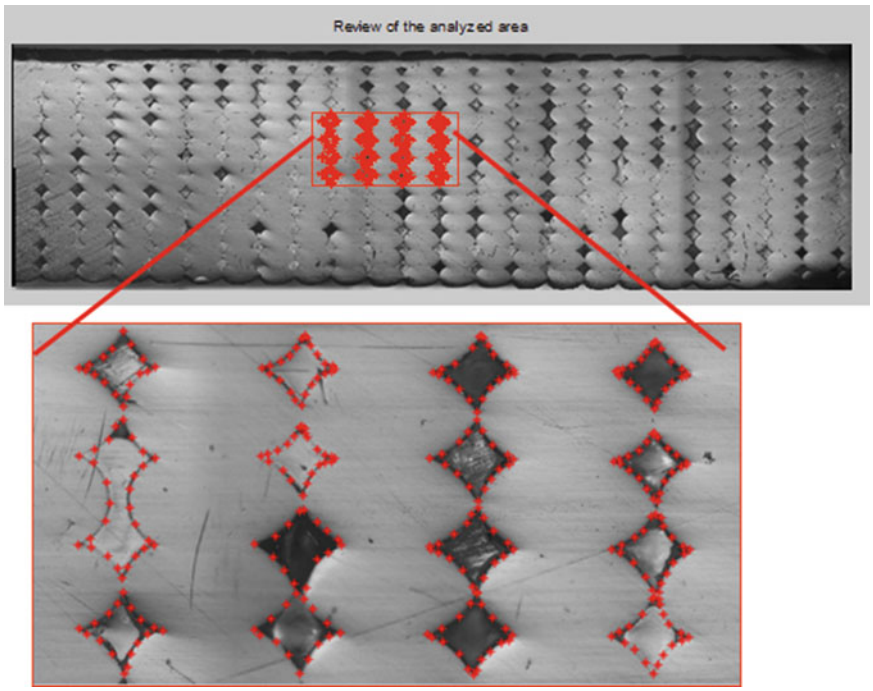

Fig. 8.5 Image analysis of "low" road density specimen yielding a pore volume fraction of 15.02 %

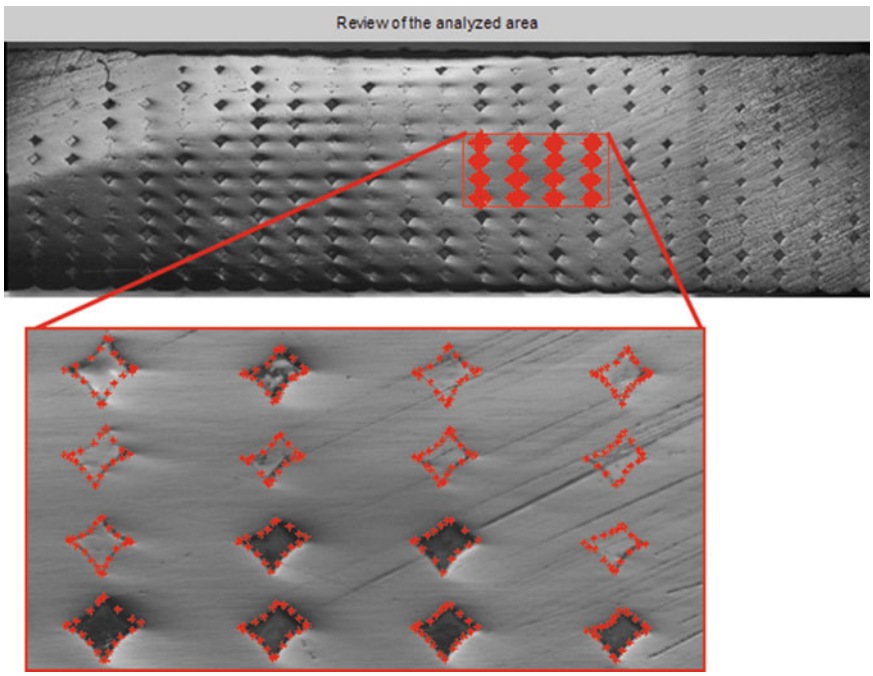

Fig. 8.6 Image analysis of "nominal" road density specimen yielding a pore volume fraction of 9.826 %

ellipse for all three road densities. There is little difference between the average road dimensions and the calculated area for low, normal and high density specimens. Table 8.3 lists the average contact length measurements between adjacent roads for low, normal and high density specimens. It is seen that the contact length measurements between adjacent roads increase with increasing road density in both in-plane and thickness directions.

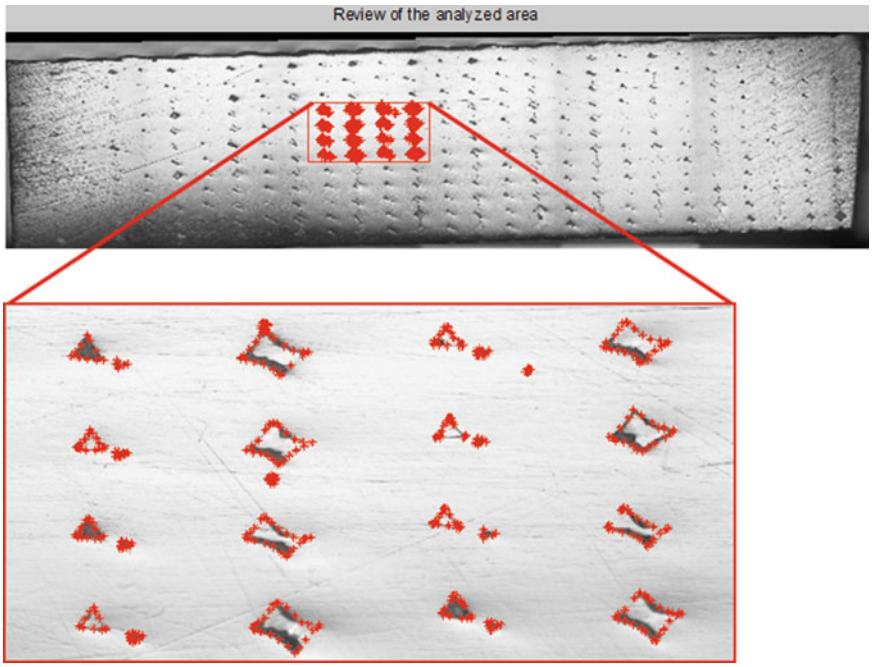

Fig. 8.7 Image analysis of "high" road density specimen yielding a pore volume fraction of 4.725 %

Table 8.1 Pore volume fraction evaluation using image analysis

Specimen ID	Pore volume fraction (%)	Pore size (μm^2)
Low density	15.02	4.7 (10^4)
Nominal density	9.83	1.3 (10^4)
High density	4.73	3.8 (10^3)

8.3.2 Fracture Toughness Characterization of Printed Roads

The first few trial specimen blanks were tested without a notch and a starter crack but they all failed at the drilled hole edges. As such it was decided that further testing would be performed with notched specimens. A 'natural' crack was then produced in each specimen by placing a single-edged razor blade in the notch and tapping the back edge of the razor blade with a small hammer. The initial crack length 'a' was then measured for all specimens. (The standard calls for 'a' to be from 0.45 W to .55 W from the centerline of the loading holes. In almost all of the specimens the value of 'a' was less than the value called for in the standard.) Several attempts were made to fatigue the specimen to meet standard value, but all attempts caused the premature failure of the specimen. Therefore, the 'best' 6–8 specimens from each plaque were selected for testing.

All specimens were tested on a 500 lb capacity MTS Insight electromechanical test frame at a crosshead displacement rate of .05 in/min. The specimen was loaded until a drop in load occurred. Table 8.4 lists the specimen dimensions along with the maximum load recorded for all the specimens tested. The plane strain fracture toughness was computed using Eq. (8.1), where P_Q is the maximum load, t is the thickness, w is the width and a is the crack length.

$$K_Q = \left(P_Q/t\,w^{1/2}\right).f(a/w) \tag{8.1}$$

where, $f(a/w) = \frac{(2+a/w)\left(0.886+4.64a/w-13.32a^2/w^2+14.72a^3/w^3-5.6a^4/w^4\right)}{(1-a/w)^{3/2}}$

The average plane strain fracture toughness for specimens with low, nominal and high road density is measured as 417.72 ± 105.87, 1337.08 ± 161.48, and 1990.46 ± 261.89 psi × $in.^{0.5}$, respectively. Thus, not only the pore volume fraction decreases and the contact length between adjacent roads increases with decreasing air-gap distance, the fracture toughness of the printed material increases by approximately five times on reducing the lateral raster-to-raster distance

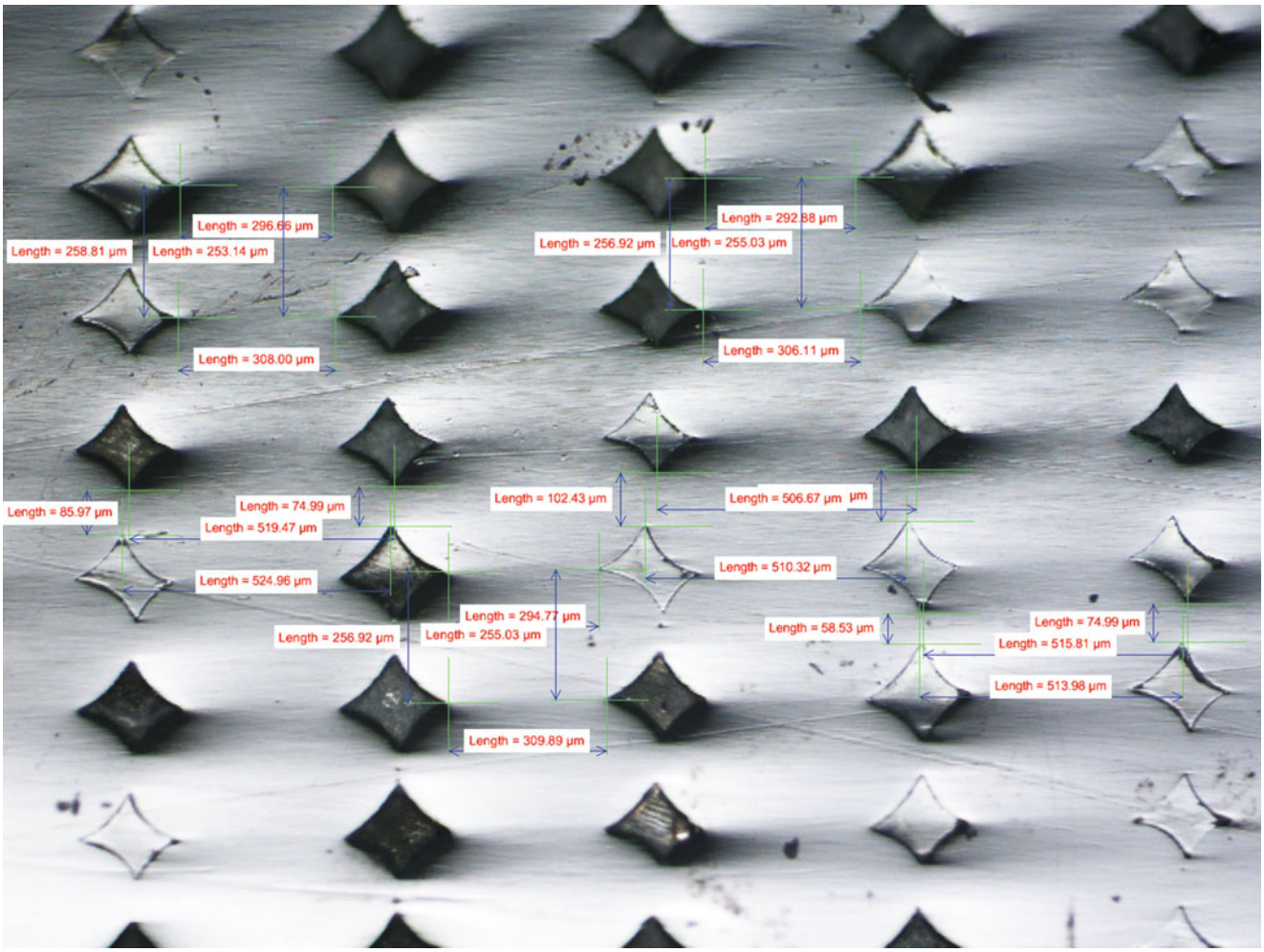

Fig. 8.8 Contact length measurements between adjacent roads for "nominal" road density specimen

Table 8.2 Overall road dimensions for "low", "nominal", and "high" road density specimens

	Overall road dimension		
Specimen ID	Width, µm	Height, µm	Area, mm^2
Low density	511.76 ± 4.69	256.8 ± 2.47	0.1032
Nominal density	510.32 ± 6.44	250.97 ± 6.94	0.1006
High density	512.76 ± 2.80	256 ± 6.83	0.1031

Table 8.3 Contact length measurements between adjacent roads

	Contact length measurement	
Specimen ID	In-plane direction, µm	Thickness direction, µm
Low density	31.17 ± 7.63	285.54 ± 7.94
Nominal density	94.81 ± 9.28	322.76 ± 9.77
High density	152.36 ± 33.9	377.53 ± 30.13

between successive prints. This large improvement in the mechanical performance of the printed material therefore signifies that the quality of FDM processed parts strongly depends on careful selection of process variables.

The fracture surface of all specimens tested was examined using optical microscopy. Figures 8.9, 8.10, and 8.11 are the representative photomicrographs of compact tension specimens with low, nominal and high road density values. Depending upon the initial location of the notch and the starter crack relative to the road, it is seen that the starter crack either advances

Table 8.4 Fracture toughness measurements for "low", "nominal", and "high" road density specimens

	Specimen ID	t (thickness), in.	w (width), in.	a (crack length), in.	P_Q (max load), lb	F (a/w)	K_Q, psi × $in.^{0.5}$
Low density	#1-6	0.131	0.516	0.134	6.82	5.05	366.32
	#1-7	0.131	0.510	0.132	7.307	5.03	392.91
	#1-8	0.131	0.513	0.129	6.006	4.95	316.91
	#1-9	0.13	0.514	0.134	10.893	5.06	591.26
	#1-10	0.131	0.515	0.134	6.305	5.08	340.40
	#1-13	0.131	0.446	0.138	7.57	5.76	498.49
Average							417.72
Nominal density	#2-7	0.13	0.513	0.122	25.681	4.76	1313.63
	#2-8	0.131	0.512	0.127	26.103	4.89	1362.72
	#2-9	0.131	0.523	0.166	22.631	5.87	1403.10
	#2-10	0.131	0.513	0.128	29.509	4.92	1545.85
	#2-11	0.131	0.512	0.123	27.033	4.79	1381.10
	#2-12	0.132	0.513	0.148	17.531	5.46	1012.50
	#2-13	0.131	0.512	0.133	24.85	5.06	1340.67
Average							1337.08
High density	#3-5	0.132	0.513	0.124	38.09	4.81	1939.56
	#3-6	0.131	0.509	0.122	39.68	4.79	2032.32
	#3-7	0.132	0.508	0.124	44.20	4.85	2276.72
	#3-8	0.133	0.510	0.126	29.50	4.89	1517.44
	#3-9	0.131	0.508	0.127	43.88	4.92	2314.56
	#3-10	0.132	0.511	0.122	34.68	4.78	1754.94
	#3-11	0.132	0.575	0.199	31.64	6.33	2000.49
	#3-12	0.133	0.574	0.201	32.90	6.39	2087.66
Average							1990.46

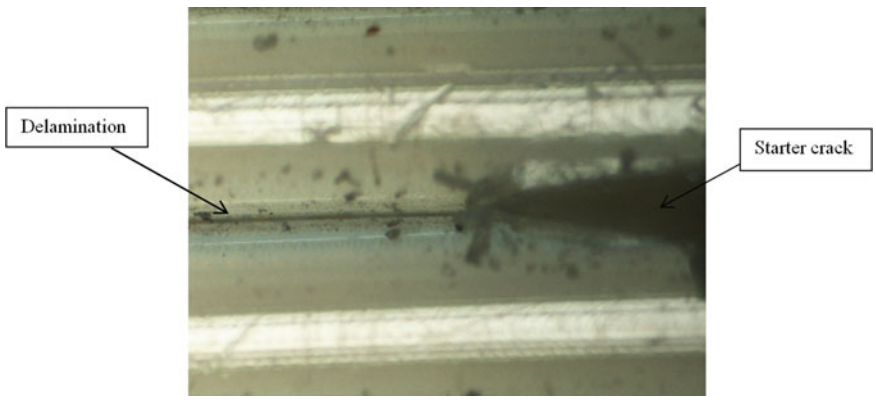

Fig. 8.9 Photomicrograph showing crack growth in "low" density compact tension specimen # 1-7

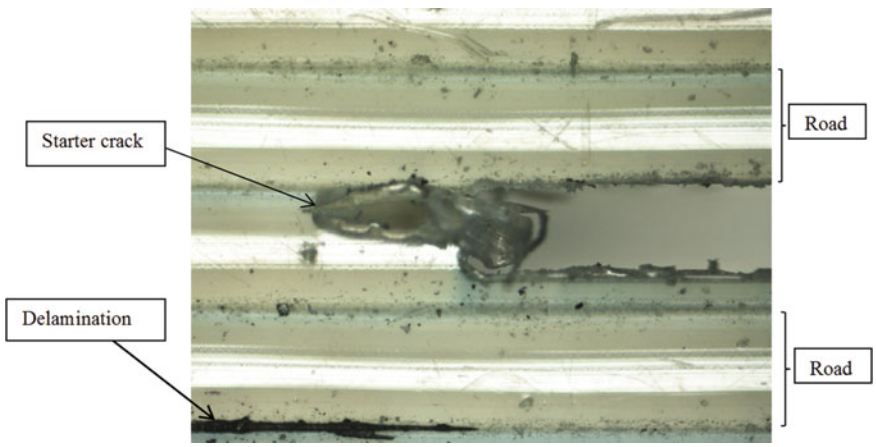

Fig. 8.10 Photomicrograph showing crack growth in "nominal" density compact tension specimen # 2-9

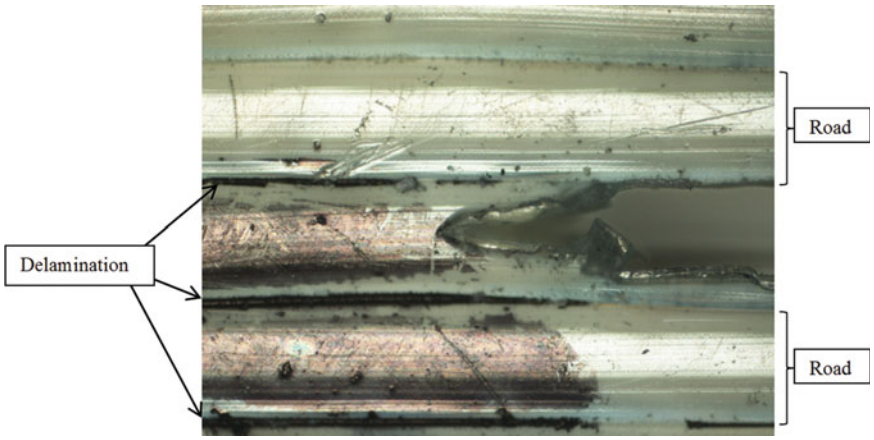

Fig. 8.11 Photomicrograph showing crack growth in "high" density compact tension specimen # 3-9

in a self-similar manner and/or jumps to neighboring road interfaces when loaded perpendicular to the initial crack. Further, the observed interface delamination is not necessarily confined to the nearest road interface and more than one interface can debond simultaneously on further loading. No damage (or fracture) was observed within the beads for all three printed road densities.

8.4 Conclusions

Three different plates measuring $6'' \times 6''$ were printed on the FORTUS 400MC with ULTEM 9085 material with "low", "medium" and "high" density of the roads. Compact tension specimens were prepared for fracture toughness evaluation, and the measured values correlated with the microstructure of the printed roads. The pore volume fraction calculation for low, normal and high density specimens shows a decrease with increase in road density. There is little difference between the average road dimensions and the calculated cross-sectional area for low, normal and high density specimens. It is seen that the contact length measurements between adjacent roads increase with increasing road density in both in-plane and thickness directions. The average plane strain fracture toughness for specimens with low, nominal and high road density is measured as 417.72 ± 105.87, 1337.08 ± 161.48, and 1990.46 ± 261.89 psi $\times$ in.$^{0.5}$, respectively, and these values are consistent in trend with the contact length measurements between adjacent roads. Depending upon the location of the notch and the starter crack relative to the road, it is seen that the starter crack either advances in a self-similar manner and/or jumps to neighboring road interfaces when loaded perpendicular to the initial crack. This large improvement in the mechanical performance of the printed material with increasing road density signifies that the quality of FDM processed parts strongly depends on careful selection of process variables.

References

1. Bagsik, A., Josupeit, S., Schoeppner, V., Klemp, E.: Mechanical analysis of lightweight constructions manufactured with fused deposition modeling. AIP Conf. Proc. **1593**, 696 (2014). doi:10.1063/1.4873874
2. Sun, Q., Rizvi, G.M., Bellehumeur, C.T., Gu, P.: Effect of processing conditions on the bonding quality of FDM polymer filaments. Rapid Prototyping J. **14**(2), 72–80 (2008). doi:10.1108/13552540810862028
3. Bagsik, A., Schöppner, V.: Mechanical properties of fused deposition modeling parts manufactured with Ultem*9085. In: ANTEC 2011, Boston (2011)
4. Bellini, A., Guceri, S.: Mechanical characterization of parts fabricated using fused deposition modeling. Rapid Prototyping J. **9**(4), 252–264 (2003). doi:10.1108/13552540310489631
5. Mohamed, O.A., Masood, S.H., Bhowmik, J.L.: Optimization of fused deposition modeling process parameters: a review of current research and future prospects. Adv. Manuf. **3**, 42–53 (2015). doi:10.1007/s40436-014-0097-7
6. El-Gizawy, A.S., Cardona, J., Graybill, B.: An integrated approach for characterization of properties and mesostructure of fused deposition modeling ULTEM 9085 products. In: International SAMPE Symposium and Exhibition (Proceedings), SAMPE 2010 Conference and Exhibition "New Materials and Processes for a New Economy" (2010)

Chapter 9
Constitutive Equations for Severe Plastic Deformation Processes

Robert Goldstein, Sergei Alexandrov, and Marko Vilotic

Abstract Processes of severe plastic deformation significantly change material properties. Therefore, it is reasonable to expect that conventional constitutive equations of plasticity theory are not applicable for severe plastic deformation processes. The main assumption made in the present paper is that the relative spin (the difference between the velocity spin and the spin of the principal axes of stress) should be included in constitutive equations to adequately describe severe plastic deformation processes. An experimental procedure to verify this assumption is proposed and partly carried out.

Keywords Severe plastic deformation • Ideal flow • Material spin • Upsetting • Constitutive equations

9.1 Introduction

Severe plastic deformation is a widely used method to improve material properties. Reviews of this method are provided, for example, in [1, 2]. During such deformation, intensive microstructural rearrangements occur in the metal. Therefore, it is reasonable to assume that constitutive equations for describing material flow in severe plastic deformation processes should be different from conventional constitutive equations used for analysis and design of traditional metal forming processes. Analysis of the mode of deformation in typical severe plastic deformation processes shows that an essential difference between severe plastic deformation processes and traditional metal forming processes is that the difference between the velocity spin and the spin of the principal axes of stress is more pronounced in the former processes. Therefore, it is reasonable to hypothesize that a measure of this relative spin should be included in constitutive equations. It is interesting to note that the relative spin referred to above may be very large in the vicinity of frictional interfaces in traditional metal forming processes. For example, in the case of rigid perfectly plastic material the theoretical relative spin approaches infinity in the vicinity of maximum friction surfaces [3]. However, a narrow layer of intensive plastic deformation often appears in the vicinity of frictional surfaces in real metal forming processes [4–7], which confirms the hypothesis made above. Note that constitutive equations that include various relative spins are widely adopted in the mechanics of granular materials [8, 9]. An attempt to use such models for describing material flow in severe plastic deformation processes has been made in [10, 11].

The present paper further develops the approach introduced in [10, 11]. In particular, the process of multi-stage upsetting of a long bar between V-shape dies is considered. It is shown that the mode of deformation of infinitesimal line segments on the axes of symmetry of the process possesses some qualitative properties inherent in severe plastic deformation processes and some qualitative properties inherent in ideal flow processes. A review of the ideal flow theory is provided in [12]. A property of ideal flows is that the velocity spin is equal to the spin of the principal axes of stress. Therefore, in a sense, ideal flow processes are opposite to severe plastic deformation processes. An experimental procedure to reveal a possible effect of the relative spin on material response is proposed. In particular, the procedure includes the process of the multi-stage upsetting of a long bar between V-shape dies. The distribution of the equivalent strain in this process is determined experimentally. This distribution can be used to select an appropriate ideal flow process and a appropriate severe deformation process, which are also included in the general experimental procedure.

R. Goldstein (✉) • S. Alexandrov
Laboratory on Mechanics of Strength and Fracture of Materials and Structures, Institute for Problems in Mechanics of the Russian Academy of Sciences, Prospect Vernadskogo, 101-1, 119526 Moscow, Russia
e-mail: goldst@ipmnet.ru

M. Vilotic
Faculty of Technical Sciences, University of Novi Sad, Obradovich Street, 6, 21000 Novi Sad, Serbia

W.C. Ralph et al. (eds.), *Mechanics of Composite and Multi-functional Materials, Volume 7*,
Conference Proceedings of the Society for Experimental Mechanics Series, DOI 10.1007/978-3-319-41766-0_9

9.2 Conceptual Approach

In the interests of simplicity, the analytical framework is restricted to plane strain deformation. Introduce a rectangular Cartesian system of coordinates (x, y). Let σ_1 and σ_2 denote the principal stresses in planes of flow. It is assumed that $\sigma_1 > \sigma_2$. Consider an infinitesimal line segment δl embedded in a continuing deformation (Fig. 9.1). Let ϕ be the angle that this segment makes with the x-axis and ψ be the angle that the principal stress direction corresponding to the stress σ_1 makes with the x-axis. It is evident that $\dot{\phi}$ is the material spin and $\dot{\psi}$ is the spin of the principal axes of stress. Here a dot denotes the rate of change relative to the Cartesian coordinate system. The relative spin is defined as $\omega = \dot{\psi} - \dot{\phi}$. It is worthy of note that the relative spin is frame indifferent and hence may appear in constitutive equations. In some cases

$$\dot{\phi} = \dot{\psi}. \tag{9.1}$$

In particular, this equation is satisfied in standard tests such as the uniaxial tensile test during uniform deformation and the uniaxial compression test in conjunction with Rastegaev's method (a description of the method is given, for example, in [13]). Equation (9.1) is also satisfied at axes of symmetry and in ideal flows (a review of the ideal flow theory is provided in [12]). On the other hand, Eq. (9.1) is never satisfied in severe plastic deformation processes. In a sense, severe plastic deformation processes are opposite to ideal flow processes. In particular, all plastic work in severe plastic deformation processes is redundant work whereas there is no redundant work in ideal flow processes. It is not obvious whether or not excessive redundant work needed for severe plastic deformation processes is to be taken into account in the formulation of constitutive equations. Nevertheless, it has been recognized that an accurate theoretical description of material behavior in the primary shear zone in metal cutting requires a material test in conditions similar to those found in cutting rather than conventional material tests [14]. It is worthy of note that Eq. (9.1) is never satisfied in the primary shear zone. Actually, the mode of deformation in this zone is very similar to that in the equal channel angular extrusion process, which is a widely used severe plastic deformation process [1, 2]. Therefore, a comprehensive experimental program is to be designed and carried out to formulate constitutive equations for severe plastic deformation processes. This paper presents a possible starting point of this program.

Consider a generic severe plastic deformation processes. In course of this deformation, the infinitesimal line segment δl (Fig. 9.1) is subject to uniaxial tension under superimposed hydrostatic pressure when it is aligned with the principal stress direction corresponding to the principal stress σ_1 and to uniaxial compression under superimposed hydrostatic pressure when it is aligned with the principal stress direction corresponding to the principal stress σ_2. In a generic ideal flow process, the infinitesimal line segment δl that is aligned with one of the principal stress directions at the initial instant is aligned with this directing during the entire process. This is one of two major differences between severe plastic deformation processes on one hand and conventional tests, such as the uniaxial tensile test during uniform deformation and the uniaxial compression test with no barreling, or ideal flow processes on the other hand. The second major difference is that in severe plastic deformation processes the infinitesimal line segment δl accumulates some strain while it rotates from one of the principal stress direction to the other. This mode of deformation does not exist in ideal flow processes. The main idea of the approach proposed in the present paper is to design experiment such that an effect of each of the aforementioned major differences on the evolution of microstructure might be revealed.

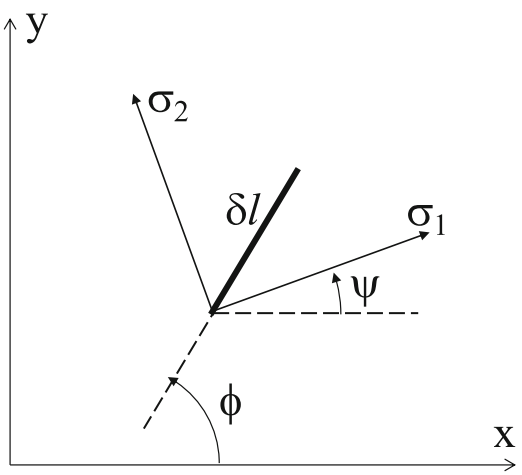

Fig. 9.1 System of coordinate, principal stress directions and infinitesimal line segment fixed in material

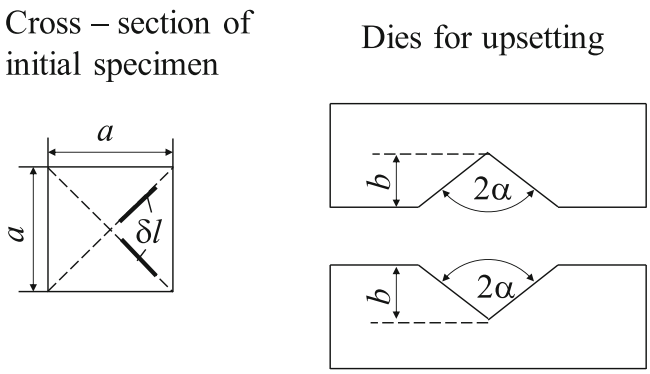

Fig. 9.2 Schematic diagram of dies for upsetting and the initial cross-section of specimens

It is known that no change in microstructure occurs after a certain amount of the equivalent strain [1, 15–19]. This strain is regarded as a reference strain. Any conventional severe plastic deformation process can be used to generate microstructural rearrangements of material at the reference strain. Parameters that characterize this microstructure may be regarded as reference parameters. An ideal flow process can be adopted to deform the same material to the reference strain. A possible process in which a high level of strain can be reached with no fracture is extrusion through a sigmoidal die [20]. An alternative process is uniaxial compression, which is simpler to carry out. However, the possibility to use this process depends on the level of the reference strain. A process that is different from both a generic ideal flow process and a conventional severe plastic deformation process is multi-stage upsetting of a long bar between V-shape dies. The initial cross-section of the bar is a square. A schematic diagram of the dies is shown in Fig. 9.2. Also shown is the initial cross-section of the specimen. The first three stages of the process are illustrated in Fig. 9.3. The second and third stages can be repeated as many times as necessary. Consider an infinitesimal line segment on one the diagonals of the initial cross-section, for example, as shown in Fig. 9.3. Symmetry demands that this line segment is aligned with one of the principal stress directions and, therefore, ideal flow conditions are satisfied for this segment during any individual stage of the process. However, the entire process is not an ideal flow process because $\phi \neq \psi$ or $\phi \neq \psi + \pi/2$ during the entire process. In the multi-stage process $\phi = \psi$ during the first stage, $\phi = \psi + \pi/2$ during the second stage, $\phi = \psi$ during the third stage and so on. Therefore, the mode of deformation for the line segment under consideration is similar to that in a typical severe plastic deformation process except that in the upsetting process there is no mode of deformation corresponding to continuous rotation of the infinitesimal line segment from one of the principal stress direction to the other. Hence this process possesses some properties of a typical ideal flow process and some properties of a typical severe plastic deformation process. For this reason, it is of interest to study the generation of microstructure by the multi-stage upsetting between V-shape dies and compare this microstructure with those generated by a typical ideal flow process and by a typical severe plastic deformation process.

9.3 Experiment

Experimental results reported in the present paper are restricted to the distribution of the equivalent strain along the two diagonals of specimens in the multi-stage upsetting of a long bar between V-shape dies (Fig. 9.3). The specimens were made of commercial low carbon steel C15E. The initial cross-section was a square with $\alpha = 14$ mm (Fig. 9.2). The initial length of the specimens was 70 mm. The main geometric parameters of the dies were $\alpha = 60°$ and $b = 7.5$ mm (Fig. 9.2). A uniform rectangular grid was placed on the lateral edges of the specimens to measure the distribution of strain. The nominal grid spacing was 2 mm. The distribution of the equivalent strain along the axes of symmetry of the specimen is illustrated in Fig. 9.4 for several stages at the beginning of the process and in Fig. 9.5 for several stages at the end of the process.

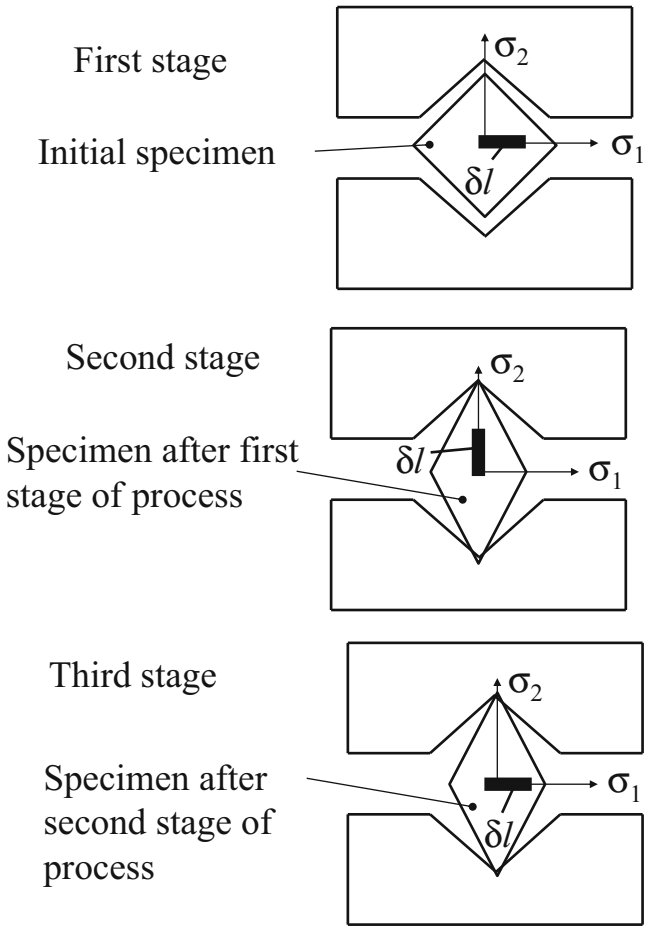

Fig. 9.3 First three stages of multi-stage upsetting

9.4 Conclusions

A methodology of experiment to reveal a possible effect of the relative spin (the material spin relative to the spin of the principal axes of stress) on microstructural rearrangements in metals has been introduced. The experimental procedure consists of three basic tests, namely (1) a typical ideal flow process, (2) a typical severe plastic deformation process, and (3) multi-stage upsetting of a long bar between V-shape dies (or a similar process). The main differences between these tests are that (1) the relative spin always vanishes in any ideal flow process, (2) the relative spin never vanishes in typical severe plastic deformation processes (and this spin is usually quite large as compared to typical metal forming processes), and (3) there are infinitesimal material segments that deform under ideal flow conditions during each stage of the multi-stage upsetting but the overall process of deformation of these segments is not an ideal flow process. It is assumed that the same level of the equivalent strain can be reached in each test. Then, comparison of microstructural arrangements between all three tests should demonstrate whether or not the relative spin contributes to the generation of microstructure. If it does then constitutive equations for severe plastic deformation processes should include the relative spin.

The experimental procedure proposed has been initiated in the present paper. In particular, the distribution of the equivalent strain in multi-stage upsetting of a long bar between V-shape dies has been determined for several stages (Figs. 9.4 and 9.5). These experimental data supplemented with the observation of microstructure at the end of each stage can provide information on the possibility to use the uniaxial upsetting of circular cylinders by means of Rastegaev method (the method is described in [13]) as an ideal flow process. In particular, the change in microstructure in the multi-stage upsetting should become negligible at the level of strain that can be reached in the uniaxial upsetting.

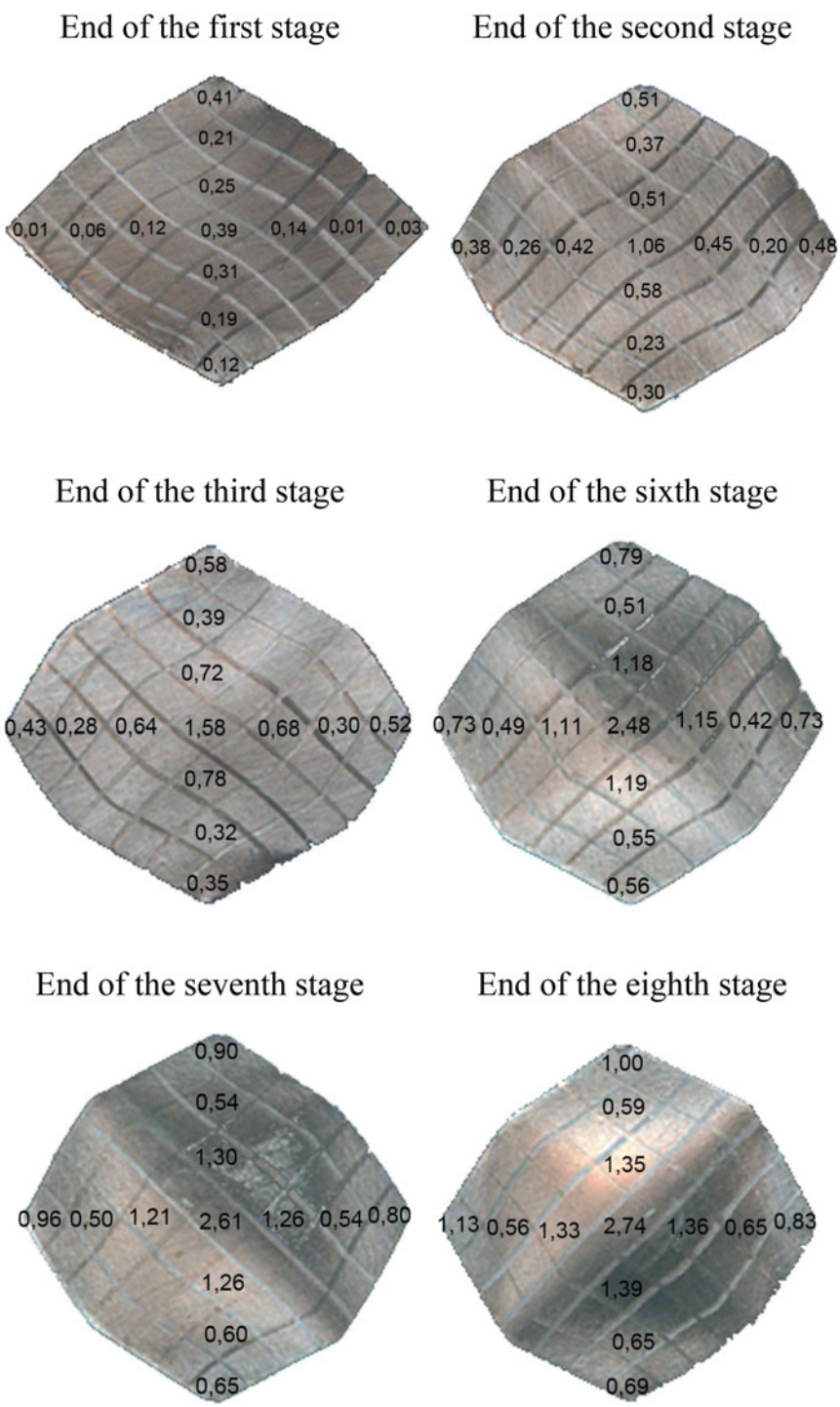

Fig. 9.4 Distribution of the equivalent strain for several stages of multi-stage upsetting at the beginning of the process

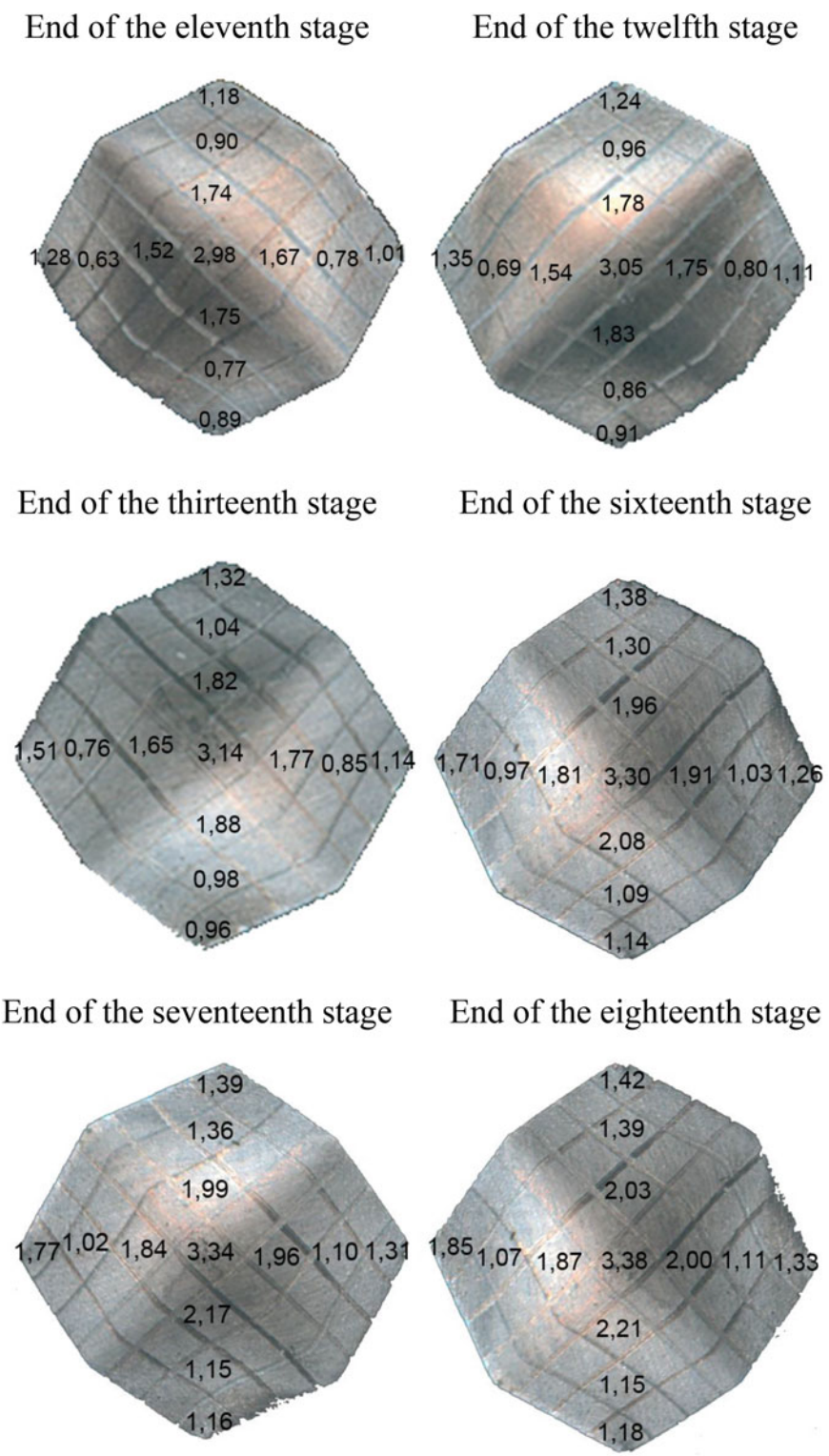

Fig. 9.5 Distribution of the equivalent strain for several stages of multi-stage upsetting at the end of the process

Acknowledgment This research was made possible by Grant No. RSCF-14-11-00844 (R.G., S.A.).

References

1. Humphreys, F.J., Prangnell, P.B., Bowen, J.R., Gholinia, A., Harris, C.: Developing stable fine-grain microstructures by large strain deformation. Phil. Trans. R. Soc. Lond. A **357**, 1663–1681 (1999)
2. Azushima, A., Kopp, R., Korhonen, A., Yang, D.Y., Micari, F., Lahoti, G.D., Groche, P., Yanagimoto, J., Tsuji, N., Rosochowski, A., Yanagida, A.: Severe plastic deformation (SPD) processes for metals. CIRP Ann. **57**, 716–735 (2008)
3. Alexandrov, S., Richmond, O.: Singular plastic flow fields near surfaces of maximum friction stress. Int. J. Non Linear Mech. **36**(1), 1–11 (2001)
4. Griffiths, B.J.: Mechanisms of white layer generation with reference to machining and deformation processes. ASME J. Trib. **109**(3), 525–530 (1987)
5. Murai, T., Matsuoka, S., Miyamoto, S., Oki, Y.: Effects of extrusion conditions on microstructure and mechanical properties of AZ31B magnesium alloy extrusions. J. Mater. Process. Technol. **141**, 207–212 (2003)
6. Kajino, S., Asakawa, M.: Effect of "additional shear strain layer" on tensile strength and microstructure of fine drawn wire. J. Mater. Process. Technol. **177**(1–3), 704–708 (2006)
7. Alexandrov, S., Jeng, Y.-R., Hwang, Y.-M.: Generation of a fine grain layer in the vicinity of frictional interfaces in direct extrusion of AZ31 alloy. ASME J. Manuf. Sci. Eng. **137**(5), 051003 (2015)
8. Spencer, A.J.M.: A theory of the kinematics of ideal soils under plane strain conditions. J. Mech. Phys. Solids **12**, 337–351 (1964)
9. Harris, D.: A hyperbolic augmented elasto-plastic model for pressure-dependent yield. Acta Mech. **225**, 2277–2299 (2014)
10. Alexandrov, S.E., Goldstein, R.V.: Kinetic equation for the grain size in processes of intensive plastic deformation. Dokl. Phys. **54**(12), 553–556 (2009)
11. Goldstein, R., Alexandrov, S.: A new evolution equation for average grain size in processes of severe plastic deformation. J. Eng. Math. **78**(1), 67–81 (2013)
12. Chung, K., Alexandrov, S.: Ideal flow in plasticity. Appl. Mech. Rev. **60**(6), 316–335 (2007)
13. Reiss, W., Pohlandt, K.: The Rastegaev upset test—a method to compress large material volumes homogeneously. Exp. Tech. **10**, 20–24 (1986)
14. Jaspers, S.P.F.C., Dautzenberg, J.H.: Material behaviour in conditions similar to metal cutting: flow stress in the primary shear zone. J. Mater. Process. Technol. **122**, 322–330 (2002)
15. Rabinovich, M.K., Markushev, M.V., Murashkin, M.Y.: Effect of initial structure on grain refinement to submicron size in Al-Mg-Li alloy processes by severe plastic deformation. Mater. Sci. Forum **243–245**, 591–596 (1997)
16. Hebesberger, T., Stuwe, H.P., Vorhauer, A., Wetscher, F., Pippan, R.: Structure of Cu deformed by high pressure torsion. Acta Mater. **53**, 393–402 (2005)
17. Hafok, M., Vorhauer, A., Keckes, J., Pippan, R.: HPT-deformation of copper and nickel single crystals. Mater. Sci. Forum **503–504**, 621–626 (2006)
18. Pippan, R., Wetscher, F., Hafok, M., Vorhauer, A., Sabirov, I.: The limits of refinement by severe plastic deformation. Adv. Eng. Mater. **8**, 1046–1056 (2006)
19. Hafok, M., Pippan, R.: High-pressure torsion applied to nickel single crystals. Philos. Mag. **88**, 1857–1877 (2008)
20. Richmond, O., Morrison, H.L.: Streamlined wire drawing dies of minimum length. J. Mech. Phys. Solids **15**, 195–203 (1967)

Chapter 10
Merging Experimental Evidence and Molecular Dynamics Theory to Develop Efficient Models of Solids Fracture

C.A. Sciammarella, F.M. Sciammarella, and L. Lamberti

Abstract Causes of failure mechanisms can only be found at the level of the dynamics of atoms and molecules. However, the subject of dynamics at the level of atomic structure is very complex, especially in terms of modeling and computations. An interesting way to better understand relationships between macro world and atomic realm is to develop Experimental Mechanics techniques that can provide a verification of developed models at the nanometric and subnanometric levels, guiding the derivation of comprehensive but manageable models. This paper will describe how to apply classical EM methods to establish a bridge between classical continuum mechanics variables and the atomistic analysis of solid mechanics. In particular, we analyze the role of the Cauchy-Born rule as standard tool applied in theoretical and numerical methods to describe the continuum utilizing atomistic arguments. Experimental evidence of the validity of the Cauchy-Born rule will be discussed for the case of SiC crystal including dislocations. Likewise, we will examine how to handle the onsets of plasticity and fracture.

Keywords Molecular dynamics • Experimental mechanics • Crystalline arrays with edge dislocations • Image analysis • Onset of plasticity and fracture

10.1 Introduction

In the solution of engineering problems involving the Mechanics of solids it is well known that the macro behavior of materials is a consequence of the interactions of atoms and molecules at the nanometer range. Answers to the century's old problem of how and why things fail and break are sought at the level of the dynamics of atoms and molecules [1–6]. The subject of the dynamics at the level of the atomic structure is very complex because it forms part of the many body's interaction in physics. This is a very ancient problem that started in Greek times in the astronomy field and today forms part of Quantum Mechanics. In quantum systems, the repeated interactions between particles create quantum correlations. These correlations will be included in a wave function that will describe such a system of multiple particles. The extraordinary amount of information included in the wave function makes it extremely difficult to find solutions, even approximated ones. Approaching the problem of the interactions of atoms and molecules from the point of view of classical Mechanics presents similar obstacles. The search for neighbors within an elementary cell that is, the evaluation of all the atoms that influence a given atom to create a multi-body potential, poses a big problem of computational power. An interesting alternative to get a better understanding of the connection between macro world and atomic realm is to develop further Experimental Mechanics techniques that can verify developed models at the nanometric and subnanometric levels and can guide analysts in derivation of comprehensive but manageable models from the point of view of required computational power.

C.A. Sciammarella (✉)
Department of Mechanical, Materials and Aerospace Engineering, Illinois Institute of Technology, 10 SW 32nd Street, Chicago, IL 60616, USA

Department of Mechanical Engineering, College of Engineering and Engineering Technology, Northern Illinois University, 590 Garden Road, DeKalb, IL 60115, USA
e-mail: sciammarella@iit.edu

F.M. Sciammarella
Department of Mechanical Engineering, College of Engineering and Engineering Technology, Northern Illinois University, 590 Garden Road, DeKalb, IL 60115, USA

L. Lamberti
Dipartimento Meccanica, Matematica e Management, Politecnico di Bari, Viale Japigia 182, Bari 70126, Italy

W.C. Ralph et al. (eds.), *Mechanics of Composite and Multi-functional Materials, Volume 7*,
Conference Proceedings of the Society for Experimental Mechanics Series, DOI 10.1007/978-3-319-41766-0_10

10.2 Interaction Between Atoms

The internal energy of a material is a consequence of the atomic arrangement and depends on the forces that keep together the atoms. There are forces that bind together the elementary particles that form an atom [7]. In the current theory of constitution of matter these forces are the weak forces, the strong forces and the electromagnetic forces. The terms weak or strong have nothing to do with the actual magnitude of the forces but it results from a comparison of the product of the force between two particles, called F_m, times the square of the distance between the two particles r, $F_m r^2$ compared to the product $(h/2\pi)c$, where h is the Plank constant and c is the speed of light. The electromagnetic forces are the forces that bind together or repel charged particles. The positively charged protons are bound to electrons to form atoms, this binding effect results in the neutral charge of atoms. Atoms are neutral, then: what forces make atoms to stick together to form a crystal? The forces that bind together atoms are called in the literature of physics residual electromagnetic forces and result from sharing electrons that is, electrons of one atom interact with the protons of the other atom. These forces are weak forces in the sense that has been previously defined and the carriers of these forces are photons.

The main types of bonding between atoms of interest to mechanics of materials are classified as hetero-polar, mono-polar, Van der Waals, and metallic bonding [8]. In the hetero-polar (ionic) bonding, one atom gives up one electron to become positive and the other atom gains an electron to become negatively charged. In the homopolar (covalent) bonding, both atoms remain neutral and share an electron pair. Van der Waals forces include attraction and repulsion forces between atoms, molecules, resulting from changes in the polarization of the interacting particles, for example repulsion forces caused by the Pauli Exclusion Principle. Metallic bonding is a very important category for the mechanics of materials because of the importance of metals in technical applications. Metals are characterized by delocalization of electronic shells, that is, electrons are shared by all the atoms in a cluster, the Fermi layer. The bonding can be characterized by the attractive force of the non localized electrons and positively charged metallic ions.

From the point of view of mechanics of materials it is interesting to point out relative magnitude of different types of bonds with distances between particles. The covalent bonds change as e^{-r}, the ionic bond as $1/r$ and the Van der Waals force as $1/r^6$. The ionic forces that bind metals are very strong and reflect in the high temperature of melting of metals and high modulus of elasticity.

10.3 Models of Chemical Bonds

In Sect. 10.2 a summary of the principal types of chemical bonds between atoms has been presented and the dependence of these bonds with the distance between nuclei indicated. The actual force fields between atoms require Quantum Mechanics computations. In classical Mechanics, in the process of molecular modeling, a force field is represented by a selected function that includes parameters that can be experimentally determined. The function provides the potential energy of a system of particles, atoms or molecules.

An example is given in Fig. 10.1, the Lennard-Jones potential is given by [9, 10],

$$\Phi_{lJ} = 4\boldsymbol{\varepsilon}_{LJ}\left\{\left[\frac{\boldsymbol{\sigma}_{LJ}}{r}\right]^{12} - \left[\frac{\boldsymbol{\sigma}_{LJ}}{r}\right]^{6}\right\} \tag{10.1}$$

The meanings of the parameters $\boldsymbol{\varepsilon}_{LJ}$ and $\boldsymbol{\sigma}_{LJ}$ included in Eq. (10.1) are given in Fig. 10.1. $\boldsymbol{\varepsilon}_{LJ}$ is a bonding energy, the order of magnitude is 10^{-1} (nN)nm; $\boldsymbol{\sigma}_{LJ}$ is a distance, in the equilibrium position it is approximately $\boldsymbol{\sigma}_{LJ} = r_o = 0.3\,\text{nm}$. Following the conventional symbols utilized in the literature, the subscripts LJ have been added to avoid confusion with the same symbols used in Continuum Mechanics to indicate strain and stress as well. The atoms adopt a position that minimizes their potential energy for a given temperature. As indicated in Fig. 10.1, if $r < \boldsymbol{\sigma}_{\mathbf{LJ}}$, the atoms experience repulsive forces that become extremely high, that is in 3-D the atom becomes an almost rigid sphere. On the contrary, the separation of the atoms reduces the binding forces that asymptotically become zero. In Fig. 10.1, it is also represented the harmonic potential used as an approximation for the analysis of dynamical problems.

If we compute the derivative of energy function E_g (see Fig. 10.2a), the inter-atomic force function is obtained. It can be seen that when the energy has a minimum, the mutual forces are zero, condition of equilibrium at a given temperature. Assuming that the force is equal to a constant E (modulus of elasticity, see Fig. 10.2b) times the displacement Δr, $F = E\Delta r$, leads to

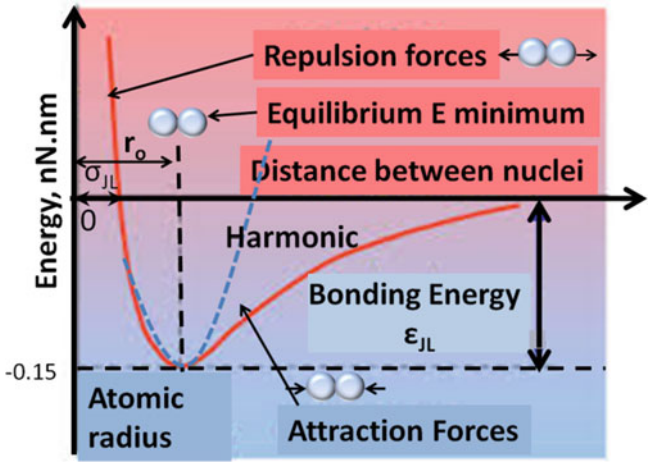

Fig. 10.1 Lennard-Jones potential and harmonic potential

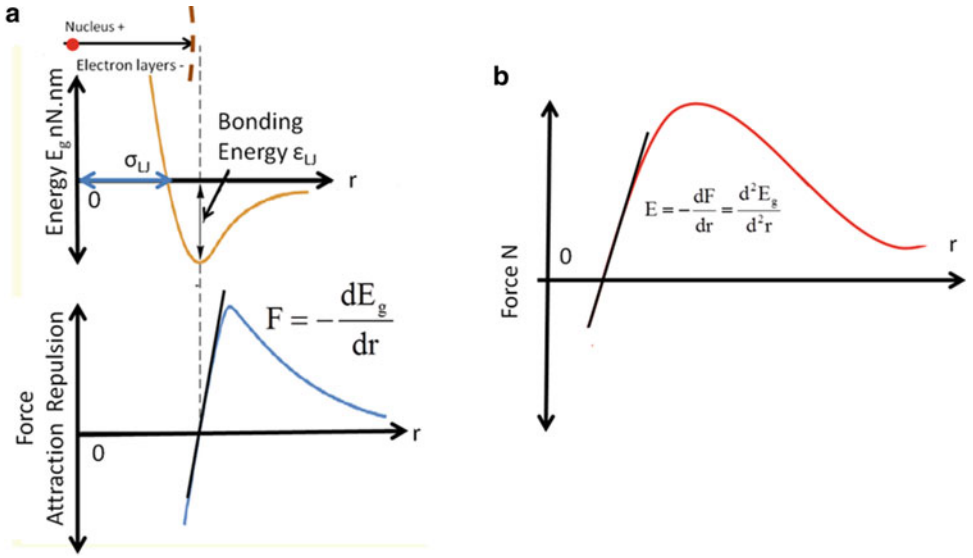

Fig. 10.2 (**a**) Inter-atomic force is the derivative of the potential energy with respect to distance; (**b**) elastic modulus is the first derivative of the inter-atomic force and the second derivative of the atomic potential with respect to distance

$$E = -\frac{dF}{dr} = \frac{dE_g^2}{dr^2} \tag{10.2}$$

The minus sign corresponds to the assumption that repulsive forces are negative and attractive forces are positive. It is possible to see that materials that have high bonding energy will have a high modulus of elasticity and the value of the modulus will be a constant in a limited range of deformations. The sharpness of the minimum of the energy function is called the potential well of the corresponding material.

10.4 Further Analysis of the Molecular Dynamics

The Lennard-Jones potential function that has been introduced in the preceding section is a particular form of a general technique called pair potentials. In 1903, Mie proposed a potential function that can take care of both repulsion and attraction of the following form [11],

$$\Phi(r) = -\frac{A}{r^n} + \frac{B}{r^m} \tag{10.3}$$

There are a number of potential pair functions that have been proposed in the literature. Since they are semi-empirical expressions that reflect basic aspects of inter-atomic forces outlined in Figs. 10.1 and 10.2, they may fail in other aspects, thus provide results that do not always agree with experimental observations. An alternative approach is to increase the number of functions and parameters. From the energetic point of view one can consider different energy contributions to the atomic arrangement. These contributions depend on the active degrees of freedom present in the system. Taking into consideration the principle that the potential energy is additive, it is possible to make a basic division of the energy into:

$$E_g = E_{lc} + E_{nlc} \tag{10.4}$$

where E_{lc} represents the local terms and E_{nlc} stands for nonlocal effects or effects at a distance. One of the classifications of local effects is the following,

$$E_{lc} = E_{bond} + E_{bond-angle} + E_{dihedral} + E_{improper-dihedral} \tag{10.5}$$

In Eq. (10.5), the term E_{bond} refers to the effect of the change of the distance Δr between nuclei that leads to Eq. (10.1), graphically represented in Figs. 10.1 and 10.2. As illustrated in Fig. 10.2, the Lennard-Jones potential contains this effect. However, at large changes of Δr that lead to bond breakage the pair potential proposed by Morse in 1929 [12, 13], takes care better of this effect,

$$\Phi(r) = \varepsilon_{LJ}\left[\exp 2\alpha\left(1 - \frac{r}{r_0}\right) - 2\exp 2\alpha\left(1 - \frac{r}{r_0}\right)\right] \tag{10.6}$$

The parameter α can be adjusted to control the curvature of the minimum of the potential energy. Both Lennard Jones and Morse assume a spherical symmetry and hence cannot take care of spatially oriented bonds. This effect corresponds to the term $E_{bond-angle}$ that is fashioned in a way that takes care of the bond geometry reproducing the effects of bond geometry; this term includes either angles or trigonometric functions. The dihedral angle potential is introduced to take care of effects observed in proteins. The improper dihedral term takes care of the chiral effects on organic molecules.

The non-localized energy potentials include the Van der Waals potential and the electrostatic potentials. The term $1/r^6$ in the Lennard-Jones potential takes care of these effects at long distances and also the negative term in the Morse potential has similar effect. In problems concerning vibrations of the atomic lattice, the harmonic potential graphically shown in Fig. 10.1 is utilized. The Morse potential is also utilized to analyze vibrations of the lattice. In this brief summary of the molecular dynamics, the aspects connected with the mechanics of engineering materials have been emphasized. One important conclusion of this analysis from the point of view of the fracture of materials is the asymmetry between the shortening of the parameter r_o illustrated in Fig. 10.1 and its stretching.

10.5 Atomic Modeling of the Continuum

The search of the solution of the connection between structure of matter and macroscopic properties can be traced back to early XIX century with Cauchy and his attempt to relate Continuum Mechanics with the atomic structure of matter that resulted in the Cauchy-Born rule [14, 15], initially introduced by Cauchy and then generalized by Born in 1915. The Cauchy-Born rule or approximation establishes a connection between atoms' positions in a crystal and the overall deformation of the crystal as predicted by Continuum Mechanics within a limited range of strains. It is necessary to relate the energy E_g defined in Figs. 10.1 and 10.2 with the elastic energy expressed as a function $W(\mathbf{E}_{ij})$ of a given strain tensor E_{ij}, assuming that the internal energy depends on deformation gradients only and one ignores thermodynamic variables and energy dissipation processes. This relationship brings the kinematics of the continuum and relates it to the changes of the atomic distances. In Sect. 10.3, it was introduced the lattice vector $\mathbf{r}$ as a parameter defining the inter-atomic potential. In order to go from an initial configuration or undeformed configuration $\boldsymbol{B_o}(X_i)$, where X_i represent the Lagrangian coordinates of the continuum points, to a deformed configuration $\boldsymbol{B_d}(x_i)$, where x_i are the Eulerian coordinates of the final positions of the points of the continuum, one can assume that a nonlinear transformation is introduced represented symbolically by $\Psi(\mathbf{X_i})$ [3]. Applying

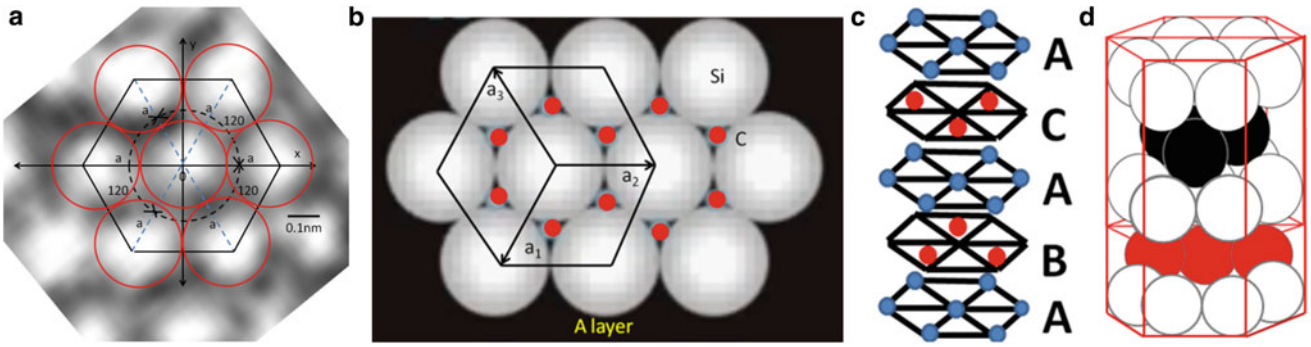

Fig. 10.3 (**a**) Elementary cell of the hexagonal packing identified in the HRTEM pattern resembling the theoretical structure of a 4HSiC crystal; (**b**) theoretical structure: the red dots indicate the position of the following atom layer shown in (**c**); (**c**) stacking sequence ACABA of the crystal [16, 17]: position of atoms in the stack; (**d**) side view of the stack

the Cauchy-Born rule we can represent the lattice vectors $\mathbf{r}$, in the Eulerian coordinates of the continuum as resulting from the application of the deformation gradient $\mathbf{F}(x_i) = \nabla_X \Psi(X_i)$,

$$\mathbf{r}_i(x_i) = \mathbf{F}(x_i)\mathbf{R}_i(X_i) \tag{10.7}$$

In Eq. (10.7), $\mathbf{r}_i$ is the vector distance between interacting atoms in the Eulerian coordinates, and $\mathbf{R}_i$ is the vector distance of the corresponding atoms in the Lagrangian coordinates. To get a visual image of these two quantities, it is necessary to go to Fig. 10.3 where side by side there are represented the ideal configuration of a hexagonal atomic arrangement and the actual image obtained from transmission electron microscopy. In Fig. 10.3a, $\mathbf{R}_i = a_o = a_1 = a_2 = a_3$, where a_o is the atomic distance in the undeformed position. Figure 10.3a is an actual HRTEM image of the arrangement of an actual hexagonal crystal, and $r_i = a_0 = a$.

We can define the total energy density as the summation of the total contributions of individual atoms uniformly distributed over a certain volume V_i,

$$W = \frac{E_g}{NV_i} = \frac{1}{NV_i}\sum_i^N E_{gi}(r_{i1} \ldots r_{iN}) \tag{10.8}$$

In Eq. (10.8), E_g is the bonding energy illustrated in Fig. 10.2 and expressed in Eq. (10.4) as the addition of local bonding energies and nonlocal bonding energies, N is the number of atoms in the considered volume V_i that interact with the atom labeled "i" and r_{ij} correspond to all the atomic distances between the atom "i" and all the atoms "j" interacting with the atom "i". Equation (10.8) is a very general expression and can be applied to the different energy potentials mentioned in Sect. 10.4. For example, if we introduce $\mathbf{\Phi}_{LJ}$, the Lennard Jones potential, it follows

$$W = \frac{1}{2V_i}\sum_{i \neq j}(\Phi_{LJ})_{ij} \tag{10.9}$$

10.6 Experimental Verification of the Cauchy-Born Rule

In Sects. 10.2–10.5 we have analyzed the whole process of merging the Continuum Mechanics approach with the atomistic description of a crystal via the bonding energy potentials. We are going to concentrate in the Experimental Mechanics verification of the merger of the two approaches to the mechanics of crystalline solids and the important conclusions that can be extracted from experimental observations. In earlier publications of the present authors [18–20], an image of a 4HSiC crystal was analyzed [21]. This particular image was selected because it is supported by extensive relevant information concerning the different steps involved in the process of generating the image. It was also of interest to study the basic unit of a hexagonal polytype of SiC whose schematic spatial organization is shown in Fig. 10.3.

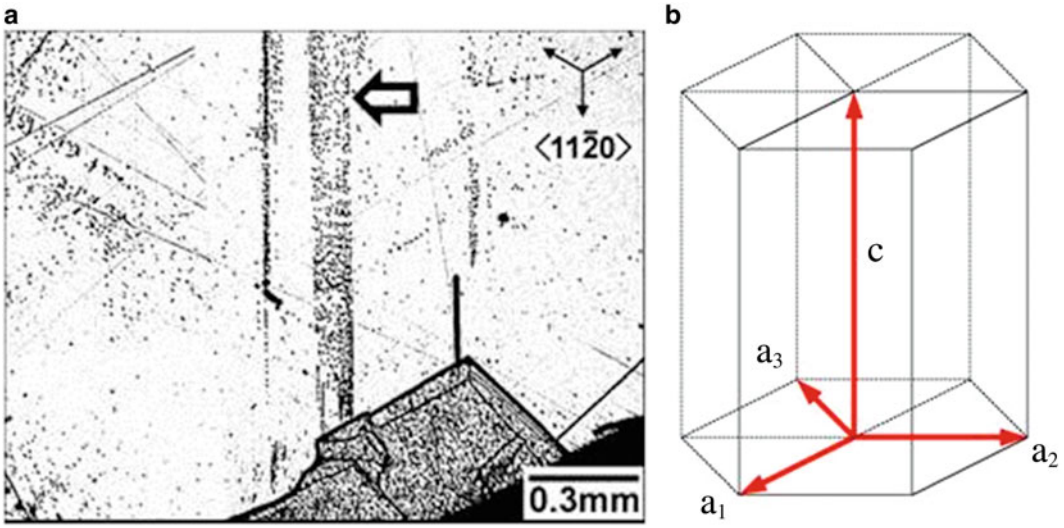

Fig. 10.4 (**a**) Optical micrograph of etch pit bands—(0001) face—of a 4HSiC wafer with bands of dislocations along directions $<11\bar{2}0>$; (**b**) theoretical structure of the hexagonal polytype of silicon carbide with $a_1 = a_2 = a_3 = a$

The basic aspects of the analyzed image are briefly described in the following paragraphs. The image source is a crystal grown by vapor deposition oriented along the plane (0001) within $\pm 0.5°$ of SiC crystal (see Fig. 10.4). Experimental measurements of the different parameters relevant to the crystal were performed. Crystals of a given material arrange in more than one given configuration. SiC can adopt a very large number of crystal configurations, in the literature more than 250 arrangements called polytypes have been identified. The analyzed crystal belongs to one of the most common polytypes. Figure 10.3c shows the sequence ACABA of the 4HSiC crystal; this sequence is relative because the radii r_o of the atomic regions corresponding to each atom all have the same magnitude. Hence, relative positions result from the possible geometrical arrangements of spheres. Figure 10.3b shows the arrangement denoted by the letter A and assuming a Si atom starts the sequence. The stacking arrangement is outlined in Fig. 10.3b and a perspective of a sequence ACABA is illustrated in Fig. 10.3c. SiC is a covalent crystal (Sect. 10.2), referred also as macromolecular substance or covalent network. All the covalent bonds join together the atoms into a crystal that can be considered as a giant molecule. Ideal crystals have perfect geometrical configurations but real crystals include defects (dislocations) that depend on the fabrication process. Hence their structures are not only determined by the ideal energy potentials that have been discussed in the preceding sections but by the configurations that result from the presence of these defects and the elastic energy arising from the residual stresses generated by the defects. The analyzed crystal thus shows dislocations that originated during the fabrication process.

Figure 10.4a shows an optical micrograph of the etch pit bands—(0001) face—of the 4HSiC wafer, these bands are the manifestation of the dislocations. The bands run along directions $< 11\bar{2}0 >$ and reveal the presence of threading edge dislocations. The theoretical structure of the hexagonal polytype of silicon carbide with $a_1 = a_2 = a_3 = a$ is shown in Fig. 10.4b.

Figure 10.5 shows more details of the dislocations seen in Fig. 10.4. This type of threading edge dislocation originated from the cooling of the SiC crystal which then caused a misoriented crystal to grow (bottom right of Fig. 10.5). The large amount of energy that concentrated in that region led to the formation of dislocations (slip bands) that caused the plane to slide as illustrated in Fig. 10.5 by the corresponding Burger's vector direction. As a result of these dislocation movements two extra half planes were generated. This re-arrangement of the crystalline structure reduced the total stored elastic energy in the crystal, thus achieving atomic configuration stability.

Figure 10.5 shows together the optical micrograph (see Fig. 10.5a) with an electron microscope image of an etch pitch (see Fig. 10.5b) and a high resolution transmission electron microscope (HRTEM) image that has two edge dislocations in the atomic array (see Fig. 10.5d). The Burger's vectors of the edge dislocations are of the type $a/3 <11\bar{2}0>$ (see Fig. 10.5c) where "a" is the 4HSiC lattice parameter.

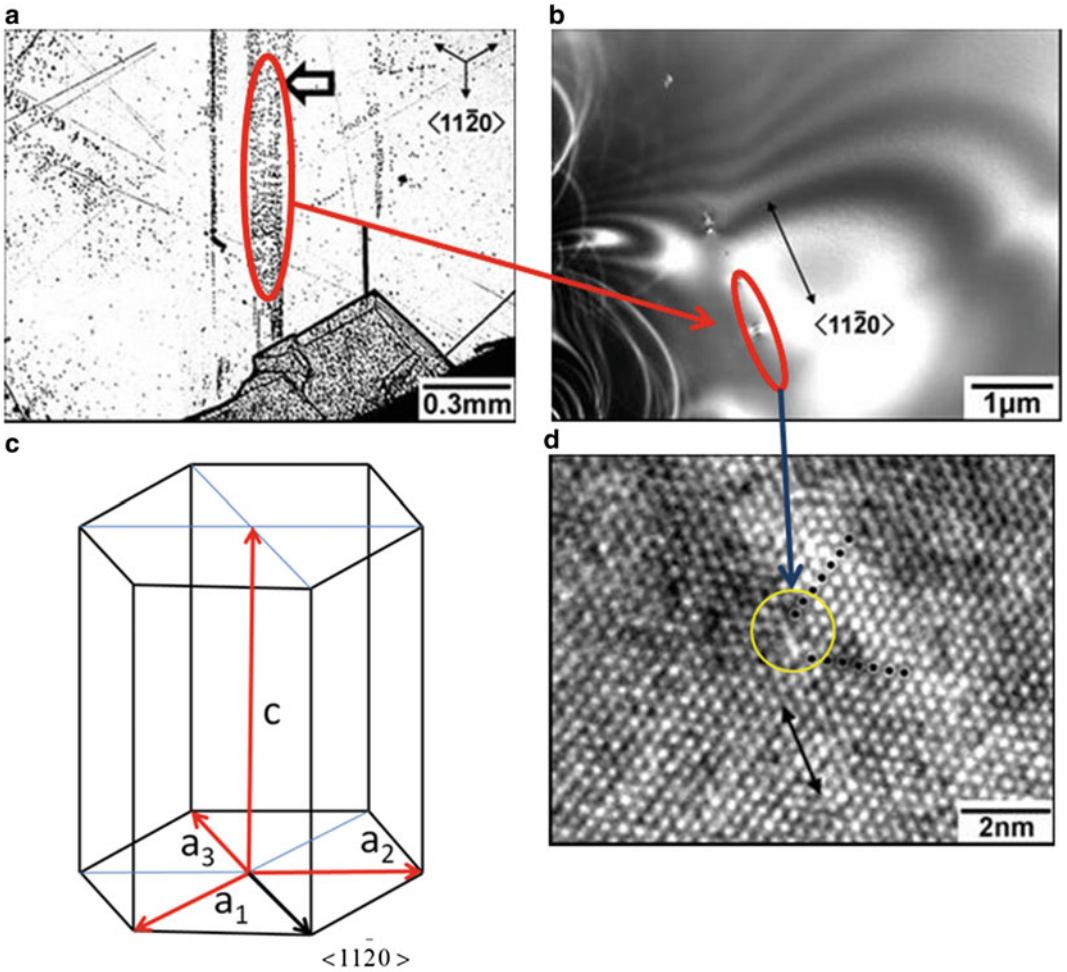

Fig. 10.5 Gliding of dislocations in slip system $<11\bar{2}0>\{\bar{1}100\}$ during post-growth cooling: (**a**) optical micrograph; (**b**) electron microscope image of a dislocation inside the red circled region; (**c**) HRTEM pattern of the crystal (dark dots indicate extra-atomic planes); (**d**) theoretical SiC structure with $a_1 = a_2 = a_3 = a$ and dislocation Burger's vector oriented as $<11\bar{2}0>$

10.7 HRTEM Image Analysis

The HRTEM image (Fig. 10.5d) contains areas where the basic cell of the crystal is very close to the ideal geometrical configuration and other regions where the crystal arrangement is highly distorted. Thus it provides information suitable to perform the analysis of the kinematics of the elementary cell under diverse conditions and to evaluate the theoretical configurations vs. actual ones. It is necessary to make an evaluation of the studied image from the experimental point of view to see if this image represents with enough accuracy the main variables of interest. In HRTEM, image formation is the result of complex processes involving subject matters of great theoretical complexity and difficulty. There are two critical points to be discussed, the image resolution and the two dimensional rendering of a 3-D object.

The resolution of the microscope from the point of view of the image formation can be expressed in terms of the classic Rayleigh criterion. The smallest distance that can be observed is given by the equation

$$\delta = \frac{0.61\lambda}{n_r \sin\alpha} \tag{10.10}$$

where λ is the wavelength of the radiation, n_r the index of refraction of the medium between the imaging lens and the image plane, α the semi-angle of the imaging lens. The wavelength associated with electrons can be approximately computed as [22],

$$\lambda = \frac{1.22}{\sqrt{E_w}} \tag{10.11}$$

In Eq. (10.11), the wavelength of the wave associated with the electron propagation is given in nm and E_w is the energy imparted to the wave expressed in eV. For the microscope utilized to get the image of Fig. 10.5d, the power of electron beam is 400 KeV. Applying Eq. (10.11), one obtains the value $\lambda = 0.00193$ nm. Since atomic radii are of the order of magnitude of 0.3 nm, the wavelength of the electron beam of the utilized microscope is well within the resolution of the atomic radii.

It should be noted that Eq. (10.10) applies to the case of incoherent illumination while the HRTEM image has a high degree of coherence. Furthermore, microscope resolution is affected by lens aberrations: the quality of magnetic lenses is poor and affects the information retrieved from image. In the present case, an alternative definition of resolution is more meaningful than the classical one. Resolution is defined as the minimum distance that can be measured in the image plane [22]. As we are going to see, by utilizing pixel interpolation in the image plane, resolution in measuring distances can be increased.

The information content of the image is represented by the mathematics of amplitude and phase modulation. The emerging wavefronts are given by a phasor (see Chap. 7.4 of Ref. [23]):

$$\vec{\mathbf{E}}_{\mathbf{L}}(\mathbf{r}, t) = E_L(\mathbf{r}, t)\, e^{i\boldsymbol{\phi}(\mathbf{r},t)} \tag{10.12}$$

In Eq. (10.12), bold letters indicate vectors, $E_L(\mathbf{r},t)$ is the amplitude of the wave associated with the electron propagation and ϕ the corresponding phase, $\mathbf{r}$ is the position vector and t is the time.

Magnetic lenses have aberrations (e.g. astigmatism, spherical, chromatic) that are included in the information retrieved by the wavefront. The information is captured as an intensity distribution detected in modern HRTEM by a raster sensor similar to electronic cameras. Image resolution is affected by the sensor similarly to what occurs in electronic cameras [24]. It is possible to correct the experimentally determined intensity via software by utilizing the concept of contrast transfer function, the equivalent of the optical transfer function used in visible optics.

It is important to understand the source of intensity distribution observed in electron microscopy. For this purpose, it is necessary to briefly analyze the interaction of matter with an electronic beam. This is an extremely complex subject which can be rigorously explained only in quantum mechanics terms. When an electronic wave impinges in the cross-section of an atom different interactions take place; of interest in our case is the stimulated emission of waves of the same frequency of the incident radiation. This interaction gives rise to waves of amplitudes proportional to the electronic density of the atom or ionic structure. This electronic density, since we are dealing with images captured on a plane, is a two dimensional density.

If we are observing an image plane, the maximum observed intensity will take place in the region where the maximum electronic density will be located. The maximum density occurs where the atomic nucleus is placed and then the observed intensity distribution can be utilized as a tool to define the position of the atom in 2-D.

In order to locate atoms in 3-D the different operation modes of the electron microscope can be used taking advantage of other types of interactions between electronic waves and observed atoms. Absorption is a very important mechanism: electronic waves can only penetrate matter in a dimensional range of few nm to 100 nm. Because the absorption coefficient increases with the energy of the electronic wave, if one uses 400 KeV the specimens must have a thickness of few nm [22].

To complete the understanding of the observed images, it is necessary to analyze the process of image formation in some more detail. One is observing a specimen of a certain thickness, d_{ob}, and this thickness is imaged at a given plane. It is necessary to find out what it is the relationship of the observed image and d_{ob}. We can go back to basic concepts of classical geometrical optics: depth of field and depth of focus. The depth of field is measured in the object space and tells us how much of d_{ob} is in focus, that is how much the object can be displaced from a given position back and forth without losing the focus in the image plane. The depth of focus refers to the image plane and tells us how much back and forth from the focal plane one can move the detector plane without an apparent loss of focus. The very thin specimen investigated in this study is the order of 10 nm and hence contains a large number of atomic planes, more than 30. In electron microscopy [22], usually the depth of focus is large enough that the whole depth of the very thin specimen is in focus and features at different depths may appear in the image. To evaluate the image content, we can analyze the actual HRTEM image of a hexagonal elementary cell shown in Fig. 10.3a. The cell was extracted away from the region circled in yellow in Fig. 10.5d and matches the theoretical atomic structure shown in Fig. 10.3b.

Different aspects of the image formation can be evaluated. It is easy to notice the similitude between the experimentally observed image and the theoretical structure. First it is necessary to explain the process followed to put together this image. From the original image (Fig. 10.5d), a small square region containing the elementary cell was cropped. A bicubical spline interpolation of the pixels was applied resulting in the scale shown in Fig. 10.3. The red circles in the figure have the radius

of the spheres $r_0 = a/2 = 0.3073/2 = 0.1537$ nm, that corresponds to the lattice parameter of SiC, $a = 0.3073$ nm at 300 K. With the above parameter the corresponding hexagon connecting the center of the spheres has been drawn.

The question of the minimum distance that can be measured in the image can now be addressed. The image of the crystal was recorded with a HRTEM JEOL 4000 EX-TEM operating at 400 KeV [25]. According to Eq. (10.11), the wavelength of the electron wave is 0.00193 nm that is of the order of 0.002 nm. Since the lattice parameter "a" is 0.3073 nm the ratio a/λ is 159. According with the criteria of optical microscopy, the mentioned wavelength λ should be able to resolve $\lambda/2$: that is, we should be able to measure 0.001 nm. We have seen that this is not feasible in electron microscopy from the point of view of the resolution defined as the fine detail of an image. The HRTEM JEOL 4000EX-TEM utilized to get the image is rated [25] as having a maximum classical resolution of 0.14 nm. Utilizing the alternative definition of resolution, the point to point distance can be evaluated as follows. The original of the picture has a pixel value S = 0.0368 nm/pixel, the sub-image has a pixel value S = 0.0011 nm/pixel that is a gain in resolution of 33 times. The bicubical spline interpolation has yielded a pixel resolution of the order of 0.001 nm. Since the arguments that follow concerning the atomic configuration are based in distance measurements one can say with confidence that the obtained conclusions are well founded.

10.8 FT of the Image and Implications for the Cauchy-Born Rule

The next step in the image analysis is to perform a Fourier Transform and observe the spectrum of the amplitudes of the image Fourier components (see Chap. 10 of Ref. [23]). Figure 10.6a shows the positions of crystallographic axes in the electron microscope pattern. The red dots show the extra atomic rows that create the two dislocations present in the image. Figure 10.6b shows an enlargement of the dislocation region showing the position of two edge dislocations generated by the added extra atomic planes (inverted green T's).

The analysis of the kinematics of the elementary cells is based on the framework and limitations that came from the idealization of 3-D array of atoms as a superposition of identical 2-D array of atoms stacked in the vertical direction. Since this stack is not identical in depth due to the sequence shown in Fig. 10.3 based in the covalent bonding of Si atoms and C atoms, the analysis is restricted to a two-dimensional array.

Figure 10.7 represents the FFT of the HRTEM pattern of the crystal shown in Fig. 10.5d. The image of Fig. 10.7a has been rotated to make the e_1 axis horizontal. The direction f_x corresponds to the family of crystallographic directions $\mathbf{a_1} \equiv [1000]$ (see Fig. 10.6a). Figure 10.8 provides a statistical average of the changes of the elementary cells in the region under analysis. The hexagon represented in Fig. 10.8 corresponds to the average size of **a** at 300 K. The departures of the positions of the corners of the hexagon with respect to the statistically observed average position reflect the distortions of the elementary cells caused by the presence of the dislocations. Figure 10.8a represents the elementary undeformed cell that is characterized for this particular crystal by the constancy of the atomic vector **a**. This vector reflects the spatial configuration of the atomic bonds that bind together the atoms. Since atoms are in continuous oscillatory motion caused by the temperature T, **a** is a statistical average in time. Figure 10.8 shows that upon the deformation caused by the presence of the dislocations the value

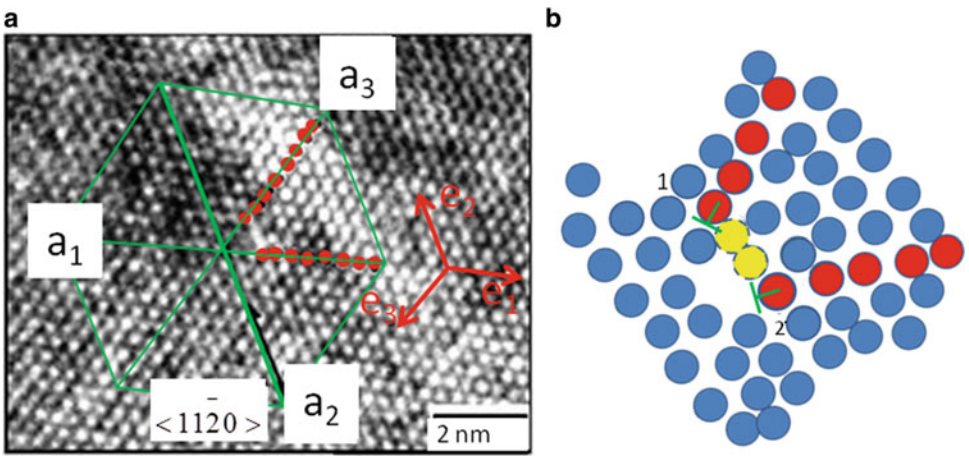

Fig. 10.6 (**a**) Crystallographic directions $< 11\bar{2}0 > \equiv \mathbf{a}_2$ as shown in Fig. 10.5c and reference coordinate system; (**b**) schematic view of the position of atoms in the neighborhood of the edge dislocations

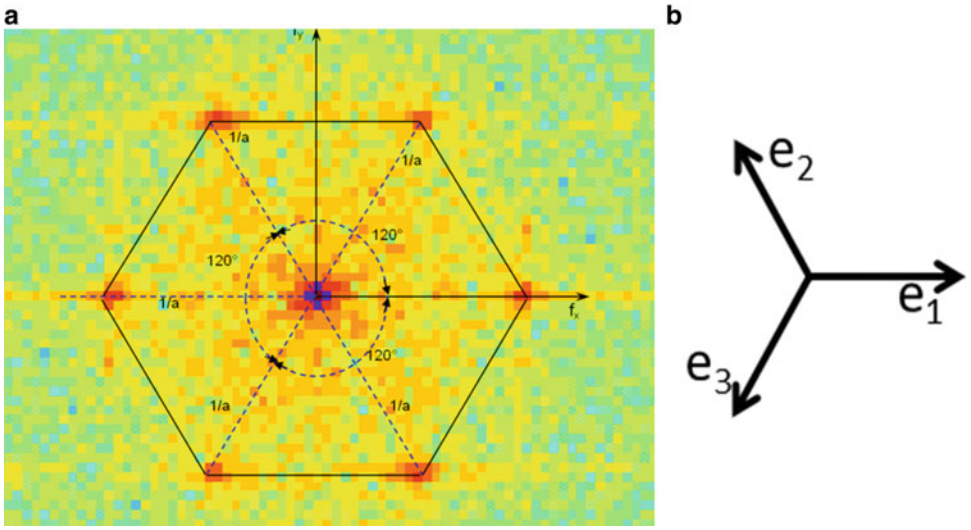

Fig. 10.7 (**a**) FFT of the HRTEM pattern shown in Fig. 10.5d; (**b**) reference system associated with the FFT (the axis $\mathbf{e}_1$ is made to be horizontal)

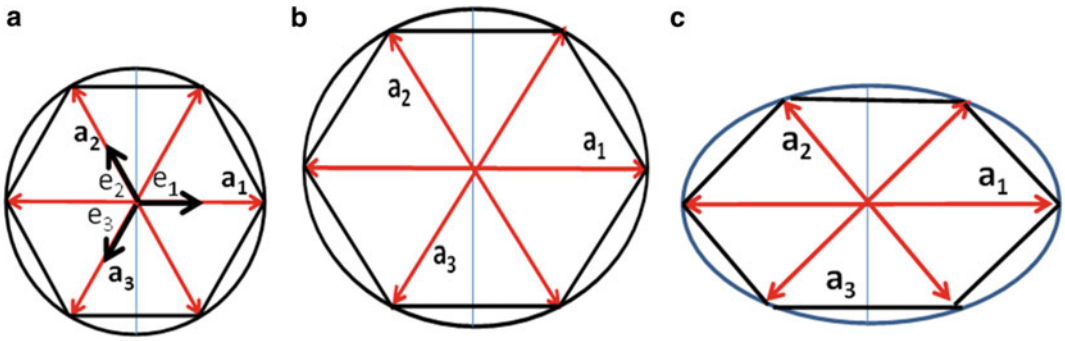

Fig. 10.8 (**a**) Fundamental 4HSiC cell; (**b**) biaxial deformation (tension); (**c**) shear deformation of the elementary cell

of **a** is modified. In the 2-D approach we can analyze the changes of the elementary cell as superposition of different changes in the dimensions and orientations of **a**.

Figure 10.8 shows the changes of the elementary cell that can be superimposed to get the different configurations statistically observed in Fig. 10.7. All the main diagonals of the hexagon show increases and decreases of the value of the modulus of **a**. Increasing frequencies correspond to shortening of a_1, modulus of **a** in the direction [1000]. Lower frequencies correspond to elongations of a_1. Let a_{1r} be the value of a_1 for 300 K and $a_1(+f)$ the value of a_1 for increasing frequencies: it holds $a_1(+f) < a_{1r.}$ Conversely, if $a_1(-f)$ is the value of a_1 for decreasing frequencies, it holds $a_1(-f) > a_{1r}$. The corresponding distribution of a_{1r} is asymmetric with wider ranges for the $a_1(-f)$ than for the $a_1(+f)$. This distribution reflects the asymmetry of the potential function that determines the forces binding atoms. From the position of equilibrium a_{1r}, the repulsion forces between atoms have a much steeper gradient that the attraction forces between atoms as they move apart (see Fig. 10.1). This asymmetry is very important in the analysis of the kinematics of the elementary cell. In solid mechanics and for small deformations, compression and tension displacements are considered symmetric. Looking at Fig. 10.2a, at the minimum of E_g the second derivative of the energy has a value that can be assumed linear for a small range of variation of the value of r_o. This is true for molecular arrangements that have a deep well at the minimum of the potential energy. This is the case of the SiC that has a high modulus of elasticity and high specific energy density.

It is possible to see also in Fig. 10.7 that the diameters of the hexagon experience rigid body rotations. The reason for this conclusion comes from the analysis of Fig. 10.7: it is possible to get pixels that can be connected to the undeformed hexagon but that are slightly rotated in the plane under analysis.

The above experimental observations provide a verification of the validity of the Cauchy-Born rule applied to the kinematics of the continuum, within the range of deformations present in the analyzed images away from the proximity of the dislocation region.

10.9 Mathematical Expressions of the Cauchy-Born Rule in Eulerian Coordinates

Figure 10.9 shows the basic system of reference with the versors $\mathbf{a_i}$ (i = 1, 2, 3). The displacements of the atomic positions in the deformed configuration in the hexagon can be expressed as:

$$\mathbf{u} = u_{a1}\mathbf{a}_1 + u_{a2}\mathbf{a}_2 + u_{a3}\mathbf{a}_3 \tag{10.13}$$

If the displacement components along three versors are available one can define the tensor of the deformations for the considered hexagon. The displacement derivatives with respect to these directions can be computed and finally one can obtain the derivatives that enter into any selected definition of a strain tensor that satisfy the conditions imposed by Continuum Mechanics. Looking at Fig. 10.9, the following equations can be written:

$$\begin{cases} \dfrac{\partial u_{a1}}{\partial a_1} = \dfrac{\partial u}{\partial x}\cos^2\theta_{a1} + \dfrac{\partial v}{\partial y}\sin^2\theta_{a1} + \left[\dfrac{\partial u}{\partial y} + \dfrac{\partial v}{\partial x}\right]\cos\theta_{a1}\sin\theta_{a1} \\ \dfrac{\partial u_{a2}}{\partial a_2} = \dfrac{\partial u}{\partial x}\cos^2\theta_{a2} + \dfrac{\partial v}{\partial y}\sin^2\theta_{a2} + \left[\dfrac{\partial u}{\partial y} + \dfrac{\partial v}{\partial x}\right]\cos\theta_{a2}\sin\theta_{a2} \\ \dfrac{\partial u_{a3}}{\partial a_3} = \dfrac{\partial u}{\partial x}\cos^2\theta_{a3} + \dfrac{\partial v}{\partial y}\sin^2\theta_{a3} + \left[\dfrac{\partial u}{\partial y} + \dfrac{\partial v}{\partial x}\right]\cos\theta_{a3}\sin\theta_{a3} \end{cases} \tag{10.14}$$

From the above equations, it is possible to determine the principal derivatives with respect to coordinate system x − y and the orientation of the principal directions with respect to these axes:

$$\begin{cases} \dfrac{\partial u_1}{\partial x} = \dfrac{\dfrac{\partial u}{\partial x} + \dfrac{\partial v}{\partial y}}{2} + \sqrt{\left[\dfrac{\frac{\partial u}{\partial x} - \frac{\partial v}{\partial y}}{2}\right]^2 + \left[\dfrac{\partial u}{\partial y} + \dfrac{\partial v}{\partial x}\right]^2} \\ \dfrac{\partial u_2}{\partial y} = \dfrac{\dfrac{\partial u}{\partial x} + \dfrac{\partial v}{\partial y}}{2} - \sqrt{\left[\dfrac{\frac{\partial u}{\partial x} - \frac{\partial v}{\partial y}}{2}\right]^2 + \left[\dfrac{\partial u}{\partial y} + \dfrac{\partial v}{\partial x}\right]^2} \end{cases} \tag{10.15}$$

$$\tan 2\boldsymbol{\theta} = -\frac{\frac{\partial u}{\partial y} + \frac{\partial v}{\partial x}}{\frac{\partial u}{\partial x} - \frac{\partial v}{\partial y}} \tag{10.16}$$

The above quantities can be determined experimentally and introduced in Eqs. (10.14)–(10.16). It is important to realize that the above relationships provide an Eulerian description of the deformed crystal and the adopted system of reference is attached to the structure of the crystal. In the derivation of Eqs. (10.14)–(10.16) it was assumed that, upon deformations, the directions $\mathbf{a_1}$, $\mathbf{a_2}$ and $\mathbf{a_3}$ change orientations with respect to the initial configuration.

There is an alternative analysis procedure based in extending Continuum Mechanics to the field under observation. Figure 10.7 showed the FFT of the crystal structure and the labeling of the corresponding axes in the physical space. These

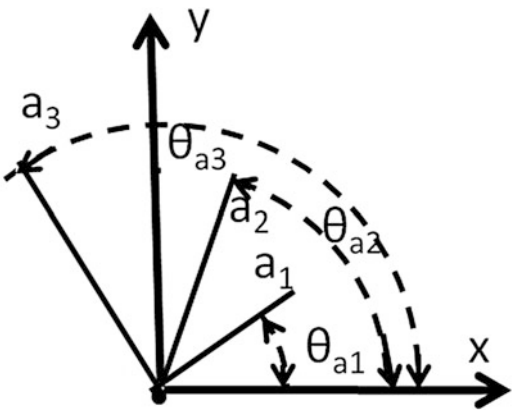

Fig. 10.9 Relationship between derivatives of displacements measured along three different versors and Cartesian coordinates

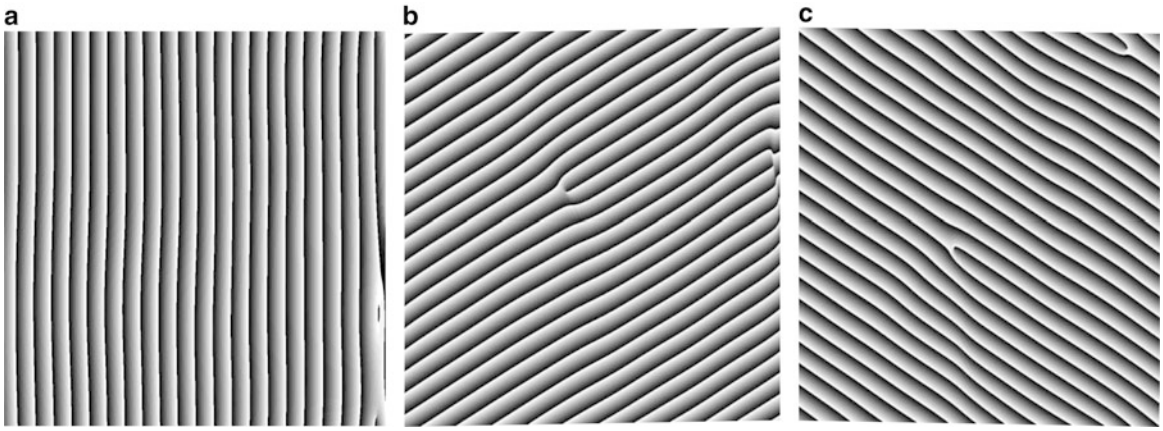

Fig. 10.10 Phases of the harmonics that modulate the deformed structure of the crystal: (**a**) direction $\mathbf{e}_1$; (**b**) direction $\mathbf{e}_2$); (**c**) direction $\mathbf{e}_3$. These images do not correspond to actual position in the image shown in Fig. 10.5d because they came from Fig. 10.7 where $\mathbf{e}_1$ has been made horizontal

axes correspond to the undeformed crystal orientations, with axis $\mathbf{e}_1$ oriented along the crystallographic family of directions $\mathbf{a_1} \equiv <1000>$ (see Fig. 10.8a). We can introduce the concept of digital moiré (see Chap. 13.8 of Ref. [23]) and through this procedure provide a tool to analyze the kinematics of the hexagonal crystal at the level of the elementary cell.

Symbolically, the deformation of the elementary cell can be represented as a function $F(\mathbf{e}_1,\mathbf{e}_2,\mathbf{e}_3,t)$ and the gradient of this function represented by $\nabla F(\mathbf{e}_1,\mathbf{e}_2,\mathbf{e}_3,t)$ provides the derivatives that characterize the state of deformation. From the inverse FFT of Fig. 10.7a we can get the three systems of fringes at orientation 120° to each other (see Fig. 10.10 presented later in this section). We also know the undeformed configuration of the crystal and can generate the phases corresponding to the undeformed crystal. From the wrapped phases of the crystal through differentiation in the frequency space we can compute the derivative of the displacements (see Chap. 13.8 of Ref. [23]). We have the equivalent of a three-elements rosette with arms at 0°, 120° and 240°. The correspondence between rosette orientations and directions (orthogonal to fringe orientation) in the FFT space is also shown in the figure. Calling $\mathbf{e_1}$, $\mathbf{e_2}$ and $\mathbf{e_3}$ the axes of the rosette (as shown in Figs. 10.7b and 10.8a) and following a similar argument to that utilized for deriving Eqs. (10.14)–(10.16), principal derivatives can be obtained as a function of the derivatives measured along the rosette axes:

$$\frac{\partial u_1}{\partial x_1}, \frac{\partial u_2}{\partial x_{2p}} = \frac{1}{3}\left(\frac{\partial u_{e1}}{\partial e_1} + \frac{\partial u_{e2}}{\partial e_2} + \frac{\partial u_{e3}}{\partial e_3}\right) \pm \frac{\sqrt{2}}{3}\left[\sqrt{\left(\frac{\partial u_{e1}}{\partial e_1} - \frac{\partial u_{e2}}{\partial e_2}\right)^2 + \left(\frac{\partial u_{e2}}{\partial e_2} - \frac{\partial u_{e3}}{\partial e_3}\right)^2 + \left(\frac{\partial u_{e3}}{\partial e_3} - \frac{\partial u_{e1}}{\partial e_1}\right)^2}\right] \tag{10.17}$$

where x_1 and x_2 are the coordinate axes, $e_1 \equiv x_1$ and the x_2-axis is orthogonal to x_1.

The principal directions of the derivatives are obtained from the following relationship:

$$\boldsymbol{\theta} = \frac{1}{2}\text{arctg}\left\{\frac{\sqrt{3}\left(\frac{\partial u_{e3}}{\partial e_3} - \frac{\partial u_{e2}}{\partial e_2}\right)}{2\frac{\partial u_{e1}}{\partial e_1} - \left(\frac{\partial u_{e2}}{\partial e_2} + \frac{\partial u_{e3}}{\partial e_3}\right)}\right\} \tag{10.18}$$

From Eqs. (10.17) and (10.18), one can compute principal derivatives and obtain all the necessary information on the elementary cell that has been analyzed.

Figure 10.10 shows the phase of the fringes obtained filtering the diffraction pattern of Fig. 10.7a. The HRTEM patterns were processed with the Holo Moiré Strain Analyzer image processing software developed by C.A. Sciammarella and his coworkers [26].

10.10 Analysis of Elementary Cells

In order to further shed light on the proposed approach to the crystal kinematics, it is interesting to survey some regions of the HRTEM pattern shown in Figs. 10.5d and 10.6a. The selected cell is located in the tension region of the stress distribution produced by the dislocation region (see Fig. 10.11a). The scale of Fig. 10.11a is $S_c = 0.000900$ nm/pixel, the axis $\mathbf{a_1}$ is oriented in the crystallographic direction [1000]. In Fig. 10.11a, the green lines represent the limits of the region of influence of each atom.

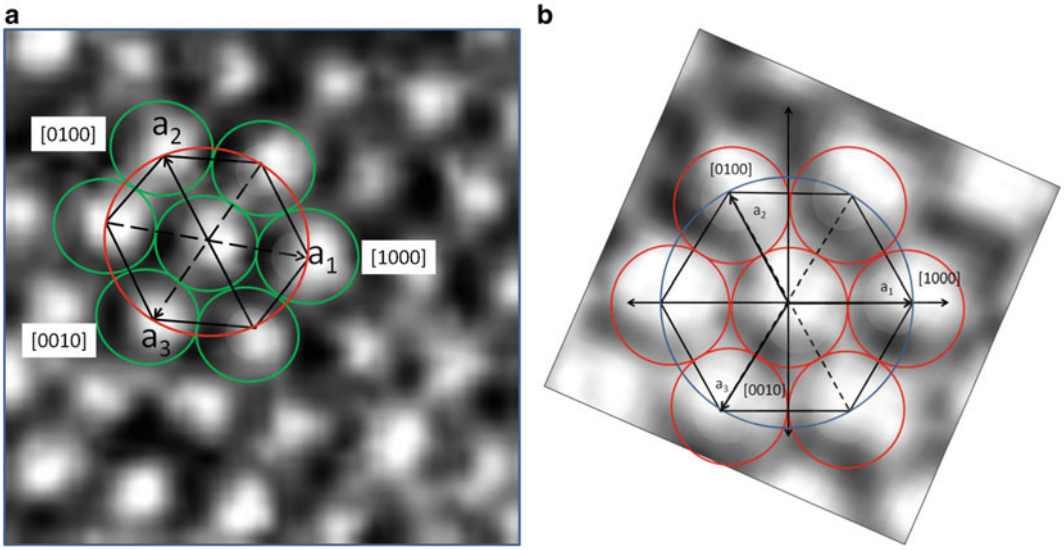

Fig. 10.11 Elementary cells in the tension region (**a**) and compression region (versors) of Figs. 10.5d and 10.6a

These outlines are no longer circles but ellipses, they fit the elementary cell configuration and the elementary cell is contained in an ellipse that is very closely similar to the shapes of the green ellipses that define the atoms positions of equilibrium. These ellipses are similar to the ellipses of the classical continuum kinematics that define the principal strains. Principal strains can be computed taking into consideration the changes of the $\mathbf{r}_{ij}$. The following values are obtained: $\varepsilon_1^e = 0.0501$, $\varepsilon_2^e = 0.0487$, the principal direction $\boldsymbol{\varepsilon}_1{}^e$ lays along the crystallographic direction [1000] while the other principal direction $\boldsymbol{\varepsilon}_2{}^e$ is perpendicular to it. Similar results have been obtained by applying numerical methods based on molecular dynamics to the analysis of homogeneous states of deformation [3]. In space we can assume that the original spheres shown in Fig. 10.3 become ellipsoids. Hence, the initial isotropy of the field is broken and each elementary cell becomes an anisotropic crystal (similar to Photoelasticity). Figure 10.11b shows an elementary cell located in the compression region. The scale of Fig. 10.11b is $S_c = 0.0009789$ nm/pixel. The principal strains are $\varepsilon_1^e = -0.02550$, which coincides with the direction [1000], and $\varepsilon_2^e = -0.0260$ which is perpendicular to this direction. It is interesting to observe that in the tension region the inter-atomic distances (black area) are more noticeable that in the compression region reflecting the asymmetry of the inter-atomic potential.

10.11 Extension of Continuum Kinematics to the Full Field

In the preceding sections, the individual cells were considered as three arms rosettes. In this section, the experimental method is applied to the aggregate of elementary cells, including the dislocation region. We will start with the analysis of Fig. 10.10. As mentioned before, three systems of fringes at orientation 120° to each other can be obtained from the FFT shown in Fig. 10.7: this is the equivalent of a three arm rosette applied to the full field of the analyzed image. From the patterns of Fig. 10.10 one can get the necessary derivatives to get the following tensor **J**.

$$\mathbf{J} = \begin{bmatrix} \dfrac{\partial u_1}{\partial x_1} & \dfrac{\partial u_1}{\partial x_2} \\ \dfrac{\partial u_2}{\partial x_1} & \dfrac{\partial u_2}{\partial x_2} \end{bmatrix} \tag{10.19}$$

Having obtained the components of the tensor **J**, one can compute the components of the Almansi's strain tensor as follows:

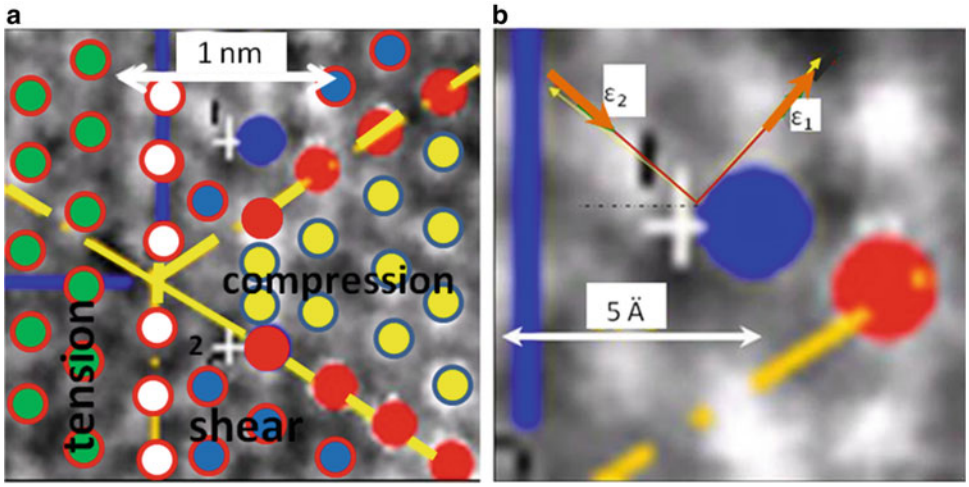

Fig. 10.12 (**a**) Image position of atoms in neighborhood of two edge dislocations; (**b**) magnified region around point 1 showing the principal strains of the Almansi's strain tensor and corresponding rigid body rotation of principal strain directions

$$\boldsymbol{\varepsilon}_{11}^{\mathrm{A}} = \frac{\partial \mathrm{u}_1}{\partial x_1} - \frac{1}{2}\left[\left(\frac{\partial \mathrm{u}_1}{\partial x_1}\right)^2 + \left(\frac{\partial \mathrm{u}_2}{\partial x_1}\right)^2\right] \tag{10.20}$$

$$\boldsymbol{\varepsilon}_{22}^{\mathrm{A}} = \frac{\partial \mathrm{u}_2}{\partial x_2} - \frac{1}{2}\left[\left(\frac{\partial \mathrm{u}_1}{\partial x_2}\right)^2 + \left(\frac{\partial \mathrm{u}_2}{\partial x_2}\right)^2\right] \tag{10.21}$$

$$\boldsymbol{\varepsilon}_{12}^{\mathrm{A}} = \frac{1}{2}\left[\frac{\partial \mathrm{u}_1}{\partial x_2} + \frac{\partial \mathrm{u}_2}{\partial x_1}\right] - \left[\frac{\partial \mathrm{u}_1}{\partial x_1}\frac{\partial \mathrm{u}_1}{\partial x_2} + \frac{\partial \mathrm{u}_2}{\partial x_1}\frac{\partial \mathrm{u}_2}{\partial x_2}\right] \tag{10.22}$$

Figure 10.12a shows the image corresponding to Fig. 10.6b where the two edge dislocations are represented by the two green inverted T's. The converging yellow lines correspond to the lines that are the axis of the two added extra rows of atoms. In the neighborhood of the dislocation, the basic atomic arrangement shown in Fig. 10.8a is distorted. The region of the yellow circles is under compression and corresponds to a shortening of the parameter "a" of Fig. 10.8a. The region of the green circles is under tension as shown in Fig. 10.8b: the parameter "a" is increased. The region of the blue circles is subjected to shear as shown in Fig. 10.8c. For example, the angles of the fundamental hexagon are changed: the "a_1" parameter is elongated, "a_2" and "a_3" are shortened.

The moiré fringe pattern analysis provides important information that is being retrieved from the 2-D image produced by the electron microscope. The kinematics of the continuum has been merged to the inter-atomic spaces via the utilization of digital moiré. The presence of fringe dislocations in the fringe patterns in the same position as physical dislocations indicates the place where there are discontinuities in the displacement field (see Chap. 10.5 of Ref. [23]).

Figure 10.13a corresponds to the derivative $\partial \mathrm{u}e_2/\partial e_2$ in the direction $\mathbf{e_2}$ versor shown in Fig. 10.6a and it is obtained from the moiré pattern of Fig. 10.10b and approximately corresponds to the upper portion of the region marked "compression" in Fig. 10.12a. In this region there is a shortening of the parameter "a": there are the yellow circles and the corresponding level lines are reddish. The blue level lines correspond to tensile deformations (parameter "a" increasing) and correspond to the green circles in Fig. 10.12a. The greenish level lines correspond to the region of transition between the compression and tension, white circles, "0" deformation. In this region the parameter "a" keeps its undeformed value, a = 0.3073 nm. Similar conclusions apply to Fig. 10.13b that corresponds to the versor $\mathbf{e_3}$ and represents the upper part of the region labeled "compression" in Fig. 10.12a.

Since the rotations in the analyzed region are small, derivatives of displacements computed from the patterns of Fig. 10.10 provide close enough values of local strains in the dislocation region. It is interesting to observe that these derivatives show a spatial distribution very similar to the pattern corresponding to the theory of elasticity solution shown in Fig. 10.13c. However, while the theoretical solutions include symmetric values the patterns of Fig. 10.13a, b show larger gradients in compression than in tension. This asymmetry is connected with the asymmetry of the energy potential in the atoms illustrated in Fig. 10.1. Through the above analysis it is possible to have an idea of the magnitude of the deformation

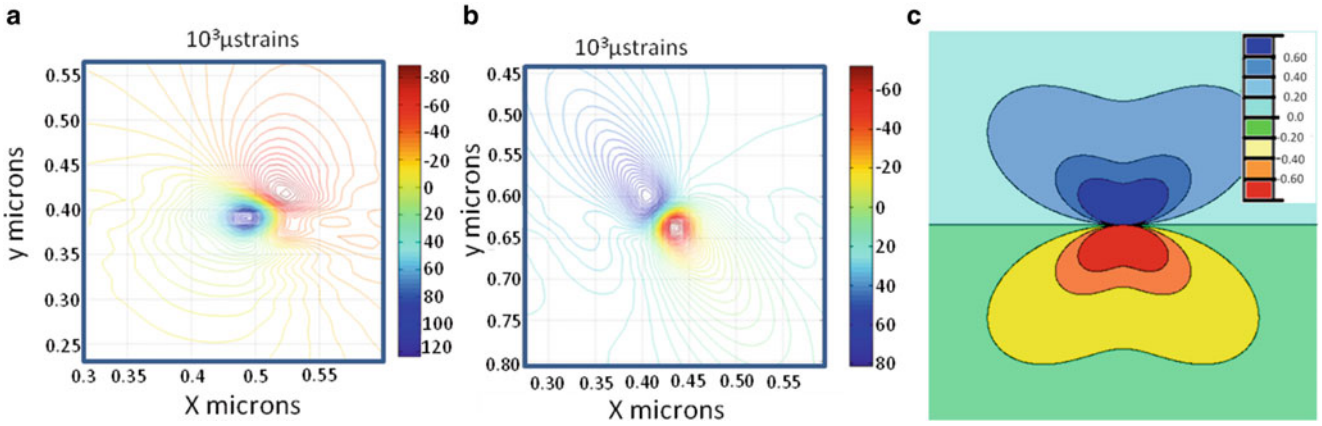

Fig. 10.13 (**a**) Displacement derivative $\partial u_{e2}/\partial e_2$ in the direction $\mathbf{e_2}$; (**b**) displacement derivative $\partial u_{e3}/\partial e_3$ in the direction $\mathbf{e_3}$; (**c**) theory of elasticity solution stresses in the direction parallel to the line of separation between tension and compression [27]. The derivatives are not plotted in their actual position of Fig. 10.5d

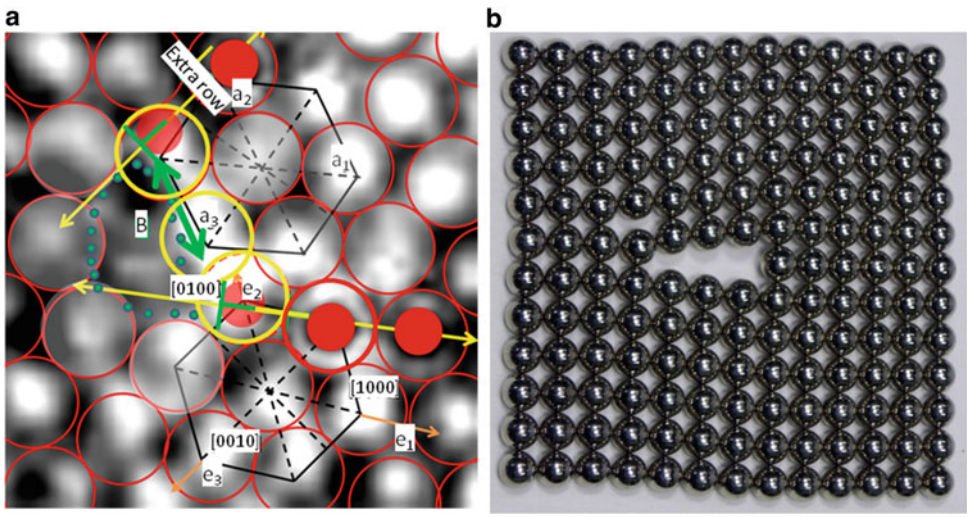

Fig. 10.14 (**a**) Atoms location in the crystal region hosting the dislocation; (**b**) simulation of the presence of a dislocation using magnetic spheres [27]

caused by dislocations generated during the growth stage of a 4HSiC crystal in the region where the cooling rates have altered the regularity of the crystalline array: about 0.05 in tension and about 0.03 in compression. It is interesting to point out that in Sect. 10.10 from the analysis of the elementary cells the values computed in tension were $\varepsilon_1^e = 0.0501$, $\varepsilon_2^e = 0.0487$ while the corresponding values for compression were $\varepsilon_1^e = -0.02550$, $\varepsilon_2^e = -0.0260$. These values are in good agreement in the order of magnitude with the results of the moiré analysis.

10.12 Analysis of the Dislocation Region

In the atomistic theory of the continuum it is accepted that the Cauchy-Born rule describes the behavior of the continuum provided the regular atomic arrangement does not experience large perturbations [3]. In this section we will analyze what occurs in an actual dislocation. The dislocation area creates an interruption of the orderly sequence of the SiC crystal. Figure 10.14a shows a closer look at the region of the two dislocations present in Fig. 10.12a and the positions of the atoms in this region. The red dots represent the atoms of the extra-rows and correspond to the red dots of Fig. 10.12a. The yellow lines indicate again the direction of the extra rows. The edge dislocations are indicated with the green symbols $\perp$, the vector **B** indicates the direction of the Burger's vector of the edge dislocations. Two basic hexagonal cells are indicated in the

vicinity of the extra atomic rows. The dislocations interrupt the basic cell arrangement corresponding to the equilibrium condition shown in Fig. 10.8a. The red circles indicate the intersections of the plane of the image with the spherical regions that correspond to the equilibrium positions. The intensity distributions within these circles are functions of the electron density with the maxima in correspondence with the nuclei of the atoms. The atoms positions are outlined by the corresponding circles with the exception of the atoms just after the extra-rows end indicated by yellow circles in Fig. 10.14a and outlined by yellow dots in Fig. 10.6b. These images show high intensity with little variation like blurred images. Just behind this atoms row there is a region of very low light intensity indicating a low density of the electron field. This region interrupts the sequence of the hexagonal patterns corresponding to the equilibrium positions of the atoms and is outlined with green dots. This region is the beginning of a sort of cavity that is almost located in the intersection of the yellow lines defining the orientation of the extra-rows. The next row of atoms, close to the yellow lines shows a deformation in the direction of the Burger's vector, $< 11\overline{2}0 >$ of approximately $\varepsilon^e = 0.130$.

Figure 10.14b shows the packing of rigid magnetic spheres. It is possible to see that the model of attracting rigid spheres, although an interesting visualization for an edge dislocation, does not provide the actual field of atomic arrangement. Atoms evidently cannot be modeled as rigid spheres: the cavity in the dislocation region of the rigid spheres is about $6.5r_o$ long while in the actual dislocation is roughly about $2r_o$, and actually it is not a cavity in the strict sense of the word as the image shows the presence of some electron density in the cavity. The cavities formed between atoms due to the presence of structural defects have an interesting property that makes its presence experimentally detectable. Due to the low electronic density if positrons are sent to this cavity, an electron and a positron form a pair, this pair is not stable and decays into two γ-rays. Using a γ-rays detector it is possible to count the number of events and this number can be used to provide a measure the number of cavities present in a specimen [28].

It is interesting to notice here that the application of the Cauchy-Born rule as a homogenization technique provides a displacement field that yields high derivative values indicating the presence of a dislocation and merges with the theory of elasticity modeling of an edge dislocation. The problem that the molecular dynamics attempts to solve is the problem of the instability of the molecular arrangement that leads to the actual onset of plasticity and eventually to the fracture of the crystal.

From Fig. 10.13, it can be concluded that the elasticity solution of an edge dislocation mimics what actually occurs at an actual dislocation: there is a region with very high compressive strains (the main parameters of the elementary cells are shortened), followed by a neutral region where the atoms remain in the equilibrium configuration (no deformation occurs), followed by a region where the basic parameters of the elementary cell are increased (tension region). However, while the theory of elasticity provides symmetrical compression and tension regions, the experimental results shows that these two regions are not symmetric due to the property of the modulus of elasticity as a derivative of the potential energy (see Fig. 10.2b), which is not symmetric with respect to the equilibrium position.

It is important to realize that the observed image is a snap shot of events that occur in time. For example, the blurred images of the electronic density after the extra atomic rows end could mean that the electronic density fluctuates during the picture exposure time due to the energy imparted by the electron beam of the microscope to the atoms located at the dislocation edge [22].

10.13 Discussion and Conclusions

The main objective of this paper was to utilize Experimental Mechanics methods to establish a bridge between classical continuum mechanics variables and the atomistic analysis of solid mechanics, thus providing experimental evidence that supports the Cauchy-Born conjecture and shedding light on the connection between atomic configuration changes and continuum mechanics solutions as homogenizing functions of these changes. There are two important aspects to this problem, the description of the motion of the continuum in function of a parameter (for example, the time), the kinematics of the continuum. The other fundamental aspect is the dynamics of the motion, the connection of the kinematic variables with the forces that cause the motion. This paper has focused on the kinematics of atomic motions and its connection with the kinematics of the continuum. The fundamental question that is investigated is the connection between the phenomenological description of the deformation of solids by Continuum Mechanics and the basic geometrical changes that take place at the level of crystalline organization.

The basic question that the theoretical efforts of atomistic based models as well as the Continuum approach try to answer has deeper practical consequences for scientists and engineers: Which are the mechanisms of atomic configurations or of the parameters of the Continuum approach that lead to the fracture of crystals? In simple words, a reiteration of centuries old question: Why things fracture, why things fail? Throughout centuries multiple paths have been followed to get partial

answers to this question. Currently the advent of computer sciences, computing hardware and numerical methods for the solution of partial differential equations have provided the means to get solutions for complex theoretical models of molecular dynamics that provide limited answers to the above posed questions. It is possible to summarize the current state of the art of the partial answers that have been obtained. In a few words, the problem of the stability of crystalline arrays is formulated in terms of the stability of the internal energy W expressed as a function of suitable tensorial forms of the displacement gradient field **F** and a corresponding form of a stress tensor **P** [3]. In this process, appears one important event: for example, the onset of plasticity in metals. This subject also has been and is the subject of extensive theoretical and experimental research. As a physical phenomenon the onset of plasticity implies the beginning of the motion of dislocations through the crystalline array: this is the point of view of the dynamic time dependent plasticity evolved in the Science of Materials. In the Mechanics of the Continuum, the transition from the elastic behavior to the plastic behavior is idealized through the model of time independent plasticity. In Continuum Mechanics, the time dependent departure from elasticity is related to transient creep and strain-rate sensitive behavior of metals where time effects are important. There is another important event to account for, the transition from plasticity to fracture. The current state of the art from the engineering point of view is Fracture Mechanics. The near field at the tip of a crack is modeled by an approximate solution of the theory of elasticity that assumes the existence of a singularity at the crack tip where the stresses become infinite. The extensions of this approach including the presence of a plastic zone at the crack tip still assume the existence of a singularity at crack tip.

This approach leads to the formulation of the transition from plasticity to fracture by introducing for example the J-integral formulation. In essence, both the elastic and the elastoplastic approaches to establish the instability of the crack propagation are based on the balance of the elastic energy stored in the material and the energy required to form new crack surfaces. These approaches do not consider the molecular dynamics phenomena that are the events leading from the onset of plasticity to the actual fracture. In the approach of the atomistic-quasi-continuum mechanics [3], transition from plasticity to fracture is also formulated on the basis of the energy analysis.

There is another approach to the formulation of the onset of plasticity and of the transition from plasticity to fracture. This approach [29–36] is based on experimental observations of the transition of elastic to plastic behavior of tensile specimens and the passage of plastic behavior to actual fracture of these specimens. The experimental tool that could be called cine-speckle interferometry provides a visualization of the process of loading a tensile specimen by recording successive frames of the loading process (Fig. 10.15). Speckle interferometry fringes of the tensile specimen are isothetic lines or lines of equal projected displacements that for the particular interferometer utilized in the experiments provide fringes of lines of equal vertical displacement. At the transition from elasticity to plasticity a particular fringe formation takes place that propagates from the end of the specimen that is being pulled to the fixed end. This particular fringe formation indicates the presence of a plastic wave, a sort of a soliton wave that propagates from the moving end to the fixed end and reflects back. Figure 10.15a shows the beginning of the wave propagation; Fig. 10.15b–c show further advance of the plastic wave; Fig. 10.15d shows the stage when the plastic region remains localized at the middle of the specimen before the specimen brakes; Fig. 10.15e shows the broken specimen.

The plastic wave fringes are oriented at 45° to the vertical axis and represent lines of maximum shear. The propagation back and forth ends when the elongation of the specimen through this mechanism of plastic wave propagation is exhausted

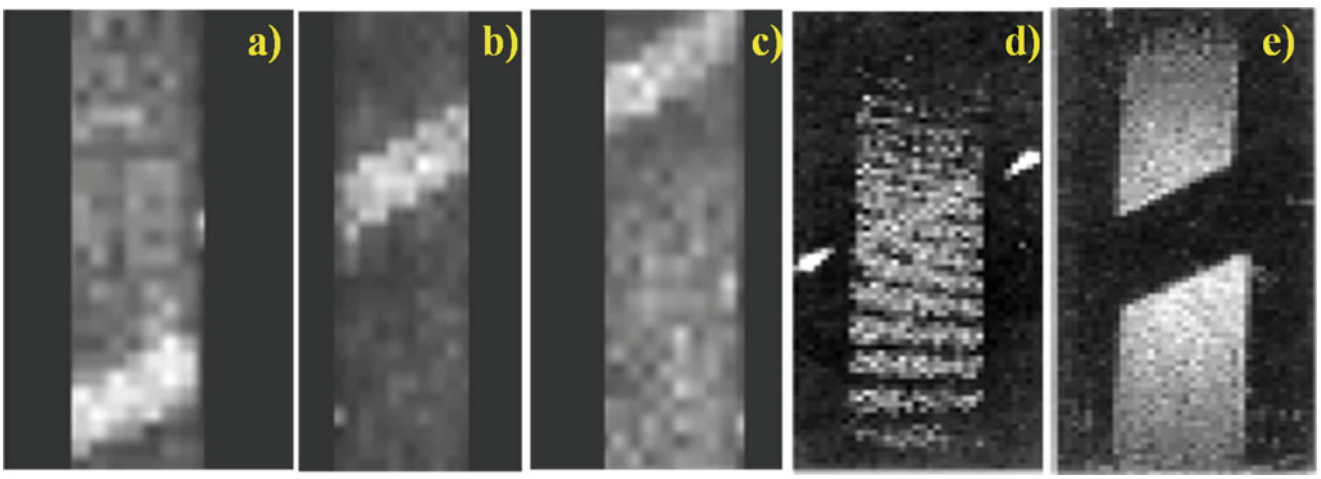

Fig. 10.15 Tensile specimen: propagation of a plastic wave from the loading end (*bottom*) to the fixed end (*top*) and localization (*arrows*), and final fracture [29]

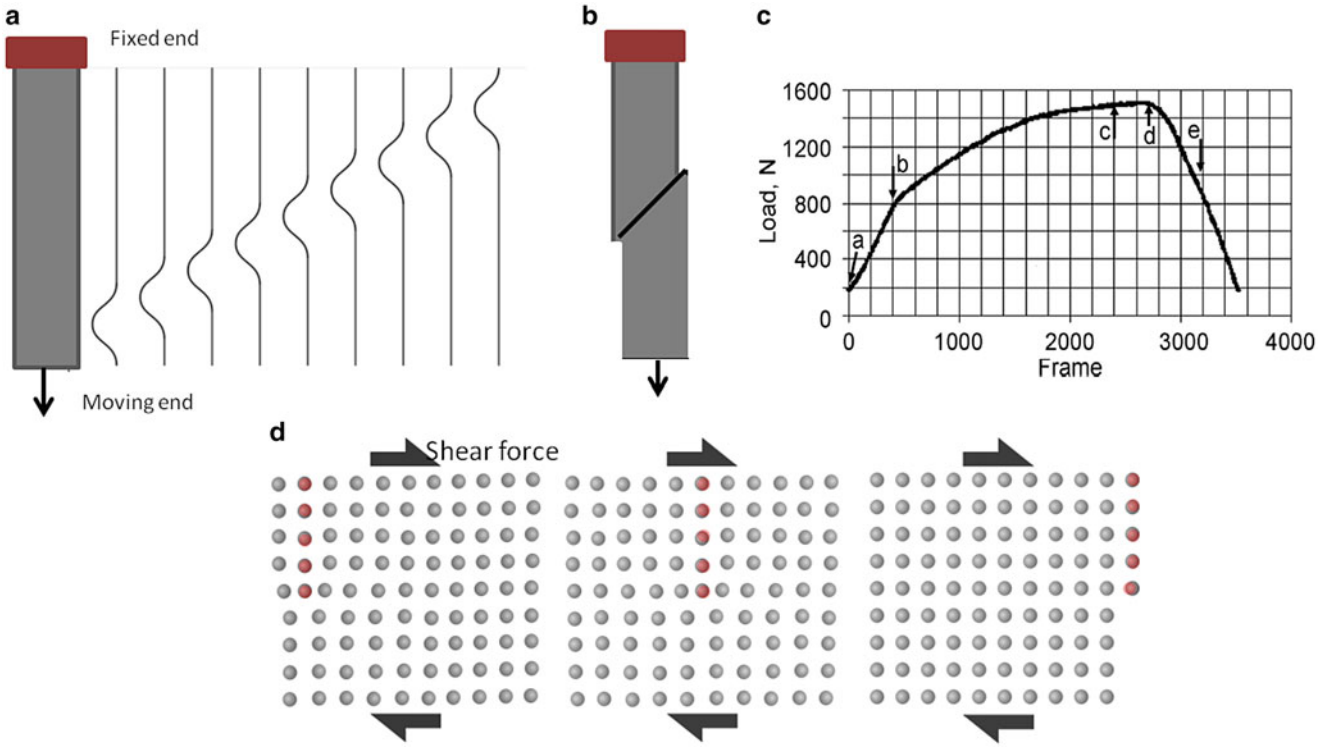

Fig. 10.16 Sequence of events leading to the fracture of a ductile material: (**a**) plastic wave propagating from moving end; (**b**) plot of picture frames vs. applied load in a tensile test; (**c**) line at 45° of the axis of the specimen; (**d**) dislocation motion

and changes in the geometry of the specimen take place that reduce the cross section of the specimen. If the specimen is homogeneous the fracture takes place at the mid-line of the specimen as it can be seen in Fig. 10.15d. If there are defects that produce stress concentration, the localization takes place where these defects are located.

Figure 10.16 shows a schematic representation of the events leading to the fracture of a ductile material in a tensile specimen according with the experimental evidence illustrated in Fig. 10.15. Figure 10.16a shows the tensile specimen and the plastic wave propagating from the loading end to the fixed end. Figure 10.16b shows a line inclined at 45° while Fig. 10.16d shows the corresponding shear stresses that activate and propagate an edge dislocation in a crystal with a favorable orientation producing a step at the end of the crystal. Figure 10.16c is a representation of the load vs. frame number on a sequence of the cine-speckle interferometry.

Referring to steps (a–e) indicated in Fig. 10.15, we can see that elastic loading starts at point (a); dislocations although present in the specimen are not activated. At point (b), dislocations begin their motion and a soliton plastic wave propagates from the bottom to the top of the specimen (Fig. 10.16b). Since the specimen is polycrystalline, these events take place in those grains whose orientation is favorable to the motions of dislocations (frames 10.15b to 10.15c). At point (d), enough dislocations have joined together to reach the free surface of the specimen and very likely merge with surface irregularities to create a crack that reaches the instability condition (schematically represented by a discontinuity in the specimen representation of Fig. 10.16b). Finally, from point (d) to point (e) the load falls in accordance with the dynamics of the specimen-machine interaction.

Figure 10.14a shows a snap shot of two edge dislocations that have merged together and are in elastic equilibrium under the presence of the elastic residual stresses generated by the interruption of the regular arrangement of the crystal. The presence of the dislocations have generated a configuration of the crystal that includes a quasi-cavity and abnormal atomic positions around which the atoms will be oscillating as a function of the temperature of the crystal. Through the application of external stresses, the atoms in the dislocation area will start to move creating a plastic wave carrying the crystalline abnormal configuration and producing at the same time oscillation of the array thus generating phonon waves that can be captured with special equipment and analyzed using wavelet based software. Finally, when the mechanism of plastic deformation produces enough surface discontinuities which merge to a dimension that creates a crack whose size makes it unstable, then actual fracture occurs. The above described process depends on the specimen-machine interaction and hence is a function of the velocity of application and form of application of the load to the specimen. Careful experimental

observations lead to a very important conclusion, plasticity and the transition of plasticity to fracture are fundamentally dynamic events. Many of the theoretical approaches of plasticity and fracture that are utilized in engineering applications are not connected to equations of motion and therefore are restricted in the validity of their prediction. More general approaches based on molecular dynamics are hence needed. Field equations that include both dynamic and kinematic variables are required for a complete formulation.

In the present paper, we have been limited to the two dimensional analysis of kinematic variables taken from snap shots of a crystalline array containing diverse regions from the point of view of deformation, including a dislocation area. This area shows the perturbations in the regular crystalline array caused by the merger of two edge dislocations. One question is very important: How far Continuum Mechanics kinematic variables can be useful in the representation of crystalline arrays? The experimental observations have provided an answer to this question. Looking to a hexagonal array it has been shown that continuum kinematic variables can be utilized at the level of the basic unit of the atoms configuration. Utilizing digital moiré even dislocation areas can be represented by continuum mechanics variables in the same sense that theory of elasticity solutions can approximate the actual dislocation kinematic variables as a homogenization tool. In conclusion, Continuum Mechanics is a powerful tool to predict the stability of a metal under general loading conditions. The reason for this fact lays in the geometrical basis of the organization of matter that underlines the observable behavior in the macro world. Although the derived conclusions have the narrow basis of a single image, careful observations of the geometrical changes seem to support the idea that the continuum can be modeled by interacting atoms and kinematics is represented by the distance vectors of these atoms. In this research work one more step was taken extending interaction kinematics to the atomic space. Further research is needed to verify that through the image light intensity distribution inference of the electron density can be extracted indicating the field configuration inside an atom [37].

References

1. Wagner, G.J., Liu, W.K.: Coupling of atomistic and continuum simulations using a bridging scale decomposition. J. Comput. Phys. **190**(1), 249–274 (2003)
2. Tadmor, E.B., Philips, R., Ortiz, M.: Hierarchical modeling in the mechanics of materials. Int. J. Solids Struct. **37**(1–2), 379–389 (2000)
3. Steinmann, P., Elizondo, A., Sunyk, R.: Studies of validity of the Cauchy Born rule by direct comparison of continuum and atomistic modeling. Model. Simul. Mater. Sci. Eng. **15**(1), 271–283 (2007)
4. Shenoy, V.D., Miller, R., Tadmor, E.B., Rodney, D., Philips, R., Ortiz, M.: An adaptive finite element approach to atomic-scale mechanics-the quasicontinuum model. J. Mech. Phys. Solids **47**(3), 611–642 (1999)
5. Arroyo, M., Belytschko, T.: An atomistic-based finite deformation membrane for single layer crystalline films. J. Mech. Phys. Solids **50**(9), 1941–1977 (2002)
6. Clayton, J.D., Chung, P.W.: An atomistic-to-continuum framework for nonlinear crystal mechanics based on asymptotic homogenization. J. Mech. Phys. Solids **54**(8), 1604–1639 (2006)
7. Philips, R.: Crystals, defects and microstructures. Cambridge University Press, Cambridge (2001)
8. Gray, H.B.: Chemical bonds, 2nd edn. University Science Book, Sausalito (1996)
9. Lennard-Jones, J.E.: On the determination of molecular fields—Part II. From the equation of state of a gas. Proc. R. Soc. London A **106**(738), 463–477 (1924)
10. Frenkel, D., Smit, B.: Understanding molecular simulation, 2nd edn. Academic, London (2002)
11. Mie, G.: Zur kinetischen theorie der einatomigen körper. Ann. Phys. **316**(8), 657–697 (1903)
12. Morse, P.M.: Diatomic molecules according to the wave mechanics. II. Vibrational levels. Phys. Rev. **34**, 57–64 (1929)
13. Le Roy, R.J., Huang, Y., Jary, C.: An accurate analytic potential function for ground-state N_2 from a direct-potential-fit analysis of spectroscopic data. J. Chem. Phys. **125**(16), 164310 (2006)
14. Cauchy, A.L.: De la pression ou tension dans un système des points matériels. Sur le équilibre et le mouvement d'un système de points matériels sollicités par des forces d'attraction ou de répulsion mutuelle. Sur l'équilibre et le mouvement intérieur des corps considérés comme masses continues. In: Cauchy Augustin-Louis, Ouvres Complétés, Tomes 20-21. Gauthier-Villars et fils, Paris (1882–1974)
15. Born, M.: Atomtheorie Des Festen Zustandes [Dynamik der Kristallgitter]. In: Taubner, G.B. (ed.), Fortschritte der Mathematischen Wessenschaften, Berlin (1923)
16. Cheung, R.: Silicon carbide microelectromechanical systems for harsh environments. Imperial College Press, London (2006)
17. Kelly, J.F., Fisher, P., Barnes, P.: Correlation between layer thickness and periodicity of long polytypes in silicon carbide. Mater. Res. Bull. **40** (2), 249–255 (2005)
18. Sciammarella, C.A., Lamberti, L., Sciammarella, F.M.: Measurement of deformations at the sub-nanometric level. In: Proceedings of the NANOMEC06 Symposium on Materials Science and Materials Mechanics at the Nanoscale, Bari, 19–23 Nov 2006
19. Sciammarella, F.M., Sciammarella, C.A., Lamberti, L.: Processing of a HRTEM image pattern to analyze an edge dislocation. In: Gdoutos, E.E. (ed.) Experimental Analysis of Nano and Engineering Materials and Structures. Springer, Rotterdam (2007)
20. Sciammarella, F.M., Sciammarella, C.A., Lamberti, L.: Experimental nanomechanics: a look at edge dislocations in 4HSiC crystals. In: Proceedings of the Materials Science and Technology Conference and Exhibition (MS&T'07), Detroit, Sept 2007
21. Ha, S.Y., Nuhfer, N.T., De Graef, M., Rohrer, G.S., Skowronski, M.: Origin of threading dislocation arrays in SiC boules grown by PVT. Mater. Sci. Forum **338–342**, 477–480 (2000)

22. Williams, D.R., Barry Carter, C.: Transmission electron microscopy, a textbook for materials science, 2nd edn. Springer, New York (2009)
23. Sciammarella, C.A., Sciammarella, F.M.: Experimental mechanics of solids. Wiley, Chichester (2012)
24. Boreman, G.D.: Modulation transfer function in optical and electro-optical systems. SPIE, Bellingham (2001)
25. JEOL USA: Transmission electron microscopes. http://www.jeolusa.com
26. General Stress Optics Inc.: Holo-Moiré Strain Analyzer Software HoloStrain, Version 2.0. General Stress Optics Inc., Chicago. www.stressoptics.com
27. Subramaniam, A., Balani, K.: Materials Science and Engineering (MSE). Chapter 5b: Crystal imperfections dislocations. Indian Institute of Technology, Kanpur. http://home.iitk.ac.in/~anandh/E-book (2013). Accessed 5 Mar 2016
28. Sciammarella, C.A.: Positron annihilation spectroscopy for life assessment of super alloys. In: Viswathnathan, R. (ed.) Proceedings for the NDE for Damage Assessment Workshop, EPRI TR-110291 (1998)
29. Yoshida, S., Muchiar, I., Muhamad, R., Widiastuti, R., Kusnowo, A.: Optical interferometric technique for deformation analysis. Opt. Express **2**(13), 516–530 (1998)
30. Panin, V.E.: Wave nature of plastic deformation in solids. Sov. Phys. J. **33**(2), 99–110 (1990)
31. Yoshida, S., Siahaan, B., Pardede, M.H., Sijabat, N., Simangunsong, H., Simbolon, T., Kusnowo, A.: Observation of plastic deformation wave in a tensile-loaded aluminum alloy. Phys. Lett. A **251**(1), 54–60 (1999)
32. Yoshida, S.: Consideration on fracture of solid-state materials. Phys. Lett. A **270**(6), 320–325 (2000)
33. Yoshida, S.: Physical mesomechanics as a field theory. Phys. Mesomech. **8**(5–6), 15–20 (2005)
34. Yoshida, S.: Dynamics of plastic deformation on restoring and energy dissipative mechanisms in plasticity. Phys. Mesomech. **11**(3–4), 137–143 (2008)
35. Yoshida, S., Rourks, R.L., Mita, T., Ichinose, K.: Physical mesomechanical criteria of plastic deformation and fracture. Phys. Mesomech. **12** (5–6), 249–253 (2009)
36. Yoshida, S.: Deformation and fracture of solid-state materials, field theoretical approach and engineering applications. Springer, New York (2015)
37. Sirelson, V.G., Ozerov, R.P.: Electron density and bonding in crystals: Principles, theory and X-ray diffraction experiments in solid state physics and chemistry. Taylor and Francis, Abingdon (1996)

Chapter 11
Comparison of Patch and Fully Encircled Bonded Composite Repair

Stephen A. Theisen and Michael W. Keller

Abstract Fully encircled bonded composite repairs in pipelines have proven effective since their introduction in the early 1990s. These fully encircled repairs completely wrap around the pipe and the defect like a sleeve. As operators became more familiar with fully encircled repairs, and as their capabilities improved, application in larger pressure equipment became viable. Increase in equipment application size corresponds to an increase in material cost and application difficulty. As such, the effectiveness of smaller patch-type repairs is of interest. Patch-type repairs, as opposed to fully encircled repairs, do not completely surround the pipe and defect, but rather only a specified area over the defect. This paper presents pressure fatigue tests comparing the performance of fully encircled and patch-type repairs installed on 6-in. nominal steel pipe with through-wall defects. Repair strain, substrate strain, and fatigue life are compared for both the fully encircled and patch-type repair. Finite element simulation results are compared to the experimental results to validate existing material models and simulation boundary conditions.

Keywords Composite repair • Pipelines • Full-encirclement repair • Patch repair • Fatigue testing

11.1 Introduction

Over the last 15 years, fiber reinforced composites have gained acceptance in a variety of industries such as automotive, infrastructure, aerospace, and oil and gas. This acceptance can be attributed to the increased familiarity of these industries with composites and superior strength to weight ratio compared to more traditional materials. These factors, among others, have convinced certain industries to use composites as a viable repair option in damaged pressure equipment. One of the most suitable applications for composite repairs is in oil and gas pipelines. Across all sectors, the US spends $137.9 billion dollars annually on repairing corrosive damage with $29.7 billion dollars in the transportation sector alone [1]. Traditionally, pipelines undergoing maintenance would have to be taken offline, but with recent advancements in composite repair systems [2–5], pipelines can be repaired while still online. Online repairs coupled with lower material and labor costs can make composites repair systems an attractive option from a cost-savings prospective [6].

Damaged sections of pipeline are typically repaired using a fabric with continuous fiber reinforcement combined with a thermoset matrix. The substrate is prepared by thoroughly cleaning the surface, which can be achieved by sanding or grit blasting depending on the sensitivity of the damaged section, and then applying a primer to ensure bonding. The repair is then installed by wrapping the wetted out fabric around the damaged section of pipe and then left alone to cure.

Traditionally, repairs completely encircle the pipe as shown below on the left side of Fig. 11.1. This type of repair is referred to as a full-encirclement repair and is accepted as the industry standard approach for installing composite repairs. However, as familiarity with composite repairs increased in the oil and gas industry, engineers and technicians began to consider larger pipelines and pressure vessels as potential sites for composite repair application. These larger pipelines can be significantly more expensive to repair due to an increase in material and labor cost. Additionally, larger full-encirclement installations can be cumbersome to wrap completely around damaged pressure equipment. Therefore, patch-type repair systems have been considered as a viable alternative. Patch repairs, shown below on the right side of Fig. 11.1, differ from full-encircle repairs in that they do not completely wrap the composite around the damaged section of pipe, but rather only over a specified section, or patch, of the pipe. These patch type repairs have yet to become widely accepted in industry due to the lack of relevant performance data.

S.A. Theisen (✉) • M.W. Keller
Department of Mechanical Engineering, University of Tulsa, Tulsa, OK 74104, USA
e-mail: stephen-theisen@utulsa.edu

W.C. Ralph et al. (eds.), *Mechanics of Composite and Multi-functional Materials, Volume 7*,
Conference Proceedings of the Society for Experimental Mechanics Series, DOI 10.1007/978-3-319-41766-0_11

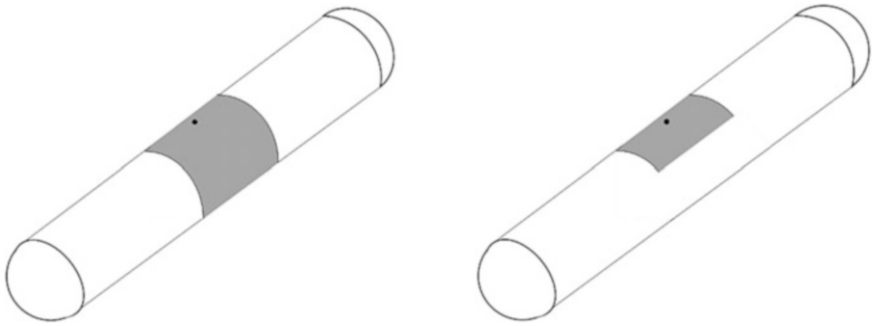

Fig. 11.1 Illustration of full encirclement (*left*) and patch repairs (*right*)

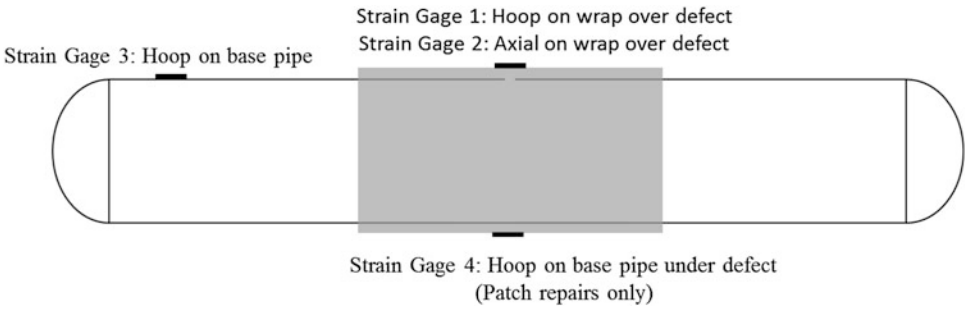

Fig. 11.2 Strain gage application locations

This study presents results from both theoretical FEA simulations and experimental fatigue data for both patch and full-encirclement repairs on through-wall defects. Fatigue data is of interest because it represents the fluctuation in pipeline pressure that can occur during operation. Additionally, this data gives reasonable life estimates for composite repair systems. These life estimates are important in determining the economic viability of composite repairs in damaged pipelines.

11.2 Experimental

11.2.1 Sample Specifications

The specimens were 4 ft long sections of 6-in. schedule 40 ASTM 106B pipes. Hemispherical end caps were welded on to each pipe along with two male couplings. The defect of interest for these pipes was a 0.25″ through-wall hole drilled into the side of the pipes. These defects are represented by the small black dots present on both specimens in Fig. 11.1. A 0.50″ Teflon disk was applied directly of the drilled hole to simulate a 0.50″ through-wall defect. The Teflon disks ensure that the defect size being tested remains consistent even after sand-blasting has occurred. The damaged section of the pipe was then wrapped with either a patch or full repair by one of two groups. Equal number of patch and full repairs were present in this study.

11.2.2 Experimental Procedure

Strain gages were applied at critical locations on the repair and on the substrate in order to quantitatively measure the differences between the two repair types. Pipe specimens with full encirclement repairs had three strain gages applied in two different locations as shown in Fig. 11.2. A biaxial strain gage was applied on the surface of the repair directly above the defect and a uniaxial strain gage was applied in the hoop direction on the base pipe at an adequate distance from the wrap. An additional strain gage was applied to pipe specimens with patch type repairs. This strain gage was located on the underside of the pipe directly below the defect on the base pipe.

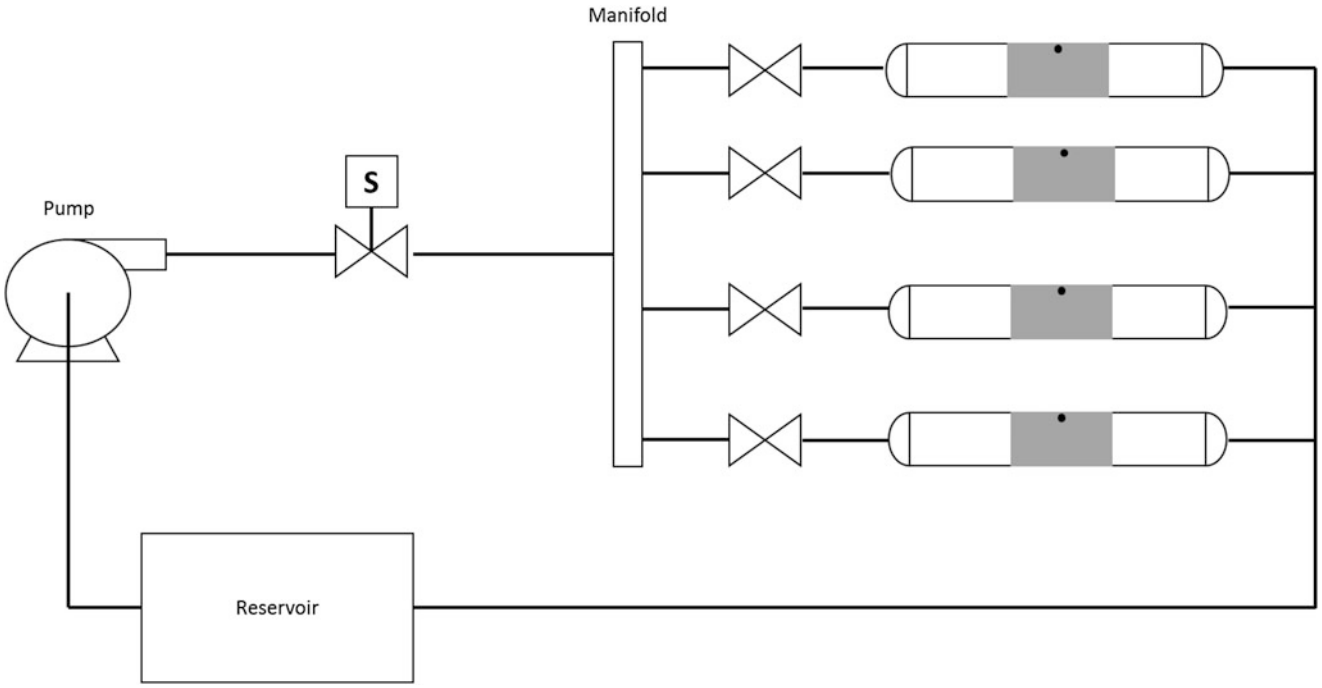

Fig. 11.3 Experimental setup

Pressure fatigue testing was conducted using a closed experimental setup consisting of a reservoir, solenoid valve with pressure switch, a manifold, and a pump. Specimens were cycled from 50 to 500 psi, which was well below maximum allowable operating pressure (MAOP) of 2038 psi. The cycling rate was approximately 25 cycles per minute. A complete schematic of the experimental system is shown in Fig. 11.3.

11.3 Finite Element Analysis Configuration

Small scale specimens for both patch and full encircle repairs were simulated in Abaqus finite element analysis software. The pipe was modelled as a quarter section with two symmetry boundary conditions. The composite was then perfectly bonded to the substrate and given appropriate anisotropic material properties. Substrate material properties for the ASTM 106B specimens were obtained using quasi-static coupon testing from representative pipe sections. Using this data, an elasto-plastic hardening model was constructed using data from previous research [7]. Composite material properties were also taken from previous research [8]. As an example system, full encirclement repairs were modelled with a 0.25″ composite layer bonded to the substrate using tie constraints. Patch repairs extended at least 2.4″ axially from the defect with a minimum circumferential distance of 2.4″. The axial repair length of 2.4″ was the minimum length required by PCC-2 repair standard and it was matched in the circumferential direction. A mesh convergence study was conducted to determine minimum global and local seed sizes to decrease computational time without sacrificing accuracy. Global seed sizes were reduced at fixed increments and the resulting Von Mises stresses were extracted from the model. This method continued until the percent difference between maximum stresses in consecutive models was acceptably small. In this case, a global seed size of 2.0 for the pipe and a local seed size of 0.5 immediately surrounding the defect resulted in a 0.33 % difference in Von Mises stress compared to a slightly larger seed size. A 500 psi internal pressure was applied to both full encirclement and patch type repairs. All simulations were run with non-reduced integration methods.

11.4 Results and Discussion

11.4.1 Finite Element Analysis

Figure 11.4 shows the maximum strain in the composite for both the full encircle and patch-type repairs. Strain increases linearly with pressure for both repair types because the applied loading remains entirely elastic. The patch repair exhibits slightly higher strain levels than the full encircle repair with the difference increasing as pressure increases. At the maximum pressure of 500 psi there is a 29.4 % difference between the strains in the patch and full encircle repairs.

Figure 11.5 shows the maximum principal strains in the region near the through-wall defect. In the figure, the steel substrate has been removed to better show the distribution of strains around the defect. As expected, the largest strain in the repair is located at the edge the defect where the repair is directly exposed to the internal pressure. Additionally, the

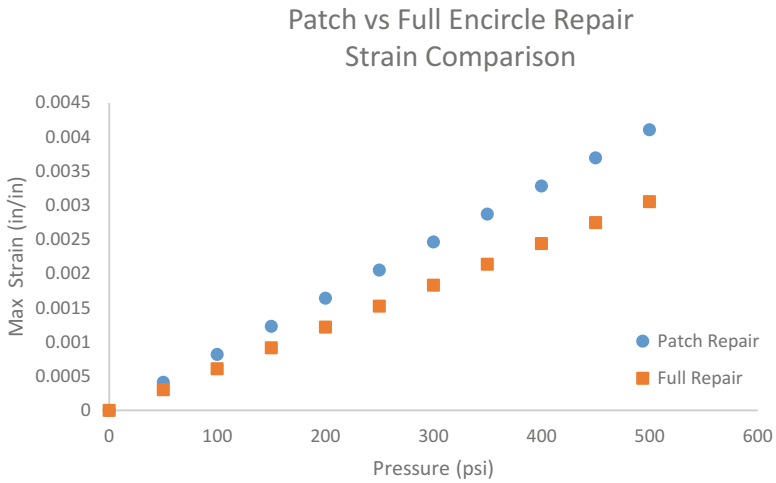

Fig. 11.4 Maximum strain in composite comparison between patch and full encircle repairs

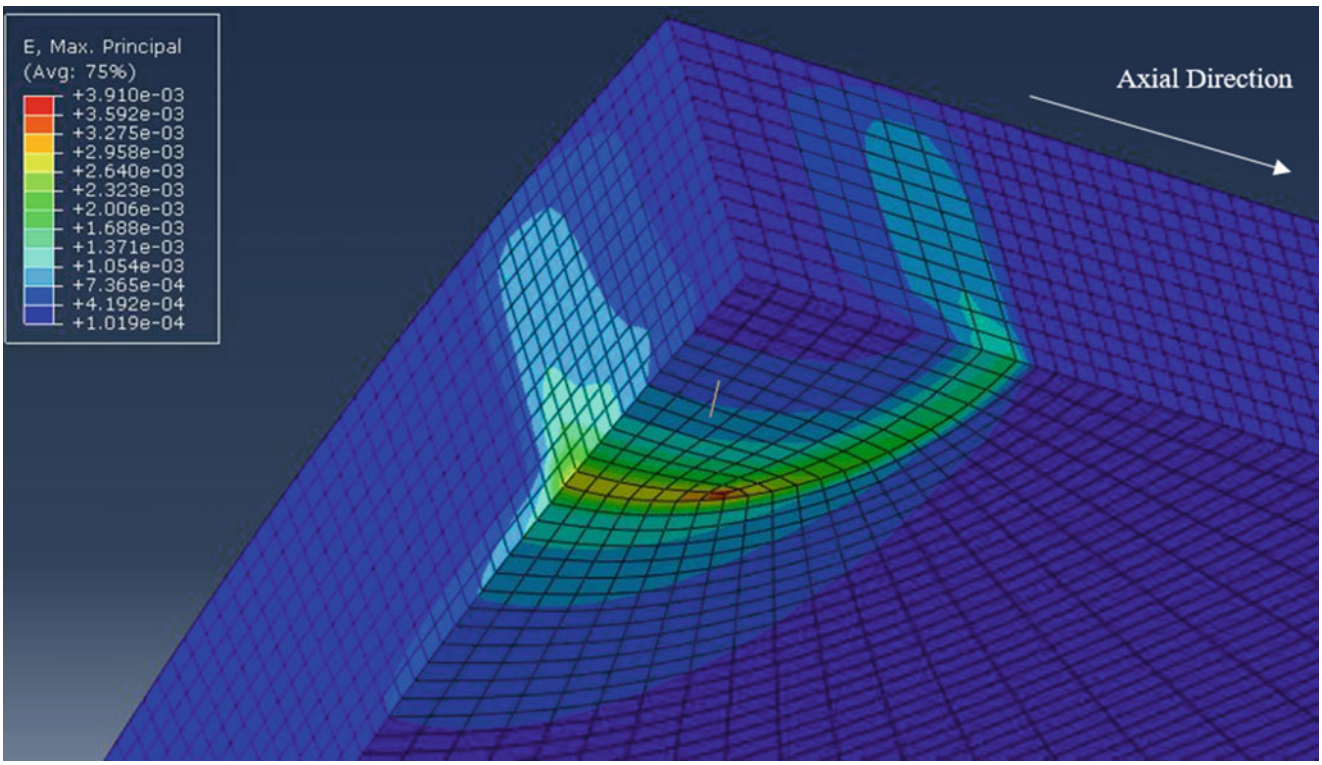

Fig. 11.5 FEA showing strain distribution in the composite repair

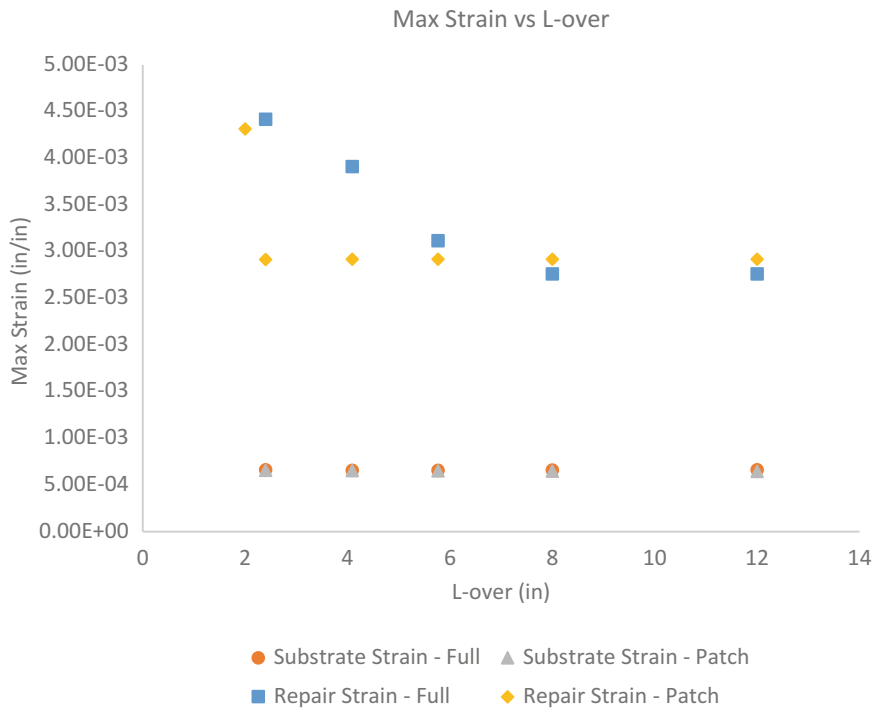

Fig. 11.6 Max strain vs. L-over

expanding strain distribution along the bottom surface of the repair indicates that the repair will likely fail due to interfacial delamination before bulk composite failure.

The extent of the repair past the defect is referred to as L-over. In a full encirclement repair, L-over refers to the distance the repair must extend axially, but for patch type repairs, it is the distance it must extend both axially and circumferentially. Traditional pressure repair systems often perform best when extending far past the defect. This idea leads to the assumption that the same may be true for patch type composite repairs. The effect of L-over on repair performance can be assessed by calculating the maximum strain in the composite for a given loading. Figure 11.6 shows the maximum strain in the steel substrate and the composite repair for both repair types as L-over increases past the edge of the defect. As L-over increases, the strain levels in the steel substrate remain relatively constant with only a 2.3 % difference between an L-over of 2 in. and 12 in. in the patch type repairs. Strain levels in the composite decrease as L-over increases, but do level out at a critical length of approximately 8 in. This is expected as adding more repair material far away from the defect is unlikely able to contribute to repair performance. Experimental testing would likely reveal a larger dependence of maximum strain on L-over as it is impossible to perfectly bond the repair to the substrate. As such, maximum strains would likely be higher than indicated in Fig. 11.6, especially at L-over values smaller than required by PCC-2.

11.5 Experimental

Figure 11.7 shows a comparison of experimental strain data taken from two specimens with strain gages applied at location one (see Fig. 11.2). One of the specimens was repaired with a patch type repair while the other was repaired with a full encirclement repair. The strains increase linearly with pressure in both specimens as expected since the loading is not sufficiently large to cause plastic deformation. Similar to the FEA results in Fig. 11.4 above, experimental results show that the patch repair exhibits slightly higher strains than the full repair with a 23.8 % difference in strain at 500 psi.

Table 11.1 shows the average fatigue life exhibited by eight specimens prepared by two different groups. Two of the specimens prepared by each group were patch-type repairs and two were full-encirclement repairs. A paired, two tailed t-test was run on the two sets of data and yielded a p-value of 0.411, which is not statistically significant. A 95 % confidence interval of 55,505 $\pm$ 44,016 was calculated for patch repair fatigue lives. The full repairs showed a similar result with a confidence interval of 54,998 $\pm$ 45,002. This large range can be attributed to a number of factors including the wide statistical variation in fatigue testing and differences in repair technique between the two groups.

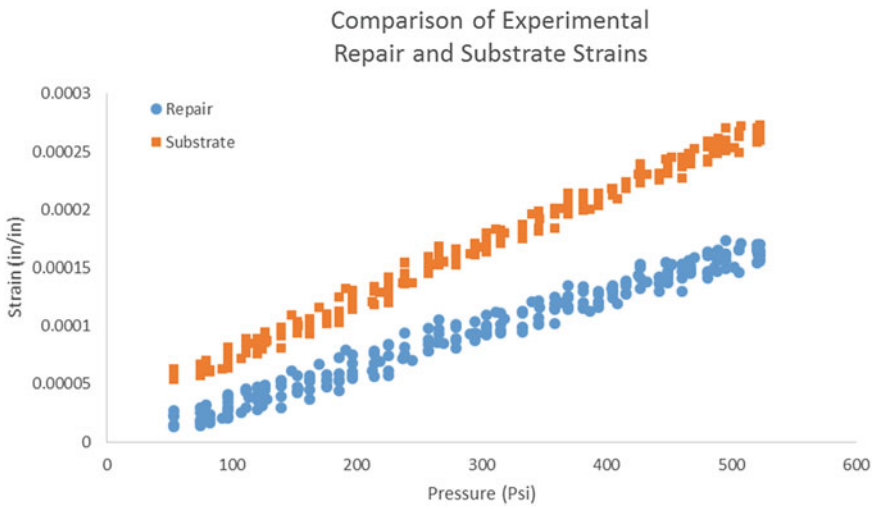

Fig. 11.7 Experimental strain data from patch and full encircle repairs

Table 11.1 Average fatigue lives of both repair types

Fatigue life averages	
Patch repair	Full encircle repair
56,012	54,998

11.6 Conclusions

Repair type does not have a statistically significant effect on the fatigue lives of small scale 6″ ASTM 106B pipe specimens according to a t-test run on fatigue data gathered from eight sample specimens. Initial comparisons of FEA strain results with experimental strain data indicate that although overall trends compare well, FEA significantly over predicts strain levels in the composite repair. This over prediction could be attributed to actual effective repair thickness exceeding simulated repair thickness. Research will continue in order to discover the reason behind these differences.

Acknowledgments This work was made possible by the Department of Transportation Cooperative Agreement (FOA #DTPH5614SN000006) and The University of Tulsa.

References

1. Gerhardus, H., Koch, M.P.H., Brongers, N.G.T.Y.P.V.J.H.P.: Corrosion costs and preventive strategies in the United States. Summary, 1–12 (2002). http://doi.org/FHWA-RD-01-156
2. Greenwood, C.: Composite pipe repair method shows versatility, long-lasting. Pipeline Gas J. **228**(2), 58 (2001)
3. Alexander, C., Wilson, F.: Development and testing of the Armor plate pipeline repair system. In: Proceedings of the 1999 ASME Energy Sources Technology Conference, American Society of Mechanical Engineers, Petroleum Division, Houston (1999)
4. Mableson, R., Patrick, C., Dodds, N., Gibson, G.: Refurbishment of steel tubulars using composite materials. Plast. Rubber Compos. **29**(10), 558–565 (2000)
5. Smith, P., Cuthill, J.: Patching up pipework with carbon–fiber composites. Mater. World **10**(5), 28 (2002)
6. True, W.: Composite wrap approved for US gas-pipeline repairs. Oil Gas J., **93**(41) (1995)
7. Duell, J.M.: Characterization and FEA of carbon composite overwrap repair system. University of Tulsa, Tulsa (2006)
8. Wilson, J.: Characterization of a carbon fiber reinforced polymer repair system for structurally deficient steel piping, p. 226. University of Tulsa, Tulsa (2006)

Chapter 12
Comparison of Composite Repair Performance on Drilled and Simulated Defects

O. Ramirez and M.W. Keller

Abstract Erosion is a common failure mechanism in pipework. Particulate-laden flows are common in many industries and these particulate can quickly deteriorate piping at bends, transitions, and, if conditions are correct, straight line sections. Repair of damaged piping and pressure vessels has traditionally been accomplishing using welded repairs. During the past two decades, the use of composite materials to repair damaged pipelines has experienced a considerable increase as these repairs have become more cost effective and efficient. These repairs are frequently installed on erosion, or corrosion, damage that is on the interior of the pipe and can become through-wall. Design qualification of repairs for through-wall defects are performed using simulated flaws manufactured by drilling through the pipe wall. This creates straight-sided flaws with significant remaining stiffness, very different from the diffuse, tapered flaws produced by erosion or corrosion. In this study we investigate the performance of through-wall composite repairs installed on flaws generated by an erosion process. Hydrostatic pressure testing of these eroded flaws is performed and compared to failure pressures of repairs installed on drilled flaws. Digital image correlation is performed to understand the development of strains in the repair and to provide a quantitative comparison between the two flaw types. Recommendations are made regarding the influence of flaw shape on overall repair performance.

Keywords Pipeline • Erosion • Composite Repair • Pressure equipment • Fracture

12.1 Introduction

Carbon steel materials are commonly used in a wide variety of industrial settings. These materials are cost-effective and possess mechanical properties that are attractive for many applications. One of the downsides of these materials is that they are susceptible to both erosion and corrosion [1]. For many applications, carbon steel materials are in contact with fluids that can chemically attack the material or the fluids contain small particulate that can remove material through an erosion process. Erosion can actually promote corrosion by removing a protective surface treatment or protective corrosion products [2]. In pressure equipment, erosion or corrosion can occur both internally and externally. In both cases, the removal of material can severely degrade the mechanical integrity of the system and lead to failures. As such, considerable research efforts have been expended to investigate strategies for the mitigation of this damage and the repair of already damaged equipment [3, 4].

Traditionally, damaged pressure equipment have been rehabilitated using welded metallic repairs. These are effective, but can be difficult to fabricate for complex shapes and are sometimes challenging to install on operating pressure equipment. Since the 1990s, composite materials have been seen as an alternative to repair and reinforce pressure equipment [5]. A composite repair is formed from three general components. A reinforcement phase, which is typically a woven reinforcement cloth, a matrix material, epoxy and polyurethanes are common, and a dimensional restoration epoxy, which returns the substrate to the original exterior profile [6]. The reinforcement and the matrix material form the load-bearing, structural repair system. While the dimensional restoration epoxy is used to fill surface defects in the corroded pipe wall to allow for a uniform surface for the over-wrap to be applied. Additionally, the dimensional restoration epoxy material is the medium through which the internal pipe pressure is transferred to the repair.

There are two design codes, ASME PCC-2 and ISO T/S 24817, that provide guidance for repair design and qualification. Both documents classify damage into two broad classes, through-wall defects and non-through wall defects. For the case of through-wall defects, the critical material parameter is the interfacial fracture behavior of the substrate-composite interface [7].

O. Ramirez • M.W. Keller (✉)
Department of Mechanical Engineering, University of Tulsa, Tulsa, OK 74104, USA
e-mail: mwkeller@utulsa.edu

W.C. Ralph et al. (eds.), *Mechanics of Composite and Multi-functional Materials, Volume 7*,
Conference Proceedings of the Society for Experimental Mechanics Series, DOI 10.1007/978-3-319-41766-0_12

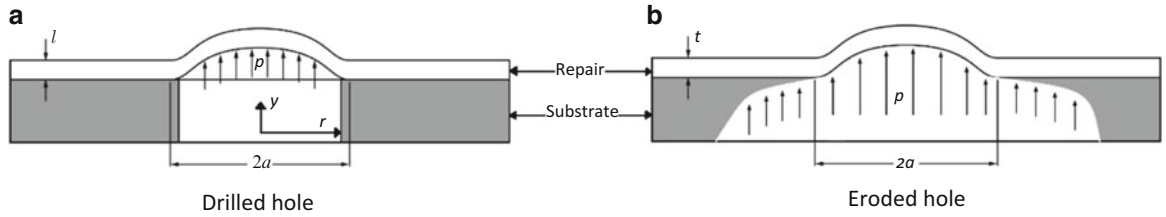

Fig. 12.1 Schematic of a repair over a drilled hole and eroded defect

The starting point for the analysis is a Griffith criteria for fracture that uses the change in volume of the repair V due to crack area extension A to define the fracture energy Γ

$$\Gamma = \frac{1}{2} P \frac{\partial V}{\partial A} \tag{12.1}$$

To apply this relation a theoretical prediction of the vertical displacement of the repair is required to calculate the volume change as a function of crack radius. The relationship is taken from plate theory and is

$$y(r) = p\left[\frac{3(1-\nu^2)}{16Et^3}\left(a^2 - r^2\right)^2 + \frac{3}{8Gt}\left(a^2 - r^2\right)\right] \tag{12.2}$$

Combining this relationship with Eq. (12.1)), we can derive a relationship between composite material properties, defect geometry and applied pressure.

$$\Gamma = p^2\left[\frac{1-\nu^2}{E}\left(\frac{3}{32t^3}a^4 + \frac{2}{\pi}a\right) + \frac{3}{16Gt}a^2\right] \tag{12.3}$$

Where the modulus E is the sum square of composite axial and hoop modulus, G is the composite shear modulus, ν is the in-plane Poisson ratio, t is the repair thickness, and p is the internal pressure. This approach has worked well for design, but has limits when attempting to extend or improve the design equations. Figure 12.1a shows the current model flaw geometry, which does not take into consideration that most flaws are not straight sided holes, but have regions of diffuse damage, as shown in Fig. 12.1b. In this paper, the results from a study on the comparison of repair performance on drilled and diffuse flaws generated through erosion are presented.

12.2 Experimental

12.2.1 Simulated Flaw Generation

A diffuse flaw was generated using dry erosion in a 152.4 mm diameter schedule 40 ASTM A106b straight pipe. A custom-built nozzle was design to achieve high particle velocity to ensure that the erosion process was completed in a reasonable amount of time (8 h). Dry compressed air was used as the gas stream and the blast media was ground glass. Flaws were produced by eroding in a specific location until a through-wall defect of approximately 6.25 mm was formed. After completing the erosion, end caps were welded onto the pipe specimen to form the sample for hydrostatic pressure testing (Fig. 12.2).

12.2.2 Eroded Flaw Characterization

Since the flaw was generated inside the pipe, as shown in Fig. 12.3a, an epoxy mold was made of the flaw to allow for characterization via 3D profilometry. To fabricate this mold, the through-hole was sealed using plastic film and then a liquid epoxy was poured into the flaw and allowed to cure. Figure 12.3b shows a representative mold of the flaw. After curing this mold was analyzed using optical profilometry (model).

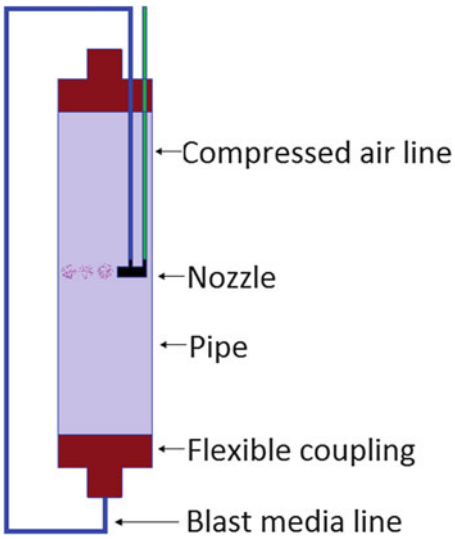

Fig. 12.2 Schematic for erosion generation

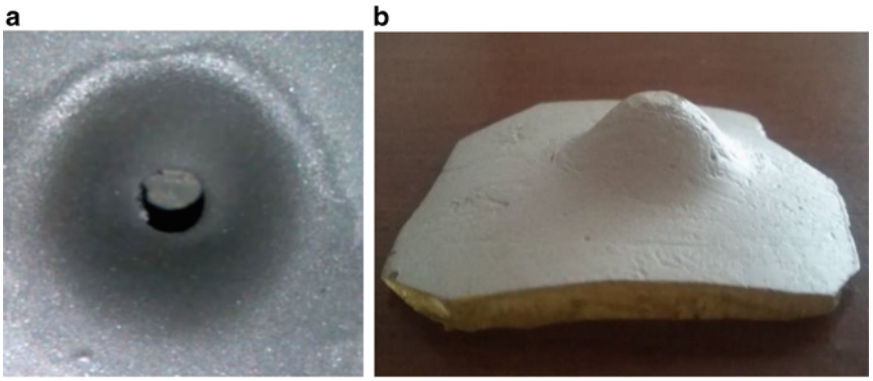

Fig. 12.3 Erosion generated inside the specimen

12.2.3 Repair Installation

Prior to installation of the repair, the exterior surface of the substrate was grit-blasted to a NACE 2 finish (near white-metal). The composite repair was installed using two concentric carbon fiber layers which has an approximate thickness of 1.14 mm [8]. The install procedure followed the manufacturer's suggested protocol. After the composite repair was installed, the repair was allowed to cure for at least 48 h at room temperature.

12.2.4 Hydrostatic Pressure Testing

Once the sample was cured, the specimen is filled with water and then pressurized using an air driven hydraulic pump (Sprague S216J100). Pressure is increase at a rate of 0.69 MPa every 15 s until failure. Once the failure occurs, the maximum pressure is recorded using a digital pressure gage. For a test to be considered valid under PCC2, the failure must be a leak at the edge of the repair, shown schematically in Fig. 12.4. This means that the failure mode should be interfacial delamination, to ensure that the measurement is a valid interfacial fracture energy measurement. Simultaneously to hydrostatic pressure testing, digital image correlation was performed to the area around the hole. This will allow us to obtain strains and displacements around the defect.

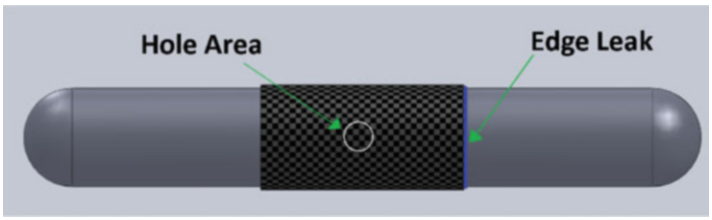

Fig. 12.4 Schematic valid data point

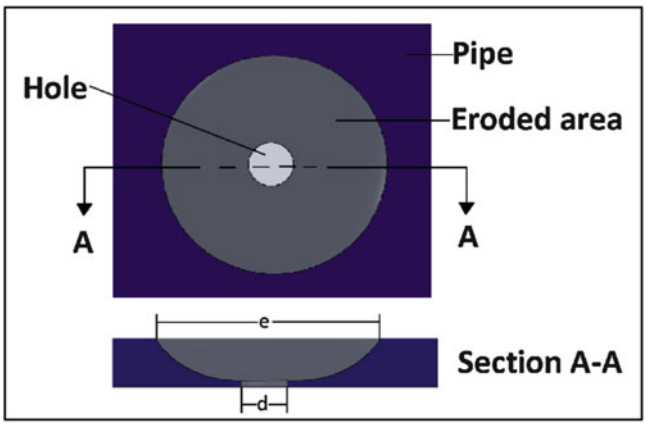

Fig. 12.5 Modeled erosion area

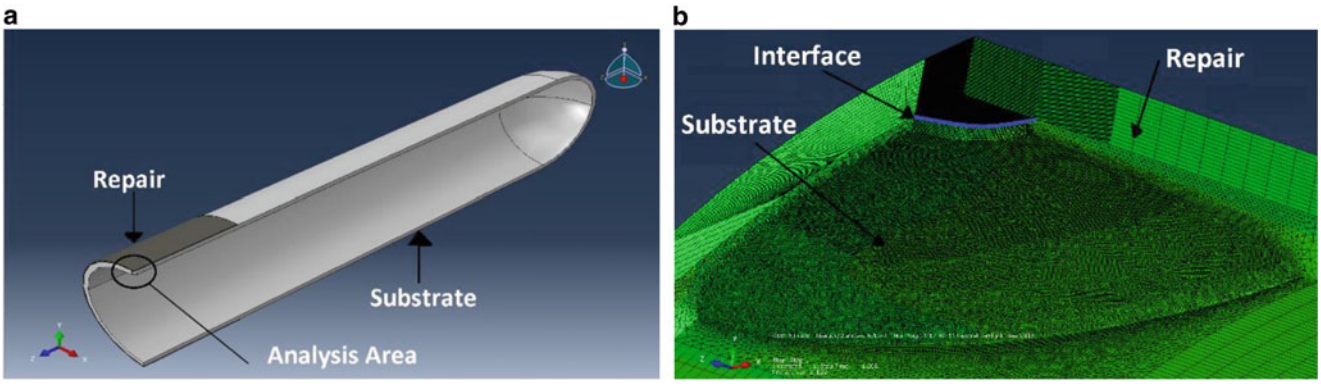

Fig. 12.6 Finite element analysis

12.3 Finite Element Analysis

Eroded defects and a drilled hole defect were simulated using a commercial finite element code (Abaqus). Six different erosion geometries were simulated to investigate the effect of varying damage geometry on the performance of the repair. A schematic view of an example erosion geometry is illustrated in Fig. 12.5 when the erosion diameter (e) around the hole is five times the hole diameter (d). The composite material was modeled as a linear-elastic, orthotropic material with material parameters taken from experimental data [8]. For all simulations, the repairs consisted of a 6.25 mm thick and 292.1 mm long composite layer that was assumed to be perfectly bonded to the substrate. An internal pressure of 6.89 MPa was applied for all simulations and a mesh convergence study was performed. Figure 12.6a shows an example ¼ model that was modeled. Figure 12.6b shows the interface along which the opening strains ε_{22} were obtained. This interface is the location where the crack is expected to initiate and grow.

12.4 Results

12.4.1 Eroded Flaw Characterization

After scanning the mold in the optical profilometer, a full 3D profile was obtained. Figure 12.7a shows the top view of the profile. From this view it was observed the width of the eroded area along with its shape. This shape is very close to a symmetric circle around the hole. Figure 12.7b shows the lateral view of the profile. Both measures are needed in order to obtain a full 3D geometry to be able to properly simulate the eroded flaw the in the finite element analysis. Based on this measurement, the diameter of the eroded area is, on average, four times bigger than the hole diameter.

12.4.2 Finite Element Analysis

Figure 12.8 shows that the opening strains in the interface are higher for the drilled hole. As the diameter of the diffuse region increases, the interface opening strains tend to decrease. This is likely the result of the thin walls of the damage region deforming, which would tend to reduce the opening strain on the composite-substrate interface. When the damage area

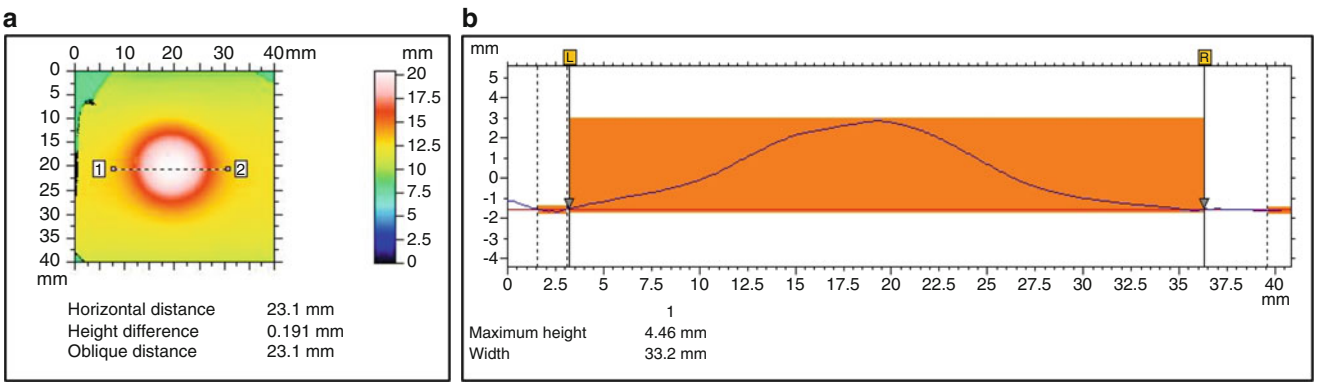

Fig. 12.7 Profilometer plots

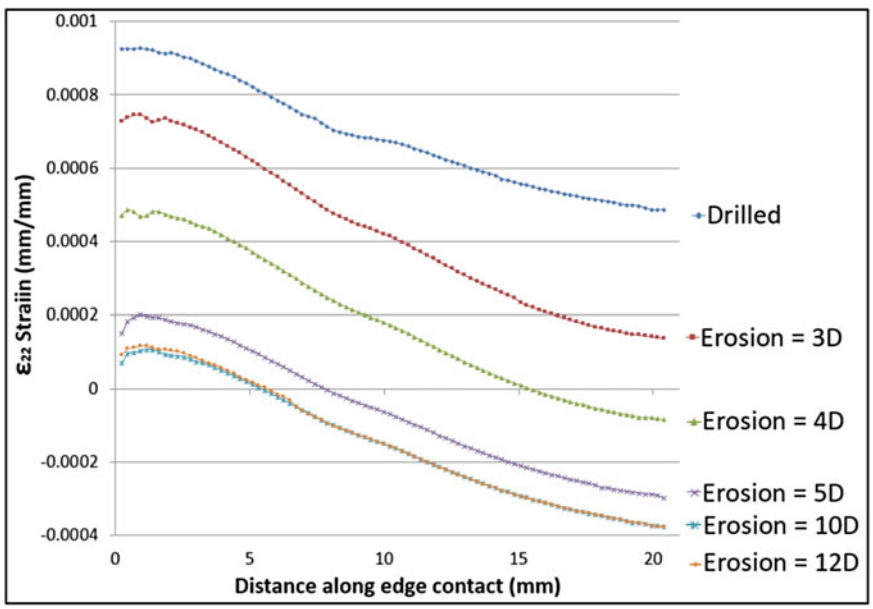

Fig. 12.8 Opening strains at the repair-substrate interface

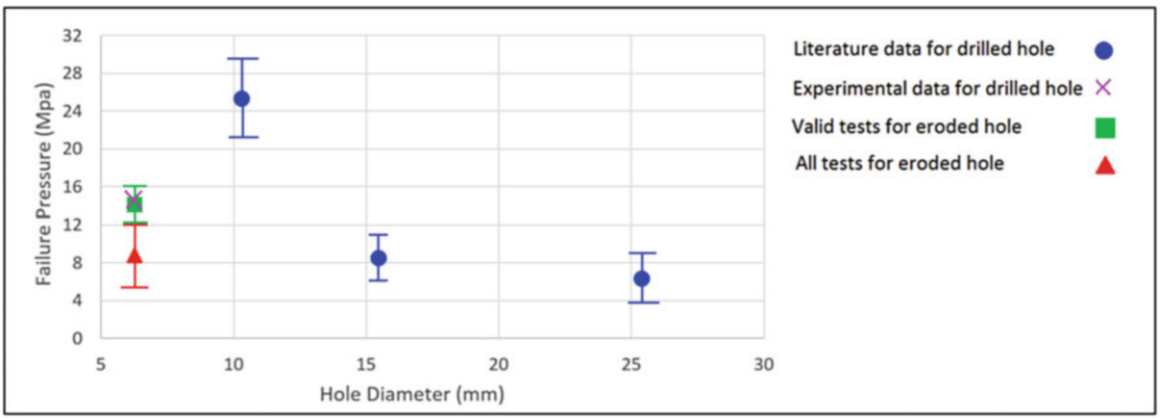

Fig. 12.9 Experimental data for failure pressure for drilled holes and eroded flaws

approaches five times the diameter of the hole, the strain becomes insensitive to the size of the erosion. This may indicate that erosion far from the defect does not influence the repair performance.

12.4.3 Hydrostatic Pressure Testing

Ten hydrostatic tests were performed on damaged and repaired substrates. Nine for eroded holes and one for drilled hole. For these tests only four valid interface failures were observed, three for the eroded flaws and one for the drilled hole. This low percentage of valid tests may be due to the fact that the repair is very thin, so the failure mechanism changes from interfacial to through-repair pin holes or this could be the result of the reduction in interface strains predicted by FEA. Reducing the interface strains could shift the failure mode from an interfacial failure to a bulk composite failure. The average of the valid tests for eroded defects was 14 $\pm$ 2.15 MPa. Plotting this value along with experimental data for drilled holes taken from the literature, it was observed that eroded flaws were below the trend [6]. However, a single experimental data point obtained for a drilled hole with the same through-wall damage size as the eroded flaw matches well the average value obtained for eroded holes (Fig. 12.9). This seems to indicate that fracture energy does not have any significant variation from drilled to eroded flaws. Adding in all tests regardless of failure mode, the average failure pressure is significantly less than would be expected from the drilled specimens. Further studies are underway to determine if the through-repair failures are the result of the thin wrap or a more systematic change in failure mode.

12.4.4 Digital Image Correlations

Figure 12.10 shows the out of plane displacement obtained from the DIC analysis. As expected, the largest displacement occurs near the center of the defect. The DIC data was also compared to the theoretical displacement profile used by ASME and ISO given in Eq. (12.2) above. From this comparison, it is observed that the predicted profile significantly overpredicts the measured displacement profile. This overprediction will tend to lead to a more conservative design as any increase in pressure will lead to a larger increase in volume. The larger volume increase will, in turn, lead to higher driving energies for the crack, causing designers to apply thicker repairs as a result. Further study of the theoretical and experimental determined deformation profiles is ongoing.

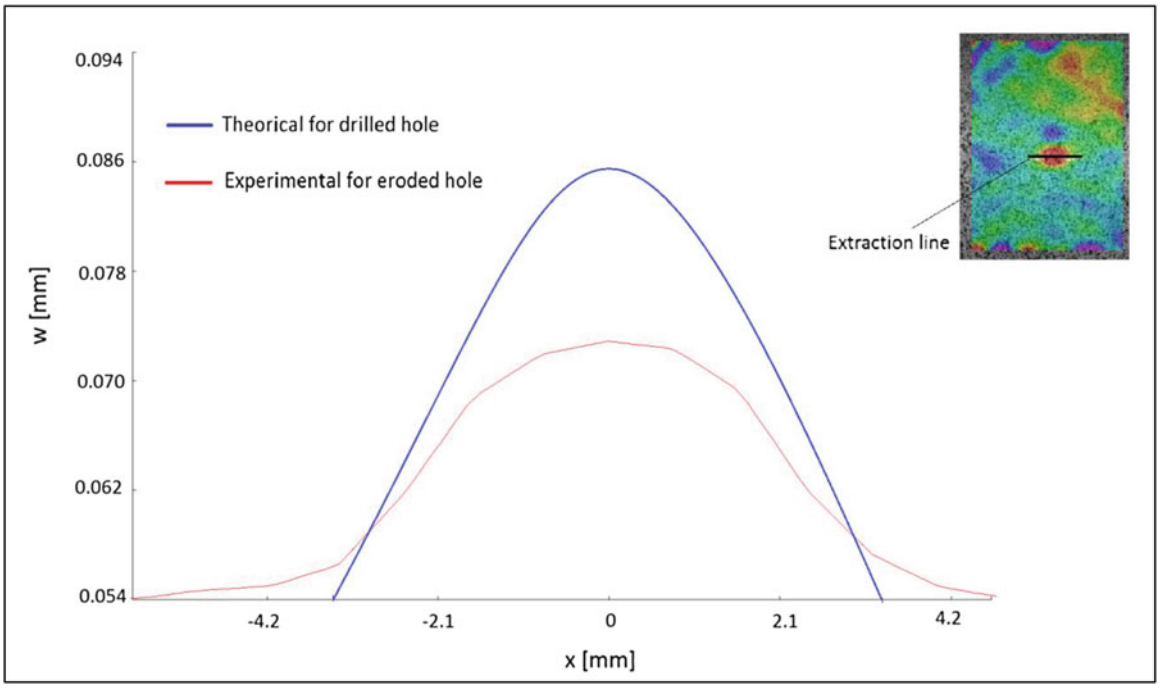

Fig. 12.10 Out of plane displacement obtained by digital image correlation and PCC code

12.5 Conclusions

Comparisons between opening strains at the substrate—repair interface for drilled holes and eroded holes were made in FEA. Opening strains were found to decrease for increasing eroded damage area as a result of increasing substrate deformation. This prediction did not correlate to an increase in failure pressures for eroded flaws as measured by hydrostatic pressure testing. However, an increase in the frequency of through-repair failures was observed during this testing indicating a change from interface failure to composite failures. Comparisons between the theoretical out-of-plane displacement and experimentally measured displacements were made using DIC measurements. The experimental deformation profiles were determined to be approximately 1.50 times smaller than the theoretical predictions. This overprediction may indicates that the current design codes are conservative when predicting interfacial failure.

Acknowledgment This work was supported in part by PHMSA/DOT through CAAP DTPH56-14-H-CAP02.

References

1. Shirazi, S., Shadley, J.R.: A procedure to predict solid particle erosion in elbows and tees. J. Pressure Vessel Technol. **117**(1), 45–52 (1995)
2. Combined Cycle Journal Team: What's eating up your LP evaporators: FAC or LDI? (2014)
3. Mableson, R., Patrick, C., Dodds, N., Gibson, G.: Refurbishment of steel tubulars using composite materials. Plast. Rubber Compos. **29**(10), 558–565 (2000)
4. Greenwood, C.: Composite pipe repair method shows versatility, long-lasting. Pipeline Gas J. **228**(2), 58 (2001)
5. Alexander, C.: Advances in the repair of pipelines using composite materials. Stress Engineering Services, Houston (2009)
6. Wilson, J.: Characterization of a carbon fiber reinforced polymer repair system for structurally deficient steel piping. University of Tulsa, Tulsa (2006)
7. ASME: Post construction code. In: Nonmetallic and bonded repairs. ASME, New York (2011)
8. Duell, J.: Characterization and FEA of carbon composite overwrap repair system. University of Tulsa, Tulsa (2006)

Chapter 13
Measuring How Overlap Affects the Strength of Composite Tubes in Bending-Torsion

Sean Rohde and Peter Ifju

Abstract A novel design for composite tubes possessing bend-twist coupling has been presented. The design requires a series of layers overlapping at two locations around the tube. This was suspected to create a weak point in the strength of the composite structure. To test this, multiple tubes possessing bend-twist coupling were constructed out of carbon fiber/epoxy prepreg. The tubes were then cut and prepared for torsional loading. A combined axial-torsion loading machine was used to steadily rotate the specimens while measuring torque and adjusting the cross-head to keep the axial load zero. DIC was used to measure the strains on the surface of the tubes. The results show the tubes fracturing with a lengthwise crack during an average torque of 44.2 lb-in (5.00 N-m). The location of the cracks and the stress at failure are consistent with failure occurring where the inner layers overlap. Micrographs of cross-sections are needed to confirm this. Further testing is also needed for the case of tension-torsion and compression-torsion that occurs during the bending-torsion the shafts would normally be subject to.

Keywords Bend-twist coupling • Composite tubes • Extension-shear coupling • Digital image correlation • Overlap

Nomenclature

COV	Coefficient of variation
DIC	Digital image correlation

13.1 Introduction

A design for a composite tube possessing bend-twist coupling has been presented [1]. The beams posses an off-axis shear center. If a load is applied at the shear center location, the beam-bends with-out twisting. Similarly if a load is applied through the centroid the beam will bend and twist as illustrated in Fig. 13.1. This property has applications for sporting-equipment, wind turbine blades [2, 3], propeller blades [4], and wings [5]. Sankar et al. has derived and validated an analytical model for predicting how the shafts considered here deform under loads [6].

The shafts are designed as shown in Fig. 13.2. Teflon is wrapped around an aluminum mandrel. A layer with fibers oriented in the 0° (measured from the beam axis) is wrapped all the way around the mandrel. Then the biased layers are wrapped such that the top half is +23° and the bottom half is −23°. It now looks like the left shaft in Fig. 13.1. Two of these biased layers are added, one on top of the other. Then another zero degree layer is wrapped all the way around. The 0° layers do not contribute to the bend-twist coupling but are added to increase flexural rigidity and structural integrity. Finally a heat shrink wrap is added to apply pressure during the cure cycle. The carbon fiber/epoxy prepreg used was tested to have the following properties: $E_1 = 81.0$ GPa, $E_2 = 5.45$ GPa, $\nu_{12} = 0.3$, $G_{12} = 3.0$ GPa, $G_{13} = 3.0$ GPa, $G_{23} = 2.0$ GPa, with a thickness of 0.16 mm.

The overlap for the two 0° layers can be anywhere and are placed as far from the other overlaps as possible. But the overlaps for the inner two layers are required to be at the same location because of the nature of the design: the top half and bottom half are mirror images of each other. This creates a weak point in the structure.

S. Rohde (✉) • P. Ifju
Mechanical and Aerospace Engineering Department, University of Florida, 571 Gale Lemerand Dr., MAE-C 134, Gainesville, FL 32611, USA
e-mail: seanerohde@gmail.com

W.C. Ralph et al. (eds.), *Mechanics of Composite and Multi-functional Materials, Volume 7*,
Conference Proceedings of the Society for Experimental Mechanics Series, DOI 10.1007/978-3-319-41766-0_13

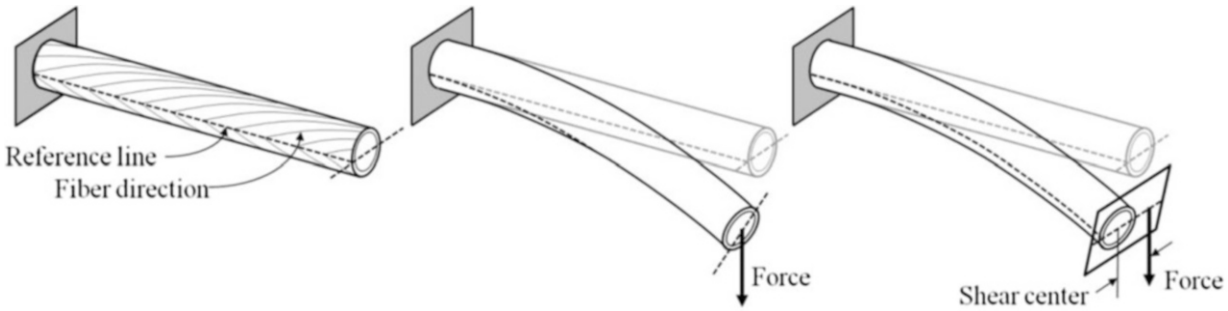

Fig. 13.1 Bend-twist coupling of a composite tube

Fig. 13.2 Laminate design with overlaps indicated

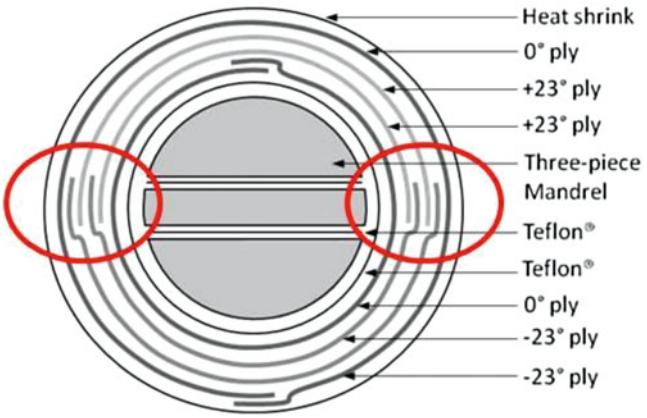

The primary motivation for this research has been golf clubs. After manufacturing numerous clubs possessing bend-twist coupling it was noticed that the clubs fractured easily. Since the main difference between the design possessing bend-twist coupling and traditional constructions of golf clubs is the preponderance of overlaps in the same location, it is suspected that failure initiates at the overlap and that the torque the shafts can handle is dominated by the properties of the overlap.

The overlaps circled in Fig. 13.2 are nominally 2 mm long but there is a large amount of uncertainty in the actual amount of overlap due to the hand layup process. Micrographs will be needed to measure and confirm how long the overlaps actually are.

13.2 Experimental Set-Up

The samples were prepared by cutting 4.5″ carbon fiber tubes out of a larger construction that was 18″ long. Care was taken not to damage the outer layer of carbon fiber during cutting. A source of difficulty was gripping the specimens to apply the loads. Attempts were made to grip the specimens using torsion grips which tighten three points of contact to apply inward pressure. The round surface of the tubes caused the specimens to slip in the grips before fracture could occur. To solve this problem, aluminum ends were added to the hollow carbon fiber tubes as in Fig. 13.3. Aluminum round stock of 0.5″ diameter were cut into 1.5″ long sections. These aluminum sections were roughened with sandpaper. The aluminum pieces were adhered with epoxy to the inside ends of the carbon fiber tubes. This left 1.5″ of hollow section in the middle. The outside surface of this middle 1.5″ section was then painted white. It was then speckled with small black dots using spray paint in preparation for digital image correlation, DIC.

A 3/16″ hole was then drilled out of the ends using an end mill. Two 3/16″ steel pins were then slid through the ends of the sample and the special aluminum grips. The grips were drilled with a 3/16″ transverse hole to apply the torque to the steel pins while the specimens spun freely in the center. All parts are shown in Fig. 13.4.

A Test Resources tension/torsion testing machine was used in these experiments. For this experiment the torsion mechanism was under angular control at 0.2°/s until just after the specimen failed. The cross-head was under load control

Fig. 13.3 The aluminum ends help to apply the loads

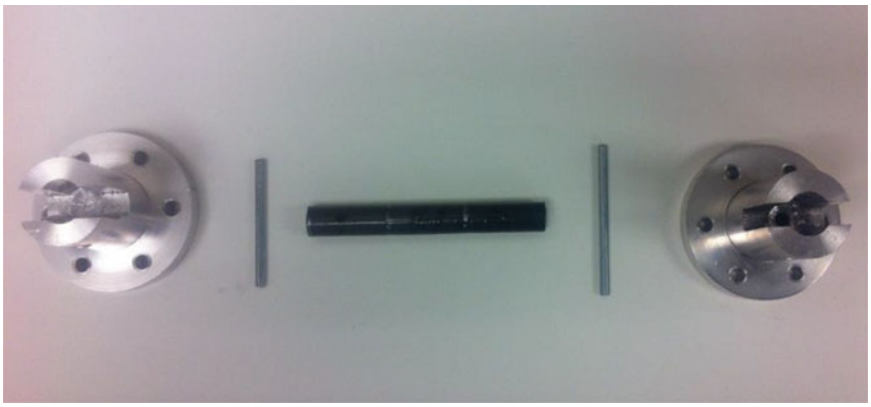

Fig. 13.4 Torsion grips, 3/16" steel pins, and unpainted specimen

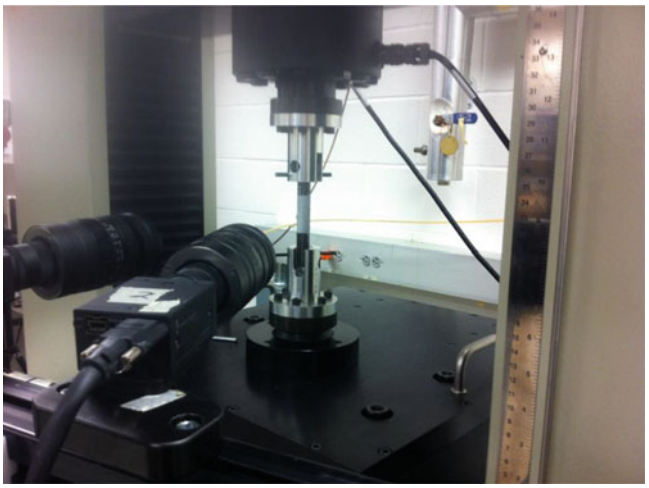

Fig. 13.5 Experimental set-up

and adjusted itself by 0.5 lb/s (2.2 N/s) towards an axial load of 0 lb. Hence, any tendency for the applied torque or grips to cause tension or compression was negated. The axial load was recorded and showed that the load was successfully kept at zero axial load. Without this feature the axial load rose to as much as 55.0 lb (245 N) of tension from shifting in the grips. The assembled experiment is shown in Fig. 13.5.

The strain was measured on the surface of the cylinders using DIC. This provided full-field measurements of displacements and strains. Two cameras were used to achieve three-dimensional measurements which were necessary for the curved surfaces of the specimens. During the experiment, one pair of images was taken per second.

The DIC software used was VIC-3D 2007 and 2009. For processing the data, a rectangular area of interest was selected so that as the tube rotated it would remain in all the frames. The subset was 35 pixels and the step was 5 pixels.

13.3 Results

It should be noted that the bend-twist coupling of these composite structures implies that the torque being applied to the shafts makes them want to bend. Because the grips prevent the shafts from curving, a bending moment reaction is occurring at the grips. This means that axial stresses resulting from this bending moment will be present in the shaft while the torque is

being applied. This is true even if the crosshead reads zero axial load. Fortunately, Sankar et al. has derived an equation for predicting the bending moment that would result from the bend-twist coupling [6]:

$$\begin{bmatrix} \overline{E}_x I & \frac{AR}{\pi}\Delta E_x \\ \frac{AR}{\pi}\Delta E_x & \overline{E}_x I \end{bmatrix} \begin{Bmatrix} \varepsilon_{x0} \\ \kappa_z \end{Bmatrix} = \begin{Bmatrix} P \\ M_y \end{Bmatrix} + \begin{Bmatrix} \overline{\eta}_{x,xs}/R \\ \Delta\eta_{x,xs}/\pi \end{Bmatrix} T$$

$$\overline{E}_x I \kappa_y = -M_z$$

E is the modulus, A the area, I the moment of inertia, R is the mean radius of the tube, η is the coefficient of mutual influence, k the curvature, ε the strain, P the axial load, M the bending moment, and the superscripts (*1*) and (*2*) indicate the top and bottom halves respectively. Furthermore: $\overline{E}_x = \left(E_x^{(1)} + E_x^{(2)}\right)/2$, $\Delta E_x = E_x^{(1)} - E_x^{(2)}$, $A = 2\pi Rh$, $I = \pi R^3 h$.

For the case where the top half is a mirror image of the bottom half: $\overline{E}_x = E_x^{(1)}$, $\Delta E_x = 0$, $\overline{\eta}_{x,xs} = 0$, $\Delta\eta_{x,xs} = 2\eta_{x,xs}^{(1)}$.

Setting $\kappa_z = 0$ and reducing for the structurally symmetric case, solving for M_y:

$$M_y = \frac{-2\eta_{x,xs}^{(1)} T}{\pi}$$

$$\sigma_x = \frac{M_y z}{I}$$

Where $z = R\sin\theta$

And θ is measured as in Fig. 13.6.

The maximum torque observed during testing was 53.6 lb-in (6.06 N-m). Plugging this value into the equations above for T yields the axial stress as a function of θ shown in Fig. 13.7. The maximum axial stress occurs at a θ of ±90. Here the axial stress is ±44.5 MPa. This stress is equivalent to an axial load on the sample of 343 lb (1530 N). Fortuitously, the maximum axial stresses occur farthest from the overlaps which are being studied here. The axial stress is zero at the center of the overlaps (θ is 0° and 180°). But the overlap could experience anything in the region of ±10°, where its edges are located. At ±10° the axial stress is ±7.7 MPa which is equivalent to pulling on the sample with 60 lb (267 N) of force. This value is relatively low as the samples have been pulled with 334 lb (1490 N) without fracturing. However, it should not be forgotten that this experiment does not result in pure shearing stress even though the crosshead records zero axial load.

Figure 13.8 shows images taken by a single camera recording the fracture of Sample 5. The pictures shown here were taken every 5 s as a crack formed. Beneath these images is the torque and angular rotation recorded by the testing machine for this same sample. Each of the eight squares in the graph illustrates the moment when an image was taken. Notice that as soon as the crack becomes visible, the amount of torque that can be sustained drops off. Each sudden decrease in torque was also accompanied by an audible cracking sound.

In Fig. 13.9, the DIC results are superimposed over the image. This color grid illustrates the amount of shearing strain on the surface.

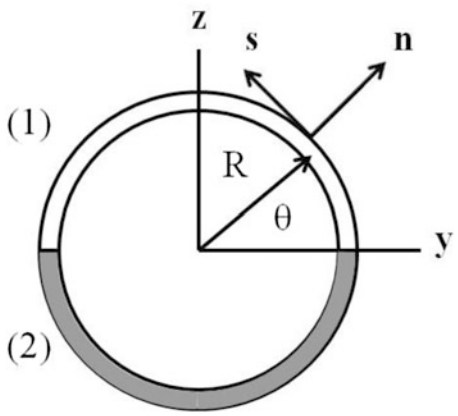

Fig. 13.6 Coordinate system, (*1*) and (*2*) refer to (0/23/23/0) and (0/−23/−23/0) laminates respectively

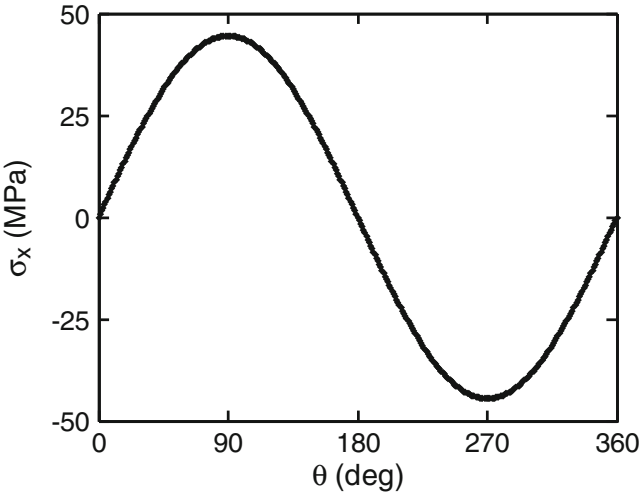

Fig. 13.7 Axial stress experienced by the specimen under 53.6 lb-in, where θ is defined in Fig. 13.6

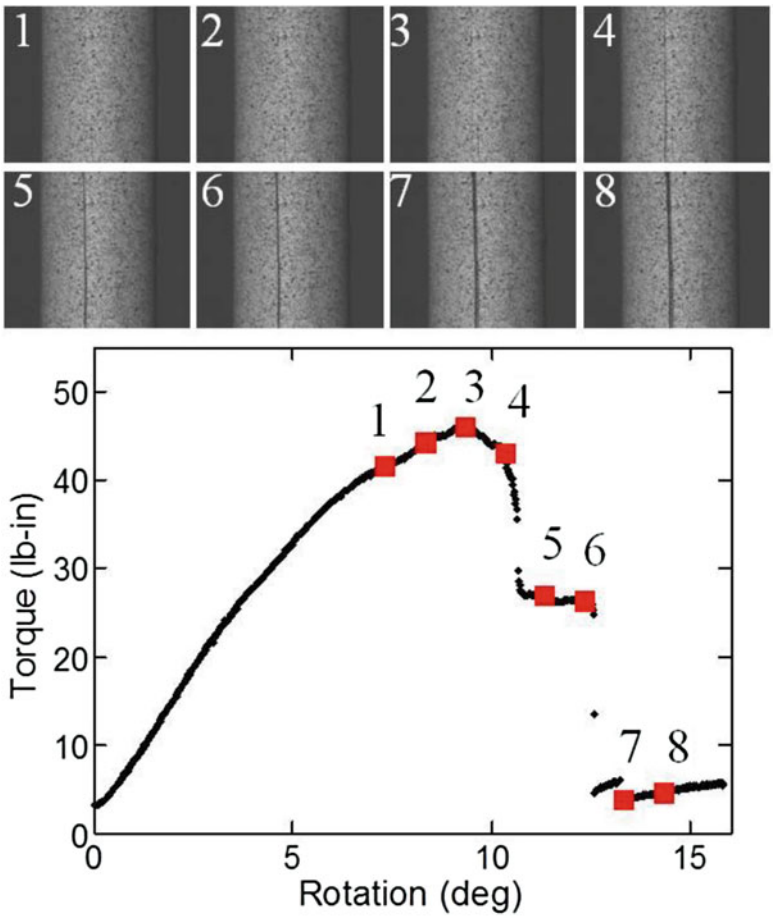

Fig. 13.8 Images of Sample 5 from 115 to 150 s at 5 s intervals with torque/rotation plot

Note that the localized shear strain predicts the location of where a crack will form. Once the crack is complete in the final image of Fig. 13.9 the correlation can no longer cross the divide and data is only present for one side of the crack. Also notice that two areas of strain localization occur. And a crack ends up forming at both of them. This hints at the cracks forming at both edges of a single overlap, not just at the center of the overlap region. This is consistent with the expectations of Fig. 13.2.

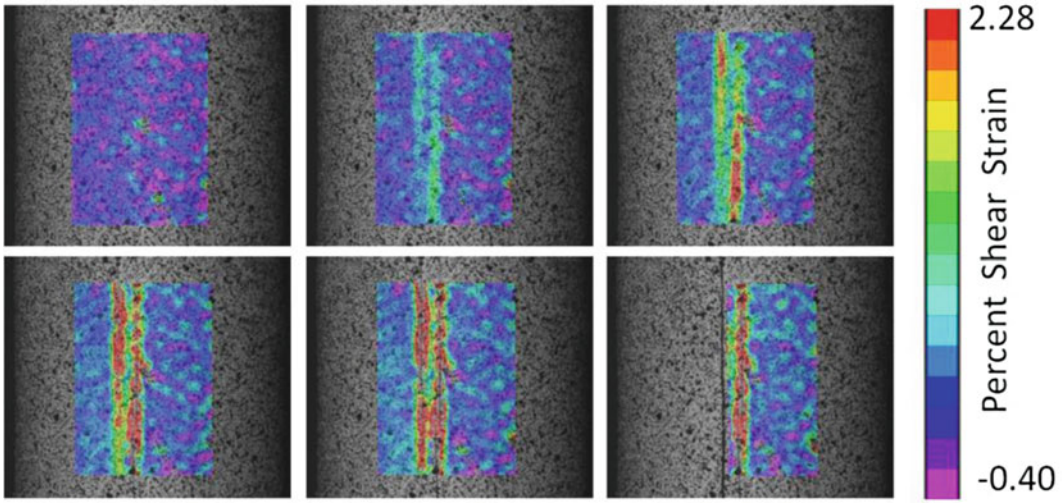

Fig. 13.9 Sample 5, shear strain from 80 to 130 s at 10 s intervals

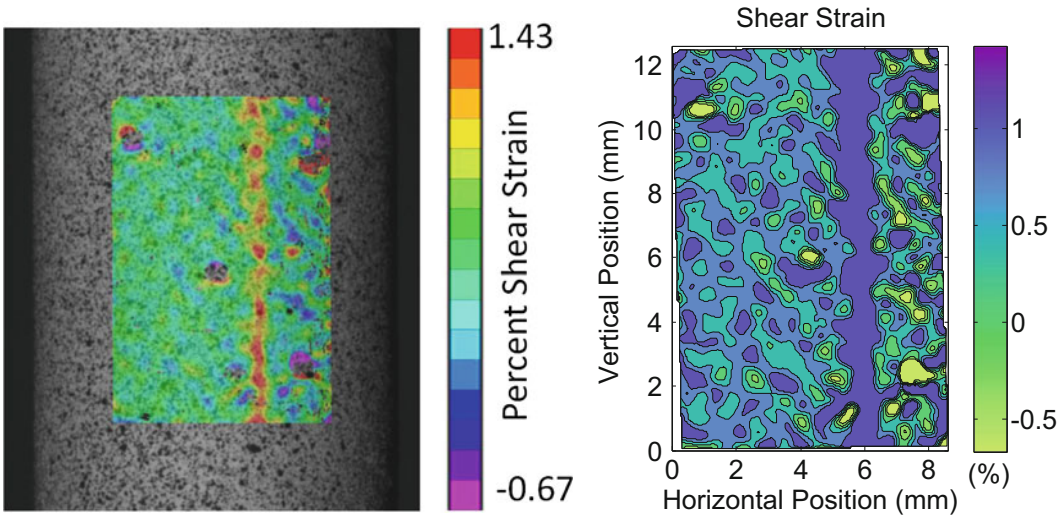

Fig. 13.10 Shear strain of Sample 6, 1 s before a crack occurs on the opposite side

During testing there was a 50 % chance that the side with the crack propagation would be the side that was being photographed. Figure 13.10 illustrates the case when the non-cracking side is facing the cameras. Note the localized region of shearing strain forming a vertical line. Apparently a crack was about to form, but 1 s later the crack propagated on the opposite side. The side facing the camera remained intact. Once the crack formed, the torque carried by the specimen dropped and the localized strain shown in Fig. 13.10 disappeared.

The side shown in Fig. 13.10 did not crack and is still intact. This indicates two weak regions of low strength and low stiffness where potential longitudinal cracks can form. This is to be expected from the overlap. Whether the sample fractures on one side or the other seems to be random and dependant on which side is weakest. There was a 50 % the cameras were placed on the side that the crack would form (Tables 13.1 and 13.2).

The average is 44.2 lb-in (5.00 N-m) with a standard of deviation of 6.9 lb-in (0.78 N-m). There is less variation among samples that were cut from the same shaft. The average standard of deviation per shaft (A, B, C) is 2.7 lb-in (0.31 N-m).

The crack propagates the full length of the specimen. This includes the sections that are adhered to the aluminum ends. In one case the rotation was continued for 30° after initial fracture and this resulted in an entire aluminum end becoming debonded from the tube. In all other experiments the aluminum ends remained adhered to the specimen after the crack propagated the length of the specimen.

Table 13.1 Ultimate torque achieved by each sample

Maximum torque	
Sample 1 (A)	36.5 lb-in
Sample 2 (A)	38.5 lb-in
Sample 3 (B)	40.1 lb-in
Sample 5 (B)	46.2 lb-in
Sample 6 (C)	53.6 lb-in
Sample 7 (C)	50.2 lb-in

Table 13.2 Average ultimate torque per original shaft

Average maximum torques per shaft	
Shaft A	37.5 $\pm$ 1.4 lb-in
Shaft B	43.2 $\pm$ 4.3 lb-in
Shaft C	51.9 $\pm$ 2.4 lb-in

The location of each crack seems to be where the overlap of each shaft is located. Micrographs need to be taken to prove this. This will be done by cutting a cross-section of the fractured shafts with a diamond saw. Then placing the cut cross-section into epoxy. Then polishing the surface until a picture of the laminate can be taken with a microscope. This micrograph will then confirm where the location of the cracking is taking place. Particularly, if the cracking is happening at the overlaps as is expected.

13.4 Conclusion

The results show an average torque at failure of 44.2 lb-in (5.00 N-m) with a standard of deviation of 6.9 lb-in (0.78 N-m). Samples that came from the same shaft were much closer in value to each other. This implies much of the uncertainty is in the construction of the shafts. Failure results from a crack propagating longitudinally down the length of the tubes. This is consistent with failure due to overlap weakness. Furthermore the strength is much lower than would be expected for a pure laminate. More work remains to be done to prove conclusively that the crack is propagating along the overlap. Cutting out cross-sections of the fractured shafts and performing abrasive polishing on them should allow for images to be taken of the fracture section using micrographs. This will have the added benefit of allowing for the precise measurement of the overlap length. More shafts can be constructed with longer overlaps and their respective strengths can be compared as a function of overlap length. This can then be used to recommend a minimum overlap length.

References

1. Rohde, S.E., Ifju, P.G., Sankar, B.V., Jenkins, D.A.: Experimental testing of bend-twist coupled composite shafts. Exp. Mech. **55**(9), 1613–1625 (2015)
2. Jureczko, M., Pawlak, M., Mezyk, A.: Optimization of wind turbine blades. J. Mater. Process. Technol. **167**(2), 463–471 (2005)
3. Malcolm, D.J., Laird, D.L.: Extraction of equivalent beam properties from blade models. Wind Energy **10**(2), 135–157 (2007)
4. Liu, Z., Young, Y.L.: Utilization of bend-twist coupling for performance enhancement of composite marine propellers. J. Fluid. Struct. **25**, 1102–1116 (2009)
5. Kosmatka, J.B.: Extension-bend-twist coupling behaviour of nonhomogeneoud anisotropic beams with initial twist. AIAA J. **30**(2), 519–527 (1992)
6. Jonnalagadda, A.K., Sawant, A.S., Rohde, S.E., Sankar, B.V., Ifju, P.G.: An analytical model for coposite tubes with bend-twist coupling. Compos. Struct. **131**, 578–584 (2015)

Chapter 14
Thermal Cycling and Environmental Effect on Tensile Impact Behavior of Adhesive Single Lap Joints for Fiber Metal Laminate

N. Mehrsefat, S.M.R. Khalili, and M. Sharafi

Abstract This experimental study investigates the effects of sea water and thermal cycling conditions on strength of adhesive lap joints made for fiber metal laminate (FML) and 430 stainless steel adherends subjected to standard tensile impact loading condition. The FMLs (three and five layers) were fabricated using 430 stainless steel sheets and fiberglass prepreg layers. The joints are kept in the sea water taken for 30 days in the laboratory. Some of the specimens are then thermally cycled in an oven (5 and 10 cycles, 40/100 °C, dwell time 20 min) and also the others are kept in liquid N_2 (5 and 10 cycles, −40/−100 °C, dwell time 10 min), and afterwards tested. Experimental results shown that the absorbed energy by adhesive lap joint specimens that are subjected to sea water is reduced. The adhesive joint strength is improved at high thermal cycling, but decreased at cryogenic temperatures with respect to sea water without thermal cycling.

Keywords FML • Adhesive joint • Sea water • Impact tensile test • Thermal cycling • Cryogenic temperature

14.1 Introduction

There are two main types of joints: mechanical joints and adhesively bonded joints. Adhesive joining is among the most important joining techniques used for bonding composite structures. Joint design technology has become a main factor in structural integrity to design of composite sub-structures in various engineering disciplines such as aerospace structures, marine engineering, automotive structural parts and also civil structures for strengthening.

However, the mechanical performance of adhesively bonded joints is strongly affected by the environment of the joint because the epoxy adhesive properties of adhesively bonded joints can be weakened by temperature or humidity [1, 2]. When moisture is absorbed into the epoxy adhesive layer, it can reduce the glass transition temperature of the adhesive and can generate stress in the adhesive layer due to volume expansion of the epoxy [3]. Kootsookos and Mouritz have investigated the effect of seawater immersion on the durability of glass- and carbon-fibre reinforced polymer composites experimentally [4]. da Silva and Adams used a mixed adhesive joint instead of a joint with a high-temperature adhesive alone which provided a joint that was strong from low to high temperatures [5].

In many real life cases, for instance in applications related to transportation systems, bonded joints may undergo impact loads that, conceptually, can be of two different types. The first type belong to the occasional heavy impacts that cause irreversible damage (i.e. automotive crash), the main issue in this case is the absorption of the kinetic energy obtained through plastic deformation. Of the second type are the frequent low-energy impacts, that the structural members and the joints must withstand without serious damage; in this case the issue is high elastic strength. The present paper deals with this latter aspect. The basic test to obtain experimental information on this topic is based on the impact of a pendulum onto a block bonded on a base (ASTM D950) [6]. The performance of adhesive bonds when subjected to dynamic loads also depends on many parameters such as temperature, moisture, stress ratio, strain rate and environmental conditions.

N. Mehrsefat (✉)
Department of Mechanical Engineering, Islamic Azad University, South Tehran Branch, Tehran, Iran
e-mail: Navid.meh@outlook.com

S.M.R. Khalili
Faculty of Mechanical Engineering, Center of Excellence for Research in Advanced Materials and Structures, K.N. Toosi University of Technology, Tehran, Iran

M. Sharafi
Department of Mechanical Engineering, Islamic Azad University, South Tehran Branch, Tehran, Iran

Faculty of Mechanical Engineering, Center of Excellence for Research in Advanced Materials and Structures, K.N. Toosi University of Technology, Tehran, Iran

W.C. Ralph et al. (eds.), *Mechanics of Composite and Multi-functional Materials, Volume 7*,
Conference Proceedings of the Society for Experimental Mechanics Series, DOI 10.1007/978-3-319-41766-0_14

An increase in adhesive thickness results in a decrease in the stress concentration, but decreases in joint strength [7]. da Silva and Adams [5] used a mixed adhesive joint instead of a joint with a high-temperature adhesive alone which provided a joint that was strong from low to high temperatures. They found that, if the coefficients of thermal expansion are such that the thermal loads decrease the load capacity, then the mixed adhesive joint is beneficial. Pires et al. [8] used a mixed adhesive joint with different stiffness along the overlap in a single lap joint and observed that the stress concentrations decrease at the ends of the joint, if a lower stiffness adhesive was employed.

In the present paper, the effect of sea water and heating and cryogenic thermal cycles on the tensile impact behavior of adhesive joint between FML and stainless steel is investigated experimentally. The joints are kept in the sea water for 30 days in the laboratory. Some of the specimens are then thermally cycled in an oven and also the others are kept in liquid nitrogen for 0, 5 and 10 cycles and then subjected to mechanical tensile impact test. Then, the effect of the thermal cycles on the enhancement of mechanical strength of the adhesive lap joints are investigated.

14.2 Experimental Procedure

14.2.1 Material, Adhesives and Adherends

The fiber metal laminates (FMLs) were manufactured three layers from two sheets of 430 Stainless steel and between them one woven fiberglass prepreg (G10) Hankuk Carbon Co., Ltd (KOREA), and five layers from three sheets of 430 Stainless steel and between them two fiberglass prepreg (G10) (1000 × 600 mm). In order to promote better adhesion, the stainless steel sheets were abraded using silicon grit paper and cleaned with acetone. The surface preparation method had no effect on the mechanical properties of the stainless steel. Glass fiber interlayer (G10) was placed at the interface between the layers of stainless steel. Various layers were stacked on a plate, heated to the processing temperature of the composite (160 °C) and cold stamped in an initially cold press at a constant pressure.

The stacking sequence of the FMLs is illustrated in Fig. 14.1. FML adherends were cut and drilled by KMT water jet (USA).

The dimensions of FML and St 430 adherends were fixed to be 120 × 25 × 1.7 mm and 120 × 25 × 4 mm, respectively. The adherends were infused with AD-314 Mokarar® resin mixed with HA-34 Mokarar® hardener (Tehran-Iran). The

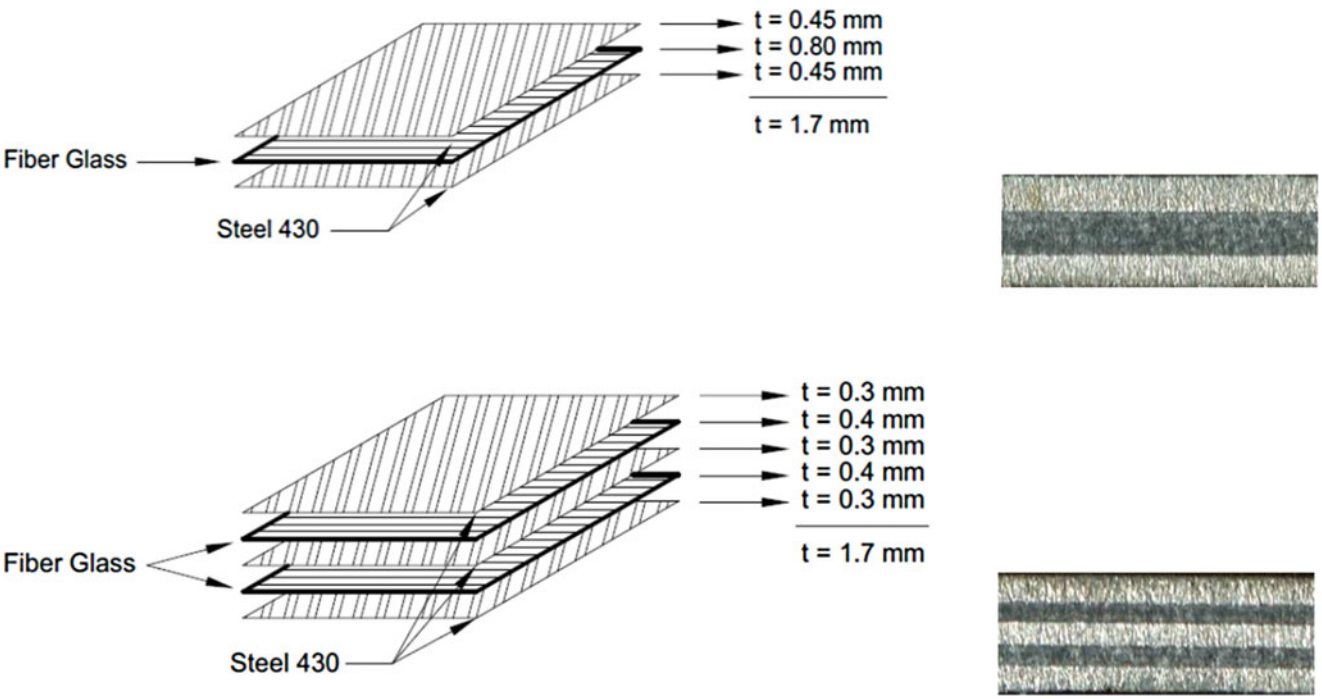

Fig. 14.1 Stacking sequence of the FMLs

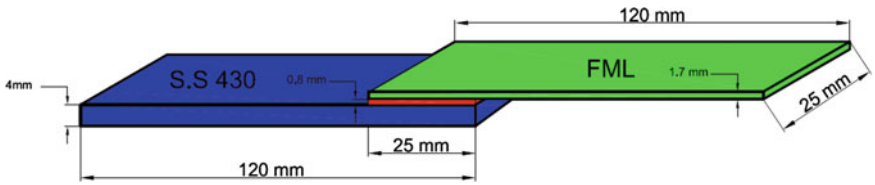

Fig. 14.2 Specimen configuration of the joint

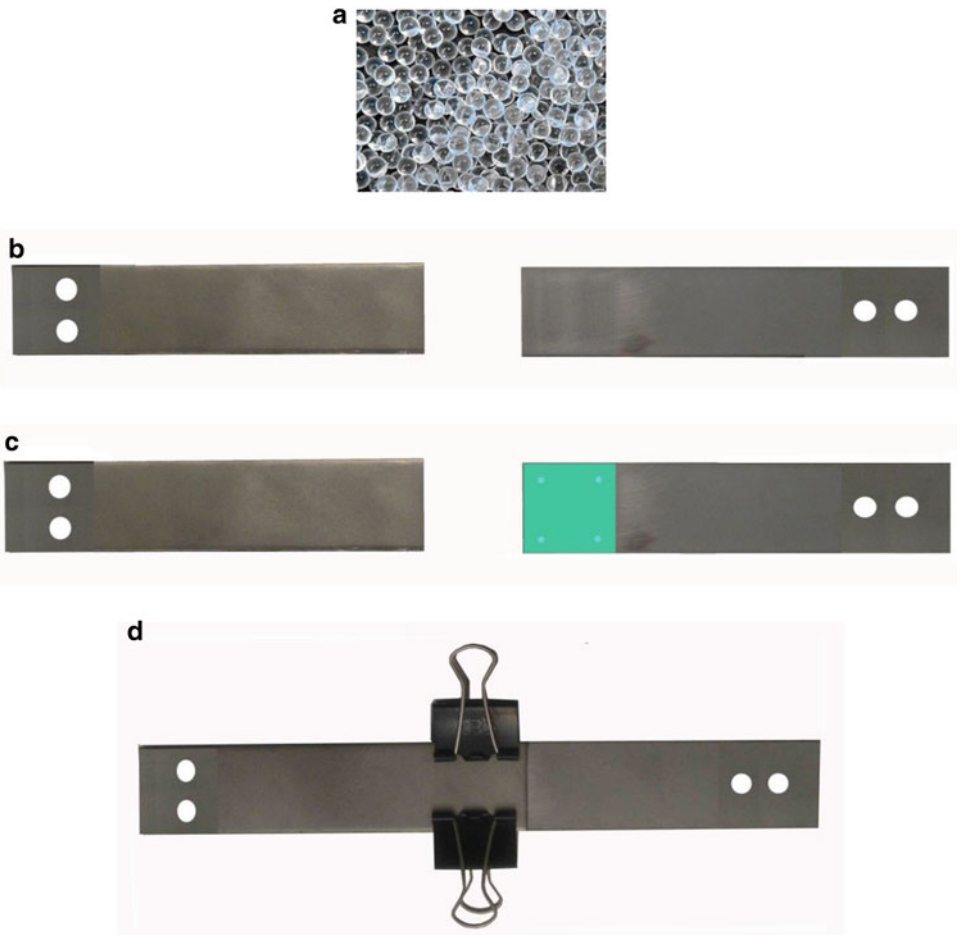

Fig. 14.3 Adhesive joint fabrication process. (**a**) Glass beads; (**b**) the surface preparation of the adherends; (**c**) wetting the surface area and put the glass beads; (**d**) adhesive joint

overlap length was 25 mm and the thickness of the adhesive was kept as 0.8 mm. Therefore the overall dimensions of the adhesive region which were constant for all the test specimens were 25 × 25 × 0.8 mm. Figure 14.2 shows the geometry and the dimensions of the test specimens.

The quality of the bonded joint depends strongly on the surface preparation of the adherends. To ensure good bond strength and durability, production of a roughened surface, cleaned of contaminants (particularly any chemicals, wax, or grease resulting from environmental exposure or after the composite fabrication process), is required.

The bonding surface was first cleaned with acetone, and then sanded then immersed in dichromate sulphuric acid solution for 60 min at 20–30 °C and cleaned with acetone again and wiped in dry air at 40 °C with lint-free paper to remove any foreign particles. The joint fabrication started by wetting the surface area to be joined then a bead of adhesive was placed along the centre line of the bond area and four numbers glass bead were used to control the thickness (0.8 mm) of the adhesive in the joint and then the adherends were placed (Fig. 14.3). The specimens were then allowed to cure at room temperature for 7 days. Figure 14.3 shows a typical specimen prepared for tensile impact test.

14.2.2 Environmental Conditions and Thermal Cycling

14.2.2.1 Sea Water

Specimens of adhesive joints were immersed in a tank containing natural sea water at a temperature of 28 °C, for a specified duration of time (30 days). The sea water in the tank was circulated by a water pump. Figure 14.4 shows the joints after sea water treatment.

14.2.2.2 Thermal Cycling

After 30 days in the sea water, the specimens of adhesive joints had been thermal cycled for five and ten times, some of the specimens for heat cycle treatment and the others for cryogenic cycle treatment. For heat cycle, a dry oven is used to elevate the temperature to a target temperature (100 °C). After the temperature reached to the target temperature, the specimens were placed in the oven at the temperature (100 °C) for 20 min, and then cooled to 40 °C and were kept at this temperature for another 20 min. This cycle continued for five and ten times, Fig. 14.5.

For cryogenic cycle, liquid nitrogen is used. According to Fig. 14.6, the specimens of adhesive joints had been cycled for five and ten times at cryogenic temperature of −100 and −40 °C, Fig. 14.6.

Fig. 14.4 Adhesive joints after 30 days in the sea water

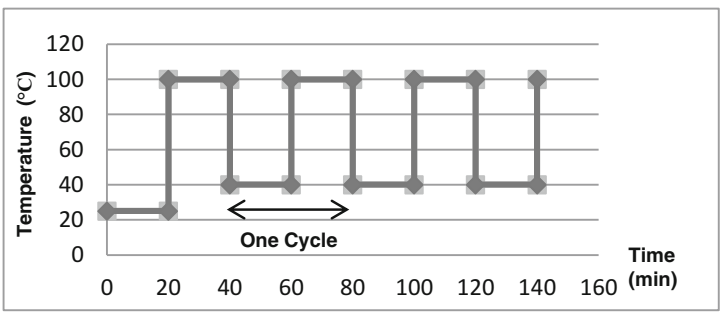

Fig. 14.5 Thermal cycling (heat cycle)

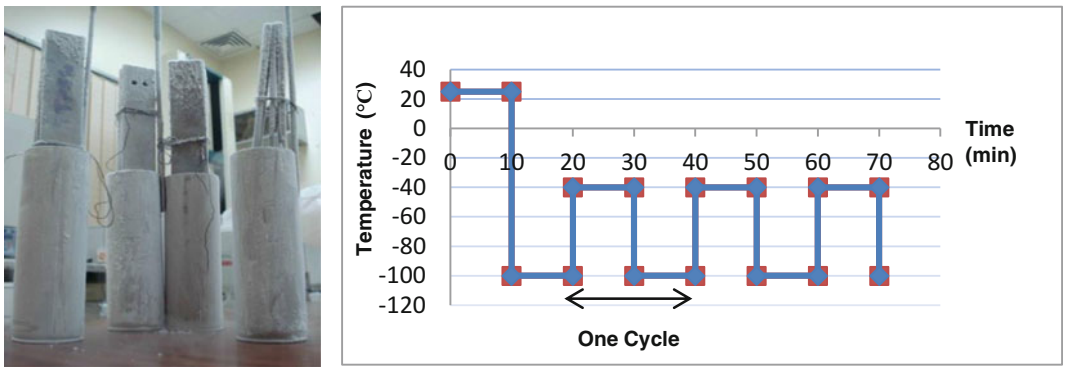

Fig. 14.6 Thermal cycling (cryogenic cycle)

Fig. 14.7 Test apparatus with the fixture and the specimen

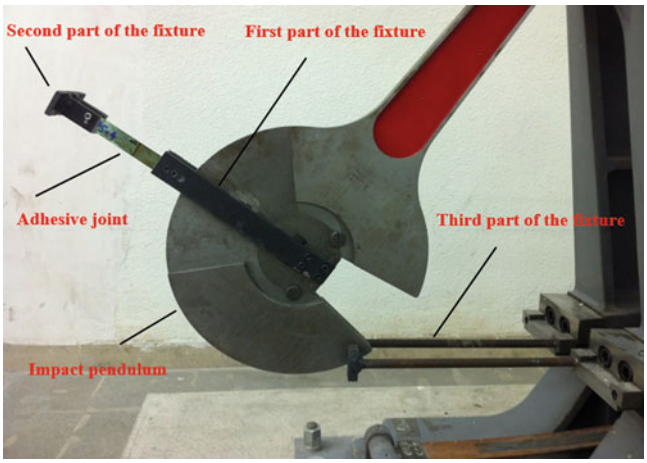

Table 14.1 Type and code no. of adhesive joints

Environmental conditions	Code no. A B C D (YY) A: Adhesive joint B: 3 or 5 (FML layers)
Atmosphere	AR00
Sea water (30 days)	SR00
Sea water (30 days) + 5 heat cycles	SH05
Sea water (30 days) + 10 heat cycles	SH10
Sea water (30 days) + 5 cryogenic cycles	SC05
Sea water (30 days) + 10 cryogenic cycles	SC10

14.2.3 Test Apparatus and Fixture

The testing machine used in this work is an instrumented Charpy pendulum. Charpy test machine was originally developed for high strain rate three-point bending testing of metals, yet, many of the early impact studies on composite materials were undertaken using the Charpy impact test method [9]. The Charpy impact test is widely used in the industry mainly as a quality control mean [10]. In order to use Charpy impact machine for tensile impact testing, design of a fixture which changes the loading direction seems essential. The experimental tests of this research work were carried out using a special fixture designed for CI-30 type Charpy machine (Tokyo Testing Machine MFG. Co., LTD. Max capacity: 300 J) which was prepared regarding the machine and the specimen limitations and geometry. All parts of the fixture were made by CK-45 steel. Figure 14.7 shows the Charpy impact device with the fixture and the specimen during the test.

Adhesive joints with six environmental testing conditions (Table 14.1) were prepared and for each condition, at least three tests were conducted and the results were averaged. After the tests, the fracture mode of each specimen was photographed with a digital camera.

14.3 Results and Discussion

In this section, the experimental results of the tensile impact energy absorption of the adhesive joints are obtained and illustrated in Fig. 14.8. The tensile impact tests were carried out in laboratory situation, using the Charpy impact machine and the designed fixture. The total friction and windage losses of the machine during the swing were calculated using the ASTM E23-07 standard. This value for the apparatus and the fixture on it was 0.215 J. For achieving the absolute energy absorbed by the specimens, this value must be subtracted from the raw amount of energy absorption by each specimen. Summaries of the test results are given in Tables 14.2 and 14.3.

As can be seen in Table 14.2, the absorbed energy by the adhesive joint coded A5AR00 is 27.3 J. Absorbed energy by adhesive joint code A5SR00 is 10.1 J and was decreased by 63 % when compared to A5AR00. The specimens of adhesive joints coded A5SH05 and A5SH10 could absorb more energy as compared to A5SR00, but the specimens of adhesive joints coded A5SC05 and A5SC10 could absorb less energy as compared to A5SR00.

As can be seen in Table 14.3, the absorbed energy by the adhesive joint coded A3AR00 is 28.3 J. Absorbed energy by adhesive joint code A3SR00 is 9.7 J and was decreased by 65.7 % when compared to A3AR00. The specimens of adhesive joints coded A3SH05 and A3SH10 could absorb more energy as compared to A3SR00, but the specimens of adhesive joints coded A3SC05 and A3SC10 could absorb less energy as compared to A3SR00.

As for all cases, the fracture occurred in the adhesive mode, but not in the adherends (FML and St 430). Most of the adhesive remained stuck on one surface and, correspondingly, a thin layer remained on the other side. The failure mode is adhesive failure with almost equal distributions on both surface, Fig. 14.9.

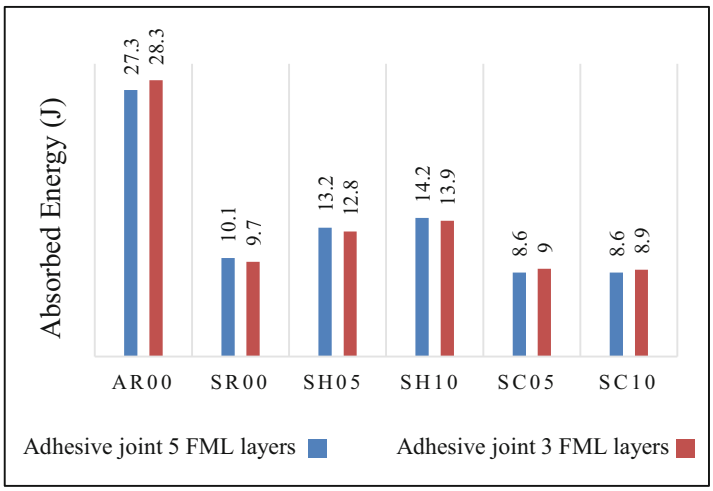

Fig. 14.8 Absorbed energy by adhesive joints

Table 14.2 The experimental results of the tensile impact energy absorption of the adhesive joints (five layers FML)

Code no.	Pure absorbed energy (J)	Increase in absorbed energy (%)
A5AR00	27.3	–
A5SR00	10.1	−63
A5SH05	13.2	−52
A5SH10	14.2	−48
A5SC05	8.6	−68.4
A5SC10	8.6	−68.4

Table 14.3 The experimental results of the tensile impact energy absorption of the adhesive joints (three layers FML)

Code no.	Pure absorbed energy (J)	Increase in absorbed energy (%)
A3AR00	28.3	–
A3SR00	9.7	–65.7
A3SH05	12.8	–54.7
A3SH10	13.9	–51
A3SC05	9	–68.1
A3SC10	8.9	–68.5

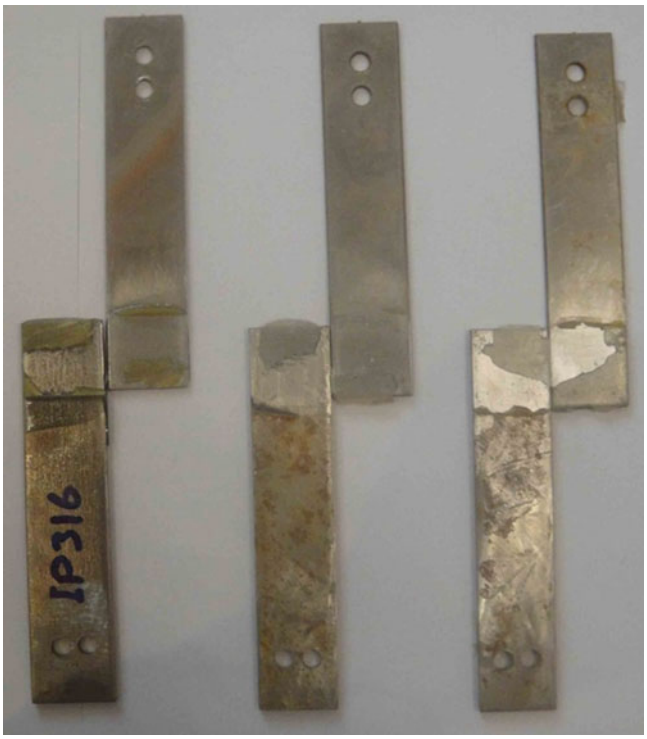

Fig. 14.9 Adhesive failure in the adhesive joints

14.4 Conclusion

This experimental study investigates disruptive effect of sea water on adhesive lap joints made with Fiber Metal Laminate (FML) and 430 Stainless steel adherends. The joints were kept into sea water for 30 days and then thermally cycled separately in an oven and also in liquid N_2 afterwards tested on tensile impact loading. Experimental investigations revealed that the absorbed energy by adhesive lap joint that subjected to sea water was less than of the same in the ambient environment and they improved for five and ten high thermal cycling, but decreased by for five and ten low thermal cycling. The failure mode for the adhesive is the mixed failure. Therefore, high thermal cycle have effective role to increase the absorbed energy in adhesive joints that were subjected to disruptive environment (sea water) in the case of dynamic loading.

References

1. Kinloch, A.J.: Adhesion and adhesives, pp. 2–3, 18–55, . Marcel Dekker, New York (1987)
2. Bikerman, J.J.: The science of adhesive joints, 2nd edn, pp. 309–316. Academic, Waltham (1968)
3. Dodiuk, H., Sharon, G., Kenig, S.: Hydrothermal properties of adhesively bonded joints and their correlation with bulk adhesive properties. J. Adhes. **33**, 45–61 (1990)
4. Kootsookos, A., Mouritz, A.P.: Seawater durability of glass- and carbon polymer composites. Compos. Sci. Technol. **64**, 1503–1511 (2004)
5. da Silva, L.F.M., Adams, R.D.: Int. J. Adhes. Adhes. **27**, 216 (2007)
6. ASTM D950-03: Standard test method for impact strength of adhesive bonds. ASTM International, West Conshohocken (2003)
7. Less, W.A.: Int. J. Mater. Prod. Technol. **2**, 168 (1987)
8. Pires, I., Quintino, L., Durodola, J.F., Beevers, A.: Int. J. Adhes. Adhes. **23**, 215 (2003)
9. Kelly, G.: Load transfer in hybrid (bonded/bolted) composite single lap joint. Compos. Struct. **69**, 35–43 (2005)
10. Hart-Smith, L.J.: Bonded-bolted composite joints. J. Aircr. **22**, 993–1000 (1985)

Chapter 15
Design of Hybrid Composites from Scrap Aluminum Bronze Chips

L.F.P. Ferreira, E. Bayraktar, I. Miskioglu, and D. Katundi

Abstract Aluminum bronze material has high thermal conductivity, wear resistance, corrosion resistance, and good mechanical strength which is widely used in structural applications, grinding tools, etc. Certain studies have shown that these composites containing a small amount of iron and nickel exhibit improved bending strength and higher strain energy.

The main purpose of the present work is to apply the liquid phase sintering process to determine the optimal sintering conditions and to evaluate the interface of aluminum and the scrap aluminum bronze chips with different reinforcement elements (TiC, BN, Gr etc.). A second aspect of this work is to evaluate the effect of the sintering conditions on the microstructure and mechanical properties such as hardness and compression behavior. In the frame of the present work, an original idea of producing a hybrid composite has been developed by using scrap aluminum bronze chips. This consists of mixing and compacting aluminum with aluminum bronze (ASTM B148) chips through press moulding and sintering.

Keywords Recycled aluminum bronze • Hybrid materials • Liquid phase sintering • Mechanical properties

15.1 Introduction

Aluminum bronzes consist of very different kind of compositions with a wide range of properties for industrial applications due to high thermal conductivity, wear resistance, corrosion resistance, and good mechanical strength, etc. The hardness of aluminum bronzes increases with aluminum content as well as with stresses caused through cold working. Certain numbers of manganese and nickel aluminate bronzes exhibit a quasi-similar martensitic transformation that could increase mechanical properties, evidently, there are other mechanisms that increase strength but they are not generally thought of as primary strengthening mechanisms. Generally, these alloys are ductile as the result of short cooling cycle during annealing. They show quasi pure metal solidification behavior [1–5].

Aluminum bronzes are used for replacing other expensive materials in marine applications, hardware and its equipment and recently they are being used more and more in aeronautical, automotive and railway engineering applications.

Another real question in manufacturing engineering is recycling of the scraps resulting from production depending on their quality and the cost of the recycling process (clean, less number of inclusions, etc.). Among the available methods, very economical production of recycled metal matrix composites (MMCs) is achieved by classical powder metallurgy sintering, thixoforming, etc. [6–11]. Essentially, thixoforming or sintered forging give composites much more advantages such as virtually porous free end product, very good interface between the reinforcements and the matrix, homogeneous distribution of the particles in the matrix and improved mechanical properties [6, 7].

The present work proposes low cost of manufacturing of a novel hybrid composite based on scrap aluminum bronze chips. A novel production method of these composites from aluminum bronze chips has been developed through cleaning of chips, addition of the reinforcements, milling, cold compaction, liquid phase sintering followed by heat treatment (tempering) [9–11]. The influence of the reinforcement particles and sintering temperature on the mechanical behaviour of these composites are evaluated. Microstructures and fracture surfaces were analyzed by Scanning Electron Microscope (SEM).

L.F.P. Ferreira
Materials Science Department, Unicamp-University of Campinas, São Paulo, Brazil

School of Mechanical and Manufacturing Engineering, Supmeca-Paris, La Garde Cedex 83957, France

E. Bayraktar • D. Katundi
Materials Science Department, Unicamp-University of Campinas, São Paulo, Brazil

I. Miskioglu (✉)
ME-EM Department, Michigan Technological University, Houghton, MI 49931, USA
e-mail: imiski@mtu.edu

W.C. Ralph et al. (eds.), *Mechanics of Composite and Multi-functional Materials, Volume 7*,
Conference Proceedings of the Society for Experimental Mechanics Series, DOI 10.1007/978-3-319-41766-0_15

15.2 Experimental Conditions

Basically, fresh scrap aluminum bronze chips (provided by French Aeronautics) were used as a matrix for this work; the chemical composition of the bronze chips is given in the Table 15.1. As the main reinforcement element, titanium carbide (TiC), in three different percentages (variable from 5, 10 up to 15 wt%) was added to the structure. Low percentages of graphite, 2 %; Si, 1.5 %; Al, 1 %; boron nitrate—BN, 2.5 %; were also used as additional reinforcements. The composites were produced by using classical powder metallurgy—liquid state sintering. After blending and milling of the mixture for 3 h, cold compaction was carried out at 650 MPa to produce green compact specimens according to ASTM-E 9-89a with a diameter of 11 mm. Aspect ratio (L/D) 1.5 or 1.75 was kept for all of the specimens. Sintering process was carried out at three different temperatures (850, 900 and 950 °C) in an argon inert atmosphere. All of the specimens were initially subjected to solubilizing treatment at a heating rate of 10 °C/min for 1 h to a maximum temperature (T_{max} = 850–900 and 950 °C) and quenched in water and subsequently tempering treatment was applied at 490 °C for 2 h and finally they were left in the oven for cooling. The nomenclature used for the three compositions (called here after as BR1, BR2, BR3) is given in Table 15.2. Dispersion of the reinforcement particles in the matrix and the final shapes of the bronze chips were characterized by Optical Microscopy (OM) and Scanning Electron Microscopy (SEM). The surfaces of the specimens were prepared by grinding, polishing, and etching using ferric nitrate (10 % in water). Micro hardness values $HV_{0.5}$ were measured by taking several measurements in different zones for each composition. All the density measurements of the specimens were carried out by using Archimedes method and the results were then compared. Sintered products were then tested in quasi-static compression tests, carried out in a servo-hydraulic INSTRON Universal test system (model Instron 5500R, equipped with a load cell of 25,000 kgf) at an initial rate of 10 mm/min and second rate of 5 mm/min. Maximum load endpoint was 4500 N.

15.3 Results and Discussion

The main alloying element in aluminum bronze is aluminum. Binary phase diagram of the Cu–Al in the equilibrium state is shown in Fig. 15.1. The figure shows that the maximum solubility of aluminum in solid copper is 9.4 wt%. As the temperature increases from 565 to 1035 °C the solubility of aluminum in the copper decreases and reaches 7.5 wt%. The stable phase of Cu–Al are α, β, γ_2 and α_2 phases.

"EDS" analysis presented in Fig. 15.2 depicts the general structure of the composites, along with the basic reinforcement elements in the structure.

The established temperature cycles during the manufacturing process are responsible for the formation of different phases that directly influence the mechanical strength of the material. For this reason, general characterization of the microstructures of these hybrid composites should be made for each heat treatment.

Figure 15.3 presents the general microstructures of all the sintered samples at 900 °C quenched in water followed by tempering treatment at 490 °C for 2 h. Well distribution of reinforcement elements is observed in the microstructure and they have given a good interface (good bonding between the matrix and the reinforcement with large bronze chip particles.

Some detailed microstructure indicates that a bonding diffusion takes place with partial eutectic solidified zones. Mainly, mutual diffusion of copper and aluminum was observed during the heat treatment applied in two stages (Fig. 15.3, right column). These types of heat treatment can only lead to good surface (wear) properties of these composites and also eliminate the porosities in the structure and could increase the strength of these composites.

Table 15.1 Chemical composition of aluminum bronze provided by French Aeronautics

Element	Cu	Al	Fe	Ni	Mg	Zn	Si
(%)	80.4	8.92	4.75	4.6	0.51	0.60	0.19

Table 15.2 Weight percent of the reinforcements

Composite	TiC	Graphite	Si	Al	BN
BR1	5	2	1.5	1	2.5
BR2	10	2	1.5	1	2.5
BR3	15	2	1.5	1	2.5

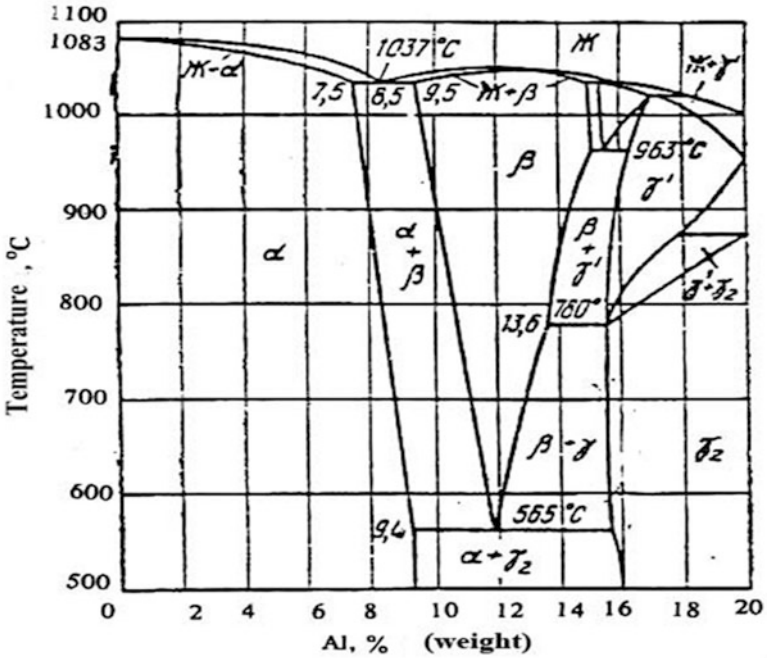

Fig. 15.1 Binary phase diagram of aluminum bronze (Cu–Al couple) [1]

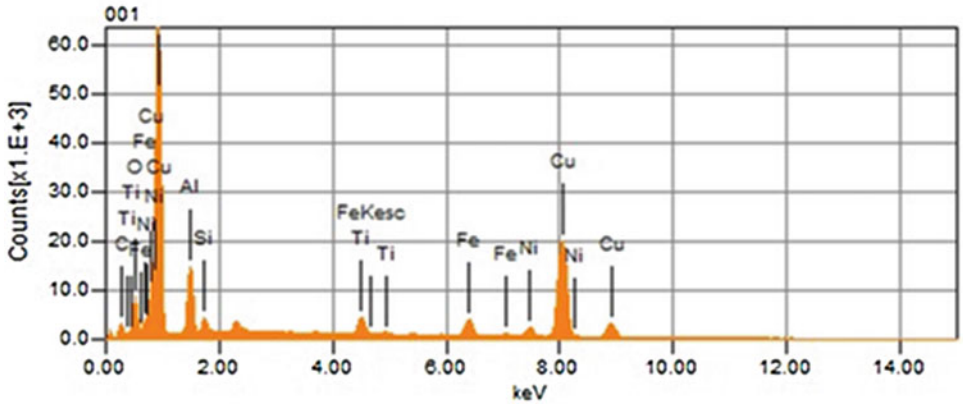

Fig. 15.2 "EDS" analysis of the general structure of the composites developed here

Much more detailed analysis of the microstructure of the composites is given in Fig. 15.4. Interface relation of the matrix with the reinforcements was discussed for the specimens sintered at 850, 900, and 950 °C for 1 h followed tempering at 490 °C for 2 h.

Interface relation and bonding diffusion at higher temperatures (900 and 950 °C) were better regarding to those of the specimens treated at 850 °C.

Experimental measurements of absolute density were carried out by Archimedes method for the three different compositions manufactured under three different heat treatments. All of these results are compared in Fig. 15.5. For all practical purposes all of the specimens have resulted in the same density with slight variations from 5.2 to 5.8 g/cm^3.

In the same way, measurements of microhardness "$HV_{0.5}$" values for the three different compositions are presented in the Fig. 15.6. All of the values are mean values of three measurements taken on each specimen. Apparently, a considerable scatter in the measured values coming from the heterogeneous structure composites (mainly in the composite called BR1) related to the chip size in the structure and distribution of the reinforcement elements. As a simple comparison of these values, composite "BR3" treated at 950 °C, showed very little scatter in data. However, these values are only preliminary values and they should be improved by improving structure by ball milling for longer time and compacting.

Quasi-static compression test results carried out on all of three compositions is presented in Fig. 15.7. All of the compression tests have been made with minimum three specimens according to the ASTM-E 9-89a with a diameter of

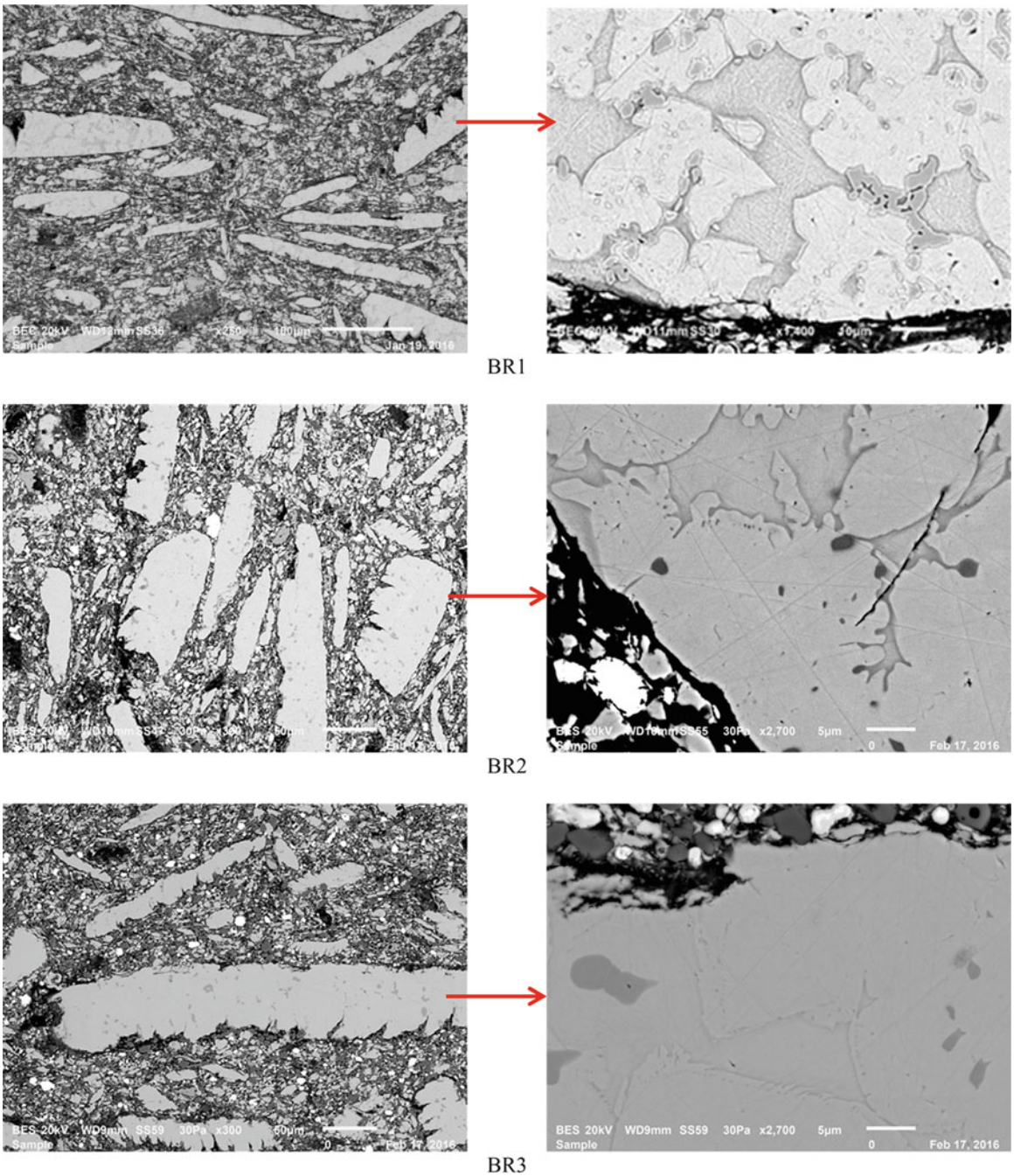

Fig. 15.3 General microstructure of the composites I, II and III at 900 °C developed in this work

11 mm. Aspect ratio (L/D equal 1.5 or 1.75) was kept the same for all of the specimens of a composite. These test results have indicated that all of the compositions treated at 950 °C have shown higher maximum forces even if scatter in the data is high. Among them the composition called "BR2", gives largest load values at 950 °C.

Evaluation of impact energies made on the three composites treated at different temperatures is presented in Fig. 15.8. For each composition, at least five or six specimens have been tested to evaluate their damping capacities. First of all, the composition "BR3" has given higher energy values at all the treatment conditions (Fig. 15.8a). However, all of the compositions have shown high impact values when they were treated at 950 °C (Fig. 15.8b). Optimal values are obtained with a composition containing 10 % TiC (BR2) treated at 950 °C. And also, for the composition containing 15 % TiC (BR3), higher energy values are obtained at three treatments, 850, 900, 950 °C regarding to other compositions. These values can help to optimize the compositions (the role of the reinforcement elements, and also the role of the treatment temperatures, etc.).

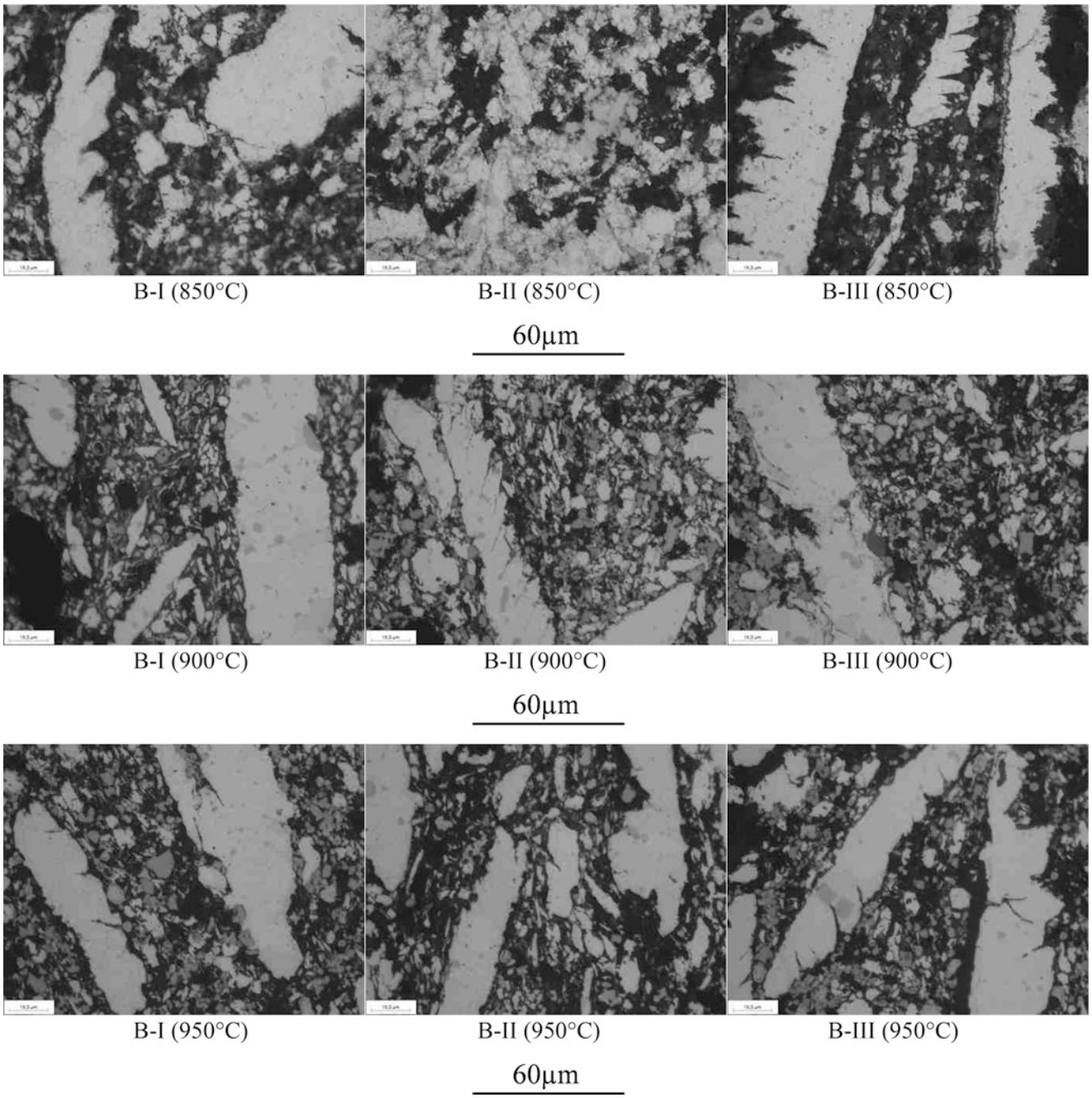

Fig. 15.4 General microstructure of the composites developed in this work: specimens sintered at 850, 900, and 950 °C for 1 h followed tempering at 490 °C for 2 h

15.4 Conclusions

In the present work, low cost design and manufacturing of novel hybrid composites for engineering applications was presented. For this research, fresh scrap aluminum bronzes were utilized in the design of novel hybrid compositions. Evidently reinforcement elements have played important role on the damping capacity at different treatment conditions. During the new process of the composites, a simple and low cost method was used for the conversion into compact metal by using fresh scrap coming from cutting chips: Quenching in water after liquid sintering at high temperature followed by tempering at 490 °C for 2 h can eliminate heavy, long and expensive metallurgical processes. These novel composites can be safely used in different engineering applications including plain bearings and landing gear components on aircraft, etc.

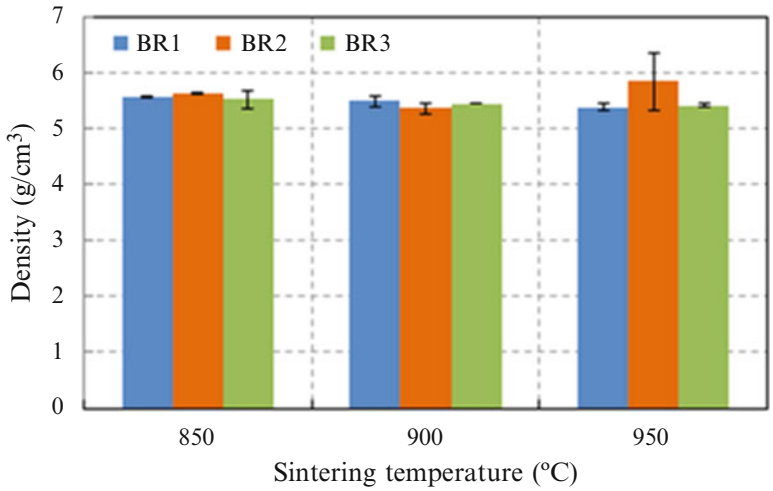

Fig. 15.5 Experimental measurements of absolute density for the three different compositions

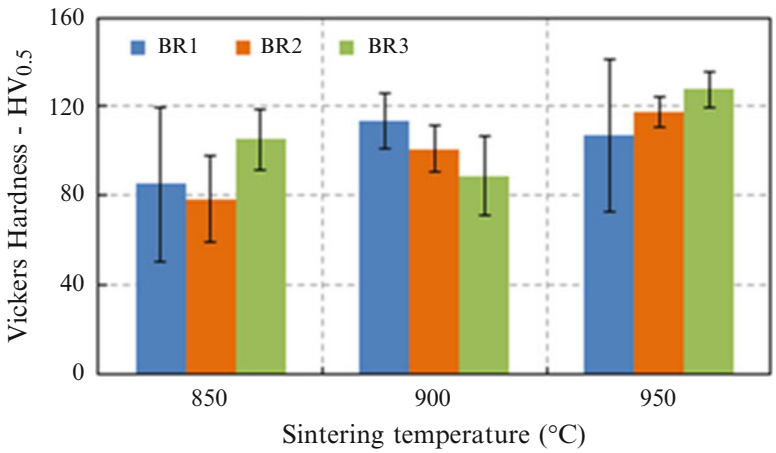

Fig. 15.6 Microhardness $HV_{0.5}$ measurements for the three different compositions

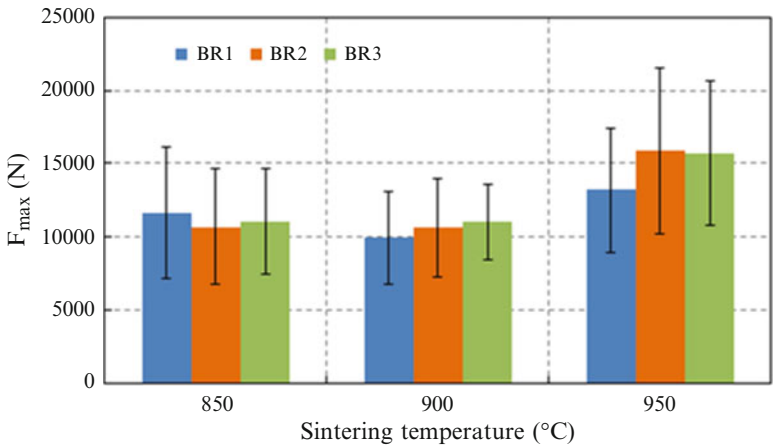

Fig. 15.7 Quasi static compression test results for the three compositions

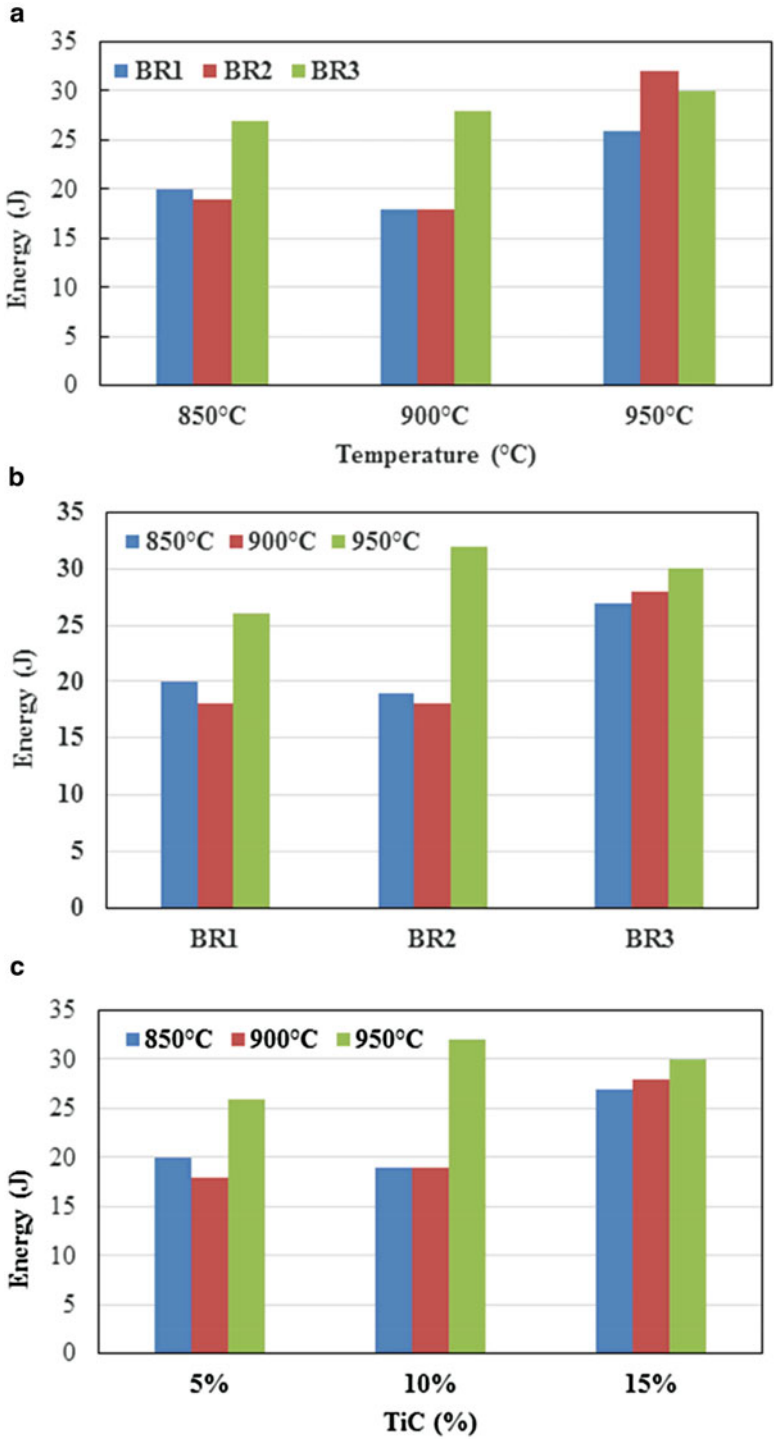

Fig. 15.8 Evaluation of Impact energies depending on (**a**) temperature, (**b**) composition, (**c**) TiC content

Evaluation of the microstructure and the mechanical properties of composites are correlated to phases created according equilibrium diagram. The kinetics of phenomena taking place during heat treatment (solubilizing and tempering) has the distinct effect on the microstructure and composite properties. Microstructure indicates that a bonding diffusion takes place with partial eutectic solidified zones. Mainly, mutual diffusion of copper and aluminum was observed during the heat treatment applied in two stages.

On the basis of practical experiments, the following optimum parameters for these composites: sintering temperature at 950 °C with a holding time maximum 1 h and tempering process should be made at 490 °C for 2 h for eliminating the porosity and increasing strength of these composites. Addition of TiC, as the reinforcement element, should be around 10–15 wt%.

References

1. Veasey, T.J., Wilson, R.J., Squires, D.M.: The physical separation and recovery of metals from wastes: process engineering for the chemical, metals and minerals industries, vol. 1. Gordon and Breach, Amsterdam (1993)
2. Skalova, L., Luka, J.: Optimization of recycling process of white bronze chips. 12th International Research/Expert Conference–TMT 2008, Turkey, Istanbul, August 2008, ISBN: 995861741-2
3. Gronostajski, J., Gronostajski, Z.: Sintering criterion in metal working processes. J. Mater. Process. Technol. **133**, 99–102 (2003)
4. van der Heide, E., Stama, E.D., Giraud, H., Lovato, G., Akdut, N., Clarysse, F., Caenen, P., Heikill, I.: Wear of aluminium bronze in sliding contact with lubricated stainless steel sheet material. Wear **261**, 68–73 (2006)
5. Pawlak, Z., Kaldonski, T., Pai, R., Bayraktar, E., Oloyede, A.: A comparative study on the tribological behaviour of hexagonal boron nitride (h-BN) as lubricating micro-particles: an additive in porous sliding bearings for a car clutch. Wear **267**(5–8), 1198–1202 (2009)
6. Lu, H., Wang, X., Zang, T., Cheng, Z., Feng, Q.: Design, fabrication, and properties of high damping metal matrix composites, a review. J. Mater. **2**, 958–977 (2009)
7. Bayraktar, E., Ayari, F., Tan, M.J., Tosun Bayraktar, A., Katundi, D.: Manufacturing of aluminum matrix composites reinforced with iron-oxide nanoparticles: microstructural and mechanical properties. In: Laughlin, D.E. (ed.) Metallurgical and Materials Transactions B, vol. 45, pp. 352–362. Springer, New York (2014)
8. Chmura, W., Gronostajski, Z.: Bearing composites made from aluminium and aluminium bronze chips. J. Mater. Process. Technol. **178**, 188–193 (2006)
9. Ferreira, L.-M.-P., Bayraktar, E., Robert, M.-H., Miskioglu, I.: Optimization of magnetic and electrical properties of new aluminium matrix composite reinforced with magnetic nano iron oxide. In: Zimmerman, K.B. (ed.) Mechanics of Composite and Multifunctional Materials, vol. 7, pp. 11–18. Springer, New York (2015). ISBN: 978-3-319-21761-1
10. Bayraktar, E., Robert, M.-H., Miskioglu, I.: Design of Al-Nb2Al composites through powder metallurgy. In: Zimmerman, K.B. (ed.) Mechanics of Composite and Multifunctional Materials, vol. 7, pp. 131–139. Springer, New York (2015). ISBN: 978-3-319-21761-1
11. Lu, H., Wang, X., Zhang, T., Cheng, Z., Fang, Q.: Design, fabrication, and properties of high damping metal, matrix composites—a review. Materials **2**, 958–977 (2009). doi:10.3390/ma2030958

Chapter 16
Impact Response of Waste Poly Ethylene Terephthalate (PET) Composite Plate

Ibrahim Bilici, Ali Kurşun, and Merve Deniz

Abstract Poly ethylene terephthalate (PET) is considered one of the most important engineering polymers for the last two decades due to its rapid growth of usage, aesthetic appearance, good light transmittance, and smooth surface. It is highly preferable for the food and soft drink bottle packaging industry because of its low gas permeability and recycling potential. For this reason, vast amount of PET's is used daily and mandates an effective recycling process. The recycling of PET can be performed using two different methods, which are chemical and mechanical methods. In this study, chemical recycling method was chosen as a recycling method. Waste PET bottle evaluated as a binder for composite materials. Obtained glycolized products and binder are characterized by OH number (hydroxyl), acid number and FTIR. Then E-glass/recycle resin composite plates were manufactured via Vacuum Assisted Resin Transfer Molding (VARTM). Drop weigh tests were applied to measure the general mechanical and damage behavior of these composites.

Keywords Polyethylene terephthalate • Glycolysis • Recycle • Composite • Impact response • Damage analysis

16.1 Introduction

PET, is the one of the most important representative of the thermoplastic polyester group by the virtue of its lightness, cheapness, toughness, clearness, chemical resistance and non-toxicity. It can be used in the manufacture of barrier material, mostly disposable plastic bottles, different types of flexible food packaging etc. Even though there is no direct damage to the environment, the extensive usage of the PET brings about tons of waste each year. In recent years, many researchers have evaluated various plastic waste recycling methods due to the growing production, use of plastics associated with environmental concerns and space problems. In order to overcome these problems, PET can be recycled by chemically or mechanically and then the recycled PET can be blended with other polymers [1] or modified concrete/mortars (cement [2], glass fiber [3], sand [4], fly ash and aggregates [5], asphalt [6], etc.). Among the recycling methods, chemical recycling is the most favorable and established one, by using this method the PET can be converted into the monomers and oligomers [7, 8]. After an effective chemical recycling process, obtained products can be used for production of unsaturated poly(ester-urethane) [8], biodegradable polyurethanes [9], polyester polyols [10], unsaturated polyesters [11, 12], waterborne polyurethane adhesives [13], polyurethane dispersions [14], polyurethane foams [15, 16], saturated polyester and polyurethane nanocomposites [17, 18]. Various methods such as hydrolysis (water), alcoholysis (alcohols), glycolysis (glycols), aminolysis (amines) can be used for chemical recycling of PET. Glycolysis is the most favorable, the oldest and simplest degradation process for PET among these methods, because by using this method new raw materials (monomers) can be obtained in order to use in the manufacturing of the advanced plastics. Ethylene glycol (EG), diethylene glycol (DEG), propylene glycol (PG) and dipropylene glycol (DPG) are commonly used glycols for glycolysis of PET [19]. Canaday and Skowronski [20] reported that, reactivity of the recycling reaction depends on temperature, catalyst and PET/glycol ratio [21]. However, if the short chain diols are used in glycolysis process, obtained polyols has some drawbacks such as the presence of cyclic oligomers in the product. Therefore, final product properties can be affected negatively depending on the

I. Bilici (✉) • M. Deniz
Department of Chemical Engineering, Hitit University, Çorum, Turkey
e-mail: ibrahimbilici@hitit.edu.tr

A. Kurşun
Department of Mechanical Engineering, Hitit University, Çorum, Turkey

W.C. Ralph et al. (eds.), *Mechanics of Composite and Multi-functional Materials, Volume 7*,
Conference Proceedings of the Society for Experimental Mechanics Series, DOI 10.1007/978-3-319-41766-0_16

reduction in total functionality and hydroxyl number of the polyols [13]. Improving the mechanical properties of the recycled plastic is important with regards to finding new application area. Theoretically, mechanical properties of recycled polymer can be enhanced by the addition of any fiber. The important thing is interaction between the matrix and fiber and choosing the right features for fiber length [22]. The E-glass Fiber Reinforced Plastic (GFRP) is a composite product which is made from glass fiber-resin and used as the construction material. In recent years, this material is widely used for its lightness, mechanical performance and shapeability [23–26].

16.2 Materials and Methods

16.2.1 Test Specimen

GFRP used in the study were manufactured via VARTM which is also known as Vacuum Infusion (VI). During VI, the vacuum pressure drives resin into a previously compacted reinforcement material. Different from RTM (resin transfer molding), VI uses a vacuum bag as the upper mold. The compaction pressure on the reinforcement material is also applied with vacuum. When the vacuum pressure is applied inside the mold, the atmospheric pressure applies the compaction pressure. VI is used widely in marine and automotive industry because of its ability to manufacture large parts and relatively low cost. The GFRP composites were produced using six layers of biaxial stitched E-glass fabrics having a density of 450 g/m^2 and two different resin one of them was recycled and the other was virgin. The dimensions were 70 × 70 mm with a thickness of 2.5 mm for the samples used.

16.2.2 Experimental Procedure

Collected PETs were purged from contaminations such as PVC, labels, and then were cut by a shredder into small pieces less than 10 mm flakes. The glycolysis reactions of PET were carried out in a 1 L five necked flask equipped with a stirrer, thermocouple, and refluxing condenser unit. Experiments were carried out at 180 °C. Time of the reaction was a maximum of 4 h. Glycolized products were labeled according to moiety of the PET: DPG and after that these acid and hydroxyl number estimated and glycols were reacted with phthalic and maleic anhydrite for the production of the polyester as a binder.

The acid number defined as the amount of potassium hydroxide required for neutralizing 1.00 g of polyol and it was determined by titration of the sample solution with 0.1 N KOH solutions (ASTM D3644). During the glycolysis reaction the acid numbers was measured at 1 h time interval.

The hydroxyl number [OH number] was defined as the amount of potassium hydroxide equivalent to the amount of acetic acid involved in the esterification reaction with 1.00 g of polyol and determined by the conventional acetic anhydride/pyridine method (ASTM D4662-03).

The samples chosen from GFRP plate with a 2.5 mm thickness of the plates, have been prepared according to impact test conditions with dimensions of 2.5 × 70 × 70 mm. CEAST 9350 drop weight impact test machine was used for the low velocity impact test characterization to analyze deformation and damage behaviour of GFRP plates. Impact test were performed with respect to the standard of ASTM D5628 FE, and two impact energy levels 20 and 40 J. The GFRP plate were placed between two steel blank holders as opposite supports containing a 40 mm circular hole. The pressure applied on the samples by means of blank holders can supply a rigid position for not allowing the slipping between the blank holders during impact. In the upper part of the machine, the mass of dropping tool that includes the weight box for adding mass in and the striker was approximately 5.295 kg. The striker is composed of the rod attached with force transducer and the impactor nose. The contact load between the impact nose and the GFRP composite specimens versus time was measured by the force transducer. CeastVIEW Software based on Newton's Second Law and kinematics converted the time–force history taken from the force transducer to the velocity and displacement histories.

16.3 Results and Discussion

16.3.1 Materials Characterization

In Fig. 16.1 acid number changing vs. time can be seen. In first hour acid number is very low because of the reactant were not react completely. After 2 h Acid number decreased dramatically and reacted were ended after 3 h. Furthermore, OH numbers were estimated according to ASTM D4662-03 and found that 1292, 1388, 274 and 388 mg KOH/g sample respectively DEG moiety. According to OH and acid numbers obtained polyols can be used as a polyol to get polyester binder.

In Fig. 16.2 reveal that reaction was successful and polyols can be used as a polyester raw material. Around 3400–3500 cm^{-1} free glycols effect can be seen clearly and 1:1 moiety polyols agreed on use as a binder.

In Fig. 16.3 reveal that esterification reaction with maleic and phthalic anhydrite has been completely successfully. Small amount of peak differences can be negligible because of contamination.

16.3.2 Mechanical Properties and Damage Analysis

Different mechanical and physical properties are evaluated in this stage; several impact drop weight tests have been carried out. Figure 16.4 gives the force—time and force—displacement histories of the composite plates and compares the results for virgin and recycled PET. In general, the contact force level increases rapidly at the beginning, which is the result of an oscillation of the composite plate after first contact with the impactor. When the plate reach maximum displacement, the force level decreases to zero again. For the same impact energies, the maximum force was obtained as a polyester composite, however the maximum displacement was obtained as a recycled PET composite. It is reveal that recycled PET based composite much more elastic behavior than virgin PET composite. It is also recycled PET composite showed that 84 % similar impact response.

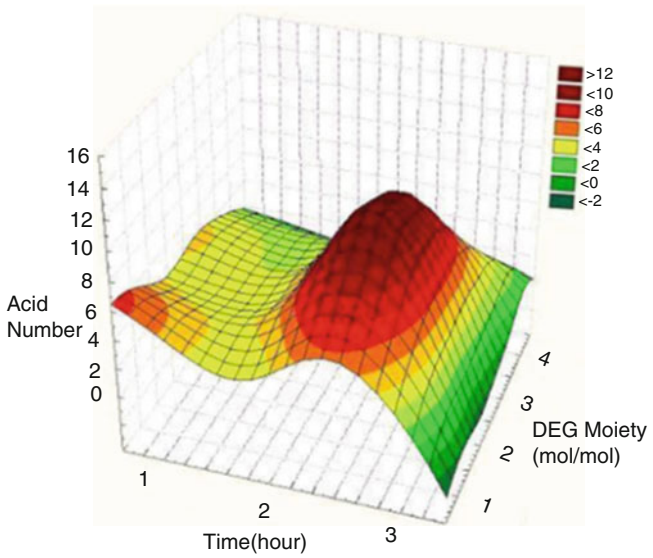

Fig. 16.1 Acid number vs. time according to DEG moiety

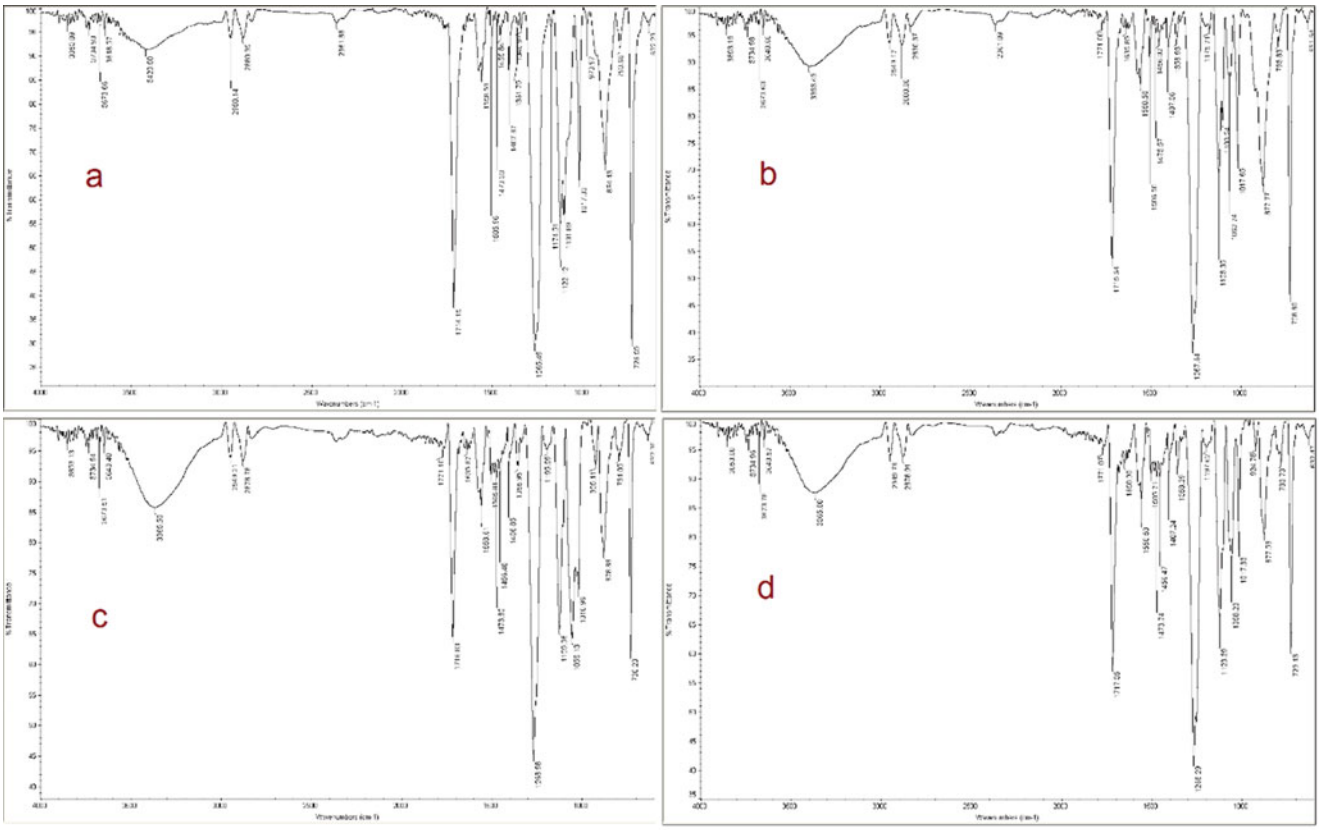

Fig. 16.2 FTIR spectrum of polyol (**a**) 1:1 DEG/PET (**b**) 1:2 DEG/PET (**c**) 1:2.7 DEG/PET (**d**) 1:3.6 DEG/PET

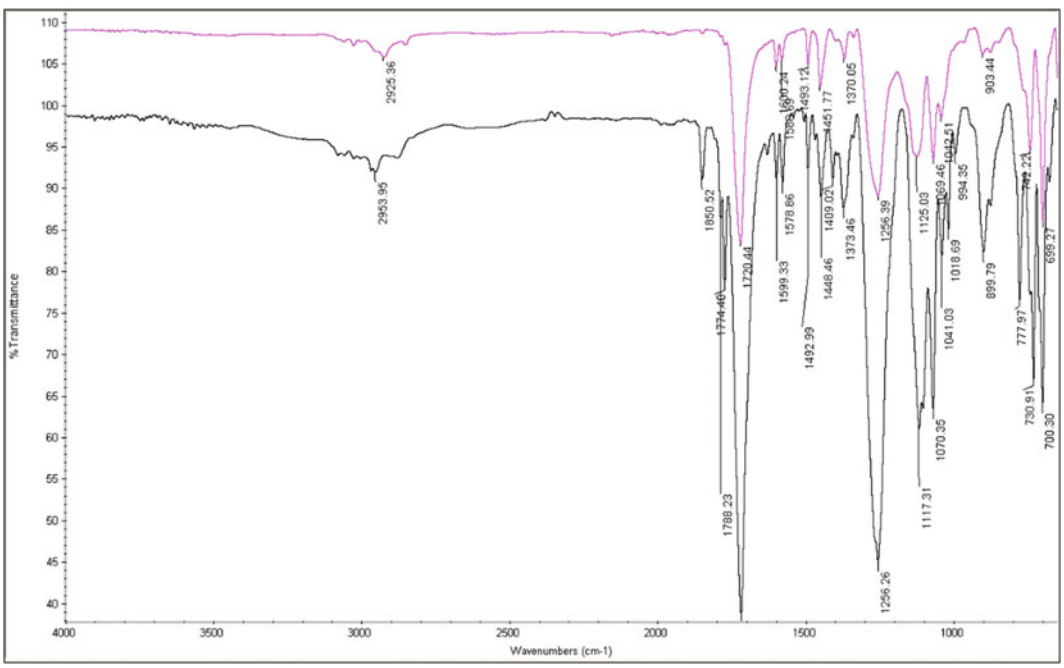

Fig. 16.3 FTIR spectrum of recycled (*black*) and commercial polyester (*pink*)

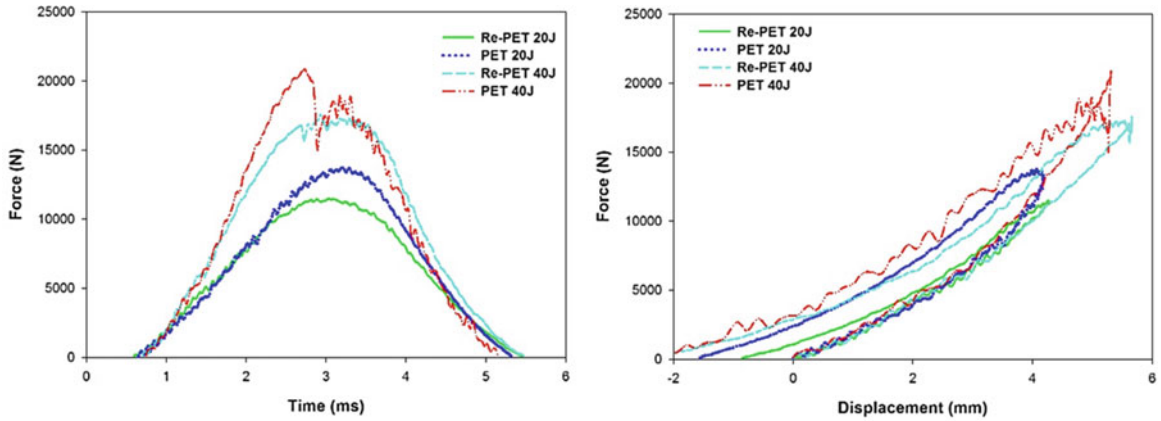

Fig. 16.4 Low velocity impact test results for recycled and virgin PET composite at two impact energy levels

16.4 Conclusion

As a conclusion;

- In this study polyester binder successfully produced from waste bottles. In addition to this study, furthermore investigation about types of glycols, types of acid could be tried, because mechanical properties are depends on the glycol and acid types.
- According to OH and acid values, these types of glycolized product can be used as a raw material such as polyurethane or polyester. Several types of material could be try via this method and analysis.
- Impact results show that mechanical properties of virgin binders just 15 % greater than waste based binder. The mechanical differences between the virgin and recycled PET can be decrease furthermore investigation and soft drink bottle waste can be used as a binder for laminated composites instead of virgin polyester. In this way, recycled or reused methods, waste bottles evaluated environmentally and ecologically.

Acknowledgment This study was supported by Hitit University Scientific Research Project, which name is "Investigation of Chemical Recycling of Waste PET (Polyethylene terephthalate) Bottles" No. MUH19002.15.001.

References

1. Lin, X., Qian, Q., Xiao, L., Chen, Q., Huang, Q., Zhang, H.: Influence of reactive compatibilizer on the morphology, rheological, and mechanical properties of recycled poly(ethylene terephthalate)/polyamide 6 blends. J. Macromol. Sci., Part B: Phys. **53**(9), 1543–1552 (2014)
2. Fraternali, F., Spadea, S., Berardi, V.P.: Effects of recycled PET fibres on the mechanical properties and seawater curing of Portland cement-based concretes. Constr. Build. Mater. **61**, 293–302 (2014)
3. Cornier-Ríos, H., Sundaram, P.A., Celorie, J.T.: Effect of recycling on material properties of glass-filled polyethylene terephthalate. J. Polym. Environ. **15**(1), 51–56 (2006)
4. Aghazadeh Mohandesi, J., Refahi, A., Sadeghi Meresht, E., Berenji, S.: Effect of temperature and particle weight fraction on mechanical and micromechanical properties of sand-polyethylene terephthalate composites: A laboratory and discrete element method study. Compos. Part B. **42** (6), 1461–1467 (2011)
5. Marthong, C., Marthong, S.: Enhancing mechanical properties of concrete prepared with coarse recycled aggregates. IES J. Part A Civil Struct. Eng. **8**(3), 175–183 (2015)
6. Almeida e Silva, J., Lopes Lucena, L.C., Guedes Rodrigues, J., Carvalho, M.W., Beserra Costa, D.: Use of micronized polyethylene terephthalate (PET) waste in asphalt binder. Pet. Sci. Technol. **33**(15–16), 1508–1515 (2015)
7. George, N., Kurian, T.: Recent developments in the chemical recycling of postconsumer poly(ethylene terephthalate) waste. Ind. Eng. Chem. Res. **53**(37), 14185–14198 (2014)
8. Issam, A.M., Hena, S., Nurul Khizrien, A.K.: A New unsaturated poly(ester-urethane) based on terephthalic acid derived from polyethylene terephthalate (PET) of waste bottles. J. Polym. Environ. **20**(2), 469–476 (2011)
9. Mir Mohamad Sadeghi, G., Shamsi, R., Sayaf, M.: From aminolysis product of PET waste to novel biodegradable polyurethanes. J. Polym. Environ. **19**(2), 522–534 (2011)

10. Mukerjee, S.L., Tabor, R., Emerson, A.W., Rogers, K.A., Vrabel, E.D., Brown, M.T., et al. (Resinate Materials Group, Inc.): Polyester polyols from thermoplastic polyesters and dimer fatty acids. US Patent US20150344622, 3rd Dec. 2015
11. Rusmirović, J.D., Trifković, K.T., Bugarski, B., Pavlović, V.B., Džunuzović, J., Tomić, M., et al.: High performance unsaturated polyester based nanocomposites: effect of vinyl modified nanosilica on mechanical properties. Express Polym Lett **10** (2), 139–159 (2016)
12. Marinkovic, A.D., Radoman, T., Dzunuzovic, E.S., Dzunuzovic, J.V., Spasojevic, P., Isailovic, B., et al.: Mechanical properties of composites based on unsaturated polyester resins obtained by chemical recycling of poly(ethylene terephthalate). Hem. Ind. **67**(6), 913–922 (2013)
13. Cakić, S.M., Ristić, I.S., M-Cincović, M., Stojiljković, D.T., János, C.J., Miroslav, C.J., et al.: Glycolyzed poly(ethylene terephthalate) waste and castor oil-based polyols for waterborne polyurethane adhesives containing hexamethoxymethyl melamine. Prog. Org. Coat. **78**, 357–368 (2015)
14. Cakić, S.M., Ristić, I.S., M-Cincović, M., Nikolić, N.Č., Ilić, O.Z., Stojiljković, D.T., et al.: Glycolyzed products from PET waste and their application in synthesis of polyurethane dispersions. Prog. Org. Coat. **74**(1), 115–124 (2012)
15. Luo, X., Li, Y.: Synthesis and characterization of polyols and polyurethane foams from PET waste and crude glycerol. J. Polym. Environ. **22**(3), 318–328 (2014)
16. Roy, P.K., Mathur, R., Kumar, D., Rajagopal, C.: Tertiary recycling of poly(ethylene terephthalate) wastes for production of polyurethane–polyisocyanurate foams. J. Environ. Chem. Eng. **1**(4), 1062–1069 (2013)
17. Nikje, M.M.A., Farazfar, M.: Synthesis and characterization of polyurethane nanocomposites formulated by incorporation of polyols from PET waste. Cell. Polym. **31**(2), 69–82 (2012)
18. Katoch, S., Sharma, V., Kundu, P.P.: Synthesis and characterization of saturated polyester and nanocomposites derived from glycolyzed PET waste with varied compositions. Bull. Mater. Sci. **36**(2), 277–286 (2013)
19. Leian, B., Muhammad, I., Bong Gyoo, C., Waheed, A.M., Do Hyun, K.: Recent developments in the chemical recycling of PET. In: Achilias, D. (ed.). Material Recycling-Trends and Perspectives, pp 65–84 InTech, Croatia (2012)
20. Canaday, J.S., Skowronski, M.J.: A comparison of aromatic polyester polyols for rigid urethane and isocyanurate foam. J. Cell. Plast. **21**(5), 338–344 (1985)
21. Pardal, F., Tersac, G.: Comparative reactivity of glycols in PET glycolysis. Polym. Degrad. Stab. **91**(11), 2567–2578 (2006)
22. Carnier-Rios, H.: Effect of recycling on material properties of polyethylene terephthalate at various recycling ratios and recycling generations. University of Puerto Rico, San Juan (2003)
23. Kurşun, A., Senel, M.: Investigation of the effect of low-velocity impact on composite plates with preloading. Exp. Tech. **37**(6), 41–48 (2013)
24. Corinaldesi, V., Donnini, J., Nardinocchi, A.: Lightweight plasters containing plastic waste for sustainable and energy-efficient building. Constr. Build. Mater. **94**, 337–345 (2015)
25. Kurşun, A., Şenel, M., Enginsoy, H.M.: Experimental and numerical analysis of low velocity impact on a preloaded composite plate. Adv. Eng. Softw. **90**, 41–52 (2015)
26. Radenkov, P., Radenkov, M., Grancharov, G., Troev, K.: Direct usage of products of poly(ethylene terephthalate) glycolysis for manufacturing of glass-fibre-reinforced plastics. Eur. Polym. J. **39**(6), 1223–1228 (2003)

Chapter 17
Particles Reinforced Scrap Aluminum Based Composites by Combined Processing Sintering + Thixoforging

L.F.P. Ferreira, E. Bayraktar, M.H. Robert, and I. Miskioglu

Abstract Scrap aluminium (AA 7075) chips are recycled for new composite design through combined method of powder metallurgy and thixoforging as a more economic method. Thixoforging processing is already known as low cost manufacturing of the structural materials. In this work, we have used an additional route (powder metallurgy) to facilitate the thixoforging processing. This new approach can help for improving performance and efficiency of the processing. AA7075 Aluminium chips are used as matrix and boron is used as main reinforcement element and others such as BN, TiO_2, graphite, and spherical ceramics are used as minor reinforcements, respectively. Graphite powders are added for their good lubrication and improving damping behavior. Microstructure, mechanical properties and Impact performance are compared depending on the reinforcement elements.

Keywords Recycle of AA7075 • Powder metallurgy • Thixoforging • Impact damage • SEM analysis

17.1 Introduction

Aluminium matrix composites (AMMCs) are mainly used in aeronautics engineering applications as matrix with different particulate reinforcements such as alumina, SiC, boron and/or intermetallics and other ceramic oxide, etc. [1–7]. Up to now, different processing methods have been developed for these composites, among which liquid state and solid state sintering as powders and also the semi-solid processing SSP, (thixoforming mainly for graded materials) are well known. Usually for this process, supplementary application of pressure is necessary to decrease internal (structural) defects and improve homogeneity of the final product. Employing SSP is very useful compared to methods involving liquid metal, which tend to result in products with a certain degree of heterogeneity due to particles agglomeration and associated porosity, especially once the reinforcing particles present small dimensions. Powder metallurgy techniques also allow better particles dispersion and higher particles content than process involving liquid, but are more lengthy, energy consuming and expensive than thixoforming techniques. Therefore, thixoforming may be an efficient and economic route to produce AMMCs. Additionally, Functionally GRaded Materials (FGRMs) are used in many engineering applications such as turbine blades, implants and piston heads, where parts are required to have hard surfaces for abrasive resistance and a more ductile core, for example. FGRMs can be manufactured by different techniques; centrifugal or squeeze casting, separation by electromagnetic field, infiltration of liquid metal into graded pre-forms, among others [5–7]. Surface treatments and different kinds of surface modifications and deposition [8, 9] as well as cladding, welding, etc. can also result in layered composites.

The present work proposes a new and a simple idea for the development of low cost engineering manufacturing of AMMCs using scrap aluminium chips, via a combined method of powder metallurgy (pre-sintering) and thixoforming

L.F.P. Ferreira
Materials Science Department, UNICAMP-University of Campinas, São Paulo, Brazil

School of Mechanical and Manufacturing Engineering, Supmeca-Paris, Paris, France

E. Bayraktar (✉)
School of Mechanical and Manufacturing Engineering, Supmeca-Paris, Paris, France
e-mail: bayraktar@supmeca.fr

M.H. Robert
Materials Science Department, UNICAMP-University of Campinas, São Paulo, Brazil

I. Miskioglu
ME-EM Department, Michigan Technological University, Houghton, MI 49931, USA

W.C. Ralph et al. (eds.), *Mechanics of Composite and Multi-functional Materials, Volume 7*,
Conference Proceedings of the Society for Experimental Mechanics Series, DOI 10.1007/978-3-319-41766-0_17

of reinforced with particulates such as metallic and ceramic oxides. Mechanical behaviour—impact damage—analyses have been carried out. Microstructural evaluation and fracture surfaces as well as interface analyses by Scanning Electron Microscopy (SEM) were studied in detail.

17.2 Experimental Procedures

Scrap aluminium (AA7075) alloy (5.1 wt% Zn, 2.2 wt% Mg, 1.5 wt% Cu), as recycled chips ($d < 1.7$ mm) coming from cutting process of aeronautical parts was used as matrix of the composites proposed in the present work. Scrap aluminium chips were initially processed by milling in a conventional ball mill to reduce their dimensions to desired conditions as presented highly deformed structure in the Fig. 17.1. A little amount recrystallization can be observed after milling (Fig. 17.1b). Addition of pure aluminium fine powder (A1050-5 wt%) during milling as stabilizer together with the ceramic particles seems to improve distribution of particles homogenously. Boron was chosen as main reinforcing elements and also BN, TiO_2, graphite, and spherical ceramic particles were added in different amounts to the matrix (Table 17.1).

Total milling time of the mixture was chosen as 2 h after that hot compaction of the mixture was performed under a double action pressure of 250 MPa at the temperature of 200 °C for 30 min. At the second step, these preformed specimens (diameter: 40 mm and thickness: 15–20 mm) were placed in the tool die and heated in the oven under argon atmosphere up to 600 °C with a waiting time of 10 min, and then followed by thixoforging at two stages: first pressure was 15 MPa and 20 s later, final pressure applied was 70 MPa. After thixoforming final diameter of the specimens was 40 mm and their thickness varied from 8 to 10 mm.

Thixoforming conditions of AA7075 alloy and the value of liquid fraction, df_l/dT (f_l = liquid fraction) in the solidification range have been studied using differential scanning calorimetry (DSC) and the actual thixoforming temperature was determined. For this case, software called "Thermocalc®" (version 4.1) was used for the calculation of phase transformation temperatures of AA7075 and liquid percentage in the solid matrix was chosen for the test temperature. Fine microstructural evaluation and fracture surfaces after impact test as well as interface analyses by Scanning Electron Microscopy (SEM) were carried out in detail.

Microhardness measurements ($HV_{0.25}$) were made on the polished and etched metallographic specimens. Seven measurements were taken for each composition in three different zones, matrix, interface and reinforcement particles,

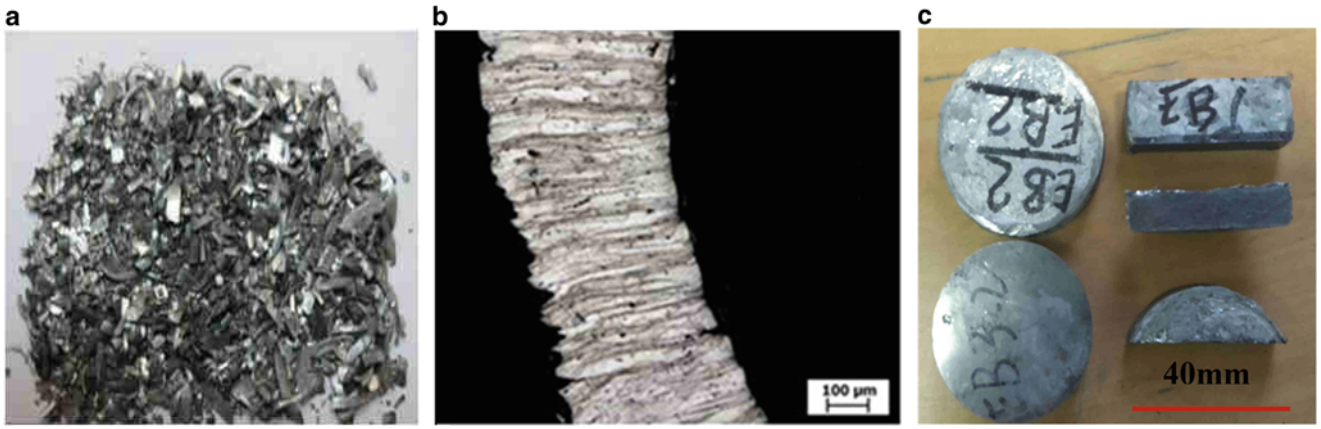

Fig. 17.1 (**a**) Al-chips as raw materials and (**b**) microstructure of Al-chips after milling and (**c**) preformed specimens compacted at 200 °C before thixoforming

Table 17.1 Weight percentage of reinforcement particles for the compositions of the Al-chips based composites (EB)

Composites	AA7075	**Boron**	TiO_2	BN	TiC	Graphite	Spherical ceramic
EC-1	B	**5**	3	2	3	3	3
EC-2	B	**10**	3	2	3	3	3
EC-3	B	**15**	3	2	3	3	3

respectively. The same specimens were also used in microindentation tests. Instrumented micro-indentation testing was conducted to estimate certain micro mechanical properties using CSM indentation test device with a Vickers diamond indenter. Nine indentations were performed one millimeter apart from each other and then the results were averaged. The maximum indentation load (F_{max}) was 600 mN. The indentation hardness and indentation modulus were measured by using the Oliver and Pharr method [10, 11].

Impact tests (EN-10045) were performed to determine the energy absorption capacity of the composites manufactured in this study. Four or five specimens were tested for each composition. The fracture surfaces of the failed specimens were analyzed by SEM.

17.3 Results and Discussion

From DSC results, the variation of liquid fraction (f_l) with temperature ($f_l \times T$) of the AA7075 chips was determined and results are shown in Fig. 17.2. In the present work, processing temperature was defined as 600 °C at which the liquid fraction was about 15 % (Table 17.2). As the total liquid fraction in the processing is not so high, this sensibility can be afforded without much risk for the processing stability. Because thixoforming processing of these composites were designed at two steps: thixoforging operation was performed on the compacted and presintered specimens in the matrix at this temperature (600 °C) at 15 MPa pressure at the beginning and at 70 MPa as final pressure.

In fact, a special case for thixoforming process is to create globular structure that interactions among globules in the semi-solid structure are important parameters as far as viscosity is concerned. These structural characteristics depend on the mechanisms involved in the spheroidization of the structure during the heating to the semi-solid condition. In this work, globular structure was carried out quasi perfectly thanks to a novel combined process that was explained in the former section (experimental conditions).

As known, ideal mechanism for globular structure is recrystallization phenomenon contained by the heavily deformed material. In this case, ideal thixotropic structure was obtained by the combined method; presintering at low temperature and large deformation after thixoforming [5, 7]. In the production of AMMCs, it would then be projected the separation of globules and penetration of particulate reinforcements in the liquid area among them, providing a good dispersion in the matrix to give a strong a tough structure [2, 5, 7].

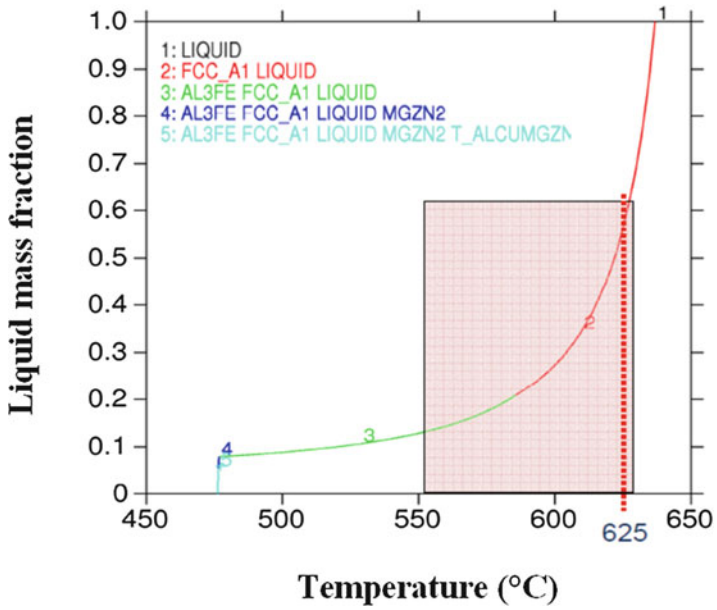

Fig. 17.2 Liquid mass fraction as function of temperature obtained by Thermocalc® software [5, 7]

Table 17.2 DSC analysis for AA7075 chips: liquid fraction (f_l) as a function of temperature

Temperature (°C)	550	560	570	580	**600**	620	625	660
f_l (%)	–	0.02	1.05	3.38	**14.50**	40.40	51.30	100

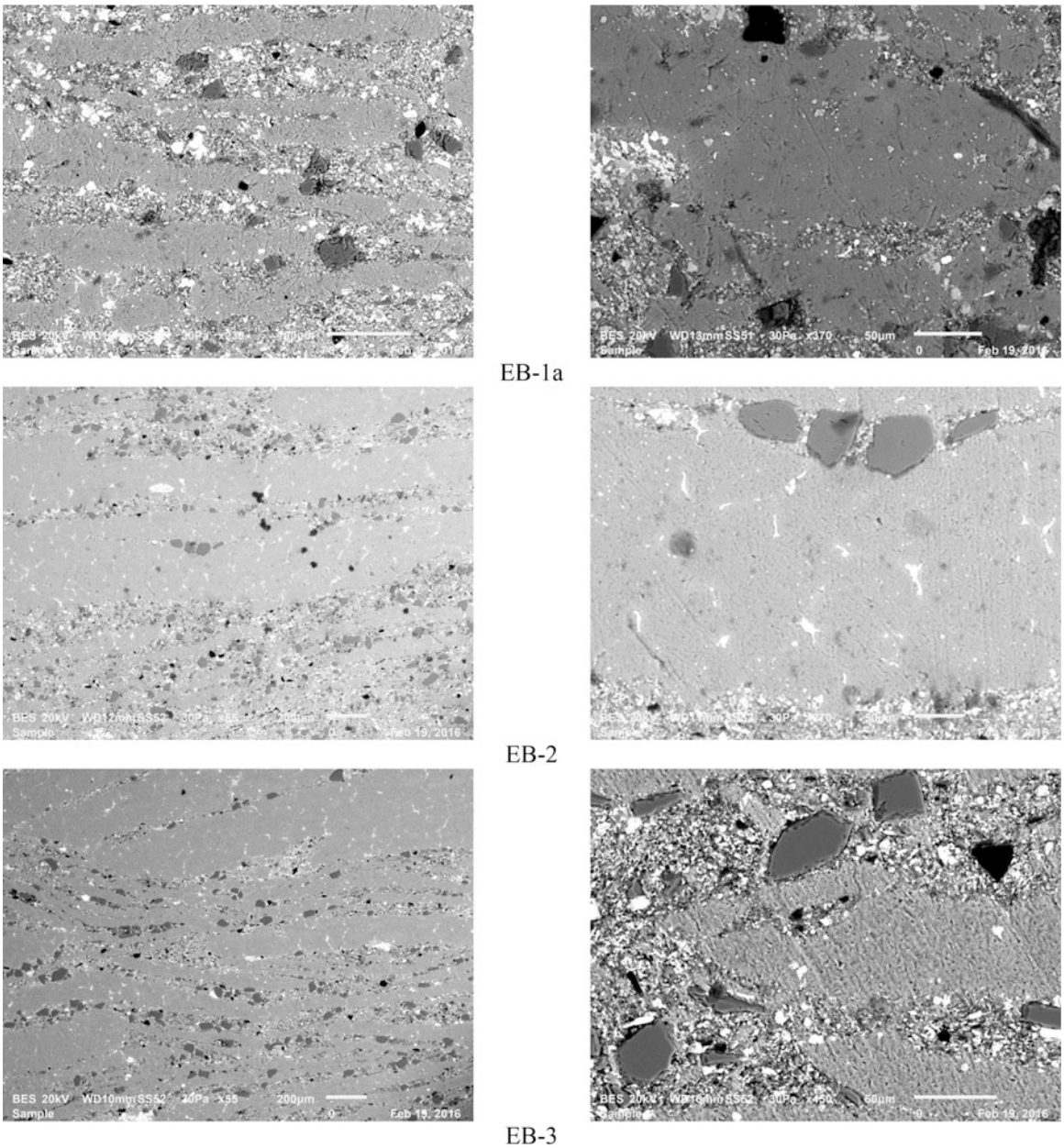

Fig. 17.3 General microstructure and some details of the compositions EB-1, EB-2 and EB-3, obtained by SEM

General microstructure and some details of the interfaces between matrix and reinforcements are presented in Fig. 17.3 obtained by SEM. The general appearance for structural information (first column) and more details of the structure related to the interfaces inside of the matrix (second and third columns) have been presented for three compositions EB-1, EB-2 and EB-3,

Again, Fig. 17.4 gives more detail about the thixotropic structure and evolution of globular forms as well as general microstructural analysis made by EDS was presented in this figure. However, from these pictures, another critical observation should be explained here. It means that there is not perfect globular structural formation in everywhere of the specimen, mainly certain chips keep their structure even if they contain eutectic zones solidified after the pushing of the reinforcement inside of the matrix with liquid parts. Although their internal structure is globular, as shown in Figs. 17.3 and 17.4, globules were not entirely detached.

Therefore, even though the heating temperature and time were enough to cause partial melting and to stimulate a globular microstructure in the chips, those with large dimensions were not desegregated during thixoforming. Most probably, the

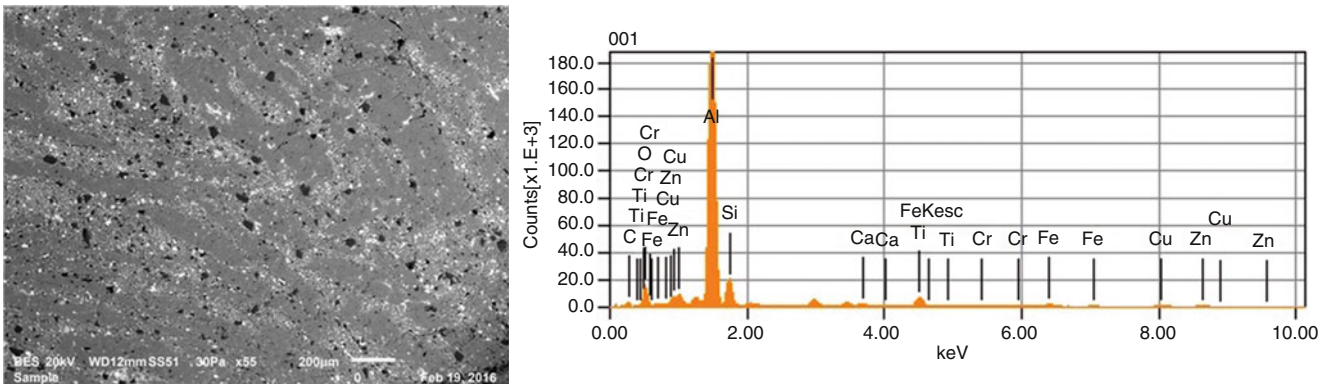

Fig. 17.4 General morphologies of AA7075 based composite observed by SEM and also "EDS" spectrum analysis

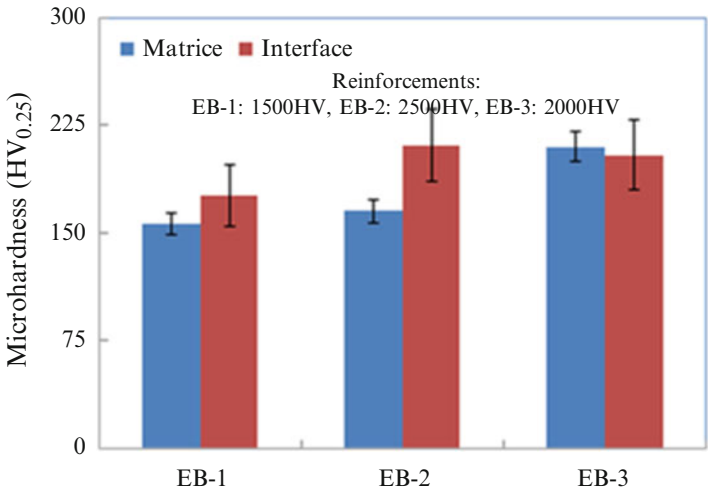

Fig. 17.5 Microhardness ($HV_{0.25}$) measurements taken from three different zones: matrix, interface and reinforcement

main reason is the heating time that should be optimized and thixoforging pressure should be increased for improving the formation of the globular structure [5, 7].

As for the porosity in the final structure, all of the produced samples presented here, does not contain porosity or very low porosity (quasi zero) is observed in the structure that is much lower than products obtained by conventional manufacturing process (simple sintering in powder metallurgy and or other classical foundry etc.).

Microhardness ($HV_{0.25}$) measurements were taken from three different zones: matrix, interface and reinforcement respectively and these results were compared in the Fig. 17.5 for all of compositions discussed here. Each test was repeated minimum three times.

All of the measurements for each composition do not change significantly for the matrices EB-1 and EB-2. And the last composite, EB-3 shows higher values for the matrix and interface. Most probably these results are due to the homogenous structures of the composites proposed in this study; it means that the distribution of reinforcement are more homogeneous thanks to the combined process applied for each composition carried out in two steps with application of high pressure in final stage of the process. Higher values measured for the composite, EB-3 that contains much higher boron as reinforcements. Many of these hard particles were distributed in the matrix and the micro hardness measurements give sometimes much higher values than expected.

For the comparison of micromechanical properties, microindentation tests results are presented in the Table 17.3. The penetration depth and contact area between the indenter and the sample describe the mechanical properties of the material. Consequently, if the structure contains very hard particle reinforcements such as boron, they can behave as barriers to the penetration movement, and evidently there will be less area of contact between the bodies and better mechanical properties are observed. As a typical example, boron can evidently cause to the increment of the indentation hardness and indentation Modulus. The maximum indentation load (F_{max}) was taken as 600 mN for all of three composites.

Table 17.3 Micromechanical properties of AA7075 composites obtained from instrumented microindentation testing only for the comparison; the value taken from literature [9] for AA7075, T6 (HV175, and E = 72 GPa)

Composition N°	Fmax (mN)	**Indentation hardness (MPa)**	**Indentation modulus (GPa)**
EB-1	600	**1964**	**152**
EB-2	600	**2410**	**167**
EB-3	600	**2280**	**172**

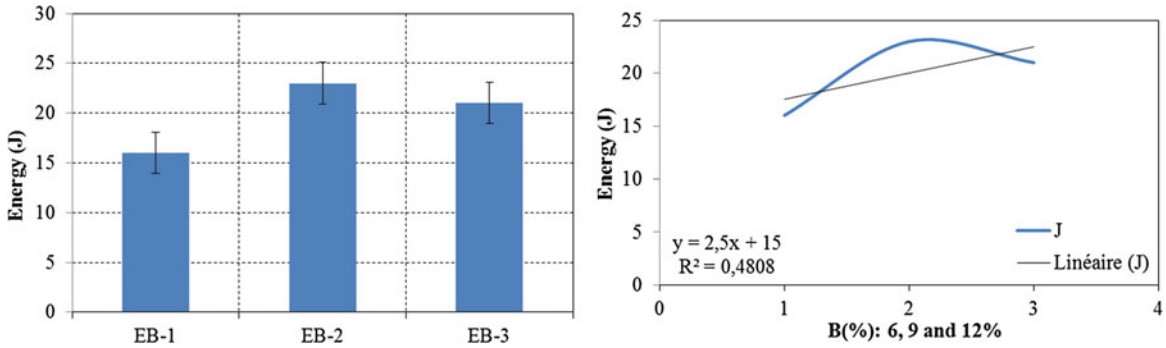

Fig. 17.6 Absorbed energy (*left side*) and linear tendency (*right side*) during impact test for three compositions

The indentation hardness and indentation modulus values measured here have shown that both of these values increase reasonably depending on the amount of boron in the structure. It means that the structures of three composites are tough and solid. They have homogeneous structures with well distributed reinforcements in the matrix. For this reason, addition of boron has a reasonable effect on the mechanical properties. Similarities of these results for the three compositions are related essentially to the homogeneous distribution of the hard particulate reinforcements in the structure obtained with the combined process used for the production of the composites.

Energy absorption capacity of the three composites, EB-1, EB-2 and EB-3 were determined by means of impact tests. Figure 17.6 shows the impact responses of the three composites. The energy (absorbed energy) values presented are the average of four or five tests for each composite. It can be observed that there is reasonable increment on the absorbed energy values of the composites. These results confirm what is discussed in Figs. 17.5 and 17.6 and also in Table 17.3; homogenous structure and well distributed particle reinforcements with very low porosity (quasi zero) in the structure.

And also the effect of main particulate reinforcement should influence these results. Here, the addition of boron in the structure gave high impact absorbed energies (composites, EB-2 and EB-3) and in case of higher boron contents (EB-3), brittleness effect on the composite can be observed.

Fracture surfaces taken from failed specimen during impact tests are presented in Fig. 17.7. Fracture surfaces have shown that rigidity increased with higher pressure during the thixoforming. There is any internal defect and/or porosity observed from these pictures. Reinforcements are well integrated in the matrix without debonding during impact due to strong interface of the particles with matrix.

17.4 Conclusions

Novel composites created by combined method of sintering + thixoforming have been carried out successfully in an economic way with quasi zero porosity. Homogenous microstructure with graded distribution of the reinforcing particles could be obtained successfully by novel process proposed in this work. Addition of pure Al fine powder as stabilizer together with the ceramic particles seems to improve homogenous distribution of the particles at the beginning of the process (milling + compacting, etc.).

Fracture surfaces of the broken specimens have shown that rigidity increased with higher pressure during the thixoforming. For this reason, interfaces between matrix and reinforcing particles can be improved by increment of dwell time at the maximum temperature during this processing and also it is worthy to increase applied pressure at the second stage of thixoforming process.

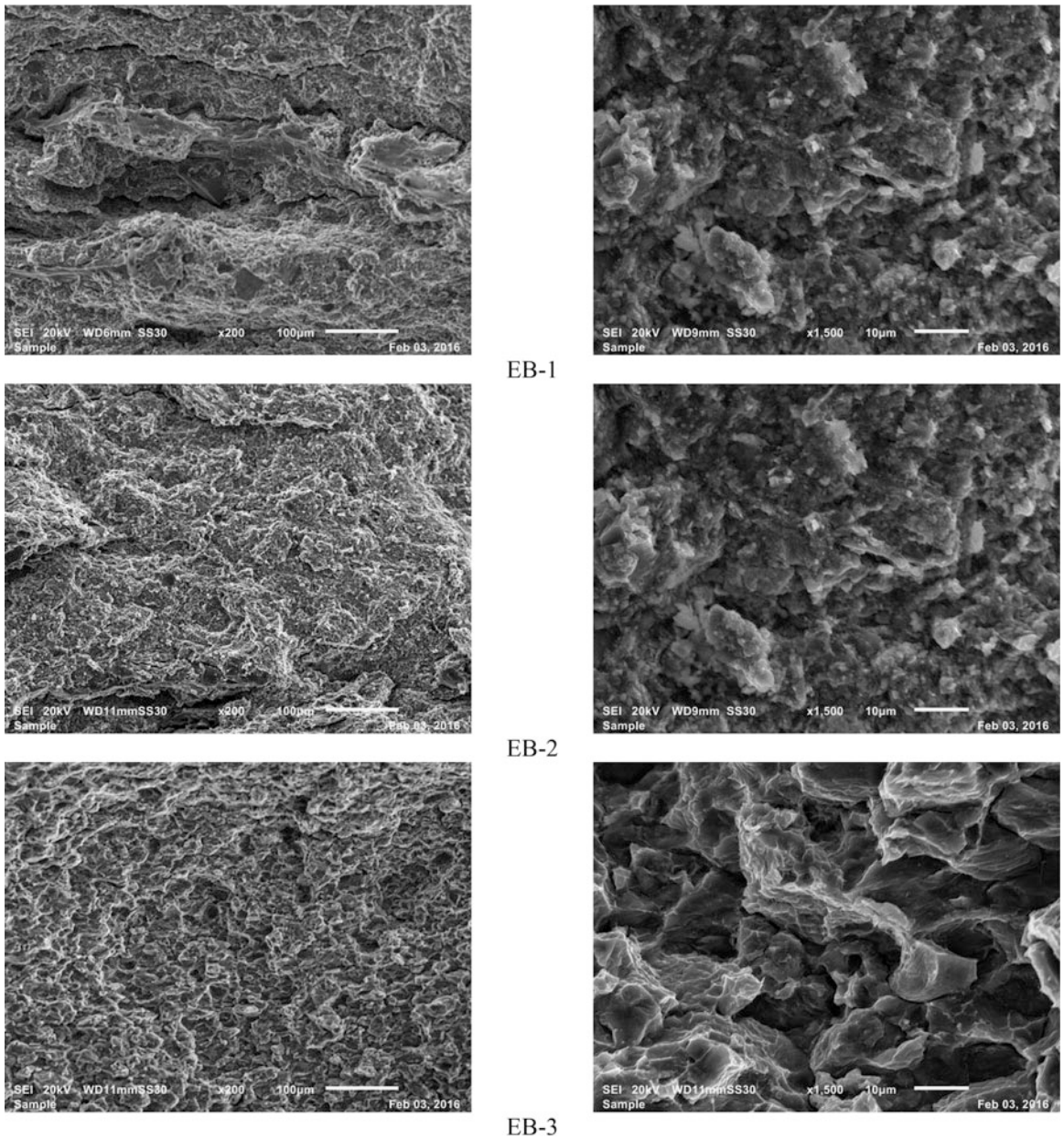

Fig. 17.7 Fracture surfaces taken from broken specimen by impact test

In summary, processing conditions still needs to be optimized, in order to achieve high homogeneity of reinforcement with high distribution in the matrix.

By this way, semi solid aluminium chips in the structure can be disaggregated very easily and then globules can be detached from original structure by penetration of hard particles of the reinforcement in the liquid phase.

References

1. Ferreira, L. M. P., Robert, M. H., Bayraktar, E.: Effect of operational parameters in the semi-solid processing of Al/SiC composites from machining chips. ECCM16—16th European Conference on Composite Materials, Seville, Spain, 22–26 June 2014
2. Huang, Y., et al.: Characterization of a powder metallurgy SiC/Cu–Al composite. J. Mater. Process. Technol. **197**, 43–48 (2008)

3. Ferreira, L.M.P., Robert, M.H., Bayraktar, E., Zaimova, D.: New design of aluminium based composites through combined method of powder metallurgy and thixoforming. Adv. Mater. Res. **939**, 68–75 (2014)
4. Ferreira, L.-M.-P., Bayraktar, E., Miskioglu, I., Robert, M.-H.: Effect of the reinforcement particles on the microstructure and electrical properties of aluminium matrix composites (AMCs). AMPT-2015, International Conference of, Advanced Materials Processing Technologies, Madrid, Leganes, Spain, 14–17 Dec 2015
5. Ferreira, L.: Design of novel composites from scrap aluminium chips (AA7075) through by combined methos, sintering + thixoforming. M.Sc. thesis, University of Campinas, UNICAMP-SP (2013)
6. Lang, Y.J., et al.: Effect of strain- induced precipitation on the low angle grain boundary in AA7050 aluminum alloy. Mater. Des. **32**, 4241–4246 (2011)
7. Min, S.: Effects of volume fraction of SiC particles on mechanical properties of SiC/Al composites. Trans. Nonferrous Met. Soc. China **19**, 1400–1404 (2009)
8. Ferreira, L., Robert, M.H., Bayraktar, E.: Production of aluminum/SiC/$NiAl_2O_4$ AMMCs by thixoforming of recycled chips. Solid State Phenom. **217–218**, 286–293 (2015)
9. Zoqui, E.J., Paes, M., Robert, M.H.: Effect of macro and microstructure on the viscosity of the A356 alloy in the semi-solid state, JMPT. J. Mater. Process. Technol. **153–154**, 300–306 (2004)
10. MATWEB: Material Property data. Information was taken from the website of met web: www.matweb.com
11. Oliver, W.C., Pharr, G.M.: An improved technique for determining hardness and elastic modulus using load and displacement sensing indentation experiments. J. Mater. Res. **7**, 1564–1583 (1992)

Chapter 18
Recycle of Aluminium (A356) for Processing of New Composites Reinforced with Magnetic Nano Iron Oxide and Molybdenum

L.F.P. Ferreira, E. Bayraktar, I. Miskioglu, and M.H. Robert

Abstract The microstructural and tribological behavior of Aluminium Matrix Composites (AMCs with scrap A356) reinforced with nano iron oxide (Fe_3O_4) and Molybdenum (Mo) produced by powder metallurgy was investigated with low cost manufacturing of light and efficient multifunctional materials for aeronautical applications. Molybdenum (Mo) is a refractory material with a high melting temperature and used essentially as high-temperature resistant materials for applications in the fields of aerospace engineering such as rocket nozzles, high-temperature resistant pieces, etc. It shows a low thermal expansion coefficient, excellent electrical conductivity and higher corrosion resistance. However, it becomes very brittle after recrystallization. Generally, AMCs reinforced with magnetic iron (Fe_3O_4) exhibit good physical (electrical and magnetic) properties, which make them excellent multifunctional lightweight materials.

Normally, they do not present high wear resistance. To overcome this shortcoming, very fine Mo (1–3 μm) powders was added to the AMCs. The main purpose of this work is to show the influence of molybdenum on the AMCs reinforced by 10 % of Fe_3O_4 to increase wear resistance of these novel composites. Matrix/reinforcement interface was also evaluated due to addition of Mo to the matrix. Two groups of composites were prepared: First group contains only Fe_3O_4, Cu and Mo. Second group contains Fe_3O_4 doped with TiO_2 (thermomechanical treatment), Cu and Mo. For processing, a novel combined method of sintering + forging was performed. Experimental results have revealed that even small additions of Mo can drastically improve wear performance of AMCs reinforced with magnetic iron (Fe_3O_4). Morphology of the composites was evaluated by Scanning Electron Microscopy (SEM). Scratch tests were conducted to evaluate wear properties.

Keywords Recycled materials • Aluminium matrix composites • Magnetic iron oxide • Damage analysis • Molybdenum

18.1 Introduction

Aluminium Matrix Composites (AMCs with scrap A356) reinforced with nano iron oxide (Fe_3O_4) and Molybdenum (Mo) produced by powder metallurgy was investigated with low cost manufacturing of light and efficient multifunctional materials for aeronautical applications. AMCs reinforced with particles tend to offer enhancement of properties processed by different. In the last few decades, high performance AMCs have been widely developed with high strength, high stiffness, low density, and good wear resistance capacity [1–5].

Among them, A356 aluminium is widely used as matrix. A356 is an interesting option for military and automobile applications as the alloy has important properties of high strength, light weight and good capacity for foundry (fluidity). This alloy can also be successfully used as matrix from recycled fresh scrap (chips) to produce high quality metal matrix composites in an economic way [6–11]. Molybdenum was chosen as a basic reinforcement to the AMCs structures reinforced with magnetic iron oxide to increase wear resistance of these composites [7–13].

L.F.P. Ferreira
Materials Science Department, UNICAMP-University of Campinas, São Paulo, Brazil

School of Mechanical and Manufacturing Engineering materials science department-composite lab, Supmeca-Paris, 93407- St Ouen, France

E. Bayraktar (✉)
School of Mechanical and Manufacturing Engineering materials science department-composite lab, Supmeca-Paris, 93407- St Ouen, France
e-mail: bayraktar@supmeca.fr

I. Miskioglu
ME-EM Department, Michigan Technological University, Houghton, MI 49931, USA

M.H. Robert
Materials Science Department, UNICAMP-University of Campinas, São Paulo, Brazil

W.C. Ralph et al. (eds.), *Mechanics of Composite and Multi-functional Materials, Volume 7*,
Conference Proceedings of the Society for Experimental Mechanics Series, DOI 10.1007/978-3-319-41766-0_18

Generally, AMCs reinforced with magnetic iron (Fe_3O_4) exhibit good physical (electrical and magnetic) properties, which make them excellent multifunctional lightweight materials. But, they have not high wear resistance. Very fine Mo (1–3 μm) powder was added to the AMCs.

The main idea for this work is to show the influence of molybdenum on the AMCs reinforced by 10 % of Fe_3O_4 to improve the mechanical quality of these novel composites.

This work is concentrated on the manufacturing of AMCs using recycled A356 chips as raw material. Two groups of composites were prepared: First group contains only Fe_3O_4, Cu and Mo. Second group contains Fe_3O_4 doped with TiO_2 (thermomechanical treatment), Cu and Mo. For processing, a novel combined method of sintering + forging was performed. Experimental results have revealed that even small additions of Mo can drastically improve wear performance of AMCs reinforced with magnetic iron (Fe_3O_4). Morphology of the composites was evaluated by Scanning Electron Microscopy (SEM). Scratch tests were conducted to evaluate wear properties.

18.2 Experimental Procedures

Two groups of composites were prepared: first group contains only Fe_3O_4, Cu and Mo. Second group contains Fe_3O_4 doped with thermomechanical treatment with TiO_2, Cu and Mo. For processing, a novel combined method of sintering + forging was performed. Effectively, this process aims to improve the quality and wear behaviour of the composites created in this project. The thermo-mechanical treatment was conducted as a novel and economic process to dope Fe_3O_4 with TiO_2. First of all, Fe_3O_4 and 10 % of TiO_2 were mixed for 30 min and then heated in the oven at 400 °C during 30 min. After that, this mixture was milled during 1 h. Finally this mixture can be added to the main structure. This main structure was mixed with ball milling during 3 h to homogenize the mixture. Initial size of scrap A356 chips was variable from 400 μm up to 1 mm. Scrap A356 powders was successfully incorporated with particulate reinforcements. Thanks to combined process of sinter forging, porosity and other inconvenient defects were eliminated. The general composition of scrap A356 was given in the Table 18.1 and also, the compositions of the composites were presented in two groups (Table 18.2).

Microstructural characterization was done by means of scanning electron microscope (SEM). The dispersion of reinforcement particles in the matrix and interface at matrix/reinforcements was evaluated.

Microhardness tests (HV0.25) have been carried out on the polished and etched specimens. Measurements were taken in different zones (interface, reinforcement, and matrix) for each composition. All the density measurements of the specimens were carried out by using Archimedes method and then, these results were compared.

Sintered products were then tested in quasi-static compression tests, carried out in a servo-hydraulic INSTRON Universal test system (model Instron 5500R, equipped with a load cell of 25,000 kgf) at an initial rate of 10 mm/min and second rate of 5 mm/min. Maximum load endpoint was 4500 N.

Wear resistance was measured by scratch wear tests at a frequency of 15 Hz. All of the compositions were tested in three different number of cycles, $10 * 10^3$, $20 * 10^3$ and $30 * 10^3$cycles. After scratch test, damaged zone was investigated by 3D optical roughness meter. Volume loss/time, maximum depth, and friction coefficient were evaluated.

Table 18.1 Chemical composition of scrap A356 chip

Element	Al	Cu	Fe	Mg	Mn	Si	Ti	Zn
wt%	Balance	≤0.20	≤0.20	≤0.25	≤0.10	6.5–7.5	≤0.20	≤0.10

Table 18.2 Compositions of the composites prepared in two groups (wt%)

First group	Fe_3O_4	Cu	Mo	Second group	Fe_3O_4 doped with TiO_2	Cu	Mo
A356-1	10	2	2	A356-11	10	2	2
A356-2	10	2	3	A356-22	10	2	3
A356-3	10	2	4	A356-33	10	2	4

18.3 Results and Discussion

General Microstructure of the composite was given in the Fig. 18.1a only as an example to see well homogeneous distribution of the particle reinforcement in the matrix and also the final arrangement of interface at the matrix/reinforcements. Figure 18.1b indicates EDS analyses taken from overview microstructure to check the elements participated in the microstructure.

Again, general microstructures of the first series of the composites were presented in the Fig. 18.2. As an example, only the first composition of this series (A356-1) was given in this Fig. 18.2a. The distribution of particle reinforcements and the position of the scrap A356 in the matrix were perfectly arranged thanks to the combined method of sintered forging.

In the Fig. 18.2b–d, detail information was given about the globular structure and perfect interface at the matrix/reinforcement. The same evolution was observed on these pictures; eutectic structure is formed always around the globular grains and many others are observed inside of the grains. As for the big size particulate reinforcements, they are at the border of interface and/or to be pushed in the aluminium particles (small size chips).

All of these evaluations of the microstructure give a clear idea about the combined process (sintered forging). This process applied for these composites is caused by bonding diffusion at the interface between matrix and reinforcement and some of the particles were forced into the grains during the forging (second) stage of this process. For this reason, very tough, solid and homogeneous structure could be obtained. Porosity and other structural defects were quasi eliminated. The same microstructure was given in the Fig. 18.3 for the second composition (for the sample A356-2). The same microstructural evolution was also observed in this composition with perfect interface and homogenous distribution of the reinforcements.

In fact this idea can be applied very well on the industrial parts in an economic way. Even if scrap aluminium particles are used as matrix, the microstructure can be improved by this process very well. Actually, sintered forging process is a novel process mainly called as near-net shape process for the manufacturing of the pieces in the automotive industry [13]. Mainly, this process is used for bulk materials in industrial applications. In fact, low-cost sinter-forging approach to processing of particle-reinforced metal matrix composites gives always high performance (fatigue-creep, etc.) applications of the industrial pieces. In the frame of this present work, only an application was given in the laboratory scales for creating novel composites from scrap aluminium reinforced with particulate reinforcements. This idea should be developed very well on the many other composites. It means that very tough and strong pieces can be obtained with a microstructure similar to the thixoforming but cheaper than the other manufacturing processes.

Evolution of the density and micro hardness ($HV_{0.25}$) evolution of these composites are presented in the Figs. 18.4 and 18.5 for two groups of the compositions. For density values, there are not so much differences between two groups Firstly, the percentage of Mo added in the matrix is not so high (Mo: 2, 3, 4 wt%) and not so much effect of other elements in the density. For micro hardness evaluation, three different zones were evaluated to compare mechanical properties of these composite structures.

Not so big differences are observed for both of two groups, but the values measured at the interface and also on the particulate reinforcements can show big differences depending on the type of the particles.

As indicated in the former section, the influence of the Mo should be evaluated in detail because high wear resistance is needed for the pieces that should be contact during the function in the mechanical systems. For this reason, we have made a comprehensive study has been carried out on theses composites to compare their wear resistance in case of Mo addition in

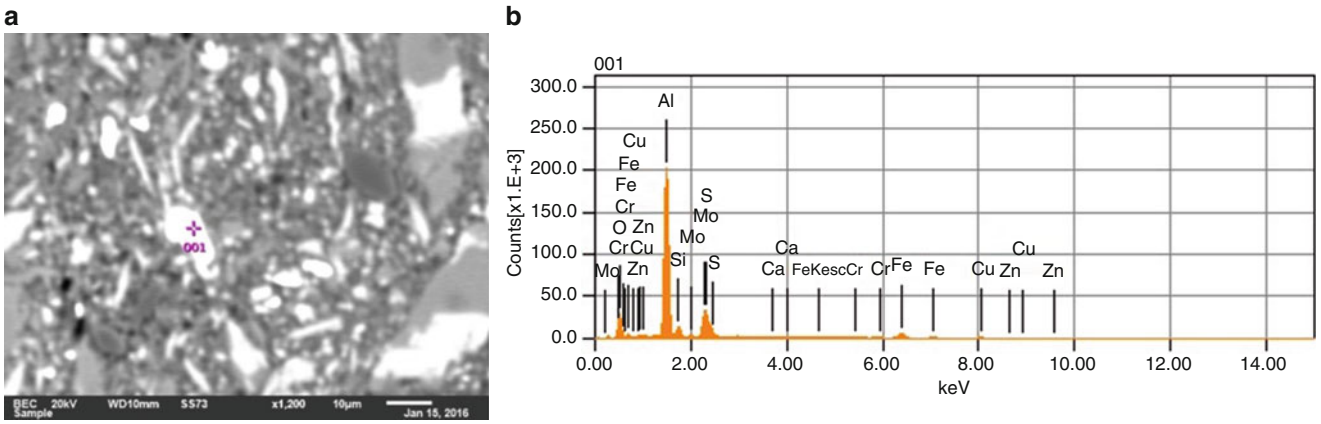

Fig. 18.1 (**a**) General microstructure of the composite A356-1 and (**b**) EDS analyses taken from overview microstructure

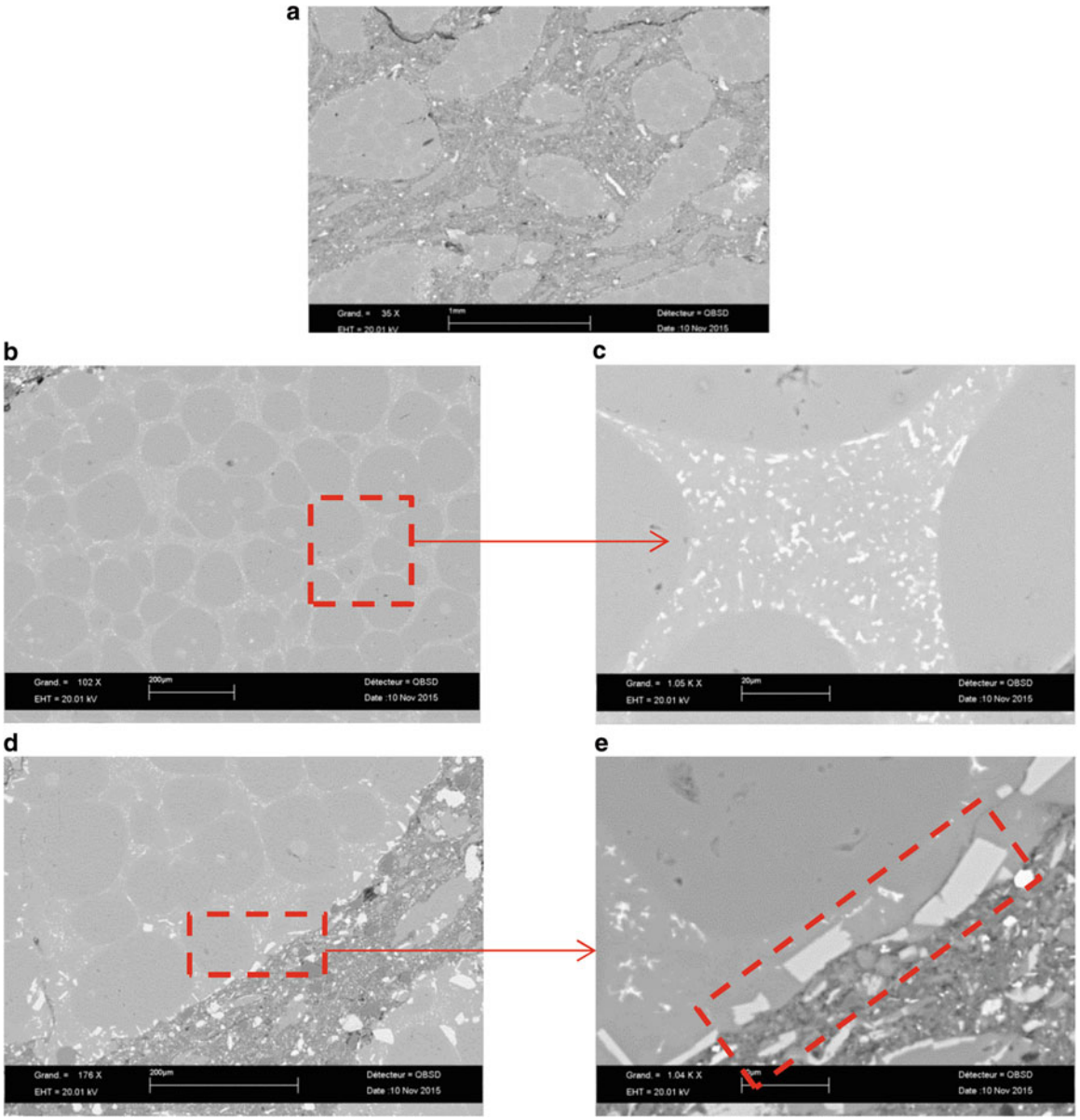

Fig. 18.2 (**a**) General microstructure of the composite A356-1 and (**b–d**) detail of matrix/reinforcement interface

different percentages. Tables 18.3 summarize the results of scratch wear test results. All the tests were performed with a small size of zirconium ball (diameter: 2 mm) and test zones were chosen randomly. For this reason, the values measured under different scratch cycles should be indicative and give a general idea on the wear resistance of these composites.

Surface damage images were presented in the Figs. 18.6 and 18.7 for the first and second groups of the composites respectively. All of these values on the wear resistance of the compositions were calculated from these images for all of the test cycles, $10 * 10^3$ cycles, $20 * 10^3$ cycles, and $20 * 10^3$ cycles respectively.

In the same way, volume lost values have been also calculated depending on the time for both of two groups of composites and these values were compared for the compositions presented in this work (Fig. 18.8). If two groups of composites are compared, a big difference should be appeared between two groups. Mainly the doping effect of Fe_3O_4 with TiO_2 is much more effective than other parameters with addition of Mo. Again, these values should be accepted as indicative values that give general idea on the effect of reinforcement and doping treatment.

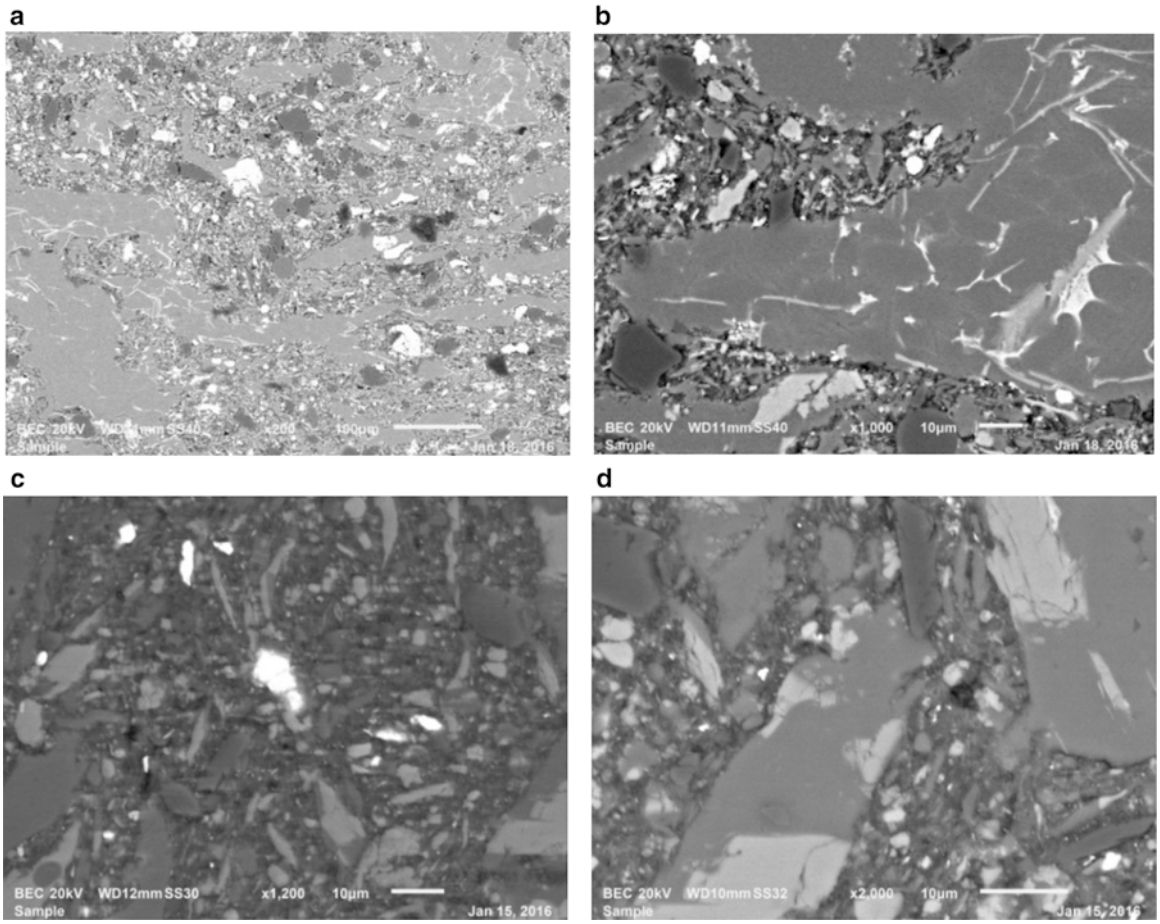

Fig. 18.3 (**a**) General microstructure of the composite A356-2 and (**b–d**) detail of matrix/reinforcement interface

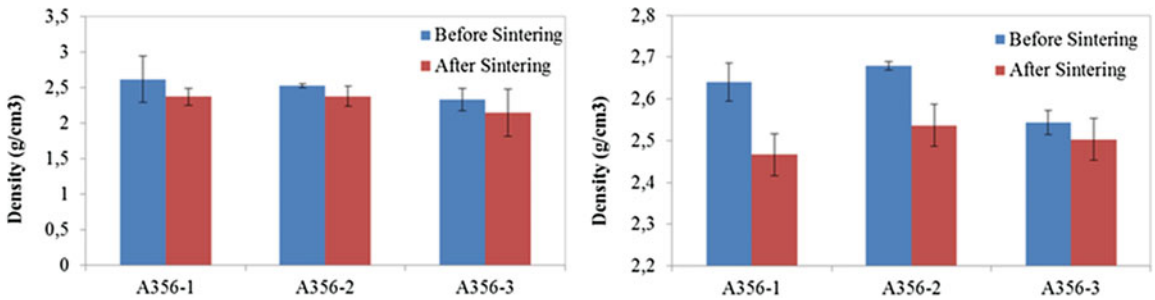

Fig. 18.4 Evolution of density of the composites: first group (*left side*) and second group (*right side*)

Figure 18.9 presents mean values friction coefficients calculated from scratch tests as a function of number of cycles. As indicated just above, these values were calculated as means values for each composition, especially percentage of Mo added in the structure. Friction coefficients increase slightly with the increased values of Mo.

Some compression test values were presented in the Fig. 18.10 conducted on the three compositions for each group. For sake of simple comparison, all of the values for maximum force have been shown in the Fig. 18.11.

First of all, increment of Mo values increases brittle fracture behaviour in case of static and dynamic test conditions. Even if small increment of this element alone can changes drastically test results. Evidently, brittleness of Mo can be improved by doping of Mo with other elements such as La_2O_3, Si or Y_2O_3, etc. In literature, some valuable works have shown that doping of Mo with certain elements can increase ductility very well [11, 12].

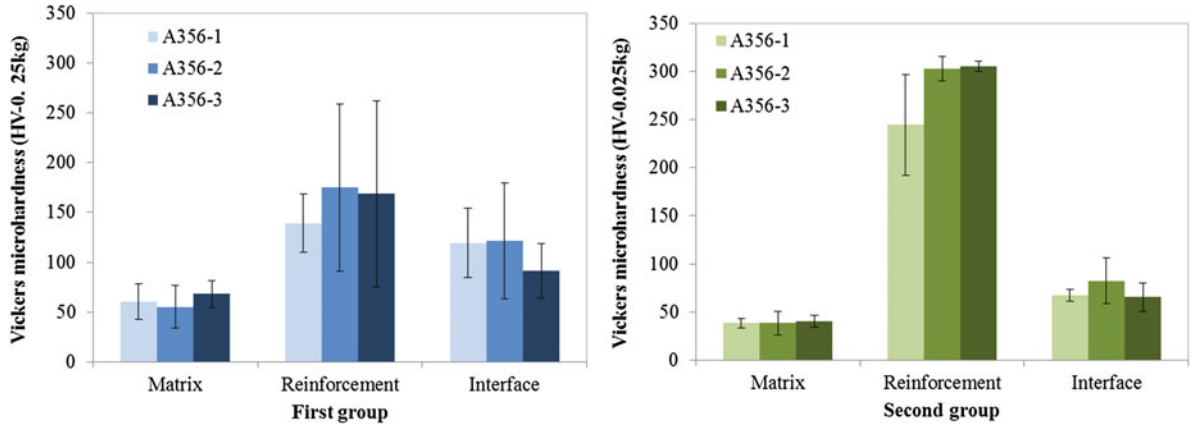

Fig. 18.5 Microhardness measurements ($HV_{0.25}$) of the composites: first group (*left side*) and second group (*right side*)

Table 18.3 Maximum depth (μm) observed during scratch tests using 10, 20 and 30 thousand cycles, for the first group of A356-Mo composites

First group	$10 * 10^3$ cycles	$20 * 10^3$ cycles	$30 * 10^3$ cycles	Second group	$10 * 10^3$ cycles	$20 * 10^3$ cycles	$30 * 10^3$ cycles
A356-1	110	142	187	A356-1	44.6	69.3	65.3
A356-2	242	187	236	A356-2	35	111	162
A356-3	99.5	127	135	A356-3	95.8	156	110

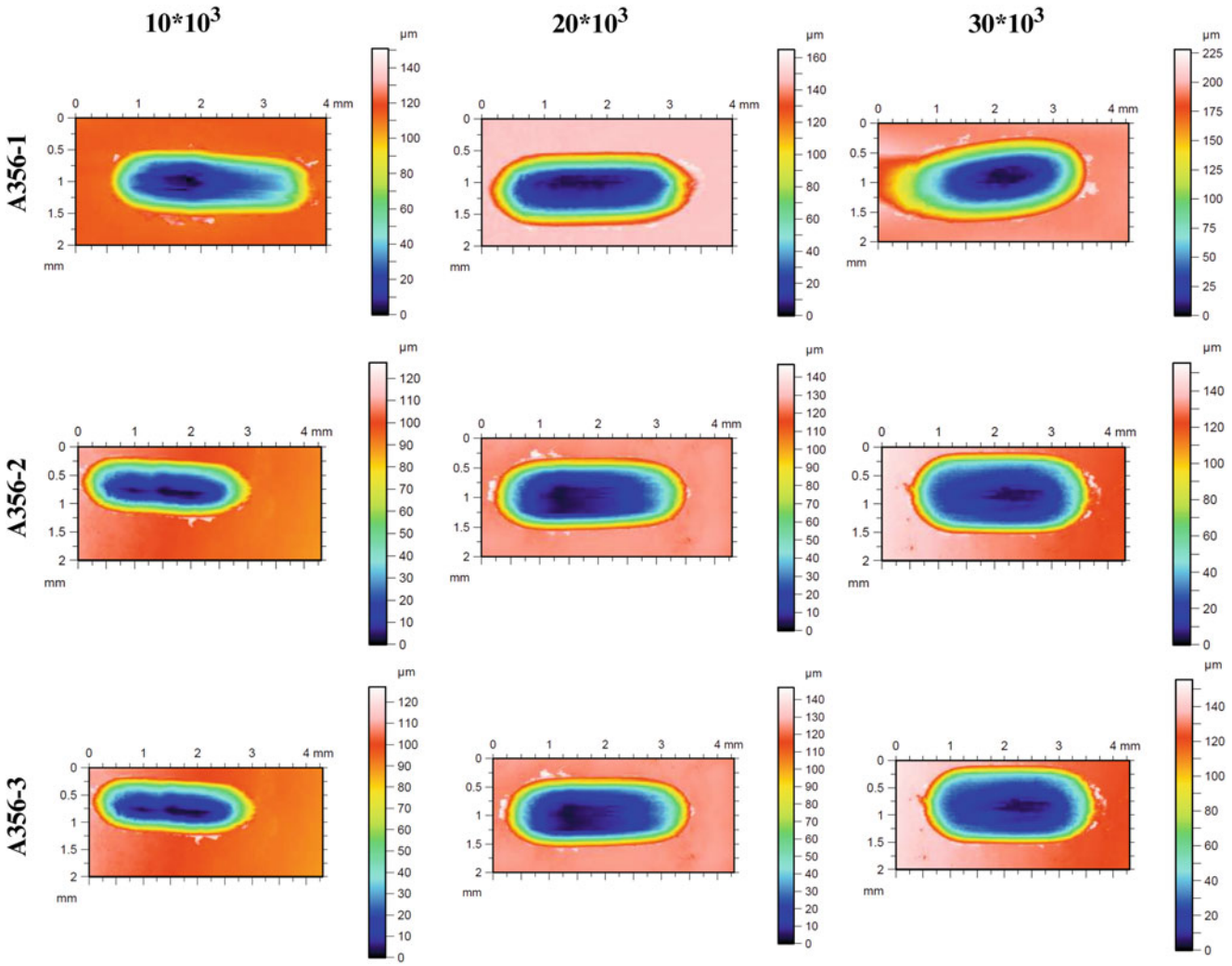

Fig. 18.6 Images of surface damage zones produced by scratch wear tests; first group composites

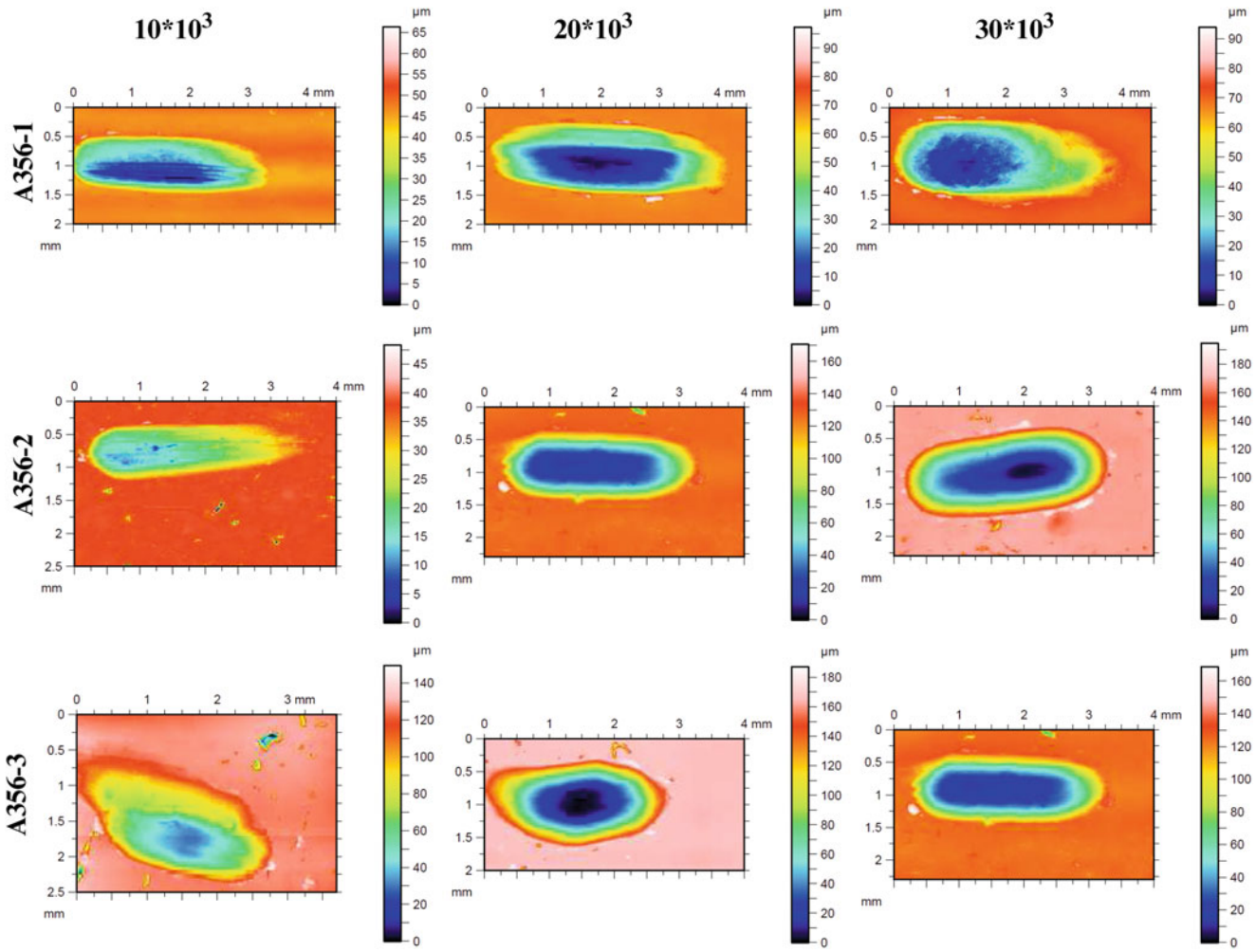

Fig. 18.7 Images of surface damage zones produced by scratch wear tests; second group composites

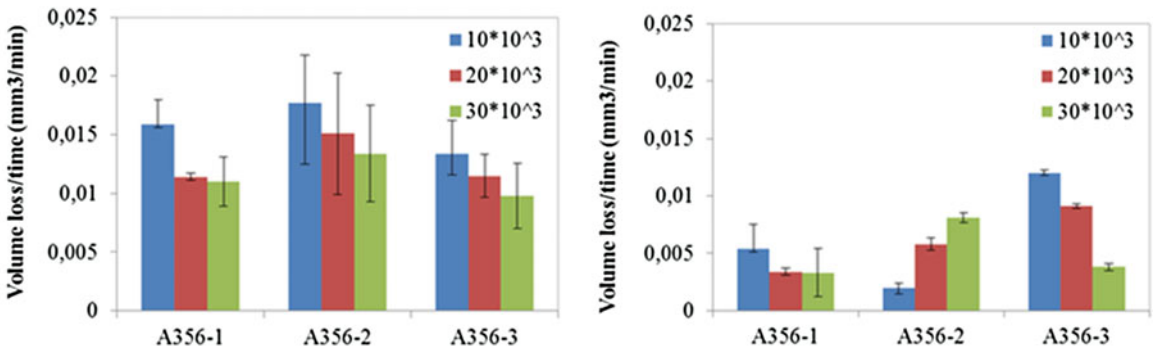

Fig. 18.8 Volume lost values depending on the time for the first (*left side*) and second (*right side*) groups of the compositions for three different numbers of cycles (10, 20 and 30 * 10^3 cycles respectively

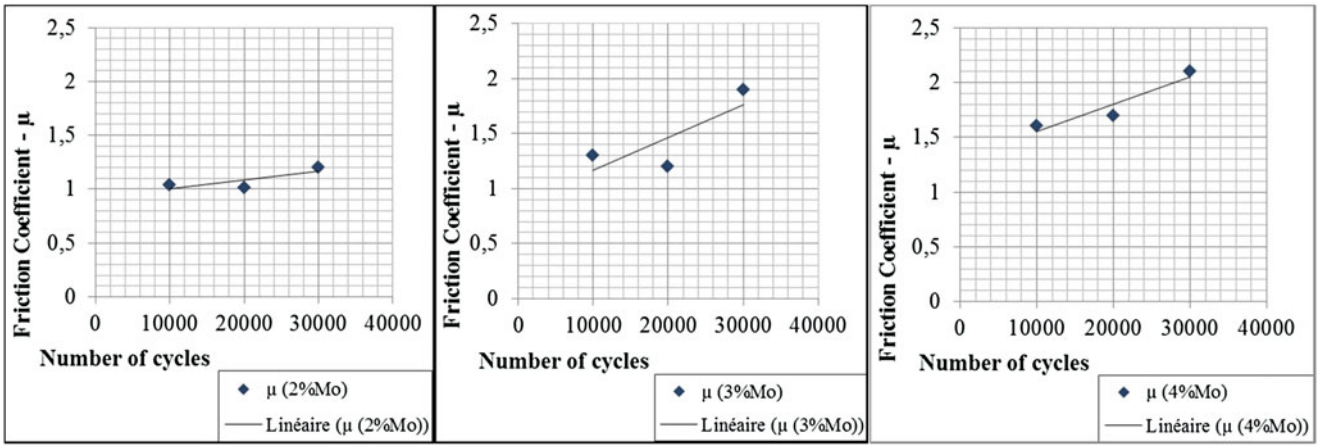

Fig. 18.9 Mean friction coefficient values as a function of number of cycles for each Mo value added in the structure

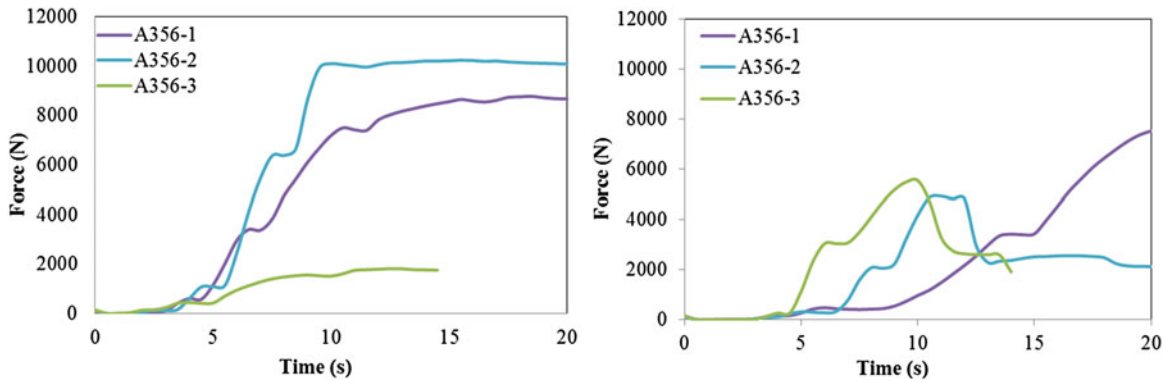

Fig. 18.10 Compression test results for three compositions of the first (*left side*) group and second group (*right side*)

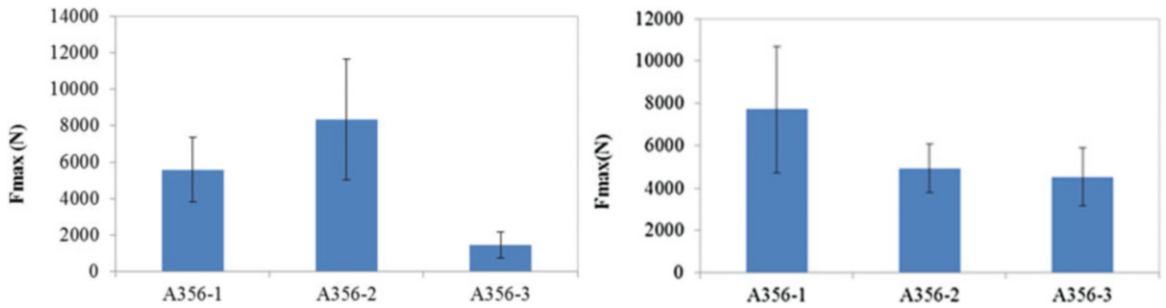

Fig. 18.11 Comparison of F_{max} values obtained from compression tests for three compositions of the first (*left side*) group and second (*right side*) group

18.4 Conclusion

In the frame of this common project, novel composites have been developed from fresh scrap aluminium A356 reinforced with magnetic iron oxide (Fe_3O_4) and main reinforcements of molybdenum. Iron oxide was doped with TiO_2 by means of a novel thermomechanical treatment in an economic way. Low cost manufacturing of these composites have been successfully managed in this work by combined method of sinter forging.

Microstructural analysis has shown that a good bonding at interface of matrix-reinforcement thanks to combined process sinter-forging, a tough and sound microstructure was obtained without porosity. Wear resistance and ductility of these structures should be improved with doping process and good preparation conditions; ball milling in longer time is needed for helping the fine and homogeneous distribution of the particles in the matrix.

References

1. Rebba, B., Ramanaiah, N.: Evaluation of mechanical properties of aluminum alloy (Al-2024) reinforced with molybdenum disulphide (MOS2) metal matrix composites. Procedia Mater. Sci. **6**, 1161–1169 (2014)
2. Majumdar, S., Kale, G.-B., Sharma, I.-G.: A study on preparation of Mo–30W alloy by alumina thermic co-reduction of mixed oxides. J. Alloys Compd. **394**, 168–175 (2005)
3. Cannillo, V., Manfredini, T., Montorsi, M., Boccaccini, A.R.: Investigation of the mechanical properties of Mo-reinforced glass-matrix composites. J. Non-Cryst. Solids **344**, 88–93 (2004)
4. Zhou, Y., Wang, Q., Han, X.-L., Sun, D.-L.: Fabrication and properties of continuous unidirectional Mo fiber reinforced TiAl composites by slurry casting and vacuum hot pressing. Compos. Sci. Technol. **83**, 72–78 (2013)
5. Chen, L.-G., Lin, S.-J., Chang, S.-Y.: Tensile properties and thermal expansion behaviors of continuous molybdenum fiber reinforced aluminum matrix composites. Compos. Sci. Technol. **66**, 1793–1802 (2006)
6. Din, T., Campbell, J.: High strength aerospace aluminum casting alloys a comparative study. Mater. Sci. Technol. **12**, 644–650 (1996)
7. Choi, D.-H., et al.: Microstructure and mechanical property of A356 based composite by friction stir processing. Trans. Nonferrous Met. Soc. China **23**, 335–340 (2013)
8. Srinivasu, R., Sambasiva, A., Madhusudhan, G., Srinivasa, K.: Friction stir surfacing of cast A356 aluminum end silicon alloy with boron carbide and molybdenum disulphide powders. Def. Technol. **11**, 140–146 (2015)
9. Santella, M.-L., Engstrom, T., Storjohann, D., Pan, T.-Y.: Effects of friction stir processing on mechanical properties of the cast aluminum alloys A319 and A356. Scripta Mater. **53**, 201–206 (2005)
10. Chainarong, S., Muangjunburee, P., Suthummanon, S.: Friction stir processing of SSM356 aluminium alloy, 12th global congress on manufacturing and management, GCMM 2014. Procedia Eng. **97**, 732–740 (2014)
11. Ma, Z.-Y., Sharma, S.-R., Mishra, R.-S.: Effect of friction stir processing on the microstructure of cast A356 aluminum. Mater. Sci. Eng. A**433** (1), 269–278 (2006)
12. Xu, B., et al.: Preparation and properties of sintered molybdenum doped with $La_2O_3/MoSi_2$. Int. J. Refract. Met. Hard Mater. **28**, 150–154 (2010)
13. Chawla, N.: Industrial paper, "Metal Matrix Composites in automotive applications", advanced materials and processes, pp. 26–31 (2006)

Chapter 19
A New Multiscale Bioinspired Compliant Sensor

Hugh A. Bruck, Elisabeth Smela, Miao Yu, Ying Chen, and Joshua Spokes

Abstract A challenge in fabricating compliant electrical sensors for various applications, such as wearable electronics, has been the lack of compatible connection concepts that are reliable and can support large levels of force without failure. Recently, we have developed compliant, carbon-based strain and thermal sensors using nanosized exfoliated graphite (EG) dispersed in latex that are highly deformable (>50 % strain) and piezoresistive. They undergo large changes in electrical resistance, resulting in highly sensitive strain (1×10^{-3}/μstrain) and thermal (1×10^{-3}/K) measurement sensors. Such compliant sensors are typically attached to external wiring using conductive silver epoxies or paints. However, the silver epoxy and the metal wires are rigid, and they detach from the compliant sensor at low load levels. By using micron-sized braided carbon fibers instead of metal, and a carbon-based composite instead of silver epoxy, a mechano-electrical interface to the sensor is created that has a significantly higher load bearing capacity than achieved with metal wires, with an inherent electrical resistivity of only 1.7×10^{-3} Ω−cm. The resulting sensor is similar to a sensory nerve receptor where the percolated network of nanosized EG act as "receptors," while the micro-sized carbon fiber acts as the sensory ganglion attaching to the central nervous system. The resulting "biologically inspired" multi-scale strain and temperature sensor has advantages in addition to durability, including amenability to additive manufacturing processes, ease of fabrication, and scalability. We also demonstrate the ability to use the new sensing material to make "sensing gloves" that could potentially be used in applications such as recording signals during manual tasks by human hands or for providing sensing capability to robotic hands.

Keywords Co-robots • Sensing skin • Multi-scale carbon composite • Sensing glove • Bio-inspired sensor

19.1 Introduction

There is considerable interest in developing new compliant materials for tactile sensing applications, such as robotics and sensing gloves. Microfabricated and nanostructured materials have good performance at the cost of relatively complex fabrication, and they can be difficult to scale up to cover large surfaces.

Recently, we have investigated the development of compliant sensing materials using exfoliated graphite (EG) dispersed in a latex matrix [1, 2]. The EG can percolate at volume fractions as low as 15 wt%, at which the polymer composite remains elastic. Thus, the sensing material remains highly compliant with the capability of being stretched >50 % and with the resistance increasing until failure. Furthermore, EG and latex are both low cost materials. Latex can be made into a paint by dissolving it in water, so the composite is easily applied to the surfaces of a variety of substrate materials, making it amenable to use at either large or small scales, as well as use in additive manufacturing processes.

The piezoresistive latex/EG composite sensing materials has good sensitivity (high gauge factor): it is able to detect a normalized change in resistance of 1×10^{-3}/μstrain. (Piezoresistors change electrical resistance under strain. One μstrain corresponds to a change in length, ΔL/L, of 10^{-6}.) Thus, the material is well suited for tactile sensing applications, such as "sensing skins" for robots, particular for "co-robots" that work alongside people. The material also has good thermal sensitivity, and we have used it to generate thermal images of surfaces [3]. Electrical impedance tomography (EIT) was used to deconvolve signals obtained from the boundary of a sensing area, obviating the need for grid-based sensing approaches.

H.A. Bruck (✉) • M. Yu • Y. Chen • J. Spokes
Department of Mechanical Engineering, University of Maryland, College Park, MD 20742, USA
e-mail: bruck@umd.edu

E. Smela
Department of Mechanical Engineering, University of Maryland, College Park, MD 20742, USA

Institute for Systems Research, University of Maryland, College Park, MD 20742, USA

W.C. Ralph et al. (eds.), *Mechanics of Composite and Multi-functional Materials, Volume 7*,
Conference Proceedings of the Society for Experimental Mechanics Series, DOI 10.1007/978-3-319-41766-0_19

The sensing skin consists of a thin film of the piezoresistive composite painted onto a stretchable membrane. We have also developed a multi-layer tactile sensing material system consisting of alternate layers of "sensing skin" and foam padding [4]. This increases the sensitivity and the force range for sensing contact and interactions.

In this work, we present a new multiscale bioinspired compliant device for tactile sensing. By using micron-sized braided carbon fibers and a nano-carbon network, it was possible to employ conductive carbon both as a good electrical conductor for the electrical signals and within the composite to create a resistance change. The more closely matched mechanical stiffness of the sensor and the conductor resulted in significant load bearing capacity over that obtained with an interface to metal wires, with an increase in electrical resistance of the fiber of only 1 Ω/cm. The resulting sensor can be compared to a sensory nerve receptor, where the percolated network of nanosized EG act as the "receptors", while the micro-scale carbon fibers act analogously to the peripheral process of sensory ganglion that are part of the central nervous system. The resulting "biologically inspired" multi-scale strain, and even temperature sensing, has advantages in addition to the greater durability, including amenability to additive manufacturing processes, ease of fabrication, and scalability. We also demonstrate the ability to use the new sensing material in sensorized gloves.

19.2 Experimental Procedure

19.2.1 Nanosized EG Sensing Material

The procedure we use for creating the sensing material the same as reported in earlier publications [2, 5]. EG particles were exfoliated from graphite flake by the microwave exfoliation process as used in [6], originally presented by Falcao et al. [7] and Wei et al. [8]. Acid-washed graphite flake (Ashury Graphite Mills, Inc.) was microwaved (1100 W, 2.45 GHz) for 1 min. The particles became worm-like, increasing in volume 200–300-fold [6].

An aqueous EG solution was also prepared as described in previous references. We took 0.75 g of Triton X-100 surfactant (Sigma Aldrich), and added it to 100 g of deionized water. This solution was placed on top of a hotplate (Fisher Scientific) at 90 °C and stirred at 500 rpm. During stirring, 1.0 g of EG was slowly added over 1 min, followed by four drops of Antifoam SE-15 (Sigma Aldrich) as a dispersant. The container was then placed in an ice bath, and horn sonicated (QSonica, Q700) with a 0.5 in. tip (solid, tip 201) at 100 % amplitude until 100 kJ of energy was added to the system (45 min) in order to mechanically disperse the EG.

When dispersed in an insulating polymer host at sufficiently high concentration, the conductive particles form a percolated network that can conduct current. To create a composite solution, vortex mixing (Fisher Scientific, 3000 rpm, 60 s) was used to combine the EG solution with a mask-making latex (RD-407, ArtMolds) [3]. Sensors were typically made with 30 wt% EG, which is well above the 3 wt% percolation threshold [2]. The resulting solution is easily spray-coated, like paint, and amenable to a variety of 3D additive manufacturing processes.

19.2.2 Carbon Microfiber

The carbon material selected for this investigation was braided carbon fiber tow in the form of a braided carbon fiber sleeve of 2 mm diameter. The sleeve contained ten tows of Toray T300 carbon fibers with ±45° fiber orientations (Fig. 19.1a). Each tow consisted of 1 K carbon fibers, with a weight of 7.8 g/100 m, yielding a calculated total cross-sectional area of 0.385 mm^2 for the braided sleeve, which is similar to a 22 gauge wire. Two carbon fiber tows 6″ in length were attached in parallel to multi-strand copper wire using heat shrink tubing.

19.2.3 Electrical Connection to the Strain Sensor

Latex sheets were cut into strips of 15 × 2 cm and temporarily fixed onto a work surface using painter's tape in a pattern that left a 5 × 1.3 cm section open, which served as a stencil for the definition of the sensor area. The ends of the carbon fibers were manually spread out and laid flat onto the surface of the sensor, overlapping the sensor area by 0.5, 1, and 2 cm. Another set of sensors was created with a 1 cm length of carbon fiber but varying gauge (sensor) length (2.5, 3.8, and 5 cm.). A drop of

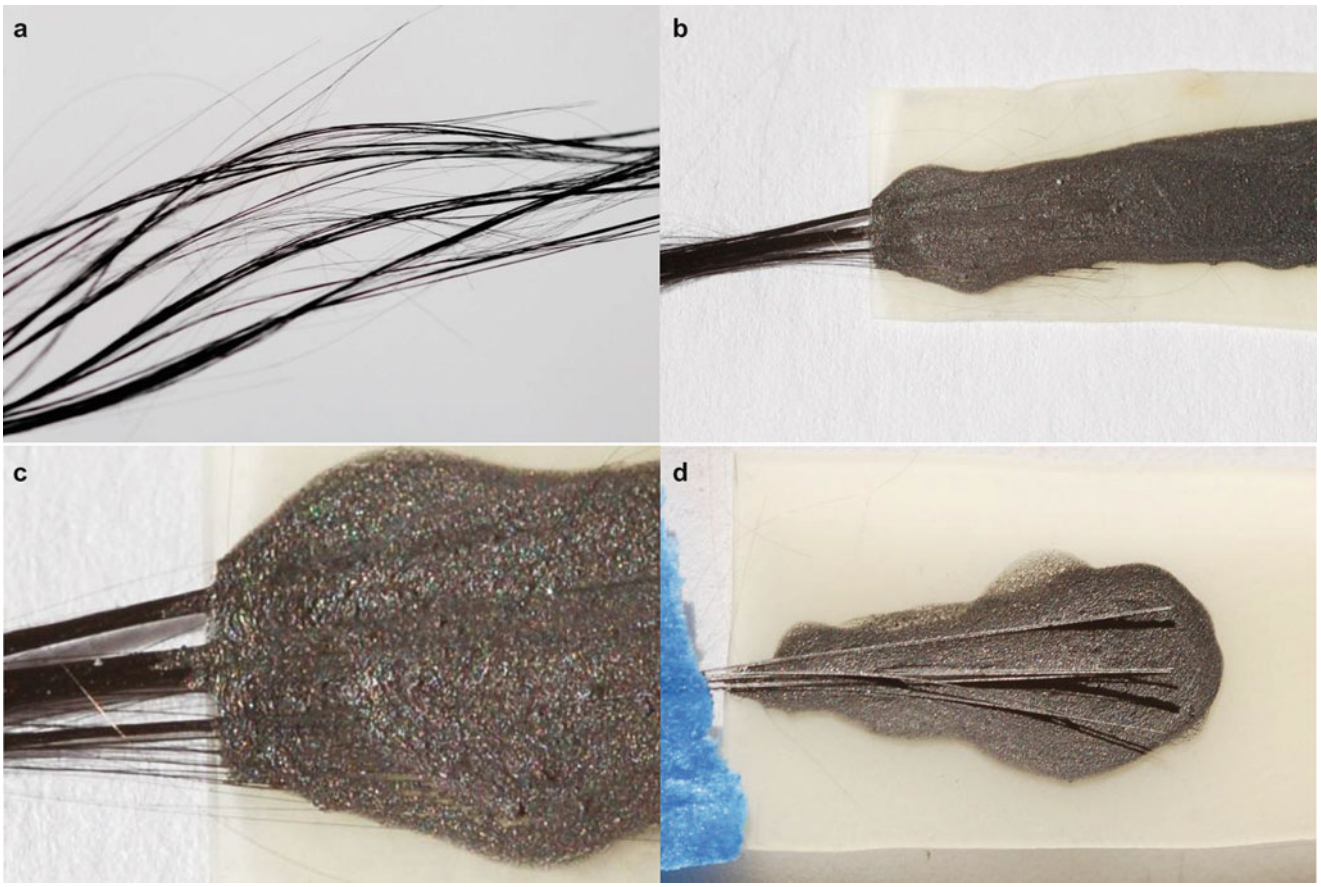

Fig. 19.1 (**a**) A close-up of a carbon fiber bundle, with the strands slightly spread out. (**b**) Latex loaded with exfoliated graphite (EG) (black film, *right*) painted over a carbon fiber bundle (black fibers, *left*) over a rubber sheet (*yellowish*). (**c**) Close-up of (**b**) showing the latex "wicking" along the fibers. (**d**) The same procedure followed with a bundle of metal wires

EG/latex solution was placed over the carbon fibers on the latex and allowed to air dry. Droplets were added until the fibers were no longer visible (Fig. 19.1b, c). For comparison, a sensor made with conventional metal wires using the same fabrication technique is also shown (Fig. 19.1d). The metal strands were too stiff to be adhered by the polymer composite.

19.2.4 Mechanical Testing of the Sensors

The sensors were subjected to cyclic tensile strain and strain to failure. The latex membrane on either side of the sensor area was clamped into the mechanical testing apparatus in series with a load cell, and the sensor was connected as part of a voltage divider to a DAQ. Load and sensor voltages were recorded simultaneously by NI SignalExpress. Samples were first cyclically strained and then strained at the same rate to the point of failure.

19.3 Experimental Results

19.3.1 Qualitative Characterization

A demonstration of the load-bearing capability of the carbon fiber interconnection is shown in Fig. 19.2, up to 100 % increase in length. In this figure, the specimen was gripped on the carbon microfiber connections. These connections have an inherent resistivity measured to be 1.7×10^{-3} Ω−cm using a shunt resistor for current with a variable voltage profile. The measured value was similar to the specifications reported by the manufacturer of the Toray T300 fiber. Thus, a typical bundle

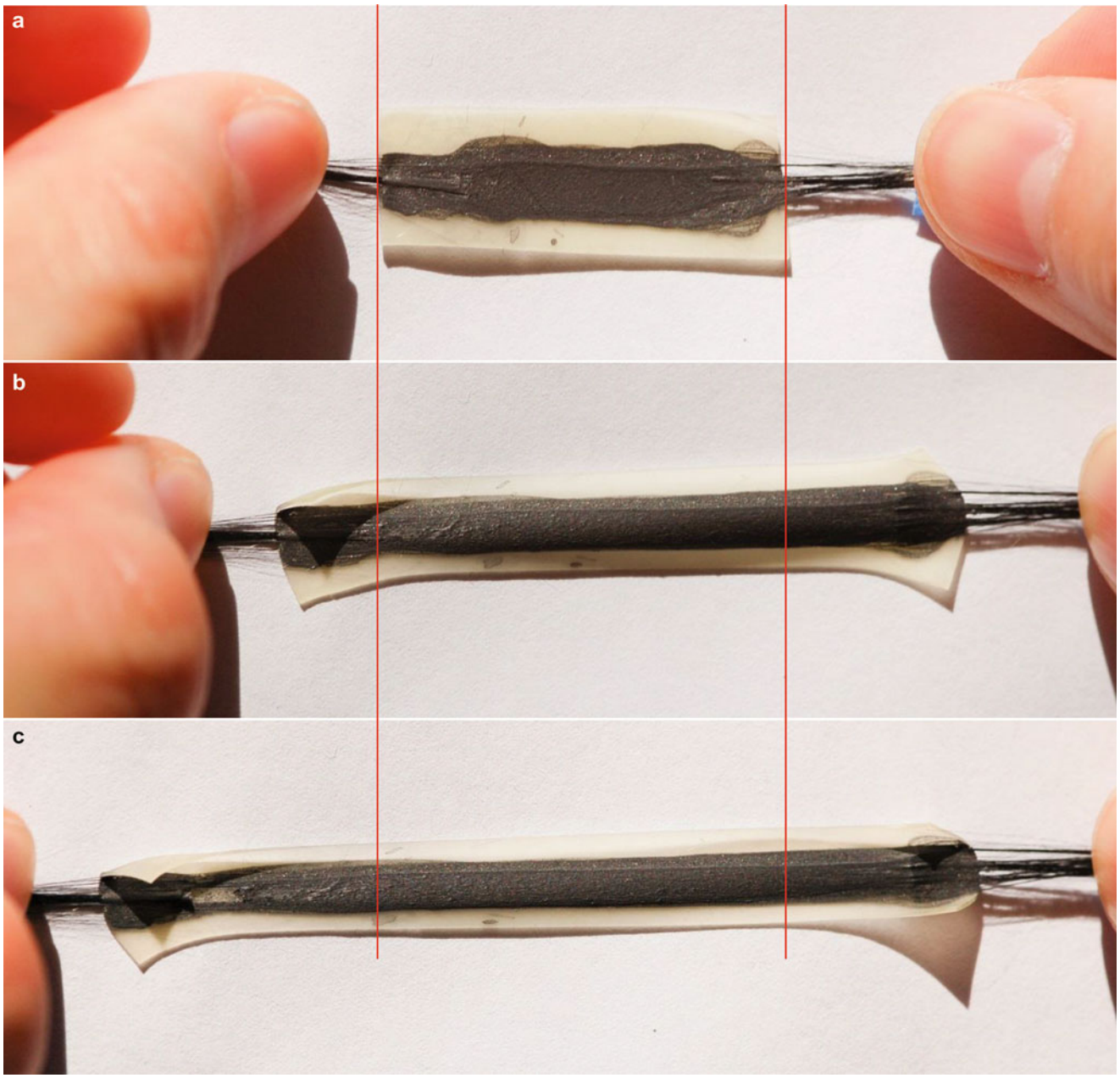

Fig. 19.2 The carbon fiber connection used on either side of a latex/EG film painted onto a latex membrane. (**a**) Under no tension. (**b**) The film was stretched by pulling on the carbon fiber yarn. (**c**) The interconnect delaminates from the membrane upon further stretching, but the fiber yarn does not pull out from the latex/EG sensing material

of carbon microfibers (e.g., 1 K tow) will have a substantially lower electrical resistance of 2 Ω/cm of length compared to the inherent resistance of the percolated EG network.

19.3.2 Mechanical Characterization of Sensing Response

To demonstrate the quality of the signal obtained from the carbon–carbon interface, cyclic tensile loading data were obtained. Sensors with a gauge length of 50 mm were gripped on the latex substrate and strained to $\Delta L/L = 0.25$ for three consecutive cycles at a rate of 0.1 mm/s during loading and unloading. Typical results are shown in Fig. 19.3. The normalized change in sample resistance, $\Delta R/R_0$, increased with strain with a sensitivity of at 2.4×10^{-6}/μstrain. There

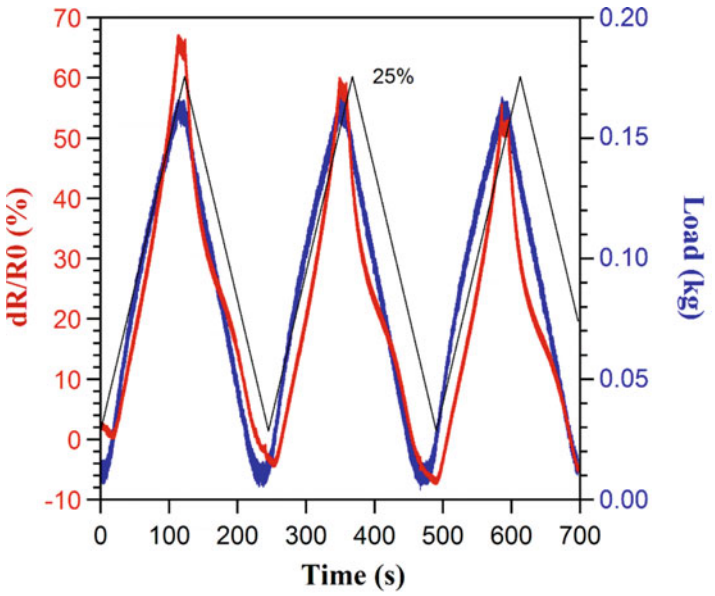

Fig. 19.3 Change in resistance (*red*) and force (*blue*) during cyclic tensile testing (10 mm embedded fiber length). The strain (*black*) is also shown ramping between 0 and 25 % (sensor 5 cm long, carbon fiber embedded 10 mm)

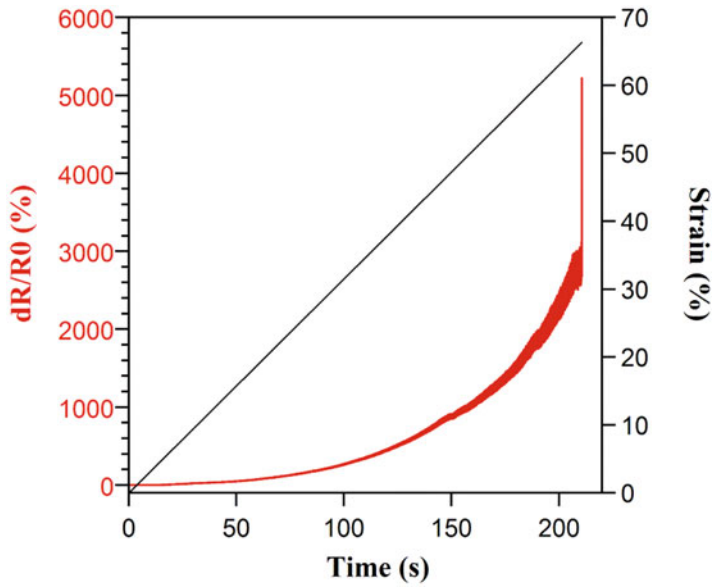

Fig. 19.4 Change in resistance (*red*) upon straining to failure (sensor 5 cm long, carbon fiber embedded 10 mm)

is a decrease in sensitivity over the three cycles, but this is due to viscoelastic effects [4] and not degradation of the electrical connection.

To demonstrate the robustness of the connection, the samples were strained to failure, as shown in Fig. 19.4 for the same sample that was used in Fig. 19.2. The device survived to 70 % strain, at which point it failed. The change in resistance near failure reached several thousand percent, with a sensitivity of normalized resistance approaching 1×10^{-4}/μstrain.

19.4 Application to a Robot Hand

Sensorized data gloves measure applied force on the fingers from contact of the hand. To demonstrate the application of the new multiscale sensing device, we applied the material to the fingers of a latex glove by spray coating. The glove was put onto to a 3D printed robot hand, and used to sense interactions with different structures, including humans as shown in Fig. 19.5. A video of the robot hand while sensing can be seen at https://youtu.be/raJdigbeFL4. From the images on the computer display, the finger is able to detect repeated squeezing by a human with real-time response.

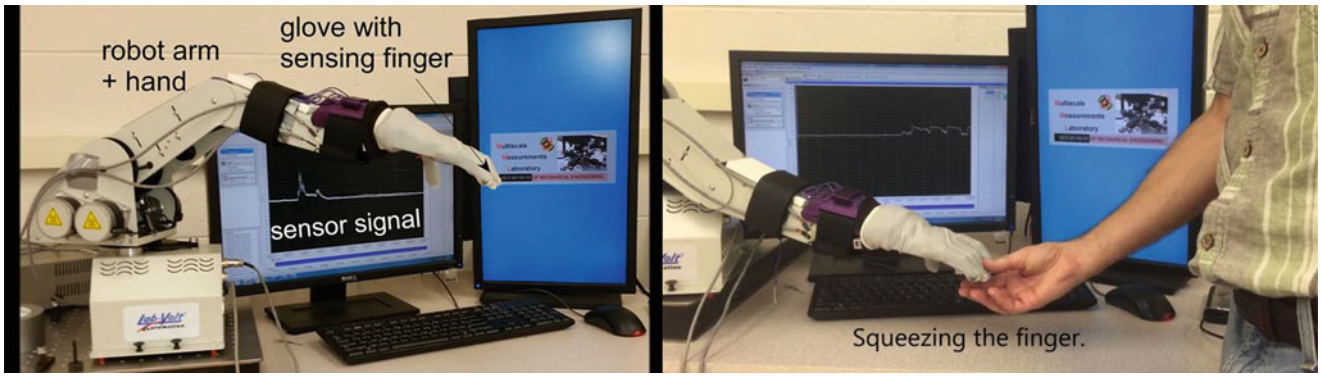

Fig. 19.5 Sensing glove on robot hand for co-robots

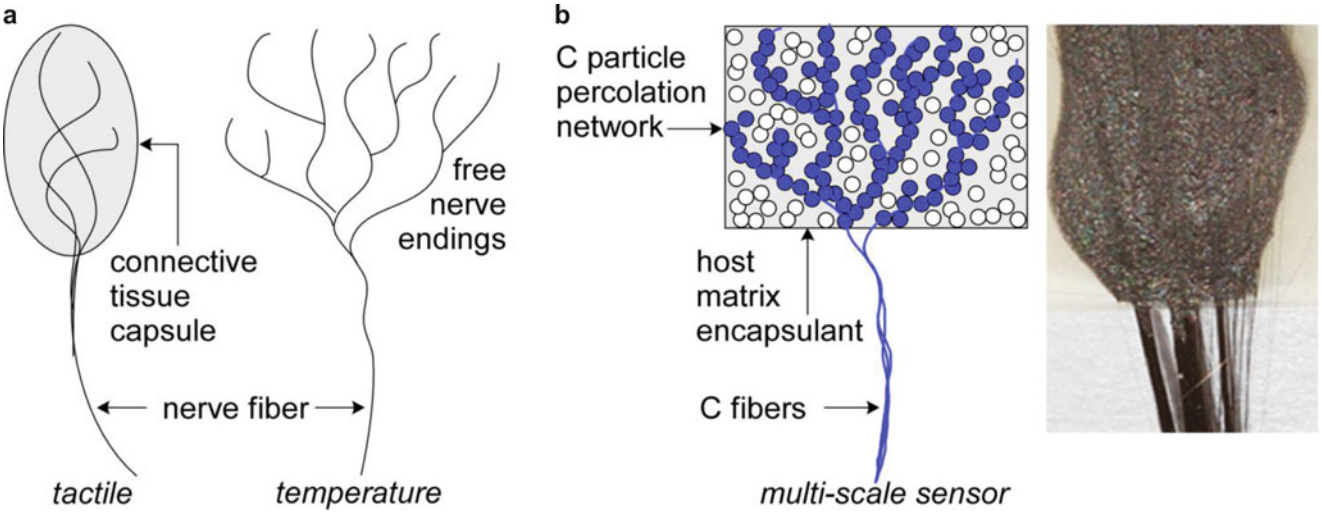

Fig. 19.6 (*left*) Schematic of sensory receptor with connective tissue capsule encapsulating a nerve ending, (*right*) new biologically inspired multiscale sensing material

19.5 Conclusions

A nerve-like sensor comprising a polymer composite with embedded carbon fibers has been demonstrated. The sensing element contains nanoscale carbon (exfoliated graphite), and sensing is based on changes in electrical percolation through the EG network in the polymer host. Such a network is responsive to stimuli such as strain and temperature. The connecting element contains micro-scale carbon, which is better matched, both mechanically and chemically, to the composite than are metal wires and metal-filled epoxies. The mechanical characteristics of the resulting multi-scale sensor were determined. The use of carbon at both the nanoscale and microscale provide high compatibility between the polymer matrices, allowing for greater load-bearing capacity, and thus robustness.

The strain and temperature sensor can be easily fabricated using a variety of manufacturing processes, wherein the composite can be deposited, injected, or molded. The resulting "biologically inspired" multi-scale strain and temperature sensor has advantages in addition to durability, including amenability to additive manufacturing processes, ease of fabrication, and scalability.

Biological temperature and mechanoreceptors are found in the skin, the latter sensing pressure and distortion (Fig. 19.6a) and changing their electrical output in response. The ends of the temperature-sensing nerve fibers branch into free nerve endings, while one type of tactile sensor is encapsulated in connective tissue. The architecture of our multi-scale carbon-based device is analogous (Fig. 19.6b), consisting of micron-scale fiber conductors (which can be liked to a bundle of nerve fibers) connected to a percolation network of nano-scale conductors, which has a large number of branches. The percolation network is encapsulated by the host matrix, which mechanically affects the network based on applied pressure or distortion, changing the electrical signal through the network.

Acknowledgments Funding for this research was provided by NSF through the National Robotics Initiative (NRI) under award number IIS1317913.

References

1. Wissman, J., Perez-Rosado, A., Edgerton, A., Levi, B.M., Karakas, Z.N., Kujawski, M., Philipps, A., Papavizas, N., Fallon, D., Bruck, H.A., Smela, E.: New compliant strain gauges for self-sensing dynamic deformation of flapping wings on miniature air vehicles. Smart Mater. Struct. **22**, 085031 (2013)
2. Kujawski, M., Pearse, J.D., Smela, E.: Elastomers filled with exfoliated graphite as compliant electrodes. Carbon **48**, 2409–2417 (2010)
3. Sauerbrunn, E., Chen, Y., Didion, J., Yu, M., Smela, E., Bruck, H.A.: Thermal imaging using polymer nanocomposite temperature sensors. Phys. Status Solidi A **212**, 2239–2245 (2015)
4. Chen, Y., Yu, M., Bruck, H.A., Smela, E.: Stretchable touch-sensing skin over padding for co-robots. Smart Mater. Struct. **25**, 055006 (2016)
5. Kujawski, M., Pearse, J., Smela, E.: Graphite/PDMS stretchable electrodes for dielectric elastomer actuators. Paper presented at Electroactive Polymer Actuators and Devices (EAPAD) XII, SPIE Symposium on SPIE Smart Structures and Materials and Nondestructive Evaluation and Health Monitoring, San Diego, 7–11 Mar 2010
6. Kalaitzidou, K., Fukushima, H., Drzal, L.T.: Mechanical properties and morphological characterization of exfoliated graphite–polypropylene nanocomposites. Compos. A: Appl. Sci. Manuf. **38**, 1675–1682 (2007)
7. Falcao, E.H., Blair, R.G., Mack, J.J., Viculis, L.M., Kwon, C.W., Bendikov, M., Kaner, R.B., Dunn, B.S., Wudl, F.: Microwave exfoliation of a graphite intercalation compound. Carbon **45**, 1367–1369 (2007)
8. Wei, T., Fan, Z.J., Luo, G.L., Zheng, C., Xie, D.S.: A rapid and efficient method to prepare exfoliated graphite by microwave irradiation. Carbon **47**, 337 (2009)

Chapter 20
Effect of Microstructure on Mechanical Response of MAX Phases

Prathmesh Naik Parrikar, Rogelio Benitez, Miladin Radovic, and Arun Shukla

Abstract High density samples of Ti_2AlC, a MAX Phase material, with three different grain sizes were processed by Reaction Sintering. The dynamic thermo-mechanical response of these samples was investigated by a modified Split Hopkinson Pressure Bar in conjunction with induction heating. Ti_2AlC exhibits high compressive strength (above 600 MPa) for temperatures as high as 1100 °C under dynamic loading. The peak compressive stress decreases with increasing temperatures. Specimens exhibited catastrophic brittle failure at room temperature but graceful failure at high temperatures. Moreover, the temperature at which graceful failure occurs decreases with increasing grain size. Also, a Hall-Petch like relationship was observed between compressive strength and the grain diameter.

Keywords MAX phase • Thermo-mechanical loading • Kink bands • SHPB • Graceful failure

20.1 Introduction

Ti_2AlC is a member of the family of ternary carbides and nitrides generally referred to as MAX phases that have a unique combination of properties that makes it attractive for different applications. All MAX phases share the general chemical formula of $M_{n+1}AX_n$ (where M is an early transition metal, A is a group element, and X is carbon and/or nitrogen), and distinctive interleaved nanolayered structure of $M_{n+1}X_n$ layers with pure A-group element layers [1–3]. MAX phases have an unique combination of metal and ceramic like properties such as high stiffness, good thermal and electrical conductivity, excellent thermal shock resistance, high damage tolerance, high fracture toughness and ease of machinability with conventional tooling [1–5]. Of the discovered MAX phases, Ti_2AlC is considered to be the most promising candidate for high temperature applications. Ti_2AlC has superior oxidation resistance owing to the formation of a self-healing Al_2O_3 protective layer that is well adhered and spallation resistant even during thermal cycling [6–9]. In addition, it has low density (4.11 g/cm^3) [3], high thermal (46 W/(m · K)) and electrical (4.42 × 106 S/m) [6] conductivities, and a high Young's modulus (≈280 GPa) [10].

The quasi-static studies on all MAX phases show that the mechanical response of changes from brittle-like at room temperatures to pseudo-plastic at elevated temperatures [2, 5, 11–13]. At elevated temperatures, they all show brittle-to-plastic transition (BPT) usually at temperatures between 900 and 1100 °C [2, 5]. Above the brittle-to-plastic transition temperature (BPTT), their strength decreases rapidly with temperature and their mechanical response becomes pseudo-ductile with strains to failure in both tension and compression exceeding 25 % [1, 2, 14–18]. MAX phases are highly plastically anisotropic as basal and only basal plane dislocations can easily move, multiply, and arrange either in pileups or in walls/arrays even at room temperature. In addition, MAX phases can also deform by kinking and kink band formation throughout the temperature ranges tested. To the best of the authors' knowledge, only a few high strain rate studies for MAX phases have been reported to date [19, 20]. Experiments conducted by Bhattacharya et al. [19] on coarse grained Ti_2AlC in 2600–4700 s^{-1} strain rate range show no apparent strain rate dependencies for the strain rates tested. Their analysis of fracture surfaces showed that kinking was an active deformation mechanism, even at the high strain rates tested. Parrikar

P. Naik Parrikar • A. Shukla (✉)
Department of Mechanical, Industrial and Systems Engineering, University of Rhode Island, Kingston, RI 02881, USA
e-mail: shuklaa@uri.edu

R. Benitez
Mechanical Engineering Department, Texas A&M University, College Station, TX 77843, USA

M. Radovic
Mechanical Engineering Department, Texas A&M University, College Station, TX 77843, USA

Materials Science and Engineering Department, Texas A&M University, College Station, TX 77843, USA

W.C. Ralph et al. (eds.), *Mechanics of Composite and Multi-functional Materials, Volume 7*,
Conference Proceedings of the Society for Experimental Mechanics Series, DOI 10.1007/978-3-319-41766-0_20

et al. [20] tested fine grained Ti_2AlC under quasi static and dynamic conditions and showed the relation between fracture characteristics and the strength of the material.

The purpose of this experimental study was to investigate the effect of grain size on the dynamic behavior of Ti_2AlC. An experimental investigation of its constitutive behavior under dynamic loading was conducted at different temperatures ranging from room temperature to 1100 °C. Under dynamic loading Ti_2AlC has brittle failure and the failure transitioned from catastrophic failure at lower temperatures to graceful failure at higher temperatures.

20.2 Material Fabrication

A two-step process was used prepare specimens. Ti, Al and TiC powders with a molar ratio of Ti:Al:TiC = 2:1.05:0.95 were mixed homogeneously by ball milling. The mixture was sintered in a high vacuum tube furnace at a temperature of 1400 °C under high purity argon flow. The sintered compact of reacted powder was then drill-milled to produce Ti_2AlC powders. This powder was processed in spark plasma sintering for 45 min at 1300 °C to produce high density samples. Those samples are further denoted as fine grained or FG. To explore the effect of grain size, samples were further subjected to 8 and 24 h of heat treatment. These samples are referred to as medium grained and coarse grained or MG and CG, respectively. A back-scattered electron detector technique was utilized to obtain the microstructure of the prepared specimens. The average grains in FG are 6.1 μm in length and 4.6 μm thick, in MG are 13.9 μm in length and 7.3 μm thick and in CG are 17.4 μm in length and 8.2 μm thick.

20.3 Experimental Setup

A Split Hopkinson Pressure Bar (SHPB) was used to study the dynamic behavior of Ti_2AlC and effect of grain size (Fig. 20.1). The striker bar, incident bar and transmission bar in the SHPB setup were all made out of Maraging steel. The incident and transmission bars had a diameter of 12.5 mm and lengths of 2133 mm and 1524 mm, respectively. The striker bar was propelled using an air-operated gun. The Ti_2AlC specimens with the three different grain sizes had a diameter of 5 mm and a length of 8 mm. Modifications were made to the SHPB setup following procedures used to test other ceramic materials [21] to account for the hard and brittle nature of Ti_2AlC. Copper pulse shaper was placed at the impact end of the incident bar. Tungsten-carbide (WC) inserts whose impedance was matched to that of the bars were placed between the two bars and the specimen was sandwiched between the inserts. The inserts were used to reduce stress concentration in the specimens and to prevent indentation of the specimens into the bars. Molybdenum disulfide was used to lubricate the specimen-insert interface and bar–insert interface.

For high temperature experiments an induction coil heater was used in conjunction with the SHPB setup. The Ti_2AlC specimens are electrically conductive, and therefore could be heated by electromagnetic induction using coiled loops around the specimen. The WC inserts prevented the development of a sharp temperature gradient in the bars and also protected the strain gauges mounted on the bars.

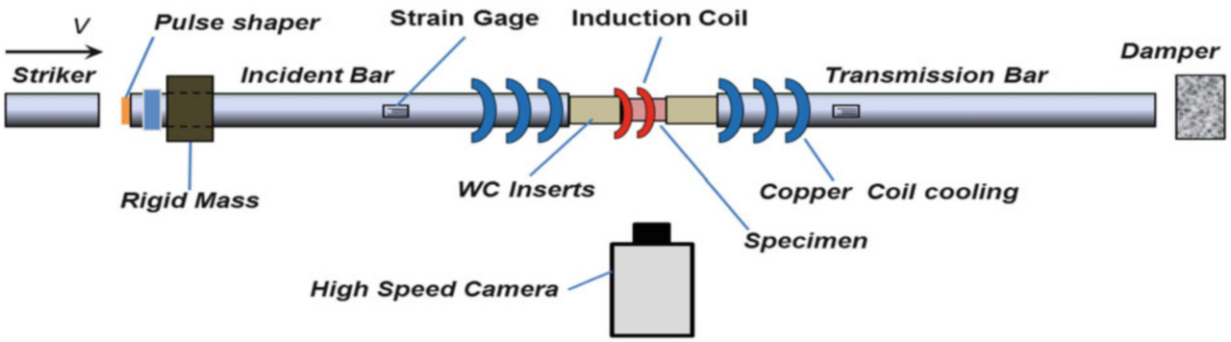

Fig. 20.1 Schematic representation of SHPB setup

Using one-dimensional wave theory, the stress and strain in the specimen can be determined from the transmitted and reflected strain pulses, respectively, as

$$\sigma_s = E_b \frac{A_b}{A_s} \varepsilon_t(t) \tag{20.1}$$

$$e_s = \frac{-2c_b}{L_s} \int_0^t \varepsilon_r(t) dt \tag{20.2}$$

Where σ_s and e_s are stress and strain in the specimen, ε_r and ε_t are the time resolved strain values of reflected and transmitted pulses, c_b is the longitudinal bar wave speed, E_b is the Young's modulus of the bar material, A_b is the cross-sectional area of the bar, A_s is the cross-sectional area of the specimen and L_s is the thickness of the specimen.

20.4 Results

Three grain sizes, fine (6.1 μm dia.), medium (13.9 μm dia.) and coarse (17.4 μm dia.) were studied. The specimens displayed brittle catastrophic failure at room temperature and a graceful failure at high temperatures. Figure 20.2a shows the typical time shifted segments of the recorded pulses and Fig. 20.2b shows the corresponding force ratio variation observed for the specimens which exhibited a catastrophic brittle failure. The specimen fails at 39 μs. The occurrence of failure is marked by the peak value of the transmitted pulse, after which the magnitude of transmitted pulse drops sharply. Figure 20.2b shows that the dynamic stress equilibrium was attained at about 15 μs and was maintained up to the point of specimen failure. The pulses were analyzed only up to the point of failure (corresponding to peak transmitted) to generate the stress strain curves for the specimens showing catastrophic failure.

The true compressive stress-strain curves of medium grained Ti_2AlC during dynamic loading at various temperatures are represented in Fig. 20.3. A '⋆' symbol is used in these plots to represent points of catastrophic failure. The dynamic experiments were conducted at an average strain rate of 500 s^{-1}. The peak compressive stress decreases with increasing in temperature. For the experiments conducted, graceful failure was beginning to occur at 1100 °C for fine grain, at 900 °C for medium grain and at 600 °C for coarse grain specimens.

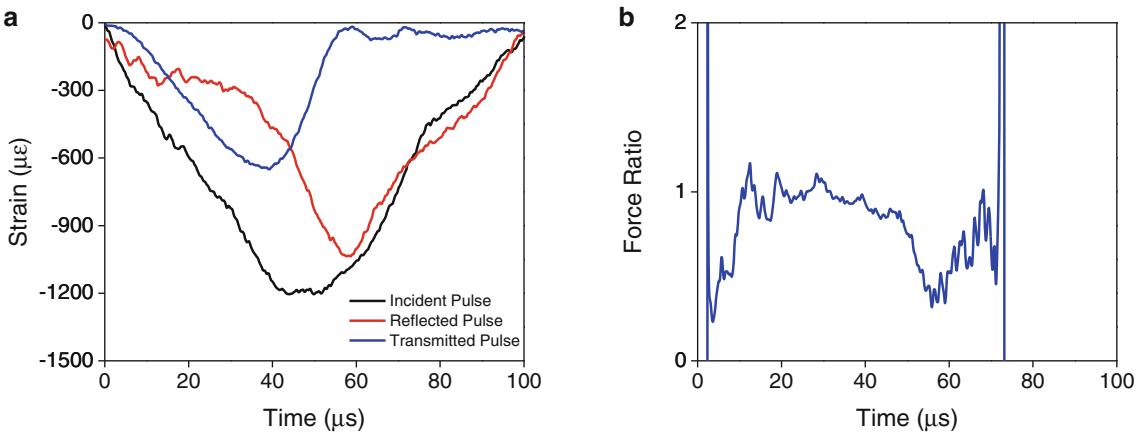

Fig. 20.2 (**a**) Typical pulses recorded when specimen undergoes catastrophic brittle failure. (**b**) Corresponding force ratio variation with time during the experiment

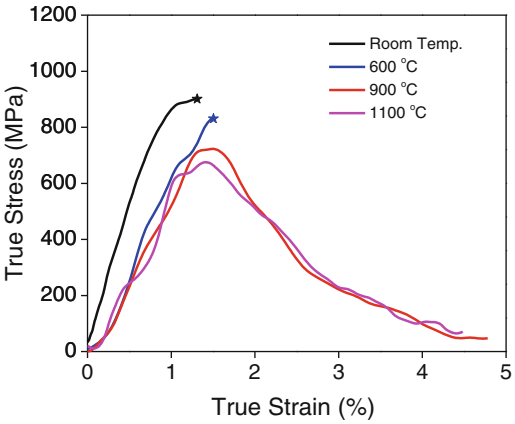

Fig. 20.3 True compressive stress-strain curve of medium grained Ti_2AlC at various temperatures

20.5 Conclusions

Ti_2AlC exhibits high compressive strength (above 600 MPa) for temperatures as high as 1100 °C under dynamic loading. The peak compressive stress decreases with increasing temperatures. The specimens had catastrophic brittle failure at room temperature and a graceful failure at high temperatures. The temperature at which graceful failure occurs decreases with increase in grain size.

Acknowledgment Authors acknowledge the financial support from CMMI, NSF, Grant Nos. 1233887 and 1233792 at the University of Rhode Island and Texas A&M University, respectively.

References

1. Barsoum, M.W.: MAX phases: properties of machinable ternary carbides and nitrides. Wiley. http://www.wiley.com/WileyCDA/WileyTitle/productCd-3527330119.html (2015). Accessed 15 June 2015
2. Barsoum, M.W., Radovic, M.: Elastic and mechanical properties of the MAX phases. Annu. Rev. Mater. Res. **41**(1), 195–227 (2011)
3. Barsoum, M.W.: The MN + 1AXN phases: a new class of solids: thermodynamically stable nanolaminates. Prog. Solid State Chem. **28**(1–4), 201–281 (2000)
4. Barsoum, M.W., El-Raghy, T.: Synthesis and characterization of a remarkable ceramic: Ti_3SiC_2. J. Am. Ceram. Soc. **79**(7), 1953–1956 (1996)
5. Radovic, M., Barsoum, M.W.: MAX phases: bridging the gap between metals and ceramics. Am. Ceram. Soc. Bull. **92**(3), 20–27 (2013)
6. Yang, H.J., Pei, Y.T., Rao, J.C., De Hosson, J.T.M., Li, S.B., Song, G.M.: High temperature healing of Ti2AlC: on the origin of inhomogeneous oxide scale. Scr. Mater. **65**(2), 135–138 (2011)
7. Basu, S., Obando, N., Gowdy, A., Karaman, I., Radovic, M.: Long-term oxidation of Ti2AlC in air and water vapor at 1000–1300°C temperature range. J. Electrochem. Soc. **159**(2), C90–C96 (2011)
8. Wang, X.H., Zhou, Y.C.: High-temperature oxidation behavior of Ti2AlC in air. Oxid. Met. **59**(3–4), 303–320 (2003)
9. Byeon, J.W., Liu, J., Hopkins, M., Fischer, W., Garimella, N., Park, K.B., Brady, M.P., Radovic, M., El-Raghy, T., Sohn, Y.H.: Microstructure and residual stress of alumina scale formed on Ti2AlC at high temperature in air. Oxid. Met. **68**(1–2), 97–111 (2007)
10. Radovic, M., Barsoum, M.W., Ganguly, A., Zhen, T., Finkel, P., Kalidindi, S.R., Lara-Curzio, E.: On the elastic properties and mechanical damping of Ti3SiC2, Ti3GeC2, Ti3Si0.5Al0.5C2 and Ti2AlC in the 300–1573 K temperature range. Acta Mater. **54**(10), 2757–2767 (2006)
11. Radovic, M., Barsoum, M.W., El-Raghy, T., Wiederhorn, S.M., Luecke, W.E.: Effect of temperature, strain rate and grain size on the mechanical response of Ti3SiC2 in tension. Acta Mater. **50**(6), 1297–1306 (2002)
12. Zhen, T., Barsoum, M.W., Kalidindi, S.R.: Effects of temperature, strain rate and grain size on the compressive properties of Ti3SiC2. Acta Mater. **53**(15), 4163–4171 (2005)
13. Zhang, H., Wang, X., Wan, P., Zhan, X., Zhou, Y.: Insights into high-temperature uniaxial compression deformation behavior of Ti3AlC2. J. Am. Ceram. Soc. **98**, 3332–3337 (2015)
14. Barsoum, M.W., El-Raghy, T., Ali, M.: Processing and characterization of Ti2AlC, Ti2AlN, and Ti2AlC0.5N0.5. Metall. Mater. Trans. A **31**(7), 1857–1865 (2000)
15. El-Raghy, T., Barsoum, M.W., Zavaliangos, A., Kalidindi, S.R.: Processing and mechanical properties of Ti3SiC2: II, effect of grain size and deformation temperature. J. Am. Ceram. Soc. **82**(10), 2855–2860 (1999)
16. Radovic, M., Barsoum, M.W., El-Raghy, T., Seidensticker, J., Wiederhorn, S.: Tensile properties of Ti3SiC2 in the 25–1300°C temperature range. Acta Mater. **48**(2), 453–459 (2000)

17. Tian, W., Sun, Z., Hashimoto, H., Du, Y.: Compressive deformation behavior of ternary compound Cr2AlC. J. Mater. Sci. **44**(1), 102–107 (2008)
18. Wan, D.-T., He, L.-F., Zheng, L.-L., Zhang, J., Bao, Y.-W., Zhou, Y.-C.: A new method to improve the high-temperature mechanical properties of Ti3SiC2 by substituting Ti with Zr, Hf, or Nb. J. Am. Ceram. Soc. **93**(6), 1749–1753 (2010)
19. Bhattacharya, R., Benitez, R., Radovic, M., Goulbourne, N.C.: High strain-rate response and deformation mechanisms in polycrystalline Ti2AlC. Mater. Sci. Eng. A **598**, 319–326 (2014)
20. Naik Parrikar, P., Benitez, R., Gao, H., Radovic, M., Shukla, A.: Mechanical response of fine grained Ti2AlC under extreme thermo-mechanical loading conditions. Mater. Sci. Eng. A **658**, 176–184 (2016)
21. Subhash, G., Ravichandran, G.: Split-Hopkinson pressure bar testing of ceramics—ASM International. In: Kuhn, H., Medlin, D. (eds.) ASM Handbook, Mechanical Testing and Evaluation, vol. 8, pp. 497–504. ASM International, Materials Park (2000)

Chapter 21
Controlled Placement of Microcapsules in Polymeric Materials

Matthew D. Crall and Michael W. Keller

Abstract A wide variety of functional materials are based on microcapsules, including self-healing and self-sensing composites. In this paper, we demonstrate the ability to guide microcapsules to a desired location in an epoxy specimen using magnetic fields. Guidable microcapsules are synthesized by the inclusion of magnetic nanoparticles in the microcapsule core and shell. Nanoparticles are surface modified to enhance compatibility with emulsion-based encapsulation processes. Transmission Electron Microscopy (TEM) is used to determine nanoparticle crystal structure and overall size, found to be 7 nm in diameter. Microcapsules are characterized using optical microscopy and Scanning Electron Microscopy (SEM). The influence of microcapsule diameter and nanoparticle concentration is studied to optimize the placement efficiency of the microcapsules. Microcapsule dispersion and location are analyzed using optical and electron microscopy. The impact of the placed microcapsules on fracture toughness is evaluated using a Tapered Double Cantilevered Beam (TDCB) specimen geometry.

Keywords Microcapsules • Magnetic nanoparticles • Self-healing • Controlled placement • Fracture toughness

21.1 Introduction

Within the past 15 years, materials science has seen significant advances in the area of multi-functional materials. A subset of this field studies materials with the capability to self-repair, called self-healing materials. There are several mechanisms that can be used to achieve self-healing functionality. One particularly successful approach is to sequester a liquid "healing agent" that can be delivered to autonomically repair damaged regions [1–3]. Healing agents can be delivered using vascular networks embedded in the material or through the use of liquids sequestered in microcapsules. Microcapsule-based materials are synthesized by simply mixing in microcapsules into a polymer before it cures. An approaching crack ruptures the embedded microcapsules and releases the healing agent. The healing agent then reacts and bonds the crack faces, restoring the fracture toughness of the material [2, 3]. Various types of microcapsules have been synthesized for these types of applications, including microcapsules with diverse core and shell materials, different shell thicknesses, and varying numbers of shell layers. These improvements serve to make the microcapsules more robust or to expand the range of healing chemistries that can be used [4–6]. Such developments are geared towards creating intelligently designed materials with unique properties desirable for specific applications.

The inclusion of microcapsules in polymeric materials can alter material properties in several ways. Typically, fracture toughness increases, as should be expected for the inclusion of particles in the matrix [7]. In addition, overall material modulus and ultimate strength can decrease as microcapsules are added [7]. Therefore, optimization of the microcapsules in order to minimize cost and any negative impact on material properties is desirable. One possible approach is to guide microcapsules to locations that have been identified as regions of high failure probability. This guiding can be accomplished using magnetic fields in a manner similar to targeted drug delivery methods being developed in biomedicine [8]. The ability to selectively locate the microcapsules to a specific region helps minimized the number of microcapsules necessary to achieve self-healing. In this paper, we detail the synthesis and performance of such magnetic microcapsules in a solvent-based self-healing epoxy.

M.D. Crall • M.W. Keller (✉)
Department of Mechanical Engineering, The University of Tulsa, 800 South Tucker Drive, Tulsa, OK 74104, USA
e-mail: michael-keller@utulsa.edu

W.C. Ralph et al. (eds.), *Mechanics of Composite and Multi-functional Materials, Volume 7*,
Conference Proceedings of the Society for Experimental Mechanics Series, DOI 10.1007/978-3-319-41766-0_21

21.2 Experimental

21.2.1 Nanoparticle Synthesis

Nanoparticles were synthesized using a modified version of the procedure described by Zhao et al. [9]. An iron salt solution was created by the addition of $FeCl_2 \cdot 4H_2O$ (0.266 g) and $FeCl_3 \cdot 6H_2O$ (0.723 g) to 20 mL of deionized water. This solution was combined with an equal volume of 4 M ammonium hydroxide solution by a high speed injection process [10]. The resulting precipitate was separated from the solution with a magnet and washed three times with deionized water. Silica coating was carried out via the Stöber process [11]. Nanoparticles were suspended in a solution of 16.7 mL ethanol, 1 mL ammonium hydroxide concentrate, and 5 mL deionized water. Next, 0.8 mL tetraethyl orthosilicate (TEOS) was added to the solution. After mixing overnight, the nanoparticles were separated from the solution with a magnet and washed three times with ethanol. Nanoparticles were then coated in a hydrophobic silane via established methods [12]. The nanoparticles were suspended in 30 mL ethanol and 0.05 mL of ammonium hydroxide concentrate in a round bottom flask under nitrogen protection at 60 °C. Lastly, 0.465 mL of phenyltriethoxysilane was added to the solution which was then mixed overnight. Nanoparticles were separated from the solution with a magnet and washed three times with ethanol.

21.2.2 Microcapsule Synthesis

Microcapsules were created using an in-situ urea-formaldehyde encapsulation technique [4]. Batch size was decreased to ¼ of a standard sized batch. Differing concentrations of nanoparticles (0.25, 0.5, 1, 2 wt%) were suspended in vials of phenyl acetate core material and vigorously shaken before being added to the microcapsule bath, which was mechanically agitated at 600 rpm. Upon completion of the reaction, the microcapsules were separated from the bath with a magnet and manually washed three times with deionized water. Microcapsules were then vacuum filtered and washed with deionized water and ethanol before drying at room temperature. Microcapsules were sieved before use to break up clumps.

21.2.3 Specimen Manufacturing

Test samples were created using a TDCB geometry to measure fracture toughness and healing efficiency of the material [13]. A short groove version was used because it has been shown to be suitable for testing the effectiveness of our chosen healing chemistry [2, 3]. Neodymium magnets were placed on the outer surface of the mold along the groove in order to guide the microcapsules to the intended fracture location (Fig. 21.1). Control specimens without microcapsule guiding were created using magnetic microcapsules without any magnets on the outside of the molds. All samples were fabricated with EPON 828 epoxy resin heated to 90 °C to decrease viscosity and facilitate the movement of the microcapsules during cure. Diethylenetriamine (DETA) was added in a ratio of 12:100 with the resin, and was also heated to 90 °C prior to being mixed in. Microcapsules were added to the epoxy resin in varying weight percentages, and the resulting mixture was immediately poured into the mold while still hot. The specimens were left to cool and cure at ambient temperature for 24 h, at which point the clamps and magnets were removed and the specimen put in an oven to post-cure for 24 h at 35 °C.

21.2.4 Fracture Testing

Specimens were removed from the molds after post-cure and pre-cracked with a razor blade just before testing. Specimens were tested in displacement control at a rate of 5 $\mu m \cdot s^{-1}$. Once the fracture propagated along the grove, the specimen was unloaded and removed from the testing machine. Specimens were tested again after 24 h to assess healing performance. The chosen TDCB geometry allows specimen compliance to be used as a measure of crack length, and max load to be directly

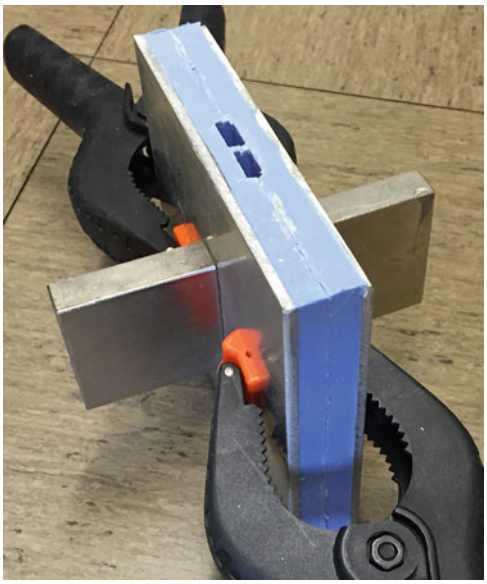

Fig. 21.1 Mold for making TDCB specimens with a pair of neodymium magnets on the outside

proportional to fracture toughness [13]. Healing is assessed by a recovery of sample stiffness and healing efficiency can be defined as the max load reached during the second test at the original compliance, over the max load reached during the initial test (Eq. 21.1).

$$\eta_{healing} = \frac{P_{healed}}{P_{initial}} \tag{21.1}$$

21.3 Results and Discussion

21.3.1 Microscopy

Transmission Electron Microscopy (TEM) was performed on the magnetic nanoparticles, showing that they are typically 7 nm in diameter and have a square or hexagonal shape consistent with the isometric hexoctahedral crystal structure of magnetite [14] (Fig. 21.2). The microcapsules were characterized with optical microscopy after synthesis. As can be seen in Fig. 21.3, the microcapsules are rather uniform in shape and contain a noticeable amount of the nanoparticles in the core. A magnetized razorblade can be used to manipulate the nanoparticles floating within the microcapsules from the outside, and crush tests confirm that the microcapsules contain liquid. Scanning electron microscopy was used to get more precise measurements of microcapsule diameter (350 μm) and shell thickness (200 nm).

Visual inspection of guided specimens shows that the microcapsules are concentrated in the intended location along the TDCB groove, as can be seen from Fig. 21.4. After fracture testing, both optical microscopy and SEM were used to analyze the location and number of microcapsules along the fracture surface. This showed that microcapsules tend to congregate along the outer face of the groove. Because of the presence of the side grooves on the TDCB, the magnetic field strength is less in the center of the crack plane when compared to the outer surface. This causes microcapsules to pile up at the outer faces of the groove, eventually forcing more microcapsules into the center of the groove. If enough microcapsules are available, the fracture plane can be completely filled with microcapsules (see Fig. 21.5). Increasing the nanoparticle concentration within the microcapsules also leads to a more effective filling of the fracture plane, as more magnetic nanoparticles allows a larger force to be applied to the microcapsules by the magnetic field. Larger microcapsules also appear to be more easily guided than smaller microcapsules, again, likely due to increased magnetic force caused by the presence of a greater number of nanoparticles. In all cases, the application of a localized magnetic field during cure guided the microcapsules towards the groove, leading to an increased concentration near the fracture location compared to control specimens. SEM of the fracture plane was used to estimate the apparent microcapsule volume fraction on the fracture surface for guided specimens since the bulk concentration was no longer representative. As can be seen from Fig. 21.6, a control

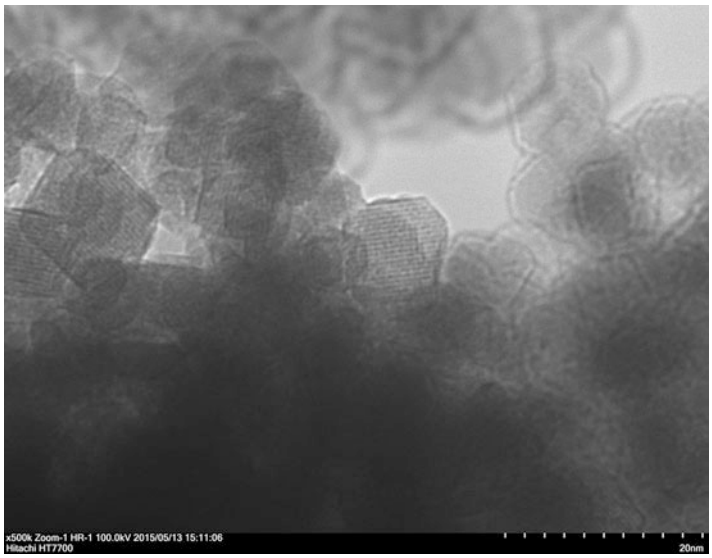

Fig. 21.2 TEM of magnetic nanoparticles

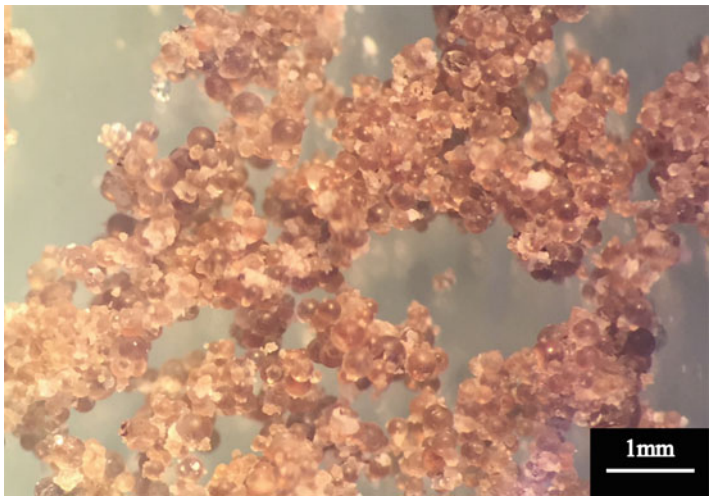

Fig. 21.3 Optical microscopy of microcapsules. Nanoparticles are the brown substance seen through the microcapsule shell walls

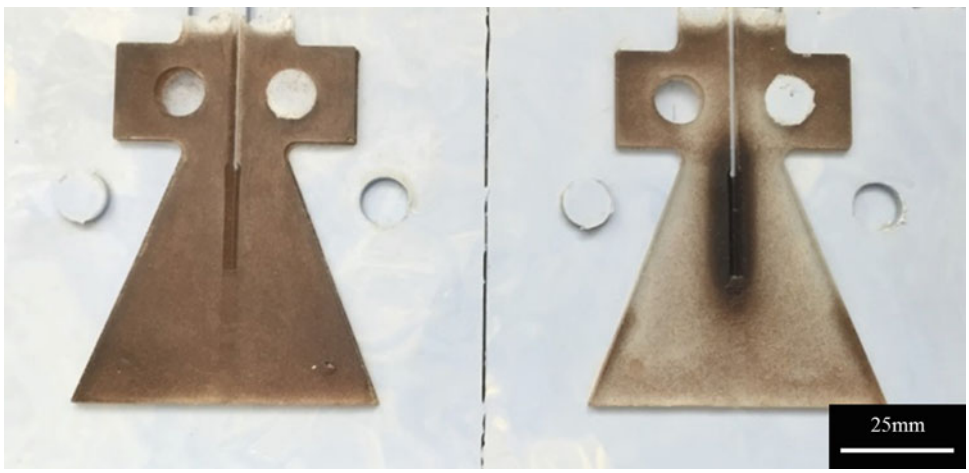

Fig. 21.4 TDCB control specimen (*left*) containing 5 % uniformly dispersed microcapsules, and a TDCB guided specimen (*right*) also containing 5 % microcapsules

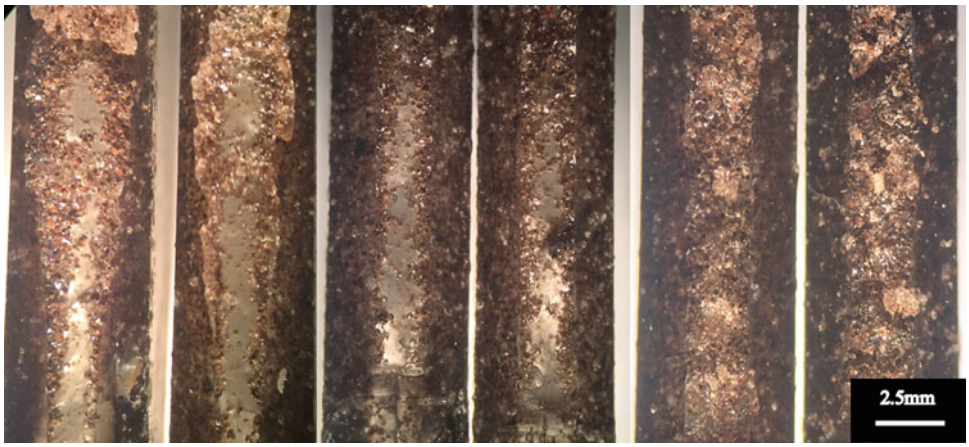

Fig. 21.5 Optical microscopy of the fracture surface of guided specimens containing (*left* to *right*): 2, 2.5 and 3 % microcapsules by weight. Note how the area fills from the outside inwards as the microcapsules stack up

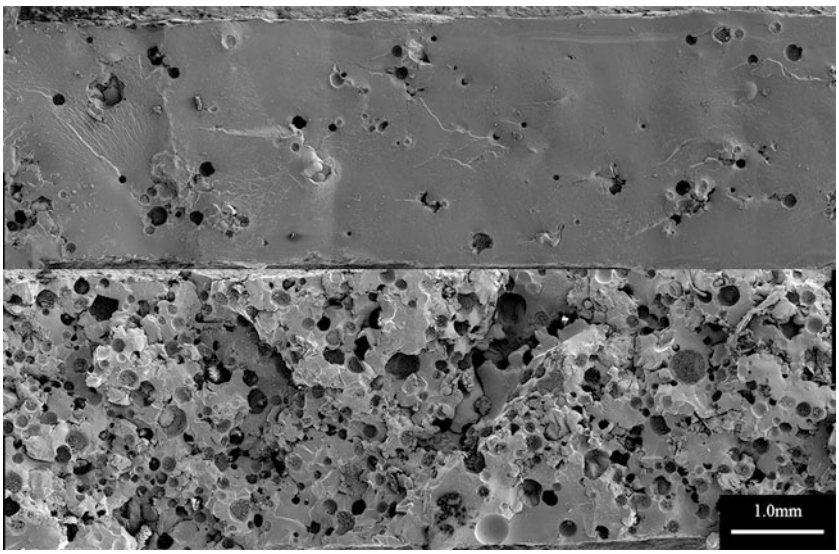

Fig. 21.6 SEM of the fracture surface of control (*top*) and guided (*bottom*) specimens, both containing nominal 4 % microcapsules by weight. Area-based estimates along the fracture indicate an apparent volume fraction of 4.1 % microcapsules for the control and 43 % for the guided specimen

specimen containing 4 % nominal weight percent microcapsules had an apparent volume fraction of 4.1 % on the fracture surface, while a guided specimen containing 4 % nominal weight percent of the same microcapsules had an apparent volume fraction of 43 % on the fracture surface, indicating that guiding achieves a tenfold increase in local microcapsule concentration.

21.3.2 Quasi-static Fracture Testing and Self-Healing Performance

A series of quasi-static fracture tests were performed using guided specimens with varying weight percentages of microcapsules. As seen in Fig. 21.7, an increase in nominal microcapsule concentration initially causes an increase in fracture toughness from 2 to 2.5 % microcapsules by weight, as expected from prior work [7]. This increase is followed by a transition from a brittle fracture failure mode to a non-linear fracture as the nominal microcapsule weight percent approaches 3–5 %. Figure 21.8 illustrates how a control specimen within this weight percent range still exhibits brittle fracture under load, while the guided specimen at that same nominal microcapsule weight percent exhibits a non-linear fracture. This difference is likely caused by high local concentrations of microcapsules displacing most of the epoxy in the test region of

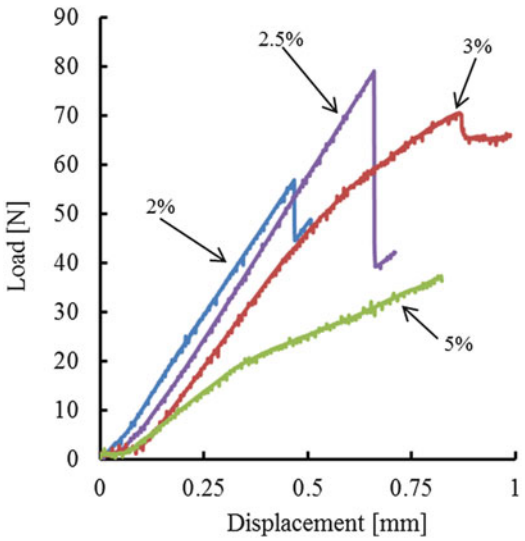

Fig. 21.7 Fracture testing for guided specimens containing microcapsules at different weight percentages

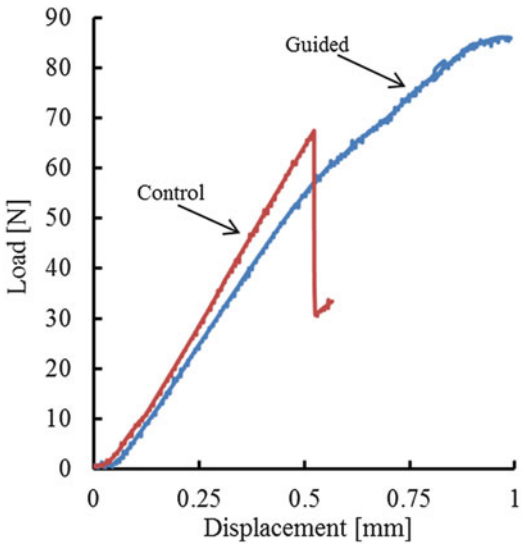

Fig. 21.8 Fracture testing comparing a control specimen and a guided specimen, each containing 4 % microcapsules by weight

guided specimens. This same change in failure mode is seen at fixed microcapsule weight percentages as nanoparticle concentration goes up. Even slight increases in microcapsule size, weight percent, or nanoparticle concentration can lead to dramatically altered material properties when the microcapsules are guided to the intended fracture location. This is because the apparent volume fraction of microcapsules in the fracture plane is higher for guided specimens than controls, even when the same nominal weight percent of microcapsules is used.

Healing efficiency was investigated for both guided specimens and controls to see what impact guiding the microcapsules had on the self-healing material performance. As can be seen from Fig. 21.9, a guided specimen at only 2 % microcapsule nominal weight percent achieved a healing efficiency of around 52 %. This is higher than the efficiency of 40.4 % observed in a control specimen at 5 % microcapsule nominal weight percent (Fig. 21.9). This implies that microcapsule guiding may actually increase self-healing performance where the microcapsules are placed. Future work will focus on using more precise microcapsule placement to improve self-healing performance at low (<1.0) microcapsule nominal weight percentages.

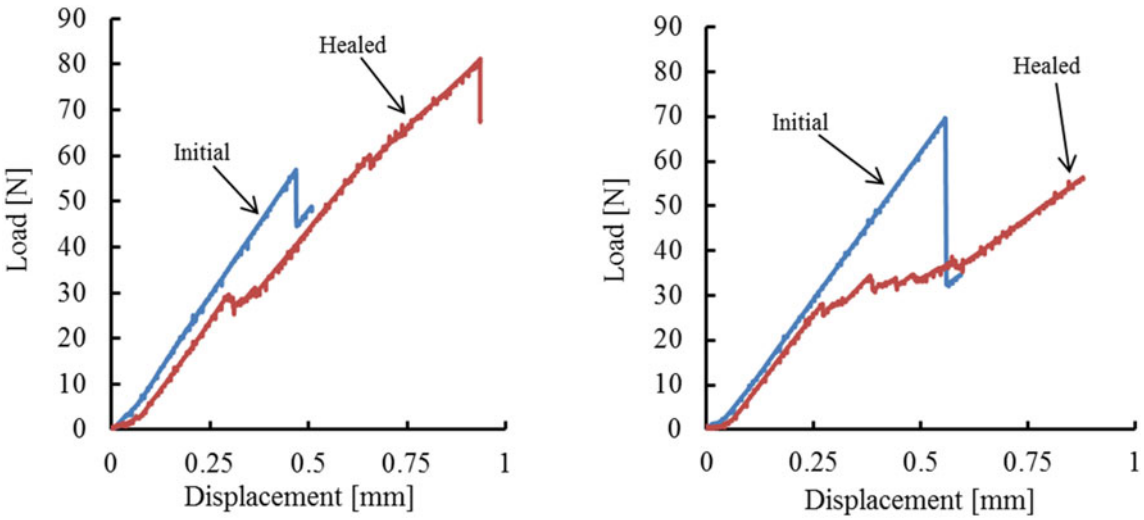

Fig. 21.9 Healing tests for a guided specimen with 2 % microcapsules by weight (*left*) and a control specimen with nominal 5 % microcapsules by weight (*right*)

21.4 Conclusions

Microcapsules containing magnetic nanoparticles were synthesized and incorporated into self-healing epoxy specimens for fracture testing. The microcapsules were successfully guided to the intended fracture location using magnetic fields. SEM of the fracture surface showed an estimated apparent volume fraction of 4.1 % for controls and 43 % for guided specimens both at 4 % microcapsule nominal weight percent. Specimens containing guided microcapsules displayed an increase in fracture toughness over control specimens when low weight percentages of microcapsules were used (less than 3 % by weight). At higher microcapsule weight percentages, guided specimens showed a transition to non-linear fracture as opposed to the brittle fracture exhibited by control specimens. These same trends were observed as nanoparticle concentration was increased within the microcapsules at fixed microcapsules weight percentages. Successful self-healing was achieved in guided specimens, with a potential increase in performance over controls.

Acknowledgment The work presented in this paper was supported by an NSF Grant (CMMI 1351760).

References

1. Trask, R.S., Bond, I.P., Williams, G.J., Williams, H.R.: Bioinspired self-healing of advanced composite materials. Collection of Technical Papers—AIAA/ASME/ASCE/AHS/ASC Structures, Structural Dynamics and Materials Conference, ISSN: 02734508 (2008)
2. Caruso, M.M., Blaiszik, B.J., White, S.R., Sottos, N.R., Moore, J.S.: Full recovery of fracture toughness using a nontoxic solvent-based healing system. Adv. Funct. Mater. **18**, 1898–1904 (2008)
3. Rule, J.D., Sottos, N.R., White, S.R.: Effect of microcapsule size on the performance of self-healing polymers. Polymer **48**, 3520–3529 (2007)
4. Brown, E.N., Kessler, M.R., Sottos, N.R., White, S.R.: In situ poly(urea-formaldehyde) microencapsulation of dicyclopentadiene. J. Microencapsul. **20**(6), 719–730 (2003)
5. Caruso, M.M., Blaiszik, B.J., Jin, H., Schelkopf, S.R., Stradley, D.S., Sottos, N.R., Moore, J.S.: Robust, double-walled microcapsules for self-healing polymeric materials. ACS Appl. Mater. Interfaces **2**(4), 1195–1199 (2010)
6. Kang, S., Baginska, M., White, S.R., Sottos, N.R.: Core-shell polymeric microcapsules with superior thermal and solvent stability. ACS Appl. Mater. Interfaces **7**(20), 10952–10956 (2015)
7. Brown, E.N., White, S.R., Sottos, N.R.: Microcapsule induced toughening in a self-healing polymer composite. J. Mater. Sci. **39**, 1703–1710 (2004)
8. Laurent, S., Saei, A.A., Behzadi, S., Panahifar, A., Mahmoudi, M.: Superparamagnetic iron oxide nanoparticles for delivery of therapeutic agents: opportunities and challenges. Expert Opin. Drug Delivery **11**(9), 1449–1470 (2014)
9. Zhao, Y., Fang, J., Wang, H., Wang, X., Lin, T.: Magnetic liquid marbles: manipulation of liquid droplets using highly hydrophobic Fe3O4 nanoparticles. Adv. Mater. **22**, 707–710 (2010)

10. Fang, M., Ström, V., Olsson, R.T., Belova, L., Rao, K.V.: Rapid mixing: a route to synthesize magnetic nanoparticles with high moment. Appl. Phys. Lett. **99**, 222501 (2011)
11. Stöber, W., Fink, A., Bohn, E.J.: Controlled growth of monodisperse silica spheres in the micron size range. J. Colloid Interface Sci. **26**, 62–69 (1968)
12. Laurent, S., Forge, D., Port, M., Roch, A., Robic, C., Vander, E.L., Muller, R.N.: Magnetic iron oxide nanoparticles: synthesis, stabilization, vectorization, physicochemical characterizations and biological applications. Chem. Rev. **108**(6), 2064–2110 (2008)
13. Brown, E.N.: Use of the tapered double-cantilever beam geometry for fracture toughness measurements and its application to the quantification of self-healing. J. Strain Anal. Eng. Des. **46**, 167–186 (2011)
14. Hamoudeh, M., Fessi, H.: Preparation, characterization and surface study of poly-epsilon caprolactone magnetic microparticles. J. Colloid Interface Sci. **300**(2), 584–590 (2006)

Chapter 22
Converse Magneto-Electric Coefficient of Composite Multiferroic Rings

Mario Lopez and George Youssef

Abstract Composite multiferroic materials for magneto-electric coupling have been investigated in the past decade as an alternative for intrinsic materials especially at room temperature. In this configuration, the magneto-electric coupling is based on the transduction of the strain between laminated piezoelectric and magnetostrictive layers. Thus, the mechanical interface plays a crucial role in the converse magneto-electric coefficient (CME). The focus of this research is to understand the dependence of CME on the bonding interface of a composite annulus with an outer axially or radially polarized piezoelectric and an inner magnetostrictive (Terfenol-D, TD) rings. The rings were epoxy-bonded in one arrangement and shrink-fitted in another. This resulted in three different sample arrangements: axially-poled PZT/epoxy/TD, axially-poled PZT/shrink/TD, and radially-poled PZT/epoxy/TD. The shrink-fit arrangement for the radially poled PZT was forfeited since the shrink-fit bonding interface under performed in axially poled configuration. The composite rings were characterized by changing the electric field from 20 to 80 kV/m, varying the frequency between 4 and 50 kHz, and the bias magnetic field between 0 and 2300 Oe. The maximum CME for epoxy-bonded rings was found to occur at lower bias magnetic field than for the shrink-fitted rings. The results show that the resonance frequency of the composite ring shifted due to change in the interface. Finally, it was found that the CME of an axially poled PZT ring arrangement is higher than a radially poled one due to saturation.

Keywords Composite multiferroics • Converse magneto-electric coefficient • Piezoelectric • Magnetostrictive • Bonding interface

22.1 Introduction

Multiferroics heterostructures consisting of ferromagnetic and ferroelectric phases have been considered for energy efficient memory and electronic devices due to its strong strain-mediated electromagnetic coupling [1–5]. Thus, the efficiency of transferring the strain from the ferromagnetic to the ferroelectric phase, in direct magneto-electric coupling, or from the ferroelectric to the ferromagnetic phase, in the converse coupling, hinges on the interface, where the strain transduction takes place [6]. When assembled epitaxially at the nanoscale, the mismatch between the lattice parameters of the ferroelectric and ferromagnetic phases results in residual strain that affect the strain transduction and in turn reduces the energy efficiency [7]. This is usually remedied by choosing materials with small lattice mismatch; nonetheless, the material candidates are limited with a quest for new materials that are stable at room temperature is an ongoing effort by scientists and engineers. Similarly, on the macroscale, the bonding layer between the heterostructure phases plays a vital role in strain-mediation, which is affected by mechanisms such as attenuation through the bonding layer thickness and shear lag [8, 9]. Majority of the research done at the macroscale focused on using a thin conductive polymer as a bonding layer, which limits the geometries that can be used due to the conformity of the adhesive tape [10–12]. Thus, experimental investigation of disc or cylindrical geometries has been limited despite the effect of the shape on magnetization, i.e. shape anisotropy [13–16]. Hence, the focus of this research on dependence of the converse magneto-electric coupling on bonding interface in composite annulus structure.

The linear constitutive piezoelectric and piezomagnetic laws, Eqs. (22.1) and (22.2), respectively, define the relationship between the mechanical, electrical, and magnetic applied and resulting fields. When combined, the strain-mediated

M. Lopez
Mechanical Engineering Department, California State University Northridge, 18111 Nordhoff Street, Northridge, CA 91330-8348, USA

G. Youssef (✉)
Mechanical Engineering Department, San Diego State University, 5500 Campanile Drive, San Diego, CA 92182-1323, USA
e-mail: gyoussef@mail.sdsu.edu

W.C. Ralph et al. (eds.), *Mechanics of Composite and Multi-functional Materials, Volume 7*,
Conference Proceedings of the Society for Experimental Mechanics Series, DOI 10.1007/978-3-319-41766-0_22

electro-magnetic coupling is achieved by applying an electrical field (E_n) across a piezoelectric layer to generate strain (ε_{ij}) that is then transduced to the ferromagnetic layer and a magnetic flux density (B_m) is induced.

$$\varepsilon_{ij} = S^p_{ijkl}\sigma_{kl} + d_{nij}E_n, \quad D_m = d_{mkl}\sigma_{kl} + \beta_{mn}E_n \tag{22.1}$$

$$\varepsilon_{ij} = S^m_{ijkl}\sigma_{kl} + \gamma_{nij}H_n, \quad B_m = \gamma_{mkl}\sigma_{kl} + \mu_{mn}H_n \tag{22.2}$$

Where, σ_{kl} is the stress tensor and D_m is the electric displacement vector. S_{ijkl} (superscript p = piezoelectric and m = piezomagnetic), d_{nij} and β_{mn} are the elastic compliance, piezoelectric coefficient, and dielectric permittivity tensors. Similarly, H_n is the magnetic field intensity vector, while γ_{nij} and μ_{mn} are the piezomagnetic coefficient and magnetic permeability tensors. Recently, Chavez and coworkers assumed force equilibrium at the interface and assumed $\varepsilon_{1,p} = \xi\varepsilon_{1,m}$ (ξ is bonding interface quality factor) to calculate the converse magneto-electric coupling coefficient (α)

$$\alpha = \left[\frac{d_{31,p}\gamma_{11,m}}{t_m S^p_{11} + \xi t_p S^m_{11}}\right] \tag{22.3}$$

where, t_p is thickness of the piezoelectric phase and t_m is thickness of ferromagnetic phase [8]. They hypothesized that $\xi \geq 1$ and discussed as the values of quality factor increases, the ability of the interface to transfer strain degrades.

22.2 Experiment Setup

22.2.1 Specimen Preparation

In this research, concentric composite ring structures consisted generally of an outer lead-zirconate-titanate (PZT, APC International: P/N-841) ring and an inner magnetostrictive Terfenol-D (ETREMA Products) ring. The nominal dimensions of the PZT rings were 30 mm-OD and 20 mm-ID, while the Terfenol-D has a nominal outer diameter of 25 mm and 5 mm wall thickness. All the rings were 5 mm in height. Three different sample configurations were constructed and characterized. Figure 22.1 shows 3D and cross-sectional views of all three-sample configurations. First (Fig. 22.1a), an axially-poled PZT and Terfenol-D rings were adhered together using a polymer epoxy (Pro-Set LAM 125/226). The two-part polymer epoxy was first thoroughly mixed, and the mixture was then applied to the inner surface of the PZT and the outer surface of the Terfenol-D rings. The latter was then inserted into the PZT ring, and the two rings were rotated with respect to one another to ensure all surfaces were properly wetted and to allow any entrapped air bubbles to escape. The composite ring was placed in an oven at 100 °C for 1 h for the epoxy to fully harden. In the second sample configuration (Fig. 22.1b), a Terfenol-D ring was cold shrink fitted into an axially-poled PZT ring, which created a negative allowance (interference). In the shrink fit process, the PZT ring was kept at room temperature while the Terfenol-D ring was cooled down in a dry ice bath. The shrunken Terfenol-D ring was then carefully inserted into the PZT ring and the assembly were kept at room temperature to reach thermal equilibrium. Finally, in the third configuration (Fig. 22.1c), a radially-poled PZT ring was adhered to Terfenol-D using conductive silver epoxy (MG Chemicals 8331-14G). The assembled composite annulus was then left to cure in ambient conditions for 24 h. In the first and second configurations, the top and bottom surfaces of the PZT rings were coated with silver and were used as electrodes to apply the electric field. In the third sample arrangement, the outer surface of the PZT and the Terfenol-D ring acted as the outer and inner electrodes, respectively. A copper search coil was wrapped radially around the composite structure to measure the strain-induced magnetic flux density, where each search coil consisted of 16 turns of 134-AWP wire.

22.2.2 Measurement Process

Figure 22.2 shows a schematic of the experimental setup used in the characterization of the converse magneto-electric coupling of concentric composite multiferroic rings. In which, a function generator (Agilent, 33210A) was used to generate a sinusoidal waveform with frequencies between 4 and 50 kHz. The output waveforms were then amplified using a high

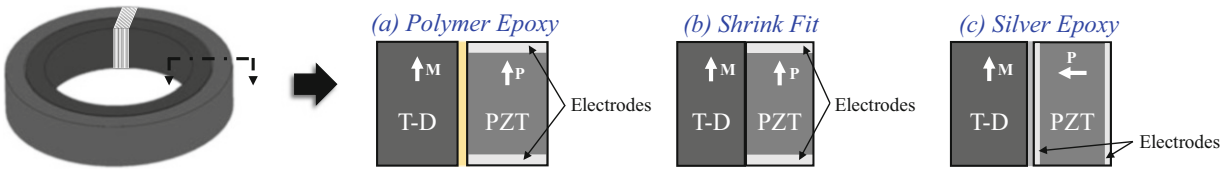

Fig. 22.1 Sample configurations

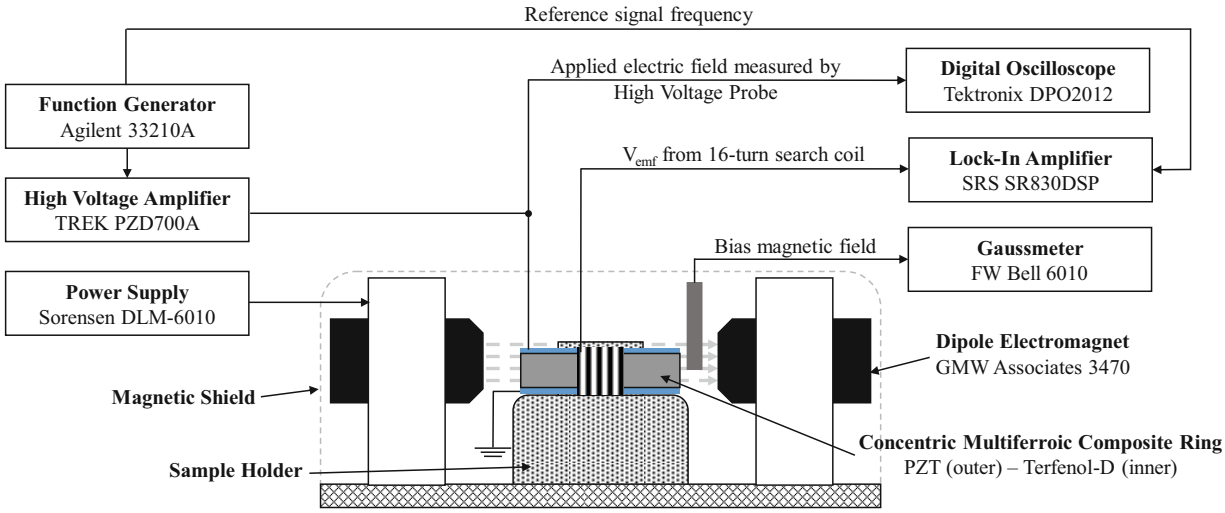

Fig. 22.2 Schematic of experimental setup (modified from [8])

voltage amplifier (TREK, PZD700A) with a set gain of 100. The amplified signal was applied across the silver electrodes (Fig. 22.1) while being monitored using high voltage probe on a digital oscilloscope (Tektronix, DPO 2012). Each sample configuration was tested at four electrical fields that ranged from 20 to 80 kV/m. Throughout the experimental investigation, the composite ring structure was placed between the poles of an electromagnet (GMW Associates, 3470) and were subjected to DC bias magnetic field that ranged from 0 to 2300 Oe. The strength of the bias magnetic field was measured using a gaussmeter (FW Bell, 6010). The strain-induced magnetic flux density was measured through a Helmholtz coil and Lock-In amplifier (Stanford Research Systems, SR830DSP). The electromagnet, the sample holder, the sample, and the gaussmeter were enclosed in magnetically shielded chamber to eliminate electromagnetic interference. The experimental setup closely mimicked the one used by Chavez et al. [8].

During the experimental characterization, first, an electric field was applied across the height and the wall thickness of the PZT ring for axially-poled and radially-poled sample configurations, respectively. The bias magnetic field was then adjusted from 0 to 2300 Oe with step size of 125 Oe. The upper limit of the bias magnetic field was selected above the field required for Terfenol-D saturation (i.e., 2000 Oe) [17, 18]. At each bias field level, the root mean square value of V_{emf} was measured and the magnetic flux density was calculated as a function of the frequency based on the number of turns in the search coil [8]. Lastly, the converse magneto-electric coefficient (CME) was calculated as the ratio of the induced magnetic flux density to the applied voltage. These steps were repeated at different applied electric fields; namely 20, 40, 60, and 80 kV/m.

22.3 Results and Discussion

Figures 22.3, 22.4, and 22.5 show the dependence of the converse magneto-electric coupling coefficient for all three-sample configurations on the bonding interface; namely epoxy-bonded axially-poled (Fig. 22.1a), shrink-fit axially-poled (Fig. 22.1b), and epoxy-bonded radially-poled (Fig. 22.1c) PZT/Terfenol-D composite ring structure, respectively. These figures also elucidate the dependence of the coupling coefficient on applied electrical field and the frequency (i.e., Fig. 22.3a–d). However, the measurements were done over a range of frequencies (4–50 kHz) as shown in Table 22.1, the figures herein only include the results in the vicinity of the resonance frequency (italicized in Table 22.1) where the

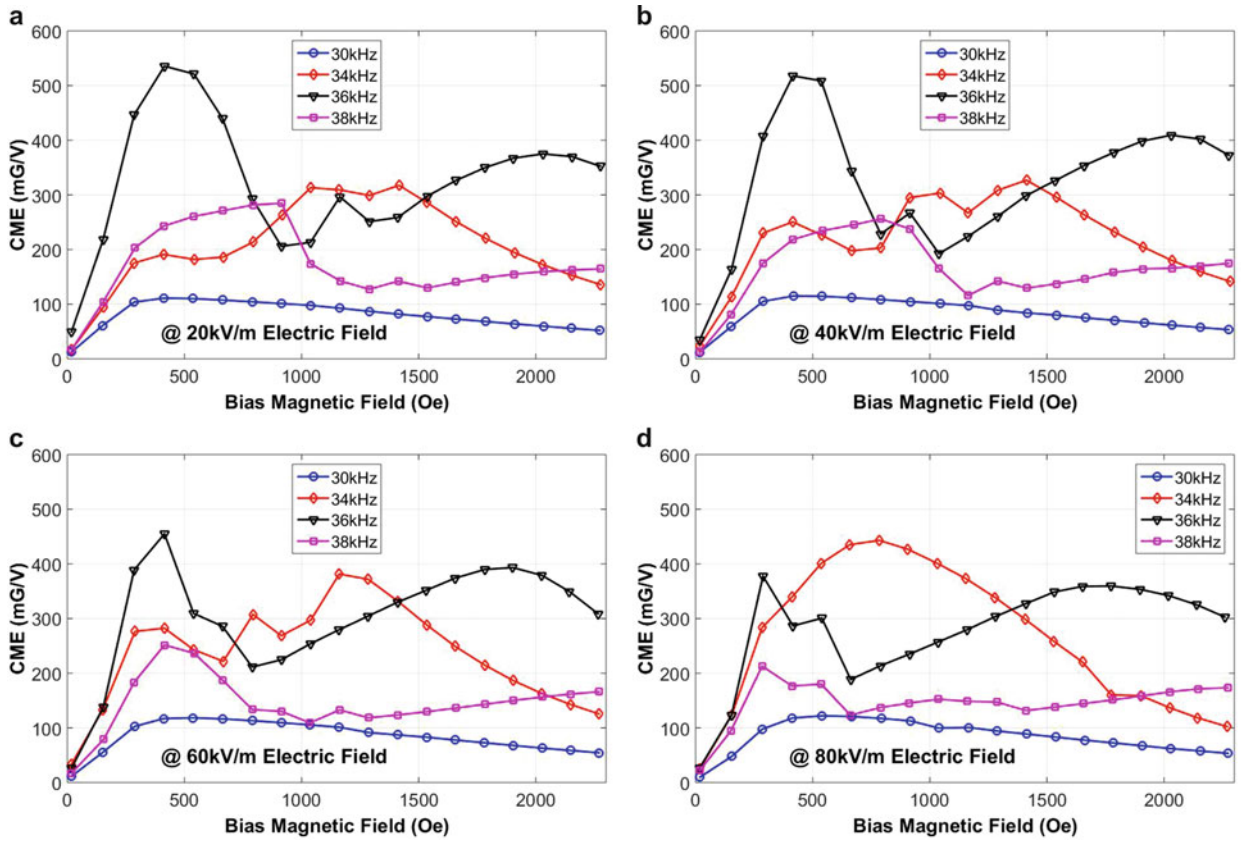

Fig. 22.3 CME response of axially-poled PZT epoxy-bonded composite multiferroic ring

maximum CME (bold in Table 22.1) is reported in all three-sample configurations. Generally, the resulting values of the CME coefficient are based on the contribution to the mechanical strain from: (1) the piezoelectric effect due to the applied electric field; (2) the magnetostriction effect due to the bias magnetic field; and (3) the interface between these phases. Important to note that generated piezoelectric and magnetostrictive strain depend on the piezoelectric and piezomagnetic properties of the specific type of PZT and Terfenol-D used in the composite structure, respectively, which have been shown previously to depend on the frequency [19–24]. In all, the experimental results expose the contribution of each of the experimental variables (electrical field, bias magnetic field, frequency, and bonding interface) to the values and behavior of CME.

Here, we emphasize four important observations based on the experimental results. First, the epoxy-bonded axially-poled PZT/Terfenol-D composite ring (Fig. 22.3) outperformed the other two configurations (Figs. 22.4 and 22.5) in magneto-electric coupling, where the maximum CME of 536 mG/V is reported at the lowest applied electrical field of 20 kV/m and a bias magnetic field of 415 Oe. The striking differences between the CME behaviors when comparing all three-sample configurations can be explained by considering the interface. The quality of the bonding interface between the ferroelectric and ferromagnetic phases of the ring structure affects the strain transduction and in turn the indirect coupling between electrical and magnetic energies [8].

Second, the shrink-fit based composite structure underperformed despite the expectation otherwise due to poor strain transfer through the interface. This underperformance is attributed to the geometrical tolerances, where the difference between the maximum material condition and least material condition of an external and internal geometrical feature, respectively, specifies the interference. It appears that the negative allowance in axially-poled shrink-fit sample configuration was small, which in turn adversely affected the strain transfer. It is then hypothesized that maximizing the negative allowance will improve the strain transfer and result in higher CME, however attaining higher degree of interference between PZT and Terfenol-D ring is an experimental challenge. Third, the maximum CME for axially-poled, polymer-epoxy sample occurred at 36 kHz, while it was reported at 34 kHz for the remaining configurations. The slight shift in the resonance frequency is mainly attributed to the change in the effective stiffness of the composite structure $\left(\omega = \sqrt{k/m}\right)$, which can be realized by considering a mechanical spring analogy of three springs connected in series to represent PZT,

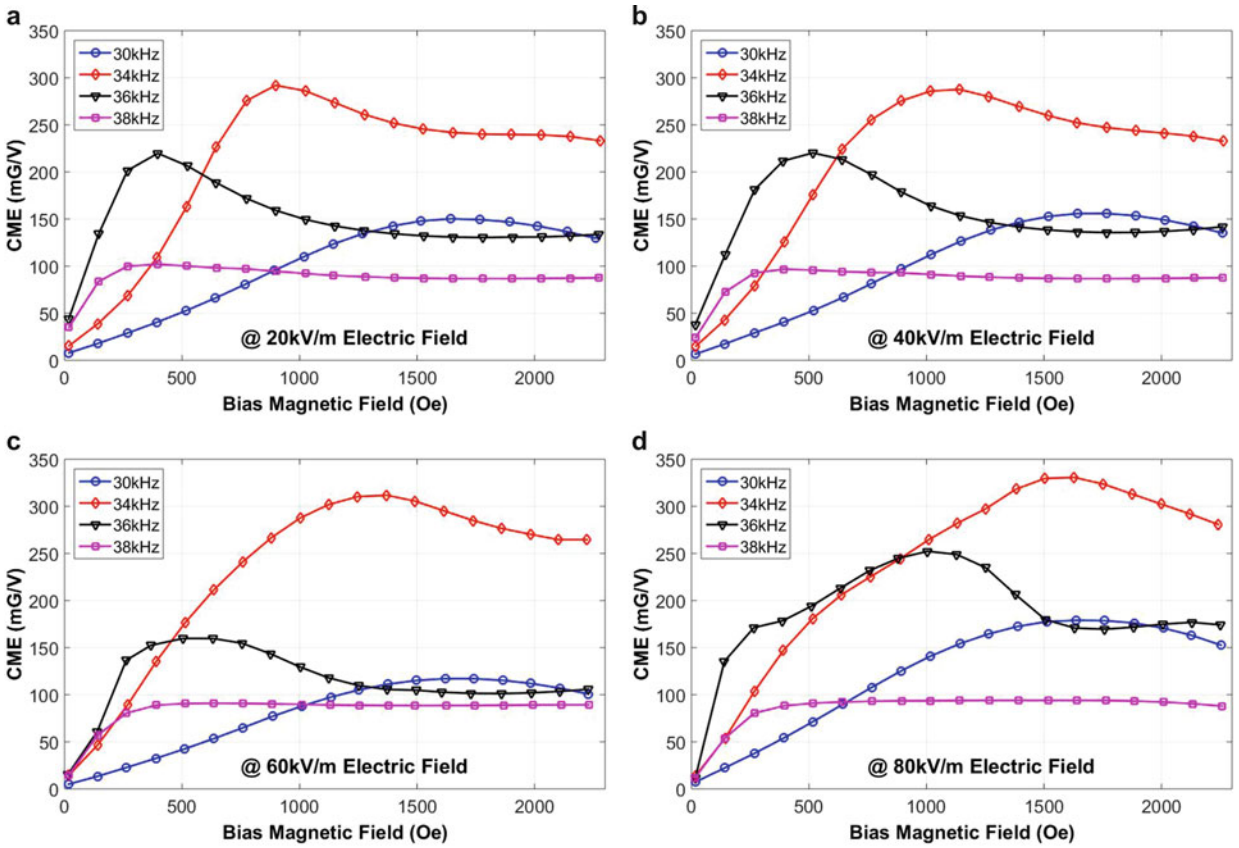

Fig. 22.4 CME response of axially-poled PZT shrink-fit composite multiferroic ring

Terfenol-D, and interface between, respectively. The middle spring, i.e. the interface, changes in stiffness from one sample configuration to another due to change in the epoxy type or the removal of epoxy (shrink-fit). For example, the elastic modulus of the polymer-epoxy is 3.39 GPa as it compares to merely 0.76 GPa for the silver-epoxy; such a difference will reduce the overall stiffness and in turn cause shift in the resonance frequency. The latter will also affect the overall generated piezoelectric and magnetostrictive strains since the properties are frequency-dependent.

Finally, however the CME values in the samples with radially-poled PZT are 7 % lower than those with axially-poled rings, the CME appeared to be clipped off at ~500 mG/V between ~400 and ~1100 Oe. When the electric field is applied across the wall-thickness, the generated piezoelectric strain that is transferred to the Terfenol-D ring is higher than in the axially-poled configuration, in which the transferred strain is based on the Poisson's effect because the electric field is applied across the height. As a result, the radial piezoelectric strain applies pressure on the Terfenol-D ring, thus lowers the magnetostriction strain and limits the strain-induced magnetic flux. The pressure-imposed limitation in magnetostriction is the primary reason for the maximum CME to occur at 20 kV/m.

22.4 Conclusion

The indirect magneto-electric coupling is based on the transduction of mechanical strain through the interface whether epoxy bonded or geometrical interference upon the application of electrical field. The strain transduction rests on the poling direction of the piezoelectric layer in relation to the direction of strain transfer; the magneto-mechanical coupling due to applied bias magnetic field; and the quality of the bonding interface. The first of which dictates the amount of pressure applied on the Terfenol-D and the corresponding limitation in the magnetostrictive strain. In summary, the CME effect of multiferroics heterostructure has been reported for three sample configurations and the results, however on the macroscale, can be used to determine the optimal configuration for fabrication of nanoscale electronic devices.

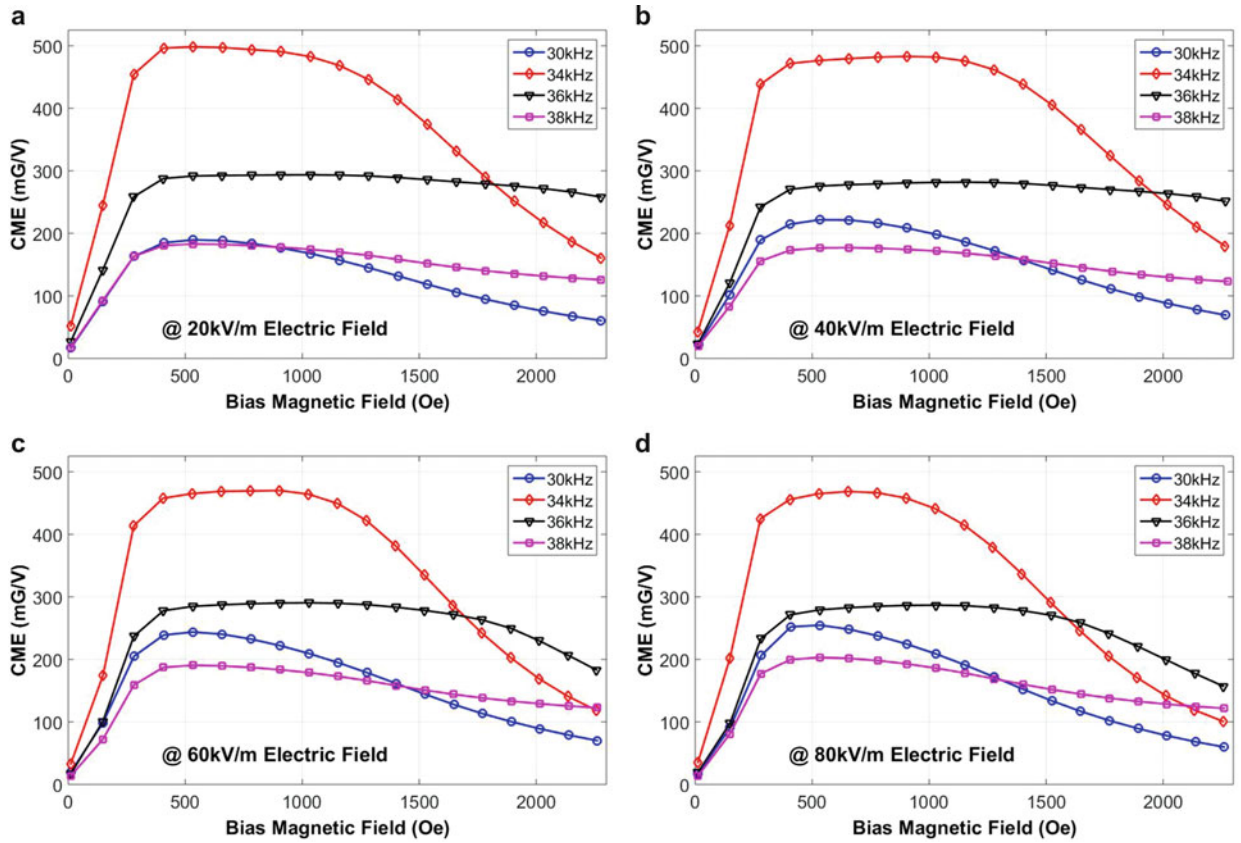

Fig. 22.5 CME response of radially-poled PZT shrink-fit composite multiferroic ring

Table 22.1 Summary of the maximum CME at different frequency and different bonding interface

	Axial epoxy			Axial shrink			Radial epoxy		
Freq. (kHz)	CME_{max} (mG/V)	H (Oe)	E (kV/m)	CME_{max} (mG/V)	H (Oe)	E (kV/m)	CME_{max} (mG/V)	H (Oe)	E (kV/m)
4	32	417	80	37	1515	80	51	658	40
6	34	415	80	46	1515	80	57	533	60
12	35	411	60	24	1642	20	35	535	80
18	94	538	40	44	1515	80	51	535	80
24	52	541	80	52	1513	80	96	535	80
30	*122*	*540*	*80*	*179*	*1637*	*80*	*255*	*533*	*80*
34	*443*	*784*	*80*	**331**	**1628**	**80**	**498**	**533**	**20**
36	**536**	**415**	**20**	*252*	*1005*	*80*	*294*	*1034*	*20*
38	*285*	*914*	*20*	*102*	*397*	*20*	*203*	*531*	*80*
45	87	1163	60	81	765	60	66	657	60
50	98	1290	60	40	393	20	31	659	60

Acknowledgment This work was supported in part by the National Science Foundation (NSF under Contract No. EEC-1160504).

References

1. Zhang, Y., Li, Z., Deng, C., Ma, J., Lin, Y., Nan, C.W.: Demonstration of magnetoelectric read head of multiferroic heterostructures. Appl. Phys. Lett. **92**(15), 7–10 (2008)
2. Priya, S., Islam, R., Dong, S., Viehland, D.: Recent advancements in magnetoelectric particulate and laminate composites. J. Electroceram. **19** (1), 149–166 (2007)
3. Srinivasan, G.: Magnetoelectric composites. Annu. Rev. Mater. Res. **40**(1), 153–178 (2010)

4. Nan, C.W., Bichurin, M.I., Dong, S., Viehland, D., Srinivasan, G.: Multiferroic magnetoelectric composites: historical perspective, status, and future directions. J. Appl. Phys. **103**, 031101 (2008)
5. Hu, J.-M., Nan, T., Sun, N.X., Chen, L.-Q.: Multiferroic magnetoelectric nanostructures for novel device applications. MRS Bull. **40**(09), 728–735 (2015)
6. Nan, C.W.: Magnetoelectric effect in composites of piezoelectric and piezomagnetic phases. Phys. Rev. B **50**(9), 6082–6088 (1994)
7. Arnaudas, J.I., De La Fuente, C., Ciria, M., Benito, L., Dufour, C., Dumesnil, K., Del Moral, A.: Magnetoelastic stresses in epitaxial (1 1 0) Terfenol-D thin films. J. Magn. Magn. Mater. **240**(1–3), 389–391 (2002)
8. Chavez, A., Lopez, M., Youssef, G.: Converse magneto-electric coefficient of concentric multiferroic composite ring. J. Appl. Phys. **119**, 233905 (2016)
9. Chang, C.-M., Carman, G.: Modeling shear lag and demagnetization effects in magneto-electric laminate composites. Phys. Rev. B **76**(13), 132116 (2007)
10. Hockel, J.L., Wu, T., Carman, G.P.: Voltage bias influence on the converse magnetoelectric effect of PZT/terfenol-D/PZT laminates. J. Appl. Phys. **109**(6), 064106 (2011)
11. Wu, T., Chang, C.M., Chung, T.K., Carman, G.: Comparison of effective direct and converse magnetoelectric effects in laminate composites. IEEE Trans. Magn. **45**(10), 4333–4336 (2009)
12. Wu, T., Chung, T.K., Chang, C.M., Keller, S., Carman, G.: Influence of electric voltage bias on converse magnetoelectric coefficient in piezofiber/Metglas bilayer laminate composites. J. Appl. Phys. **106**(5), 054114 (2009)
13. Wu, G., Zhang, R., Li, X., Zhang, N.: Resonance magnetoelectric effects in disk-ring (piezoelectric - magnetostrictive) composite structure. J. Appl. Phys. **110**(12) (2011)
14. Dong, S., Li, J.F., Viehland, D.: Voltage gain effect in a ring-type magnetoelectric laminate. Appl. Phys. Lett. **84**(21), 4188–4190 (2004)
15. Dong, S., Bai, J.G., Zhai, J., Li, J.F., Lu, G.Q., Viehland, D., Zhang, S., Shrout, T.R.: Circumferential-mode, quasi-ring-type, magnetoelectric laminate composite-a highly sensitive electric current and/or vortex magnetic field sensor. Appl. Phys. Lett. **86**(18), 182506 (2005)
16. Leung, C.M., Or, S.W., Zhang, S., Ho, S.L.: Ring-type electric current sensor based on ring-shaped magnetoelectric laminate of epoxy-bonded Tb0.3Dy0.7Fe1.92 short-fiber/NdFeB magnet magnetostrictive composite and Pb(Zr, Ti)O3 piezoelectric ceramic. J. Appl. Phys. **107**(9), 09D918 (2010)
17. Sandlund, L., Fahlander, M., Cedell, T., Clark, A.E., Restorff, J.B., Wun-Fogle, M.: Magnetostriction, elastic moduli, and coupling factors of composite Terfenol-D. J. Appl. Phys. **75**(10), 5656–5658 (1994)
18. Dapino, M.J., Faidley, L.E., Flatau, A.B., Smith, R.C.: A coupled structural-magnetic strain and stress model for magnetostrictive transducers. J. Intell. Mater. Syst. Struct. **11**(2), 135–152 (2000)
19. Zhang, Q.M., Zhao, J.: Electromechanical properties of lead zirconate titanate piezoceramics under the influence of mechanical stresses. IEEE Trans. Ultrason. Ferroelectr. Freq. Control **46**(6), 1518–1526 (1999)
20. Aljanaideh, O., AL-Tahat, M.D., Al Janaideh, M.: Rate-bias-dependent hysteresis modeling of a magnetostrictive transducer. Microsyst. Technol. **22**(4), 883–892 (2016)
21. Ruiz De Angulo, L., Abell, J.S., Harris, I.R.: Magnetostrictive properties of polymer bonded Terfenol-D. J. Magn. Magn. Mater. **157–158**, 508–509 (1996)
22. Greenough, R.D., Wharton, A.D.: Methods and techniques to characterise Terfenol-D. Science **258**, 114–117 (1997)
23. Masys, A.J., Ren, W., Yang, G., Mukherjee, B.K.: Piezoelectric strain in lead zirconate titante ceramics as a function of electric field, frequency, and dc bias. J. Appl. Phys. **94**(2), 1155–1162 (2003)
24. Benčan, A., Malič, B., Drnovšek, S., Tellier, J., Rojac, T., Pavlič, J., Kosec, M., Webber, K.G., Rödel, J., Damjanovic, D.: Structure and the electrical properties of Pb(Zr, Ti)O_3—zirconia composites. J. Am. Ceram. Soc. **95**(2), 651–657 (2012)

Chapter 23
In-Situ Sensing of Deformation and Damage in Nanocomposite Bonded Surrogate Energetic Materials

Engin C. Sengezer and Gary D. Seidel

Abstract The current work aims to explore the potential for in-situ structural health monitoring in polymer bonded energetic materials through the introduction of carbon nanotubes (CNTs) into the binder phase as a means to establish a significant piezoresistive response through the resulting nanocomposite binder. The experimental effort herein is focused towards electro-mechanical characterization of surrogate materials in place of actual energetic (explosive) materials in order to provide proof of concept for the strain and damage sensing. The electrical conductivity and the piezoresistive behavior of samples containing randomly oriented MWNTs introduced into the epoxy (EPON 862) binder of 70 wt% ammonium perchlorate-epoxy hybrid composites are quantitatively and qualitatively evaluated. Brittle failure going through linear elastic behavior, formation of microcracks leading to reduction in composite load carrying capacity and finally macrocracks resulting in eventual failure are observed in the mechanical response of MWNT-ammonium perchlorate-epoxy hybrid composites. Incorporating MWNTs into local polymer binder improves the effective stiffness about 42 % compared to neat ammonium perchlorate-polymer samples. The real time in-situ relative change in resistance for MWNT hybrid composites captured low values of applied strains less than 0.2 %.

Keywords Energetics • Carbon nanotube • Nanocomposite • Piezoresistivity • Structural health monitoring

Nomenclature

CNTs	Carbon nanotubes
MWNTs	Multi walled carbon nanotubes
PBXs	Polymer bonded explosives
SHM	Structural health monitoring
wt	Weight

23.1 Introduction

Energetic materials, such as polymer bonded explosives (PBXs) [1–9] which are composed of two phases, namely, the explosive material and a polymeric binder, are a class of composite materials designed to a chemical reaction in response to a trigger, releasing a large amount of energy. These energetic materials are comprised of crystals of explosives such as HMX (cyclotetramethylene-tetranitramine), RDX (Trinitroperhydro-triazine), PETN (pentaerythritol-tetranitrate), or TATB (triamino-trinitrobenzene) which are present with grain size around 200 μm [10]. Polymer binder materials, e.g. estane (thermoplastic polyurethanes), Viton-A (fluoropolymer binder), KEL-F (poly(chlorotrifluoroethylene-*co*-vinylidene fluoride)), BDNPA (bis(2,2-dinitropropyl)acetal) are used in these composites which typically constitute around 10 % or less of the volume. Peeters et al. [1] performed tensile and compression testing for different strain rates at room temperature on PBX 9501, PBX 9502, and 900-10 mock materials, as wells as creep and cyclic tests for each material not only to provide a data set for energetic materials constitutive model development, but also to obtain a phenomenological characterization of

E.C. Sengezer (✉) • G.D. Seidel
Department of Aerospace and Ocean Engineering, Virginia Polytechnic Institute and State University, Randolph Hall (0203), Blacksburg, VA 24061, USA
e-mail: sengezer@vt.edu

W.C. Ralph et al. (eds.), *Mechanics of Composite and Multi-functional Materials, Volume 7*,
Conference Proceedings of the Society for Experimental Mechanics Series, DOI 10.1007/978-3-319-41766-0_23

energetics. Liu et al. [2] investigated the fracture process of PBS 9501 sugar mock, a PBX 9501 high explosive simulant mock. The most dominating mechanical failure mechanism in high explosives of microcrack initiation and propagation was similarly observed in PBS 9501 sugar mock material. Liu et al. [3] also tested Mock 900-21, a PBX 9501 high explosive simulant which was subjected to monotonic and cyclic loading in order to assess the macroscopic crack formation and its extension in these materials. It was postulated that the heterogeneity in the microstructure of the energetic material led to macroscopic crack formation.

The explosive event is usually divided into various stages: ignition, the growth of deflagration (burning) and deflagration to detonation transition (DDT). In many situations which involve accidental low velocity impact during transportation and handling or tool drop, ignition of energetic material make PBXs highly sensitive. Therefore, what is needed is a way to monitor in situ microstructural changes in real time during a mechanical insult event via structural health monitoring. At present structural health monitoring efforts focus primarily on the sensors and sensing systems for detecting instances and locations of damage through techniques such as X-ray, microCT, acoustic emission, lamb wave, impedance methods, etc., which only detect cracks at relatively large length scales above 100 μm and rely on rely heavily on sensors and sensing systems which are external to the material system. Distributing the sensing network throughout the binder phase of energetic composites in an effort for real time embedded sensing of strain and damage in energetic materials through piezoresistive response for structural health monitoring in energetic materials may be invaluable in reducing the stochastic nature of safety characterization and may help in designing insult tolerant energetic materials. In the current work, the electro-mechanical characterization of surrogate ammonium perchlorate-MWNT-epoxy hybrid composites is conducted in order to provide proof of concept for in-situ strain and damage sensing in nanocomposite bonded energetics. It is expected that the results presented in the current work will provide basis to explore in-situ detection of strain and damage state and prognostocation of remaning life of nanocomposite bonded polymer explosives.

23.2 Experimental

23.2.1 Preparation of MWNT-Ammonium Perchlorate-Epoxy Hybrid Composites

In this preliminary study, MWNTs and ammonium perchlorate have been dispersed in the EPON™ Resin 862/EPIKURE™ Curing Agent W. The epoxy system was selected as the binder for its general coating and bonding applications along with its low viscosity and very long working life at room temperature. The pristine MWNTs (PD15L1-5) (NanoLab) were reported to have a purity of more than 95 %, ~15 nm outer diameter and average nanotube lengths between 1 and 5 μm. Ammonium perchlorate (NH_4ClO_4) was used as a surrogate material in place of actual explosive materials. Neat ammonium perchlorate-epoxy samples were prepared with a weight ratio of 70/30 (corresponding to 59 vol.% NH_4ClO_4) to obtain the neat ammonium perchlorate-epoxy mixture, with this ratio likewise being maintained in the preparation of hybrid binder samples having concentrations of 0.5 wt% MWNTs relative to the entire MWNTs-ammonium perchlorate-epoxy sample (corresponding to 1.65 wt% MWNTs relative to the epoxy). In preparing hybrid composite samples, MWNTs were added first to the lower viscosity fast evaporating acetone solvent with 2.5 mL acetone used for each 0.01 g of MWNTs. MWNTs were dispersed in acetone using bath sonication for 1 h with a QsonicaSonicator 4000 operating at 20 kHz and amplitude of 25 % in order to obtain a more uniform initial dispersion of MWNTs. EPON™ Resin 862 was added to the predispersed MWNTs-acetone solutions and resonicated for an additional hour with the same settings to obtain a homogeneous MWNT distribution within the epoxy. Acetone was evaporated from the solutions using a Buchi Rotavapor RII rotary evaporator with heating bath at 50 °C. The evaporated solution was mixed at 20 kHz and amplitude of 10 % with a 3/16″ Microtip probe for 5 min on a pulse mode 1 min on/1 min off. The aforementioned curing agent was added to the viscous final mixture and blended thoroughly with lab spoon using mechanical stirring. Then, 70 wt% (59 vol.%) surrogate material was added the prepared solution and blended thoroughly with the same method. The prepared mixtures were degassed under vacuum for an hour and then cast into silicon mold and cured at 121 °C for 4 h. Figure 23.1 shows the resulting specimens prepared for quasi-static tensile testing. The neat ammonium perchlorate-epoxy and MWNTs-ammonium perchlorate-epoxy hybrid composite specimens have a gage length of 50 mm corresponding to ASTM standard D638 for specimen type I.

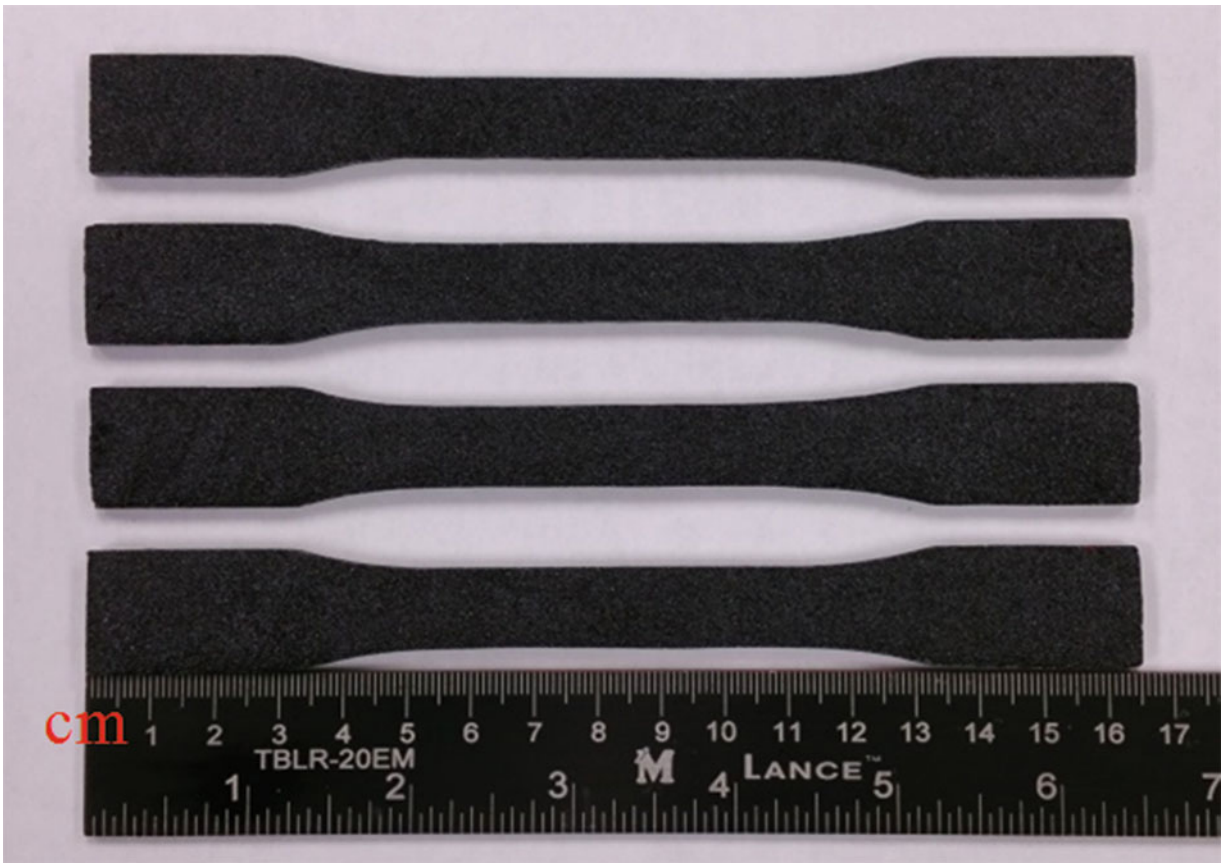

Fig. 23.1 As-produced, randomly oriented 0.5 wt% MWNT-70 wt% ammonium perchlorate-epoxy hybrid composites

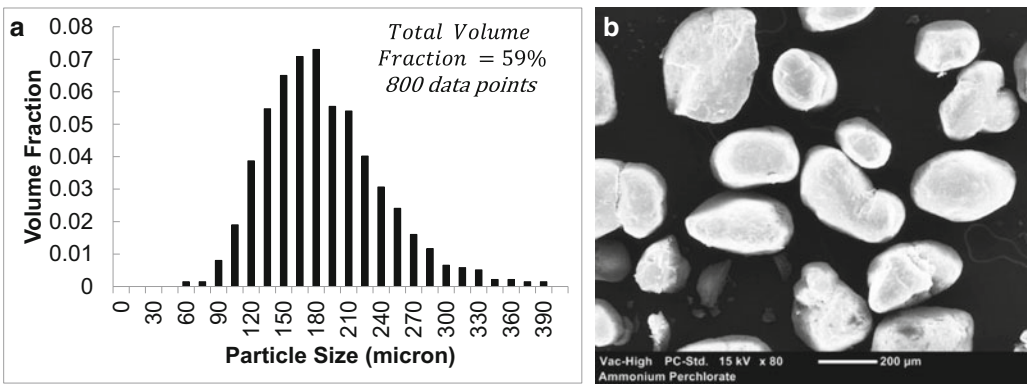

Fig. 23.2 (**a**) Ammonium perchlorate crystals size distribution correlated to 59 vol.% and (**b**) SEM micrograph of NH_4ClO_4

23.2.2 Morphological Characterization

Ammonium perchlorate were firstly investigated using a Hirox high magnification (350–7000×) optical microscope to assess the surrogate crystal size distribution. The size distribution of ammonium perchlorate crystals can be observed with associated average length scales of ~180 µm in Fig. 23.2. A NeoScope JCM-5000 Benchtop scanning electron microscope was used to conduct fracture surface topography characterization of neat and MWNTs-ammonium perchlorate-epoxy hybrid composites after mechanical testing.

23.2.3 Electrical and Piezoresistive Characterization

The electrical properties of as-produced neat ammonium perchlorate-epoxy and randomly oriented MWNT-ammonium perchlorate-epoxy hybrid composite samples were measured using an Agilent Technologies E4980A Precision LCR Meter via a two terminal method. The 8331 Silver conductive epoxy was used as to construct electrodes. The piezoresistive behavior of the as-produced hybrid composites were obtained using LCR meter by applying 2 V at 10 kHz in conjunction with mechanical testing. Average resistance readings over eight data point were obtained from LCR meter and correlated to applied strain from crosshead displacement during mechanical loading. The electrode placements for measuring piezoresistive response through instantaneous resistance change ($\Delta R/R_0$ where R_0 is initial resistance) as the specimens undergo deformation were cemented on top and bottom of the gauge section at distance 50 mm apart on alternate sides of the sample to obtain volume resistivity measurements. Tensile tests were carried out in accordance with ASTM D638. The quasi static monotonic was implemented at constant crosshead displacement rates of 0.1 mm/min corresponding to a strain rate of 0.000869 mm/mm/min.

23.3 Results and Discussion

23.3.1 Fracture Surface Topography

Hybrid surrogate material samples have inherently multiscale material architectures with microstructural features ranging the nanoscale (nanotubes) and the mesoscale (nanotube network) in the hybrid material to the microscale (grains) and macroscale of hybrid samples. In order to assess key morphological features of the as-produced neat ammonium perchlorate-epoxy and MWNT-ammonium perchlorate-epoxy hybrid composites such as MWNT and surrogate crystal distribution, Scanning Electron Microscopy (SEM) was used. Figure 23.3 provides the SEM (NeoScope JCM-5000 Benchtop) micrographs of neat-59 vol.% ammonium perchlorate-epoxy fracture surface where the size distribution of sugar crystals can be observed with associated average length scales of ~200 μm. Additionally, regions of crystal pull-outs are observed in contrast to the polymer coated crystal surfaces. The surfaces of these pull-outs appear to have epoxy polymer left behind during the fracture event indicating that fracture appears to have occurred in the binder phase. Figure 23.4 shows SEM micrographs for 0.5 wt% MWNT (1.65 wt% relative to epoxy)-hybrid composite fracture surfaces. It is not until the scale is reduced to the order of 5–10 μm in Fig. 23.4b, c that bundles/agglomerations of MWNTs are observed in the form of white clouds/specs on the fracture surface in the local binder region.

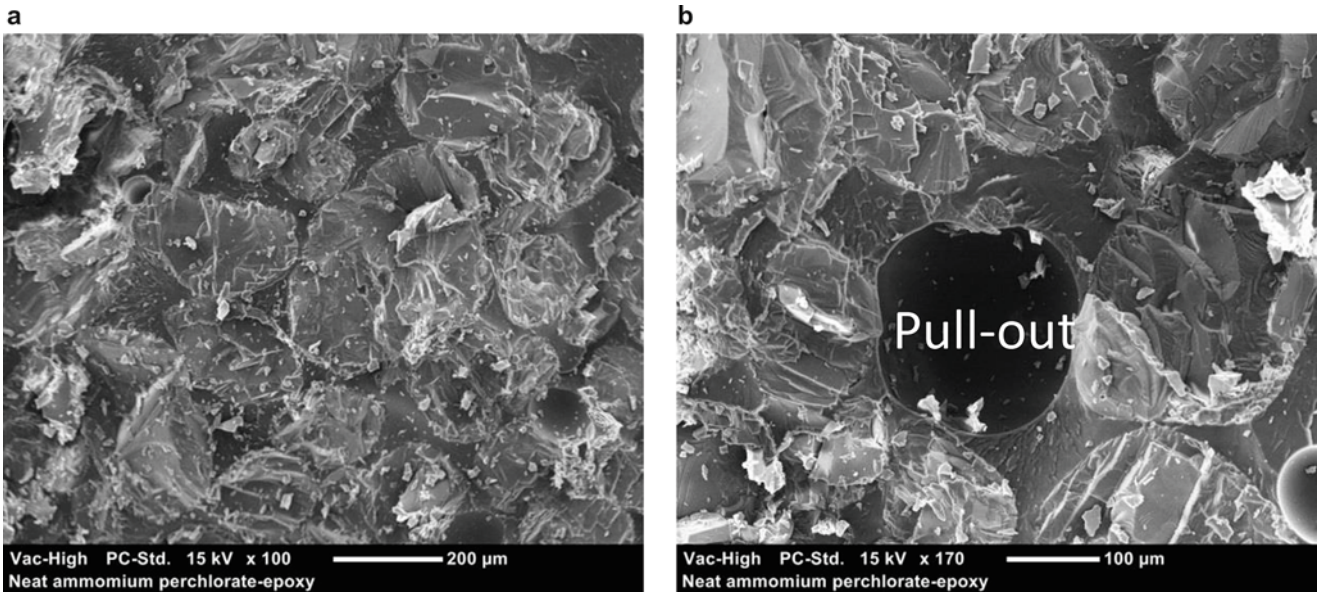

Fig. 23.3 SEM micrographs of neat-59 vol.% ammonium perchlorate-epoxy fracture surface

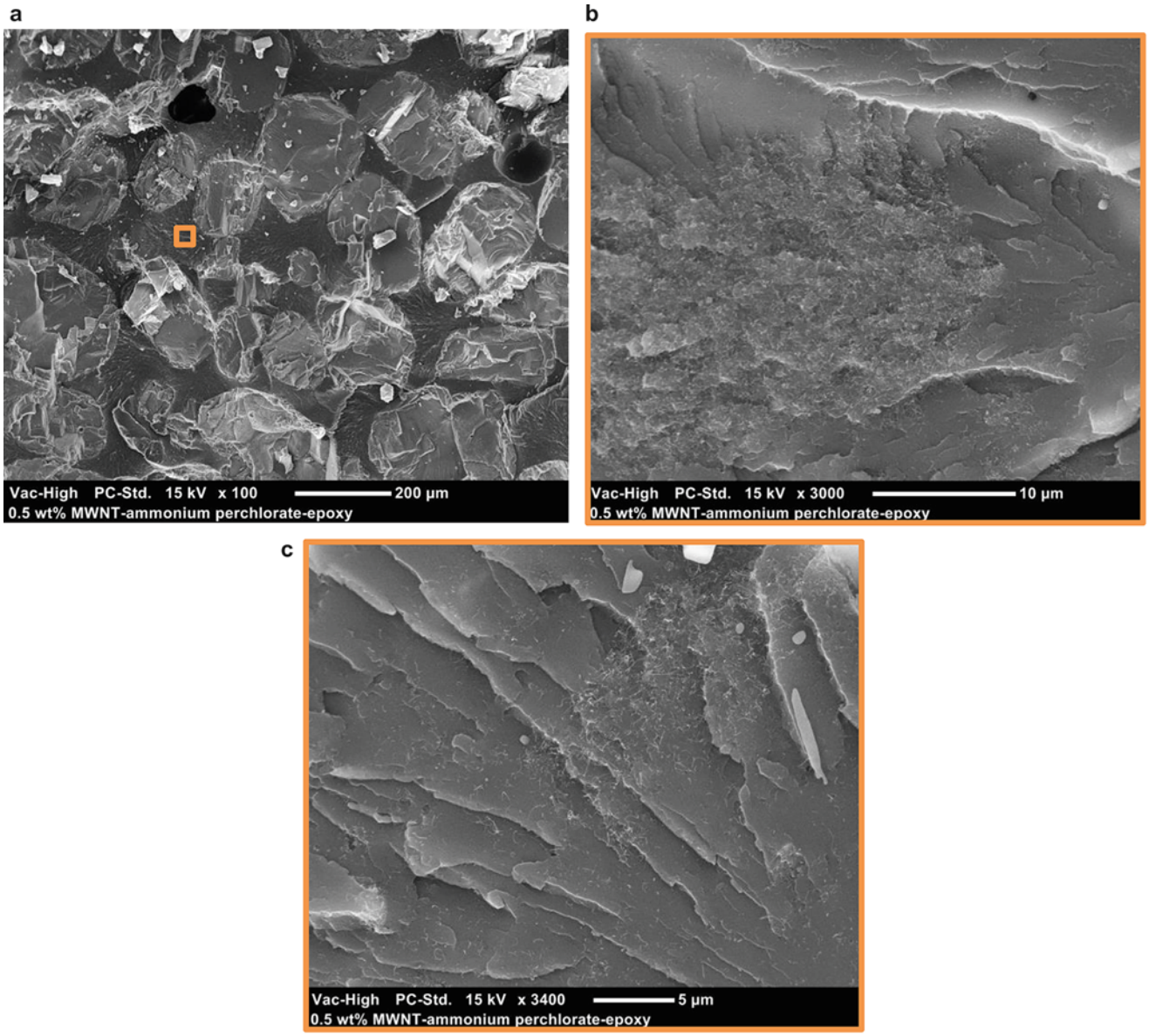

Fig. 23.4 SEM micrographs of hybrid composite fracture surface for 0.5 wt% MWNT (1.65 wt% relative to epoxy) samples at different zoomed scales

23.3.2 Electrical Properties

Figure 23.5 shows the log–log scale plot of the frequency dependence (range: 20 Hz–2 MHz) of real part, imaginary part and absolute AC conductivity for as-produced hybrid composites. Neat ammonium perchlorate-epoxy composite conductivity is plotted to provide a baseline measurement from which to assess the effect of MWNT on the electrical conductivity. For the neat ammonium perchlorate-epoxy samples, both the epoxy and the ammonium perchlorate crystals are expected to have very low conductivity and thus the effective composite displays strong insulator-like behavior, i.e. frequency dependence as a function of the input measurement frequency (20 Hz–2 MHz). It is noted that at 20 Hz measurement frequency, conductivity measurements for the neat ammonium perchlorate-epoxy show high degree of fluctuation because of their low conductivities. The absolute AC conductivity increases from ~6.7E−10 S/cm at low frequency (20 Hz) to ~2.3E−5 S/cm at high frequency (2 MHz). On addition of highly conductive MWNTs, the conductivity of the MWNT-ammonium perchlorate-epoxy composite is observed to increase from that of the baseline ammonium perchlorate-epoxy composite. As

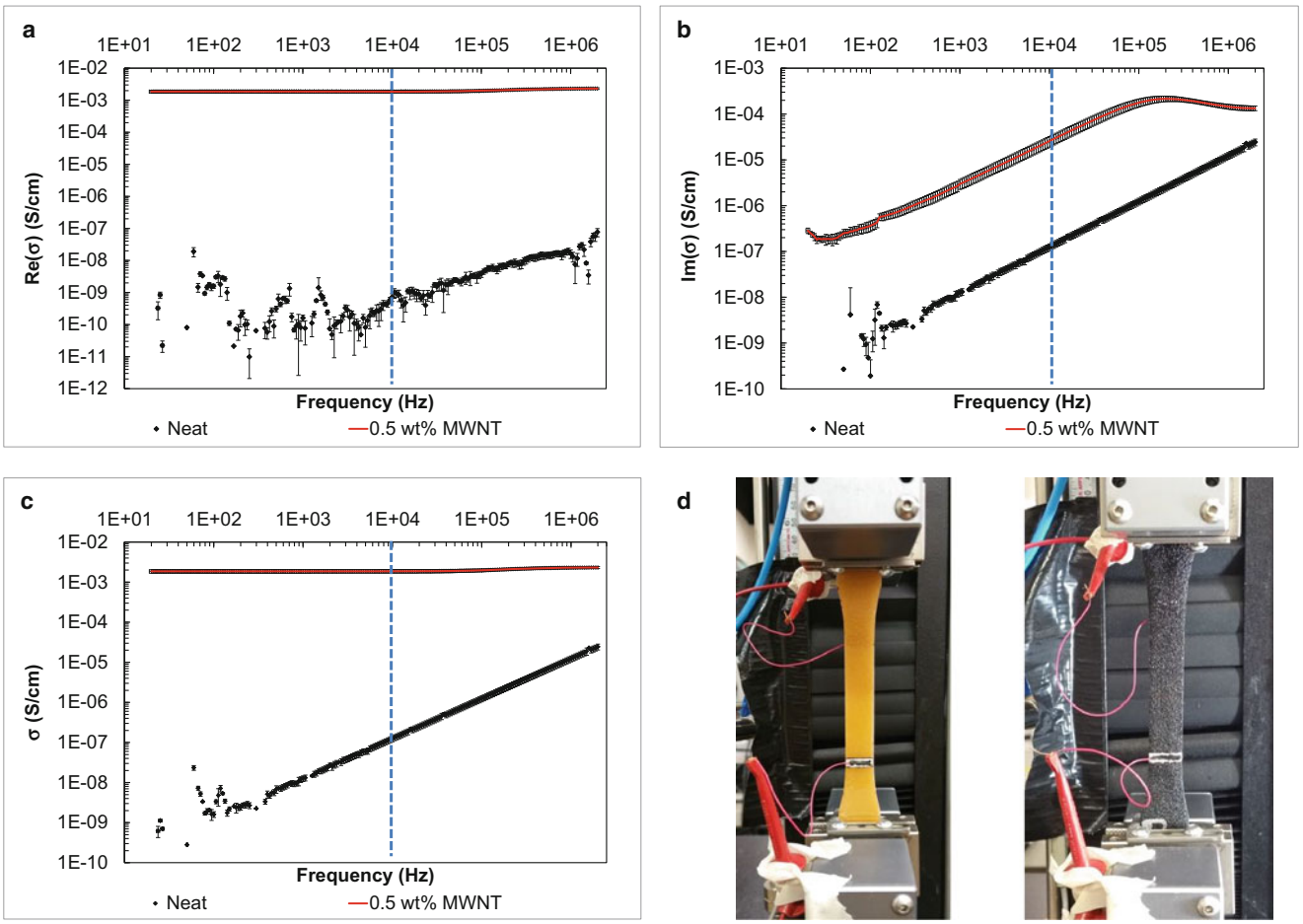

Fig. 23.5 Assessment of neat and hybrid composites' (**a**) real part (**b**) imaginary part of AC electrical conductivity (**c**) absolute AC electrical conductivity at various measurement frequencies associated (**d**) conductive epoxy electrodes cemented on top and bottom of the gauge section of the neat ammonium perchlorate-epoxy and hybrid composite dogbone specimen at distance 50 mm apart to obtain volume conductivity measurements. The marked frequency (10 kHz) indicates the frequency at which the resistance measurements were made during piezoresistive testing

an example, at 20 Hz input measurement frequency, the real part of AC conductivity of the neat and 0.5 wt% MWNT hybrid composites is observed to be about 3.26E−10 S/cm and 1.86E−3 S/cm, respectively. The increase in effective conductivity is attributed to formation of conductive pathways within the local polymer binder (i.e. nanotube networks) which make the binder more conductive as MWNT weight concentration is increased. The effective conductivity for 0.5 wt% MWNT-ammonium perchlorate-epoxy hybrid composites demonstrated a seven order of magnitude increase in conductivity at low measurement frequency (20 Hz) as compared to the neat ammonium perchlorate-epoxy samples corresponding to a value of 1.86E−3 S/cm. It was observed that the absolute AC conductivity is dominated by the real part of AC conductivity for MWNT hybrid composites. In addition, 0.5 wt% MWNT hybrid composites' conductivity was observed to be frequency independent as compared to the neat ammonium perchlorate-epoxy, which is an indication that the 0.5 wt% MWNT hybrid composites is already well above percolation threshold, which will have a negative effect in piezoresistive measurements.

23.3.3 Mechanical Properties of MWNT-Ammonium Perchlorate-Epoxy Hybrid Composites

Tensile tests were conducted to evaluate the mechanical properties of as-produced neat ammonium perchlorate-epoxy and randomly oriented MWNT-ammonium perchlorate-epoxy hybrid composite dogbone samples. Figure 23.6 shows various neat and 0.5 wt% MWNT-ammonium perchlorate-epoxy stress-strain responses in order to compare the results of mechanical testing. The corresponding stress-strain responses undergoes a brittle failure going through linear elastic behavior,

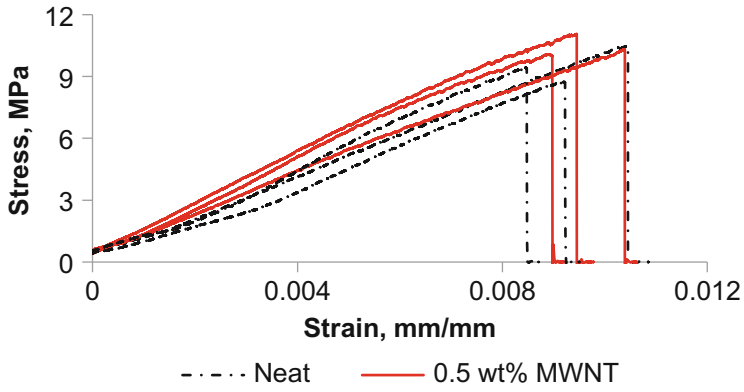

Fig. 23.6 Stress-strain curves for neat ammonium perchlorate-epoxy and randomly oriented MWNT-ammonium perchlorate-epoxy hybrid composites

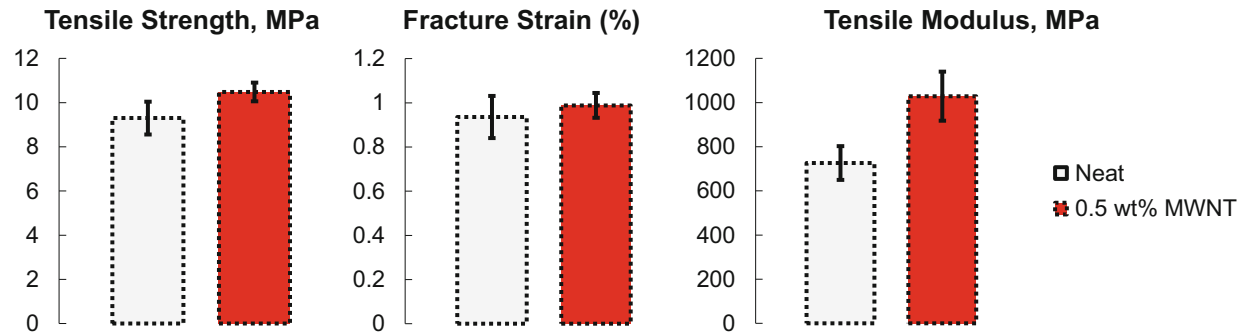

Fig. 23.7 The resulting mechanical properties: tensile strength, fracture strain and Young's modulus

formation of microcracks leading slight reductions on load carrying capacity and finally macrocracks result in eventual failure in the mechanical response of MWNT-ammonium perchlorate-epoxy hybrid composite. The resulting values for tensile strength, Young's modulus and fracture strain for the investigated samples are provided in Fig. 23.7. The average tensile strength for neat ammonium perchlorate-epoxy was measured to be 9.3 ± 0.74 MPa. Incorporation of randomly oriented MWCNT into epoxy polymer was found to lead a small improvement in the tensile strength. For instance, the nanocomposites with 0.5 wt% MWCNT relative to the entire MWNTs-ammonium perchlorate-epoxy sample (corresponding to 1.65 wt% MWNTs relative to the epoxy) have about 12 % higher strength (10.48 ± 0.42 MPa) than the neat ammonium perchlorate-epoxy samples. This increase might be explained by dispersion state of untreated (pristine) MWNTs within local polymer binder, leading to a slight improvement in the load transfer efficiency at the interface regions between MWNTs and surrounding local polymer binder. The average fracture strains for neat ammonium perchlorate-epoxy and 0.5 wt% MWCNT-ammonium perchlorate-epoxy were measured to be 0.93 ± 0.09 and 0.99 ± 0.05 %. On the other hand, addition of MWNTs into epoxy binder had a substantial effect on the stiffness of the hybrid composites. The average tensile modulus value for neat ammonium perchlorate-epoxy was measured to be 726 ± 77 MPa. The tensile modulus of 0.5 wt% MWCNT-ammonium perchlorate-epoxy hybrid composites was observed to be 1029 ± 111 MPa, which is about 42 % higher than the neat ammonium perchlorate-epoxy samples in comparing the mean values.

23.3.4 Piezoresistive Testing of MWNT-Ammonium Perchlorate-Epoxy Hybrid Composites

The volume piezoresistive measurements were recorded in terms of relative resistance change ($\Delta R/R_0$ where R_0 was initial unstrained resistance) as the specimens underwent deformation. Neat ammonium perchlorate-epoxy composites piezoresistive response was measured in order to provide a baseline measurement from which to assess the effect MWNT. The piezoresistive response of neat ammonium perchlorate-epoxy and 0.5 wt% MWNT relative to the entire MWNTs-ammonium perchlorate-epoxy samples is shown in Fig. 23.8. As expected, the relative change in resistance for the neat ammonium perchlorate-epoxy composite was insignificant. However, incorporation of MWNTs into local polymer

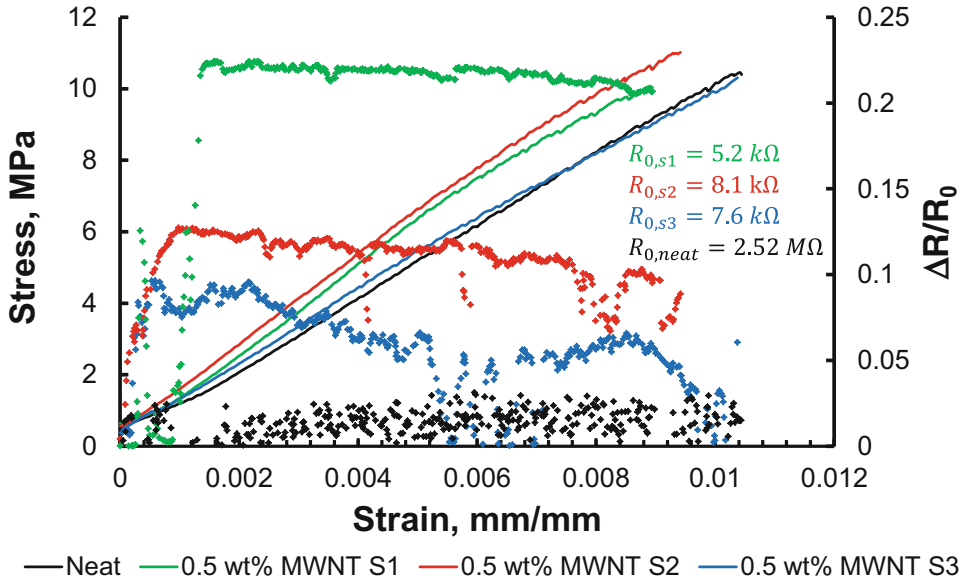

Fig. 23.8 Stress-strain and relative change in resistance-strain response of as-produced the neat ammonium perchlorate-epoxy and MWNTs-ammonium perchlorate-epoxy hybrid composites (S1, S2, S3 are sample #)

binder phase resulted in a different response. It is to be noted that the effective change in the macroscale piezoresistivity of CNT-polymer nanocomposites is believed to be attributed in large part to the rearrangement, i.e. either disruption or formation, of conductive networks of CNTs within the matrix material and the associated electron hopping in neighboring CNTs, i.e. tunneling resistance change rather than the intrinsic individual CNT piezoresistivity, i.e. CNT resistance change under deformation. 0.5 wt% MWNTs-ammonium perchlorate-epoxy hybrid composites exhibited an increase in the relative resistance change for very low values of applied strains (less than 0.2 %), which can be attributed to local deformations of the inherently piezoresistive MWNT-epoxy binder in absence of interfacial damage. However, the relative resistance change also exhibited a non-monotonic behavior. This observation might be explained by several factors. It is to be noted that the electrical conductivity measurements shows that 0.5 wt% MWNTs-ammonium perchlorate-epoxy hybrid composites are well above percolation threshold. There may not be a disruption in conductive pathways within the local polymer binder as the interfaces separation between surrogate crystals and binder due to saturated MWNT nanotube networks. Complex rearrangements of the current conductive paths makes the hybrid composite exhibit either no change in relative resistance and/or slight reduction in relative resistance change under applied strains due to formation of new conductive paths. Furthermore, for such composites with granular composite microstructure, it is difficult to constrain the developing microcracks to initiate in the gauge section. Microcracks can develop outside of the gauge section, which relax the local stresses in the gauge section. The effective resistance can reduce because of local relaxation of the specimen within the gauge section.

23.4 Conclusion

This preliminary study performs the experimental investigation of MWNT-ammonium perchlorate-epoxy hybrid composites to assess their microstructure morphology, effective conductivity and deformation based effective piezoresistive response. The current exploration of nanocomposite bonded polymer surrogate explosives includes several key observations. Neat epoxy-ammonium perchlorate samples are non-conductive and addition of MWNTs increases the effective conductivity of the hybrid composite. The stress-strain response of hybrid composites undergoes a brittle failure going through linear elastic behavior, formation of microcracks leading slight reductions in load carrying capacity and finally macrocracks result in eventual failure. Incorporating MWNTs into local polymer binder improves the effective stiffness about 42 % compared to neat ammonium perchlorate-epoxy samples. Moreover, it is observed that the relative resistance change of MWNT-ammonium perchlorate-epoxy samples captures very low values of applied strains (less than 0.2 %). Complex rearrangements of the current conductive paths makes the hybrid composites exhibit either no change in

relative resistance and/or slight reduction in relative resistance change after initial increase in the relative resistance change. Hence, it is essential to investigate a range of CNT concentrations to be starting just below and just above the composite electrical percolation concentration. The initial piezoresistive testing of MWNT-ammonium perchlorate epoxy hybrid composites indicated that addition of CNTs to the polymer binder can lead to piezoresistive response based deformation and damage sensing, which may be used to detect strain and damage initiation and its propagation for real-time SHM and self-diagnostic functionalities in energetic materials.

Acknowledgment The authors would like to acknowledge the support of Air Force Office of Scientific Research (grant FA9550-12-1 0205) in the Dynamic Materials and Interactions Program.

References

1. Peeters, R.: Characterization of plastic-bonded explosives. J. Reinf. Plast. Compos. **1**(2), 131–140 (1982)
2. Liu, C., Stouta, M., Asay, B.: Stress bridging in a heterogeneous material. Eng. Fract. Mech. **67**(1), 1–20 (2000)
3. Liu, C., Rae, P.J., Cady, C., Lovato, M.: Damage and fracture of high-explosive mock subject to cyclic loading. In: Proulx, T. (ed.) Conference Proceedings of the Society for Experimental Mechanics Series. Mechanics of Time-Dependent Materials and Processes in Conventional and Multifunctional Materials, vol. 3. Springer, New York (2011)
4. Liu, C., Thompson, D.G.: Crack initiation and growth in PBX 9502 high explosive subject to compression. J. Appl. Mech. **81**(10), 101004 (2014)
5. Liu, C., Thompson, D.G.: Macroscopic crack formation and extension in pristine and artificially aged PBX 9501. In: Proceeding of the 14th International Detonation Symposium Coeur d'Alene, ID, USA, 2010
6. Ruz-Nuglo, F., Groven, L., Puszynski, J.: Additive manufacturing for energetic components and materials. In: Proceedings 50th AIAA/ASME/SAE/ASEE Joint Propulsion Conference, Additive Manufacturing for Energetic Components and Materials, Cleveland, OH, USA, 2014
7. Paripovic, J., Davies, P.: Identification of the dynamic behavior of surrogate explosive materials. In: Proceedings of the ASME 2013 International Design Engineering Technical Conferences and Computers and Information in Engineering Conference IDETC/CIE, Portland, Oregon, USA, 2013
8. Mares, J.O., Miller, J.K., Sharp, N.D., Moore, D.S., Adams, D.E., Groven, L.J., Rhoads, J.F., Son, S.F.: Thermal and mechanical response of PBX 9501 under contact excitation. J. Appl. Phys. **113**, 084904 (2013)
9. Miller, J.K., Woods, D.C., Rhoads, J.F.: Thermal and mechanical response of particulate composite plates under inertial excitation. J. Appl. Phys. **116**, 244904 (2014)
10. Palmer, S.J.P., Field, J.E., Huntley, J.M.: Deformation, strengths and strains to failure of polymer bonded explosives. Proc. R. Soc. London, Ser. A **440**, 399–419 (1993)

Chapter 24
Quasi-Static Characterization of Self-Healing Dental Composites

Dhyaa Kafagy, Kevin Adams, Sharukh Khajotia, and Michael Keller

Abstract Self-healing in dental resin composites were successfully achieved in recently developed dental composites. A self-healing system of microcapsules was made of 30–60 μm diameter of initiator (BPO) and activator monomers. A compact version of tapered double cantilever beam (cTDCB) specimens was made of dental composites by integrating the self-healing components in the form of microcapsules. Quasi-static tests were performed to characterize specimens and to measure healing efficiency. Two sets of specimens were tested to show the healing ability of the dental composites which include: injected healing, and full in-situ self-healing specimens. The injected healing specimens were made using 40 wt% of dental resin and 60 wt% of a dental filler; the healing system of equal amounts of initiator and activator were injected in fluid form into the surface crack instantly after breaking the specimens. Full in-situ self-healing specimens of dental composites were made using 40 wt% of dental resin, 55 wt% of dental filler, and 5 wt% of equal amounts of initiator and activator microcapsules. The results show 10.31–36.62 % of self-healing efficiency was successfully achieved in 80 % of the in-situ self-healing specimens, and 94–99.5 % of healing efficiency was achieved in all of the injected specimens.

Keywords Microcapsules • Dental resin composites • Self-healing • Fracture test • Tapered double cantilever beam

24.1 Introduction

Resin-based dental composites are becoming the top choice for the restoration of damaged and decayed teeth because of the improved esthetic properties relative to amalgam. Dental resin composites are a unique class of biomaterials composed of inorganic fillers and monomers such as UDMA and Bis-GMA [1]. These materials can, upon polymerization, indistinguishably mimic the appearance of natural teeth. However, these restorations are more prone to cracks and failure than amalgam, leading to increases in the total cost of dental restorations. With the FDA predicting that nearly fifty million restorations occur every year in the United States, there are a large number of resin restorations currently in service in the US [2, 3]. Reducing the number of restoration revisions or reinstalls could significantly reduce the cost of restorative dentistry.

One potential approach for reducing restoration failure is the incorporation of a self-healing system in the dental composites. The self-healing system in this study is based on the use of embedded microcapsules within the dental composite structure. These microcapsules contain active chemical agents that can polymerize upon release from a capsule that is ruptured by a crack or other damage in the dental composite. The polymerized healing agent acts as an adhesive repair material to repair cracks before crack propagation can occur. As such, the incorporated self-healing mechanism is expected to increase the durability of composites by improving resistance to the growth of cracks in the restoration.

In this paper we present results of healing efficiency using the quasi-static test of two sets of dental composites specimens. The first, was dental composite specimens with injected healing, and the second was the fully in-situ self-healing specimens.

D. Kafagy • K. Adams • S. Khajotia • M. Keller (✉)
Department of Mechanical Engineering, The University of Tulsa, 800 Tucker Dr., Tulsa, OK 74104, USA
e-mail: michael-keller@utulsa.edu

W.C. Ralph et al. (eds.), *Mechanics of Composite and Multi-functional Materials, Volume 7*,
Conference Proceedings of the Society for Experimental Mechanics Series, DOI 10.1007/978-3-319-41766-0_24

24.2 Materials and Methods

24.2.1 Synthesis of Dental Composites

Inorganic silica Nano-fillers (about 40 nm size) are used to increase the compressive modulus and strength of the dental composite. Adding silica Nano-fillers also improves wear resistance and reduces the initial setting time [4, 5]. Traditional resin-based dental composites are made from 50 to 80 wt% inorganic filler of barium glass and 20–50 wt% of dental resin, depending on the filler size [6–10]. The dental resin in this work is made from five components: urethane di methacrylate (UDMA), bisphenol a glycidyl methacrylate (Bis-GMA), tertiary amine *N*, *N*-di methylaniline (DMA), Camphorquinone (QC), and tri methylolpropane tri methacrylate (TMPTMA).

For this study, if the batch of dental composites was to contain microcapsules, then an equal amount of barium glass was removed from the material so that the combination of filler and microcapsules was a constant 60 wt%. Table 24.1 shows the components of the dental resin incorporating the addition of 5 % of microcapsules.

The Bis-GMA, UDMA, and TMPTMA were mixed first and then transferred to a safe-light box. Then, 0.2 g of tertiary amine *N*,*N*-dimethylaniline (DMA) was added to the resin, to serve as an activator for the radical source.

24.2.2 Synthesis of Self-Healing Microcapsules

The self-healing system consists of two types of microcapsules, a benzoyl peroxide (BPO) containing capsule and a capsule that contains a mixture of a tertiary amine accelerator and monomers. Both kinds of microcapsules were made using an in-situ urea-formaldehyde (UF) encapsulation as described in the literature [11, 12]. The core materials of the initiator capsules consisted of purified BPO 90.1 wt% and phenyl acetate (PA) 9.9 wt%. The core materials of the resin capsules consisted of trimethylolpropane ethoxylate triacrylate (TMPET) 59.6 wt%, Bis-GMA 19.9 wt%, PA 20 wt%, and 4,4 ′-methylene (Bis *N*,*N*-dimethylaniline) (MBDMA) 0.5 wt%. This healing chemistry was adopted from previous work on self-healing bone cement [13, 14].

Microencapsulation is a two-step process: emulsion and shell formation. The emulsion process includes the addition of 100 mL of deionized (DI) water and 25 g of a 2.5 wt% aqueous solution of ethylene-maleic anhydride (EMA) copolymer. An overhead stirrer was started at the desired rpm. Then 2.5 g urea, 0.25 g NH_4Cl, and 0.25 g resorcinol were added, and the pH was adjusted to 3.5 by the addition of NaOH solution. Then the core material was added. The shell formation process started with the addition of 6.3 g formaldehyde solution. The portion of the beaker containing the capsule mixture was immersed in a water bath on a hot plate so that the heat could be applied gently and evenly during the encapsulation process. The hot plate was set to the desired temperature, and the mixture reaction was run for 4 h. Figure 24.1 shows a SEM micrograph of typical initiator microcapsules.

24.2.3 Fabrication of Self-Healing Dental Composite Specimens

To fabricate a fully in-situ self-healing dental composite, 40 wt% of dental resin was mixed with 55 wt% of barium glass filler in an opaque container, using a centrifugal high-speed mixer (model FlackTek DAC 150.1 FVZ-K). The mixer was used at a speed of 2800 rpm for 30 s. After mixing, the mixture was degassed to eliminate any air bubbles within the mixture.

Table 24.1 The chemical components of dental resin with 5 % of microcapsules

Component	Weight percentage (%)
Barium glass (inorganic filler)	55
Urethane dimethacrylate (UDMA)	19.01
Bisphenol A glycidyl methacrylate (Bis-GMA)	19.01
Microcapsules	5
Trimethylolpropane trimethacrylate (TMPTMA)	1.9
Camphorquinone (QC)	0.08

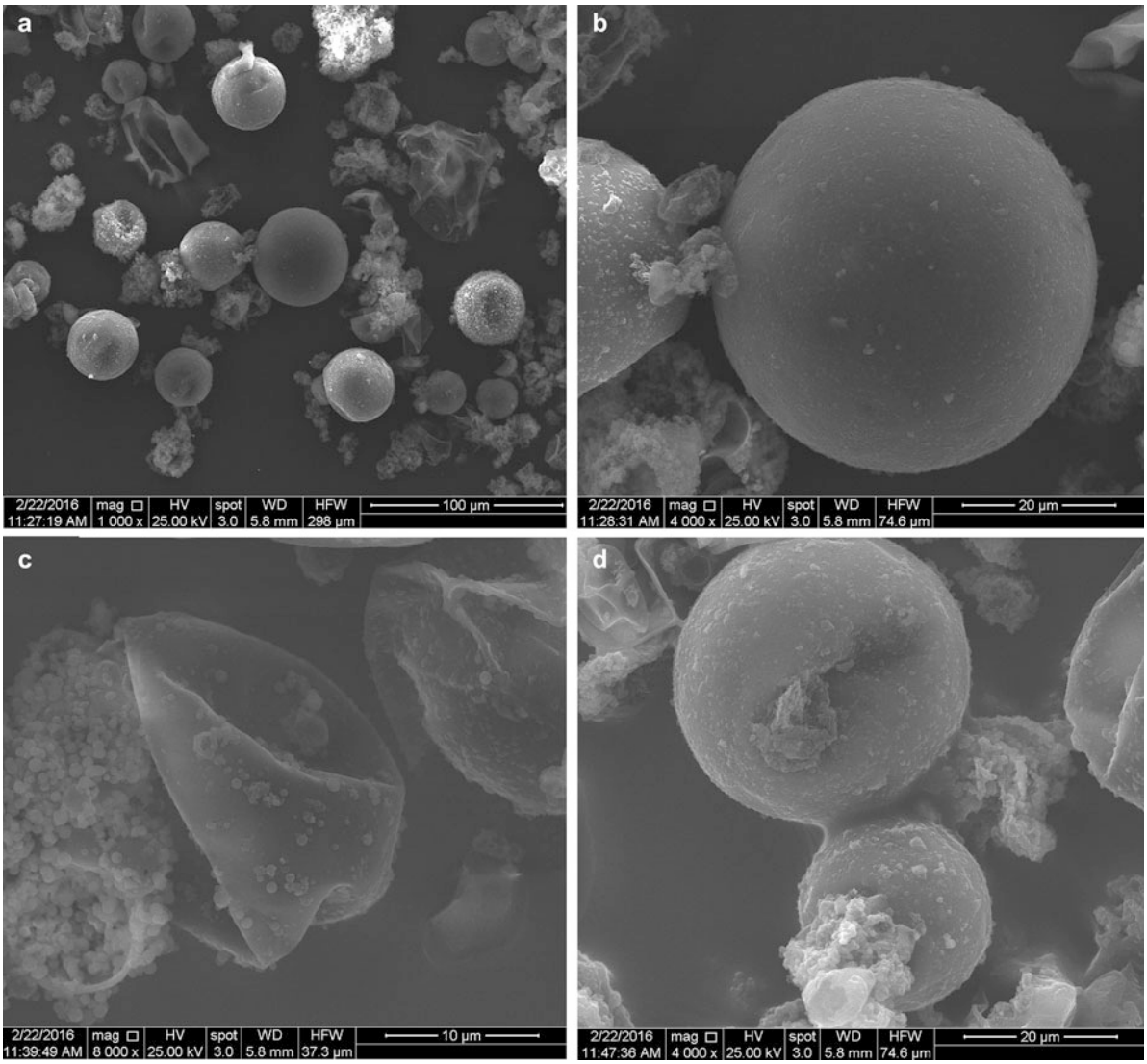

Fig. 24.1 (**a**) BPO group of urea-formaldehyde microcapsules visualized using Electro Scan Microscope (SEM). (**b**) A typical BPO microcapsule. (**c**) Ruptured microcapsule. (**d**) Release of monomers from a ruptured microcapsule

Next, 2.5 wt% of resin capsules were added and mixed, and the mixture was degassed again. Finally, 2.5 wt% of initiator capsules were added and mixed.

The mixture was transferred from the opaque container to a mold inside the light-safe box to avoid premature polymerization of the mixture Fig. 24.2b. The mold was then removed from the safe-light box and the specimen was exposed to a high-intensity LED curing light (VALO V34596) for 20 s on each side of the mold. After curing, the fully in-situ specimens were stored in DI water until testing.

The last step before testing was to make the initial crack, this was achieved by using a diamond saw (Buehler IsoMet 1000 Precision Saw) with a 1 mm thick blade to make a starter notch in the specimen. Then the crack tip was sharpened using a razor blade.

Another set of specimens were fabricated using the traditional portions of dental resin composites. The injected healing composite specimens were made by the addition of 40 wt% of dental resin with 60 wt% of barium glass filler in an opaque container. Then the healing components of initiator and activator were injected into the crack surface after the specimens were cracked. After the healing process, the specimens were kept immersed DI water in an opaque container, and the healed specimens were tested again.

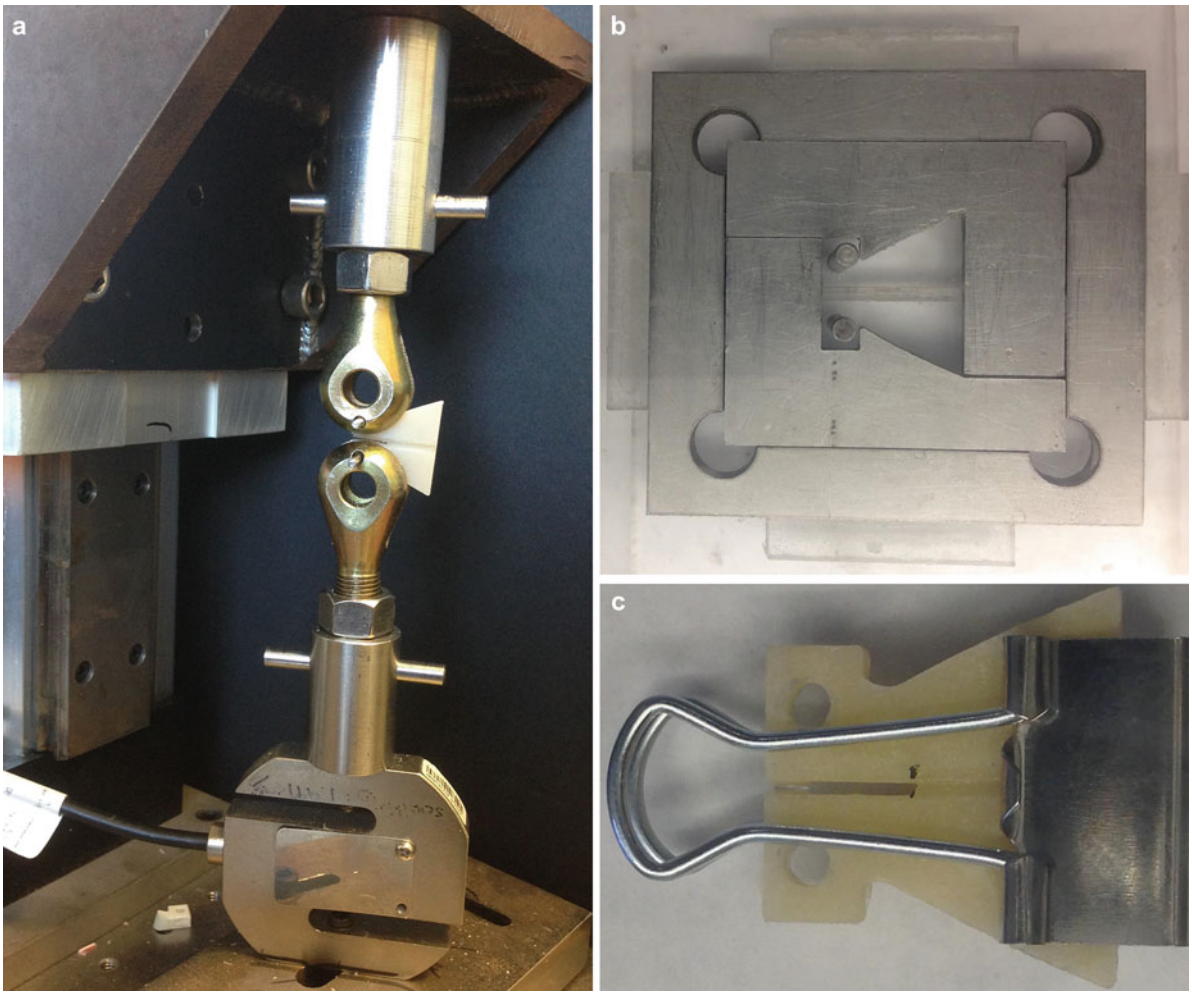

Fig. 24.2 (**a**) The quasi-static load frame used for fracture testing, shows a 25 kg load cell, upper and lower grips, pins, and a testing specimen. (**b**) The four-part mold of the cTDCB specimen. (**c**) Two halves of cTDCB specimens were clamped together during healing

24.2.4 Quasi-static Fracture Testing

Quasi-static fracture testing was performed to assess the self-healing efficiency of the dental resin composites. The test was controlled using a custom a Lab VIEW virtual instrument to collect load and displacement data. The load frame shown in Fig. 24.2a, was used to perform testing in displacement control, with a displacement rate of 0.05 mm/s. For healing tests, the samples were pre-cracked with a fresh razor blade, tested, and then stored under DI water for 24 h before retesting.

In this study, self-healing is considered successful if it shows more than 10 % of healing recovery. To test the healing efficiency of both the injected and the in-situ self-healing specimens a quasi-static test took place. Immediately following specimen fracture, the two halves of the specimen were placed back together using clamps as shown in Fig. 24.2 c to ensure good contact between the two fracture surfaces. The healing efficiency was measured by comparing the fracture toughness of the virgin and healed specimens as given by the relationship (24.1)

$$\eta = \frac{K_{IC_{Healed}}}{K_{ICInitial}} \tag{24.1}$$

The specimens were kept in DI water to approximate an oral environment.

24.3 Results and Discussion

The addition of 5 wt% microcapsules to the dental composite specimens increases the initial fracture toughness by 40 %. This increase was expected based on previous research on microcapsule-toughened composites [15, 16]. The addition of microcapsules has been found to introduce new toughening mechanisms during fracture, which increase fracture surface roughness and effective fracture area.

The injected healed specimens were successful in all the tested specimens. Healing in injected tests also shows high healing efficiency, ranging from 94 to 99.5 %, see Table 24.2. Based on this result we expect that the proposed healing chemistry will be successful at repairing crack damage in dental composites. As an initial demonstration, a series of five fully in-situ healing specimens were fabricated and tested as described above. The self-healing in the in-situ self-healing specimens was successful 80 % of the time. The successful self-healed specimens showed healing efficiencies of 10.31, 14.84, 29.61, and 36.62 %. Currently, a study is underway to optimize the healing chemistry and capsule concentration to achieve the healing indicated by the injected specimens (Fig. 24.3).

Table 24.2, summarizes the average healing efficiency of the in-situ self-healing and the injected healed specimens. The standard deviation was high in the in-situ self-healing samples, due to the variations of the quantity and the random distribution of the microcapsules in the crack site.

The measured healing efficiency in the in-situ self-healing specimens was in the range from 10.31–36.62 %. These were low healing efficiencies, but the system has not yet been optimized. A study is ongoing to understand the effect of capsule concentration and resin viscosity on healing performance. The unsuccessful healing in 20 % of the in-situ self-healing could be due to either imperfect contact of the crack planes or because of a low release of the resin components from the fractured capsules. Further study is required to understand what is more important for ensuring successful healing.

Table 24.2 The average efficiency in the in-situ self-healing dental composite and the injected healed and their standard deviation

Condition	Average healing efficiency
In-situ self-healing dental composites with microcapsules	19.08 % ± 12.49
Dental composites without microcapsules	97.46 % ± 3.13

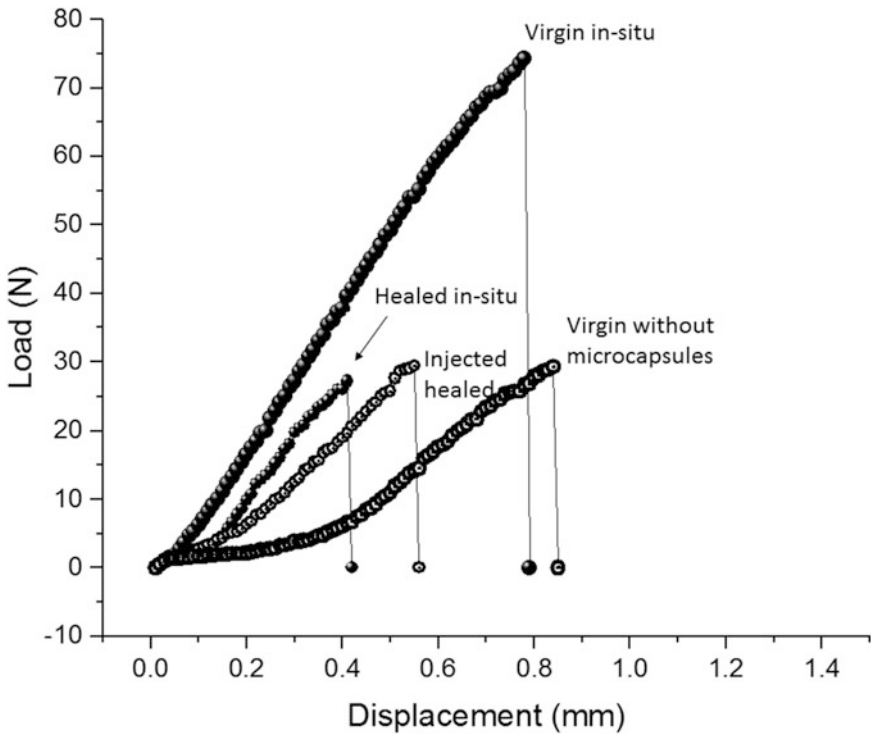

Fig. 24.3 Quasi-static test of in-situ self-healing and injected dental composite cTDCB specimens

24.4 Conclusions

The in-situ self-healing of a dental composite using microcapsules was successfully demonstrated. The addition of 5 wt% microcapsules to the dental composite served to increase the virgin toughness by 40 %. For the un-optimized system studied, self-healing was successful in 80 % of in-situ self-healing specimens. For injected specimens, all of the specimens were successfully healed with healing efficiencies averaging 97 %.

Acknowledgment This research was supported in part by the Oklahoma Center for the Advancement of Science and Technology (HR13-131). The authors would also like to thank Esstech for their gracious donation of material used in this research.

References

1. Cramer, N.B., Stansbury, J.W., Bowman, C.N.: Recent advances and developments in composite dental restorative materials. J. Dent. Res. **90**, 402–416 (2011)
2. Food and Drug Administration, H.H.S.: Dental devices: classification of dental amalgam, reclassification of dental mercury, designation of special controls for dental amalgam, mercury, and amalgam alloy. Final rule. Fed. Regist. **74**, 38685–38714 (2009)
3. http://www.intechopen.com/books/advances-in-diverse-industrial-applications-of-nanocomposites/dental-nanomaterials (2016). Accessed 17 Feb 2016
4. Uysal, T., Yagci, A., Uysal, B., Akdogan, G.: Are nano-composites and nano-ionomers suitable for orthodontic bracket bonding? Eur. J. Orthod. **32**, 78–82 (2010)
5. Basso, M.: Teeth restoration using a high-viscosity glass ionomer cement: the Equia® system. J. Min. Intervent. Dentist. **4**, 74–76 (2011)
6. Anusavice, K.J., Phillips, R.W., Shen, C., Rawls, H.R.: Phillips' science of dental materials. Elsevier, New York (2013). http://www.clinicalkey.com/dura/browse/bookChapter/3-s2.0-C20090424255
7. Moshaverinia, A., Ansari, S., Movasaghi, Z., Billington, R.W., Darr, J.A., Rehman, I.U.: Modification of conventional glass-ionomer cements with N-vinylpyrrolidone containing polyacids, nano-hydroxy and fluoroapatite to improve mechanical properties. Dent. Mater. **24**, 1381–1390 (2008)
8. Hook, E.R., Owen, O.J., Bellis, C.A., Holder, J.A., O'Sullivan, D.J., Barbour, M.E.: Development of a novel antimicrobial-releasing glass ionomer cement functionalized with chlorhexidine hexametaphosphate nanoparticles. J. Nanobiotechnol. **12**, 3 (2014). doi:10.1186/1477-3155-12-3
9. Moshaverinia, A., Ansari, S., Moshaverinia, M., Roohpour, N., Darr, J.A., Rehman, I.: Effects of incorporation of hydroxyapatite and fluoroapatite nanobioceramics into conventional glass ionomer cements (GIC). Acta Biomater. **4**, 432–440 (2008)
10. Friedl, K., Hiller, K.A., Friedl, K.H.: Clinical performance of a new glass ionomer based restoration system: a retrospective cohort study. Dent. Mater. **27**, 1031–1037 (2011)
11. Brown, E.N., Kessler, M.R., Sottos, N.R., White, S.R.: In situ poly(urea-formaldehyde) microencapsulation of dicyclopentadiene. J. Microencapsul. **20**(6), 719–730 (2003)
12. Blaiszik, B.J., Caruso, M.M., Mcilroy, D.A., Moore, J.S., White, S.R., Sottos, N.R.: Microcapsules filled with reactive solutions for self-healing materials. Polymer **50**, 990–997 (2009)
13. Caruso, M.M., Moore, J.S., Moore, J.S., Silverman, S.K., Zimmerman, S.C., White, S.R.: Solvent-based self-healing polymeric materials. University of Illinois, Urbana (2010)
14. Rochmadi, P.A., Hasokowati, W.: Mechanism of microencapsulation with urea-formaldehyde polymer. Am. J. Appl. Sci. **7**, 739–745 (2010)
15. Brown, E., Sottos, N.R., White, S.R.: Fracture testing of a self-healing polymer composite. Exp. Mech. **42**, 372–379 (2002)
16. Jin, H., Miller, G.M., Sottos, N.R., White, S.R.: Fracture and fatigue response of a self-healing epoxy adhesive. Polymer **52**, 1628–1634 (2011)

Chapter 25
Load Monitoring Using Surface Response to Excitation Method

S. Tashakori, A. Baghalian, M. Unal, V.Y. Senyurek, H. Fekrmandi, D. McDaniel, and I.N. Tansel

Abstract Surface response to excitation (SuRE) method is a low-cost alternative to the electromechanical impedance method developed for the structural health monitoring (SHM) applications. This method uses one piezoelectric transducer to excite the surface of a structure with a sweep sine wave. One or more piezoelectric sensors or scanning laser vibrometer monitors the dynamic response of the surface to the excitation. The spectrum of the dynamic response is collected at the optimal operating conditions. Any significant change of the spectral characteristics may indicate defects, improper loading or loose fasteners.

In this study, the performance of SuRE method was evaluated when the conventional piezoelectric elements and scanning laser vibrometer were used for monitoring the presence of loads on the surface. In order to determine the accuracy and reliability of both monitoring approaches two tests were performed. In the first test, one piezoelectric transducer was used as exciter and another one as a sensor. In the second test, a scanning laser vibrometer was used to measure the surface vibrations. Although the piezoelectric element collected the data with better resolution, the results with the scanning laser vibrometer were acceptable and can be used when attaching piezoelectric elements are not allowed to the surface.

Keywords SHM • Load monitoring • SuRE method • Laser vibrometer • Piezoelectric transducer

25.1 Introduction

It is essential for structures to safely work during their service life. However, defects can trigger a breakdown period for the structures. Defects also may reduce effectiveness of structure, so that defect prediction methods play a pivotal role for structural health monitoring applications and by monitoring and mending these sort of damages in structure, functional age of the structure can be improved. More to the point, existence of any undesired load on structures may affect sensor response and damage the results. Over last few years, establishing a testing method to monitor load on structures has been considered as a primary issue [1, 2].

In the Electromechanical Impedance (EMI) method, health of the structure will be investigated by measuring the mechanical impedance of the structure using piezoelectric transducers [3]. However, impedance analyzers are extremely costly and it has been tried to be replaced by cheaper alternatives such as cheaper electronic circuits [4–8]. Also, other variations of this method such as SuRE method has been recently introduced which canceled the need for impedance analyzer. By applying the SuRE method, Fekrmandi et al. [9] proposes a non-contact milling monitoring process that has the potential of monitoring the surface roughness and the dimensional accuracy of a work piece remotely. They also investigated detection of the damage of Thick Blocks using SuRE Method with the help of DSP techniques [10]. Lim et al. [11] also proposed a impedance technique at varying temperature and loading conditions for detection of bolt loosening in the metal fitting lug connecting a composite aircraft wing to a main Fuselage.

S. Tashakori (✉) • A. Baghalian • I.N. Tansel
Mechatronics Research Laboratory, Department of Mechanical and Materials Engineering, Florida International University, 10555 W Flagler Street, Miami, FL 33174, USA
e-mail: stash002@fiu.edu

M. Unal
Department of Mechatronics Engineering, Faculty of Technology, Marmara University, Istanbul, Turkey

V.Y. Senyurek
Department of Electrical and Electronics Engineering, Faculty of Technology, Marmara University, Istanbul, Turkey

H. Fekrmandi • D. McDaniel
Applied Research Center, Florida International University, 10555 W Flagler Street, Miami, FL 33174, USA

W.C. Ralph et al. (eds.), *Mechanics of Composite and Multi-functional Materials, Volume 7*,
Conference Proceedings of the Society for Experimental Mechanics Series, DOI 10.1007/978-3-319-41766-0_25

In this study, the performance of SuRE method for load monitoring was investigated. The conventional piezoelectric elements and scanning laser vibrometer were used in the course of experiments and successful performance of SURE method in load monitoring applications for aluminum plate was shown.

25.2 Method

In this study, surface response to excitation (SuRE) method has been used to monitor different levels of loads on the structure. Also, it has been tried to modify this method for load monitoring purposes by using signal processing and data analysis approaches. In the SuRE method, the surface of structure is excited by a sweep sine wave over a certain frequency range using a piezoelectric transducer and another piezoelectric transducer will be used on the other side of structure to sense dynamic response of the system. Then frequency spectrum of the signal was obtained by using Fast Fourier Transform (FFT) [12]. Then in order to decrease the effect of noises and also increase resolution of main frequencies, power spectral density (PSD) of frequency domain data was calculated:

$$PSD = \frac{1}{f} \times |X(f)|^2 \tag{25.1}$$

Frequency response of the structure will be consistent as long as there is no change in system and whenever condition changes, in terms of applying load or existence of defect, the frequency spectrum changes can be observed.

In order to quantify these changes, the sum of the squared differences (SSD) of frequency response after the changes with respect to the frequency response of pristine, is considered:

$$SSD = \sum_{i=1}^{m} |B_{m\times 1} - R_{m\times 1}|^2 \tag{25.2}$$

Here, B and R are the baseline and response signal after changes matrices and also m denotes size of FFT.

25.3 Experiment

In SuRE method-based structural health monitoring, the range of excitation is typically between 1–250 kHz. However, in order to find appropriate range of frequency for excitation for load monitoring application, different range of frequencies were studied. The optimal range in this view was considered as the highest signal to noise ratio of frequency spectrum. Also, the sampling frequency was chosen five times bigger than the highest excitation frequency.

Therefore, this area was narrowed down to a shorter range of frequency where it showed monotonic behavior to any increase or decrease in applied load and this was done by trial-and-error method.

In order to select the appropriate frequency range of excitation, the response of the plate to an excitation frequency range of 1–400 kHz was obtained and it was shown in Fig. 25.1.

From Fig. 25.1 it can be seen that we have the highest Amplitude and SNR for the response signal in the range of 1–200 kHz and after 200 kHz the rate of signal to noise ratio is meaningfully lower. Then, this area is narrowed down to 1–50 kHz by the trial-and-error method. The results of that were shown in Fig. 25.2.

25.4 Load Monitoring

In order to study the effectiveness of the SuRE method for load monitoring purposes, laser vibrometer and piezoelectric sensor, respectively, as non-contact and contact methods were utilized. A schematic of experimental setup is shown in Fig. 25.3.

In this test, applied force was increased from F1 to F3 using 1 lb steps. The schematic and experimental setup are shown in Fig. 25.4. The collected results from piezoelectric sensors and the laser vibrometer are shown in Figs. 25.5 and 25.6.

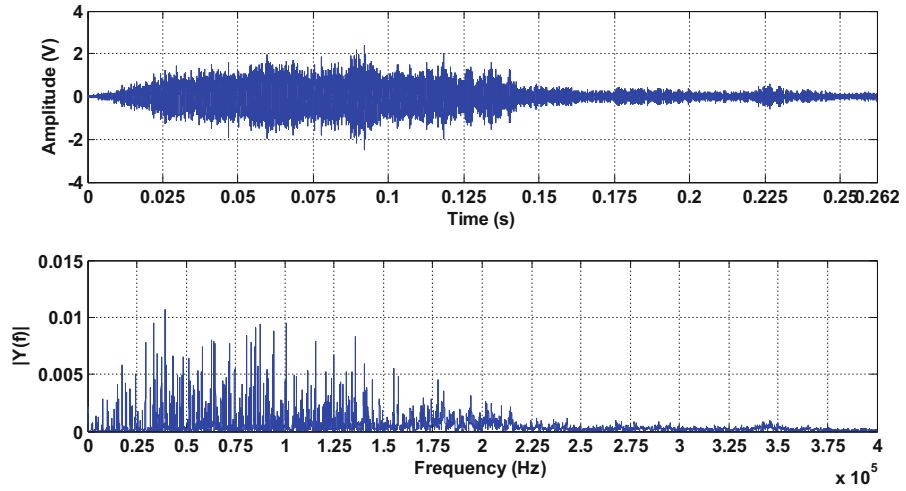

Fig. 25.1 FFT response of plate for 1–400 kHz

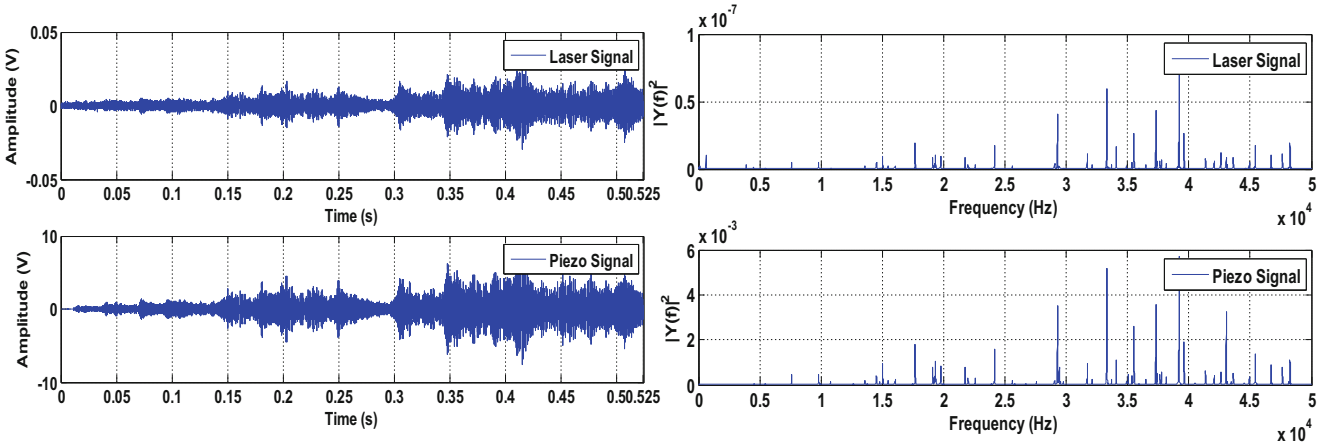

Fig. 25.2 Time domain response and FFT response of the plate for 1–50 kHz

Using PZT for data collection, PSD of frequency response of the plate for baseline (no load) and each of the applied loads were acquired. Results are plotted in Fig. 25.5 and it can be seen as the load is increased, amplitude of the PSD monotonically decreases.

In another attempt, instead of PZT transducer, in order to collecting data, a laser vibrometer was employed. Then, the changes in frequency response with the aid of FFT analysis were examined. Data acquired using laser vibrometer for different size of load in FFT and SSD analysis were represented in Fig. 25.6.

25.5 Conclusions

The purpose of this study was to evaluate the efficacy of SuRE for load monitoring purposes. A piezoelectric element was used to excite surface waves on the surface of the aluminum plate. Laser scanning vibrometer and piezoelectric transducer were employed respectively as a non-contact and contact sensor to measure the vibrations at a scan point. The spectrums of the vibration data were calculated by using the FFT analysis. In addition, in order to decrease the effect of noises and also increase resolution of main frequencies, power spectral density (PSD) was applied. Using sum of

Fig. 25.3 Experiment setup

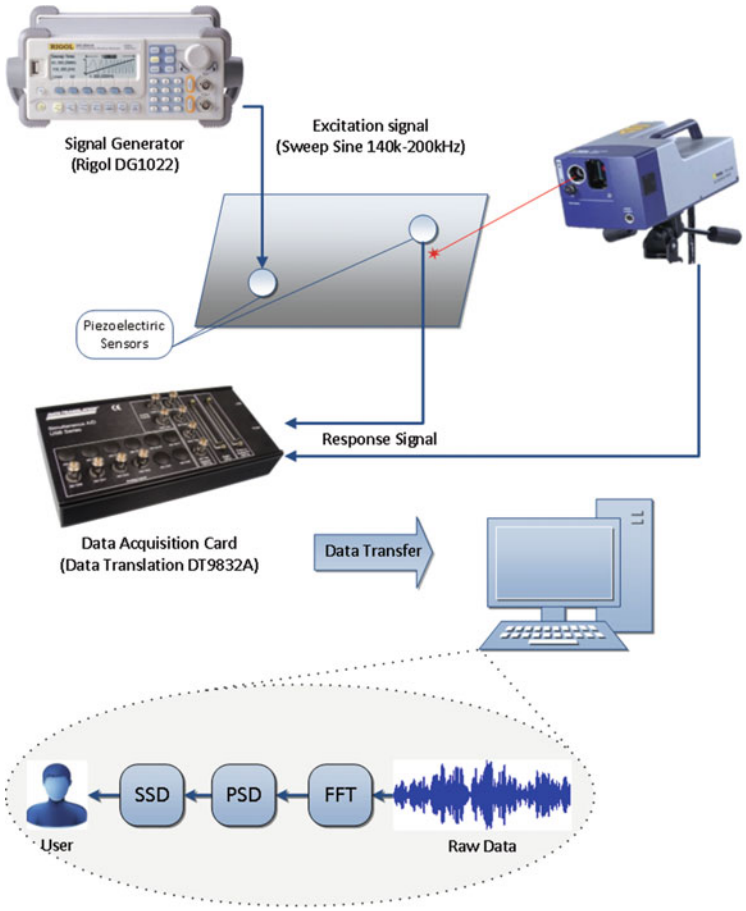

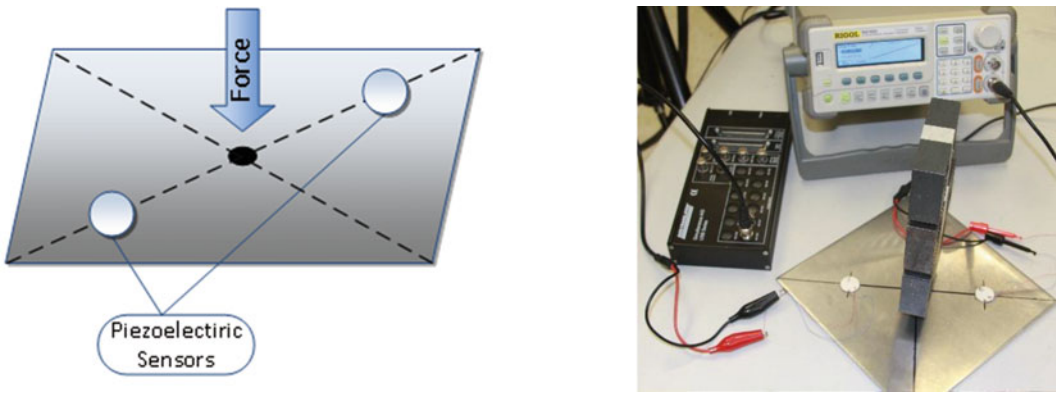

Fig. 25.4 Experimental setup for single load into the center of plate

squares of differences between the reference and spectrums after applying loads, the variation of the spectrums for difference levels of applied load was investigated and it was shown that by increase of applied load, the SSD values were increased and the reasonable sensitivity to the change of applied load was observed. More to the point, the experiment results showed that response signals which gathered by using Laser scanning vibrometer and PZT transducer had similar pattern. Although the amplitude of laser response are so much smaller in comparison with amplitude of piezoelectric response which, by considering to be non-contact approach, was conceivable. As a result, in order to reduce the cost of inspection and initial investment in load monitoring investigations, SuRE method can be considered as a promising approach.

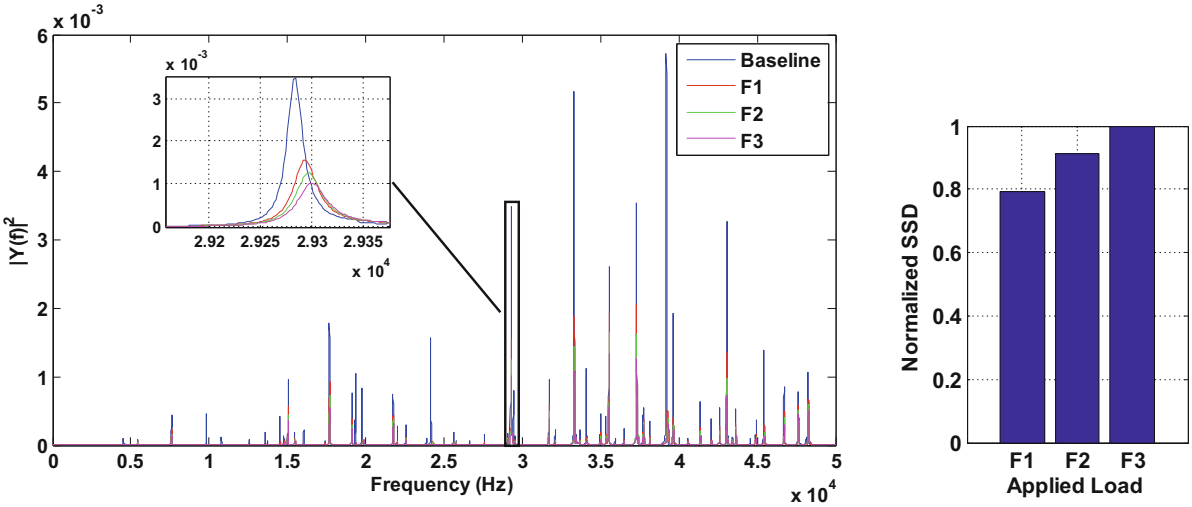

Fig. 25.5 Comparing different applying forces using PZT for data collection

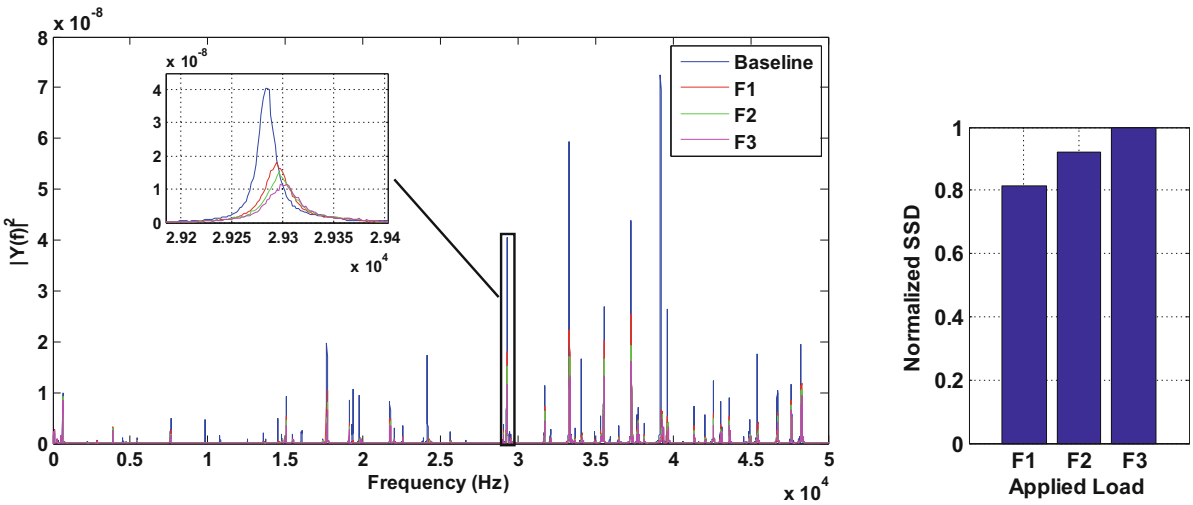

Fig. 25.6 Comparing different applying forces using laser vibrometer for data collection

Acknowledgments The authors would like to thank The Scientific and Technological Research Council of Turkey (TUBITAK) for supporting Dr. Muhammet UNAL and Dr. Volkan Yusuf SENYUREK's research at the Florida International University.

References

1. Roy, S., Ladpli, P., Chang, F.-K.: Load monitoring and compensation strategies for guided-waves based structural health monitoring using piezoelectric transducers. J. Sound Vib. **351**, 206–220 (2015)
2. Jassim, Z.A., Ali, N.N., Mustapha, F., Abdul Jalil, N.A.: A review on the vibration analysis for a damage occurrence of a cantilever beam. Eng. Fail. Anal. **31**, 442–461 (2013)
3. Fu, J., Tan, C., Li, F.: Quantitative electromechanical impedance method for nondestructive testing based on a piezoelectric bimorph cantilever. Smart Mater. Struct. **24**, 065038 (2015)
4. Park, G., Cudney, H.H., Inman, D.J.: Impedance-based health monitoring of civil structural components. J. Infrastruct. Syst. **6**, 153–160 (2000)
5. Peairs, D.M., Park, G., Inman, D.J.: Improving accessibility of the impedance-based structural health monitoring method. J. Intell. Mater. Syst. Struct. **15**, 129–139 (2004)

6. Kim, J., Grisso, B.L., Ha, D.S., Inman, D.J.: A system-on-board approach for impedance-based structural health monitoring. In: The 14th International Symposium on: Smart Structures and Materials & Nondestructive Evaluation and Health Monitoring, p. 65290O. International Society for Optics and Photonics (2007)
7. Baptista, F.G.: A new impedance measurement system for PZT-based structural health monitoring. IEEE Trans. Instrum. Meas. **58**, 3602–3608 (2009)
8. Xu, B., Giurgiutiu, V.: A low-cost and field portable electromechanical (E/M) impedance analyzer for active structural health monitoring. DTIC Document (2005)
9. Fekrmandi, H., Unal, M., Baghalian, A., Tashakori, S., Oyola, K., Alsenawi, A., Tansel, I.: A non-contact method for part-based process performance monitoring in end milling operations. Int. J. Adv. Manuf. Technol. **83**, 13–20 (2016)
10. Fekrimandi, H., Tansel, I., Gonzalez, R., Rojas, S., Meiller, D., Lindsay, K., Baghalian, A., Tashakori, S.: Implementation of the surface response to excitation (SuRE) method with DSP's for detection of the damage of thick blocks. In: 10th International Workshop on Structural Heath Monitoring 2015, Stanford University, Stanford (2015)
11. Lim, H.J., Kim, M.K., Sohn, H., Park, C.Y.: Impedance based damage detection under varying temperature and loading conditions. NDT and E Int. **44**, 740–750 (2011)
12. Fekrmandi, H., Rojas, J., Campbell, J., Tansel, I.N., Kaya, B., Taskin, S.: Inspection of the integrity of a multi-bolt robotic arm using a scanning laser vibrometer and implementing the surface response to excitation method (SuRE). Int. J. Prognostics Health Manage. **5**, 1–10 (2014)

Chapter 26
Elevated Temperature Digital Image Correlation Using High Magnification Optical Microscopy

W. Carter Ralph, Kevin B. Connolly, and Cheri B. Moss

Abstract Full-field thermally-induced strain measurement of small areas or structures is desirable for applications such as microelectronics, but is difficult to achieve at microscopic scales. This data can be used to evaluate product reliability, validate finite element models, and perform failure analysis. Digital image correlation is an ideal technique for these applications, but its feasibility has not yet been demonstrated. Two primary challenges present themselves: thermal expansion of the specimen and hardware push the viewing surface out of the small focal range of the lens, and speckle fields of sufficiently small size are difficult to prepare. In addition, the close proximity of the microscope lens to the specimen can cause the lens to be heated to harmful temperatures. This paper presents a method for successfully performing two-dimensional digital image correlation measurements over a range of temperatures though and throughout a large range of optical magnifications. Test apparatus has been designed to effectively eliminate out-of-plane thermal expansion and heating of the lens. Specimen preparation techniques provide a sufficient high-contrast surface features for strain and displacement calculations. The apparatus design and specimen preparation methods are described, and examples are presented to demonstrate capability. This provides a means to measure full-field two-dimensional strain of microscopic features over a range of temperatures using common laboratory equipment.

Keywords Optical microscopy • Digital image correlation • Thermal strain • Microelectronics • Elevated temperature

26.1 Introduction

Thermal expansion mismatches between materials can cause damage to composite structures when they are subjected to a sufficient change in temperature. Part failure can occur over a single temperature cycle, or may occur as damage propagates over multiple cycles. Testing and modeling can be used to determine the cause and location of failure, to design parts that are resistant to damage, and to assess product reliability before full-scale production. Strain measurements during thermal tests can be used to quantitatively assess the effects of the temperature profile, and is vital to the validation of both analytical and numerical models. Strain measurements over the entire surface are preferred to point and area strain measurements, such as strain gages.

Strain measurements of any kind are difficult on microscopic structures, such as microelectronic parts. These parts are primarily made up of silicon, metals, ceramics, and polymers having a wide variety of thermal expansions. The silicon processors are typically attached to polymeric or ceramic substrates, which in turn are connected to glass/epoxy wiring boards with solder joints that act as both electrical and mechanical interconnections. The processors, substrates, and printed wiring boards themselves contain metal traces and vias that carry the electrical signals, and the parts may be underfilled with resin. The components are assembled in multiple steps at elevated temperatures, and thermal stresses build up as the assembly cools down. Thermal cycles occur each time the product is powered on and off. Cracks and delaminations can occur during the manufacturing process or product use due to thermal or mechanical stress, and can extend due to thermal cycling until product failure occurs (Fig. 26.1).

Interferometry can be used to measure full-field displacement on microscopic scales, but has several practical disadvantages. Specimen preparation is labor-intensive and requires careful surface preparation and test setup [1]. A fine grating must be carefully applied to the specimen surface that is then viewed through another grating during a temperature

W.C. Ralph (✉) • K.B. Connolly • C.B. Moss
Southern Research Institute, 757 Tom Martin Drive, Birmingham, AL 35211, USA
e-mail: ralph@southernresearch.org

W.C. Ralph et al. (eds.), *Mechanics of Composite and Multi-functional Materials, Volume 7*,
Conference Proceedings of the Society for Experimental Mechanics Series, DOI 10.1007/978-3-319-41766-0_26

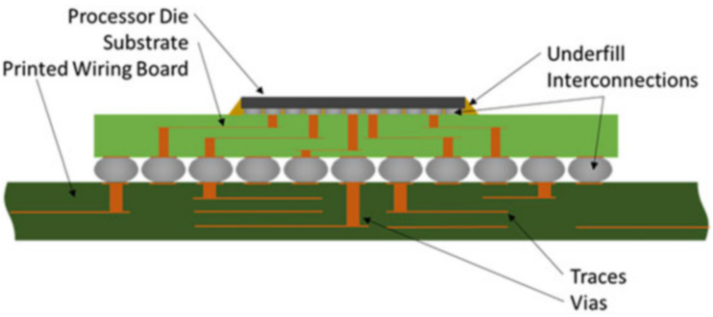

Fig. 26.1 Illustration of a microelectronics assembly

profile to measure the shape of the surface. Displacement can only be measured in one direction at a time with a typical linear grating, and can be measured in two directions with a cross-line grating. The grating pattern may be projected onto the specimen surface with less surface preparation, but this comes at the cost of lower resolution, greater susceptibility to external vibration, and more restrictive test setup due to the fact that the specimen must be located close to the grating surface. Laser interferometry techniques offer higher resolution with less surface preparation, but come at the cost of high sensitivity to environmental vibrations and air fluctuations. All of these techniques require specialized equipment and training.

Digital image correlation (DIC) is a proven and popular displacement measuring technique that offers several distinct advantages. Displacement and strain are computed by comparing deformed images to a reference image and measuring the change in location of high-contrast surface features that are common to both images. The software algorithms can locate the position of the features with sub-pixel resolution. Displacement can be measured simultaneously in three dimensions (and 6 axes) over the entire field of view with two or more cameras positioned at an angle from each other, or in two dimensions (and 3 axes) with a single camera. Surface features are either applied to the surface, or intrinsic to the material. Surface preparation is typically less labor-intensive than for interferometry because the surface does not need to be flat, as long as the regions of interest are visible and in focus. The technique is scalable to any size that can be digitally imaged, and has been applied from the meter to the nanometer scales [2].

Application of this technique to the micrometer scale, which is ideal for microelectronics structures, presents several technical challenges. The relative depth of focus for microscope lenses is very small compared to camera lenses and scanning electron microscopes, so even small out-of-plane displacement caused by thermal expansion can result in images that are too blurry for DIC calculations. Surface features of the proper size are difficult to apply: paint speckles are too large, microspheres are too tall, focused ion beam features are too small, and fine powders clump due to van der Waals forces. In addition, thermal issues become increasingly problematic: uneven heating of the air causes diffraction, the necessarily close proximity of the microscope lens to the specimen can cause the lens to be heated to damaging temperatures, and window panes can severely degrade image contrast [3].

The present study has developed from work that was published in 2013, in which DIC was used from −55 to 200 °C to measure thermal strain on electronic assemblies under reflow and temperature cycling conditions using a small reflow oven with a large window [4]. Those test methods were extended to continually smaller scales. At image widths between 4 and 10 mm, as shown in Fig. 26.2, high magnification camera lenses had to be used. At the higher magnification range individual microelectronic features begin to be significantly large to resolve. Figure 26.2b shows a 4 mm wide image of a portion of a microelectronics package overlaid with its thermal strain, and the solder interconnections between the processor and the substrate can be distinguished. At higher magnification the image quality suddenly degraded beyond usefulness due to a number of issues: the air brush paint speckling technique resulted in contrast features that were too large, the camera lens was so close to the oven that it began to get significantly hot, the window pane greatly reduced image contrast, thermal expansion of the oven and specimen caused focus to be lost, and too much light was lost due to additional extension tubes. Employing a microscope solved this last issue, but the other issues still applied, and no published study could be found that addressed them.

These technical challenges have been systematically addressed by the authors in a number of ways, which are presented in this paper. A new apparatus has been designed to minimize thermal expansion and lens heating, and specimen preparation methods have been developed for providing high contrast surface features. These developments have allowed thermal strain on microprocessors to be successfully measured at magnifications up to ×1000 and temperatures up to 200 °C using a commercially-available optical microscope.

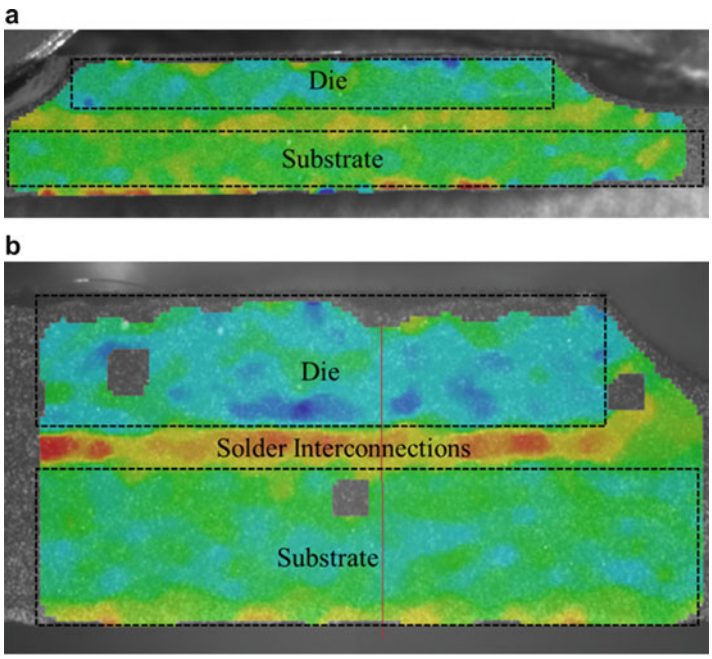

Fig. 26.2 Thermal strain measured on a microprocessor with high magnification camera lenses: (**a**) 10 mm wide field of view, (**b**) 4 mm wide field of view

26.2 Apparatus

The original test apparatus was the root cause of several of the problems with high magnification imaging. This setup consisted of a modified Bomir batch reflow oven with a 28 × 28 cm double-pane glass window. The oven uses convection heating to simulate production reflow conditions, which has the added benefit of creating turbulent air flow that reduces refractive distortions by caused by regions of unevenly heated air. The air ducts and specimen stage were re-designed to produce a more even vertical and horizontal air flow distribution across the viewing area of the oven. The two-pane window was re-designed to eliminate refractive distortions caused by air recirculation patterns that developed between the two panes. An external fan was used to blow ambient air across the outer surface of the window to eliminate refractive distortions between the window and the camera. Liquid nitrogen was used with the oven's recirculating system for below ambient temperature measurements. A stereo pair of 5 megapixel digital cameras was used with 50 mm lenses and extension tubes for higher magnifications. This apparatus is illustrated schematically in Fig. 26.3. The size and metal construction of the oven allows for a relatively large (approximately 0.2 mm) amount of thermal expansion, which is added to slightly by the expansion of the specimen. This is insignificant compared to the depth of focus of traditional camera lenses, but is much larger than the total depth of focus of high magnification lenses. Higher magnifications also require the lens to be placed closer to the specimen, so the outer window pane had to be removed and the lens reached the manufacturer's maximum use temperature before the specimen could be sufficiently heated. Image contrast degraded when viewing though the window pane at high magnifications, which was demonstrated when the plane was replaced with a metal sheet with a small viewing hole and the image quality significantly improved. In addition, this setup makes test setup difficult, since the microscope or camera must be removed and the oven top opened to place and adjust the specimen in the oven.

The new apparatus was designed with the specimen inverted on a low thermal expansion stage atop an adjustable stand. The microscope is inverted in its stand to accommodate this setup. The stage has a viewing port machined into it and rests on a vented thermal insulator, which in turn rests on an adjustable stand set above the microscope. A resistance heater is placed on top of the stage and around the specimen. This setup is shown in Fig. 26.4. This design has several specific advantages. The viewing surface does not go out of focus because the low thermal expansion of the stage material is negligible. Due to the inverted setup, all thermal expansion of the specimen occurs behind the viewing plane. Heat rises away from the viewing plane and the microscope lens, keeping the lens cool and minimizing refractive distortions in the air between the lens and the viewing plane so that a vent fan (which can cause undesirable vibrations) is not needed. The viewing port provides an unobstructed optical path between the specimen and the lens so that image contrast is not degraded. Finally, the specimen is

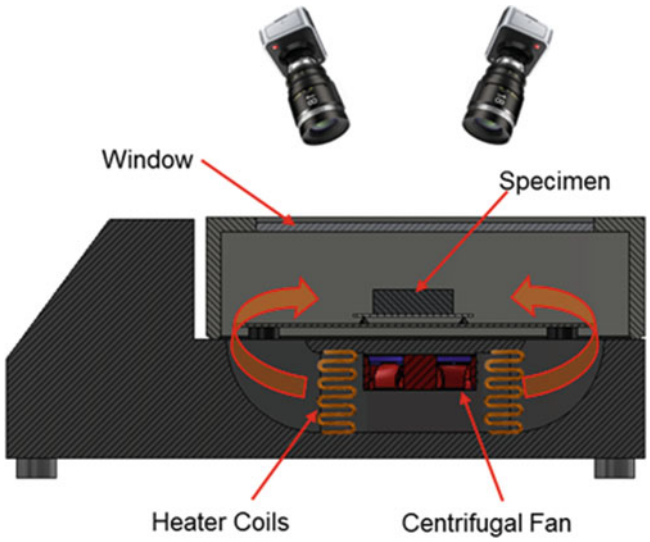

Fig. 26.3 Schematic of original test apparatus

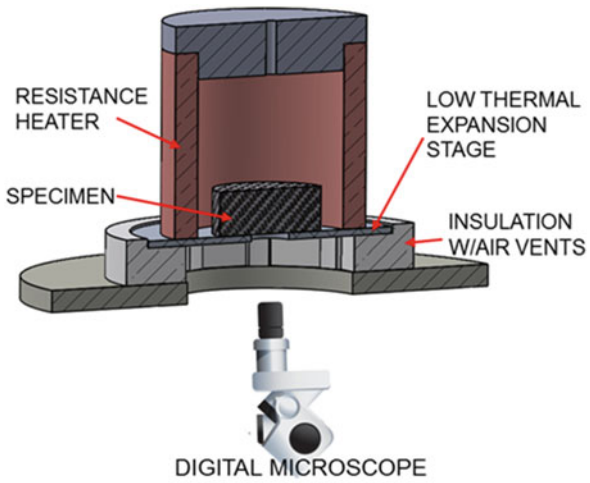

Fig. 26.4 Specially-designed microscopy apparatus

resting on the stage, supported only by its weight, and is free to expand without constraint. In addition, this setup provides easy access to the specimen for setup and adjustment, and the adjustable stage allows the specimen to be easily moved in across the field of view.

26.3 Specimen Preparation

A new method of for applying high-contrast surface features needed to be developed for this application. In order to track displacement across the image, DIC requires high-contrast surface features that remain consistently identifiable throughout the test. These features need to be about 5 pixels wide, which is approximately 1 μm wide at ×1000 magnification for the Keyence microscope that was used. Various powders with 1 μm particle size were tried using a variety of application methods, but the particles tended to aggregate into approximately 10 μm clumps due to van der Waals forces. On a few occasions the surface was found to have sufficient intrinsic contrast features, such as dendrites in the solder, that DIC data could be reduced from a finely polished specimen. An example of this is shown in Fig. 26.5, in which a pair of first-level interconnect solder bumps has been polished to reveal the solder dendrites, voids in the copper traces and silicon, along with features in the polymeric underfill and substrate resin. All of these features produced sufficient contrast for the DIC software to calculate strain data.

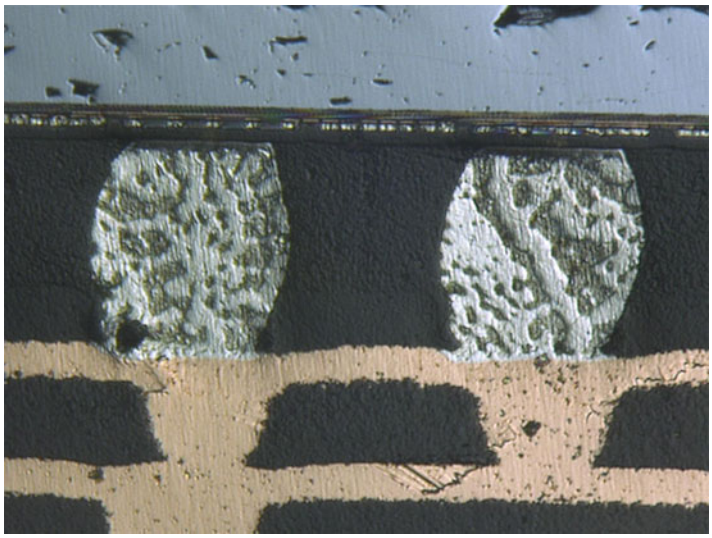

Fig. 26.5 Polished specimen with sufficient intrinsic surface features at ×1000 magnification

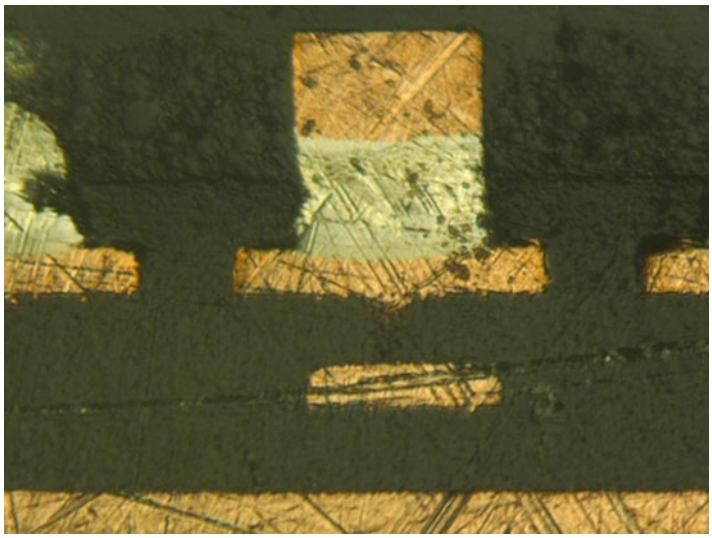

Fig. 26.6 Polished and "de-polished" first level solder bump viewed at ×1000 magnification

It has more often been the case that high-contrast features have to be added. The authors found that the surface could be finely polished and then "de-polished" in several directions with a coarser grit to add these features. The width of the features depends on the grit, and the depth of features of the proper size is typically smaller than the depth of focus for that magnification. An example of this is shown in Fig. 26.6, where small scratches produced contrast in regions of the solder microstructure with insufficient intrinsic features. Acceptably low levels of noise were achieved after some practice in specimen preparation. This was all done using typical optical microscopy sample preparation equipment and supplies.

26.4 Results

Tests have been performed over a range of temperatures up to 200 °C, over a range of magnifications between ×100 and ×1000, and on a variety of microelectronics structures and materials. The lower magnifications are appropriate for relatively large regions of microelectronic packages or for the larger interconnections between the substrate and the wiring board. The higher magnifications are more appropriate for individual structures or for the much smaller interconnections between the processor and the substrate. The higher magnification test are more difficult to set up due to the lower depth of focus and smaller field of view, but produce comparable results. Some tests at higher magnification have lost focus at elevated

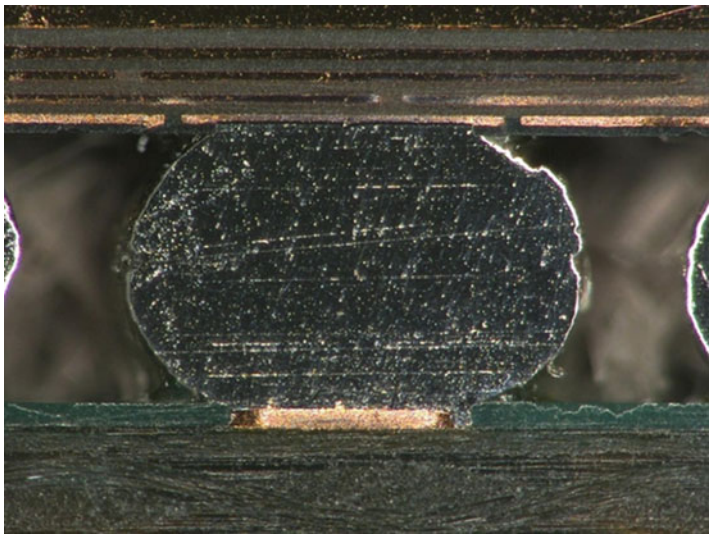

Fig. 26.7 Pre-test second level interconnect specimen at × 200 magnification

temperature due to out-of-plane warpage of the part. This was addressed by milling a groove in the upper side of the stage on either side of the viewing port so that the out-of-plane displacement goes into the groove without moving the area of interest.

In order to demonstrate the capability, two tests are presented below. The first test is of a substrate-to-board interconnection at ×200 magnification from room temperature to 170 °C. The second test is of a pair of processor-to-substrate interconnections from a different part at ×1000 magnification from room temperature to 110 °C. In both tests the reference images were taken at room temperature. In DIC post-processing, the entire area of interest was used to perform a correction to remove any rigid body motion.

The lower magnification test was performed on a flip-chip ball grid array (FCBGA) microelectronic package mounted to a 1.6 mm thick wiring board. The spacing from interconnection to interconnection is approximately 1.2 mm and the solder interconnections are approximately 1 mm wide. The part was cross-sectioned near the edge of the processor die and polished down to a 1 μm diamond paste finish. The interconnection that was imaged was the second from the last to one of the outer edges, and is shown in Fig. 26.7 at ×200 magnification, producing an image that is approximately 1.4 mm wide. The specimen was photographed every 20 °C from 30 to 170 °C. The response of the specimen was essentially uniform expansion, as shown in Fig. 26.8, with significant rigid body motion of the edge of the part in the in-plane direction due to the expansion of the package (which was removed from the data using the correction mentioned above), but negligible shear across the solder joint by the substrate and board. This is reasonable due to the fact that the overall thermal expansion of the substrate and board materials are expected to be very similar. The expansion across (in the y direction in the figures) the interconnection was measured as a function of temperature, since this motion should be solely due to the thermal expansion of the solder, and the data are plotted in Fig. 26.9, showing general agreement with typical values for the thermal expansion of tin/silver/copper solder. It is interesting to note that the x displacement reveals the difference in the thermal expansion of the bundle of glass reinforcement fibers in the wiring board that are oriented in the z direction compared to those oriented in the x direction, which illustrates the quality of the results.

The higher magnification test was performed on a FCBGA package with an integrated heat sink attached to the top of the substrate and the processor die, and with epoxy underfill between the die and substrate. The solder interconnections are approximately 100 μm wide. The part was cross-sectioned through the center of the processor die and was polished down to a 1 μm diamond paste finish. At ×1000, two interconnections fill the field of view, which is approximately 300 μm wide. The package had been tested up to 180 °C previously—well above the underfill cure temperature—and the microstructure changed significantly during the first temperature cycle, but not on subsequent cycles to lower temperatures. The original microstructure is shown in Fig. 26.5, and the subsequent microstructure is shown in Fig. 26.10. For this test a pair of bumps one quarter of the way across the length of the die was imaged. The results at 110 °C showed little strain in the x direction, but significant strain in the y direction, which is shown in Fig. 26.11. The high strain region along the middle of the image revealed that a crack had formed between the underfill and the substrate and was propagating through the lower portion of the solder interconnection. It is also interesting to note that the strain data shows the difference in thermal expansion of the thin direction copper trace and the surrounding polymer over a difference of only 80 °C.

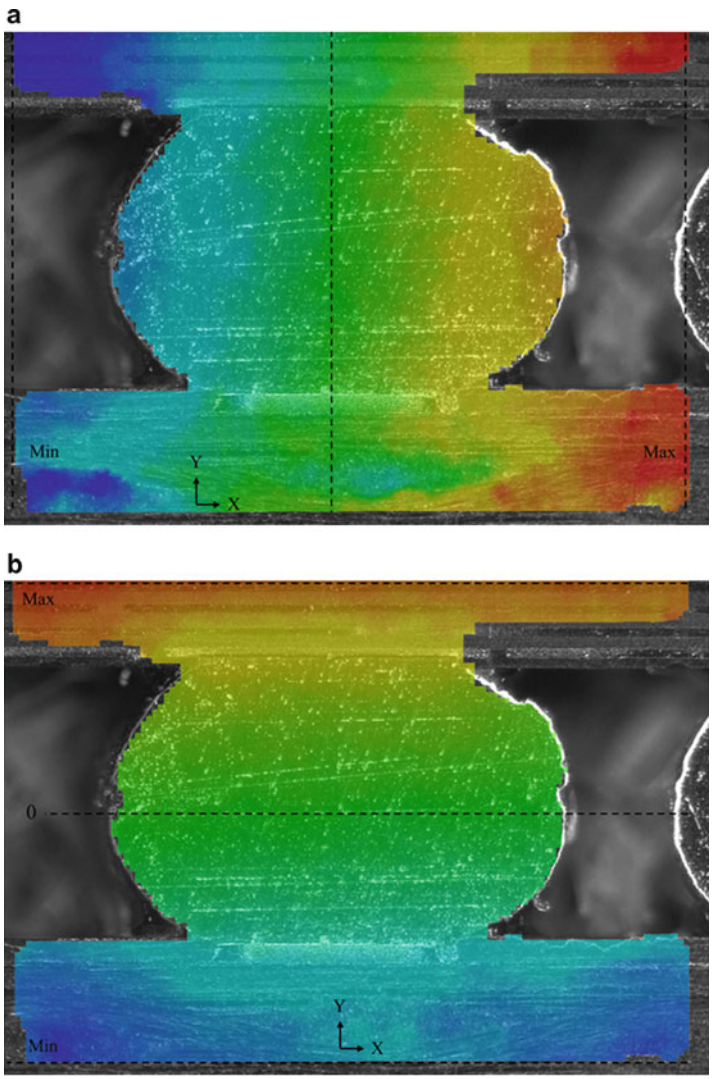

Fig. 26.8 Relative displacement at 170 °C: (**a**) X displacement, (**b**) Y displacement

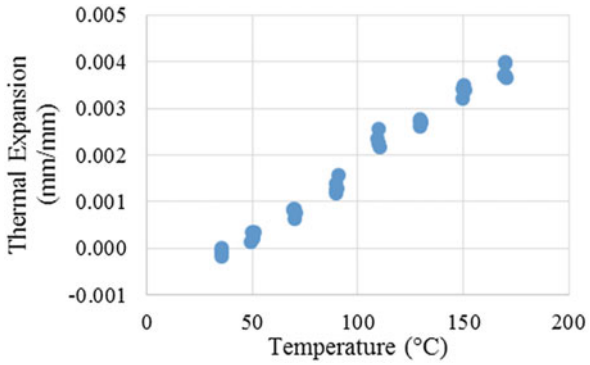

Fig. 26.9 Expansion of the solder as a function of temperature

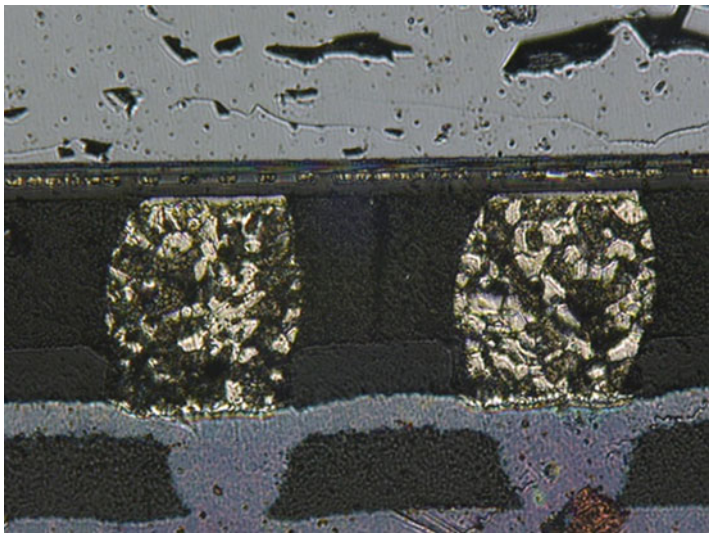

Fig. 26.10 Pre-test first level interconnect specimen at ×1000 magnification

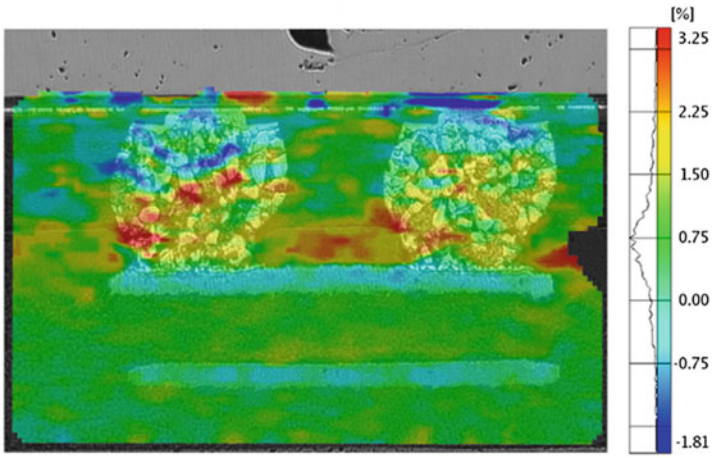

Fig. 26.11 Local Y strain response at 110 °C

26.5 Conclusions

The prototype test apparatus and specimen preparation methods have produced satisfactory displacement and strain data at magnifications between ×100 and ×1000 and at temperatures up to 200 °C. This scale is sufficient to resolve the thermal strain on microscopic features. While specimen preparation is required to polish the specimen surface and add contrast features, it is less labor-intensive and requires less specialized equipment compared to interferometry, while measuring all in-plane displacements with a single test.

Acknowledgment The authors would like to thank Kelly Davis and Janelle Chambers of Southern Research for their assistance in testing and sample preparation. In addition, we would like to thank the manufacturers of the parts for providing samples to test.

References

1. Davidson, R.J.: A comparison of Moire interferometry and digital image correlation. Air Force Institute of Technology, Wright Patterson Air Force Base (2008)
2. Kammers, D.: Digital image correlation under scanning electron microscopy: Methodology and validation. Exp. Mech. **53**(9), 1743–1761 (2013)

3. Ralph, M.: Connolly, digital image correlation using high magnification optical microscopy. In: Proceedings of SMTA International, Rosemont, 27 Sept–1 Oct 2015
4. Ralph, R.: Assembly level digital image correlation under reflow and thermal cycling conditions. In: Proceedings of the 63rd Electronic Components and Technology Conference, pp. 2223–2227, Las Vegas, 28–31 May 2013

Chapter 27
Design of Hybrid Composites from Scrap Aluminum Reinforced with (SiC+TiO_2+Gr+Ti+B)

A. Kursun, L.F.P. Ferreira, E. Bayraktar, and I. Miskioglu

Abstract Hybrid Metal Matrix Composites (HMMCs) have very light weight, high strength, and show better resistance to corrosion, oxidation, and wear. Impact resistance is an especially important property of these HMMCs which is essential for automotive applications. In this study, hybrid aluminum matrix composites were designed through the powder metallurgy route. As matrix, fresh scrap aluminium chips (AA2014), byproduct of machining, were used. Silicon carbide (SiC), boron, titanium, titanium oxide (TiO_2) and graphite (Gr) particles were used as reinforcement elements for the present work. The hybrid MMCs were prepared with SiC (5, 10 and 15 % by weight) as a main reinforcement and also certain amounts of Ti, B, TiO_2 and graphite powders were added in the matrix.

Within the framework of the present study, an original idea of producing a hybrid composite has been developed by using scrap aluminum (AA2014) chips. This consist of the mixing, blending and compacting of aluminum chips through press moulding and sintering. The influence of the reinforcement particles on the mechanical behavior of these composites was evaluated. Microstructure of each composite was analyzed by Scanning Electron Microscope (SEM).

Keywords Hybrid MMCs • Powder metallurgy • Solid state sintering • Impact test • Scanning Electron Microscopy (SEM)

27.1 Introduction

Hybrid metal matrix composites (HMMCs) are the new version of the conventional metal matrix composites (MMCs) that have many possibilities to replace simple reinforced composites with better mechanical and physical properties. They combine two or more materials in such a way as to have certain characteristics not presented by any one material alone. In fact, metal matrix composites (MMCs) should combine the physical and mechanical properties of the metallic alloys and the ceramic oxide reinforcements with high modulus and high ultimate tensile strength. By this way, they can result in better characteristics than the conventional metallic alloys [1, 2]. Among MMCs, aluminum matrix composites (AMCs) exemplifies certain MMCs possessing properties such as low density, high stiffness and strength, higher wear resistance, controlled coefficient of thermal expansion, higher fatigue resistance and better stability at elevated temperatures. Hence these composites are used in the design of a wide range of components in advanced engineering applications [3].

As a typical example, use of AMCs in engine applications can reduce the overall weight, fuel consumption and pollution in the automobiles and aircrafts [4, 5]. Generally, AMCs are reinforced with silicon carbide or alumina particles and they are attractive materials for such applications [4–6]. However, whatever the composites are used for, low cost manufacturing of MMCs with improved physical and mechanical properties became an important subject for the composite designers. Due to this, fresh scrap aluminum chips (AA2014) are used in the present work for the design of novel hybrid composites that will be pioneered in future industrial applications in automobiles and aircrafts [5–8].

A. Kursun
Department of Mechanical Engineering, Hitit University, Çorum, Turkey

School of Mechanical and Manufacturing Engineering, Supmeca-Paris, Paris, France

L.F.P. Ferreira
School of Mechanical and Manufacturing Engineering, Supmeca-Paris, Paris, France

Materials Science Department, UNICAMP—University of Campinas, Campinas, São Paulo, Brazil

E. Bayraktar (✉)
School of Mechanical and Manufacturing Engineering, Supmeca-Paris, Paris, France
e-mail: bayraktar@supmeca.fr

I. Miskioglu
Department of ME-EM, Michigan Technological University, Houghton, MI, USA

W.C. Ralph et al. (eds.), *Mechanics of Composite and Multi-functional Materials, Volume 7*,
Conference Proceedings of the Society for Experimental Mechanics Series, DOI 10.1007/978-3-319-41766-0_27

The present study deals with the development and characterization of novel hybrid composites with aluminum matrix from fresh scrap aluminum chips (AA2014). The main reinforcements in these composites should improve its physical and mechanical properties. In addition, secondary reinforcements added to the composite at low percentages should play an important role in the development of HMMCs with more enhanced characteristics. For this reason, certain elements were chosen as secondary reinforcements and added to the matrix.

In the final stage, material parameters were optimized for improving physical and mechanical properties of these composites. Further, the influence of reinforcement's type and content on the mechanical properties has also been reviewed and discussed. Damping capacities and damage were analyzed by drop weight and quasi static compression tests. Microstructures were analyzed by the Scanning Electron Microscope (SEM).

27.2 Experimental Procedures

Three different compositions were prepared for the present work with scrap aluminum AA2014 chips used as the matrix material. As a major reinforcement, silicon carbide (SiC) in three different weight percentages (5, 10 and 15 %), was used. Titanium, graphite, titanium dioxide and boron were also added in the compositions as secondary reinforcements. The three compositions were classified under the name of the following codes (AK1, AK2 and AK3) as shown Table 27.1.

All of the three compositions were milled for 1 h in a stainless steel mixer with addition of 2 % zinc stearate to facilitate the lubrication and then each composition was mixed by ball milling at a rotational speed of 6000 rpm for 1 h. To prepare green compaction of the powder mixtures, a double action—hydraulic press with a capacity of 100 tons was used. Cold compaction was carried out at 650 MPa to produce green compact specimens according to ASTM-E 9-89a with a diameter of 11 mm. Aspect ratio (L/D) was kept as 1.5 or 1.75 for all of the specimens.

Samples of green compacts were sintered under inert atmosphere with argon gas. Solid state sintering was carried out in one stage: the consolidation of sintering was completed at the temperature of 600 $\pm$ 5 °C for a total period of 1 h 30 min. Heating rate was 10 °C/min. After sintering of the density of the specimens were measured by a pycnometer (digital density meters, Webb and Orr, 1997 work with helium gas) and the results were compared.

Quasi-static compression testing of the sintered products were carried out with a servo-hydraulic INSTRON Universal test system (model Instron 5500R, equipped with a load cell of 25.000 kgf) at an initial rate of 10 mm/min and a second rate of 5 mm/min.

Maximum load endpoint was 4500 N. Furthermore, dynamic compression (drop weight tests) were carried out with a universal drop weight test device (Dynatup Model 8200 machine) with a total weight of 10.5 kg, punch height of 600 mm and with an impact velocity of 3 m/s. Microstructure and fracture surface analyses of the composites were carried out with Scanning Electron Microscopy (JOEL-SEM).

27.3 Results and Discussion

The study of microstructure was reasonably useful in evaluating the distribution of the reinforcements in the matrix and the reinforcement/matrix interface relation in these composites. Figure 27.1 shows the details of the hybrid composites designed here with interface positions of matrix/reinforcements for three compositions. Prolongation of milling time, mainly ball milling, facilitates the diffusion process at reinforcement/matrix interface.

In these structures, distribution of the main reinforcements are very similar, more or less homogenous. Basically SiC and boron have shown good cohesion with matrix containing aluminum chips. Some of the areas in the grain boundaries show precipitation of the reinforcements that were indicated in the right column for each composition. As well known, boron and SiC are harder than the aluminum matrix and they improve the hardness of HMMCs. Here, graphite plays an important role as lubricant. Combined effect of boron and graphite has significant effect on properties, such as high thermal conductivity, low thermal expansion, good thermal shock resistance, etc. [7–10].

Table 27.1 Weight percentage of the particles added as reinforcement to the Al-matrix

Composite	Al	SiC	Ti	Gr	TiO_2	B
AK1	Balance	5	5	2.5	2.5	5
AK2	Balance	10	5	2.5	2.5	5
AK3	Balance	15	5	2.5	2.5	5

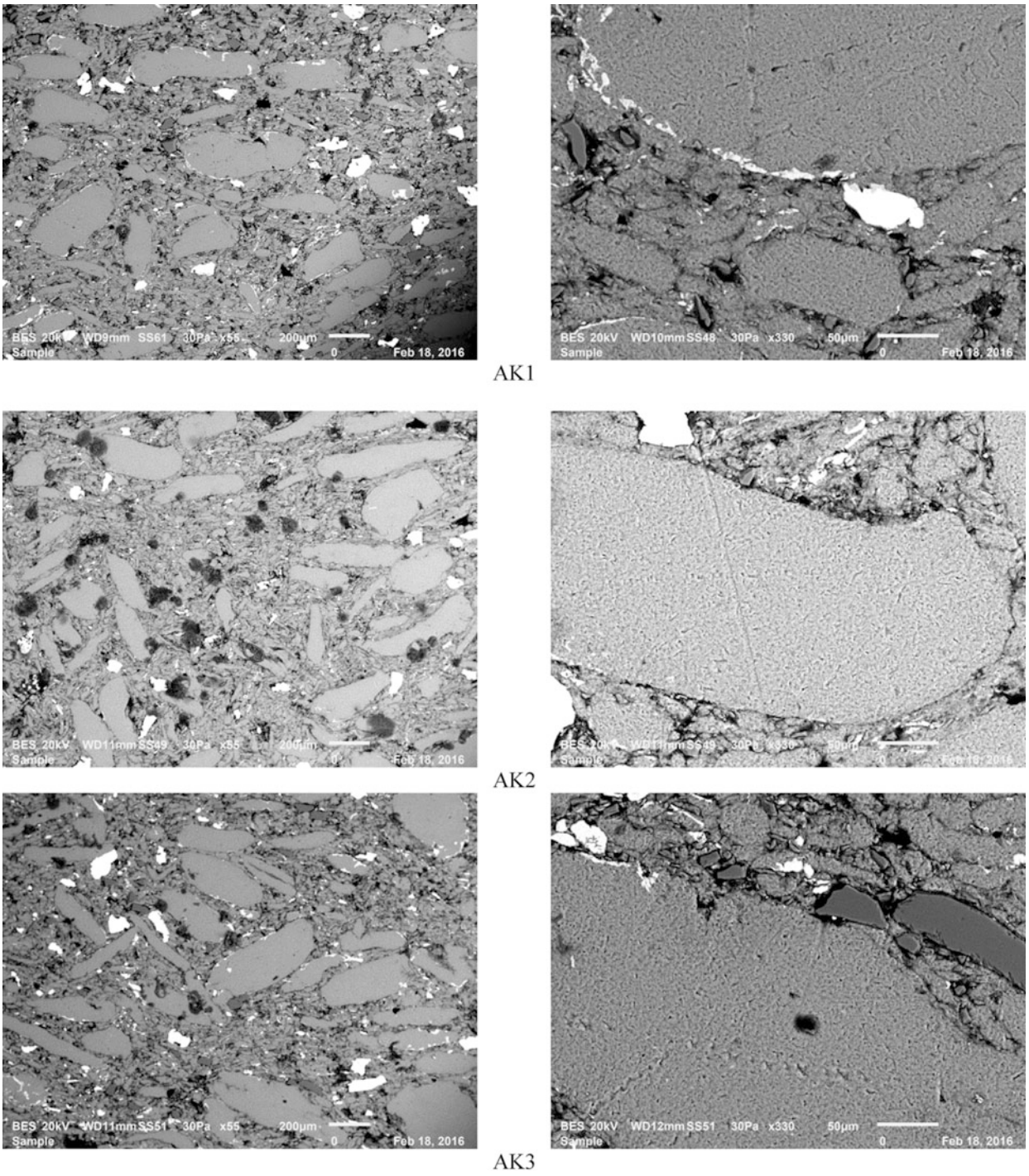

Fig. 27.1 SEM microstructures of three compositions created in this work (AK1, AK2 and AK3)

The small agglomerations observed in certain zones are due to the homogenization problem entirely related to milling. Interface is extensively influenced by blending and mixture—milling time (mixing condition of Al chips and reinforcement powders), compacting pressure and most significantly by the sintering temperature. For this reason, homogenous and fine distribution of reinforcement particles can be achieved by ball milling which in turn can results in improved physical and mechanical properties of these composites and stimulate phase transformation of reinforcements. A proper cohesion at the interface can only be carried out by milling and relatively high sintering temperatures.

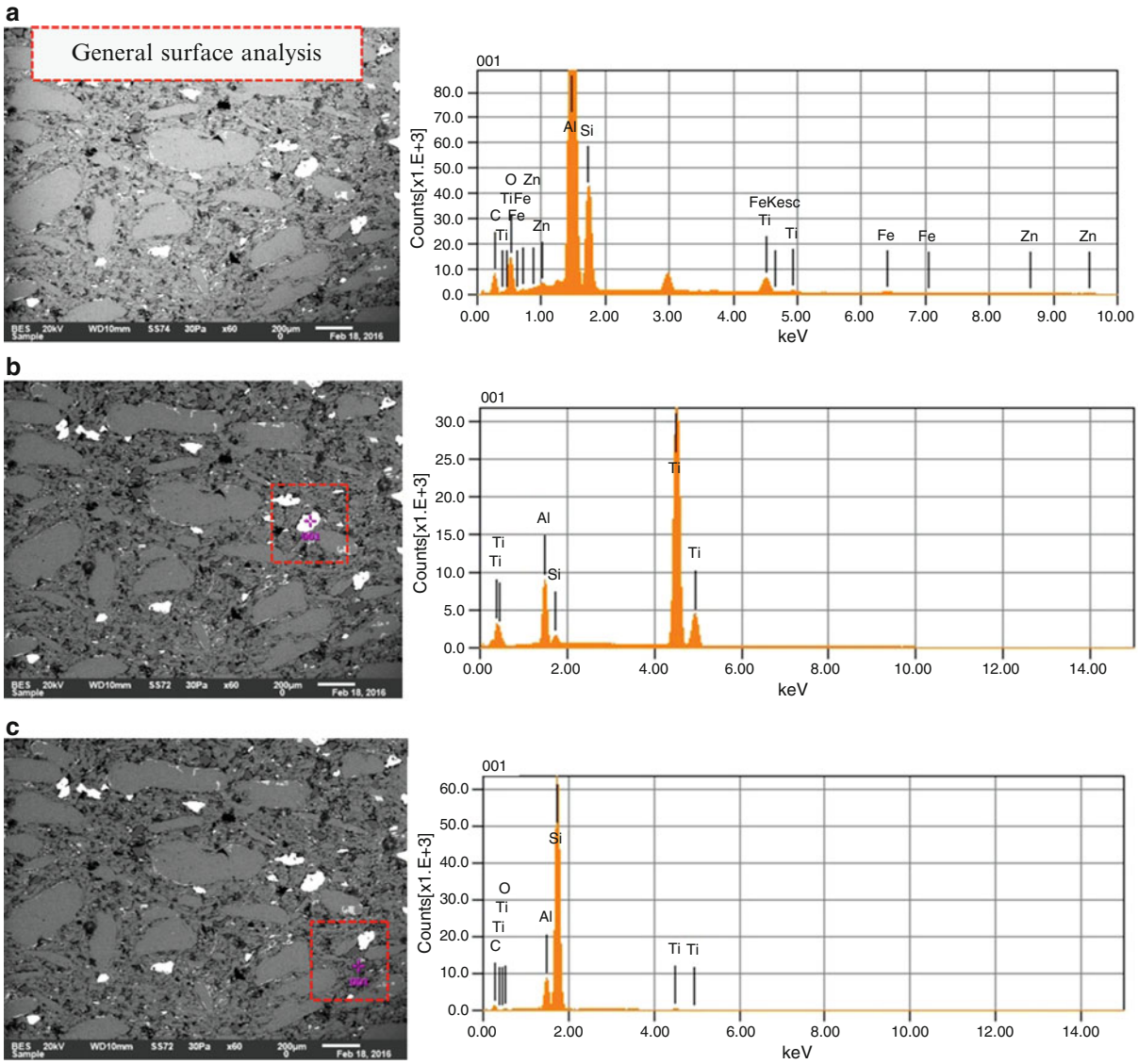

Fig. 27.2 Chemical composition of AK1: (**a**) general analysis, (**b**) white particles, (**c**) gray particles

A stable bonding diffusion occurs between the soft matrix and hard particles. In these composites this should occur between the light atoms (e.g. aluminum chips and or aluminum powders) and the heavy atoms such as B, SiC, particulate reinforcements are much simulated at the grain boundaries. Therefore, reaction phases at the interface matrix/intermetallic can be caused by a stable interface.

Figure 27.2 presents the microstructural analyses by spectrum graphics, EDS for the composite AK1. In this figure, general analysis was made only on the composite surface as an example and also, some spot analyses have been carried on the different particulates as shown in the figure.

A comparative study for density and microhardness ($HV_{0.1}$) measurements are presented in Fig. 27.3 for the three compositions. At the first time, a slight effect of the SiC is seen in the structure. Slight increase in hardness values is mainly due to the effect of SiC particulate reinforcements. It means that the density of these composites decreases linearly due to lower density of SiC and graphite (combined effect of graphite and SiC).

Secondly, the combined effect of boron and graphite can affect these results. In some areas, certain amount of agglomeration can influence the measurements.

For this reason, homogeneous distribution of hard particle reinforcements should be improved in the microstructure as can be seen from these curves (Fig. 27.3).

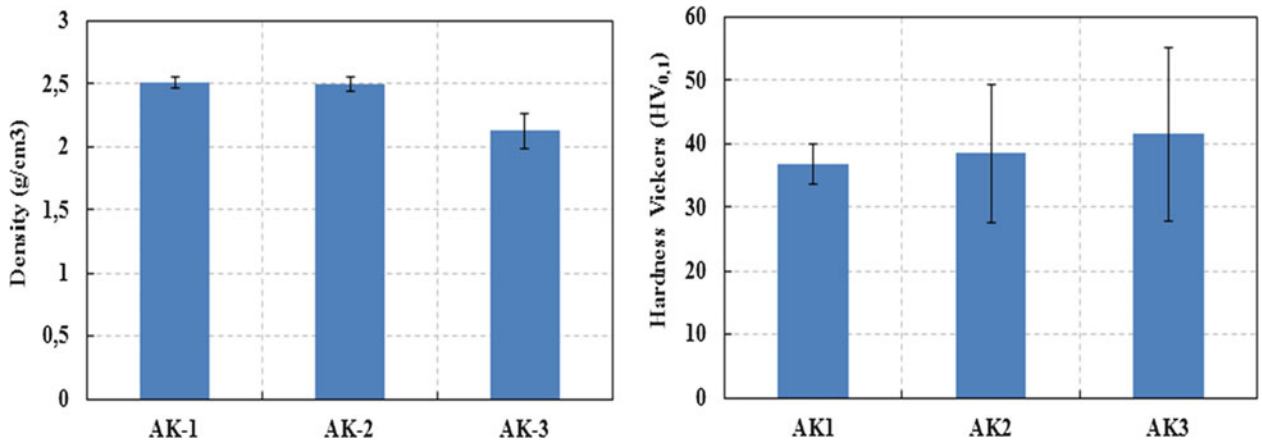

Fig. 27.3 Comparative study of the density measurements at the left column and micro hardness ($HV_{0.1}$) values at the right column for the three compositions

Low velocity or dynamic compression tests results are given in Fig. 27.4. Three typical force vs. time curves of the composites created in this work were analyzed to evaluate impact forces as a function of time; it means that the maximum force was evaluated there by the values from both support data points. Here, three series of impact tests were performed at room temperature at the centre of cylindrical specimens using the instrumented drop weight test device as explained in detail in the former section (experimental conditions). At least three specimens were tested for each composition.

First of all, the effect SiC on the impact resistance of the composites can be detected. It seems from the graphs given in the Fig. 27.4b, the composition coded AK1 shows slightly higher impact resistance (higher impact energy level). Again, the same composition gives similar absorbed energy as the composition coded AK2. In fact all of the three compositions have shown that the most part of the impact force is used to maintain the balance with the inertia force, and only a small portion of the impact force is actually used to deform and fracture the specimen. Maximum Forces as a function of time and related maximum stress levels for each composition are shown in Fig. 27.4c.

By using the former graphs, the maximum energy levels have been calculated for each composition. All of the results are presented in Fig. 27.5a. Evolution of linear energy tendency for three compositions is also shown in Fig. 27.5b.

Obviously, the specimens containing higher particulate reinforcements such as AK3 have shown higher particulate fracture behaviour. In general, the damage of the composites under low velocity impact started with matrix cracking; where compression stresses are dominant the cracks developed in the interfaces and/or continue as particulate cracking.

The dynamic responses during the impact for the specimens AK1 and AK2 are very similar and reach maximum impact forces equal 1200 N and 1300 N respectively with very high standard deviations, around 5–7 %.

All of the compositions developed in this work were also tested under quasi-static compression loading conditions. Some of the test specimens are presented in the Fig. 27.6 before and after compression test as an example. Obviously the resistance of the specimens to compressive loads is very high with the addition of the hard particulate reinforcements. Here, major effect is seen with the percentage of SiC particulates and also brittleness effect of these particles; influence of these particles on the composite AK3 is indicated in the Fig. 27.7.

27.4 Conclusion

In the present work, certain properties of hybrid metallic matrix composites (HMMCs) have been presented to recognize them as materials with suitable performance for various engineering applications and as a replacement for conventional materials. Essentially the application of HMMCs in various automotive and aeronautic components seem to be achievable.

In general, the properties of hybrid composites can be improved with the arrangement and combination of different particulate reinforcements. Usually, the ceramic reinforcements increase the density of the base alloy during manufacturing of these composites. But, the addition of lightweight reinforcements reduces the density of the hybrid composites. These could be revealed as complementary reinforcements for development of hybrid composites. As expected, the mechanical

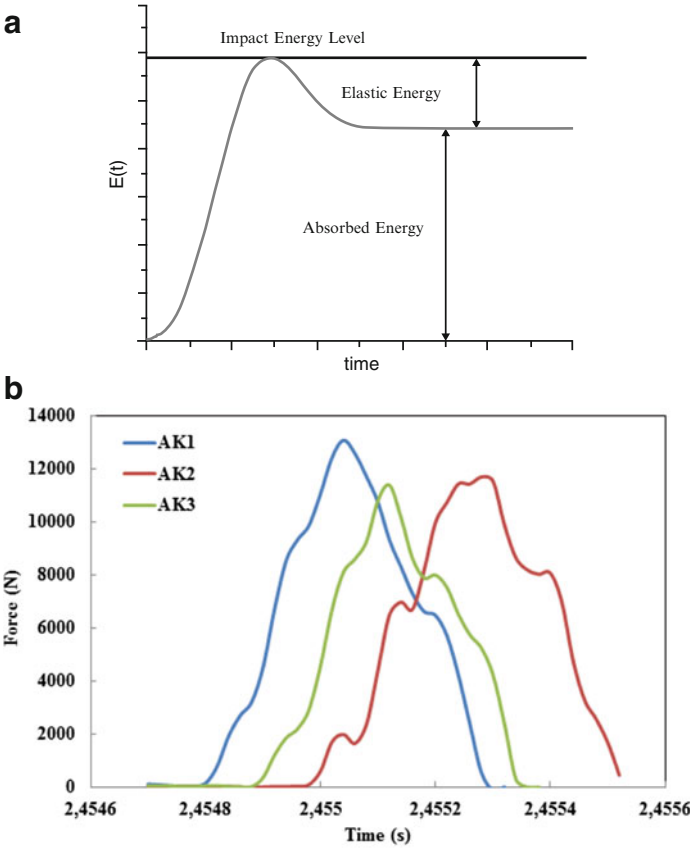

Fig. 27.4 (**a**) General presentation of impact test and (**b**, **c**) drop weight/dynamic compression test results for three compositions: AK1, AK2and AK3

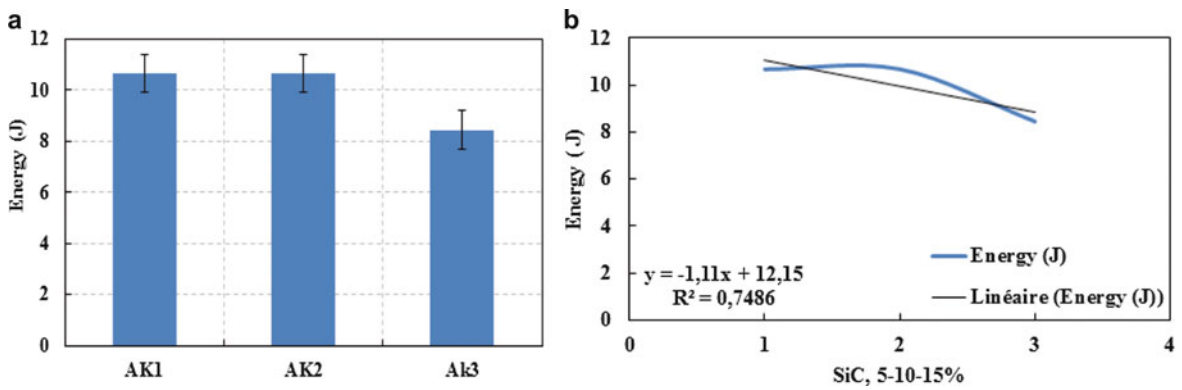

Fig. 27.5 (**a**) Maximum energy values, (**b**) evolution of linear energy tendency for three compositions

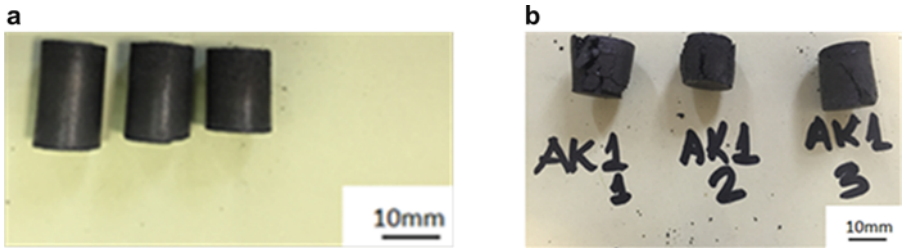

Fig. 27.6 Compression test samples before (**a**), and after the test (**b**)

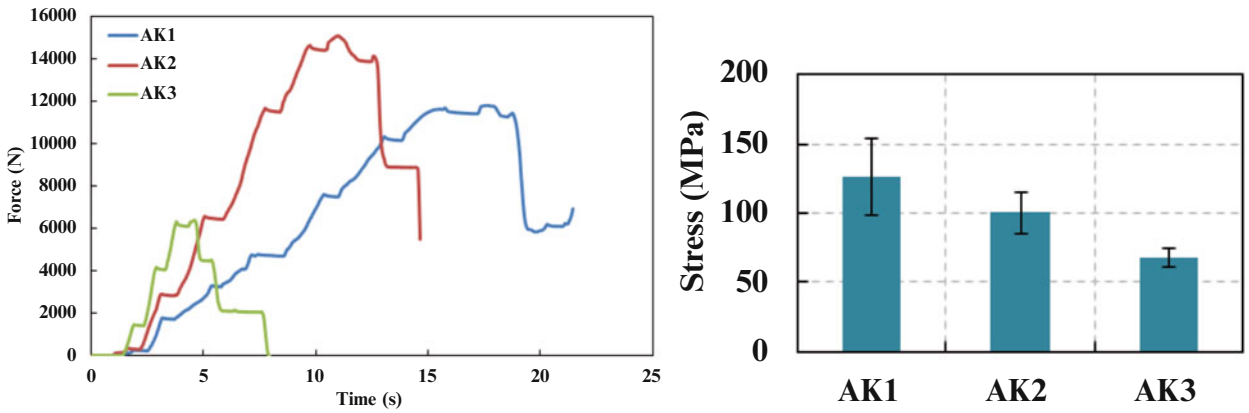

Fig. 27.7 Maximum force (Fmax) and maximum stress (MPa) obtained by compression test for the compositions AK1, AK2 and AK3

and physical properties of HMMCs are controlled by the composition and type of the reinforcements. It has also been detected that the major reinforcements like SiC, alumina and/or boron can be combined with secondary (minor) reinforcements to obtain required properties for these composites.

References

1. Milan, M.T., Bowen, P.: Tensile and fracture toughness properties of SiCp reinforced Al alloys: Effects of particle size, particle volume fraction and matrix strength. J. Mater. Eng. Perform. **13**, 775–783 (2004)
2. Ranjbaran, M.M.: Low fracture toughness in AA7191 and 20% SiC aluminum matrix composite. Eur. J. Appl. Eng. Sci. Res. **41**, 261–272 (2010)
3. Rajmohan, T., Ranganathan, S., Suryakumari, T.S.A.: Experimental study on fabrication of hybrid (Al+Tio2+Gr) metal matrix composites. Int. J. Adv. Eng. Appl. **7**(2), 11–14 (2014)
4. Sinclair, I., Gregson, P.J.: Structural performance of discontinuous metal matrix composites. Mater Sci. Technol. **3**, 709–726 (1997)
5. Hanumanth, G.S., Irons, G.A.: Particle incorporation by melt stirring for the production of metal-matrix composites. J. Mater. Sci. **28**, 2459–2465 (1993)
6. Bayraktar, E., Ayari, F., Tan, M.J., Tosun Bayraktar, A., Katundi, D.: Manufacturing of aluminum matrix composites reinforced with iron-oxide nanoparticles: Microstructural and mechanical properties. Metall. Mater. Trans. B **45B**(26), 352–362 (2014)
7. Gottesman, T., Girshovich, S.: Impact damage assessment and mechanical degradation of composites. Key Eng. Mater. **141**(1), 3–18 (1998)
8. Macke, A., Schultz, B.F., Rohatgi, P.: Metal matrix composites offer the automotive industry an opportunity to reduce vehicle weight, improve performance. Adv. Mater. Process. **170**(3), 19–23 (2012)
9. Podgornik, B., Kosec, T., Kocijan, A., Donik, C.: Tribological behaviour and lubrication performance of hexagonal boron nitride (h-BN) as a replacement for graphite in aluminium forming. Tribol. Int. **81**, 267–275 (2015)
10. Kindervater, C.M., Georgi, H.: Composite strength and energy absorption as an aspect of structural crash resistance. In: Proceedings on Structural Crashworthiness and Failure, pp. 189–235. Elsevier, London, 2003

Chapter 28
Manufacturing of Low Cost Composites with Porous Structures from Scrap Aluminium (AA2014) Chips

L.F.P. Ferreira, F. Gatamorta, E. Bayraktar, and M.H. Robert

Abstract In this study, aluminium matrix composites, (AMCs) have been created with porous structures reinforced with brown sugar, BN, graphite powders, boron and also fine glass bubbles. These composites are produced as sponge structures with low thermal and electrical conductivity. The process comprises a simple mixture of aluminium powders obtained from scrap aluminium chips (A2014) and glass bubbles with fresh scrap organic sugar coming from the excess of the production and their blending and finally followed by compacting of the mixture. Addition of the wax is variable from 0 up to 10 %. Sintering is carried out in two steps. First of all, the green compact is heated to eliminate entirely the sugar after that classical sintering of the structure is made under the inert atmosphere. Glass bubbles added at the beginning of the green compact create a net of interconnected porosity. Basically, drop weight test were applied to measure the impact behaviour of these sponge composites and acoustic emission capacity was measured. Microstructural and fracture behaviour were evaluated by Scanning Electron Microscopy (SEM).

Keywords Recycle of aluminium • Hybrid-porous composites • Impact test • Damage analysis • Clean energy

28.1 Introduction

Hybrid composites have unique structures that can be used to bring together various design requirements in a more economical way than conventional composites. Aluminium metal matrix composites (AMMCs) find many advanced materials application thanks to new manufacturing techniques and application of new particulate reinforcements. Today, through the combined methods of sintering and thixoforging/forging, many new composites especially hybrid composites are successfully used for the main manufacturing processes in aerospace and automotive industry. They are known high strength, lightweight materials very often called absorbed materials with high wear resistance, etc.

Increasingly, the demands for lightweight materials having a high strength and a high toughness capacities have attracted a lot of attention to the development of composite porous structures and/or composite reinforced with light reinforcements as nonconventional organic materials such as sugar, wax boron nitrate and/or porous ceramic oxides etc. [1–5].

The Powder Metallurgy (PM) route is known as most commonly used method for the preparation of discontinuous reinforced AMMCs. This method is generally used as low–medium cost to produce small objects, the high strength and resistant materials. For this reason, in the present work, a simple idea was established on the production of porous composites by using a low cost method (mixture of aluminum matrix with wax and/or with organic sugar and also addition of small size glass bubbles and finally cold compaction followed by sintering in two stages). Therefore, a new process was applied for the manufacturing of these composites for sake of the low-cost and simplicity of manufacturing process [1–4, 6, 7]. At the first step of this research, a typical porous structure has been created by using wax + organic sugar granular particles and an open spaces created by the volatilization of the wax and sugar constitute a net of interrelate porosity in the final product, called a low cost metallic porous structure [5–11].

L.F.P. Ferreira
Department of Materials Science and Engineering, UNICAMP—University of Campinas, Campinas, São Paulo, Brazil

School of Mechanical and Manufacturing Engineering, Supmeca-Paris, Paris, France

F. Gatamorta • M.H. Robert
Department of Materials Science and Engineering, UNICAMP—University of Campinas, Campinas, São Paulo, Brazil

E. Bayraktar (✉)
School of Mechanical and Manufacturing Engineering, Supmeca-Paris, Paris, France
e-mail: bayraktar@supmeca.fr

W.C. Ralph et al. (eds.), *Mechanics of Composite and Multi-functional Materials, Volume 7*,
Conference Proceedings of the Society for Experimental Mechanics Series, DOI 10.1007/978-3-319-41766-0_28

Procedures are very simple required for a low cost processing route of AMMCs containing glass bubbles, boron, boron nitrate, graphite reinforcements, for engineering applications. The present work uses a simple sintering technique under inert gas (argon), which has the certain advantages over liquid state methods. It presents potentially lower energy consumption, simplified operation methods with a low time scale, etc.

The present work has the following overall aims: to develop the understanding of powder metallurgy techniques in producing hybrid structure from scrap aluminum (A2014) matrix composites; to make the persistence of the lowering of costs in the processing of these composites.

Mechanical behavior was evaluated by using drop weight (dynamic compression) and quasi static compression tests. Microstructural characterization was made by Scanning Electron Microscope (SEM) for the checking of the reinforcement dispersion in the matrix and also to evaluate the interface between the matrix and reinforcements.

28.2 Experimental Procedures

Four hybrid compositions were arranged for the present work: Scrap aluminum (AA2014, Table 28.1) chips (initial size: $d \leq 80$ μm), coming from French Aeronautics was used as raw matrix m for final matrix of the composition. Glass Bubbles (GB-hollow glass microspheres produced by the company-3M with a density of 0.227 g/cm^3, specified as S38HSS & K1). Finally, for sake of simplicity, these four compositions were classified under the name of the following codes (Table 28.2):

Basically reinforcements (boron, glass bubble, boron nitrate and graphite) and also additional elements (wax and brown sugar, were analyzed in a differential thermal analyzer to determine the critical temperature-transformation points (solid-liquid zone) and mass loss *versus* temperature; they had also their size and geometry analyzed by SEM. All of the compositions were mixed during 2 h in a stainless steel mixer with addition of 2 % Zinc Stearate to facilitate the lubrication. The role of the wax and sugar granulates used in the matrix is to create nearly homogeneous distribution of porous/empty spaces in the matrix during the sintering process. To prepare green compaction of the powder mixtures, a double action-hydraulic press with a capacity of 20 tons was used. For compaction of the mixture, a stainless steel mold with a diameter of 20 mm was used, resulting in green compacts of same size, L/D = ~1.5 (diameter: 20 mm and height: 30 mm). After final blending, the mixture was compacted under pressure of 250 MPa. Green compacted samples were sintered according to the following conditions. Samples of green compacts were sintered under inert atmosphere with argon gas. The treatment for solid state sintering was carried out in two steps: firstly, the volatilization of the wax and sugar was performed at a temperature of 200 °C for a fixed time of 120 min. At the second step of the sintering of the mixture was completed at the temperature of 550 °C for a total period of 120 min. Heating rate was 10 °C/min for both steps. During the first step, removing of the wax and sugar must be complete by allowing the gas created by the melting and volatilization of the sugar granulates to scape, resulting in a porous structure with nearly homogeneous porous distribution. This structure is consolidated by the second step sintering.

Measurements of the density and porosity of the compacted specimens before and after sintering were carried out by pcynometer (digital density meters work with helium gas) before and after sintering and the results were then compared.

For mechanical tests and microstructural analyzes. Sintered products were submitted to compression tests, carried out in a servo-hydraulic INSTRON Universal test device (model Instron 5500R, equipped with a load cell of 25.000 kgf) with a quasi-static low speed (initial rate: 10 mm/min and second rate: 5 mm/min rate). Maximum load endpoint was 4500 N. All testing parameters are given in the Table 28.3.

Furthermore, dynamic drop tests were carried out on a universal drop weight test device (Dynatup Model 8200 machine) with a total weight of 1.9 kg, punch height of 1000 mm and with an impact velocity of 3 m/s.

Table 28.1 Chemical composition of scrap aluminium (AA2014) chips (wt%)

Element	Al	Cr	Cu	Fe	Mg	Mn	Si	Ti	Zn
wt%	Balance	≤0.10	4.5	≤0.70	0.55	0.8	≤0.15	≤0.15	≤0.25

Table 28.2 Reinforcement particles added to the Al-matrix (in wt%)

Composite wt%	Al A2014	Wax	Boron	Glass bubble	BN	Graphite	Brown sugar
P0	B	**0**	1	5	2	2	15
P1	B	**5**	1	5	2	2	15
P2	B	**7.5**	1	5	2	2	15
P3	B	**10**	1	5	2	2	15

Table 28.3 General conditions for compression tests of produced composites

Initial speed	10	10	10	10	mm/min
Load endpoint	4448	4448	4448	4448	N
Outer loop rate	100	100	100	100	Hz
Secondary speed	5.08	5.08	5.08	5.08	mm/min
Strain endpoint	80	80	80	80	%

Table 28.4 Experimental results of the differential scanning calorimetry analysis (DDSC) compared with calculated values

AA2014	DSC (5 °C/min)	DSC (10 °C/min)	DSC (15 °C/min)	Thermo-Calc®
$T_{liquidus}$ (°C)	642	650	660	641
$T_{solidus}$ (°C)	576	575	572	524
ΔT (°C)	66	75	88	117

28.3 Results and Discussion

Differential thermal analyses of the scrap aluminum (AA2014, glass bubbles (GB), and brown sugar (BS) in powders are shown in Table 28.4 and Fig. 28.1, respectively. In the same Figure, certain information are also given as images of these elements obtained by SEM. Basically, brown sugar powders in DTA curves show a significant transformation starting around 180 °C, followed by a heavy mass loss starting round 220 °C; these points can be assumed as melting and volatilization temperatures, respectively. The same information can be also obtained for other elements in the mixture.

Related to the Glass Bubbles, Fig. 28.1b shows some reaction when heating from room temperature to 140 °C, with around 5 % of mass addition. This can be related to some chemical reaction in the glass material and must be further investigated. SEM images show Hollow glass spheres are perfectly rounded, presenting diameters from 2 to 30 μm; Brown Sugar granulates present polygonal morphology and sizes of 200 to 250 μm.

SEM microstructures of the compositions classified as P0, P1, P2 and P3 as a function of percentage of wax (0, 5, 7.5 and 10 %) were presented in the Fig. 28.2. First of all, the combined effect of the wax and brown sugar granulates should be considerable. The presence of glass bubbles can be observed distributed more and less well in the structure, as well as the free spaces left increase with sugar percentage added in the structure.

Any trace as artifacts is observed in the structure after the volatilization of the sugar granulates. Thinner cell walls are present with high contents of sugar used together with wax. Considering theses microstructures, a new design of the structure is needed by limitation of the sugar content and wax together. However, all of these composites proposed here, give a simple idea clean process in an economic way by elaborating scrap aluminium chips coming from cutting process in industry.

Measurements of the density of the specimens before (green compact) and after sintering (composite) measured on these specimens can give an indicative results to show the idea of space holders created by wax and sugar. Density of all the green compact specimens for the four compositions investigated varies between 2.45 and 2.51 g/cm^3. After sintering these values decrease around 40–50 %, to the levels of 1.80–2.05 g/cm^3.

Specimens present lower density when the wax and brown sugar are used together. Glass Bubble addition in the structure gives high damping effect to create light composites.

These results show that free spaces/massive regions ratio increases after sintering as the sugar granulates suffer volatilization, at the same levels for all of four compositions. Sintering treatments is found correct for these compositions. For obtaining more homogenous porous structures, more carefully preparation of the mixture longer milling is need also to distribute homogenously in the matrix.

Low velocity or dynamic compression tests results were given in the Fig. 28.3. Maximum force was evaluated there by the values from both support data points. Here, a series of impact tests were performed at room temperature at the centre of cylindrical specimens using the instrumented drop weight test device as explained in detail in the second section (experimental conditions). Three specimens were tested for each composition (Fig. 28.4).

First of all, the effect combined effect of wax and sugar granulate on the impact resistance of the composites can be detected.

It seems from the graphs given in the Fig. 28.4, impact resistance is related to absorbed energy. In fact all of the four compositions have shown that the most part of the impact force is used to maintain the balance with the inertia force, and only a small portion of the impact force is actually used to deform and fracture the specimen.

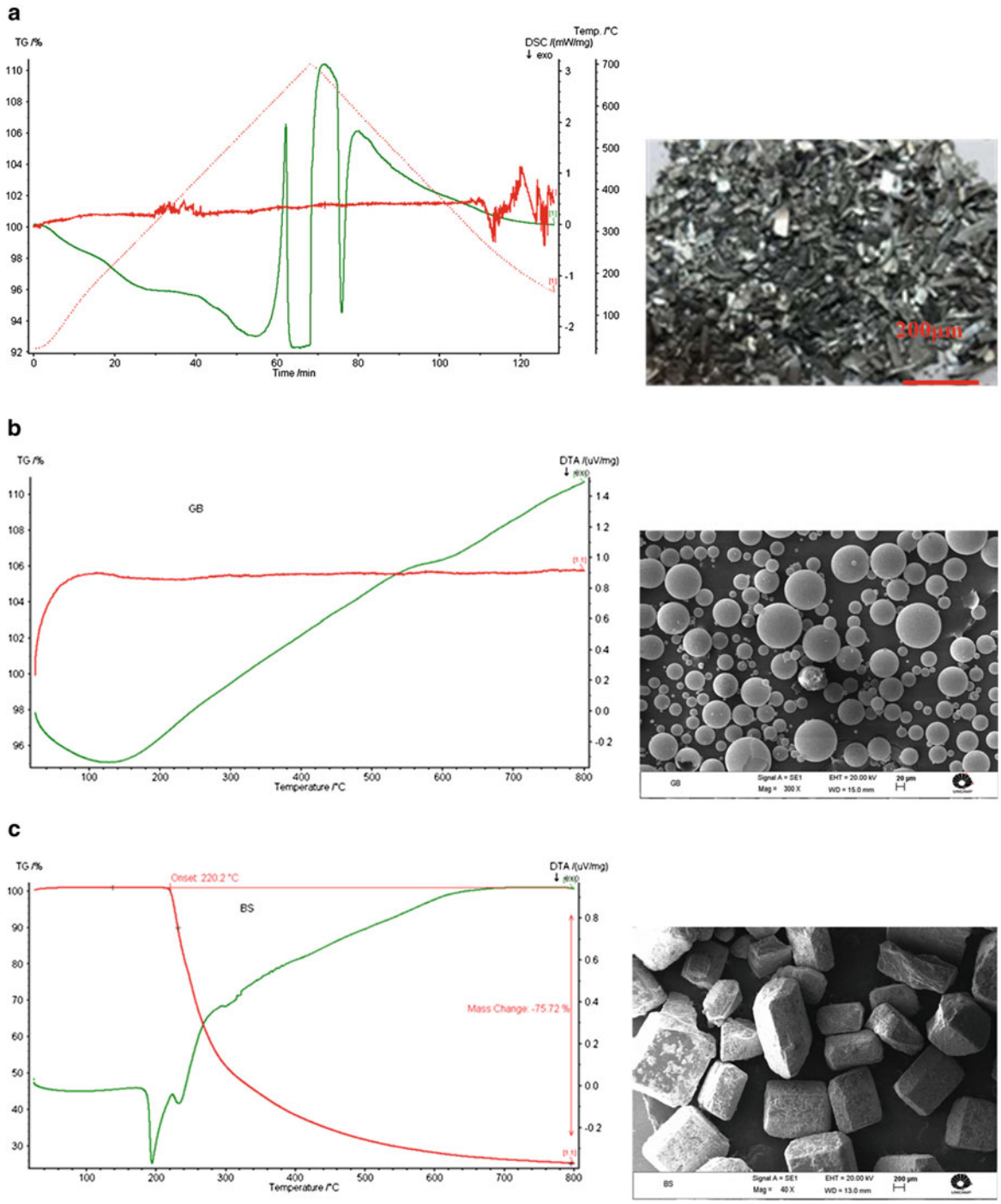

Fig. 28.1 Results of differential thermal analysis (DTA) and thermogravimetry (TG) of the glass bubbles and brown sugar granulates used in this work and images by SEM of the corresponding material: (**a**) scrap aluminium (AA2104) chips, (**b**) glass bubbles (additional element), (**c**) brown sugar (space holder)

Absorbed energy should be related with the compositions that this energy increases slightly with percentage of space holders (depending on the presence of glass bubbles distributed in the structure, as well as the free spaces left by the volatilization of the sugar granulates). Absorbed Energy and energy/linear tendency were presented in the Fig. 28.5 as a function of wax added in the structure that confirms the ideas identified in the former Fig. 28.4.

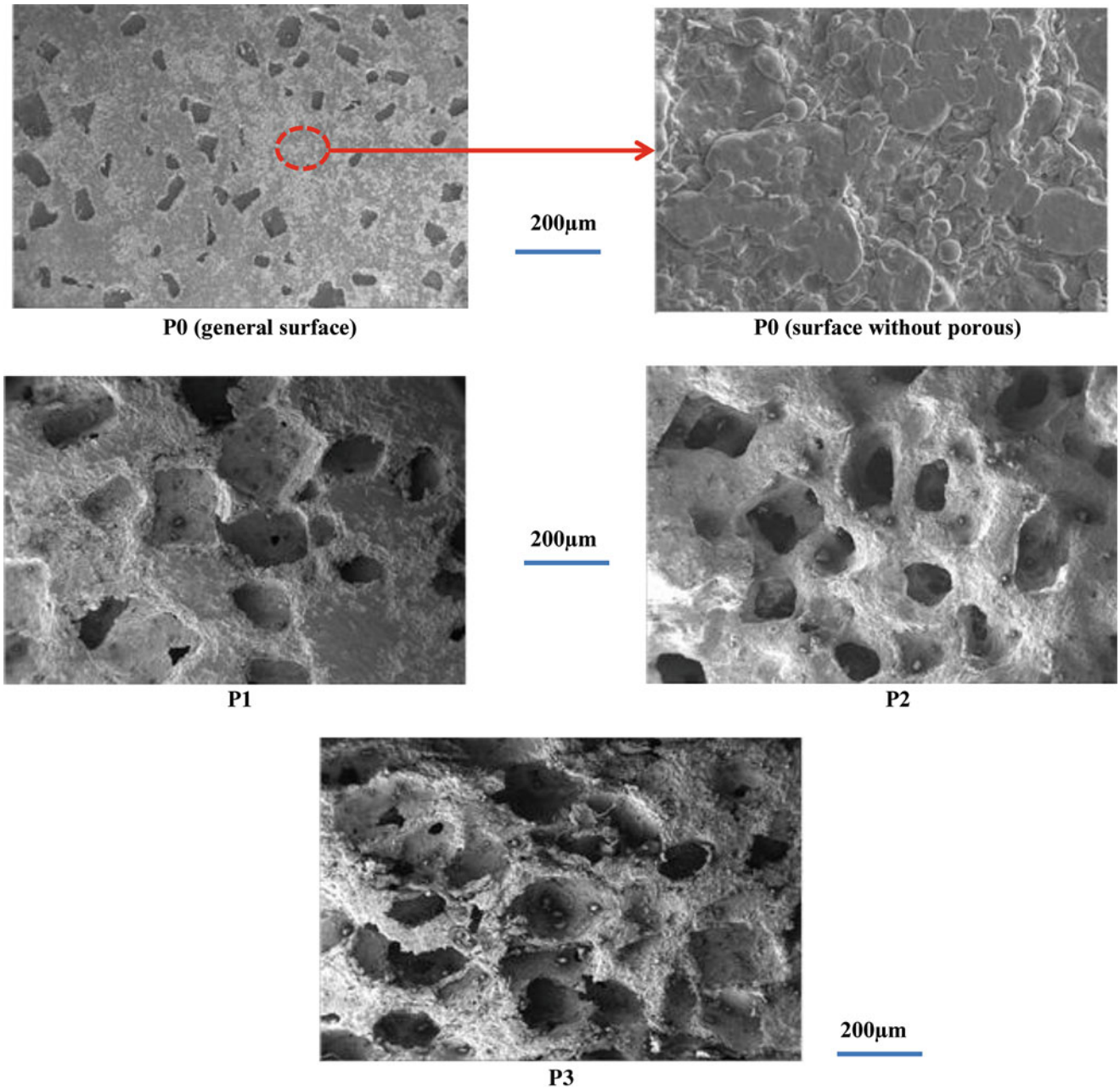

Fig. 28.2 SEM microstructure of the compositions with P0, P1, P2 and P3 with (0, 5, 7.5 and 10 % of wax)

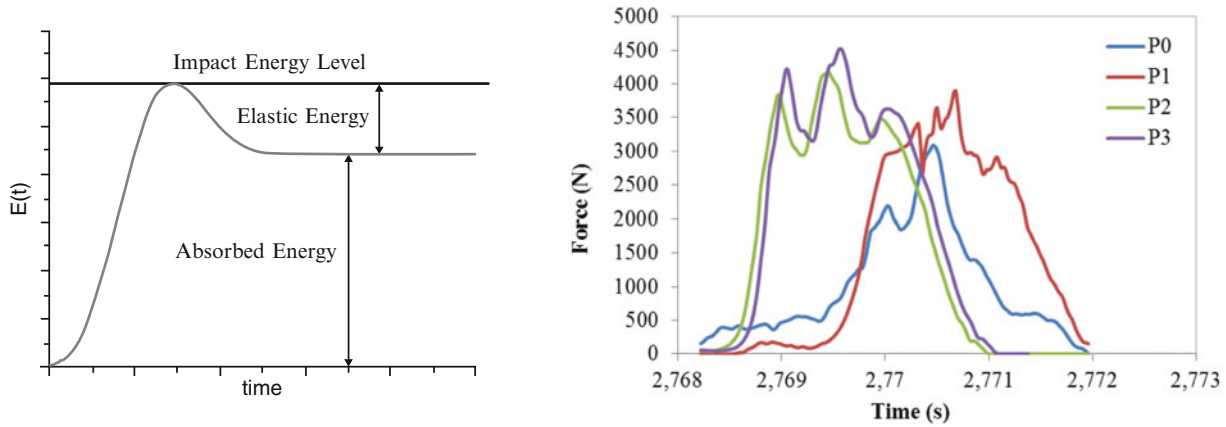

Fig. 28.3 General presentation (*left side*) of low velocity drop weight/dynamic compression test and experimental results for four compositions (*right side*)

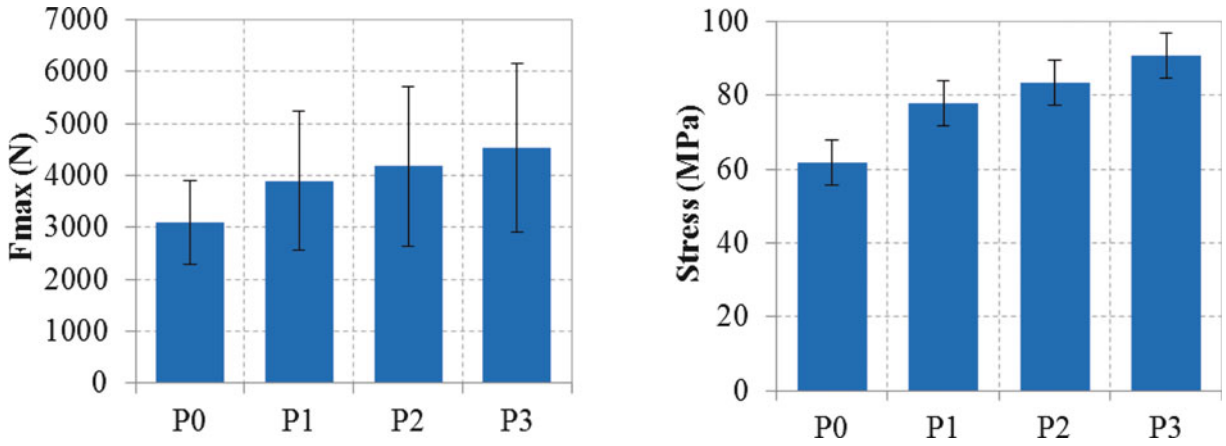

Fig. 28.4 Evolution of maximum forces (N) and stress (MPa) obtained by drop weight test depending on the composition

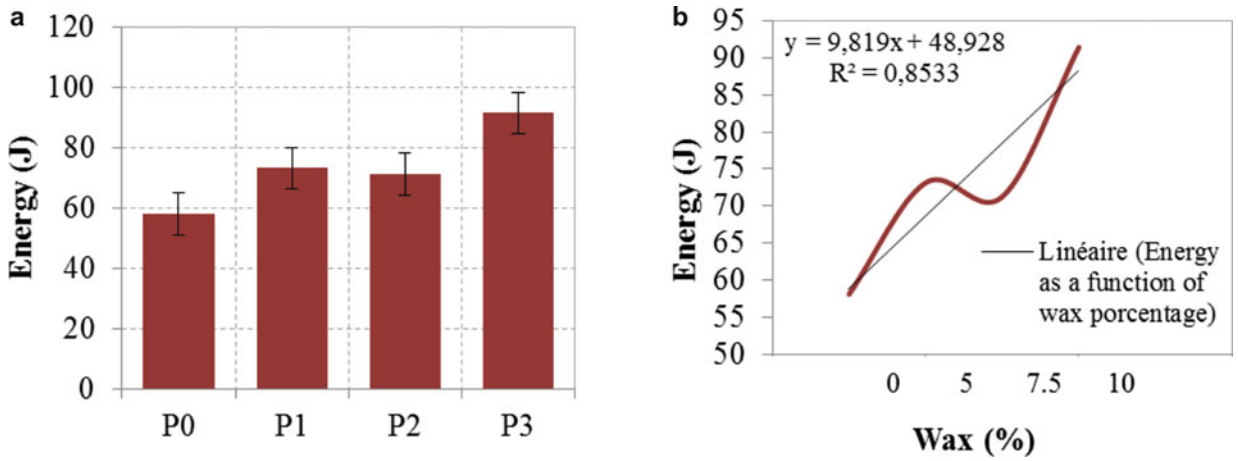

Fig. 28.5 Absorbed energy (**a**) and (**b**) energy/linear tendency as a function of wax added in the structure

Quasi-static compression test results as explained in the former section, experimental conditions) carried out on all of four compositions is presented in Fig. 28.6. All of the compression tests have been made with minimum three specimens according to the ASTM-E 9-89a with a diameter of 20 mm.

Aspect ratio (L/D minimum 1.5) was kept the same for all of the specimens of a composite. These test results have indicated that each of the compositions has shown correct behaviour suitable its content essentially wax and sugar percentage in the structure.

Figure 28.7 summarizes maximum stress values in compression. Among them the composition called "P0", gives the highest stress values with higher deviation than three other compositions that contain much more space holders than P0.

28.4 Conclusion

In the present work, a simple idea was developed on the production of porous composites by using a low cost method: mixture of aluminum matrix (obtained from scrap aluminium chip, AA2104) with organic (brown) sugar with addition of micro hollow glass bubbles and cold pressing followed sintering process at two steps. Results obtained so far indicates that the method is quite promising in producing foams with open, interconnected cells (similar to sponges) as a result of volatilization of wax and sugar granulates, and glass spheres as closed cells. Acceptable dispersion of both open and close spaces can be achieved successfully when proper mixing/pre-compacting conditions are well managed. All of the specimens

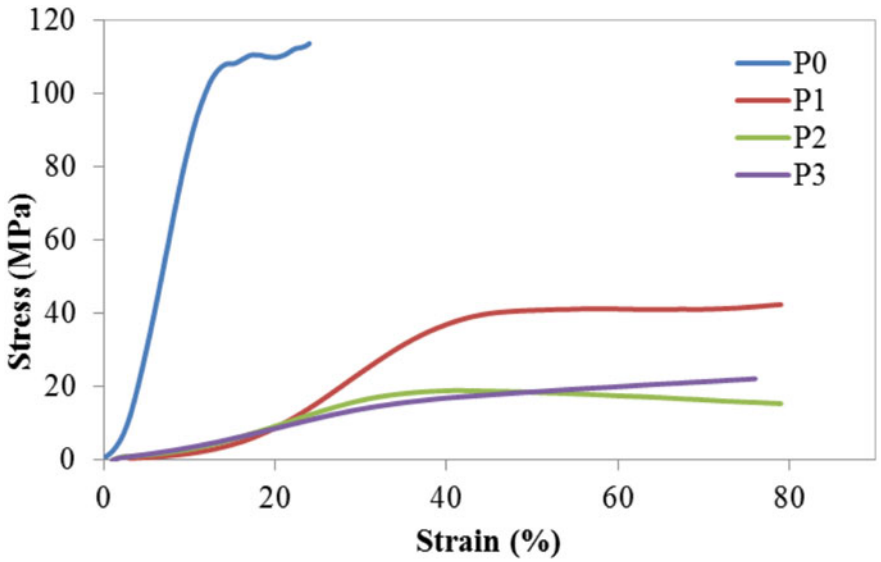

Fig. 28.6 Stress versus strain obtained by quasi static compression test carried out on the four compositions

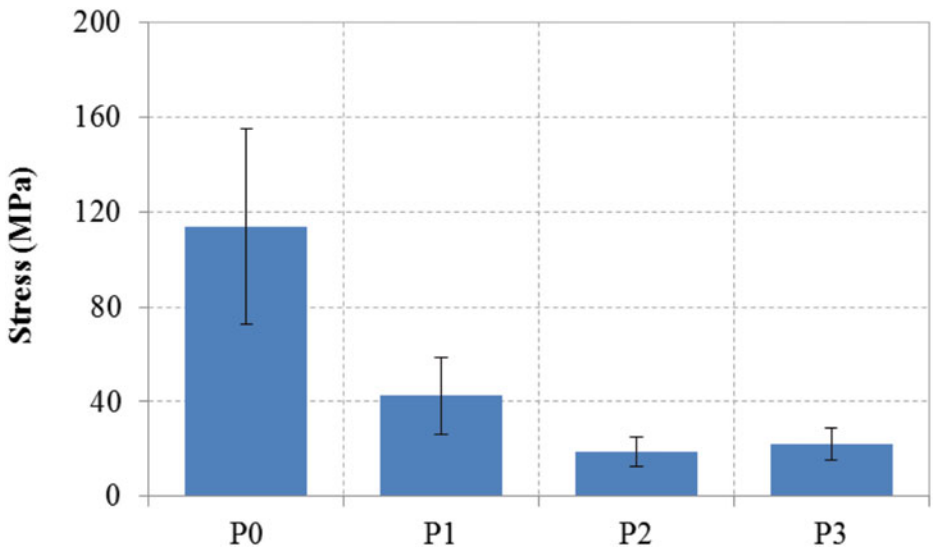

Fig. 28.7 Maximum stress values as a function of wax added in the structure used in the compositions

produced in this work show low density (relative density) and can respond well impact forces (ability of energy absorption in impacts).

Experimental results have exposed that the two parameters examined here: addition or not of wax and sugar granulate brown sugar and combined effect both of them in the composition of P0). These parameters can indicate significant effect on the density and considerable effect on the compression behavior of the products. Addition of glass bubbles tend to stimulate to increase absorbed energy level as a positive damping effect on the structure.

As a general conclusion, the present work indicated that the method can be used for the production of porous structures in an economic way with a clean energy containing both open and closed spaces, using wax and brown sugar and also hollow glass bubbles in certain amounts, by means of sintering at two steps, this is well-intentioned to develop this idea and investigate for the production in large scales.

References

1. Robert, M.H., Jorge, A.F.: Processing and properties of AA7075/porous SiO_2-MgO-Al_2O_3 composite. J. Achiev. Mater. Manuf. Eng. **3**, 1–5 (2012)
2. Torralba, J.M., Da Cost, C.E., Velasco, F.: P/M aluminum matrix composites: An overview. J. Mater. Process. Technol. **133**(1–2), 203–206 (2003)
3. Gatamorta, F., Bayraktar, E., Robert, M.H.: Preliminary study on the production of open cells aluminum foam by using organic sugar as space holders. Exp. Mech. Compos. Hybrid Multifunct. Mater. **4**, 7–14 (2014). doi:10.1007/978-3-319-06992-0
4. Irot, F.A., Queniss, J.M., Naslain, R.: Discontinuously reinforced aluminum matrix composites. Compos. Sci. Technol. **30**, 155–163 (1987)
5. Das, S.K.: Aluminum recycling: An integrated industry-wide approach. In: AIME Conference, pp. 22–24, Lausanne, July 2009
6. Slipenyuk, A., Kuprin, V., Milman, Y., Goncharuk, V., Eckert, J.: Properties of P/M processed particle reinforced metal matrix composites specified by reinforcement concentration and matrix-to-reinforcement particle size ratio. Acta Mater. **54**(1), 157–166 (2006)
7. Ferreira, L.-P.: Production of aluminum metal matrix composites by thixoforming of recycled chips. Thesis for Master of Science, Department of Mechanical and Manufacturing Engineering, University of Campinas—UNICAMP, Campinas, UNUICAMP-FEM, Campinas, SP-Brazil (2013)
8. Frosch, R.A., Gallopoulos, N.E.: Strategies for manufacturing. Scientific American. http://www.umich.edu/nppcpub/resources/compendia/IEORpdfs/IEOR_Reading.pdf (1989)
9. Shao-Yun, F., et al.: Hybrid effects on tensile properties of hybrid short-glass-fiber-and short-carbon-fiber-reinforced polypropylene composites. J. Mater. Sci. **36**, 1243–1251 (2001)
10. Bao, L., Zang, J., Li, X.: Flexible Zn_2SnO_4/MnO_2 core/shell nano cable carbon microfiber hybrid composites for high-performance supercapacitor electrodes. Nano Lett. **11**(3), 1215–1220 (2011)
11. Aerospace Manufacturing and Design (AMD): AFRA targets 90% recyclability of global fleet by 2016. http://www.onlineamd.com/aerospace-manufacturing-design-AFRA-recyclability-amd-070210.aspx (2011)

Chapter 29
Development of Functionally Graded Nodular Cast Iron Reinforced with Recycled WC Particles

Rodolfo Leibholz, Maria Helena Robert, Henrique Leibholz, and Emin Bayraktar

Abstract The work deals with the development of a graded composite based on DIN 1693 nodular cast iron reinforced with WC particles from recycled cutting tools. A superficial composite layer with a specific profile and thickness is designed to provide high wear resistance in working surfaces in products like impact crushers for sugar industries or sinter plants. The process involves the addition of the ceramic particles to the liquid metal through a specially designed casting process using EPS pattern. Different casting conditions, contents and dimensions of reinforcing particles were tested. Obtained products were characterized concerning the dispersion of the reinforcing agent and quality of reinforcement/matrix interface. Results show the possibility of incorporating WC in the cast iron matrix with the pre-designed profile of WC distribution in the working surface of the product. During processing some disaggregation of micro carbide particles from the recycled material is observed, resulting in a finer dispersion of WC in the metallic matrix. Microstructural changes in the matrix in the composite region results in higher perlite/ferrite ratio related to the non-reinforced region of the product.

Keywords Graded composites • Recycling • Cast iron composites • Impact crusher • Reinforced layer

29.1 Introduction

In many engineering applications, metallic components require distinct properties in distinct regions. Therefore, optimization of a component performance deals with pre-design of the materials characteristics and properties in different locations, according to the specific behavior demanded (mechanical or other nature). Such distinct distribution of properties in a single work piece can be accomplished by different production routes; for example, promoting a surface of high hardness for high performance in abrasion conditions by means of structure surface modifications using laser or plasma techniques, deposition of different materials in pre-prepared surfaces by different techniques, etc. Another approach is the addition of reinforcement particles in a metallic matrix in a tailored content distribution. Functionally Graded Composites Materials (FGCMs) present reinforcing elements distributed according to required gradient properties, for example presenting a content gradient from a specific surface [1–3]. This work proposes a production technique of a specific product—an impact crusher for defibration of sugar cane stalks in the sugar production plant, with tailored properties: body of the hammer presenting high weight and ductility and surface with high wear and impact properties. Such type of hammer is usually manufactured from thick cast iron plates cut to the required geometry and the work surface coated with harder material by welding. This kind of coating suffers wear and detchment as well as promotes deleterious structure modifications due to the heat input during welding. Improvements in this area are usually related to structure modifications by different thermomechanical treatments to improve wear resistance under impact for steel hammers used in the sinter industry [4], or adding reinforcing particles such as WC by laser or plasma melt injection [5–7] or even producing a bulk steel-NbC or TiC composite by hot isostatic pressing [8].

Several other techniques, with different complexity and costs have been utilized to produce taylored composites, like the time consuming additive technology [9]. Looking forward the development of more sustainable, low cost production means, this work proposes the fabrication of such kind of product by direct casting process, using nodular cast iron with graded content of WC particles from recycled machining tools.

R. Leibholz • M.H. Robert (✉) • H. Leibholz
Faculty of Mechanical Engineering, UNICAMP—University of Campinas, Campinas, São Paulo, Brazil
e-mail: rodolfoleibholz@femaq.com.br; helena@fem.unicamp.br; henrique_leibholz@femaq.com.br

E. Bayraktar
Faculty of Mechanical Engineering, UNICAMP—University of Campinas, Campinas, São Paulo, Brazil

School of Mechanical and Manufacturing Engineering, Supmeca-Paris, Paris, France
e-mail: emin.bayraktar@supmeca.fr

W.C. Ralph et al. (eds.), *Mechanics of Composite and Multi-functional Materials, Volume 7*,
Conference Proceedings of the Society for Experimental Mechanics Series, DOI 10.1007/978-3-319-41766-0_29

29.2 Experimental Procedures

GGG-50 nodular cast iron (grade according to DIN 1693—Deutsches Institut fur Normung) was used in the experiments. This sort of cast iron presents a ferrite/perlite matrix, with predominance of ferrite (circa 70–80 %); main alloying elements are C (3.2 wt%), Si (2.74 wt%) and Mn (0.46 wt%); some residual Mg around 0.035 wt% is also present due to the graphite nodularization treatment.

As reinforcement material, grinded particles of WC from recycled cutting tools were used. Chemical composition may vary from one particle to another as different cutting tools are employed in the machining shops. However, most usual compositions contain 90 to 97 wt% WC and 3 to 12 wt% Co as binder.

Scrap material supplied by machining shops was grinded and particles dimensions selected in three groups: coarse (2–10 mm), medium (2–4 mm) and fine (1–3 mm). General aspect and detail of morphology and microstructure of the reinforcing particles are shown in Fig. 29.1.

Morphology is irregular and polygonal; the microstructure of the sintered material shows the presence of localized regions of Co used as binder element and high porosity. WC individual particles present dimensions in the range 1–4 μm.

The studied product, a hammer used to promote fibres rupture of sugar cane stalks in the sugar industry, is presented in Fig. 29.2. The hammer head suffers severe wear under impact in the surface in contact with the branches of the sugar cane; therefore, a layer of reinforced material is designed to be located in this surface. The wear suffered by this product while in use is not linearly distributed in the surface, and for this reason, also a non linear profile of reinforced layer was designed.

The process investigated to produce the required configuration of reinforcing particles distribution is casting the nodular iron using lost foam pattern, which was built in EPS (expanded poly-styrene). During pouring the mould was tilted so

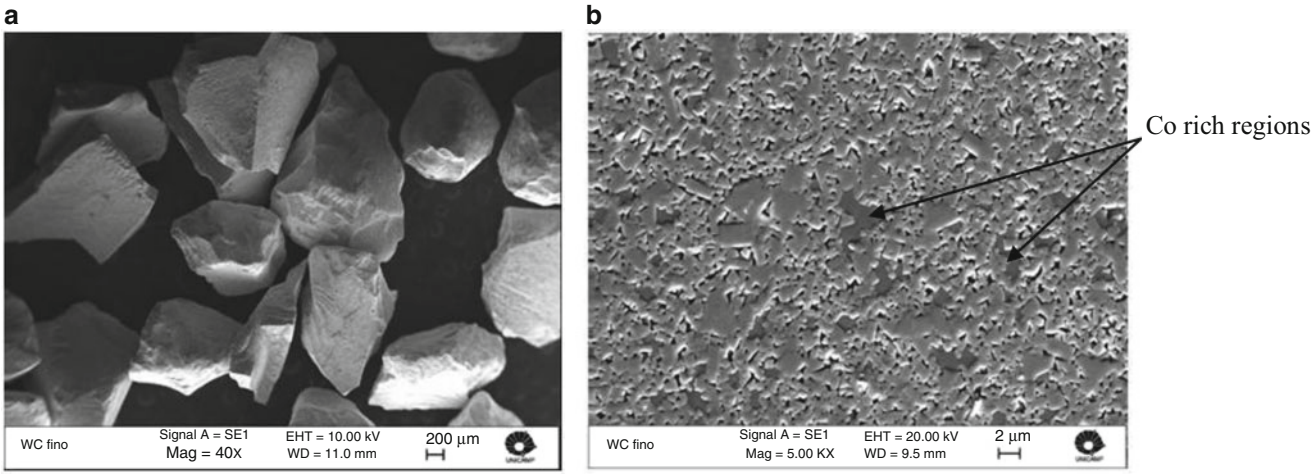

Fig. 29.1 WC particles used as reinforcement: (**a**) general aspect; (**b**) microstructure, SEM

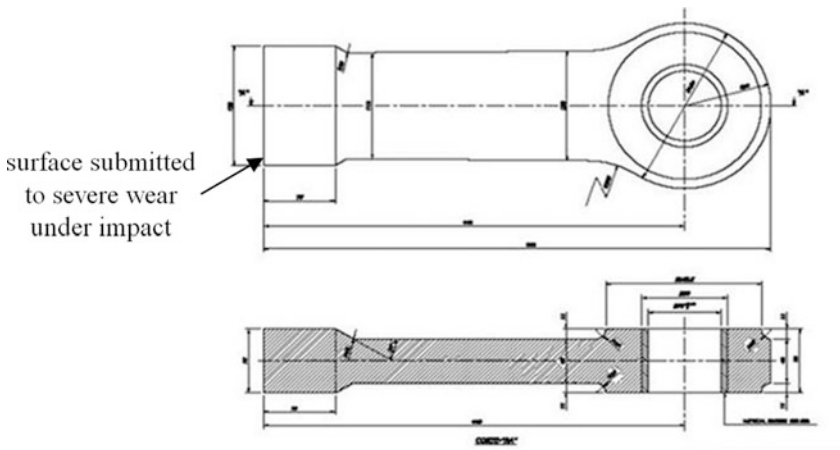

Fig. 29.2 Sketch of the artefact produced: impact crusher for sugar cane industry. Surface submitted to high abrasive and impact conditions as indicated

particles of the reinforcing WC pushed by the liquid flow are supposed to concentrate in one corner of the bottom surface of the cast part. Optimized pouring temperature was 1480 °C.

The following processing variables were investigated, after optimization of the casting procedure: dimensions of the reinforcing particles (coarse, medium and fine); WC particles content related to the total weight of the hammer head part (6 and 9 wt%). Produced samples were sectioned and prepared for metallographic analysis; optical microscopy, SEM, EDS and XRD analysis were used to analyze microstructures. The thickness of the reinforced layer was evaluated by ultra sound technique using a GE-XS Phasor equipment with a 4 MHZ, 10 mm diameter transducer.

29.3 Results and Discussions

A typical cast product is shown in Fig. 29.3; surfaces used for analysis are indicated: bottom surface, to observe the distribution and content of reinforcing particles in the region directly in contact with the abrasive environment (sugar cane branches, vegetal and mineral impurities) and longitudinal section of the hammer head, to evaluate the thickness of the reinforced layer and microstructures.

General results are shown in Fig. 29.4 which presents macro aspects of the bottom surface of the products. It is possible to observe clearly the presence of high content of WC particles in all cases; distribution seem to be acceptably homogeneous throughout. It can be observed in general better distribution of the fine particles, occupying estimated 90 % of the surface area, when compared to coarse particles, when using the same relative weight content (lower number of coarser particles). When coarser particles are used, some shrinkage is observed in the metal matrix entrapped among WC particles.

Concerning the distribution of WC in the longitudinal section of the hammer head, i.e. the thickness of the reinforced layer starting from the bottom surface of the cast product, a typical result is shown in Fig. 29.5a: the thickness of the layer shows a non linear profile, it increases towards one of the corners, due to the tilting of the mould during pouring solid WC particles concentrate in this region. This non homogeneous thickness of the reinforced layer is desirable taking in account the wear behaviour profile suffered by this kind of product during work, as presented in Fig. 29.5b. This picture was supplied by a sugar company and is related to a commercial crusher with the bottom surface of the hammer head coated with hard material by welding. It is clearly observed that one of the edges of the head is more severely affected by the impact with the abrasive material, which is actually a mixture of the sugar cane branches with circa 1 % of silica sand, among other mineral and vegetal materials [10].

The thickness of the layer containing WC particles in each composite was evaluated by ultra-sound technique. Explanation of method and typical generated data are presented in Fig. 29.6. Tests were performed in different scanning lines in axial direction as indicated; lines were equidistant 5 mm. In each line transducer was placed in different positions related to the composite layer: above (region without WC particles), transition region, and on the composite layer. As the WC particles does not present good acoustic properties, it was possible to define the transition region metal/composite considering the response echo (RE) at 100 % in the region containing no WC particles, 50 % of RE in the transition region and total loss of RE in the composite region.

Using the obtained data it was possible to estimate the general profiles of WC particles distribution in the product, which are presented in Fig. 29.7. Minimum and maximum values of the reinforced thickness layer in each case are presented in Table 29.1.

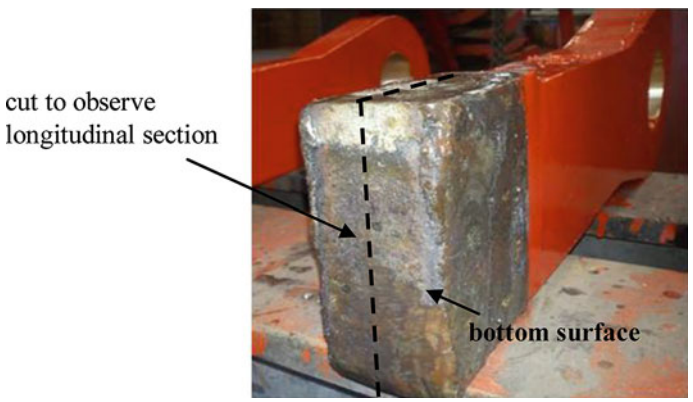

Fig. 29.3 Typical cast product: hammer head of GGG-50 nodular iron/bottom surface reinforced with WC particles

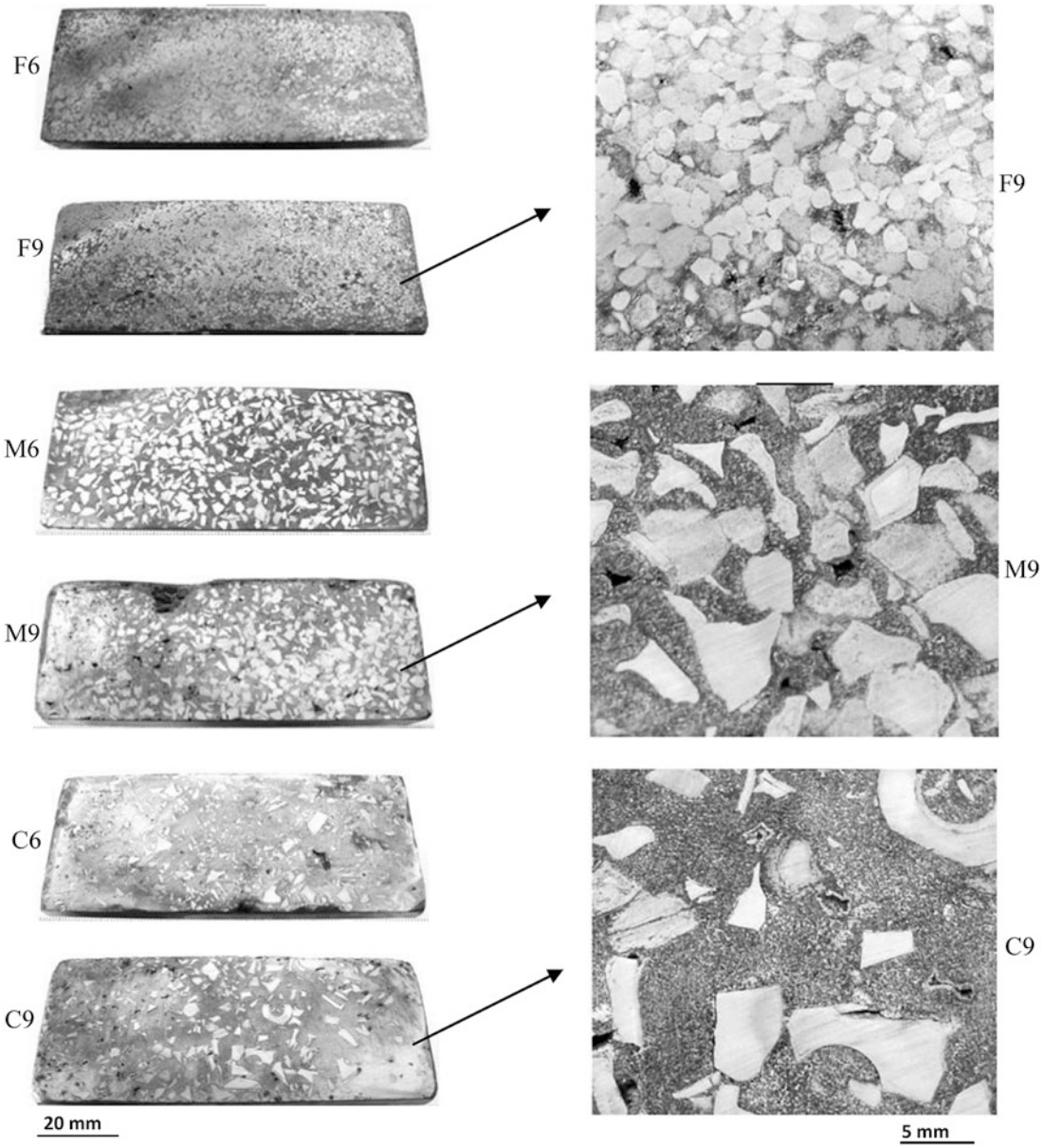

Fig. 29.4 General aspects and macrostructures of composites produced. *F*: fine; *M*: medium; *C*: coarse WC particles; *6*: 6 wt% WC; *9*: 9 w%t WC added; (OM)

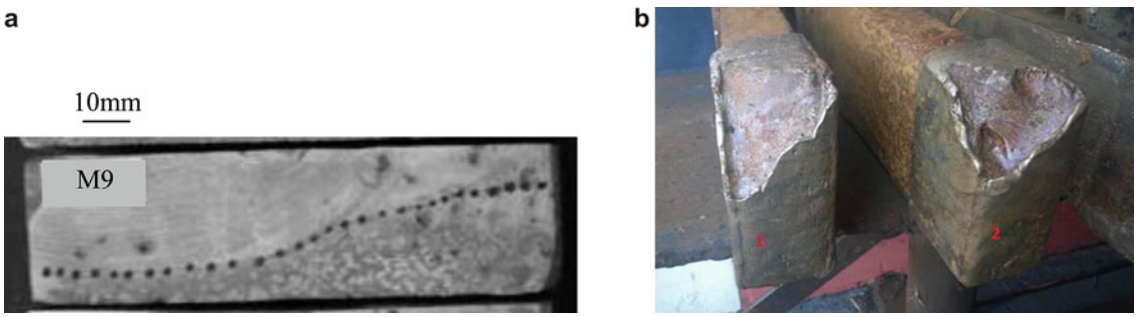

Fig. 29.5 (**a**) Typical aspects of longitudinal section of bottom surface of the hammer head of the cast crusher produced; (**b**) general aspect of the wear suffered by a commercial product with surface coated by welding [10]

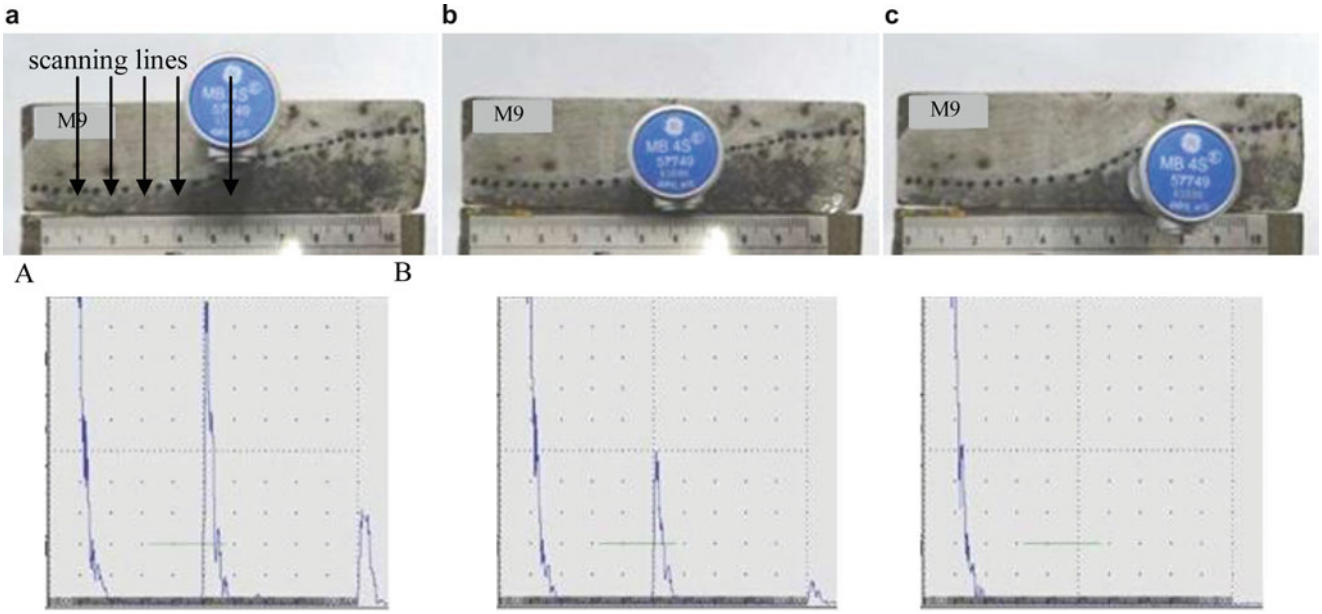

Fig. 29.6 Ultra sound tests for evaluation of composite layer thickness; typical acoustic response for one scanning line. (**a**) Transducer in region free of WC particles (RE = 100 %), (**b**) transducer in intermediate region (RE = 50 %), (**c**) transducer in composite region (RE = 0 %)

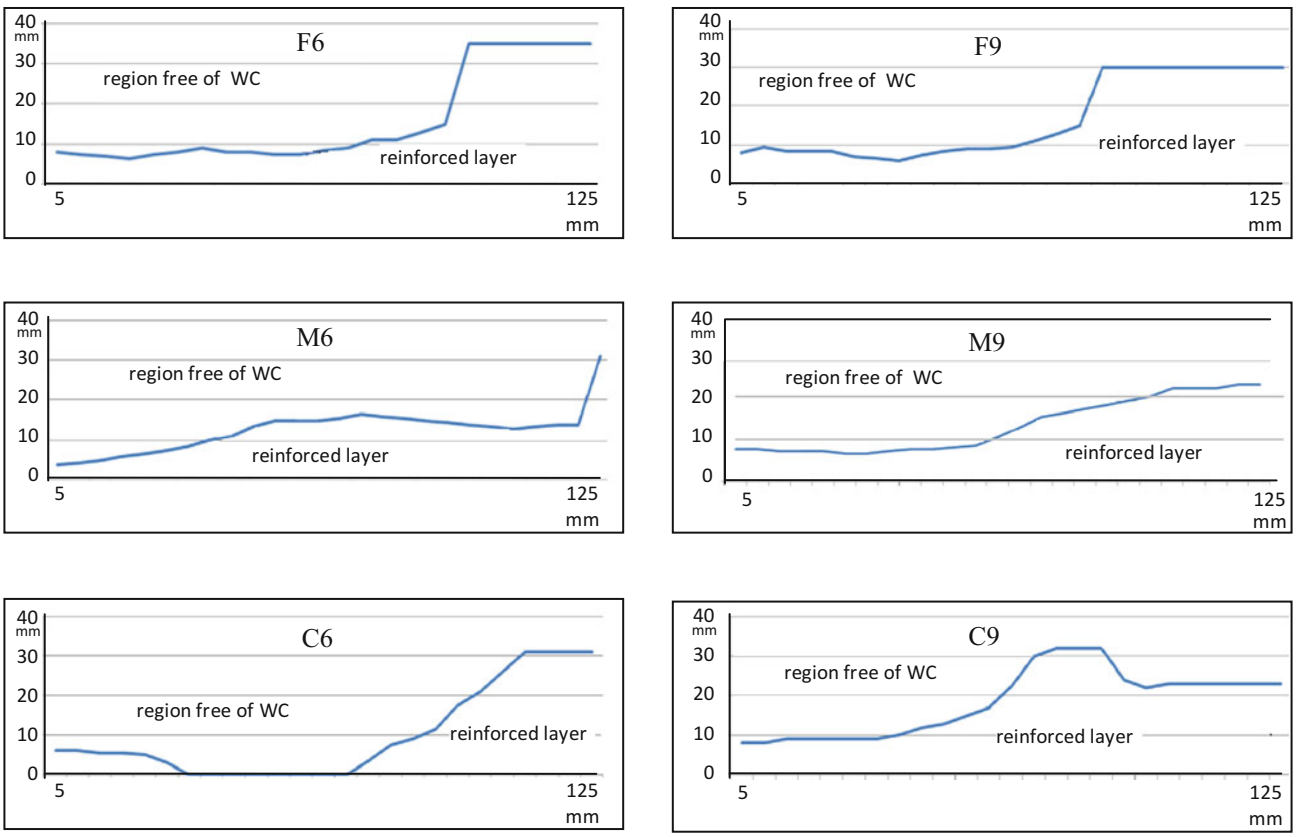

Fig. 29.7 Profile of reinforced layer in the bottom surface of cast products, using loss of back echo response in ultrasound tests. Reinforced layer containing: *F*: fine; *M*: medium; *C*: coarse WC particles. Total weight content of WC particles added *6*: 6 wt%; *9*: 9 wt%. *X*: distance from edge A to B as shown in Fig. 29.6, *Y*: thickness of layer containing WC particles

Table 29.1 Estimated thickness of reinforced layer in the products obtained in different conditions (mm)

Composite type					
F6	F9	M6	M9	C6	C9
8 to 35 mm	8–30 mm	4–31 mm	7–24 mm	0–31 mm	8–32 mm

F: fine; *M*: medium; *C*: coarse WC particles; *6*: 6 wt%; *9*: 9 w%t WC added

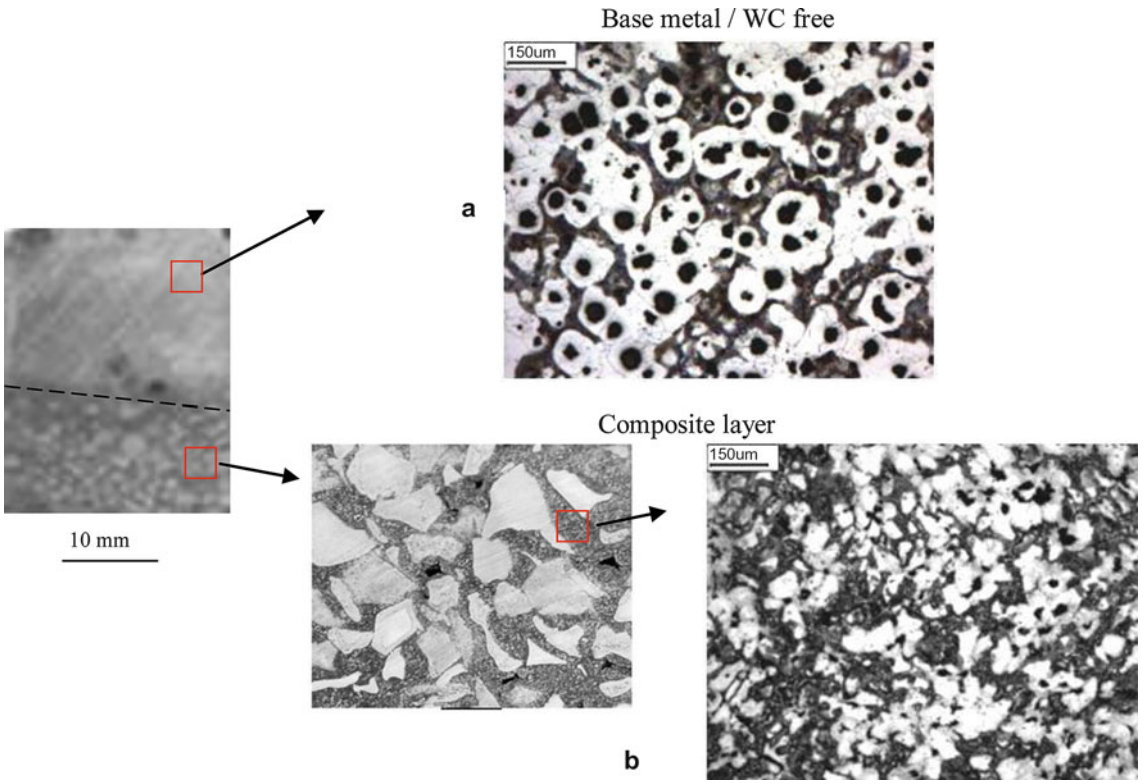

Fig. 29.8 Microstructure of the metal matrix in the AAA50007/WC composites: (**a**) region without reinforcing particles; (**b**) in the reinforced layer, among WC particles; (OM)

In all cases the profile of the reinforced layer is accordingly the required shape, with thickness increasing towards one of the edges of the hammer head. Therefore, the designed gate system and casting operation were able to promote the appropriate liquid flow to result in the expected particles distribution in the product. In most of the cases thickness varying from 8 to 30 mm were obtained; only in one situation the distribution of particles was critical, with some region in the surface with no reinforcement—this event happens eventually when low content of coarse particles of WC is employed. It was observed that more homogeneous and reliable results are obtained when using fine WC particles. Naturally the number of coarse individuals is lower than medium or fine particles as same weight content was employed in all cases, making it easier to disperse away the coarse reinforcement by the liquid flow in the pouring and filling operations.

Therefore, choosing fine particles can be more prudent as far as the regularity of the composite layer is concerned. Interfaces between WC particles and metal are free of cracks or voids.

Typical results on the microstructure of the metal matrix in different regions of the products are presented in Fig. 29.8. In the region free of reinforcement (a), the microstructure is typical of the nodular cast iron, with small nodular graphite surrounded by ferrite and perlite among ferrite grains. This grade of iron must present in cast condition a ferrite/perlite matrix with predominance of ferrite (70–80 %), as mentioned earlier. Quantitative analysis performed resulted in circa of 60 % ferrite. In the composite region, structure presents more irregular morphology: graphite nodulus are smaller, yet still globular, ferrite grains are also smaller and ferrite/perlite ratio decreases (ferrite content in the order of 50 %, according to quantitative measurements); the presence of carbides also is higher in the composite region when compared to the base matrix—around 3 and 1 % respectively. It is clear that the presence of the reinforcing WC particles influences the metal structure due to thermal as well as chemical effects on the solidification of the liquid, in case the particles suffer some

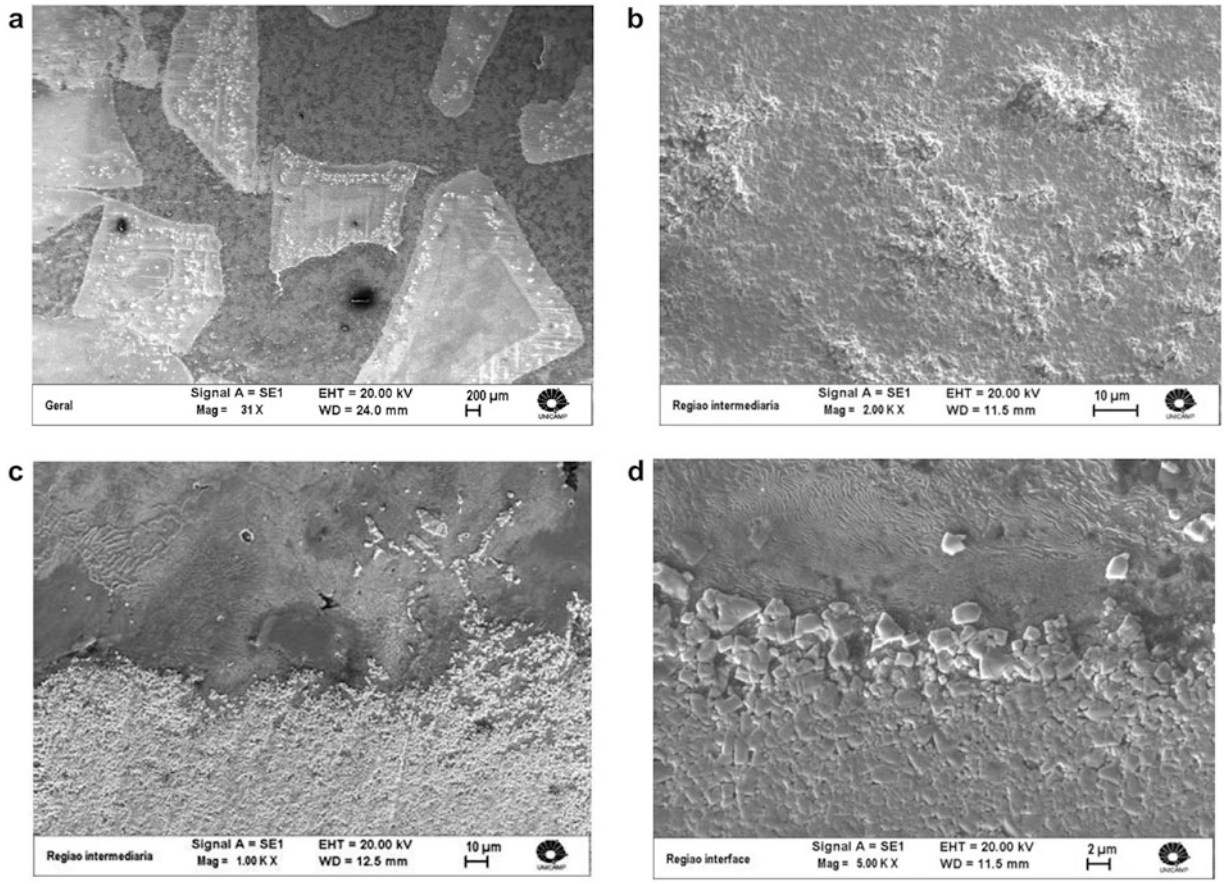

Fig. 29.9 Microstructure of the cast composite AAA50007/WC: (**a**) general aspect of the composite layer; (**b**) internal aspect of the WC particle; (**c**) interface region WC/metal; (**d**) same as (c) with higher magnification; (SEM)

modification during the processing. Concerning thermal effects, as the WC particles were not previously heated, higher cooling rate is expected both during solidification and eutectoid transformation in the metal among them, resulting in lower time for graphite decomposition and therefore lower ferrite/perlite ratio is obtained.

Concerning the possibility of WC degeneration during processing, promoting local modification in the chemical composition of the liquid metal among particles, structures analyzed by SEM presented in Fig. 29.9 can be discussed.

It is observed a reaction layer in the WC particles from external surface towards the internal region. This reaction layer becomes porous and individual WC small particles are detached to the liquid metal, where are entrapped during solidification. This effect can be interesting for wear and other properties of the material, once a finer dispersion of WC particles can be produced. Liquid metal clearly penetrates in the degenerated WC particles surface, creating a non discrete interface metal/reinforcement. This effect improves the mechanical bonding metal/reinforcement in the composite.

The degeneration of the WC particles is due to the dissolution of the Co used as binder for WC grains in the sintering of the cutting tools. It is not probable the melting of Co as its melting point is higher than the melt pouring temperature used (1495 °C and 1480 °C, respectively). Evaluation of variation of Co content in the WC particles and neighbour metal is shown in Fig. 29.10. It is observed a high Co content in the metal matrix circa 100 µm far from the particle interface, indicating the diffusion of this element from the WC particle towards the liquid metal. It is well known that the most powerful graphitizing elements in cast iron are Si, Al, Ni, Co and Cu, in decreasing order of graphitizing potency, it meaning potency of graphite formation in the solidification range and in the eutectic transformation. However, in the eutectoid transformation, Ni and Cu promote decrease in the ferrite/perlite radio by delaying C diffusion in the austenite [11]. It can be supposed that the high Co content in the liquid among WC particles could also have the same effect of reducing the C diffusion in the eutectoid transformation, resulting in higher than expected presence of perlite related to ferrite as observed.

It was also observed the presence of high W content in the iron matrix close to a FeOW phase present in grain boundaries, as shown in Fig. 29.11. Some reports [5, 6] show the formation of carbides such as Co_3W_3C, Fe_3W_3C in the matrix of steel/WC composites produced by higher energy processing (laser or plasma cladding), due to increase in W and C content in the liquid steel by dissolution of WC at high temperatures. This event should be less effective in the casting procedure adopted in

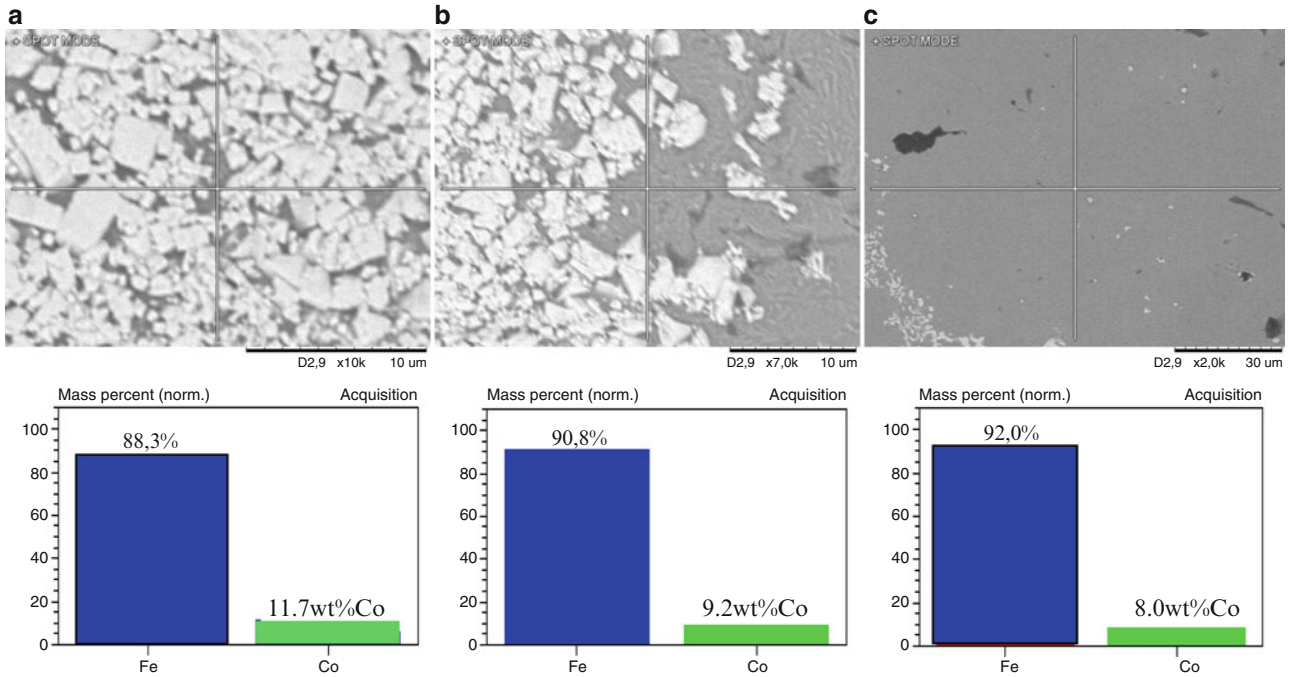

Fig. 29.10 EDS analysis showing Co content in AAA50007/WC composites: (**a**) interior of WC particles; (**b**) in the iron matrix close to the interface; (**c**) in the iron matrix circa 100 μm from the interface

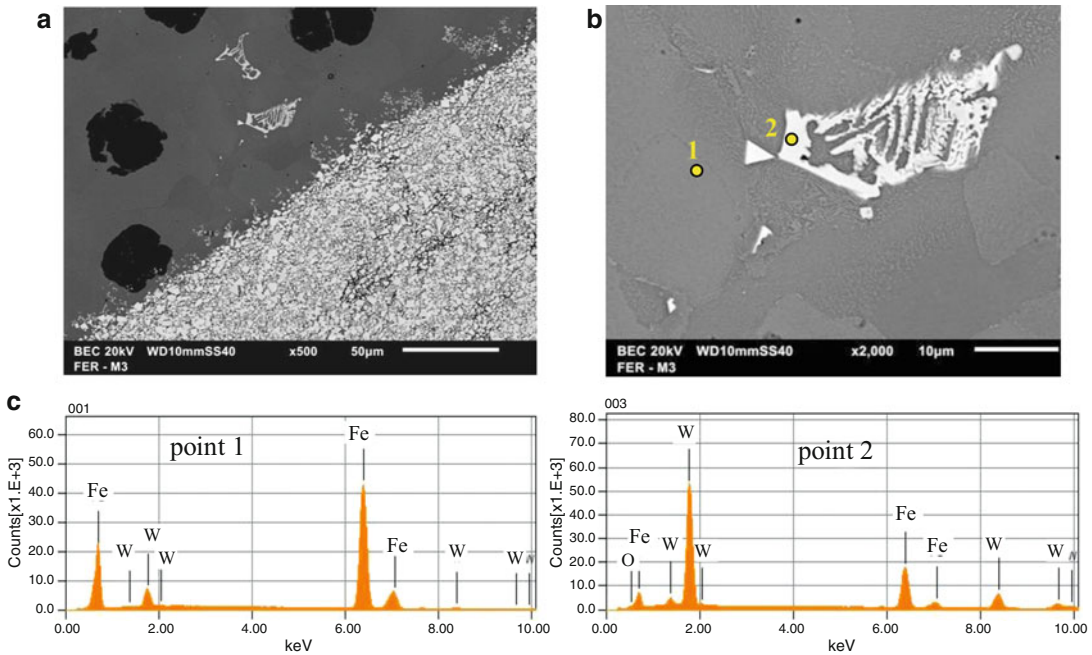

Fig. 29.11 Microstructure of the cast composite AAA50007/WC: (**a**) region close to the interface WC particle/metal; (**b**) detail of a FeOW rich phase; (**c**) main elements on points 1 and 2

this work, yet not totally absent, as increase on W content was observed in some regions, leading to the formation of the FeWO rich phase observed. These results can be interesting as the bottom surface of the hammer head shall present improved abrasion properties not only by the presence of the macro reinforcing particles added, but also the micro WC detached particles and the modification of the microstructure of the iron matrix, which contains higher perlite/ferrite ratio and higher content of carbides in the composite region.

29.4 Conclusions

Results show the possibility of producing a composite layer with pre-designed profile by simple casting operation using EPS patterns, for nodular cast iron reinforced with recycled WC particles. During processing, dissolution of the binder element from the WC macro particles towards the liquid metal promotes disaggregation of micro WC particles which are pushed to the metal, resulting in a non discrete interface between reinforcement and base material. Some of the micro particles can dissolve, increasing W and Co content in the metal; this effect, together with the higher cooling rate in the reinforced layer (addition of non heated WC particles), promotes microstructural changes in the matrix in the composite region: higher perlite/ferrite ratio and higher content of carbides. These structure modifications can promote further improvement in wear resistance of the composite layer, yet to be investigated.

Acknowledgment Thanks for financial support from CNPq—Conselho Nacional de Desenvolvimento Cientifico e Tecnológico (Brazil) and Program French Catedra UNICAMP, Brazil/French Embassy for Prof. Bayraktar's visiting period at UNICAMP.

References

1. Mortensen, A., Surech, S.: Functionally graded metals and metal-ceramic composites: Part 1. Processing. Int. Mater. Rev. **40**(6), 239–265 (1995)
2. Kieback, B., Neubrand, A., Riedel, H.: Processing techniques for functionally graded materials. Mater. Sci. Eng. A **362**(1–2), 81–106 (2003)
3. Ferguen, N., Cogné, C., Bellenger, E., Guessasma, M., Pélegris, C.: Numerical model for predicting effective thermal conductivities of alumina/Al composites. J. Compos. Mater. **47**(26), 3311–3321 (2013). doi:10.1177/0021998312464081
4. Mukhopadhyay, G., Palit, P., Bhattacharyya, S.: Development of AISI A2 tool steel beater head for an impact crusher in sinter plant. Metallogr. Microstruct. Anal. **4**(2), 114–121 (2015). doi:10.1007s/13632-015-0192-6
5. Liu, A., Guo, M., Zhao, M., Wang, C.: Microstructures and wear resistance of large WC particles reinforced surface, metal matrix composites produced by plasma melt injection. Surf. Coat. Technol. **201**, 7978–7982 (2007)
6. Cheng, F.T., Kwok, C.T., Man, H.C.: Cavitation erosion resistance of stainless steel laser-clad with WC reinforced MMC. Mater. Lett. **57**, 969–974 (2002)
7. Nascimento, A.M., Ocelík, V., Ierardi, M.C.F., De Hosson, J.T.M.: Wear resistance of WCp/duplex stainless steel metal matrix composite layers prepared by laser melt injection. Surf. Coat. Technol. **202**, 4758–4765 (2008)
8. Emamian, A., Alimardani, M., Khajepour, A.: Effect of cooling rate and laser process parameters on additive manufactured Fe–Ti–C metal matrix composites microstructure and carbide morphology. J. Manuf. Processes **16**, 511–517 (2014)
9. Ala-Klemea, S., Kivikytö-Reponenb, P., Liimatainenb, J., Hellmanb, J., Hannu, S.: Abrasive wear properties of metal matrix composites produced by hot isostatic pressing. Proc. Est. Acad. Sci. **12**(4), 445–454 (2006)
10. CTC General Annuary, Centre for Sugar Technology, Brazilian Government, Piracicaba (2015)
11. Campbell, F.C. (ed.): Elements of metallurgy and engineering alloys. ASM Interantional, Geauga (2008)

Chapter 30
Aluminium Matrix Composites Reinforced by Nano Fe_3O_4 Doped with TiO_2 by Thermomechanical Process

L.F.P. Ferreira, I. Miskioglu, E. Bayraktar, and M.H. Robert

Abstract In this work, scrap Aluminium Matrix Composites (AMCs) reinforced with 10 wt% nano iron oxide (Fe_3O_4) were produced and the influence of doping Fe_3O_4 with TiO_2 at 2.5 %, 5 %, 7.5 % and 10 % wt%, was studied. For the dispersion of the reinforcement and the study of the matrix/reinforcement, interface was evaluated by Scanning Electron Microscopy (SEM). Density and microhardness of the composites were measured and compared. Wear and creep response of the composites were evaluated by a nanoindenter, Furthermore modulus and hardness of the composites were calculated using the unloading data from the nanoindentation tests. Relatively homogenous distribution of the constituents, with a good bond between matrix and the reinforcements was observed. It was also observed that wear behaviour improved with the increase in the TiO_2 content.

Keywords Scrap Al matrix composites • Iron oxide (Fe_3O_4) • Microstructural analysis • Mechanical performance • Magnetic saturation

30.1 Introduction

Novel metal matrix composites containing magnetic particulate reinforcements with metallic matrix have been progressively used in aerospace and automotive industries due to their desirable properties [1–7]. They are very attractive if they can be produced at low cost for such engineering applications. During the last two decades, they became very popular as multifunctional materials mainly known multiferroic composites [3]. They should have high wear resistance with high performance indices high modulus or high resistance with lower density [8].

In the modern technology, there is no scene of permanent magnet applications decaying in near future. Naturally, there are optimistic prospects for innovative applications, especially if the properties of cost-effective magnetic parts can be manufactured to new requirements such as corrosive and wear stability and/or high temperature applications, etc. Today, permanent magnets are unique in their capability to deliver magnetic flux into the air gap of a magnetic circuit without any continuous expenditure of energy.

Aluminium matrix composite materials are used in aeronautical and aerospace and automotive applications especially in the thermal management areas. Aluminium Matrix Composites (AMCs) reinforced with nano iron oxide (Fe_3O_4) exhibit good physical and mechanical behaviour (electrical conductivity and magnetic permeability), which makes it an excellent multifunctional lightweight material.

In the frame of this present work, low cost-effective permanent magnetic composites are proposed by using Aluminium Matrix Composites (AMCs) reinforced basically with nano iron oxide (Fe_3O_4) and also doping of other reinforcement alloying elements such Titanium dioxide (TiO_2) as a stabilizer and protector of magnetic nano iron in the structure.

L.F.P. Ferreira (✉)
Materials Science Department, UNICAMP—University of Campinas, Campinas, São Paulo, Brazil

School of Mechanical and Manufacturing Engineering, Supmeca-Paris, Paris, France
e-mail: lygiamaria@fem.unicamp.br

I. Miskioglu
Department of ME-EM, Michigan Technological University, Houghton, MI, USA

E. Bayraktar
School of Mechanical and Manufacturing Engineering, Supmeca-Paris, Paris, France

M.H. Robert
Materials Science Department, UNICAMP—University of Campinas, Campinas, São Paulo, Brazil

W.C. Ralph et al. (eds.), *Mechanics of Composite and Multi-functional Materials, Volume 7*,
Conference Proceedings of the Society for Experimental Mechanics Series, DOI 10.1007/978-3-319-41766-0_30

As known well, dopant impurities in these composites can improve certain properties and these properties, basically, depends on the doping process and the material used as doping agent.

As for magnetic iron oxide, it is very easy to produce as nanoscale particles that were presented in the former papers. Magnetic iron oxide nanoparticles (Fe_3O_4) with a lattice parameter 0.8397 nm are very adaptable for new electromagnetic applications with good magnetic and electrical properties. For this reason, magnetite Fe_3O_4 is one of the favorite and mostly characterized filler materials [9–14]. Cost reduction can be obtained by reducing the total raw material cost as well as more efficient manufacturing and assembly. This work reviews in detail the manufacturing of magnetic MMCs based on the thermomechanical doping of Fe_3O_4 by TiO_2 in different percentages [12–20].

The influence of TiO_2 percentage on the doping process and consequently on the wear resistance of the composites were evaluated. Wear tests were carried out by using the scratch feature of a nanoindentation system. Microstructural evaluation was performed by Scanning Electron Microscopy (SEM) and EDS analyses to optimize influence of the major reinforcements distributed in the matrix.

30.2 Experimental Conditions

In this work, certain amount of aluminium scrap was mixed with 30 % aluminium nano powder (A1050) and used as matrix material. Magnetic nano iron oxide (Fe_3O_4) was pretreated via thermo-mechanical doping process with TiO_2 powders to protect iron oxide and then used as major particulate reinforcement.

The thermo-mechanical doping process of magnetic iron oxide with TiO_2 was performed is three stages:

1. Mixing of Fe_3O_4 and x wt%TiO_2 and milling for a short time (~15 min)
2. Heating this mixture in a ceramic crucible at 400 °C for 30 min at a heating rate of 10 °C/min
3. Blending of this mixture homogeneously by ball milling (4000–6000 rpm) for 30 min the small amounts of Cu and Zr_2O_3 are added and the composition is further ball milled for 2 h.

In the frame of this work, different amounts of TiO_2 were tested: 2.5, 5, 7.5 and 10 wt% and small amounts of Cu and Zr_2O_3 were added in the composition during the process. These compositions will be referred to as TiO_2-2.5, TiO_2-5.0, TiO_2-7.5 and TiO_2-10, respectively depending on the increasing amount of the TiO_2 doped with magnetic nano iron oxide.

The composites were produced by powder metallurgy route as follows: Milling 1 h followed high speed ball milling for 15 min, after that compacting at 250 MPa, and sintering at 500 °C, for 1 h under Argon atmosphere to produce specimens with a 20 mm in diameter and a height of 6 mm.

All of the specimens were prepared metallographic analyses and other examination;

The dispersion of reinforcement particles and the geometry of the final composites were structurally characterized by Scanning Electron Microscopy (SEM). The microhardness ($HV_{0.25}$) measurements were made with seven values taken in different zones for each composition. All of the density measurements of the specimens were carried out by means of Archimedes method.

Wear testing was carried out by nanoindentation run under two different normal loads (20 and 50 mN) applied over a linear track of 500 μm for 50 cycles. One cycle is defined as a pass and return over the track; the total distance for one test was 0.050 m. The speed of the tip during wear tests was 50 μm/s. A total of 10 wear tests were performed for each sample.

Creep tests were performed with a nanoindenter at two maximum loads of 20 and 50 mN. On each sample 25 indents were made on a 5 × 5 grid with a Berkovich indenter. The load was increased at a rate of 1 mN/s to the maximum load and kept at the maximum load for 500 s then unloaded. During each test, data collected was used to calculate the creep compliance by using the relationship presented in Eqs. (30.1) and (30.2). The strain is related to stress during creep as:

$$\varepsilon(t) = \sigma_0 J(t) \tag{30.1}$$

where σ_0 is the constant stress applied and $J(t)$ is calculated by:

$$\mathrm{J}(t) = \mathrm{A}(t)/(1-\nu)\mathrm{P}_0\tan\theta \tag{30.2}$$

where $\mathrm{A}(t)$ is the contact area, P_0 is the constant applied load, θ is the effective cone angle which is 70.3° for a Berkovich indenter and the Poisson's ratio ν is assumed to be 0.3. The strain versus time response of the material during creep test is characterized by a high strain rate $\dot{\varepsilon} = d\varepsilon/dt$ in the primary stage of creep.

Nano hardness (GPa) and elastic modulus (GPa) measurements were determined from the unloading data at each indent using the method developed by Oliver and Pharr. A Poisson's ratio (ν) of 0.3 was used for these calculations also.

30.3 Results and Discussion

30.3.1 Microstructural Evaluation

Distribution of magnetic iron oxide doped with TiO_2 by thermomechanical process and interface with Al matrix in different percentage of TiO_2 was examined in the microstructure as presented in the Fig. 30.1a as TiO_2-2.5, TiO_2-5.0, TiO_2-7.5 and TiO_2-10, respectively. For sake of protection of magnetic iron oxide, Doping treatment should be made at the beginning of the manufacturing of the composites. This is an economic method for the processing of these materials.

Here, doping of iron oxide with TiO_2 elements at the first stage of process resulted in a more homogenous composite. Microscopic analyses of iron oxide powders have shown that thermo-mechanical doping treatment currently work well and help to improve bonding with the matrix.

In general, all of the compositions it was found that Fe_3O_4 was dispersed homogeneously and continuously in the aluminium matrix. Porosity and abnormal distributions were not observed in the compositions.

EDS analysis of the specimen produced from the first composition, TiO_2-2.5 was indicated in the Fig. 30.1b. This is only general analysis to check the basic elements and reinforcements added in the structure.

30.3.2 Evolution of Density and Microhardness Values ($HV_{0.25}$)

Density measurements of the specimens for the four compositions (TiO_2-2.5, TiO_2-5.0, TiO_2-7.5 and TiO_2-10) were carried out by means of Archimedes method. The results were obtained from three specimens for each composition.

Density measurements varied from 3.18 up to 3.20 g/cm^3 with some scatter in data. There was no discernible difference between the densities of the four composites, i.e., TiO_2 content did not affect the density considerably.

Microhardness values ($HV_{0.25}$) are presented in Fig. 30.2. Comparing the hardness value presented for the four compositions, it is possible to see that the addition of TiO_2 during doping process has increased the hardness values from 51 up to 90 HVN. Also the addition of TiO_2 during doping process improves the surface damage of these compositions. However, these experimental results obtained under certain laboratory conditions can be accepted as a consequence of the individual hardness of the elements and their distribution on the Al-matrix. Evidently, more reliable values can be obtained with a homogeneous microstructure with well distribution of particulate reinforcements in the matrix.

30.3.3 Wear Resistance by Nanoindentation

Wear resistance of the composites were evaluated by test using a nanoindenter. Wear tracks for the compositions were performed with a conical tip (90^o cone angle) at two different normal loads, 20 and 50 mN.

For each composite 10 wear tests were performed. As an example of these tests wear tracks 7 and 8 are shown in Fig. 30.3 for the TiO_2-2.5 sample. As indicated in this figure, wear track through different parts of the microstructure; matrix, particulate reinforcement, can be observed.

A typical example for wear test data is shown in Fig. 30.4 to for track 8 on the TiO_2-2.5 sample along with the micrograph of the wear track, initial profile and residual profiles during the tests. The wear damage is characterized as the area between these two curves and the averages are presented wear track deformation (in μm^2) for each composition in Fig. 30.5.

Wear deformations obtained on the specimens were compared in this figure for two pressure loads, 20 mN and 50 mN. At the small pressure load level, wear damage values are essentially the same level. It means that at the small pressure loads, surface damage values are very small regarding to the high pressure loads, 50 mN and beyond. Wear track deformation under the load of 50 mN have shown high scatter due to composite structure; as indicated in the former section (experimental conditions).

Naturally, interface of matrix with particulate reinforcement in certain area of specimens and distribution of minor reinforcements influence these measurements. Even if there scatter in these measurements, general tendency is that wear track deformation levels decrease with the increase in TiO_2 content in the structure. Main drop in wear track deformation occurs as the TiO_2 content is increase to 5 wt%. This change is more pronounced under the high load used (50 mN).

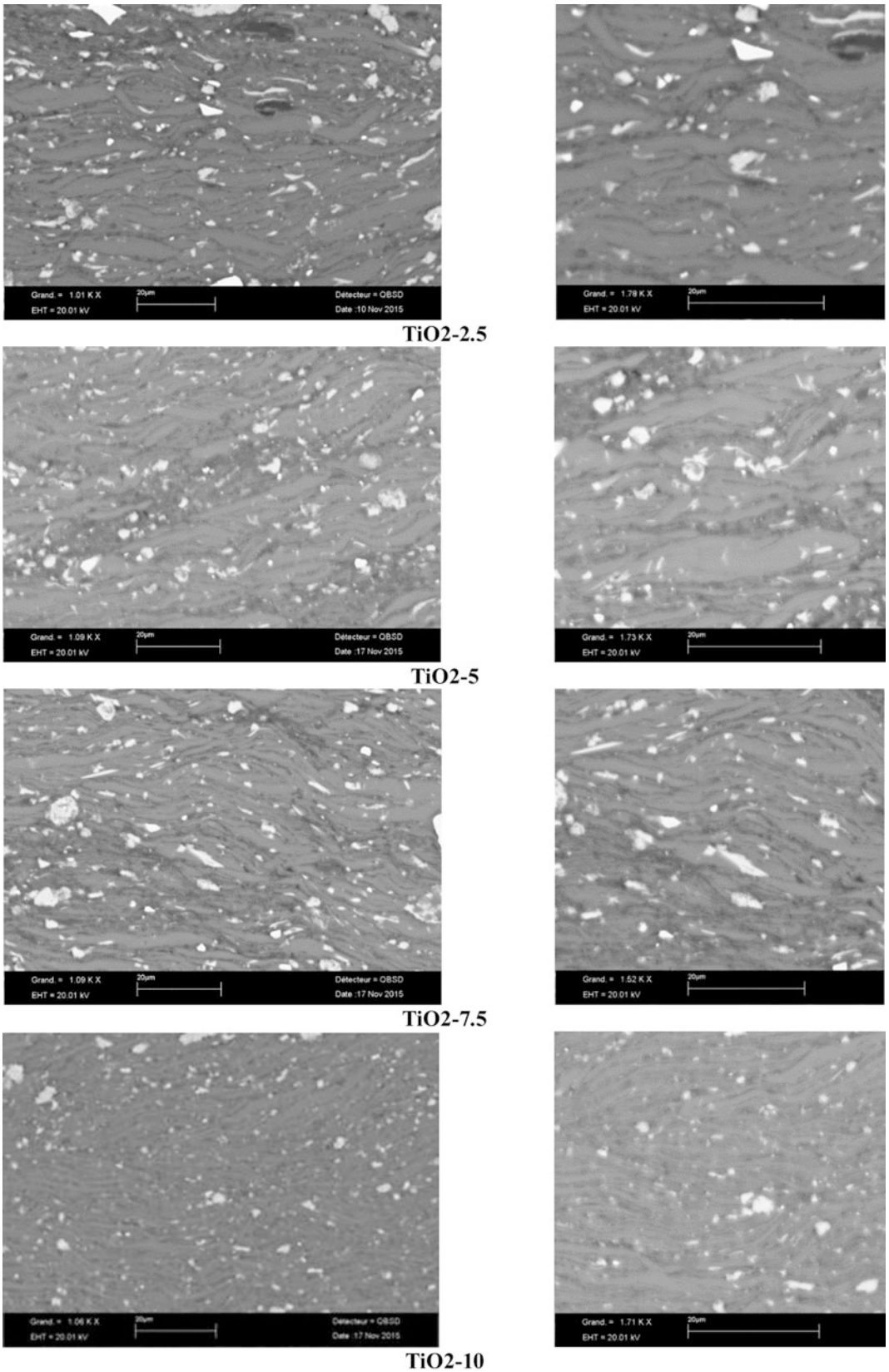

Fig. 30.1 (**a**) SEM micrographs of the compositions with different percentages of TiO_2 added in the matrix. (**b**) EDS analysis of the specimen produced from the first composition, TiO_2-2.5

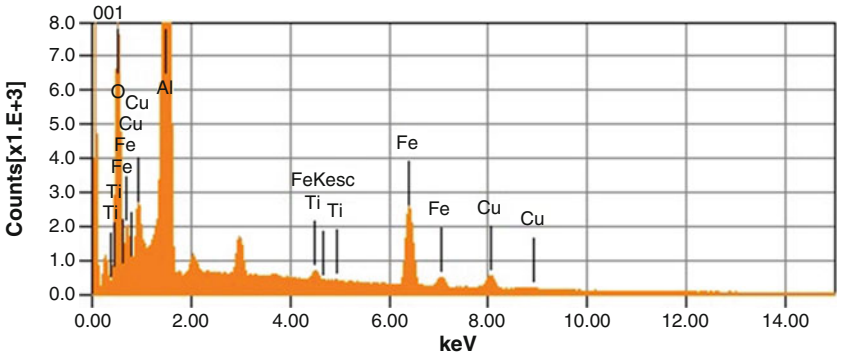

Fig. 30.1 (continued)

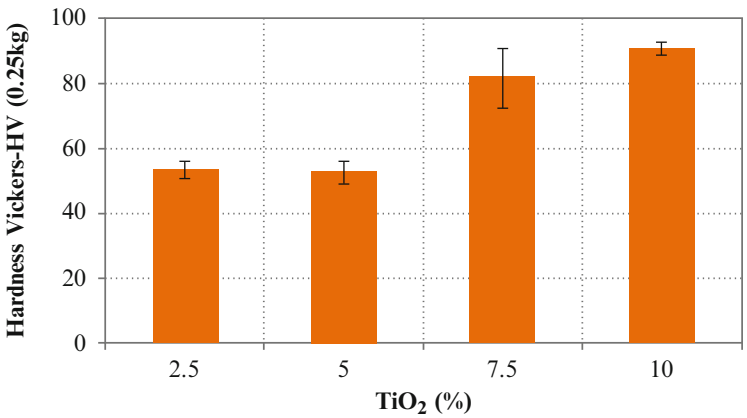

Fig. 30.2 Comparison of microhardness measurements ($HV_{0.25}$) obtained on the four compositions

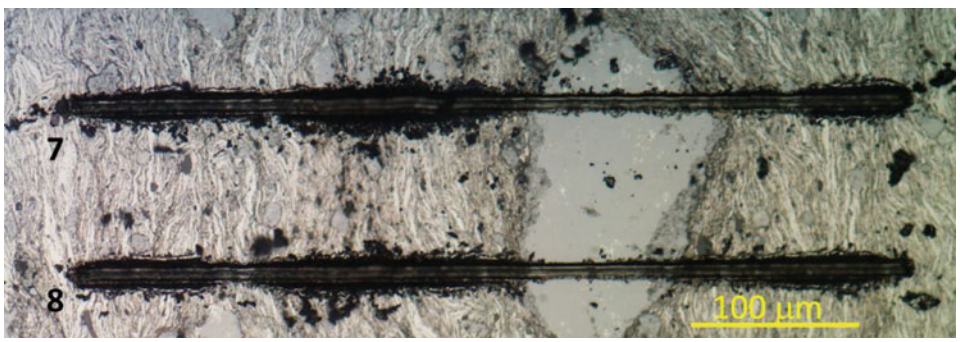

Fig. 30.3 Wear tracks obtained with a scratch application under the load of 50 mN TiO_2-2.5

30.3.4 Creep Compliance by Nanoindentation

Creep behavior of the composites was evaluated with a nanoindenter at two maximum loads of 20 and 50 mN. On each sample 25 indents were made on a 5 × 5 grid with a Berkovich indenter. The load was increased at a rate of 1 mN/s to the maximum load and kept at the maximum load for 500 s then unloaded. In fact, many extensive studies have been performed to understand the bonding characteristics near the interface between the metal and the ceramic particle [13, 15–19]. Among them, evaluation of interface has been carried out by micromechanics and metallographic analyses to show the bonding conditions at the interface of matrix with ceramic oxide, such as Al_2O_3, TiO_2, etc. very simply, the reinforcement particles are embedded into the aluminium powders and progressively during the mechanical milling process, distributed in the

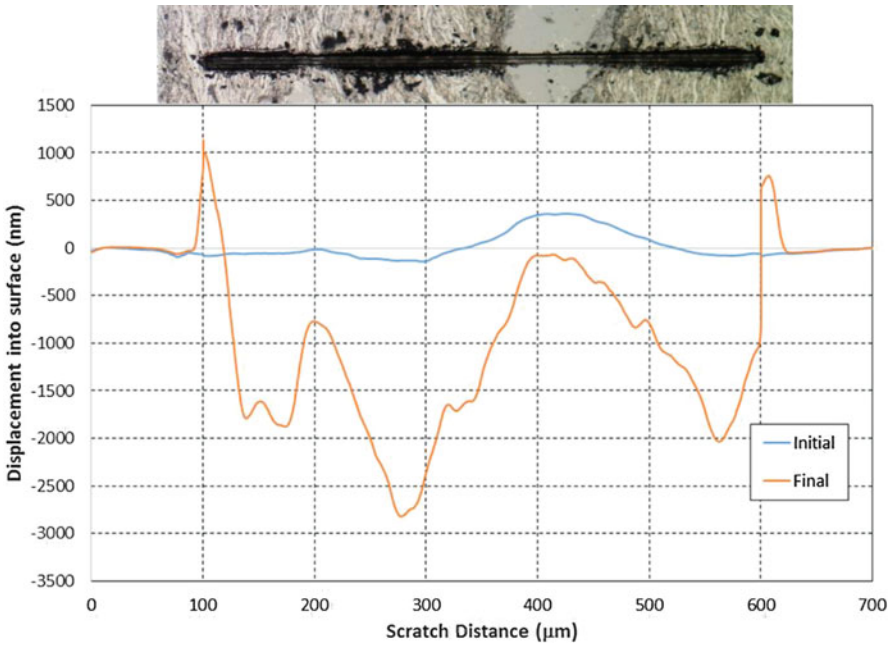

Fig. 30.4 Example of initial and residual profiles used in the calculation of wear track damage

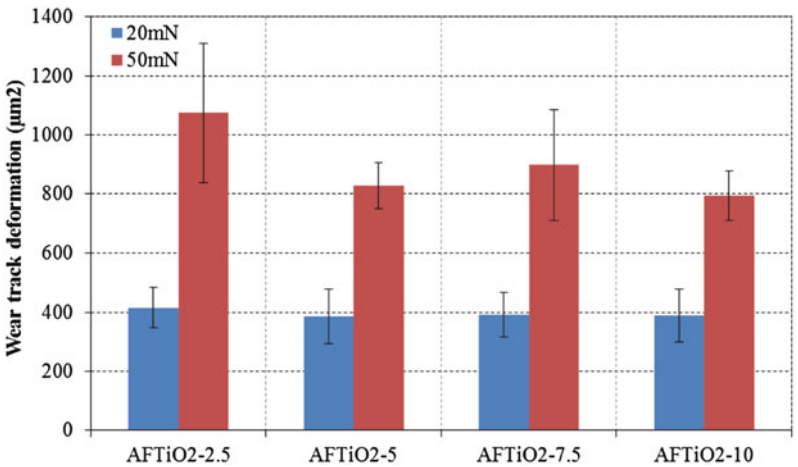

Fig. 30.5 Comparison of wear track deformation for the four compositions

matrix by repeating plastic deformation, fracture, and cold welding of the Al powders and so on. For this reason interface conditions are strongly depended on the blending and milling conditions.

In the present work, a novel thermomechanical treatment was proposed to dope magnetic iron oxide with TiO_2 powders (powder size: 3–10 µm) in an economic way. That is why creep tests by nano indentation technique should be interesting to evaluate the bonding conditions at the interface and the structure of the novel composite proposed in this paper.

Figure 30.6a–c show the micrographs taken from creep tests by nanoindentation under the load of 50 mN for two compositions (TiO_2-2.5, and TiO_2-7). More details of the indents at different locations in microstructure is shown in Fig. 30.6c for the indents 16–20 on sample TiO_2-2.5. Figure 30.7 is the corresponding load-displacement into surface graphs for the indents in Fig. 30.6c showing the localized effect related to the different constituents. These graphs illustrate the reason for the expected scatter in data due to heterogeneity of the samples at this length scale.

Creep compliance have been calculated for all of the compositions presented in this work under the pressure loads of 20 mN and 50 mN and presented in Fig. 30.8.

More details were given in the second section about the calculated values of creep compliances. As indicated in this figure, creep compliance (1/GPa) is variable from 0.4 up to 0.5 in case of 20 mN load while these values are variable from 0.5 up to 0.7 for 50 mN load. Most probably, dispersion of these values are related of the microstructure, the zone where the indentations were taken can show different distribution of particulate reinforcements as was pointed out above.

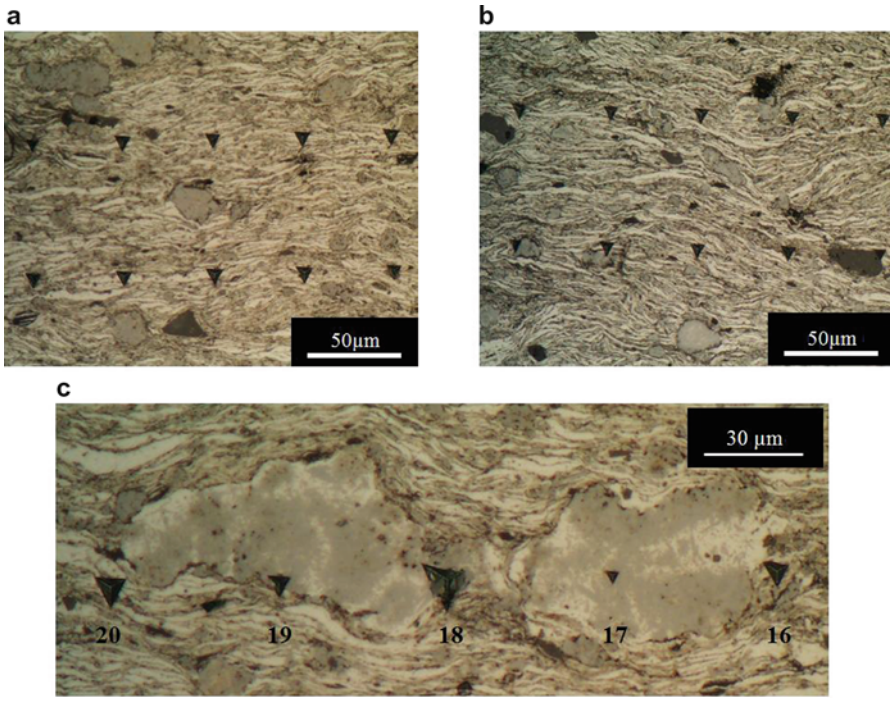

Fig. 30.6 Micrographs taken from creep tests by nanoindentation under the pressure load of 50 mN for two compositions. (**a**) TiO_2-2.5, (**b**) TiO_2-7.5, and (**c**) TiO_2-2.5

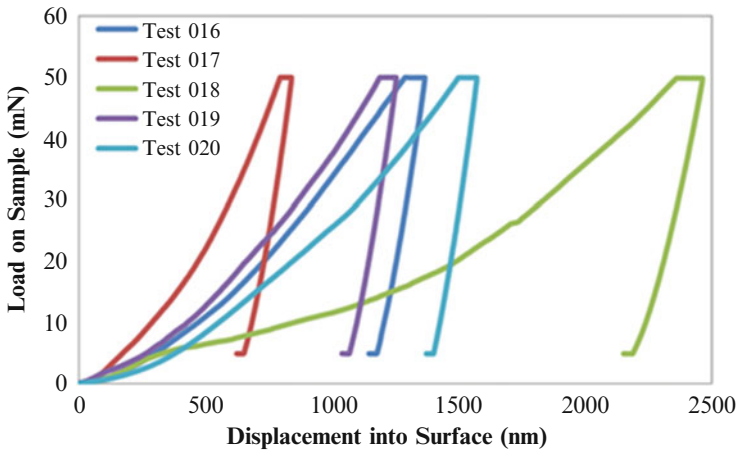

Fig. 30.7 Typical load-displacement curve for creep test data from TiO_2-2.5 under the load of 50 mN

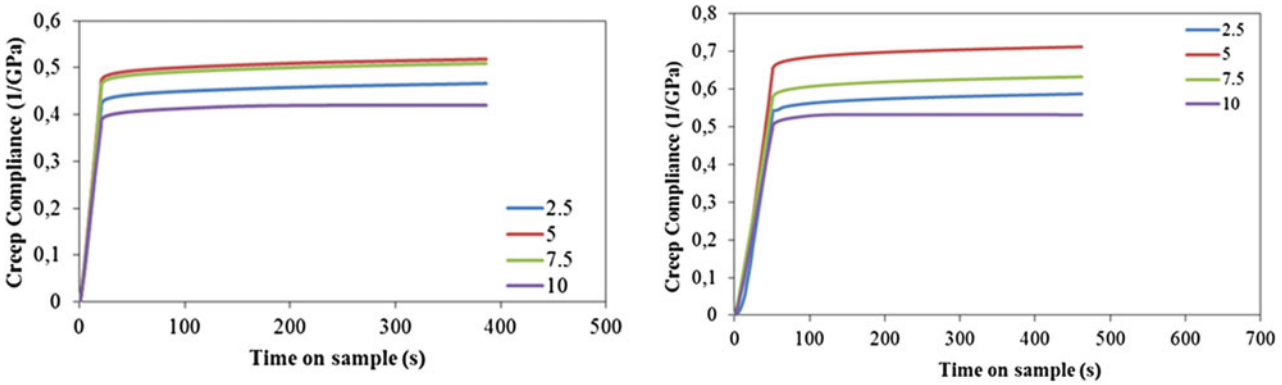

Fig. 30.8 Creep compliance curves for the all of the compositions presented in this work under the pressure loads of 20 mN (*left side*) and 50 mN (*right side*)

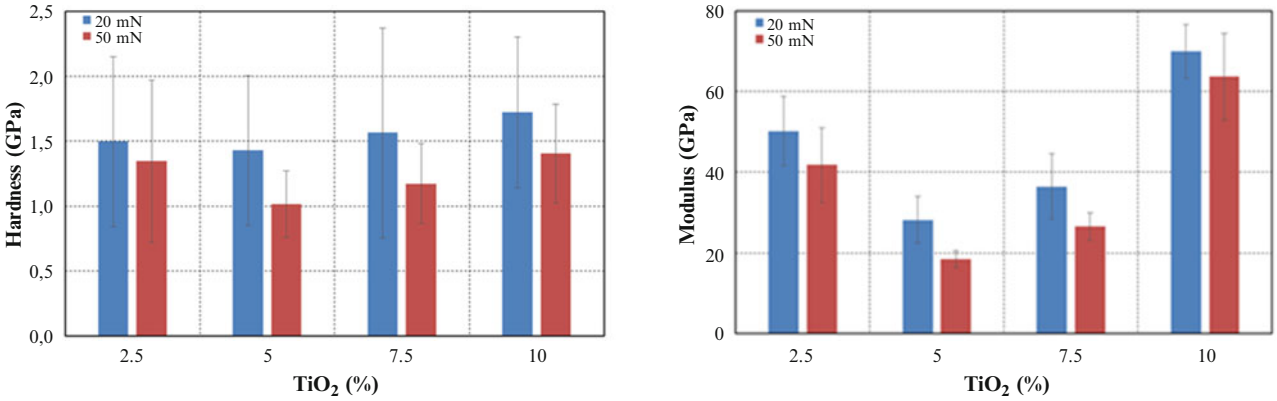

Fig. 30.9 Hardness (*left side*) and Modulus (*right side*) values of the four composites obtained by nanoindentation under the 20 and 50 mN loads

30.3.5 Evaluation of Hardness and Modulus Values by Nanoindentation

In the same way, evaluation of hardness and modulus values of the four composites is presented in Fig. 30.9. These values were calculated through the data obtained by nanoindentation under the loads of 20 and 50 mN.

Hardness values do not show big difference between the data for the composites. There is only a slight change as a function of TiO_2 added in the matrix. However, modulus values show considerable variation between the four compositions mainly the values was the highest found in the last composition (TiO_2-10).

30.4 Conclusions

In the frame of the common research project, novel composites have been proposed from scrap aluminium matrix reinforced with magnetic iron and TiO_2 in different percentages. At the beginning of the process, a novel thermomechanical treatment was applied to dope magnetic iron oxide with TiO_2 powders (powder size: 3–10 μm) in an economic way. By this way, magnetic iron oxide was protected and distributed well in the matrix.

Bonding conditions at the interface of matrix with the reinforcements (doped iron oxide with TiO_2) have been evaluated by means of micromechanics and microstructural analyses. Wear and creep tests have been successfully applied on the four compositions proposed here. Creep compliances and wear track deformations have been determined from the data obtained by nanoindentation.

The present work gives partial results of the project that is going on. Due to the limited length of the manuscript, some other mechanical tests and magnetic properties will be presented in the future publication.

References

1. Tita, V., de Carvalho, J., Vandepitte, D.: A study of the dynamic behavior for low velocity impact on thin composite laminates. In: DINAME-2007, ABCM, Proceedings of the XII International Symposium on Dynamic Problems of Mechanics, Ilhabela, 26 Feb–2 Mar 2007
2. Gottesman, T., Girshovich, S.: Impact damage assessment and mechanical degradation of composites. Key Eng. Mater. **141**(1), 3–18 (1998)
3. Bayraktar, E., Ayari, F., Tan, M.J., Tosun Bayraktar, A., Katundi, D.: Manufacturing of aluminum matrix composites reinforced with iron-oxide nanoparticles: Microstructural and mechanical properties. Metall. Mater. Trans. B **45B**(26), 352–362 (2014)
4. Kurşun, A., Bayraktar, E., Robert, M.H.: Low cost manufacturing of aluminium-alumina composites. J. Adv. Mater. Process. Technol. **1**(3–4), 515–528 (2015). doi:10.1080/2374068X.2016.1143212
5. Mondal, D.P., Das, S.: High stress abrasive wear behavior of aluminum hard particle composites: Effect of experimental parameters, particle size and volume fraction. Tribol. Int. **39**, 470–478 (2006)
6. Panuwar, R.S., Pandey, O.P.: Analysis of wear track and debris of stir cast LM13/Zr composite at elevated temperatures. Mater Charact **75**, 200–213 (2013)
7. Kolhatkar, A.G., Jamison, A.C., Litvinov, D., Wilson, R.C., Lee, T.R.: Tuning the magnetic properties of nanoparticles. Int. J. Mol. Sci. **14**(8), 15977–16009 (2013)

8. Haug, E., de Rouvray, A.: Crash response of composite structures. In: Proceedings on Structural Crashworthiness and Failure, pp. 237–294. Elsevier, London (1993)
9. Michael Hogan, C.: Density of states of an insulating ferromagnetic alloy. Phys. Rev. **188**(2), 870 (1969). doi:10.1103/PhysRev.188.870
10. Zhang, X.Y., Suhl, H.: Spin-wave-related period doublings and chaos under transverse pumping. Phys. Rev. A **32**(4), 2530–2533 (1985)
11. Kursun, A., Enginsoy, H., Bayraktar, E.: Effect of impactor shapes on the low velocity impact damage of sandwich composite plate: Experimental study and model. Composites Part B **86**, 143–151 (2016)
12. Kursun, A., Enginsoy, H., Bayraktar, E.: Experimental and numerical study of alumina reinforced aluminum matrix composites: Processing, microstructural aspects and properties. Composites Part B **90**, 302–314 (2016)
13. Ferreira, L.P., Robert, M.-H., Bayraktar, E.: Production of aluminum composites/SiC/NiAl2O4 MMCs by thixoforming of recycled chips. Solid State Phenom. **217–218**, 286–293 (2015)
14. Dong, S., Hou, P., Cheng, H., et al.: Fabrication of intermetallic NiAl by self-propagating high-temperature synthesis reaction using aluminium nanopowder under high pressure. J. Phys. Condens. Matter **14**, 11023–11030 (2002)
15. Shin, J.H., Choi, H.J., Cho, M.K., Bae, D.H.: Effect of the interface layer on the mechanical behavior of TiO_2 nanoparticle reinforced aluminum matrix composites. J. Compos. Mater. **48**(1), 99–106 (2014)
16. Ferreira, L.-M.-P., Bayraktar, E., Miskioglu, I., Robert, M.-H.: Effect of the reinforcement particles on the microstructure and electrical properties of aluminium matrix composites (AMCs). In: AMPT-2015, International Conference of, Advanced Materials Processing Technologies, Madrid, 14–17 Dec 2015
17. Shi, Z., Yang, J.M., Lee, J.C.: The interfacial characterization of oxidized SiC/2014 Al composites. Mater. Sci. Eng. A **303**, 46–53 (2001)
18. Yu, Z., Wu, G., Jiang, L.: Effect of coating Al_2O_3 reinforcing particles on the interface and mechanical properties of 6061 alloy aluminium matrix composites. Mater. Lett. **59**, 2281–2284 (2005)
19. Ferreira, L.-M.-P., Bayraktar, E., Robert, M.-H., Miskioglu, I.: Influence of nano particulate and fiber reinforcements on the wear response of multiferroic composites processed by powder metallurgy. In: AMPT-2015, International Conference of, Advanced Materials Processing Technologies, Madrid, 14–17 Dec 2015
20. Foo, K.S., Banks, W.M., Craven, A.J.: Interface characterization of an SiC particulate/6061 aluminium alloy composites. Composites **25**, 677–683 (1994)

Chapter 31
Implementation of the Surface Response to Excitation Method for Pipes

A. Baghalian, S. Tahakori, H. Fekrmandi, M. Unal, V.Y. Senyurek, D. McDaniel, and I.N. Tansel

Abstract The Surface response to excitation (SuRE) method was developed to detect the defects and loading condition changes on plates without using the impedance analyzer. The SuRE method excites the surface with a piezoelectric exciter. Generally, sweep sine wave is continuously applied and surface waves are monitored with (a) piezoelectric element(s) or noncontact sensor(s). The change of the spectral characteristics is quantified by using the sum of the squares of the differences (SSD) to detect the defects. In this study, the SuRE method was implemented for detection of the defects in pipes. The surface of a pipe was excited with a continuous sweep sine wave and the dynamic response of the pipe on selected points were monitored by using a scanning laser vibrometer. The study shows that the SuRE method can be used effectively for detection of damage and estimation of its severity in pipe like structures.

Keywords SHM • Pipe monitoring • SuRE method • Sensor networks • Guided waves

31.1 Introduction

Wave transmission technology and impedance based SHM methods are among the most successful guided wave-based SHM techniques that have been used for detecting defects in pipes. Wave transmission SHM techniques work based on monitoring propagations of excited waves through measuring reflections and/or transmission of guided waves [1–16]. Successful application of these techniques in SHM of pipes highly depends on identifying appropriate guided wave modes and frequencies for each application. In some applications, there is limited or no knowledge regarding the structure's material properties, which makes proper mode and frequency selection an even more troublesome task.

In methods that fall under the category of Impedance methods, a PZT transducer is bonded to a target structure and is used to simultaneously excite the structure with high-frequency waves and also to acquire electric impedance of a structure [17–22]. Assuming that the PZT impedance is invariant, since the mechanical impedance of the PZT and the host structure are coupled together, any changes in the measured electrical impedance by PZT can be correlated with the change of the host structure's mechanical health; therefore, by analyzing the electromechanical coupling relationship between PZT ceramic and body structure the damage condition of the structure can be monitored. In practice, an impedance analyzer such as HP 4194A that costs about $40,000 is used for characterization of the piezoelectric element when implementing the Impedance method. However, not all capabilities of such an analyzer are necessary; therefore, some researchers have substituted the impedance analyzer with an amplifier-based turnkey circuit which is capable of measuring and recording electric impedance of a PZT; where the cost of parts required to make one test device was less than $10.

In a variation of the impedance approach, dynamic characteristics of a structure are monitored using a second piezoelectric element that is also mounted on the surface of the structure. This approach is called the Surface Response to Excitation (SuRE) method and it has been successfully applied to assess the state of the health in plates and also for load monitoring in

A. Baghalian (✉) • S. Tahakori • I.N. Tansel
Mechatronics Research Laboratory, Department of Mechanical and Materials Engineering,
Florida International University, 10555 W Flagler Street, Miami, FL 33174, USA
e-mail: abagh004@fiu.edu

H. Fekrmandi • D. McDaniel
Applied Research Center, Florida International University, 10555 W Flagler Street, Miami, FL 33174, USA

M. Unal
Department of Mechatronics Engineering, Faculty of Technology, Marmara University, Istanbul, Turkey

V.Y. Senyurek
Department of Electrical and Electronics Engineering, Faculty of Technology, Marmara University, Istanbul, Turkey

W.C. Ralph et al. (eds.), *Mechanics of Composite and Multi-functional Materials, Volume 7*,
Conference Proceedings of the Society for Experimental Mechanics Series, DOI 10.1007/978-3-319-41766-0_31

plate-like structures [23–28]. The basic concept of the SuRE method is to apply high-frequency sweep sine wave to excite a piezoelectric element that is attached to surface of a target structure to monitor dynamic characteristics through acquiring the frequency response using another sensor, which contain critical information regarding state of the health of the structure. The sensor could be a piezo electric disk or laser vibrometer. In this method, SSD is used as damage metric for damage identification.

The purpose of this paper is to examine the effectiveness of SuRE-based structural health monitoring by using noncontact sensors in pipe monitoring. In this paper, the same philosophy of continuous comparison of frequency by frequency pattern of responses is followed; however, the second piezoelectric sensor is substituted with a scanning laser vibrometer. Circumferential and longitudinal defects have been created and the SSD damage metric was used to detect the presence and estimate the severity of the damages. The study shows that the SuRE method can be used effectively for detection and estimation of severity of both types of damages in pipe like structures.

31.2 Method

The SuRE method is an active structural health monitoring technique in which the surface of a structure is excited over a certain frequency range through using surface bonded piezoelectric elements. Typically, one piezoelectric element is used for excitation and one or more piezoelectric or other type of transducer could be used to acquire the response of the system. In order to monitor the dynamic response of the system, Fast Fourier Transform (FFT) of the acquired signal is obtained. This frequency spectrum remains unchanged as long as no change occurred on the structure. The frequency response matrix of the system in intact and damaged states is shown in Eq. (31.1). The response at each frequency has the unit of voltage, where f is frequency, B and D indicate the Baseline and Damage states, m is number of scanned frequencies, and n is the number of sensory points in the network. In other words, every column in the matrixes represents the frequency response spectrum of a certain sensory point over the acquired frequency range.

$$V_B(f) = B_{m*n}, V_D(f) = D_{m*n} \tag{31.1}$$

When damages occur or loads are applied on the structure of interest, the dynamic response of the structure changes. In the SuRE method, for sensory points of j = 1,. . .,n in the sensing network, SSD of the frequency response matrix of the damaged part with respect to the pristine structure (baseline state) is used as the damage metric and is calculated, as shown in Eq. (31.2).

$$SSD_{j=1,\ldots,n} = \sum_{i=1}^{i=m} \left(B_{ij} - D_{ij}\right)^2 \tag{31.2}$$

SSD is an index to quantify changes in the frequency spectrum; damages and loads application on the structure affect properties such as mass, damping and stiffness, which result in variation of the frequency response from its initial state.

31.3 Experimental Setup

In the present study, a disk-shaped piezoelectric transducer was permanently bonded to the surface of an Aluminum pipe specimen and it was excited by an external signal generator over a broad frequency range. the pipe had an external diameter of 26 mm, a wall thickness of 3 mm and a length of 226 mm. Responses at different points were sensed using the LDV (Laser Doppler Vibrometer)—Polytec 3D Laser Scanning Vibrometer PSV400 [23–28]. The received signals were in the form of V (f) curves (i.e., amplitude versus frequency).

The testing phase was broken into two main stages of damaged and pristine structure (baseline) tests; first, the dynamic response of the structure at different sensory points in a pristine state were acquired; then, to simulate defects with different sizes and degrees of severity, circumferential and longitudinal defects were created using a tube cutter and milling machine, respectively. The depth of the defect in the circumferential defect and the length of the defect in the longitudinal defect were increased in three increments, in the course of experiments. After increasing the damage characteristics in each increment, the response of the structure was acquired and the SSD vector was calculated. The schematic of experimental set up used in this experiment is shown in Fig. 31.1.

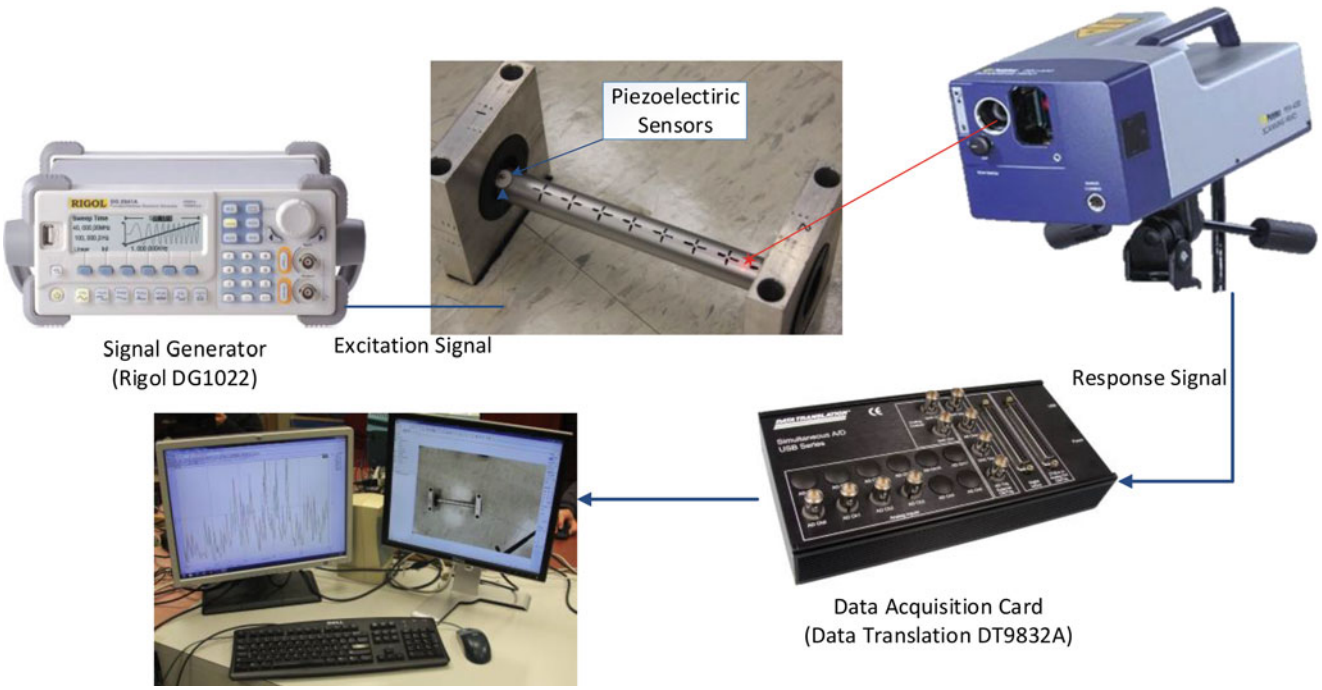

Fig. 31.1 Experimental set-up for implementation of SuRE method

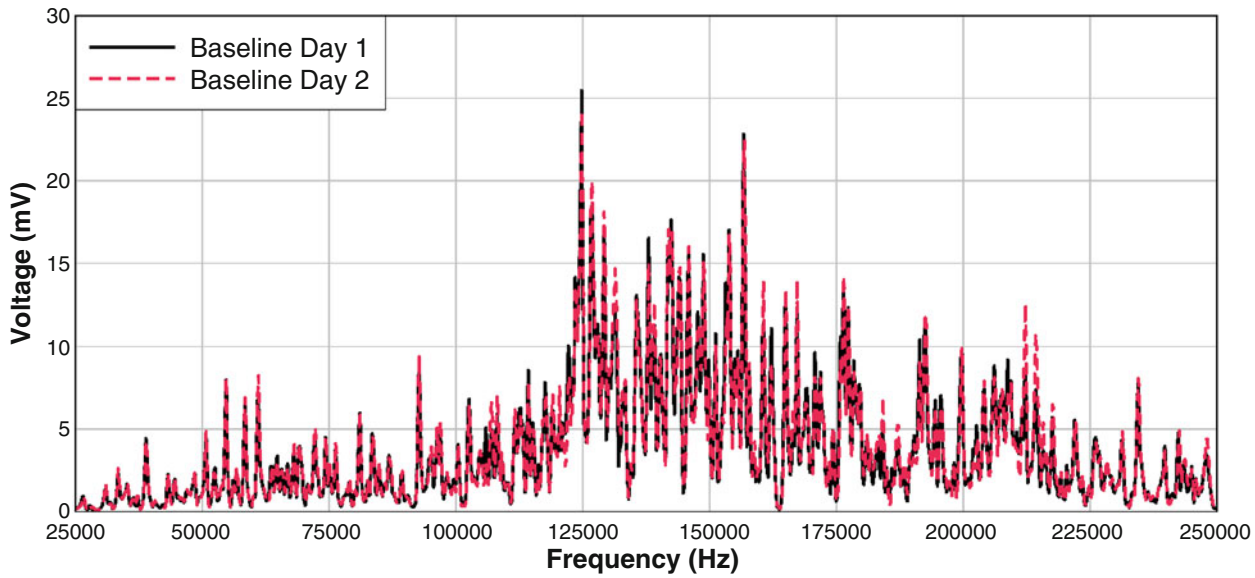

Fig. 31.2 First baseline spectrum vs. second baseline spectrum

31.4 Results and Discussion

To implement the SuRE method, in the first step, the response of the system to excitation in the situation of no-damage (baseline) was acquired. To show repeatability of the procedure, the response was captured on two different days and each time prior to data acquisition, the experimental setup was completely disassembled and once again assembled. The test was repeated three times and the average of the acquired response of the system after the three different tries was used in analysis. As it can be seen from Fig. 31.2, there is a very high match between responses acquired in the two sets of tests.

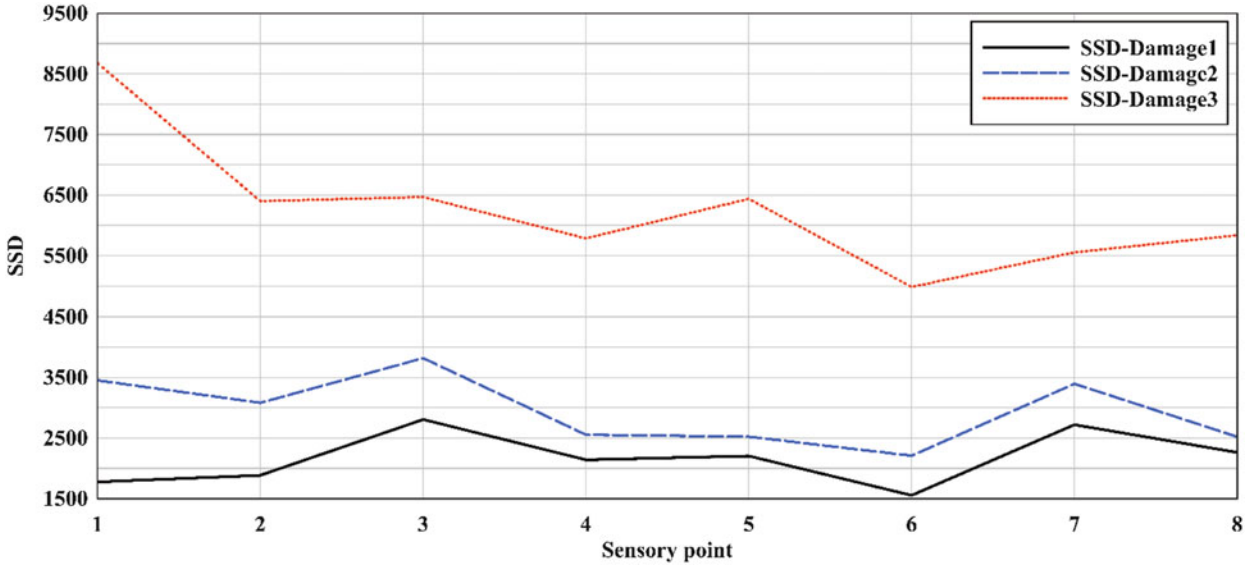

Fig. 31.3 SSD values on sensory points after each increase in circumferential damage

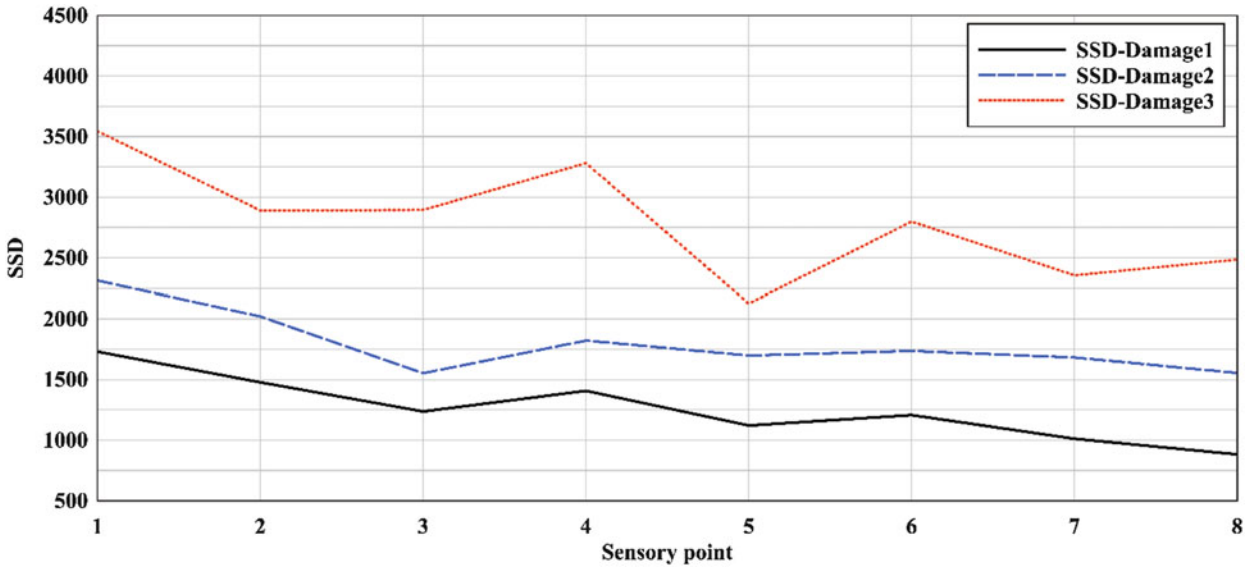

Fig. 31.4 SSD values on sensory points after each increase in longitudinal damage

A complete circumferential cut was created in the pipe using a tube cutter and depth of cut was increased in three increments, in steps of 0.5 mm. The dynamic response of the pipe in all sensory points was acquired. Using Eq. (31.2), SSD values were calculated with respect to baseline frequency spectrums; the results for all sensory points are shown in Fig. 31.3. As it can be seen from Fig. 31.3, the SuRE method was successfully able to distinguish between three damage states. As it is shown in Fig. 31.3, by increasing the damage depth, the SSD value that is an indicative of damage presence and severity in structure increases in all sensory points.

In another try it was aimed to study the effectiveness of the SuRE method in the detection of longitudinal defects and distinguishing between different levels of severity. Therefore, the length of a longitudinal defect with a width of 1 mm was increased in increments of 0.5 mm, in three steps. Using Eq. (31.2), SSD values were calculated with respect to frequency response of the pristine pipe. Similar to Fig. 31.3, it can also be seen from Fig. 31.4 that increasing the length of the damage, the SSD value monotonically increases in all sensory points.

31.5 Conclusion

For the first time, the SuRE method is applied for pipe structural health monitoring using noncontact laser doppler sensors. The differences between the FFT of the acquired signal in pristine and other damaged states were quantified by calculating the corresponding sum of the squares of differences. The SSD damage metric in pipes shows steady and monotonic change in value as the damage condition increases. Our case studies have demonstrated that SuRE method could be successfully applied for SHM of pipes.

Acknowledgment The authors would like to thank The Scientific and Technological Research Council of Turkey (TUBITAK) for supporting Dr. Muhammet Unal and Dr. Volkan Yusuf Senyurek's research at the Florida International University.

References

1. Ahmad, R., Kundu, T.: Structural health monitoring of steel pipes under different boundary conditions and choice of signal processing techniques. Adv. Civ. Eng. **2012**, 14 (2012). doi:10.1155/2012/813281
2. Amjad, U., Yadav, S.K., Kundu, T.: Detection and quantification of pipe damage from change in time of flight and phase. Ultrasonics **62**, 223–236 (2015)
3. Baltazar, A., Rojas, E., Mijarez, R.: Structural health monitoring in cylindrical structures using helical guided wave propagation. Phys. Procedia **70**, 686–689 (2015)
4. Carandente, R., Cawley, P.: The effect of complex defect profiles on the reflection of the fundamental torsional mode in pipes. NDT&E Int. **46** (1), 41–47 (2012)
5. Galvagni, A., Cawley, P.: The reflection of guided waves from simple support in pipes. J. Acoust. Soc. Am. **129**, 1869–1880 (2011)
6. Kang, T., Lee, D.H., Song, S.J., Kim, H.J., Do Jo, Y., Cho, H.J.: Enhancement of detecting defects in pipes with focusing techniques. NDT&E Int. **44**(2), 178–187 (2011)
7. Kim, H.W., Lee, H.J., Kim, Y.Y.: Health monitoring of axially-cracked pipes by using helically propagating shear-horizontal waves. NDT&E Int. **46**(1), 115–121 (2012)
8. Li, F., Liu, Z., Sun, X., Li, H., Meng, G.: Propagation of guided waves in pressure vessel. Wave Motion **52**, 216–228 (2015)
9. Liu, K., Wu, Z., Jiang, Y., Wang, Y., Zhou, K., Chen, Y.: Guided waves based diagnostic imaging of circumferential cracks in small-diameter pipe. Ultrasonics **65**, 34–42 (2016)
10. Ma, S., Wu, Z., Wang, Y., Liu, K.: The reflection of guided waves from simple dents in pipes. Ultrasonics **57**(C), 190–197 (2015)
11. Ratassepp, M., Fletcher, S., Lowe, M.J.S.: Scattering of the fundamental torsional mode at an axial crack in a pipe. J. Acoust. Soc. Am. **127**(2), 730–740 (2010)
12. Stoyko, D.K., Popplewell, N., Shah, A.H.: Detecting and describing a notch in a pipe using singularities. Int. J. Solids Struct. **51**(15–16), 2729–2743 (2014)
13. Wang, T., Yang, C., Ye, L., Spray, D., Xiang, Y.: Evaluation of guided wave propagation in steel pipes. In: Recent Advances in Structural Integrity Analysis – Proceedings of the International Congress (APCF/SIF-2014), 255–260 (2014)
14. Wang, X., Tse, P.W., Mechefske, C.K., Hua, M.: Experimental investigation of reflection in guided wave-based inspection for the characterization of pipeline defects. NDT&E Int. **43**(4), 365–374 (2010)
15. Yang, F., Jing, L., Zhang, W., Yan, Y., Ma, H.: Experimental and numerical studies of the oblique defects in the pipes using a chaotic oscillator based on ultrasonic guided waves. J. Sound Vib. **347**, 218–231 (2015)
16. Zhou, W., Yuan, F.G., Shi, T.: Guided torsional wave generation of a linear in-plane shear piezoelectric array in metallic pipes. Ultrasonics **65**, 69–77 (2016)
17. Hamzeloo, S.R., Shamshirsaz, M., Rezaei, S.M.: Damage detection on hollow cylinders by electro-mechanical impedance method: Experiments and finite element modeling. C. R. Mec. **340**(9), 668–677 (2012)
18. Min, J., Park, S., Yun, C.B., Lee, C.G., Lee, C.: Impedance-based structural health monitoring incorporating neural network technique for identification of damage type and severity. Eng. Struct. **39**, 210–220 (2012)
19. Park, G., Cudney, H.H., Inman, D.J.: Feasibility of using impedance-based damage assessment for pipeline structures. Earthquake Eng. Struct. Dyn. **30**(10), 1463–1474 (2001)
20. Park, G., Sohn, H., Farrar, C.R., Inman, D.J.: Overview of piezoelectric impedance-based health monitoring and path forward. Shock Vib. Dig. **35**(6), 451–463 (2003)
21. Park, S., Yun, C.B., Inman, D.J.: Structural health monitoring using electro-mechanical impedance sensors. Fatigue Fract. Eng. Mater. Struct. **31**(8), 714–724 (2008)
22. Xu, D., Huang, S., Cheng, X.: Electromechanical impedance spectra investigation of impedance-based PZT and cement/polymer based piezoelectric composite sensors. Constr. Build. Mater. **65**, 543–550 (2014)
23. Fekrmandi, H., Tansel, I.N., Gonzalez, R., Rojas, S., Meiller, D., Lindsay, K., Baghalian, A., Tashakori, S.: Implementation of the surface response to excitation (SuRE) method with DSP's for detection of the damage of thick blocks. In: 10th International Workshop on Structural Heath Monitoring 2015, 2 Sep 2015
24. Fekrmandi, H., Gonzalez, R., Rojas, S., Tansel, I.N., Meiller, D., Lindsay, K.: Excitation (SuRE) method by using neural networks. In: 7th International Conference on Recent Advances in Space Technologies (RAST), vol. 3420, pp. 11–16, Istanbul (2015)

25. Fekrmandi, H., Rojas, J., Campbell, J., Tansel, I.N., Kaya, B., Taskin, S.: Inspection of the integrity of a multi-bolt robotic Arm using a scanning laser vibrometer and implementing the surface response to excitation method (SuRE). Int. J. Prognostics and Health Manage. **5**(1), 1–10 (2014)
26. Fekrmandi, H., Rojas, J., Tansel, I.N., Yapici, A., Uragun, B.: Investigation of the computational efficiency and validity of the surface response to excitation method. Meas. J. Int. Meas. Confed. **62**, 33–40 (2015)
27. Fekrmandi, H., Unal, M., Baghalian, A., Tashakori, S., Oyola, K., Alsenawi, A., Tansel, I.N.: A non-contact method for part-based process performance monitoring in end milling operations. Int. J. Adv. Manuf. Technol. **83**(1), 13–20 (2015)
28. Fekrmandi, H., Unal, M., Rojas Neva, S., Tansel, I.N., McDaniel, D.: A novel approach for classification of loads on plate structures using artificial neural networks. Measurement **82**, 37–45 (2016)

Chapter 32
Thermal Methods for Evaluating Flaws in Composite Materials: A New Approach to Data Analysis

Davide Palumbo and Umberto Galietti

Abstract Lock-in thermography represents a valid and consolidated techniques capable of detecting and quantifying defects in composite materials. This technique in industry is still not widespread especially for large structures, mainly because of the overall lengthy time required for testing due to the necessary scanning approach.

In this work, the influence of the main setup parameters of the lock-in thermography technique is assessed, analysing simulated defects on a sample specimen made of GFRP. In particular, the attention was focused on the optimization of testing parameters for the improvement of signal quality and to reduce testing time. An analysis of the phase signal variations with the dimension and position of defect has been carried out and eventual implications about the quantitative evaluation of defects were discussed.

Keywords NDT • Stimulated thermography • Multi-frequency lock-in • Composite material • GFRP

32.1 Introduction

Composite materials are currently used in many applications where a high strength to weight ratio is required. Typical defects such as delamination or voids can dramatically change the strength of the structure [1]. Non-destructive techniques are currently used for defect detection in composites such as X-ray [2], ultrasound [3], shearography [4], vibration testing [5] and electrical potential technique [6], all of which have their own peculiarities and capabilities to identify and different kinds of defects to quantify.

Thermographic techniques, with respect to other traditional well established NDT techniques, potentially allows for investigation of large areas with a relatively shorter time and without the need for coupling like UT or safety issues such as with X-ray [1, 7].

With regards to test set-up and data processing, Lock-in Thermography (LT) is among the most used thermographic techniques for the non-destructive evaluation of composite materials [7–12]. All the thermographic techniques use an external heat source to stimulate the material with thermal waves in order to induce a heat flux in the material and analyse the temperature behaviour on the surface of the component. In this way, a defect can be detected since it inducing different thermophysical local properties in the material, will also induce an anomaly in the thermal diffusion and subsequently a different surface temperature in the component. In particular, the Lock-in Thermography looks for areas of differing thermal behaviour that can be correlated to a defect and that are typically dependent on different thermal-physical properties involved in the heat transmission phenomena such as the thermal conductivity, the specific heat at constant pressure and the density of material [1, 11].

The ability of thermography to detect defects in CFRP and GFRP composite materials has been demonstrated in various works and in many applications. In particular, thermal techniques have been used to investigate defects in adhesively bonded components [12–17] and many applications concern the investigation of composite material subjected to impact damage [18–21].

In this work, LT has been used to detect simulated defect on a GFRP sample specimen. In particular a modulated heat source has been used for stimulating the specimen in a desired range of frequencies and extracting information about the simulated defects.

This approach has already been used in literature with the aim of reducing testing time. In particular, a theoretical basis for describing this approach has been provided in the work of Mulaveesala et al., [22] where in a single test, hidden Teflon

D. Palumbo (✉) • U. Galietti
Department of Mechanics, Mathematics and Management (DMMM), Politecnico di Bari, Viale Japigia 182, 70126 Bari, Italy
e-mail: davide.palumbo@poliba.it

W.C. Ralph et al. (eds.), *Mechanics of Composite and Multi-functional Materials, Volume 7*,
Conference Proceedings of the Society for Experimental Mechanics Series, DOI 10.1007/978-3-319-41766-0_32

patches at various depths were detected. In this regard, Pitarresi [23, 24] proposed a numerical off-line signal processing technique for assessing flaws with lock-in thermography. This technique has been used for obtaining phase maps at various lock-in frequencies generated with pulse-modulated heat within one single experiment. However, in these works a qualitative analysis of results is only provided and, in these terms, a comparison with the classic procedure is not made.

Generally, quantitative analysis of defects is carried out considering different algorithms based on the evaluation of a threshold value of the phase signal dependent on the set-up parameters adopted for the tests and on the material [1, 11]. However, the dimensions and position (depth) of the defect affect the phase signal and then they must be taken into account for a correct quantitative analysis.

In this work it has been carried out a discussion about the influence of the dimensions and position of defects on the phase signal.

32.2 Stimulated Thermography

Lock-in thermography is based on the generation of thermal waves inside the specimen, for example, by periodically exciting the specimen surface [7, 10]. The resulting oscillating temperature field in the stationary regime can be recorded remotely through its thermal infrared emission by an IR camera. Thermal wave can be reconstructed by measuring temperature evolution over the specimen surface: by a suited algorithm, information about magnitude (A) and phase (φ) of the thermal wave can be obtained.

Phase data are relatively independent of local optical and infrared surface features and phase signal allows deeper penetration into the material than the analysis of the amplitude signal [7, 10].

In the phase image, defects appear with a different phase signal compared to sound material. Moreover, the phase of thermal wave is related directly to depth z [7, 10]:

$$\varphi(z) = \frac{2\pi z}{\lambda} = \frac{z}{\mu} \tag{32.1}$$

with λ thermal wavelength and μ the thermal diffusion length:

$$\mu = \sqrt{\frac{2k}{\omega \rho c_p}} = \sqrt{\frac{2\alpha}{\omega}} \tag{32.2}$$

where k is the thermal conductivity, ρ is the density, c_p is the specific heat at constant pressure, ω is the modulation frequency and α is the thermal diffusivity.

Equation (32.1) refers to homogeneous materials [7, 10] but qualitative considerations can also be extended to composite laminates. This equation indicates that higher modulation frequencies restrict the analysis in a near-surface region, while low-frequency thermal waves propagate deeper but very slowly [7, 10]. The main drawback of the technique is that, for depth evaluation, the operator has to change and to perform different test, each time changing the frequency of thermal excitation.

32.3 Material and Methods

A specimen with simulated defects was obtained through the vacuum infusion resin process. An epoxy-type (i.e. EC 157 by ELANTAS) resin was taken into account, reinforced with a double layer of quadriaxial glass fiber of the type 0°/+45°/90°/−45° (Fig. 32.1). Dimensions and depth of defects are reported in Table 32.1.

Lock-in thermography tests were performed by IR camera FLIR SC 640 with thermal sensitivity (NETD) < 30 mK and based on a micro bolometer detector with 640 × 512 pixels.

The set-up used is shown in Fig. 32.1 ($\beta = 30°$, DT = 30 cm, DL = 20 cm). In particular, two halogen lamps with a power of 500 W were controlled by MultiDES® system in order to heat specimens with a series of sinusoidal and square waves. Thermal data were processed by IRTA® [24] software in order to obtain amplitude and phase images from lock-in tests.

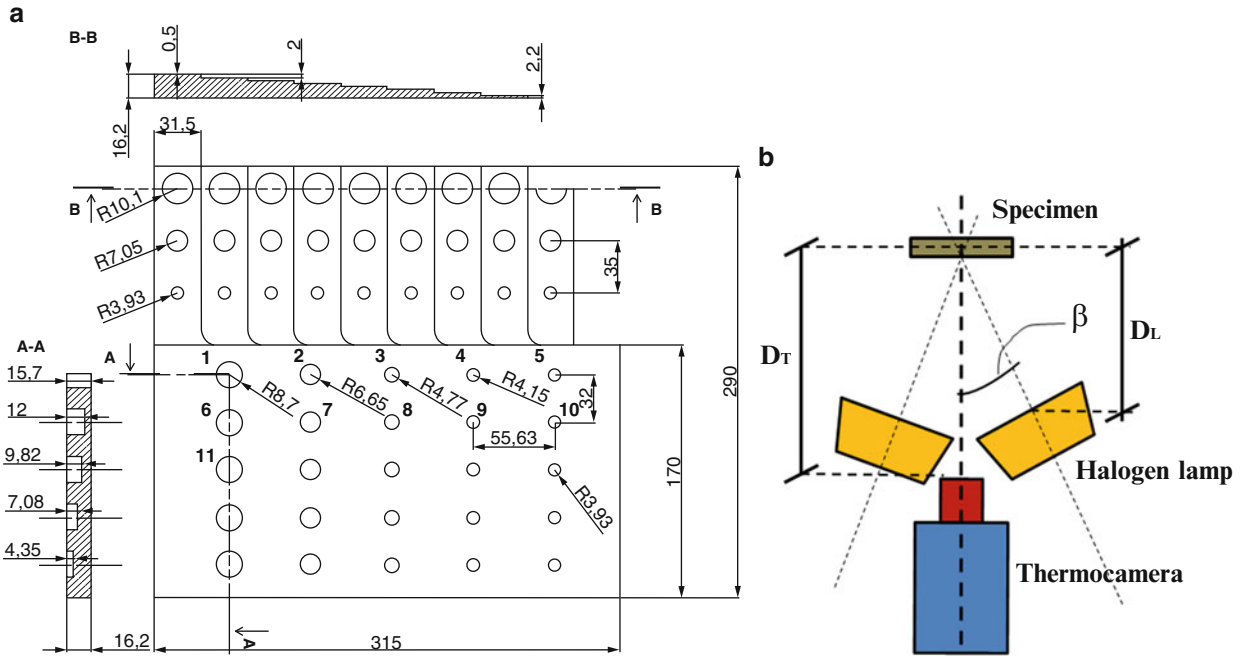

Fig. 32.1 Specimen and set-up used for tests

Table 32.1 Diameter and depth of defects indicated in Fig. 32.3

N°	Nominal area (mm^2)	Nominal diameter D (mm)	Depth p (mm)
1	237.7	17.4	0.5
2	138.9	13.3	0.5
3	71.4	9.5	0.5
4	54.1	8.3	0.5
5	48.4	7.9	0.5
6	237.7	17.4	3.8
7	138.9	13.3	3.8
11	237.7	17.4	6.4

Table 32.2 Parameters used for lock-in thermographic tests (acquired 100 frames/cycle)

Modulation period (s)	Modulation frequency (Hz)	Heat source	Number of cycles	Harmonics (Hz)	
48	0.021	square	2, 3, 5	0.021; 0.062; 0.105	I; III; V
		sin		0.021	–
72	0.014	square	2, 3, 5	0.014; 0.042; 0.069	I; III; V
		sin		0.014	–
80	0.013	square	2, 3, 5	0.013; 0.038; 0.063	I; III; V
		sin		0.013	–
120	0.008	square	2, 3, 5	0.008; 0.025; 0.042	I; III; V
		sin		0.008	–
240	0.004	square	2, 3, 5	0.004; 0.013; 0.021	I; III; V
		sin		0.004	–
360	0.003	square	2, 3, 5	0.003; 0.008; 0.014	I; III; V
		sin		0.003	–

A number of lock-in tests have been carried out, as shown in Table 32.2, with a different number of cycles analyzed, as well as shapes of thermal excitation and periods of excitation. All tests were carried out in order to always obtain 100 frames per cycle. This value represents a good compromise for obtaining both a good signal to noise ratio and lower computational times.

32.3.1 Methods and Algorithms Proposed

Generally, the lock-in thermography technique is carried out by stimulating the material with a modulated sinusoidal heat source at a fixed frequency. As just stated, this frequency allows us to investigate the material to a given depth as reported in Eq. (32.1). It follows that in order to obtain information about the full depth of a component, different tests have to be performed at different modulated frequencies and consequently, in the case of a large structure, the application of LT technique can involve elevated testing time.

As demonstrated in other works [22–24], the thermal response of material contains information about high order frequencies proportional to the main frequency. By decomposing the thermal response in time domain as the sum of a singular sinusoidal wave, we can write:

$$T_m(t) = a + bt + \sum_{n=1}^{\infty} \Delta T_n \sin(n\omega t + \varphi_n) \quad n = 1, 3, 5, 7, \tag{32.3}$$

where t is the time, a and b are two constants used to model the average temperature growth of the material, ω is the modulated frequency of the main harmonic (first Fourier component), ΔT_n and φ_n are the amplitude and the phase of n-th Fourier component.

In this work, all the constants were obtained through a least-square fit method by imposing the model of Eq. (32.3) to the thermal signal of each pixel and by considering the terms up to $n = 5$. In this way we can write:

$$T_m(t) = a + bt + \Delta T_1 \sin(\omega t + \varphi_1) + \Delta T_3 \sin(3\omega t + \varphi_3) + \Delta T_5 \sin(5\omega t + \varphi_5) \tag{32.4}$$

Equation (32.4) allows us to obtain information about the amplitude and phase signal of high order excitation frequencies with respect to the main by a single lock-in test.

32.4 Results

32.4.1 Qualitative Comparison of Sinusoidal and Square Wave Excitation

Figure 32.2 shows a comparison between the phase maps obtained by using sinusoidal wave and the first harmonic of square wave. As was expected, deeper defects appear in correspondence with a higher modulation period (lower excitation frequencies). In Fig. 32.3, the phase maps obtained with a sinusoidal wave at a modulation period of 120 s and 72 s are compared to the third and fifth harmonics obtained from a square excitation at modulated period of 360 s.

The comparison of the images seems to clearly indicate that there is no significant difference between sinusoidal and square wave excitation. The comparison of results obtained with sinusoidal heating shape with third and fifth harmonic of the square wave seems to suggest that there is a significant but yet not dramatic loss of quality.

32.4.2 Quantitative Comparison of Sinusoidal and Square Wave Excitation

In order to quantitatively compare the results obtained from sinusoidal and square wave heating shape, the behaviour of two parameters was monitored: the standard deviation of a sound area (in some ways representative of the noise) and the contrast of the phase signal between defect and sound areas (representative of the usually assessed parameter in NDE).

Figure 32.2 shows the area used for quantitative analysis. In particular, notation S is used for the sound area and d for the area with a defect (in this case, defect number 2). In detail, the phase contrast can be defined as:

$$\Delta\varphi = mean(\varphi_d) - mean(\varphi_S) \tag{32.5}$$

where $mean(\varphi)$ represents the average value of the phase signal assessed on d and S areas.

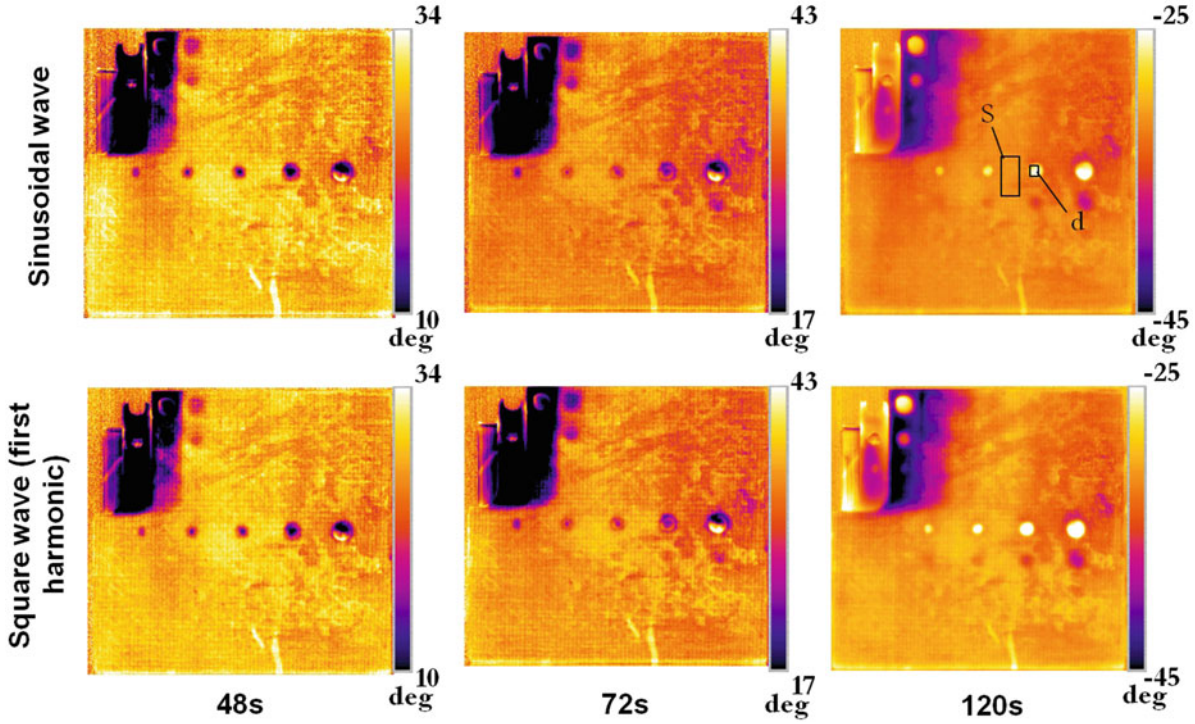

Fig. 32.2 Comparison between phase maps obtained with sinusoidal wave and the first harmonic of the square wave (modulation periods = 48 s, 72 s, 120 s)

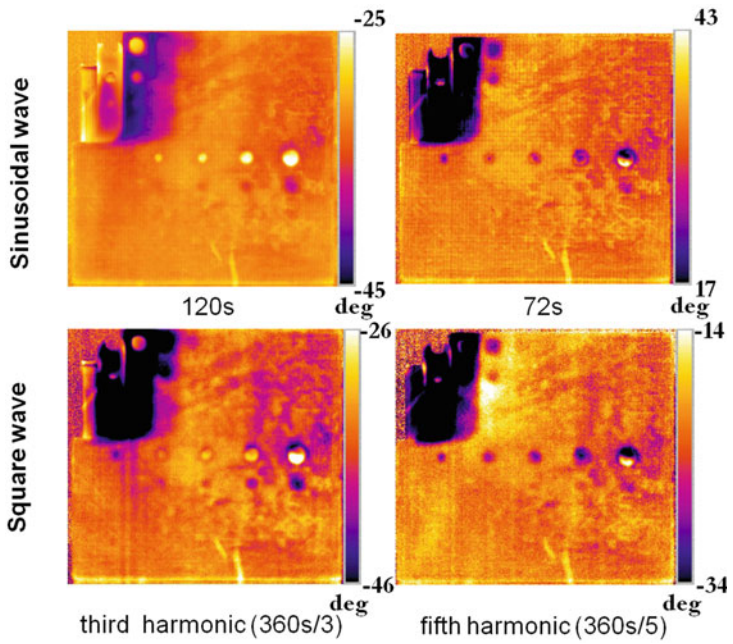

Fig. 32.3 Comparison between phase maps obtained with sinusoidal wave and the third and fifth harmonic of the square wave

In Fig. 32.4, the values of the standard deviation of the *S* area are shown as a function of the modulation period for a number of cycles set at 3. In particular, on the same graph, the results obtained are reported with the sinusoidal excitation shape and the square excitation shape in terms of first, third and fifth harmonic. The following is clear:

- Data obtained from the first harmonic of square wave are in excellent agreement with that of the sinusoidal, for each value of the modulation period,
- In the range between 48 s and 120 s, where there is the overlap of all data, the difference between the results obtained from the third and fifth harmonic (square wave) and the sinusoidal data is less than 1 deg. Yet, there is an evident trend of slight increase in noise with the order of the harmonic,

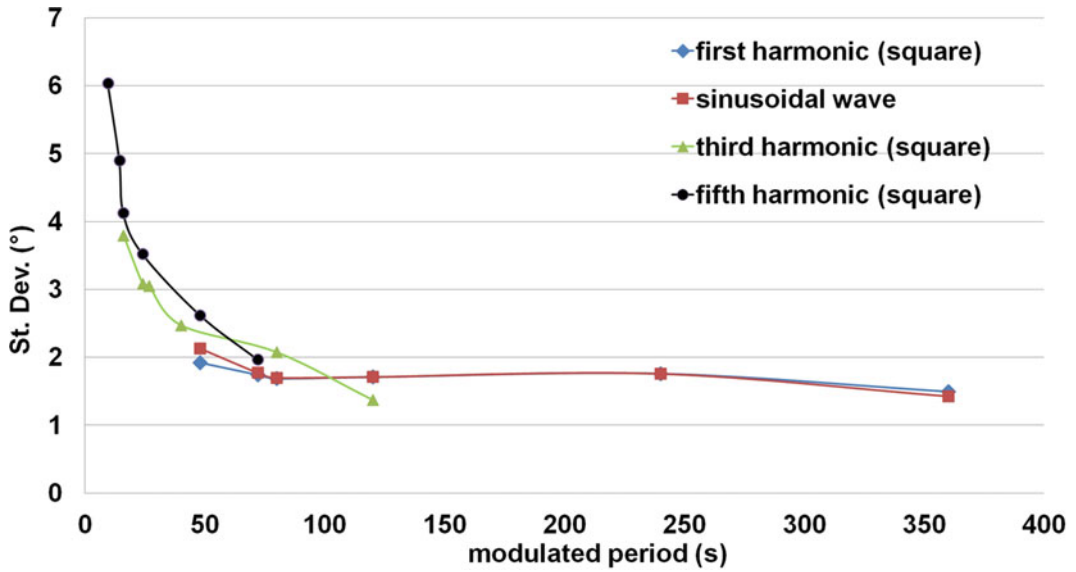

Fig. 32.4 Standard deviation vs. modulation period: comparison between sinusoidal and square wave in a sound area. SD increase for low periods for a higher influence of the surface morphology, and a higher level of noise and increase also with the considered harmonic of the square wave analyzed

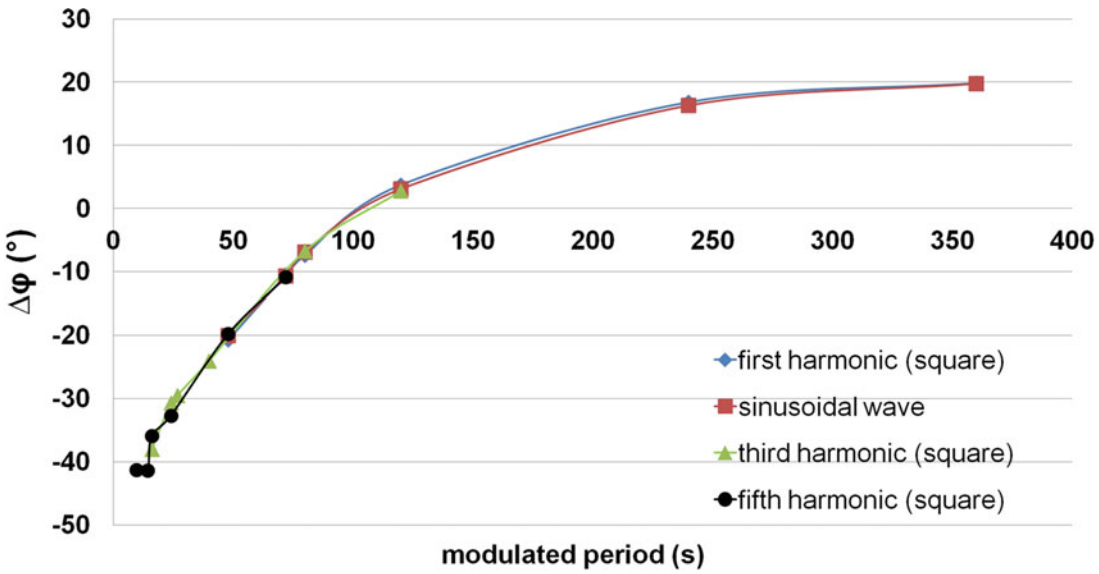

Fig. 32.5 Phase contrast vs. modulation period: comparison between sinusoidal and square wave. Signal varies with period but there is no significant difference between sinusoidal and square wave harmonics lock-in

- Standard deviation increases significantly for lower values of the period. This is due to the increasing influence on the phase signal of the morphology of the surface and of the first ply fiber distribution.

The Standard deviation trend is, in fact, due to two simultaneous effects. As illustrated in Sect. 32.2, if the modulation period increases, thermal waves propagate deeper into the material so, the thermal response of material is less influenced by the superficial phase signal variation due to a non perfect uniformity of surface of the specimen. These non-uniformities can be due to the intrinsic properties of the material or result from poor surface preparation (for example non uniform emissivity or small reflection on the surface of specimen). Moreover, the thermal signal increases as the modulation period increases and then a better signal to noise ratio is obtained for the higher modulation periods.

In Fig. 32.5, the trend of the phase contrast is reported for the varying shape of the imposed thermal waves for a cycle number set on 3. Also in this case, the results obtained with square wave are in excellent agreement with those obtained

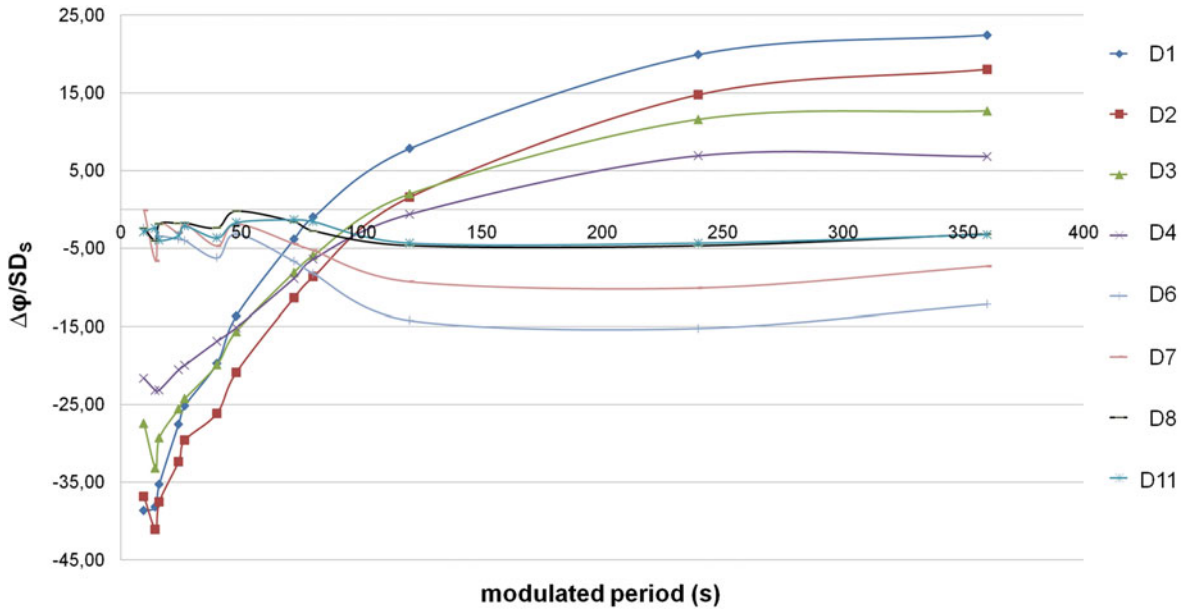

Fig. 32.6 Phase signal normalized with respect to standard deviation (SD) of the sound area vs. modulated period

with sinusoidal wave, for each value of the modulation period. It is interesting to note the superior consistency of the higher order harmonics analysis with first harmonic/sinusoidal (that are basically coincident). Data appear to be in an excellent agreement.

32.4.3 Analysis of the Influence of the Dimensions and Depth of the Defect on the Phase Signal Variation

Generally, for LT technique the quantitative analysis requires the evaluation of threshold values [1, 11] (threshold value criterion) in order to obtain binary data able to discern the detectable from the undetectable defect. These methods don't take into account the influence on the phase signal of the dimensions and position (in terms of depth inner the component) of defects. This assumption can lead to significative errors in the quantitative evaluation of defects.

As example, in Fig. 32.6 are reported the values of the phase contrast for eight defects as function of the modulated periods. In particular, it was reported the value of the phase contrast normalized with respect to the standard deviation (SD) of the sound area. This ratio provides a more significant parameter for evaluating the ability of the detection of the technique since it take into account the noise of the signal.

Figure 32.6 shows as different phase signals are obtained for defects placed at the same depth but with different dimensions (diameter). All defects reach the maximum value of the signal to noise ratio for negative values of the phase contrast. These values are plotted in Fig. 32.7 as function of defect diameter and defect depth. In this figure it is very clear as the phase signal is influenced by the dimensions and depth of defects.

32.5 Conclusions

In this work, new procedures are proposed for analyzing thermal data obtained by the lock-in thermography technique.

Different tests were carried out on a GFRP sample specimen with imposed defects. In particular, the effect on the quality of phase signal produced by the adopted heat source excitation shape and the number of cycles of excitation were evaluated.

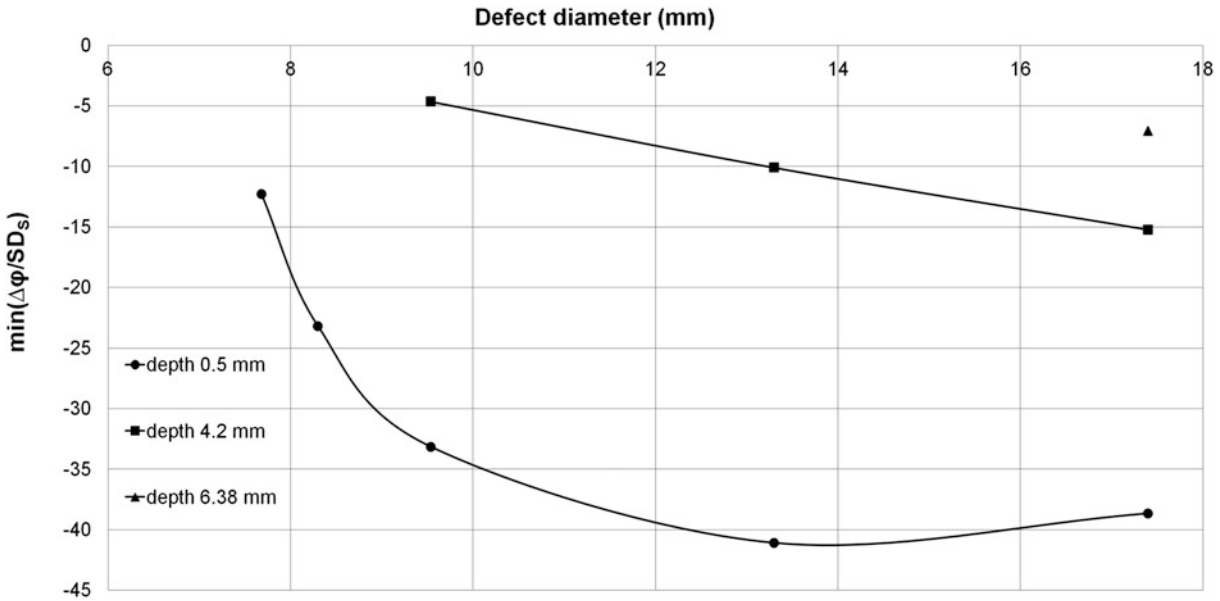

Fig. 32.7 Phase signal normalized with respect to standard deviation (SD) of the sound area vs. diameter and depth of the defect

The results can be summarized as follows:

- Shape of the heat source: the use of square waves provides basically the same results of sinusoidal excitation. Moreover, square waves allow a multi-frequency analysis to obtain information about higher order harmonics, providing in one test results usually obtained testing the specimen with sinusoidal shape three times.
- Number of cycles: The noise of phase signal slightly decreases if the number of modulated cycles increases. More than three cycles do not give significant variation for sinusoidal or first harmonic analysis but can influence the higher harmonics analysis. Shortening the testing time at two cycles gives good results, provided to take into account the thermal transient.
- The phase signal is influenced by the dimension and the depth of the defect. This analysis shows as for the quantitative evaluation of defects in a component, a sample specimen with imposed known defects and made of the same material of the component is necessary in order to calibrate the phase signal values as function of the dimension and the position of defects.

References

1. Palumbo, D., Ancona, F., Galietti, U.: Quantitative damage evaluation of composite materials with microwave thermographic technique: Feasibility and new data analysis. Meccanica **50**, 443–460 (2015)
2. Nikishkov, Y., Airoldi, L., Makeev, A.: Measurement of voids in composites by X-ray computed tomography. Compos. Sci. Technol. **89**, 89–97 (2013)
3. Hosur, M.V., Murthy, C.R.L., Ramamurthy, T.S., Shet, A.: Estimation of impact-induced damage in CFRP laminates through ultrasonic imaging. NDT&E Int. **31**(5), 359–374 (1998)
4. De Angelis, G., Meo, M., Almond, D.P., Pickering, S.G., Angioni, S.L.: A new technique to detect defect size and depth in composite structures using digital shearography and unconstrained optimization. NDT&E Int. **45**, 91–96 (2012)
5. Pérez, M.A., Gil, L., Oller, S.: Impact damage identification in composite laminates using vibration testing. Compos. Struct. **108**, 267–276 (2014)
6. Angelidis, N., Irving, P.E.: Detection of impact damage in CFRP laminates by means of electrical potential techniques. Compos. Sci. Technol. **67**, 594–604 (2007)
7. Maldague, X.P.V.: Theory and practice of infrared technology of non-destructive testing. Wiley, New York (2001). ISBN 0-471-18190-0
8. Meola, C., Carlomagno, G.M., Squillace, A., Giorleo, G.: Non-destructive control of industrial materials by means of lock-in thermography. Meas. Sci. Technol. **10**, 1583–1590 (2002)
9. Usamentiaga, R., Venegas, P., Guerediaga, J., Vega, L., Lòpez, I.: Feature extraction and analysis for automatic characterization of impact damage in carbon fiber composites using active thermography. NDT&E Int. **54**, 123–132 (2013)

10. Ibarra-Castanedo, C.: Quantitative subsurface defect evaluation by pulsed phase thermography: Depth retrieval with the phase. Ph.D. thesis, Université Laval (2005)
11. Palumbo, D., Tamborrino, R., Galietti, U., Aversa, P., Tati, A., Luprano, V.A.M.: Ultrasonic analysis and lock-in thermography for debonding evaluation of composite adhesive joints. NDT&E Int. **78**, 1–9 (2015)
12. Garnier, C., Pastor, M.L., Eyma, F., Lorrain, B.: The detection of aeronautical defects in situ on composite structures using non destructive testing. Compos. Struct. **93**, 1328–1336 (2011)
13. Tashan, R., Al-mahaidi, R.: Investigation of the parameters that influence the accuracy of bond defect detection in CFRP bonded specimens using IR thermography. Compos. Struct. **94**, 519–531 (2012)
14. Taillade, F., Quiertant, M., Benzarti, K., Aubagnac, C.: Shearography and pulsed stimulated infrared thermography applied to a nondestructive evaluation of FRP strengthening systems bonded on concrete structures. Construct. Build Mater. **25**, 568–574 (2011)
15. Omar, M., Hassan, M., Donohue, K., Saito, K., Alloo, R.: Infrared thermography for inspecting the adhesion integrity of plastic welded joints. NDT&E Int. **39**, 1–7 (2006)
16. Galietti, U., Dimitri, R., Palumbo, D., Rubino, P.: Thermal analysis and mechanical characterization of GFRP joints. In: 15th European Conference on Composite Materials: Composites at Venice, ECCM 2012, Venice, 24–28 June 2012
17. Genest, M., Martinez, M., Mrad, N., Renaud, G., Fahr, A.: Pulsed thermography for non-destructive evaluation and damage growth monitoring of bonded repairs. Compos. Struct. **88**, 112–119 (2009)
18. Krstulovic-Opara, L., Klarin, B., Neves, P., Domazet, Z.: Thermal imaging and thermoelastic stress analysis of impact damage of composite materials. Eng. Fail. Anal. **18**, 713–719 (2011)
19. Galietti, U., Palumbo, D., Calia, G., Pellegrini, M.: Non destructive evaluation of composite materials with new thermal methods. In: 15th European Conference on Composite Materials: Composites at Venice, ECCM 2012, Venice, 24–28 June 2012
20. Meola, C., Carlomagno, G.M.: Impact damage in GFRP: New insights with infrared thermography. Composites Part A **41**, 1839–1847 (2010)
21. Mulaveesala, R., Tuli, S.: Theory of frequency modulated thermal wave imaging for non destructive subsurface defect detection. Appl. Phys. Lett. **89**, 191913 (2006)
22. Pitarresi, G.: Lock-in signal post-processing techniques in infra-red thermography for materials structural evaluation. Exp. Mech. **55**(4), 667–680 (2015)
23. Pitarresi, G.: Thermal NDE of thick GRP panels by means of a Pulse modulated lock-in thermography technique. In: 14th International Conference on Experimental Mechanics, ICEM 2014, vol 6, Poitiers, 4–9 July 2010
24. Diagnostic Engineering Solutions.: IRTA Manual (DES srl) (2015)

Chapter 33
Characterising the Infrared Signature of Damaged Composites for Test Control

J.E. Thatcher, D.A. Crump, P.B.S. Bailey, and J.M. Dulieu-Barton

Abstract It has been shown that as damage grows within a composite material, there is a local temperature increase that can be measured with an infrared (IR) detector. The possibility of controlling the rate of damage evolution during a test using infrared thermography (IRT) is investigated. Unlike the point or local monitoring achieved by strain gauges, IRT is a full-field technique which can be used to monitor the whole test specimen. To control damage evolution rate, the IR response (i.e. temperature change) associated with material damage must be defined and measured, before a control methodology can be developed. The results of a series of tests conducted to establish the relationship between the recorded temperature change and damage condition in composite materials is described. Two types of glass reinforced epoxy specimens are studied with layup $(0, 90)_{3S}$ and $(\pm 45)_{3S}$ under fatigue loading.

Keywords Composite • Fatigue • Infrared • Thermography • Control

33.1 Introduction

During mechanical testing of composite materials and structures there is a recognised need to control the damage rate and to establish more effectively when the material has failed. As damage evolves, the strain increases for a given load, or in displacement control the stress decreases. A more appropriate form of test machine control could be termed 'damage evolution control' where the loading or displacement is adjusted to give a constant damage growth rate. This type of approach is well established for crack propagation in metals, using controlled level and variation in crack tip stress intensity [1]. It is well-known [2] that as damage occurs in a composite material, there is a local temperature increase in the area of the damage growth. It is proposed that the temperature increase, detected with an infrared (IR) camera, could be used for test machine damage evolution control.

Unlike the point or local monitoring achieved by strain gauges, infrared thermography (IRT) is a full-field technique which can be used to record temperature measurements over the entire specimen surface. The material damage type and the corresponding temperature evolution must be identified, characterised and quantified, before a control methodology can be developed. The specimen temperature evolution during damage is sufficient to be detected using IRT, however to identify the damage type further information is required. Therefore, during these initial studies a technique known as thermoelastic stress analysis (TSA) [3] is applied to provide more data. The thermoelastic response is proportional to stresses and enables the stress redistribution due to damage to be visualised and quantified. When capturing IR images during a fatigue test, it is also possible to process the images and apply TSA. The surface temperature captured in the IR images can then be directly compared with the damage type identified by the TSA images, to provide the specimen temperature change at which a certain damage type occurs.

Two types of glass reinforced epoxy specimen were used. A layup of $(0, 90)_{3S}$ was prepared, from which on-axis specimens were used, generating progressive defects through the fatigue cycle, i.e. matrix cracking, longitudinal splitting, delamination and finally fibre breakage. The second type of specimens were cut at 45° to the fibre directions, in order to generate internal damage. The specimens were fatigue tested to failure under a sinusoidal, load-controlled waveform, at a load ratio of $R = 0.1$, during which the temperature was mapped and recorded. The paper presents results from the two specimen types and the relationship between the damage type (from the TSA) and temperature changes measured during damage evolution is discussed.

J.E. Thatcher (✉) • D.A. Crump • J.M. Dulieu-Barton
University of Southampton, University Road, Highfield, Southampton SO17 1BJ, UK
e-mail: jet1e13@soton.ac.uk

P.B.S. Bailey
Instron Dynamic Systems, Instron Division of ITW Ltd., Buckinghamshire, UK

W.C. Ralph et al. (eds.), *Mechanics of Composite and Multi-functional Materials, Volume 7*,
Conference Proceedings of the Society for Experimental Mechanics Series, DOI 10.1007/978-3-319-41766-0_33

33.2 Methodology

Previous studies have shown that IRT can be used with a (±45) fibre lay-up, to detect matrix disbonding and delamination's during fatigue tests [4], and matrix cracking is the dominant failure mechanism [3]. Visible surface damage evolution can be created by using a lay-up of (0, 90). It has been shown [5] that axial cracks and delamination's form during tensile testing, that the specimen fractures orthogonal to the tension axis with 0° fibre failures [4] and that there is axial cracking of the matrix, with internal matrix cracking and delamination [3]. To localise the damage in the specimen it was necessary to introduce a stress concentration in the form of a central circular hole. Even though, IRT is a full field technique, to improve the resolution of the damage growth it was decided to focus on a smaller area local to the hole. It has been shown that an open hole concentrates the damage and its evolution within a localised area [5, 6]. The test specimens were 250 mm in length. The width of the specimen was determined based upon the British standard BS ISO 12817 [7] and BS ISO 14603 [8] for open hole compression of fibre-reinforced plastic composites and open hole tension of continuous fibre ceramic matrix. Both standards suggest a specimen width to hole diameter ratio of 6. It is also suggested a hole diameter of 6 mm is used giving a specimen width of 36 mm. Therefore the specimens were manufactured using E-glass fibre (1062) pre-impregnated with a MTM28-1 resin system material with an autoclave consolidation to the dimensions shown in Fig. 33.1.

Specimen thickness was an important consideration as the detection of internal damage using IRT becomes more challenging with increasing thickness. It was decided that a 12 ply stacking sequence would be used, giving an approximate thickness of 1.8 mm. This was based on [3] where IRT was used successfully on laminates of E-glass epoxy with 13 plies. Laminates of $(0, 90)_{3S}$ were manufactured and the $(\pm 45)_{3S}$ laminate was cut at 45° to the principal material axis. The front surface of all test specimens was sprayed with matt black paint to provide a uniform emissivity for the IRT.

The (±45) specimen was cyclically loaded, in load control, using a 5 Hz sinusoidal waveform. A maximum load of 6.1 kN (R = 0.1), was applied. A FLIR SC5500 series photon detector was used to record the IR images for 1000 frames at 383 Hz, every 100 cycles until 1200 cycles and then every 50 cycles. The (0, 90) specimen was loaded at the same frequency and R ratio, to a maximum load of 10.45 kN. Images were recorded every 1000 cycles until just before failure, when images were recorded after an audible ping.

33.3 Results

The TSA data was processed as follows to eliminate the effect of the surface temperature increase:

$$\frac{\Delta T}{T} = -K(\sigma_1 + \sigma_2) \tag{33.1}$$

where ΔT is the change in temperature, K is the thermoelastic constant, T is the absolute temperature of the specimen, and σ_1, σ_2, are the changes in the principal stresses.

Figure 33.2 shows the temperature evolution of (±45) specimen. Deformation of the hole during the test can be clearly seen, along with deformation along the edge due to the shear coupling. The entire specimen shows an increase in temperature as well as the damaged areas. In the $\Delta T/T$ images, the damage evolution is evident. A crack is growing from the hole signified by the stress concentration, as well as delamination, signified by the triangular area shown in images. Fig. 33.3a is a photograph of the failed specimen, showing the kink on the right side of the hole, which corresponds well to the damaged regions in the $\Delta T/T$ image. The edge deformation is also clear in the image.

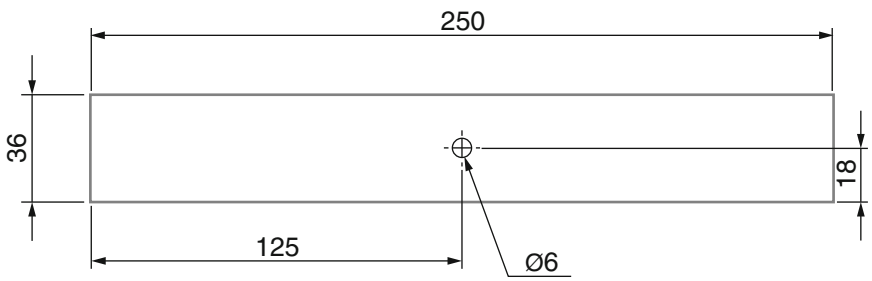

Fig. 33.1 Dimensioned drawing of the composite open hole specimen

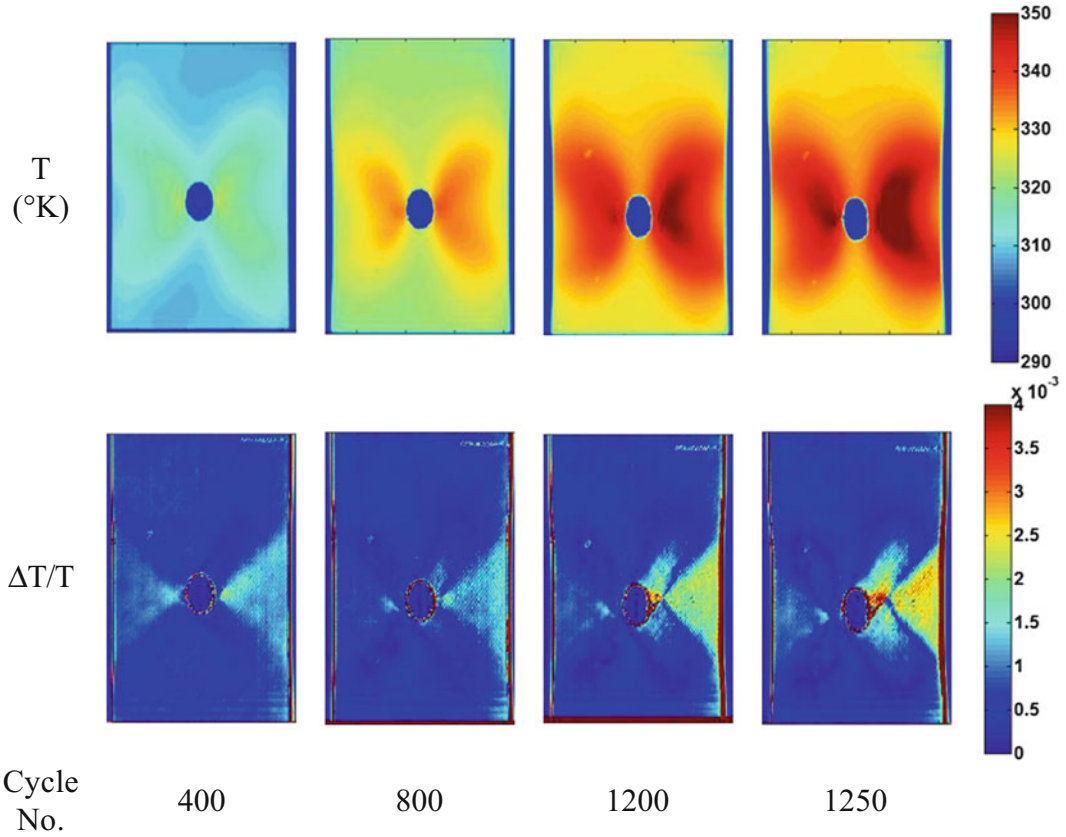

Fig. 33.2 (±45) Specimen temperature evolution

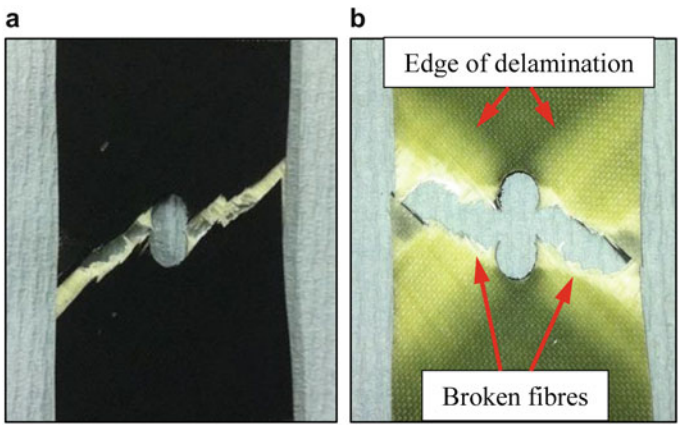

Fig. 33.3 (±45) Specimen failure image after 1291 cycles. (**a**) Front face, (**b**) back face

The temperature evolution from the (0, 90) specimen is shown in Fig. 33.4. In the early parts of the test the temperature did not change, so the data recorded, before 91,000 cycles is not presented. Instead the audible pings from the localised failure of the material were used to select the data. When the "before and after" pings (100 cycles between recordings) temperature data was compared there appeared to be little to no change, in contrast in the $\Delta T/T$ images the damage evolution could be clearly observed. The last two image sets in Fig. 33.4 shows the damage evolution just before failure. The IR image clearly shows an increase in temperature at the damage site. What is more revealing is the $\Delta T/T$ date which clearly shows how the stress is redistributed as a result of the damage progression. Local to the hole all load carrying capacity is lost as the delamination progresses away from the hole. The remaining intact material has to carry the load and this is signified by the

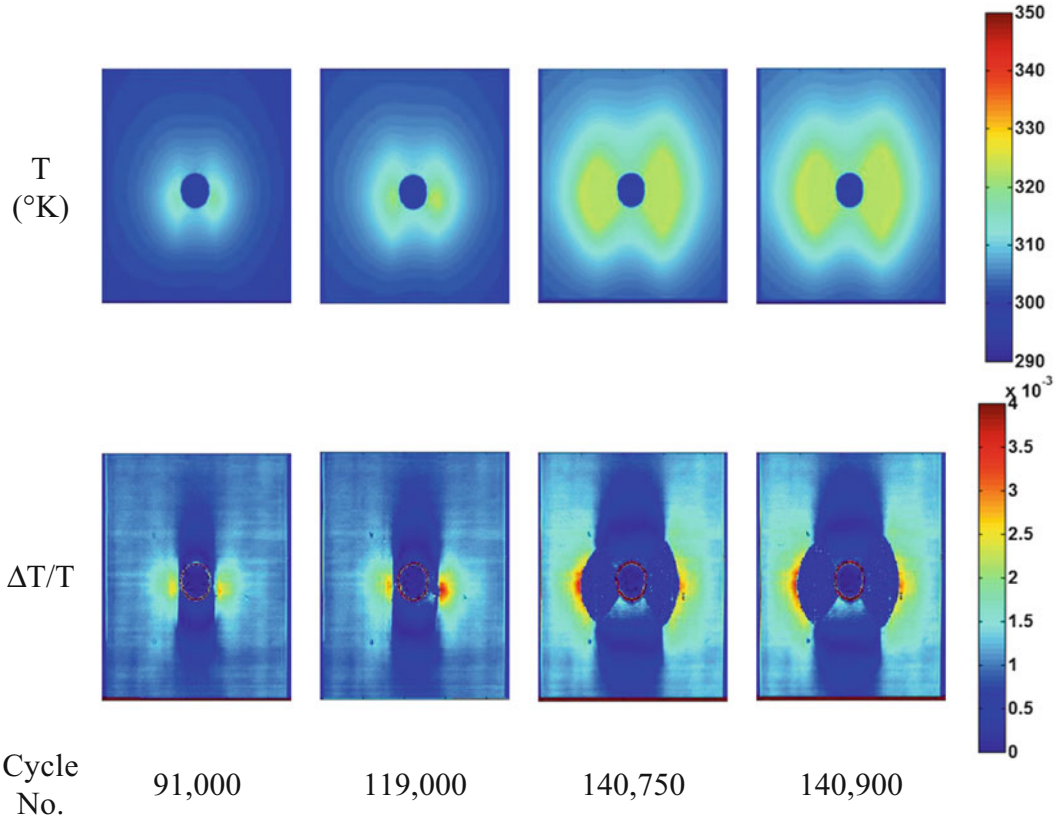

Fig. 33.4 (0, 90) Specimen temperature evolution

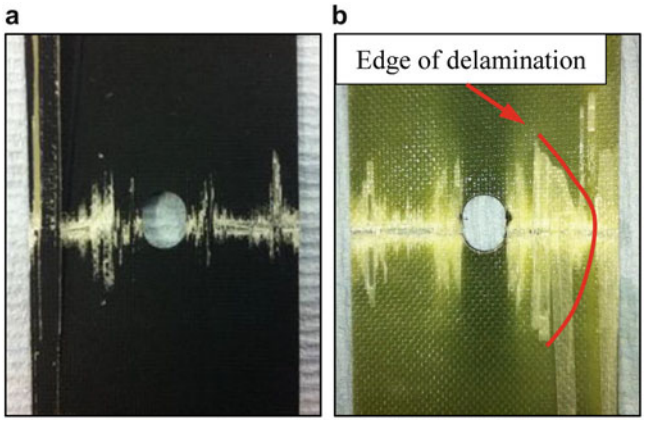

Fig. 33.5 Photo of the failed (0, 90) specimen, after 140,922 cycles. (**a**) Front face, (**b**) back face

increased response at the edge of the delamination. Figure 33.5 shows photographs of the front and back of the specimen at the end of the tests. Full failure occurred after 140,922 cycles. Here the TSA has revealed areas of sub surface damage that are not visible in the photographs. In Fig. 33.5b, the curvature of the delaminated area can be seen on the right hand side of the hole, corresponding with surface damage on the front of the specimen.

33.4 Discussion and Future Work

It has been demonstrated the surface temperature changes obtained from an IR detector can monitor damage evolution in a composite material. It is clear from this work that identifying, characterising and quantifying the damage and its severity using the surface temperature change is a difficult if not impossible proposition. The difference in the temperature changes between the (± 45) specimen and the (0, 90) specimen is as expected as the shearing causes a greater increase in temperature. The temperature difference between delamination, matrix cracking and fibre breakage as seen in the (0, 90) specimen is not detectable. Only by applying the TSA is the actual damage state revealed. Therefore it is necessary to link this with the surface temperature data, which will be the object of further investigations.

References

1. British Standards: Metallic materials—Fatigue testing—Fatigue crack growth method. BS ISO 12108. British Standards Institution, London (2012)
2. Naderi, M., Kahirdeh, A., Khonsari, M.M.: Dissipated thermal energy and damage evolution of glass/epoxy using infrared thermography and acoustic emission. Composites Part B **43**, 1613–1620 (2012)
3. Emery, T.R., Dulieu-Barton, J.M.: Thermoelastic stress analysis of damage mechanisms in composite materials. Composites Part A **41**, 1729–1742 (2010)
4. Goidescu, C.: Damage investigation in CFRP composites using full-field measurement techniques: Combination of digital image stereo-correlation, infrared thermography and X-ray tomography. Composites Part B **48**, 95–105 (2013)
5. O'Higgins, R.M., McCarthy, M.A., McCarthy, C.T.: Comparison of open hole tension characteristics of high strength glass and carbon fibre-reinforced composite materials. Compos. Sci. Technol. **68**, 2770–2778 (2008)
6. Toubal, L., Karama, M., Lorrain, B.: Damage evolution and infrared thermography in woven composite laminates under fatigue loading. Int. J. Fatigue **28**, 1867–1872 (2006)
7. British Standards: Fibre-reinforced plastic composites—Determination of open-hole compression strength. BS ISO 12817:2013. British Standards Institution, London (2013)
8. British Standards: Fine ceramics (advanced ceramics, advanced technical ceramics)—Test method for open-hole tension of continuous fibre-reinforced ceramic matrix composites at room temperature. BS ISO 14603:2012. British Standards Institution, London (2012)

Chapter 34
Thermoelastic Stress Analysis and Digital Image Correlation to Assess Composites

J.M. Dulieu-Barton and G.P. Battams

Abstract A novel methodology for the synchronised capture of white light images for digital image correlation (DIC) and infrared images for thermoelastic stress analysis (TSA) is described. The methodology enables simultaneous data capture without the requirement to pause the cyclic load necessary for the TSA to collect the DIC data. The methodology is demonstrated on cross-ply carbon-epoxy and glass-epoxy specimens that have with and without prior damage and the results from each compared. Various damage types are identified as the damage progresses.

Keywords Damage • Composites • Thermoelastic stress analysis • Digital image correlation

34.1 Introduction

An experimental methodology that combines the DIC (digital image correlation) [1] and TSA (thermoelastic stress analysis) [2] techniques for the identification of damage propagation in fibre-reinforced polymer (FRP) material under cyclic loading is developed. The use of the two techniques allows the collection of surface strain and stress sum data, with the possibility of defining a new damage parameter. Unlike point measurement methods, full-field techniques allow damage to be identified across an entire surface without prior knowledge of the material behaviour.

TSA usually requires the application of a cyclic load. The CEDIP Silver 480M camera used for the TSA in the present paper is capable of imaging full-frame (320 $\times$ 128 pixels) at a frequency of 383 Hz, more than sufficient for sampling at this loading frequency. Capturing white-light images with a high resolution low-frame rate camera during fatigue loading is more challenging. The use of high speed white-light cameras to collect a series of images throughout a loading cycle was considered but the spatial resolution of images and hence the quality of DIC data would be lower. Since high spatial resolution cameras generally have a low frame rate, accurate image timing is necessary to capture images at exactly the peak load in a cycle. A further benefit of using a methodology based around low-frame rate CCD cameras rather than high speed cameras is the decreased cost, allowing the methodology developed to be more accessible to future users. A camera triggering and data collection system has been developed [3] in LabView 9.0 around a National Instruments USB-6211 data acquisition input/output device. This system allows the automatic and repeated capture of IR and white-light image data sets on specific intervals in a fatigue cycle.

34.2 Experimental Investigation

All test specimens were of a symmetrical crossply lay-up with an outer 90° lamina, minimising any complicating effects from elastic coupling and promoting early surface damage in the form of transverse cracking. The damage behaviour of crossply material has been extensively documented, helping to simplify the interpretation of optical measurements. Four layers of Gurit SE84LV unidirectional carbon epoxy pre-preg material were used to give a $[90,0]_S$ lay-up and a panel thickness of 1.13 mm. Specimens were produced from the panels of 20 mm nominal width and 100 mm nominal gauge

J.M. Dulieu-Barton (✉)
Faculty of Engineering and the Environment, University of Southampton, Highfield SO17 1BJ, UK

Department of Mechanical and Manufacturing Engineering, Aalborg University, 9220 Aalborg, Denmark
e-mail: janice@soton.ac.uk

G.P. Battams
Faculty of Engineering and the Environment, University of Southampton, Highfield SO17 1BJ, UK

W.C. Ralph et al. (eds.), *Mechanics of Composite and Multi-functional Materials, Volume 7*,
Conference Proceedings of the Society for Experimental Mechanics Series, DOI 10.1007/978-3-319-41766-0_34

Table 34.1 Test summary for previously undamaged CFRP specimens

Specimen	Mean stress	Cyclic stress amplitude	Frequency	Loading cycles	Data collection intervals	
					<10,000 cycles	>10,000 cycles
$[90,0]_S$ CFRP	300 MPa	270 MPa	5 Hz	250,000	Every 500 cycles	Every 5000 cycles

Table 34.2 Camera settings for tests conducted on undamaged CFRP specimens

Camera	Image size (pixels)	Imaging area on specimen (mm)	Spatial resolution (mm/pixel)	Imaging frequency (Hz)	Images captured	Exposure/integration time (μs)
2 × AVT Manta G-504B	2452 × 2056	19.96 × 28.92	0.014	N/A	1 at min load 1 at max load	900
1 × CEDIP Silver 480M	320 × 256	19.96 × 67.23	0.261	383	600	1300

length. Specimens were coated in two passes of RS matt black paint followed by a light coat of Ambersil matt white paint to create a speckle pattern suitable for DIC analysis. A specimen prepared in a similar manner and examined under an optical microscope was found to have a paint coating thickness varying between 15 and 40 μm. The large variation of paint thickness is due to the high surface roughness of the material; an artefact of the peel-ply fabric required during manufacture. No difference in IR (infra-red) response could be noted as a result of the speckle pattern.

CFRP specimens were cyclically loaded under tension-tension loading in an Instron 8802 servo-hydraulic test machine operating in load control, further details are given in Table 34.1. The specimens were undamaged prior to application of cyclic load. Surface damage was expected to occur rapidly during the initial stages of fatigue life; hence data collection intervals were shorter during the initial 10,000 cycles. The Silver 480M IR camera was positioned nominally perpendicular to the specimen surface whilst being flanked by a set of two Manta G-504B 5 MPixel white-light cameras manufactured by Allied Vision Technologies. An overview of the Manta camera specifications is presented in Table 34.1.

A summary of camera settings is used for the TSA and DIC is presented in Table 34.2.

Prior to each test, two sets of white light images were taken of the specimen at zero load to provide reference images for DIC analysis. A piece of aluminium foil was also attached to the centre of the specimen and IR and white-light images taken, allowing the two datasets to be aligned during post processing. The foil was then removed prior to the test. White-light images were processed in DaVis 8.1 using a cell size of 31 × 31 pixels, a step size of 6 pixels and a sixth order spline subpixel interpolation method. IR videos were motion compensated and TSA processed using Altair LI 5.90. A Matlab code was developed to enable DIC and TSA data to be overlaid. The code uses the DIC vertical and horizontal displacement vectors to shift the DIC strain data to their correct spatial location for each image. Using the foil markers as a point of reference, the IR data is spatially interpolated to match the DIC data points, so allowing TSA and DIC data to be overlaid. Maps of longitudinal (ε_{yy}), horizontal (ε_{xx}) and shear strain (ε_{xy}) were calculated using DIC. Maps of thermoelastic temperature change (ΔT), mean temperature (T_0) and phase were also obtained. ΔT data was divided by the mean temperature T_0 at each pixel location to give a normalised thermoelastic response ($\Delta T/T_0$). Selected data sets from all data types are presented in Fig. 34.1. Despite the first data set being collected after just 10 loading cycles, significant damage has already occurred to the surface 90° layer. Multiple horizontal lines of high strain, evident in the longitudinal strain map, were found to match spatially with horizontal lines of reduced thermoelastic response. Such behaviour is expected as DIC records the crack opening displacement as an increase in longitudinal strain whilst TSA measures a decreased thermoelastic response as the cracked surface layer has a reduced load-bearing capability. Most cracks were found to form across the entire specimen width within the 500 loading cycles between data collection intervals. Transverse crack saturation is reached at around 8000 cycles. After which, a region of low thermoelastic response can be noted to form at the bottom of the data map at the right specimen edge. Between 8000 and 19,500 cycles a similar behaviour can be noted at the left specimen edge. The TSA phase and DIC shear strain (ε_{xy}) maps were studied for further information on this behaviour. Under adiabatic conditions the phase map displays either 0° or 180°, indicating areas of compression or tension. Non-adiabatic conditions, such as at locations of damage cause a shift in the phase angle of the thermoelastic response relative to the applied loading. In FRP specimens, frictional heating between damaged layers or crack surfaces takes a finite time to conduct to the surface, causing a phase change in the recorded IR signal. Whilst some undamaged patches of material remain at 0° phase at 8000 cycles, the majority of the specimen surface is out of phase, indicating widespread surface damage. From 8000 cycles onwards, a change in the response occurs. Between 8000 and 19,500 cycles an area of negative phase propagates vertically

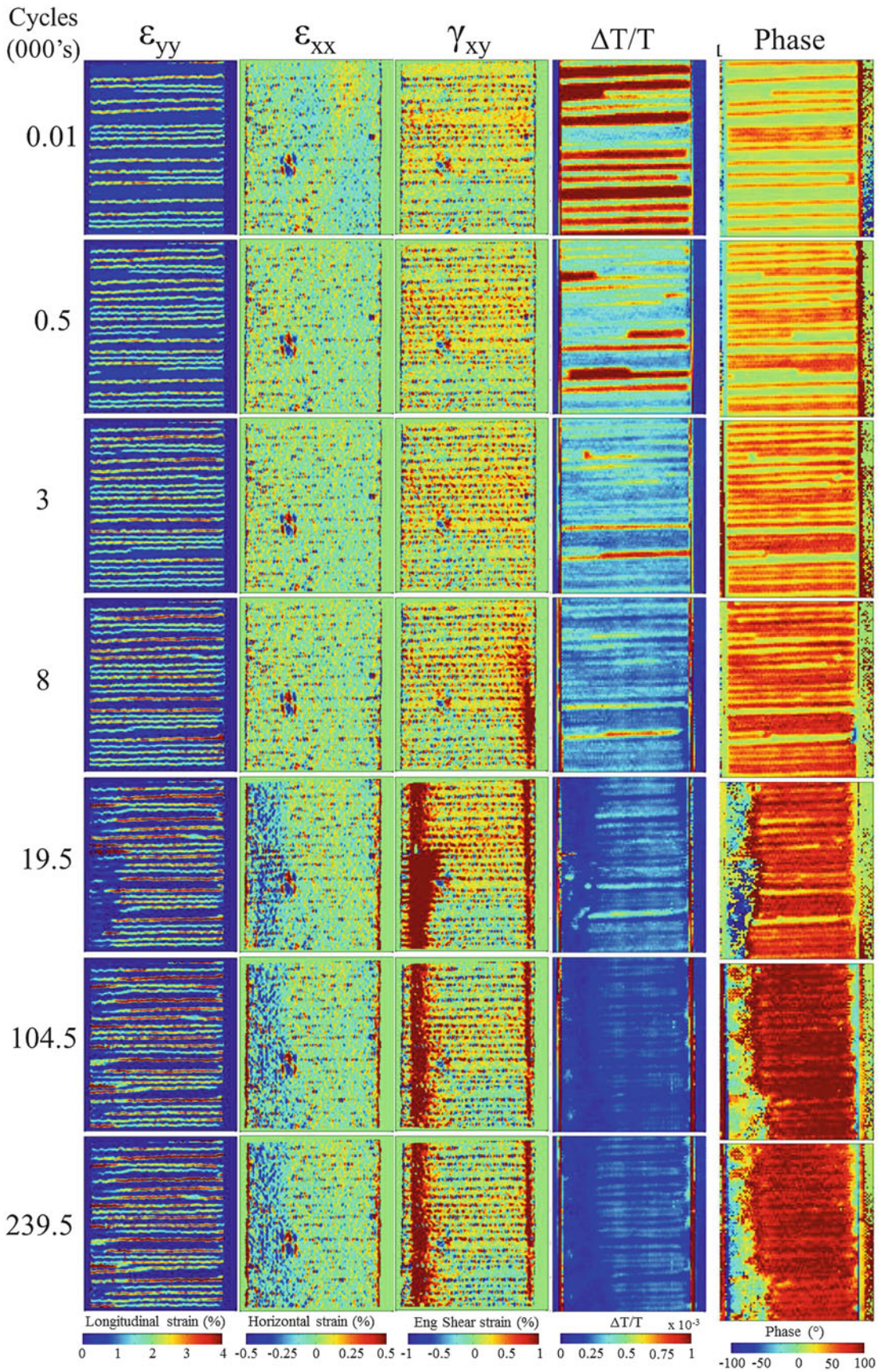

Fig. 34.1 Full-field data collected during the fatigue loading of a crossply CFRP specimen

from the bottom of the image at the left edge of the specimen. The change in response is consistent with delaminations propagating from the free edge of the specimen, which is a dominant failure mode in cross ply laminates caused by the free edge effect. CT scanning was conducted on the specimen, which validated the damage modes identified.

34.3 Summary and Conclusions

A methodology for the semi-automated collection of white-light and IR images for the study of FRP specimens during un-interrupted fatigue tests has been developed. The approach uses simple electronics, intense LED lighting and a LabView based methodology to achieve accurate camera timing, so allowing the use of low frequency, high resolution white light cameras during cyclic loading. The use of high resolution cameras has subsequently given high spatial resolution strain maps, allowing the imaging of small scale damage in CFRP specimens.

The use of a combined TSA and DIC methodology has allowed various damage types to be identified in the two types of specimen tested, including surface and subsurface damage types. Transverse cracking in CFRP laminates has been clearly identified in longitudinal strain and normalised thermoelastic data, whilst delaminations have been identified in shear strain and TSA phase data.

Acknowledgments The work presented was co-sponsored by the UK Engineering and Physical Sciences Research Council. The financial support received is gratefully acknowledged.

References

1. Sutton, M.A., Orteu, J.-J., Schreier, H.W.: Image correlation for shape, motion and deformation measurements. Springer, New York (2009)
2. Dulieu-Barton, J.M.: Thermoelastic stress analysis. In: Optical methods for solid mechanics, pp. 345–366. Wiley-VCH, Weinheim (2012)
3. Battams, G.: The use of optical techniques to assess the damage tolerance of composite materials. Doctoral thesis, Faculty of Engineering and the Environment, University of Southampton (2014)

Chapter 35
A Study on Mechanical Properties of Raw Sisal Polyester Composites

G.L. Easwara Prasad, B.S. Keerthi Gowda, and R. Velmurugan

Abstract Natural fibers are available in nature as byproducts of agricultural products of various countries around the world. It is observed that coir fibers is product obtained from coconut but jute and sisal fibers are obtained from plants grown in nature. These fibers are very abundantly available in nature can be used for structural construction practices. This increases the economic value of these fibers. In the present study an effort is made to study the mechanical properties of sisal fiber reinforced composite materials. In the present study, randomly oriented sisal fiber reinforced polyester matrix composite specimens of thicknesses 2 mm, 3 mm, 4 mm, 5 mm and 6 mm were fabricated by using hot compression moulding technique. Untreated sisal fibers of length 10 mm is used as reinforcement for casting the composite specimens. A mixture of polyester resin, methyl ethyl ketone peroxide and cobalt naphthenate of ratio 50:1:1 is used as matrix for the fabrication. Each composite panels of fiber volume fraction 10 %, 15 %, 20 %, 25 % and 30 % were tested for its tensile strength and flexural strength as per ASTM D-3039 and ASTM D-7264 respectively. From the experimental results it is observed that tensile strength and flexural strength were increasing up to 20 % fiber volume fraction and further found to be decreasing for fiber volume fractions of 25 % and 30 %. But in case of specimens of 6 mm thickness a small change in the trend of results is observed. The increase in tensile strength is found to be continuous up to 30 % of fiber volume fraction with a tensile strength of 22.938 MPa at 30 % fiber volume fraction.

Keywords Sisal • Mechanical properties • Polyester • Natural fibers

35.1 Introduction

Natural Fiber Reinforced Polymer (FRP) composites are tough and have acceptable specific strength. Natural FRP composites are also biodegradable, light weight, economical and environment friendly. Compared to the synthetic fibers, natural fibers are easily (locally) available, requires very less chemical treatment, lesser expenditure for fabrication setup. Hence in the present study one of natural fibers like sisal is used as reinforcement with polyester resin (general purpose resin). Cobalt naphthenate and methyl ethyl ketone peroxide are used as catalyst and hardener while casting the composites panels.

Earlier researchers have reported broad studies on composites by utilizing natural fibers as reinforcing material among them Ghosh et al. [1] have reported that banana fiber having high specific strength makes a light weight composite material and can be used to make light weight automobile interior parts. Lu et al. [2] have reported that the sisal/phenol formaldehyde composites made by the synthesizing method have shown an increase of 17.61 %, 7.16 % and 12.25 % in impact strength, bending strength and bending modulus respectively as compared to conventional physical blending method. Ali [3] has reported that coconut fibers are ductile and energy absorbent. Zaman et al. [4] have shown that mechanical properties of coir fiber reinforced composites have a strong association with their dynamic characteristics. Sathiyamurthy et al. [5] have reported that Artificial Neural Network (ANN) models can be used effectively for predicting the mechanical properties of inorganic fillers impregnated coir-polyester composites. Gowda et al. [6] have reported that the tensile strength of coir fiber

G.L. Easwara Prasad (✉)
Department of Civil Engineering, MITE-VTU, Moodabidri, Karnataka, India
e-mail: gle.prasad@gmail.com

B.S. Keerthi Gowda
Department of Structural Engineering, VTU, Mysore, Karnataka, India
e-mail: keerthiresearch@yahoo.com

R. Velmurugan
Department of Aerospace Engineering, IIT-Madras, Chennai, Tamil Nadu, India

W.C. Ralph et al. (eds.), *Mechanics of Composite and Multi-functional Materials, Volume 7*,
Conference Proceedings of the Society for Experimental Mechanics Series, DOI 10.1007/978-3-319-41766-0_35

reinforced polyester composite is relatively high when compared to sisal fiber reinforced polyester composites; and that natural fiber reinforced composites can be regarded as a useful light weight engineering material. Easwara Prasad et al. [7] have reported that the feed forward ANN model could be a very good mathematical tool for prediction of properties of coir fiber reinforced epoxy resin composites.

Further, Verma et al. [8] have reported that several natural fiber composites have shown mechanical properties akin to glass fiber composites and are being used in furniture and other related industries. Karthik et al. [9] have studied the surface roughness value of composites using boiled egg shell, rice husk particulate (15 %) and coir fiber (10 %). The study has revealed that higher surface roughness values are recorded when fibers of 10 mm length are used when compared with the values obtained using fiber of 30 mm length. Li et al. [10] have reported in their study that natural fibers can be a potential replacement for an artificial fiber in composite materials. Kuriakose et al. [11] have reported that adhesion at fiber—matrix interface can be improved by sodium hydroxide treatment—mercerization of the fibers. This treatment creates porous surface leading to a rough surface texture which allows coir fibers to reinforce strongly with polyester matrix. Idicula et al. [12] have reported the mechanical performance of short randomly oriented banana and sisal hybrid fiber reinforced polyester composites. With reference to the relative volume fraction of those two fibers, at a constant total fiber loading of 0.40 volume fractions, keeping banana as the skin material and sisal as the core material, the impact strength of the composites were increased with fiber loading. The tensile and flexural properties of respective composite were found to be better at 0.40 volume fraction. Girisha et al. [13] have reported that natural fibers (sisal and coconut coir) reinforced epoxy composites were subjected to water immersion tests in order to study the effects of water absorption on mechanical properties. Natural fibers like coir (short fibers) and sisal fibers (long fibers) were used in hybrid combination and the fiber weight fraction of 20 %, 30 % and 40 % for the fabrication of the composite. Water absorption tests were reported by immersing specimens in a water bath at 25 °C and 100 °C for different time durations. The tensile and flexural properties of water immersed specimens subjected to both aging conditions were evaluated and compared with dry composite specimens. The percentage of moisture uptake was found to increase along with increase in fiber volume fraction due to the high cellulose content of the fiber. The tensile and flexural properties of natural fiber reinforced epoxy composite specimens were found to decrease with increase in percentage moisture uptake. Moisture induced degradation of composite samples was observed at elevated temperature.

Additionally, Sen et al. [14] have depicted that the materials chosen for structural up-gradation must be functionally efficient, qualitatively superior and sustainable. The application of composites in structural facilities is at present mostly concentrated on increasing the strength of the structure with the help of artificial fibers and does not address the issue of sustainability of the raw materials used. Sisal is an abundant source of natural fiber used for making ropes, mats, carpets and as reinforcement with cement. In developing countries, sisal fibers are used as roofing materials in houses. Thomas et al. [15] have studied the mechanical properties of hybrid lingo-cellulosic fiber reinforced natural rubber composites. The objective of their study was to investigate the effect of the ratios of sisal and oil palm fibers on tensile properties of natural rubber composites. The mechanical properties were found to be more dependent on sisal fiber than oil palm. A positive hybrid effect was observed for the tensile properties. The extent of fiber alignment was found to be more when sisal and oil palm was present in equal amounts. Bujang et al. [16] have studied the effect of coir fibers volume on mechanical properties and dynamic characteristic of composite. They reported that the mechanical properties have a strong association with the dynamic characteristic. Both the properties are highly dependent on the volume percentage of fibers. The tensile strength of composite was found to be linearly proportional to the natural frequency. Moreover, the damping ratio was found to be increased by incorporation of coir fibers which giving an advantage to the structure in reducing the high resonant amplitude. Riedel et al. [17] reported that the fibers serve as a reinforcement and show high tensile strength and stiffness, while the matrix holds the fibers together, transmits the shear forces, and also functions as a coating. Further criteria for the choice of suitable reinforcing fibers include elongation at failure; thermal stability; adhesion of the fibers and matrix; dynamic behavior; long-term behavior; and price and processing costs. Sabah et al. [18] depicts that natural fibers, when used as reinforcement, compete with such synthetic fibers as glass fiber. Till date, the most important natural fibers used in composites are Jute, flax, sisal and coir. Natural Fibers are renewable raw materials and they are recyclable. Joshy et al. [19] have reported in their article that untreated randomly oriented isora fiber reinforced polyester composite exhibited an initial decrease in the tensile and flexural properties at 10 % fiber loadings; found to have increased up to 34 % fiber loading and then declination with higher fiber loading. 30 mm long randomly oriented isora fiber recorded as optimum length at which effective stress transfer between fiber and the matrix occurs. Authors Inferred that higher fiber lengths lead to fiber-fiber contact, fiber curling results in shortening of effective fiber length below the critical value but short fiber length leads to notching effect results in considerable stress concentration and generation of micro cracks. In evaluation of flexural properties, authors recorded flexural stress-strain behavior at 40 mm fiber length. Authors observed increase in impact strength with increase in fiber loading and recorded highest impact strength at 48 % fiber volume fraction whose further changes with respect to fiber volume fraction is negligible. As overall, authors concluded that in the present study

mechanical properties of randomly oriented isora fiber reinforced polyester matrix composite exhibits less fiber matrix interaction at the initial level of fiber loading. At its optimum level of fiber loading showed good fiber matrix interaction but after that level authors observed poor dispersion of fibers in the matrix resulted in decrease in the mechanical properties. Chandramohan et al. [20] have showed from their study that natural fibers reinforced composite can be effectively used to manufacture composite for the bone implant, automotive parts, furniture, upholstery, household goods and computer goods. Sumaila et al. [21] have reported the influence of length of banana fibers on its mechanical properties. Authors used 30 % weight randomly oriented nonwoven short banana fiber reinforced epoxy composite of 5 mm thickness for their research. With increase in the fiber length here density and impact strength of composites decreases. Tensile strength, tensile modulus and percent elongation of 15 mm long fiber reinforced composite material recorded the highest value. Here fibers were treated with 5 % NaOH solution before fabrication, and flexural strength and modulus of composite material increased with increase in fiber length up to 25 mm.

Sreekumar et al. [22] investigated the dynamic mechanical properties of sisal fiber reinforced polyester composites fabricated by Resin Transfer Moulding). Investigation proved that at all the temperature range the storage modulus value is maximum for the composite having fibers loading of 40 % volume and also observed that the loss modulus and damping peaks were lowered with increasing fiber content. Silva et al. [23] reported the potential use of long aligned sisal fibers as reinforcement in thin cement based laminates for semi-structural and structural applications. Naidu et al. [24] depicted that the tensile and flexural strength of sisal/glass fiber hybrid component is higher than sisal fiber reinforced composite, but lower than the glass reinforced composite. Ma et al. [25] have reported in their article that when there is increase in the twist level of fibers, the mechanical properties of that natural fiber-reinforced polymeric resin matrix composites decreases. Authors used Sisal fibers yarns as reinforcing material with phenolic resin as matrix to fabricate the composite panels. Gowda et al. [26] have reported in their study that Artificial Neural Network can be effectively used to predict the tensile properties of untreated coir reinforced polyester matrix composites. Gowda et al. [27] have reported in their article that probabilistic approach could be effectively utilized to predict the range of tensile properties of coir reinforced polyester matrix composites. Prasad et al. [28] have reported in their article that Artificial Neural Network is one of the better tools to prognosticate the flexural properties of coir polyester composites.

From the literature, it is observed that more detailed study is necessary in the area of study of mechanical properties of sisal fiber reinforced polymer matrix composites for different thicknesses and respective fiber volume fractions. Hence the present study aims to compute the tensile and flexural strength of sisal fiber reinforced polyester matrix composite for different fiber loadings between 10 % to 30 % and different thickness from 2 mm to 6 mm.

35.2 Materials and Methods

In the present study raw (untreated) sisal fiber is used as reinforcement, polyester resin as matrix, cobalt naphthenate as curing agent and methyl ethyl ketone peroxide as catalyst. Fabrication of specimen is carried out using manual operated, temperature controlled compression molding machine. The knotted fibers are obtained from sisal plants and are cleaned up. These fibers are passed through a Knot Separating Machine to remove the knots and to separate individual fibers. The fibers obtained from knot separating machine are dried in sunlight for a period of 48 h to remove the moisture content. Fibers are cut to a length of 10 mm to be used in randomly oriented fiber mats. In this stage, the spacers are used for casting composite panels of size 300 mm × 300 mm with varying thicknesses (2 mm, 3 mm, 5 mm, and 6 mm). These are placed on the base plate and a thick mylar (a non sticky) sheet is placed in between spacers and base plate for the easy removal of composite specimen after fabrication. Resin, catalyst and hardener are mixed in a proportion of 50:1:1 that is 1000 ml: 20 ml: 20 ml in ratio and stirred well. A 10 mm long sisal fiber of required fiber volume fraction (10 %, 15 %, 20 %, 25 % and 30 %) is weighed and distributed uniformly at the bottom of the mould inside the spacers. Compression load is then applied for 15 min on mould containing the fibers. Resin is then applied uniformly on fibers. Another releasing mylar sheet is spread over as the top surface with a steel plate and then the specimen is compressed for 1 h for uniform distribution of matrix and elimination of entrapped air bubble if any. Here the temperature of both base plates are maintained for 60 °C. The composite is removed from the mould and left for curing at room temperature for 24 h after which the desired composite specimens were cut from the casted composite panels.

The tensile and flexure strength of each specimen in the present study is carried out as per American Society for Testing and Materials (ASTM) standard D-3039 and D-7264 [29, 30] respectively. The specimens subjected to tension test were of size 250 mm × 25 mm. The thickness of test specimens varied from 2 mm to 6 mm. Test specimens were bonded with tabs of 1.5 mm thick and 50 mm length made of emery cloth to serve as grips while testing on both the ends. The tabs distribute gripping stresses and controls failure created by grip jaws. All the tension tests were conducted on a PC controlled Universal

Testing Machine of 5-ton capacity and the results were obtained. As per ASTM D7264 standards the specimens subjected to flexure test the support span-to-depth ratio is 32:1, the standard specimen thickness should be 4 mm and standard width is 13 mm with specimen length being 20 % longer than the support span. It also reveals that if the standard specimen thickness cannot be obtained in a given material system, an alternate specimen thickness shall be used while maintaining the support span-to-thickness ratio and specimen width. Optimal support span-to-thickness ratios of 16:1, 20:1, 40:1, and 60:1 may also be used. So in the present study the each specimens of thickness 2 mm, 3 mm, 4 mm, 5 mm and 6 mm of different percentages of fiber content were tested by using the optimal support span-to-thickness ratio of 20:1 respectively.

35.3 Results and Discussions

Table 35.1 depicts the tensile strength of untreated sisal fiber reinforced polyester composites. Figure 35.1 shows the variation of the tensile strength of raw sisal fiber reinforced polyester composites with fiber volume fractions. Here tensile strength of 2 mm and 3 mm thick specimens increases up to 20 % fiber volume fraction and afterward decreased by showing the highest tensile strength as 9.00 MPa and 11.60 MPa respectively. 4 mm and 5 mm thick specimen's displays increase in the tensile strength up to its 25 % fiber volume fraction and then decreased by showing highest tensile strength as 19.3 MPa and 20.56 MPa respectively. But, 6 mm thick specimens have demonstrated the increase in tensile strength up to its 30 % fiber volume fraction continuously by recording its highest tensile strength as 22.938 MPa.

Table 35.2 shows the flexural strength of untreated sisal fiber reinforced polyester composites. Figure 35.2 shows the variation of the flexural strength of untreated sisal-polyester composites with different fiber volume fraction. Specimens of all thicknesses i.e., 2 mm, 3 mm, 4 mm, 5 mm and 6 mm thick specimens shows their highest flexural strength of 110.934 MPa, 137.308 MPa, 144.230 MPa, 147.692 MPa and 151.538 MPa respectively at their 25 % of fiber volume fractions. We can observe that as the thickness of specimens increases, both the tensile and flexural strength of untreated sisal fiber reinforced polyester composite increases.

Table 35.1 Tensile strength of untreated sisal fiber reinforced polyester composites

SI No.	Thickness (mm)	Fvf[a] (%)	Ultimate load (kN)	Tensile strength (MPa)
1	2	10	0.095	01.890
2	2	15	0.178	03.559
3	2	20	0.450	09.000
4	2	25	0.289	05.770
5	2	30	0.127	02.540
6	3	10	0.551	07.340
7	3	15	0.640	08.533
8	3	20	0.870	11.600
9	3	25	0.690	09.200
10	3	30	0.605	08.064
11	4	10	1.263	12.635
12	4	15	1.320	13.200
13	4	20	1.420	14.200
14	4	25	1.930	19.300
15	4	30	1.519	15.194
16	5	10	1.640	13.120
17	5	15	2.070	16.560
18	5	20	2.100	16.800
19	5	25	2.570	20.560
20	5	30	2.460	19.680
21	6	10	2.527	16.844
22	6	15	2.792	18.613
23	6	20	2.910	19.400
24	6	25	3.249	21.660
25	6	30	3.441	22.938

Note: [a]Fiber volume fraction

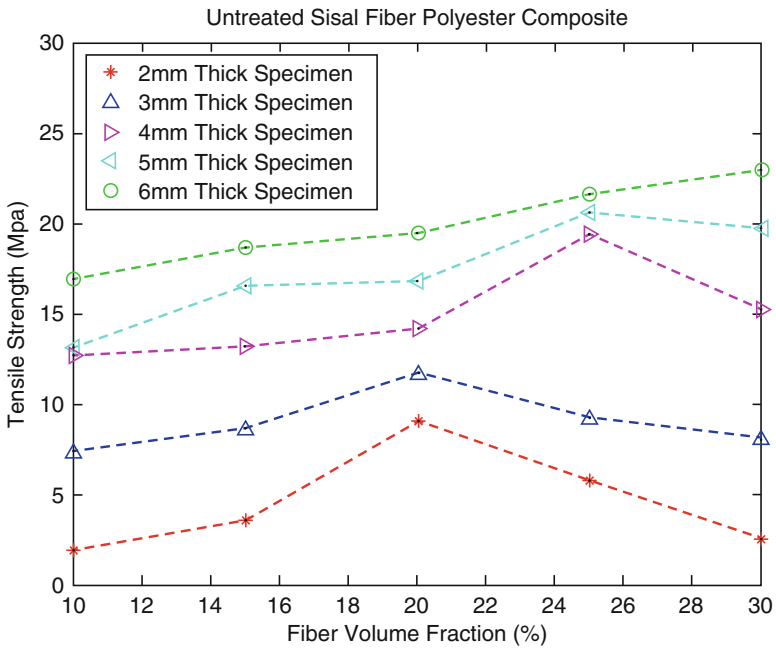

Fig. 35.1 Variation of tensile strength of untreated sisal fiber reinforced polyester composites with fiber volume fraction

Table 35.2 Flexure strength of untreated sisal fiber reinforced polyester composites

SI No.	Thickness (mm)	Fvf[a] (%)	Width (mm)	Gauge (mm)	Ultimate load (kN)	Flexure strength (MPa)
1	2	10	13	40	0.076	087.347
2	2	15	13	40	0.084	097.183
3	2	20	13	40	0.089	103.246
4	2	25	13	40	0.096	110.934
5	2	30	13	40	0.088	101.723
6	3	10	13	60	0.130	099.827
7	3	15	13	60	0.140	107.692
8	3	20	13	60	0.148	113.769
9	3	25	13	60	0.179	137.308
10	3	30	13	60	0.147	113.077
11	4	10	13	80	0.185	106.615
12	4	15	13	80	0.203	116.923
13	4	20	13	80	0.210	121.153
14	4	25	13	80	0.250	144.230
15	4	30	13	80	0.207	119.461
16	5	10	13	100	0.239	110.384
17	5	15	13	100	0.260	120.000
18	5	20	13	100	0.280	129.230
19	5	25	13	100	0.320	147.692
20	5	30	13	100	0.260	120.000
21	6	10	13	120	0.296	113.836
22	6	15	13	120	0.322	123.846
23	6	20	13	120	0.350	134.615
24	6	25	13	120	0.394	151.538
25	6	30	13	120	0.360	138.273

Note: [a]Fiber volume fraction

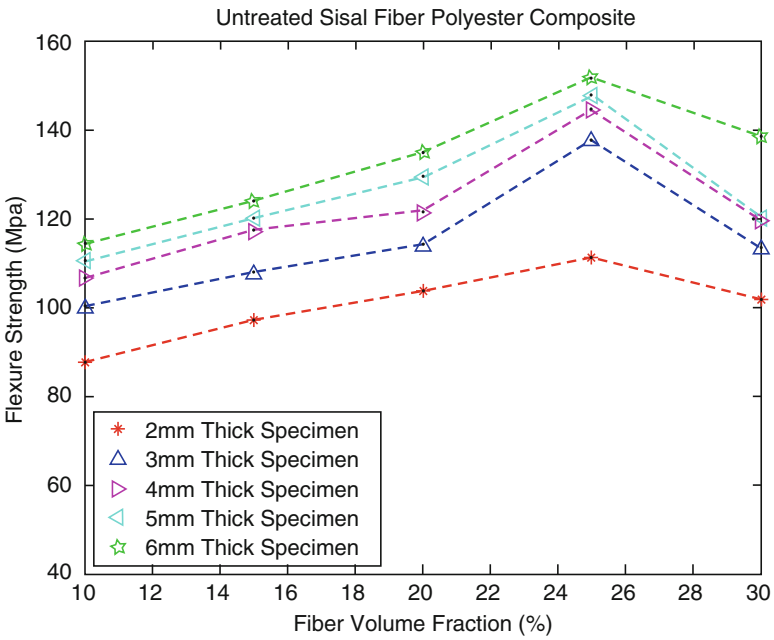

Fig. 35.2 Variation of flexure strength of untreated sisal fiber reinforced polyester composites with fiber volume fraction

35.4 Conclusion

Locally available natural fibers like sisal fibers can be used to fabricate light weight composite materials with less handling expense. The mix proportion of 50:1:1 of polyester resin, Cobalt Naphthenate, and Methyl Ethyl Ketone peroxide respectively (as matrix solution) is suitably adequate to fabricate randomly oriented sisal fiber reinforced polyester matrix composite. Figure 35.1 indicates that fiber volume fraction of 20 % to 25 % is the ideal range to get high tensile strength of untreated sisal-polyester matrix composites. Figure 35.2 shows that fiber volume fraction of 0.25 (25 %) is the optimum amount to obtain high flexure properties of untreated sisal-polyester matrix composites.

References

1. Rajesh, G., Rama Krishna, A., Reena, G., Raju, B.L.: Effect of fiber volume fraction on the tensile strength of banana fiber reinforced vinyl ester resin composites. Int. J. Adv. Eng. Sci. Technol. **4**(1), 89–91 (2011)
2. Lu, J., Zhong, J.-B., Wei, C.: Studies on the properties of sisal fiber/phenol formaldehyde resin in-situ composites. Res. J. Text. Apparel **10**(3), 51–58 (2006)
3. Ali, M.: Coconut fiber—A versatile material and its applications in engineering. In: Second International Conference on Sustainable Construction Materials and Technologies. Università Politecnica della Marche, Ancona, 28–30 June 2010
4. Zaman, I., Ismail, A.E., Awang, M.K.: Influence of fiber volume fraction on the tensile properties and dynamic characteristics of coconut fiber reinforced composite. J. Sci. Technol. **1**(1), 55–71 (2011)
5. Satiyamurthy, S., Abu Thaheer, A.S., Jayabal, S.: Prediction and optimization of mechanical properties of particles filled coir–polyester composites using ANN and RSM algorithms. Indian J. Fibre Text. Res. **38**(1), 81–86 (2013)
6. Keerthi Gowda, B.S., Easwara Prasad, G.L., Velmurugan, R., Akshay, N.K.: Comparative study of tensile strength of coir and sisal fiber reinforced composites. In: Proceedings of the Indo Russian Workshop on Tropical Problems in Solid and Applied Mechanics, Chennai, Nov 2013
7. Easwara Prasad, G.L., Keerthi Gowda, B.S., Velmurugan, R.: Prediction of properties of coir fiber reinforced composites by ANN. In: Experimental Mechanics of Composites, Hybrid and Multifunctional Materials, vol. 6, pp. 1–7. Springer, New York (2014)
8. Verma, D., Gope, P.C., Shandilya, A., Gupta, A., Maheswari, M.K.: Coir fiber reinforcement and application in polymer composites: A review. J. Mater. Environ. Sci. **4**(2), 263–276 (2013)
9. Karthik, R., Sathiyamurthy, S., Jayabal, S., Chidambaram, K.: Tribological behaviour of rice husk and egg shell hybrid particulated coir-polyester composites. J. Mech. Civil Eng., pp. 75–80 (2014). E-ISSN: 2278-1684, p-ISSN: 2320-334X
10. Xue, L., Tabil, L.G., Panigrahi, S.: Chemical treatments of natural fiber for use in natural fiber–reinforced composites: A review. J. Polym. Environ. **15**(1), 25–33 (2007)
11. Kuriakose, S., Varma, D., Vaisakh, V.G.: Mechanical behaviour of coir reinforced polyester composites—An experimental investigation. Int. J. Emerging Technol. Adv. Eng. **2**(12), 751–757 (2012)

12. Maries, I., Neelakantan, N.R., Oommen, Z., Joseph, K., Thomas, S.: A study of the mechanical properties of randomly oriented short banana and sisal hybrid fiber reinforced polyester composites. J. Appl. Polym. Sci. **96**(5), 1699–1709 (2005)
13. Girisha, C., Sanjeevamurthy, Gunti, R.S.: Sisal/coconut coir natural fibers–epoxy composites: Water absorption and mechanical properties. Int. J. Eng. Innov. Technol. **2**(3), 166–170 (2012)
14. Sen, T., Jagannatha Reddy, H.N.: Application of sisal, bamboo, coir and jute natural composites in structural upgradation. Int. J. Innovation Manage. Technol. **2**(3), 186–191 (2011)
15. Sabu, T., Varughese, K.T., John, M.J.: Green composites from natural fibers and natural rubber: Effect of fiber ratio on mechanical and swelling characteristics. J. Nat. Fibers **5**(1), 47–60 (2008)
16. Bujang, I.Z., Awang, M.K., Ismail, A.E.: Study on the dynamic characteristic of coconut fiber reinforced composites. In: Regional Conference on Engineering Mathematics, Mechanics, Manufacturing and Architecture, pp. 184–202. Noise, Vibration and Comfort Research Group, Belgium (2007)
17. Riedel, U., Nickel, J.: Applications of natural fiber composites for constructive parts in aerospace, automobiles, and other areas. Biopolymers **10**, 1–28 (2005)
18. Reem, S.M., Ansari, M., Saleh, H.M.: A study on mechanical, thermal and morphological properties of natural fibre/epoxy composite. J. Purity, Util. React. Environ. **1**(5), 237–266 (2012)
19. Joshy, M., Mathew, L., Joseph, R.: Studies on short isora fibre-reinforced polyester composites. Compos. Interfaces **13**(4–6), 377–390 (2006)
20. Chandramohan, D., Bharanichandar, J.: Studies on natural fiber particle reinforced composite material for conservation of natural resources. Adv. Appl. Sci. Res. **5**(2), 305–315 (2014)
21. Sumaila, M., Amber, I., Bawa, M.: Effect of fiber length on the physical and mechanical properties of random oriented, nonwoven short banana (Musa balbisiana) fibre/epoxy composite. Asian J. Nat. Appl. Sci. **2**(1), 39–49 (2013)
22. Sreekumar, P., Saiah, R., Saiter, J., Leblanc, N., Joseph, K., Unnikrishnan, G., Thomas, S.: Dynamic mechanical properties of sisal fiber reinforced polyester composites fabricated by resin transfer molding. Polym. Compos. **30**(6), 768–775 (2009)
23. Silva, F., Filho, R., Filho, J., Fairbairn, E.: Physical and mechanical properties of durable sisal fiber–cement composites. Construct. Build Mater. **24**(5), 777–785 (2010)
24. Naidu, V., Kumar, M., Reddy, G., Khanam, P., Reddy, M., Chakradhar, K.: Tensile & flexural properties of sisal/glass fibre reinforced hybrid composites. Int. J. Macromol. Sci. **1**(1), 19–22 (2011)
25. Ma, H., Li, Y., Luo, Y.: The effect of fiber twist on the mechanical properties of natural fiber reinforced composites. In: Proceedings of 18 th International Conference on Composite Materials. The Korean Society of Composite Materials, Jeju Island, Korea, 21–26 (2011)
26. Keerthi Gowda, B., Easwara Prasad, G., Velmurugan, R.: Prediction of tensile properties of untreated coir reinforced polyester matrix composites by ANN. Int. J. Mater. Sci. **9**(1), 33–38 (2014)
27. Gowda, B., Prasad, G., Velmurugan, R.: Probabilistic study of tensile properties of coir fiber reinforced polymer matrix composite. Int. J. Adv. Mater. Sci. **6**(1), 7–17 (2015)
28. Easwara Prasad, G.L., Keerthi Gowda, B.S., Velmurugan, R.: Prediction of flexural properties of coir polyester composites by ANN. In: Mechanics of Composite and Multi-functional Materials, vol. 7. pp. 173–180. Springer, New York (2016)
29. ASTM International: ASTM D3039/D3039M-00: Standard test method for tensile properties of polymer matrix composite materials. ASTM, West Conshohocken, www.astm.org (2006). doi:10.1520/D3039_D3039M-00R06
30. ASTM International: ASTM D7264: The standard test method for tensile properties of polymer matrix composite materials. ASTM, West Conshohocken (1995)

Chapter 36
HPHT In-Situ Strain Measurement of Polymer Composites for Oilfield Applications

Daniel Sequera, Yusheng Yuan, and John Wakefield

Abstract In recent years composite materials have been used extensively for drillable and other tools in oilfield operations because of their light weight, longer fatigue life, corrosion resistance and cost effectiveness. This requires determining their mechanical properties in such downhole conditions. Downhole tools are typically exposed to hot-wet environments above 93 °C (200 °F) and 34 MPa (5000 psi). Conventional environmental test methods conduct post-conditioning mechanical tests in dry conditions under ambient pressure, where the test condition is untrue and often giving misleading results. A previous publication presented an in-situ strain-gage measurement method using conventional resistive strain gages to determine the tensile strain and modulus of the composites in immersed hot-wet environment. However, satisfactory results were obtained only up to 93 °C (200 °F). This paper presents a new in-situ strain measurement technique, where an AC excited Wheatstone bridge with inductors is used. Thus, the sensor can operate as long as the inductors can resist the environment. Materials for the inductors were carefully selected to withstand how-wet conditions. The objective is to obtain the high-pressure-high-temperature (HPHT) in-situ tensile strain and tensile moduli of selected composite materials without discontinuing the hot-wet exposure cycle. Effect of the hydrostatic pressure on the tensile properties of the composites in hot-wet condition is presented.

Keywords Polymers • Composites • Hot-wet condition • In-situ extensometer • In-situ stress-strain • In-situ strain measurement • Hydrostatic pressure-dependent elastic modulus

36.1 Introduction

Composite materials have been used extensively for downhole application in the oil field, such as drillpipes and drillable tools, because of their lightweight, corrosion resistance, fatigue life and cost effectiveness. In these applications, tools are exposed to hot-wet conditions, typically above 93 °C (200 °F) and 34 MPa (5000 psi). Depending on the application, composite material tools are exposed to hot-wet conditions for a period of time where moisture absorption and elevated temperatures induce hygrothermal effects and deterioration on the tools, leading to performance degradation and premature failure. Under the conventional test procedure for environmental effects, material performance is evaluated by first exposing test specimens to an application fluid (i.e., brine, oil, etc.) at the desired temperature and pressure, which can be easily accomplished in pressurized autoclaves, then removing the specimen from such environment to conduct post-aging mechanical tests on a material testing system at either room temperature or elevated temperature and under ambient pressure in dry condition. This technique enables the specimens to reach exposure temperatures above the boiling temperature of the fluid. However, the moisture and pressure conditions of the test specimens under mechanical load in the conventional test procedure are not the same of those of a real application. Furthermore, the conventional test method may generate additional hygrothermal damage by thermal and pressure cycles during specimen transfer between sample conditioning and mechanical testing, by sample dry-out, and additional cracking or delamination may occur when the exposed wet specimens are tested at an elevated temperature due to dry heating. Thus, the conventional environmental-mechanical test method often provides misleading results.

Previous publications by Yuan and Goodson [1, 2] presented a high-pressure-high-temperature (HPHT) in-situ mechanical test method that has been successfully used for various mechanical tests conducted in a simulated HPHT fluid and gas environment. This in-situ test method is capable of conducting mechanical tests directly in a given fluid and gas condition under required temperature and pressure after a period of environmental exposure, which combines the specimen

D. Sequera (✉) • Y. Yuan • J. Wakefield
Baker Hughes Inc., 14990 Yorktown Plaza Dr., Houston, TX 77040, USA
e-mail: daniel.sequera@bakerhughes.com

W.C. Ralph et al. (eds.), *Mechanics of Composite and Multi-functional Materials, Volume 7*,
Conference Proceedings of the Society for Experimental Mechanics Series, DOI 10.1007/978-3-319-41766-0_36

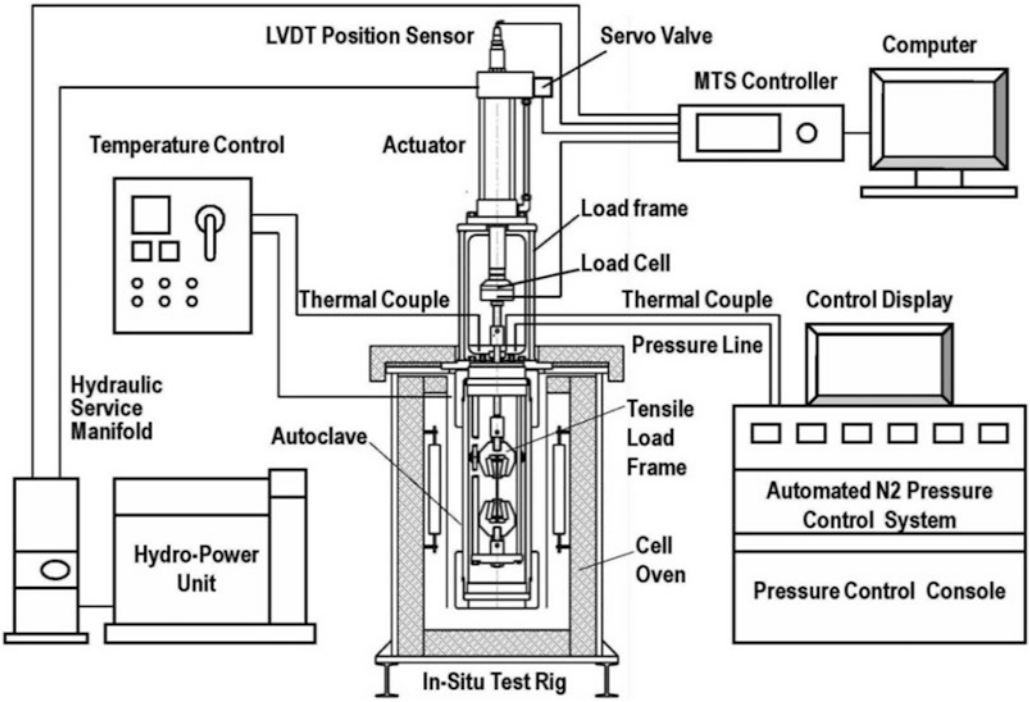

Fig. 36.1 Schematic illustration of the HPHT in-situ thermomechanical testing system with the associated hydraulic, gas pressure and control systems

conditioning and the post-conditioning mechanical testing in one procedure. This eliminates all the problems introduced by the conventional environmental-mechanical test method as mentioned above. A schematic diagram of this HPHT in-situ test system is shown in Fig. 36.1. This in-situ mechanical testing system has the capability of accommodating tensile tests per ASTM D638 test standard, among others, with the feature of being submerged in water or other fluids at elevated temperatures. This is of interest because strength and stiffness of composite materials vary with temperature and moisture content due to hygrothermal degradation [3–5]. Yet, in the above publications in-situ mechanical tests were conducted with load and displacement measurements only, and the in-situ strain measurement technique was not established.

A widely used method for strain measurement in the field of experimental stress analysis is the resistance strain gage [6]. It consists of a strain gage that changes resistance when subject to mechanical strain. However, resistance change is not practical to measure; thus, an electrical circuit is used to generate a measurable voltage output as a result of mechanical strain. This electrical circuit is called the Wheatstone bridge sensing circuit. The Wheatstone bridge is largely used in strain gage technology due to its ability to detect small changes in resistance, produce zero-output voltage when the test part is at rest, and compensate for temperature-induced resistance changes in the strain gage circuit [7]. Following, Yuan and Sequera [8] presented an in-situ tensile strain measurement method based on traditional resistive strain gage technology based on the Wheatstone bridge sensing circuit. Selected strain gages were mounted on specimens and in-situ tensile strain measurements were conducted in a submerged wet condition at an elevated temperature. A flexible water-resistant sealing material was used on one side of the specimen to seal the strain gage completely and protect it from the wet condition, yet the opposite side of the specimen, the side with no strain gage, was exposed to hot-wet conditions to allow for diffusion of fluid into the sample. It was found that the in-situ strain gage measurement technique in de-ionized water with properly selected strain gages and bonding adhesives is a valid test method for successfully measuring the in-situ tensile stress-strain curves and the elastic moduli of the polymer and composites in hot-wet condition up to 93 °C (200 °F). The strength of the backing film of the strain gage and the gage-to-specimen bonding strength in hot-wet environment were the major limits to the in-situ strain measurement technique presented in that study.

This study introduces an HPHT in-situ extensometer used in combination with the HPHT in-situ thermomechanical test system to enable the technique of in-situ strain measurements in hot-wet environment under a high pressure and high temperature, simulating conditions found in oilfield applications. Then, this study presents performance of such technique at typical oilfield HTHP conditions. The objective is to obtain the in-situ tensile stress-strain curves and determine the elastic moduli of a selected laminated composite material in a water-based fluid condition at elevated temperature under a high pressure.

36.2 Experimental

The HPHT in-situ strain measurements were conducted in the in-house developed HPHT in-situ thermomechanical testing and analysis system, as illustrated in Fig. 36.1. The HPHT in-situ thermomechanical testing and analysis system consists of an HPHT autoclave, a controlled cell oven, a hydraulic driving system, a mechanical test load frame, a high-pressure gas source and a nitrogen pressure control system. The autoclave can accommodate the in-situ tensile load frame and the environmental medium under high temperature and high pressure. The system can accommodate standard tensile tests per ASTM D638. All components exposed to the test environment are made of high-strength, corrosion-resistant alloys. The hydraulic driving system includes an actuator, a servo valve, a service manifold and a hydraulic power unit. The load frame connects the hydraulic actuator and the loading train that includes a load cell and a loading rod that passes through a high-temperature, low-friction reciprocating seal in the top plug of the autoclave. The hydraulic driving system and the mechanical test frame are controlled by a full-functional MTS controller for operation and data acquisition. The nitrogen pressure control system can control the autoclave pressure accurately to within 34 KPa (5 psi). The in-situ test system is rated to a 50 KN (11.2 kip) loading capacity in fluid and gas environment up to 260 °C (500 °F) and 69 MPa (10,000 psi). Figure 36.2 shows a photograph of the entire in-situ test rig with its controller and hydraulic pump, and more detailed information on the HPHT in-situ thermomechanical testing and analysis system can be found in author's earlier publications [8, 9].

The in-situ test system was used in combination with the HPHT in-situ extensometer, as illustrated in Fig. 36.3, purchased from Psylotech, Inc. with certain improvements and modifications for the HPHT in-situ strain measurement application. The HPHT in-situ extensometer is an AC excited Wheatstone bridge with inductors replacing traditional resistive strain gages constructed with high-strength, corrosion-resistant alloys to withstand the corrosive hot-wet testing conditions. In this design configuration, as long as the resin sealed inductors can withstand the hot-wet environment, the sensor can operate. The HPHT in-situ extensometer consists of two sets of self-gripping pairs, one pair for measuring transverse strain (top on Fig. 36.3a, b), and another pair for measuring axial strain (bottom on Fig. 36.3a, b). Each pair of grips has 30° knife edges and loading springs for efficient gripping onto the test specimens. Material tested in this study is an E-glass fabric reinforced epoxy composite laminate, commonly used in oilfield applications. The test specimens were cut from the laminate panel in principal fiber direction to 178 mm (7 in.) long, 19.1 mm (0.75 in.) wide and 3.2 mm (0.125 in.) thick as straight-side tensile specimens per ASTM D3039. Figure 36.3c shows a test specimen mounted in the in-situ tensile grips and load frame with the in-situ extensometer installed, ready to be submerged into the high-pressure autoclave for the in-situ testing.

Fig. 36.2 Overall view of a HPHT in-situ test rig with the control system and hydraulic power unit

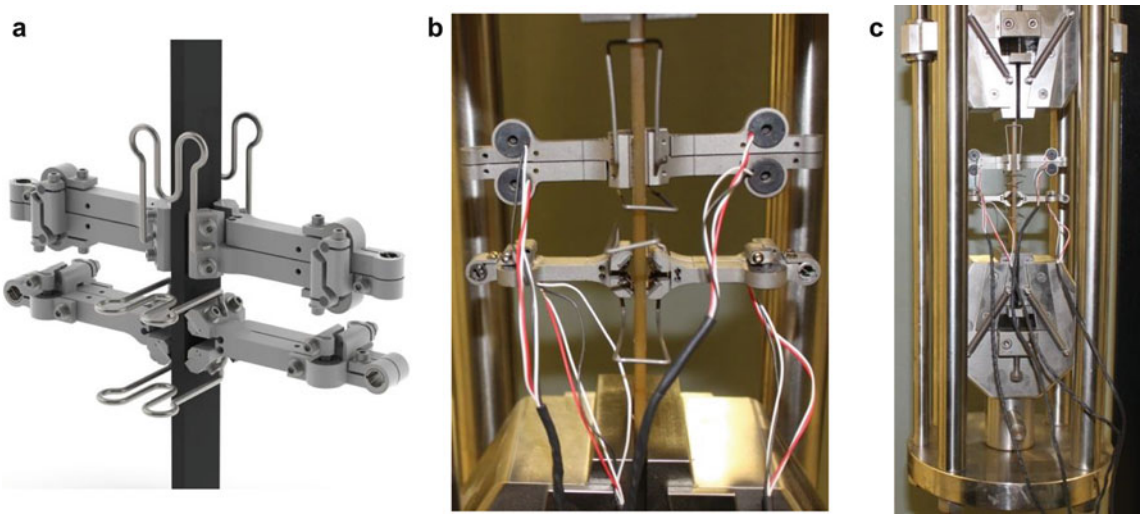

Fig. 36.3 In-situ HPHT extensometer (**a**) stock image, (**b**, **c**) mounted on the HPHT in-situ mechanical test system

36.3 Results and Discussion

Validation Experiments: Validation experiments of the HPHT in-situ extensometer were conducted on a MTS material testing system at 21 °C (room temperature) and at 149 °C (300 °F) in dry condition, and the measured results were compared with those obtained by using a calibrated conventional MTS extensometer on the same MTS system. Straight-side tensile specimens, 178 mm (7 in.) long, 19.1 mm (0.75 in.) wide by 3.2 mm (0.125 in.) thick, per ASTM D3039 were used to conduct the validation experiments. First Ply Failure (FPF) criteria was used to determine the maximum tensile stress to ensure the laminated E-glass/epoxy tensile specimen remained undamaged within the elastic region, so that the specimens could be used repeatedly in the loading and unloading runs. Thus, at each test temperature one specimen was loaded to a maximum tensile load of 35.6 KN (8000 lb-f) and the stress-strain data were obtained using the conventional MTS extensometer, then the specimen was unloaded and the extensometer was replaced with the HPHT in-situ extensometer. Specimen was loaded again to the same maximum load and stress-strain data obtained. This procedure was repeated twice for each test temperature and it allows for direct comparison between the results obtained with the two extensometers. Test specimens were loaded and unloaded in displacement-control mode at the same rate of 1.3 mm/min (0.05 in./min) per ASTM D3039. Figure 36.4 shows the stress-strain curves obtained using both conventional and in-situ extensometers and Table 36.1 shows a summary of the calculated moduli by the two extensometers at 21 °C and 149 °C, respectively. The test results show an excellent match of the elastic moduli measured by the two extensometers at each test temperature: elastic moduli calculated from the stress-strain curves obtained with either extensometer match to within 3.5 % or less. This result was consistently obtained among the repeated tests. Thus, data obtained with the in-situ extensometer was considered validated.

In-situ Experiments: In-situ tensile experiments were conducted and the in-situ strain data obtained with the validated (in dry condition) in-situ extensometer to determine the in-situ elastic moduli of composite laminate specimens in a HPHT hot-wet fluid-gas environment. Deionized water was used as the fluid environment and an automatically-controlled pressure system was used to maintain constant pressure to within 34 KPa (5 psi) during the tensile test at a controlled constant test temperature. Similar to the validation experiments, straight-side specimens 178 mm (7 in.) long, 19.1 mm (0.75 in.) wide by 3.2 mm (0.125 in.) thick were used and loaded up to a maximum of 35.6 KN (8000 lb-f) to avoid FPF and remain within the elastic region of the material without causing damage during the loading and unloading. Tensile loading and unloading was displacement-controlled at a rate of 1.27 mm/min (0.05 in./min). Baseline tests were conducted in dry condition at room temperature and ambient pressure using the in-situ extensometer in the in-situ test system. Experiments were conducted at 21 °C (room temperature) and 149 °C (300 °F) in wet condition under 1.7 MPa (250 psi), 34.5 MPa (5000 psi) and 68.9 MPa (10,000 psi), respectively. Figure 36.5 shows the in-situ stress-strain curves at different temperature and pressure conditions. Calculation of the elastic moduli were based on the stress-strain curves in the stress level between 20 MPa and 58, which is a better representative for linear elastic deformation of the test material as this remains under the elastic region of the stress-strain curve. The results indicate three major findings: (1) the in-situ extensometer is capable of measuring the true strain in a HPHT hot-wet environment successfully up to 149 °C (300 °F) and 68.9 MPa (10,000 psi). This enables new testing capabilities for material characterization for oilfield downhole applications. (2) Immersing the specimen in a

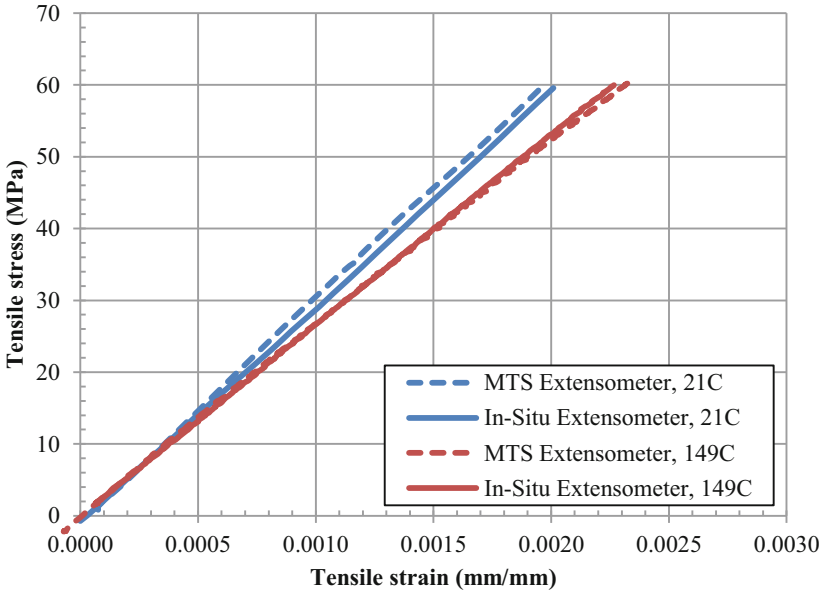

Fig. 36.4 Stress-strain of E-glass/epoxy in dry condition at different temperatures using MTS and in-situ extensometers

Table 36.1 Summary of results of preliminary experiments

Extensometer	Temperature, °C (°F)	Elastic modulus, GPa (Msi)	Variation (%)
MTS	21 (70)	31.1 (4.5)	–
In-situ	21 (70)	30.0 (4.3)	−3.5
MTS	149 (300)	25.9 (3.7)	–
In-situ	149 (300)	26.5 (3.8)	+2.3

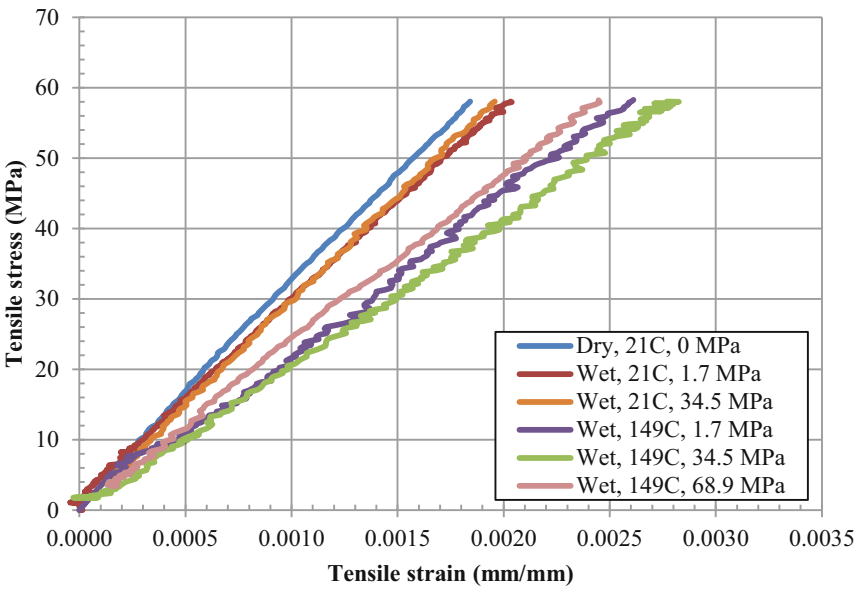

Fig. 36.5 In-situ stress-strain of E-glass/epoxy at different temperatures and pressures

high-temperature wet condition results in a significant decrease on the elastic modulus compared to that measured in dry condition at room temperature and ambient pressure. This is due to the moisture effects from the water immersion. Although stiffness of the composite laminate in tension (elastic modulus) is fiber-dominated, moisture absorption by the matrix introduces degrading mechanisms on mechanical properties, such as epoxy resin glass transition temperature (T_g) drop, collection of water at the fiber/resin interface that affect bonding. These mechanisms in turn prevent efficient load transfer. This is well known in the literature, yet careful consideration must be taken. Specimens tested were only exposed to hot-wet condition for approximately 3 h prior to conducting a test at elevated temperature and pressure, nonetheless this result

Table 36.2 Summary of results of in-situ experiments

Condition	Temperature, °C (°F)	Pressure, MPa (psi)	Elastic modulus, GPa (Msi)
Dry	21 (70)	0 (ambient)	30.1 (4.4)
Wet	21 (70)	1.7 (250)	27.7 (4.0)
Wet	21 (70)	34.5 (5000)	29.6 (4.3)
Wet	149 (300)	1.7 (250)	23.4 (3.4)
Wet	149 (300)	34.5 (5000)	21.4 (3.1)
Wet	149 (300)	68.9 (10,000)	23.3 (3.3)

indicates that the in-situ tensile tests conducted using the in-situ extensometer eliminate drying effects and steam pressure delamination introduced in conventional environmental test methods, thus this technique helps gain an accurate understanding of the effect of moisture absorption on mechanical properties of composite laminates. (3) It was observed that the hydrostatic pressure has no major effect on elastic modulus of the current laminated composite in the current tested pressure range. This observation is consistent with that observation in a previous publication by Yuan and Sequera [9]. In that study, HPHT in-situ dynamic mechanical analysis (DMA) test results were presented and it was found that pressure had a significant impact on T_g of the materials tested, yet the storage modulus, which is representative of the elastic modulus, remained unchanged under a high hydrostatic pressure. Table 36.2 shows a summary of such results. Although conventional material testing techniques have revealed the effect of temperature and hot-wet condition on composite materials, an extensometer capable of collecting data in true HPHT hot-wet conditions, thus obtaining true material performance in such conditions, has never been demonstrated.

36.4 Conclusions

An innovative, inductor-based HPHT in-situ extensometer was used and validated successfully in the in-house developed, industry-first HPHT in-situ thermomechanical testing and analysis system and the HPHT in-situ strain measurement technique and the test procedure by using a HPHT in-situ extensometer were established for the first time. This HPHT in-situ extensometer is capable of collecting axial and transverse strain data in a specified fluid and gas condition at elevated temperature under a constant autoclave pressure, and the HPHT in-situ validation tests were conducted up to 149 °C (300 °F) and 68.9 MPa (10,000 psi). Higher temperature capability is potentially feasible and will be validated further. In-situ stress-strain curves of an E-glass fabric-reinforced epoxy laminate were determined by the HPHT in-situ extensometer in de-ionized water up to 149 °C (300 °F) and 68.9 MPa (10,000 psi) autoclave pressure. Although the test specimens were exposed in the water for only a short time during the test setup and preheating, hot-wet degradation in elastic modulus of the E-glass/epoxy laminate was observed in this validation study with the use of new HPHT in-situ extensometer. No major effect of the hydrostatic pressure on elastic modulus of the material was observed under the applied hydrostatic pressure range.

Acknowledgments The authors would like to thank Baker Hughes Completions and Wellbore Intervention Technology for their permission to publish this paper. The authors would like to express sincere appreciation to Dr. Partha Ganguly, Director Research & Technology for his full support, and to Charley Tompkins, Testing & Automation Engineer at CTI Test Lab, for his work in creating the nitrogen pressure control system. Thanks also due to Shawn Young for his assistance in conducting HPHT in-situ tests.

References

1. Yuan, Y., Goodson, J.: HT/HP hot-wet thermomechanical properties and HT/HP in-situ mechanical test method of high-temperature polymer composites. In: Proceedings of the 52nd International SAMPE Symposium and Exhibition, Baltimore, 3–7 June 2007
2. Yuan, Y., Goodson, J.: HTHP in-situ mechanical test rig and test method for high-temperature polymers and composites. In: SPE 113516, in proceedings of the 2008 SPE Europec/EAGE Annual Conference and Exhibition, Rome, 9–12 June 2008
3. Ruffner, D.R.: Hygrothermal behavior. In: ASM handbook. Composites, vol. 21, pp. 246–251. ASM International, Materials Park (2001)
4. Browning, C.E.: The mechanisms of elevated temperature property losses in high performance structural epoxy resin matrix materials after exposure to high humidity environments. Ph.D. dissertation, University of Dayton, Dayton (1976)

5. Yuan, Y., Goodson, J.: HP/HT hot-wet thermomechanical behavior of fiber-reinforced high-temperature polymer composites (Chapter 16). In: Tandon, G.P., et al. (eds.) Experimental Mechanics of Composite, Hybrid, and Multifunctional Materials. Conference Proceedings of the Society for Experimental Mechanics Series, vol. 6. Springer, New York (2014)
6. ASM International: ASM handbook. In: Nondestructive Evaluation and Quality Control, vol. 17. ASM International, Materials Park (1989)
7. Cheatle, K.: Fundamentals of test measurement instrumentation. Instrumentation, Systems and Automation Society, Research Triangle Park (2006)
8. Yuan, Y., Sequera, D.: In-situ strain gage measurement technique development in hot-wet conditions. In: Proceedings of 2013 SAMPE Conference and Exhibition, Long Beach, 6–9 May 2013
9. Yuan, Y., Sequera, D.: Pressurized in-situ dynamic mechanical thermal analysis method for oilfield polymers and composites. In: Mechanics of Composite and Multi-Functional Materials. Proceedings of the 2015 SEM Annual Conference on Experimental and Applied Mechanics, vol. 7. Springer, New York (2015)

Chapter 37
Evaluation of Viscoelastic Characteristics of Polymer by Using Indentation Method

Kenichi Sakaue

Abstract Five-step indentation test is used to evaluate viscoelastic characteristic of acrylonitrile butadiene styrene resin, ABS resin. Five-step indentation test consists of two indentation cycles and the creep compliance is evaluated from the second indentation cycle, because the measured penetration depth in second cycle is unaffected by plastic deformation. The creep compliance is evaluated by the indentation theory for an axisymmetric conical indenter and elastic-viscoelastic correspondence principle. Furthermore, in order to evaluate the creep compliance, FEM is used to analyze the indentation problem, in which the conical indenter is impressed on an impression. The results show that creep compliance evaluated by FEM are comparable to that by tensile test. This result means that the creep compliance of polymer can be evaluated by 5-step indentation test.

Keywords Indentation test • Viscoelasticity • Polymer • Creep compliance • Finite element method

37.1 Introduction

Indentation test can evaluate mechanical characteristics from local surface of materials. Therefore, indentation test is useful for testing of sample pieces and inspection of products, even if making standard specimens from these samples and products is difficult. The method to evaluate elastic and plastic characteristics has been established [1]. However, the method to evaluate viscoelastic characteristics is not fully established. The most important problem with respect to evaluation of viscoelasticity is to separate viscoelastic deformation and plastic deformation.

In order to evaluate viscoelasticity by the indentation test, a theoretical equation by Sneddon [2] and elastic-viscoelastic correspondence principle [3] is widely used [4, 5]. Sneddon derived the solution for an indentation problem in which an axisymmetric conical indenter is impressed on elastic half-space. Also, elastic-viscoelastic correspondence principle gives the viscoelastic solution from Sneddon's solution. Therefore, if the theoretical equation is applied to indentation test results, the dominant deformation during the indentation test should be viscoelasticity. However, actual polymer material shows viscoelastic and plastic deformation. Thus, it is necessary to separate viscoelastic deformation and plastic deformation from the measured deformation by the indentation test.

One of the methods to separate these deformations is proposed by Sakaue et al. [6, 7]. They used atomic force microscope to measure the depth of an impression after indentation test. The plastic deformation is obtained as the depth of impression, and the viscoelastic deformation is evaluated by subtracting the plastic deformation from the measured indentation depth. However, it is required the method without measuring the depth of the impression, because their method needs additional measurement equipment.

Another method to separate these deformations is 5-step indentation test, in which two-repeated indentation tests are carried out on the same position of a specimen. It can be thought that plastic deformation does not occur in the second indentation cycle, thus, only viscoelastic is measured in the second cycle. This method was used to evaluate viscoelasticity, and the study indicated that the indentation modulus evaluated by 5-step indentation is higher than that by common indentation test [8]. This result is thought to be valid, because evaluated modulus becomes lower value if estimated elastic or viscoelastic deformation includes plastic deformation. However, test surface for the second indentation cycle has an impression and is not flat surface, thus, it is necessary validation for applicability of Sneddon's solution.

In the present study, 5-step indentation test is applied to evaluate creep compliance at high temperature. The plastic deformation is estimated from the indentation force and penetration depth curve, F-h curves. Furthermore, in order to

K. Sakaue (✉)
Department of Mechanical Engineering, Shibaura Institute of Technology, 3-7-5 Toyosu, Koto-ku, Tokyo 135-8548, Japan
e-mail: sakaue@sic.shibaura-it.ac.jp

W.C. Ralph et al. (eds.), *Mechanics of Composite and Multi-functional Materials, Volume 7*,
Conference Proceedings of the Society for Experimental Mechanics Series, DOI 10.1007/978-3-319-41766-0_37

evaluation the precise value of the creep compliance, the indentation problem is analyzed by FEM. As the results, evaluated creep compliance by general method based on Sneddon's solution and precise method by FEM are compared with the value obtained by tensile test.

37.2 Indentation Test

In the present study, a triangular pyramidal indenter, Berkovich indenter, is used. The pyramidal indenter is usually modeled as an axisymmetric conical indenter, which has the same relationship between projected area of contact and indentation depth as the pyramidal indenter. When this rigid conical indenter with a cone angle α is impressed onto an elastic-half space, the relation between indentation force F and penetration depth h is expressed as [2]:

$$h^2 = \frac{\pi(1-\nu^2)}{2\tan\alpha}\frac{F}{E} \tag{37.1}$$

where E and v are Young's modulus and Poisson's ratio of the elastic-half space, respectively. If the rigid conical indenter is impressed onto a viscoelastic-half space, the relation in Eq. (37.1) and elastic-viscoelastic correspondence principle give the following equation:

$$h^2(t) = \frac{\pi(1-\nu^2)}{2\tan\alpha}\int_0^t J(t-\tau)\frac{dF(\tau)}{d\tau}d\tau \tag{37.2}$$

where $J(t)$ is creep compliance of viscoelastic-half space. When the indentation force $F(t)$ is assumed to be a step load $F(t) = F_0H(t)$, where F_0 is the maximum indentation force in loading and holding steps and $H(t)$ is a Heaviside unit step function, the creep compliance is given by:

$$J(t) = \frac{2\tan\alpha}{\pi(1-\nu^2)F_0}h^2(t). \tag{37.3}$$

Equations (37.2) and (37.3) postulate that the deformation of the half-space is perfectly viscoelastic behavior, because the basic relation in Eq. (37.1) is elastic. However, the behavior of actual polymer materials includes viscoelastic deformation and plastic deformation. Therefore, in order to apply Eqs. (37.2) and (37.3) to evaluate creep compliance, it is necessary to separate viscoelastic and plastic deformation from measured indentation depth.

In the present study, 5-step indentation test is used to separate viscoelastic and plastic deformation. Five-step indentation test is divided into two indentation cycles. The first cycle consists of loading-unloading, and the viscoelastic and plastic deformation are dominant. Then, the second indentation cycle, reloading-holding-unloading, is carried out on the impression, which is the same position of the first indentation cycle. The deformation in the second cycle is though to be only viscoelasticity. Therefore, creep compliance can be evaluated from time variation of the penetration depth in holding part of the second cycle by Eq. (37.3).

Accurate evaluation of creep compliance from time variation of the penetration depth in second indentation cycle requires modifying Eq. (37.3). Equation (37.3) assumes that the indentation test is carried out on the flat surface. On the other hand, the second indentation cycle in 5-step indentation test is performed on the impression by the first cycle. In the present study, the indentation test on an impression is analyzed by FEM. The detail of FEM is described in later section.

The experimental condition for the indentation test is as follow. Specimen material used in the study is acrylonitrile butadiene styrene resin, ABS resin. Indentation testing machine is Shimadzu Dynamic Ultra Micro Hardness Tester, DUH-W201, with high-temperature unit. A Berkovich indenter, which coincides with an axisymmetric conical indenter with a cone angle α of 70.3°, is used. The maximum indentation force in the first and second indentation cycle is 100 mN. The loading and unloading rate are 13.2 mN/s. The interval time between the first and second indentation cycle is 300 s. The holding time in the first and second cycle are 5 s and 500 s, respectively. Test temperature is 40 °C and 60 °C and is measured on the specimen surface with thermocouple devices.

37.3 Results and Evaluation of Creep Compliance

Figure 37.1 shows the measured indentation force and penetration depth curves, *F*-*h* curves, at 40 °C and 60 °C. Each figure indicates *F*-*h* curves obtained from the first and second indentation cycle. Because the used indentation testing machine can not detect the depth of impression, the initial penetration depth of the second cycle is set to zero. As shown in Fig. 37.1, the penetration depth in the first cycle is larger than that in the second cycle. Also, creep behavior can be observed during holding step in the first cycle even if the holding time is enough short. Therefore, the dominant deformation in the first cycle is viscoelastic and plastic.

Assuming plastic deformation does not occur in the second cycle, the end of the reloading curve in the second cycle should be the same penetration depth as the end of the loading curve in the first cycle. According to this viewpoint, it is possible to shift the *F*-*h* curve of the second cycle to coincide the ends of the loading and reloading curves. Figure 37.1 also shows the shifted *F*-*h* curve in the second cycle. As shown in Fig. 37.1, the shifted *F*-*h* curves at 40 and 60 °C starts from about 2.3 μm-penetration depth. Therefore, the depth of impression by the first indentation cycle is thought to be 2.3 μm.

As mentioned in the previous section, Eq. (37.3) assumes that the indentation test is carried out on the flat surface. However, the second indentation cycle in 5-step indentation test is performed on the impression by the first cycle. Therefore, in order to evaluate viscoelastic characteristics, the precise analysis for the indentation test on an impression is needed. In the present study, FEM is used to analyze the problem. Figure 37.2 shows the finite element model used in this study. An axisymmetric model is used, and the indenter and the specimen are a rigid element and a four-node elastic element, because

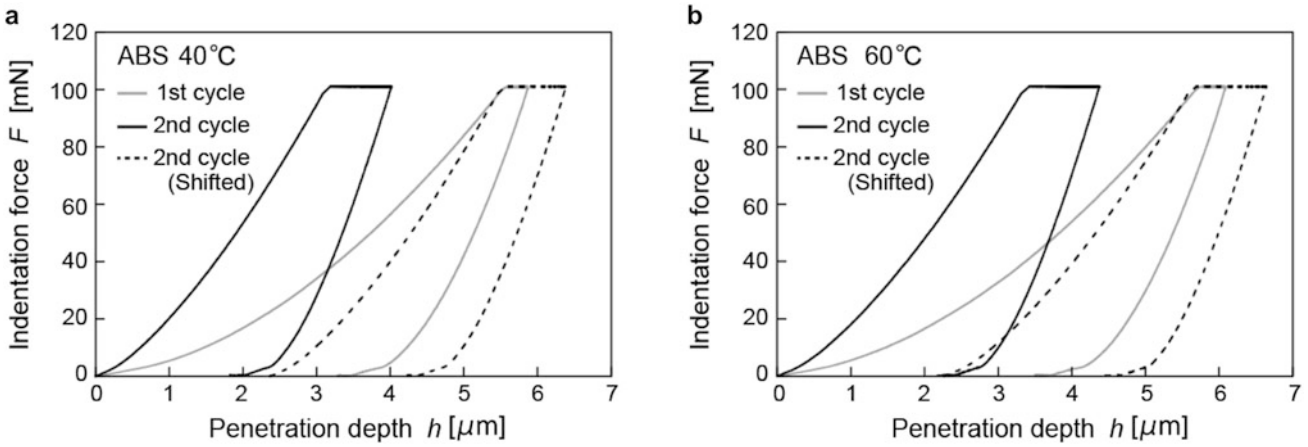

Fig. 37.1 *F*-*h* curves measured by 5-step indentation test for ABS resin. (**a**) At 40 °C, (**b**) at 60 °C

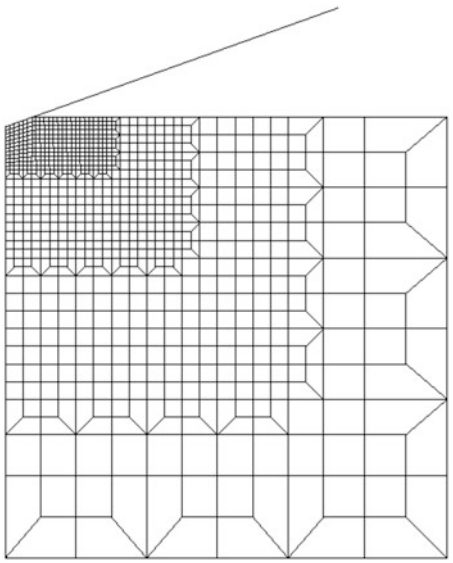

Fig. 37.2 Finite element model for indentation on impression

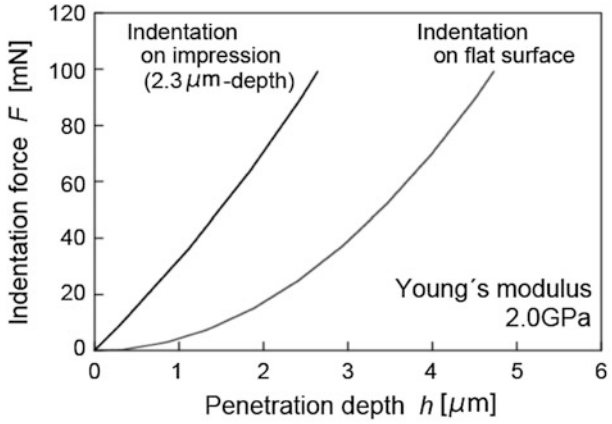

Fig. 37.3 Results of indentation force and penetration depth relation evaluated by FEM

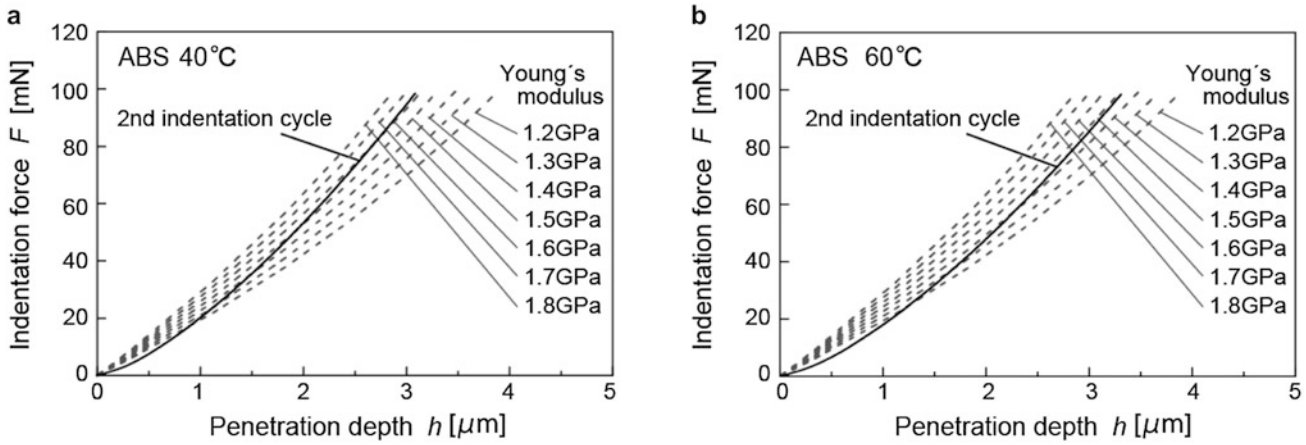

Fig. 37.4 *F-h* curves obtained by second indentation cycle and evaluated by FEM with various Young's modulus

the elastic-viscoelastic correspondence principle can be applied. The angle of the axisymmetric conical indenter is 70.3°. The height and width of the specimen are 100 μm and 100 μm, respectively. The specimen has an impression with a depth of 2.3 μm, which is estimated by 5-step indentation test. The shape of the impression is the same as the conical indenter. In the present study, the indentation on flat elastic surface is also analyzed.

Figure 37.3 indicates the numerical results of *F-h* curves in loading part for the indentation on the impression and flat surface. The results are obtained under the condition: the maximum indentation force is 100 mN, Young's modulus of the specimen is 2000 MPa, Poisson's ration is 0.35. As the results, the indentation on the impression shows higher indentation modulus than the indentation on flat surface, because the contact area for the indentation on the impression is larger than the indentation on flat surface. Therefore, Fig. 37.3 means that 5-step indentation test needs precise analysis with regard to the shape of the impression.

Figure 37.4 shows the *F-h* curves in loading part for the indentation on the impression with various Young's modulus. Figure 37.4a, b also indicate the *F-h* curves of reloading part obtained by the second cycle of 5-step indentation test at 40 °C and 60 °C, respectively. The results show that the maximum penetration depth at 40 °C coincides with the *F-h* curves for Young's modulus of 1.6 GPa. Also, the maximum depth at 60 °C is almost the same as the *F-h* curves for 1.5 GPa. Therefore, the initial creep compliance in holding part at 40 °C and 60 °C are assumed to be 0.625 GPa^{-1} and 0.667 GPa^{-1} as inverse of Young's modulus, respectively. However, the both curve obtained by the second indentation cycle are not perfectly coincide with the *F-h* curves calculated by FEM. This result is thought to be caused by the shape of the impression. The shape of an impression on polymer is different from the shape of the indenter [7], and the angle α becomes lager then that of the indenter.

Figure 37.5 is creep compliances of ABS resin at 40 °C and 60 °C, that are evaluated by tensile test and 5-step indentation test. The creep compliance by tensile test is evaluated as inverse of uniaxial relaxation modulus by stress relaxation test. The values evaluated by second indentation cycle are obtained from the measured penetration depth and Eq. (37.3), which involves an indentation problem on flat surface. Also, dashed lines indicate the values evaluated by FEM as shown in Fig. 37.4. Figure 37.5 means that the values by Eq. (37.3) are smaller than that by stress relaxation test. This result is caused

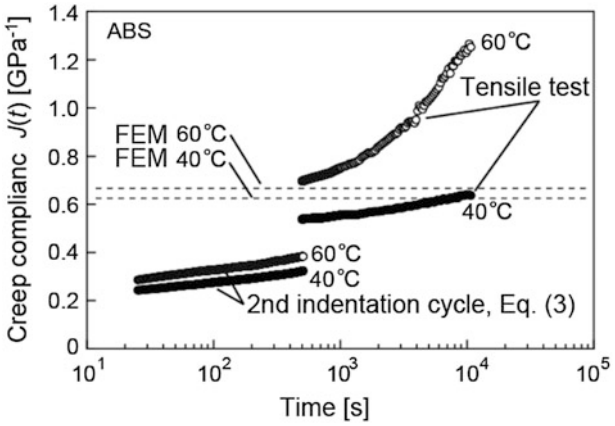

Fig. 37.5 Creep compliance evaluated by 5-step indentation test

by the fact that the indentation modulus on impression becomes higher than that on flat surface as shown in Fig. 37.3. On the other hand, the values evaluated by FEM are comparable to that by stress relaxation test. Therefore, considering the shape of impression, creep compliance of polymer can be evaluated by 5-step indentation test. Also, this result means that 5-step indentation can separate viscoelastic deformation and plastic deformation by shifting the *F*-*h* curve of the second indentation cycle. However, in order to evaluate more precise creep compliance, the effect of shape of the impression is required as mentioned above. Furthermore, the value evaluated by FEM could not account time-dependent characteristics. Therefore, it is necessary theoretical or empirical time-dependent equation with regard to the actual shape of the impression through various analyses by FEM.

37.4 Conclusions

In the present study, 5-step indentation test is applied to evaluate creep compliance of ABS resin. In order to evaluation the precise value of the creep compliance, the problem of the second cycle of 5-step indentation test is analyzed by FEM, in which an axisymmetric indenter impresses on an impression with certain depth. The results show that the values of the creep compliance evaluated by the equation for a indentation problem on flat surface are smaller than that evaluated by stress relaxation test. On the other hand, the values evaluated by FEM are comparable to that by stress relaxation test. Therefore, considering the shape of impression, creep compliance of polymer can be evaluated by 5-step indentation test.

Acknowledgments We thank T. Hoshino and K. Kato, graduate students in Shibaura Institute of Technology, for support of this study.

References

1. Fischer-Cripps, A.C.: Nanoindentation, 2nd edn. Springer, New York (2004)
2. Sneddon, I.N.: The relation between load and penetration in the axisymmetric Boussinesq problem for a punch of arbitrary profile. Int. J. Eng. Sci. **3**, 47–57 (1965)
3. Christensen, R.M.: Theory of viscoelasticity, 2nd edn. Dover, New York (2003)
4. Lu, H., Wang, B., Ma, J., Huang, G., Viswanathan, H.: Measurement of creep compliance of solid polymers by nanoindentation. Mech. Time-Depend. Mater. **7**(3), 189–207 (2003)
5. Huang, G., Wang, B., Lu, H.: Measurements of viscoelastic functions of polymers in the frequency-domain using nanoindentation. Mech. Time-Depend. Mater. **8**(4), 345–364 (2004)
6. Sakaue, K., Okazaki, S., Ogawa, T.: Indentation technique for evaluation of master curve of creep compliance. Exp. Tech. **35**(5), 16–22 (2011)
7. Sakaue, K., Isawa, T., Ogawa, T., Yoshimoto, T.: Evaluation of viscoelastic characteristics of short-fiber reinforced composite by indentation method. Exp. Mech. **52**(8), 1003–1008 (2012)
8. Stan, F., Fetecau, C.: Characterization of viscoelastic properties of molybdenum disulphide filled polyamide by indentation. Mech. Time-Depend. Mater. **17**, 205–221 (2013)